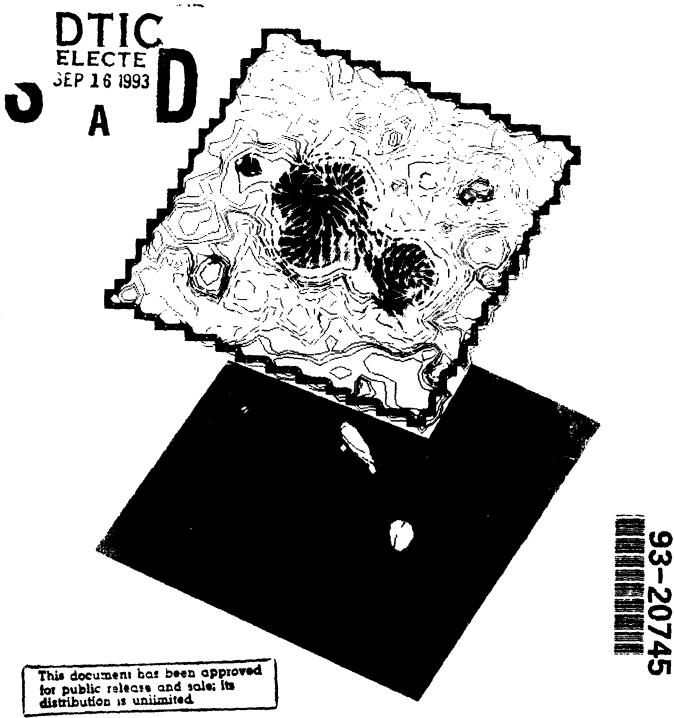
# Solar Polarimetry



Proceedings of the Eleventh National Solar Observatory/Sacramento Peak Summer Workshop



NSO/SP Summer Workshop Series No. 11

# Solar Polarimetry

Proceedings of the Eleventh National Solar Observatory / Sacramento Peak Summer Workshop, Sunspot, New Mexico 27-31 August 1990

Sponsored by:

The National Solar Observatory

The National Science Foundation

The National Aeronautics and Space Administration

The US Air Force
The Department of the Navy
The High Altitude Observatory

DITIC QUALITY INSPECTED 1.

Edited by: Laurence J. November Accesion For

NTIS CRAMI V
DITE AND
Use AND Confidence from

By
Distribution /

Availability Cones

Distribution /
Special

A-1

National Solar Observatory / Sacramento Peak Sunspot, New Mexico 88349, USA January 1991

#### Preface

One of the most beautiful astronomical spectacles is the filamentary structure that is apparent on the solar disk in  $H\alpha$ . Both amateurs and professionals can appreciate the unusual form of the fine fibril ropes which connect magnetic features on the solar surface. The form is indicative of magnetic fields. While one of the most important elements in solar dynamics, electromagnetic fields are still one of the most elusive, as their observational manifestations are subtle.

Though electromagnetic fields are mostly invisible, the interactions of fields with matter produce certain subtle observable manifestations. The magnetic fine structure in  $H\alpha$  indicates the added magnetic pressure in the gas, but this effect alone is unable to define uniquely the magnetic field parameters. Most agree that the basic physical processes of spectral line formation hold the best possibilities for making a precise determination of the electromagnetic field parameters. Section 4 of this volume contains contributions devoted to the general problem of physical interpretation.

Due to the inherent anisotropy of the electromagnetic processes, its optical manifestations contain polarization information in addition to spectral information. Precise polarimetry has been difficult in astronomical observations because the polarization transformation properties of instruments can be quite large and difficult to calibrate out in general. Instruments can be specifically designed to provide good polarization characteristics or measured so they give a known effect. With the advent of improved instrumentation and detector technology, a number of efforts are underway around the world to try to provide a precise polarization measurement. Section 1 of this volume has contributions on the technical problem: facilities (Section 1.1) and techniques (Section 1.2).

Presently there exit a number of intriguing measurements of fine structure and field morphology, observations of flare processes, and coronal investigations. The cover shows figures from Canfield et al. "Currents and Flares in a Highly Nonpotential Active Region" (page 296). The upper figure shows the derived longitudinal field strength (contours) and the transverse field strength and direction (vectors) superposed on a map of intensity showing the sunspots in the region. The data were obtained in 6302.5Å with the Haleakala Stokes Polarimeter. The lower figure shows the derived vertical current density (grey scale) with the vertical magnetic field (contours). The superposed temporal image difference in the  $H\alpha$  blue wing indicates the bright flare kernel on the magnetic neutral line nearer the larger spot in the lower image. Detailed observations of flare fields and currents is only one of the possibilities of precise polarimetric observations. Section 2 discusses observations, solar fine structure (Section 2.1), flares (Section 2.2), coronal measurements (Section 2.3), and solar/stellar polarimetry (Section 2.4).

Some of the difficulties with spectrally resolved magnetic field measurements can be avoided by making observations in infrared spectral lines. With the increased relative magnetic splitting in the infrared measurements, the true field strength and some information on the distribution of strengths within an observing element can be ascertained. The problems of instrumental polarization and atmospheric seeing are also reduced in the infrared, but only now with the advent of improved detection hardware are infrared observations becoming routine. Section 3 contains several contributions on the state of the art in infrared solar instrumentation and observations. The infrared holds the promise for some of the most elusive problems in solar polarimetry.

Existing observations are usually limited by their instrumental polarimetric precision and the accuracy of the physical interpretation. Though the basic theory of line formation in an electromagnetic field is classical, practical bridges are needed to provide useful observational tools. Spectral, spatial, and temporal resolution limit what is possible so observations must be designed with practical theoretical considerations to provide the most physical information. Section 4 presents

contributions on physical interpretation methodology, practical considerations (Section 4.1), general theoretical considerations (Section 4.2), and flux-tube models (Section 4.3).

I would like to thank the participants and contributors who have made a most interesting and successful workshop by their attentiveness and discussion. The proceedings contain much original material that I think will represent a valuable timely reference to those studying and working in this changing field. On behalf of the participants I would like to thank the National Solar Observatory for hosting the meeting and thank the NSO support staff who under the direction of Romona Elrod provided smooth logistics support and a friendly and courteous attention to our needs. Many individuals contributed to the success of the workshop, it is impossible for me to recognize them all. The members of the organizing committee were: Serge Koutchiny, David Rust, Andy Skumanich, Raymond Smartt, Jan Stenflo, and myself. Funds in support of the workshop and proceedings were provided by The National Aeronautics and Space Administration through Joseph Gurman of the Ultraviolet Spectrometer and Polarimeter (UVSP) experiment. The European Office of the Air Force Office of Scientific Research through Owen Cote provided support for travel. The Department of the Navy in their Office of Naval Research Asian Office through Sachio Yamamoto also provided support for our far east participants. Also, The High Altitude Observatory provided funds.

Laurence J. November National Solar Observatory Sunspot, NM 88349, USA

# Table of Contents

Forward
Preface
Section 1 Instrumentation and Technique (chair J.O. Stenflo)
Section 1.1 Facilities:
Preliminary Results from the HAO/NSO Advanced Stokes Polarimeter Prototype Observing Run
B.W. Lites, D. Elmore, G. Murphy, A. Skumanich, S. Tomczyk, and R.B. Dunn
Ultraviolet Polarimetry with the UVSP
Progress on the Analysis of BBSO Vector Magnetograms
Recent Results from the San Fernando Observatory Video Spectra-Spectroheliograph $\dots$ 37 $G.A.Chapman$ and $S.R.$ Walton
The Potsdam Vector Magnetograph: Methodical Experiences and Results
Solar Instruments for Magnetic and Velocity Measurements in IZMIRAN
Solar Vector Magnetic Field Measurements
Vector Magnetography
A Brief Introduction to the Multichannel Solar Magnetic Field Telescope
Section 1.2 Techniques:
Two-Dimensional Polarimeter with CCD Image Sensors and Piezo-Elastic Modulators 102 II.P. Povel, C.U. Keller, and J.O. Stenflo
2D Real Time Polarimetric Spectrograph with 64-Channel
High Spatial Resolution Polarimetry using Filtergrams

Progress Toward an Advanced Imaging Vector Magnetograph
Systematic Errors in Polarimeter Calibration due to Imperfect Calibration Optics 142 S. Tomczyk, P. Stoltz, and P. Seagraves
Using the Zeeman Spectral-Polarization Symmetry for Telescope Calibration $\dots \dots 149$ L.J. November
Fringes in Polarizing Optical Elements
Sensitivity to Polarization: How Can We Measure Weak Vector Magnetic Fields at High Angular Resolution?
Using KD*P Modulators to Measure the Stokes Vector on the Sun
Performance of the IAC Stokes I and V Analyzer
Polarization of the Domeless Solar Telescope of the Hida Observatory (Preliminary Report) 198 M. Makita, Y. Funakoshi, and Y. Hanaoka
Section 2 Polarimetric Observations (chair: S. Keil)
Section 2.1 Solar Fine Structure
Stokes Profile Analysis of a Sunspot Using the MSFC Magnetograph
Spectropolarimetry of Active Regions
High Spatial Resolution Observations of Magnetic Flux Elements
High Resolution Spectropolarimetry of an Active Region
Small Scale Magnetic Field Mapping with High Temporal Resolution
High Spatial Resolution V Stokes Polarimetry to Measure the Zeeman Effect in Flux Tubes and Prominence Filament Threads

Visualization of Intergranular Magnetic Fields
On the Complexity and Reactivity of Magnetic Features in Solar Active Regions $\dots 276$ J. Linke
The Character of Velocity Field Distribution in the Quiescent Filament Region 280 B.A. Ioshpa, I.E. Kogevatov, and E.H. Kulikova
Section 2.2 Flares
Observation and Interpretation of $H\alpha$ Polarization in Solar Flares
Currents and Flares in a Highly Nonpotential Active Region
Velocity Gradients Across a Flaring Neutral Line from Stokes II Measurements 307 A. Skumanich and B. Lites
Section 2.3 Coronal Measurements
Properties of the White-Light Corona Polarization during Maximum of the Solar Cycle 318 $J\'ulius S\'ykora$
Interpretation of Polarization Measurements of Coronal Fe XIII (10747Å) Emission 326 R.N. Smartt and C.W. Querfeld
Section 2.4 Solar/Stellar Polarimetry
Broadband Linear Polarization: the Sun and the F-G-K Stars
Section 3 Polarimetry in the IR (chair: J.B. Zirker)
Polarimetry in the IR
Sampling V-Stokes on the Solar Disk with FeI 15648Å and H Paschen $\beta$
Plage Magnetic Field Strengths from Near-Infrared Spectra

Section 4 Physical Interpretation (chair: A. Skumanich)
Section 4.1 Practical Considerations
Direct Inference of the Field Vector from Stokes Profiles
The Derivation of Vector Magnetic Fields from Stokes Profiles: Derivative versus Least Squares Fitting Techniques
Inversion of Stokes V Profiles
Measurement of Polarization-Dependent Stark Broadening as a Diagnostic of Electric Fields in the Solar Atmosphere
Polarimetric Studies of Solar Magneto-Sensitive Spectral Lines
Section 4.2 General Theoretical Considerations
Unified Classical Theory of Line Formation in a Magnetic Field
Diagnostic of the Magnetic Field Vector using the Atomic Density Matrix Formalism 434 V. Bommier, E. Landi Degl'Innocenti, and S. Sahal-Brechot
Non-LTE Formation Heights of Stokes Profiles of Fel Lines
Multiple-Line Stokes Profile Inversion
Section 4.3 Flux Tube Models
Center-to-Limb Variation of the Stokes V Asymmetry in Solar Magnetic Flux Tubes 468 M. Bünte, O. Steiner, and S.K. Solanki
Stokes Profile Formation Heights in Solar Magnetic Flux Tubes
Flux Tube Diagnostics Based on the Stokes V Profiles of Infrared H-Band Lines 489 K. Muglach, and S.K. Solanki
THEMIS Un Télescope pour Comprendre le Magnétisme Solaire
Group Picture
List of Participants
NSO/SP Summer Workshop Series

# Section 1 Instrumentation and Technique Chair: J. Stenflo

# PRELIMINARY RESULTS FROM THE HAO/NSO ADVANCED STOKES POLARIMETER PROTOTYPE OBSERVING RUN

B. W. LITES, D. ELMORE, G. MURPHY, A. SKUMANICH, S. TOMCZYK

High Altitude Observatory
National Center for Atmospheric Rese. .ch\*
P.O. Box 3000
Boulder, Colorado U.S.A

R. B. DUNN
National Solar Observatory†
Sunspot, New Mexico

#### **ABSTRACT**

A prototype version of the Advanced Stokes Polarimeter was operated at the Sunspot Vacuum Tower Telescope of the National Solar Observatory in May and June, 1990. Although the prototype instrument does not have the capability of the final instrument to be deployed in 1991, it nonetheless provided high spatial resolution Stokes profile observations of a small, symmetric sunspot. Analysis of these observations shows that the magnetic field at the outer edge of the penumbra of this sunspot is highly inclined with respect to the local normal ( $\gamma = 70-80^{\circ}$ ), in agreement with previous Stokes II measurements of larger sunspots. In addition, the axial field and flux distribution was found to be nearly identical to that of the previous Stokes II measurement.

#### I. INTRODUCTION

The scientific objectives of the Advanced Stokes Polarimeter (ASP) have been described elsewhere (Lites 1986; Lites and Skumanich 1989) so they will not be discussed extensively here. The broad objectives of this program are to expand our knowledge of MHD processes in and above active regions through high resolution, quantitative (within a few percent) measures of the vector magnetic field and, where possible, the thermodynamic properties of the magnetized plasma. Ranking high among the specific goals of the program are efforts to understand the structure of sunspots, and the observations reported herein present us with a partial but much higher-resolution picture of the variation of the magnetic field with distance from the center of a small sunspot.

The target science of the ASP and the constraints that the analysis of spectro-polarimetric measurements observed through the earth's atmosphere impose upon the observations have led to the following characteristics of ASP data (Lites and Skumanich 1989):

- Resolved, simultaneous wavelength coverage of Stokes profiles
- Strictly simultaneous measurements in two members of a multiplet
- Simultaneous measurement of B in the photosphere and chromosphere
- Angular resolution of 1" or better
- Ability to scan an active region of about  $100 \times 100 \text{ arcsec}^2$  in 10 minutes
- Polarization accuracy of about 10<sup>-3</sup> relative to the continuum

<sup>\*</sup>The National Center for Atmospheric Research is sponsored by the National Science Foundation. †Operated by the Association for Research in Astronomy, Inc., under contract with the National Science Foundation.

Given these constraints, the ASP design evolved to a scanned spectrographic system, but with the capability to simultaneously carry out narrow-band filter polarimetry as well. The design considerations are discussed in considerable detail in the ASP Design Review document (Fisher 1989).

In this paper we describe the specific goals of the ASP prototype polarimeter observing run and how the prototype instrument differs from the final instrument (Section II), the calibration and reduction of the data from these observations (Section III), and the analysis of the first high resolution Stokes profiles of a small sunspot (Section IV). In Section V we summarize the results of the prototype observing run and we indicate the major hurdles that must be overcome before the ASP is fully operational.

#### II. THE ASP PROTOTYPE INSTRUMENT

The ASP is a very complex instrument being developed jointly by two institutions. The System Block diagram given in Lites and Skumanich (1989) indicates the institution responsible for development of the various components of the system. In general, HAO is developing the polarimeter and data acquisition system, and NSO is providing the telescope and integrating the polarimeter into their Adaptive Optics complex. The participants felt strongly that a preliminary test of the entire system would be essential to a timely implementation of the full instrument in 1991. The objectives of the prototype observing run carried out in May-June 1990 were to:

- Verify the end-to-end design of the system
- Evaluate the actual performance of the calibration procedure
- Constrain the specifications of the final optical elements
- Evaluate the effects of fringing in the optical elements
- Produce sample data for software development, and
- Obtain scientifically useful observations

The prototype instrument differs from that described in the Design Review in a number of significant aspects. In the following, we describe these differences and how they compromise the data from the prototype instrument.

#### a) Single Camera, Single-Beam Polarimeter

Even though the ASP camera system operates at twice video rates (60hz), seeing-induced image motion can introduce unacceptably high levels of crosstalk among the Stokes parameters in a single-beam demodulation scheme (Lites 1987). The final ASP will employ a dual-beam demodulation scheme, which is designed to reduce the seeing-induced crosstalk by about a factor of four. Simultaneous detection of both states of modulated linear polarization will increase the signal/noise ratio (S/N) of the measurement as well. The disadvantage of the dual-beam scheme will be the necessity to carefully align the images from the two detectors before subtraction, and the final shifts will be taken out in post- observation processing.

The observations with the prototype instrument demonstrate that image motion does cause significant  $I \to Q, U, V$  crosstalk as evidenced by polarization "streaks" in wavelength within the spectral-spatial images of Q, U, V (see Figure 1) when the solar image is not stabilized with an active mirror. When the image is stabilized during periods of good seeing, the "streaks" are largely suppressed and the residual contributon due to polarization errors is larger than the streaking. Compensation for these and other errors are described in Section III below.

### b) Preliminary Optics

The mock-up of the ASP optical system used in the prototype polarimeter contained many optical elements which differ from those that will be used in the final instrument (see Fisher 1989, Figure 3-2A). The bandpass limiting filter, located just after the exit port of the Tower Telescope, was neither wedged nor made from a low-expansion substrate. Early in the observing run it was discovered that this element produced interference fringes in the spectra, so the filter was not used for the remainder of the run. The lack of a bandpass limiting filter caused a larger heat load on subsequent elements, in particular the calibration linear polarizer and retarder, and the rotating waveplate modulator of the polarimeter.

The calibration linear polarizer and retarder were PVA polarizers sandwiched between BK7 glass substrates. Each was broadband antireflection coated. The calibration linear polarizer demonstrated a small amount of stray retardance, which was shown to be dependent both upon temperature and position within the field of view. This element will be replaced in the final instrument with a polarizer sandwiched between fused silica substrates chosen for good uniformity of both the stray retardance and transmission. The calibration retarder and the waveplate modulator were both deemed suitable for the final instrument. However, the calibration retarder was positioned too close to the prime focus of the telescope and, as a result, dust on the retarder produced a 1–2% modulation of the intensity when the element was rotated into the beam. This element will be placed farther from the focus in the final instrument.

The mirror used in the image motion compensation system (hereafter IMC), degrades the image somewhat. This problem will be corrected in the final instrument. The relay lenses for the NSO/Sunspot adaptive optics system and the collimator lens for the spectrograph are those that will be in the final instrument, but they were uncoated for this run. A single polarizing beam-splitter was used in the prototype instrument, whereas the final instrument will use a compound polarizing beamsplitter and a mirror. The spectrograph grating and the camera lens from the prototype will probably be used in the final instrument. We expect some gain in system efficiency in the final instrument after coating the optics and improving the reflecting surfaces.

# c) The CCD Cameras

A major portion of the instrumentation effort for ASP centers on the CCD cameras. The cameras must not only produce 12-bit digital signals with a 60 Hz readout rate, but photon statistics must dominate read noise and the readout must be carried out in precise synchronism with the phase of the rotating modulator, which in turn is locked to the phase of the line voltage in order to stabilize any electromagnetic interference in the video signals. Two versions of the CCD camera were used during the prototype run: the evaluation camera and the prototype camera 'A'. Both versions are based upon Texas Instruments TC243 research grade CCD chips: frame store devices with three (RGB) color channels.

In the laboratory the evaluation camera assured us that the objectives for the ASP detector could be met. A read noise of about 80 e<sup>-</sup> was achieved with this camera operating at room temperature and at a 60 Hz readout rate. Readout of the chip at this rate at a depth of 12 bits requires that special electronics be fabricated to perform the A/D conversion separately for each of the three color channels, that the signals be recombined, and that the images be reduced in size before they may be processed. At the time of the observing run the "receiver board" that performs these functions was not finished, so that only the standard Datacube hardware was available to accept the digital signals from the camera. This arrangement required that only one

B. W. Lites et al.

of the three color channels be processed; hence the sampling of 3.9 pm per pixel in the spectral dimension is only 1/3 that of the final instrument.

Camera 'A' is the first version of the CCD camera to be placed on a single printed circuit board. This board includes the electronics for digitizing and processing all three color channels. This camera became available only during the observing run, and it was used to obtain the observations presented here. Camera 'A' showed some nonstationary electronic noise which will be described below, but this was found to be smaller in the polarization images than was the case for the nonstationary noise of the evaluation camera. Like the evaluation camera, camera 'A' was operated in only one of its three color channels.

# d) Scanning and Image Motion Compensation

The data presented here was obtained with active IMC, but the use of IMC precluded scanning of the Sun normal to the slit. In the final instrument, scanning of the image will be accomplished at the spectrograph, so this limitation will be avoided.

#### III. CALIBRATION

The calibration of the ASP polarimeter in conjunction with the NSO Vacuum Tower Telescope is a non-trivial task and, as will be shown below, our ability to compensate for the polarizing effects of the full instrument system falls somewhat short of our desired level of precision in polarization. The main challenge regarding the polarization calibration arises from the fact that we cannot yet introduce light of a variety of known states of polarization into the optical system, with the exception of introducing nearly unpolarized light in the continuum of the solar spectrum.

We can extract much of the needed information regarding the response of the polarimeter itself using measurements with our polarization calibration optics sampled at many of the possible combinations of orientations. This procedure appears to give us a good representation of both the polarimeter response and the imperfections in the calibration optics (refer Tomczyk, Stoltz, and Seagraves 1991; Murphy and Skumanich 1991).

The present observations represent the first attempt at calibration of the entire ASP system. Much of the observing time was devoted to the acquisition of calibration data. We measured the out-of-focus quiet Sun image with combinations of orientations of the calibration polarizers, as described above, through several hours as the pointing of the Tower Telescope changed. From these measurements we identified several shortcomings of the calibration optics (described in II.b. above) which will be corrected in the final instrument. We also carried out these calibrations during one half-day with repeated rotations of a large polarizer mounted in front of the entrance window. These data were used to evaluate the Muller matrix of the Tower telescope using the analysis summarized by Elmore (1988).

Calibration of the data described below proceeded in several steps, as outlined in the following:

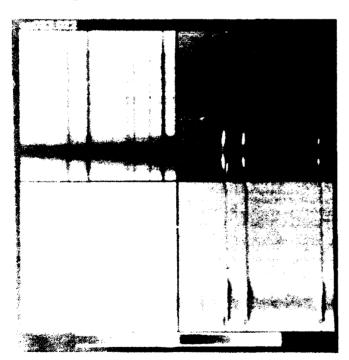
# a) The Fixed-Pattern Gain Correction (Flat-Fielding)

Certain features of the CCD image are stationary, reproducible, and independent of wavelength. By removing the entrance slit of the spectrograph, the spectral lines and any spectral

fringes are smeared out, so that one may obtain a first-order "flat-field" for correction of the pixel-by-pixel response of the CCD. The left panel of images in Figure 1 shows the Stokes spectra after flat-fielding, i.e., after correction for the fixed-pattern gain variations. Note the asymmetry present in the Q and U profiles of the Fe I lines. This asymmetry arises from the polarizing effects of the telescope and polarimeter optics.

### b) First-Order Polarization Calibration

Elmore (1990) describes the iterative method used here to derive a calibration matrix for the polarimeter. The method assumes ideal polarization calibration optics, and it yields values for the "response matrix" of the polarimeter, the retardance and transmission of the calibration retarder, the transmission of the calibration linear polarizer, the calibration Stokes vector exiting the telescope, and the "bias" offsets (i.e., the dark levels). When this procedure is applied to the entire spectral-spatial field shown in Figure 1 we note that the variation of the parameters resulting from this calibration is smooth and small across the field, except in the vicinity of spectral lines. The effects at the spectral lines appear to result from a wavelength instability in the spectrograph. Although this instability is not rapid enough to be problematic in the single-beam prototype polarimeter, rapid differential distortions in the dual-beam device of the final instrument might be of concern. The final spectrograph will be enlosed to minimize differential seeing effects between the two beams. We have adopted a single value for the response matrix derived from its average over a continuum window near the middle of the image: to the blue of the strong Fe I lines at 630.1 and 630.2 nm.



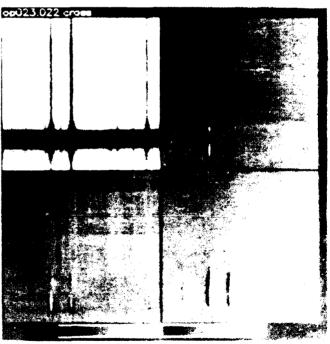


Fig. 1. Stokes split spectra of a small sunspot are shown as gray-scale images. Each of the two panels contains the four Stokes parameters, respectively, clockwise from the upper left, I, Q, V, U. A spectral region of about 0.76 nm containing the strong Fe I lines at 630.15 and 630.25 nm, slightly to the left of center, is shown. Wavelength increases to the left, and the sampling interval is 3.9 pm/pixel. The spatial extent shown along the slit is 75 $^{\circ}$ , with a pixel sampling of 0.4 $^{\circ}$ . The leftmost panel shows the instrumental Stokes images corrected only for the fixed-pattern gain. Note the asymmetry in the Q and U profiles. The panel on the right shows the physical Stokes images after calibration. Note the reversal in the polarity of the line-of-sight field at the bottom of the Stokes V image. As displayed here, the bottom of the slit corresponds to the top of the images in Figure 2; that is, North is at the bottom here.

B. W. Lites et al.

#### c) Removal of Spectral Skew

Even though the startal lines were carefully aligned with respect to the pixel columns of the CCD, the dispersion is not precisely aligned with the pixel rows. This indicates a slight misalignment of the spectrograph slit with respect to the rulings of the grating. This problem resulted in a skew of the spectrum, which was removed by linear interpolation. In the interpolated image the pixel rows accurately contain the sunspot spectra.

# d) Correction for Residual $I \rightarrow Q, U, V$ Crosstalk

After calibration we note a small residual polarization is present at continuum wavelengths in the Q, U, V images, and that this polarization varies along the slit (see Figure 1, left image). For each pixel row we derive a value for the residual crosstalk  $I \rightarrow Q, U, V$  from the continuum wavelength just to the red of the Fe I 630.2 nm line, and we use it to correct the entire pixel row using the observed intensity at each spectral location. The resulting corrected Stokes images are shown in the rightmost image of Figure 1. When compared with the uncalibrated images on the left, the Q and U profiles for the strong Fe I lines are now quite symmetric, and the V profiles are antisymmetric, as expected. Note that the physical V is reversed in sign from the instrumental V.

# e) Compensation for Residual $V \rightarrow U$ Crosstalk

At locations within the sunspot spectrum where V is large and U is small we note a significant asymmetry in the U Stokes profile. This occurs just above the dark umbral streak in Figure 1. The source of this error is not known at the present time, but the crosstalk from circular to linear polarization for the combined telescope-polarimeter system is difficult to measure without introducing a measurable and known amount of circular polarization into the system. We apply an ad hoc antisymmetric correction matrix in which the (3,4) and (4,3) matrix elements have an absolute value of 0.1. This correction, when applied to the Stokes images, has the effect of making the Stokes U profiles much more symmetric while not changing substantially the Stokes V profiles.

#### IV. ANALYSIS OF SUNSPOT MAGNETIC FIELD STRUCTURE

#### a) Analysis of the Data

The data analyzed here (Figure 1) is a single Stokes frame from a series of 100 observations made of a small sunspot shown in the slit-jaw images of Figure 2. These slit-jaw images were digitized from an analog videotape recording made during the observations. At several slices across the sunspot, 100-frame sequences of images were recorded with active IMC. We analyzed only those individual frames within each of these sequences having the highest rms fluctuation of the intensity in a continuum window along the slit. Thus, the frames shown here are those with the best seeing during each sequence.

We use the nonlinear least-squares inversion code described in several previous papers (Skumanich and Lites 1987; Lites et al. 1988; Lites and Skumanich 1990) to extract values of the magnetic field strength and orientation, and the Doppler shift of the lines. The inversion was performed on both the Fe I 630.15 and 630.25 nm lines simultaneously. The method for the multi-line inversion has been described by Lites et al. (1988), and it has been applied to inversion of Stokes I spectra of sunspots (Lites et al. 1990). The inversion incorporates a number of other techniques: nearest neighbor initialization whereby the solution of the inversion for the adjacent spectrum is used as an initial guess for the iteration, compensation for the spectral resolution of

the observations (the instrument function is assumed to be of Gaussian shape with the theoretical FWHM of 3.5 pm), and correction for a "scattered light" component.

The scattered light correction (Skumanich and Lites 1987) admits the possibility that the Stokes I profiles are contaminated with light from the surrounding nonmagnetic (and unpolarized atmosphere. The mean scattered light profile  $I^{scatt}(\lambda)$  is the average of about 10 spectra away from the sunspot having net polarization averaged over the fitted portion of the line profiles less than 0.006  $I_c$ , where  $I_c$  is intensity in the continuum. The least-squares procedure seeks an optimum fraction  $\alpha$  of  $I^{scatt}(\lambda)$  added to the observed Stokes I profile, and it also treats the wavelength shift of  $I^{scatt}(\lambda)$  as a least-squares parameter.

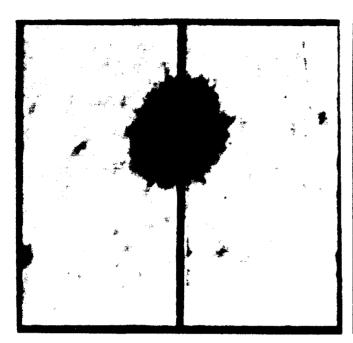




Fig. 2. Slit-jaw images are shown for the current observations. The sunspot was observed at a solar latitude of  $25^{\circ}$  N,  $16^{\circ}$  E at 16h20m UT on 1990 June 4 (heliocentric angle  $\mu = cos^{-1}(\theta) = 0.87$ ). The images shown were digitized from the analog video record of the slit-jaw monitor camera. The quality of these images is degraded by a strong video interference pattern that was present in this analog video signal at the time of observation. Granulation is nonetheless visible in the images, and fixes the scale. The sunspot is roughly 18" in diameter. The field of view in these images is smaller than that of the spectra in Figure 1. These images do not coincide precisely in time to the selected frames analyzed, but the image quality is representative of the spectral measurements, although these images represent a much shorter exposure than that of the Stokes spectra. The slit is parallel to the solar N-S direction, with solar north at the top. The left and right images correspond to Image 1 and Image 2, respectively, in Figures 4 and 5.

#### b) Scattered Light/Image Degradation in the Polarimeter

Results of the inversion of the Stokes spectrum through the center of the sunspot are shown in Figure 3. Here the continuum intensity  $I_c$  at the center of the umbra (at the slit position of about 11.5") is about 26% of the average intensity outside of the sunspot. The corrected continuum intensity inferred for the magnetized component of the profile  $I_c^{mag} = I_c^{obs} - \alpha I_c^{scatt}$ , where  $I_c^{obs}$  is the observed continuum intensity and  $I_c^{scatt}$  is the scattered light profile, only drops to 23% within the umbra. This points to a concern regarding the angular resolution and scattered light in the prototype instrument: the intensities of the sunspot umbra are apparently too large by a factor of two or more. Adjabshirzadeh and Koutchmy (1983) measured umbral intensities of about 10% in a slightly larger sunspot observed with the Vacuum Tower Telescope at Sac Peak.

10 B. W. Lites et 21

It is unlikely therefore that the large amount of scattering (or image degradation) comes from the Tower Telescope itself. It must reside in the polarimeter. Inasmuch as the scattered light correction deduced by the inversion does not remove most of the contamination of the umbral intensity, it is possible that the image is degraded by the spectrograph. In any case, the principal contamination of umbral spectra may arise from the polarized light of the surrounding penumbra.

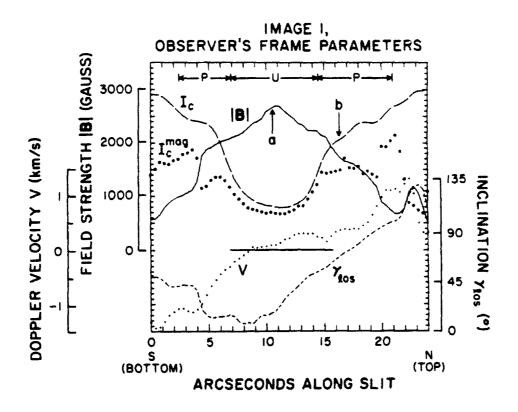


Fig. 3. Results of the inversion of a Stokes spectrum through the center of the sunspot (slit-jaw image on the left in Figure 2) are shown. Only a limited spatial region around the sunspot was processed, and the absissa gives the angular position in arcseconds. The top (north) and bottom (south) directions refer to the slit-jaw images of Figure 2. Near the top of the graph the approximate regions of penumbra and umbra are indicated by P and U, respectively. The long-dashed line indicates the variation of the continuum intensity  $I_c$  along the slit in arbitrary units, with the horizontal line indicating the zero level of intensity. The inferred magnetic field strength |B| is given as a solid line, the field inclination with respect to the line-of-sight  $\gamma_{los}$  is given as a short-dashed line, and the small dots indicate the variation of the Doppler velocity V relative to the frame average. The large dots indicate the corrected continuum intensity  $I_c^{mag}$  as inferred from the determination of the scattered light (see text.)

Another concern about the spectrograph arises from the observed depth of the line profiles. The central intensities of our observed average quiet Sun Fe I profiles are considerably brighter than expected. This also suggests the presence of either significant scattering in the spectrograph or an infrared leak, although the amount of scattering in the spectrograph required to produce the observed line center intensities cannot account for the high umbral intensities. The rather smooth variation of the continuum intensity along the slit suggests that degradation of the image may also play a role. These issues will be investigated thoroughly for the final instrument.

# c) The Inferred Variation of the Vector Magnetic Field

The inferred field strength |B| reaches a maximum of about 2700 G near the center of the umbra (Figure 3). The line-of-sight inclination  $\gamma_{los}$  varies smoothly on the northward side of the sunspot. A reversal in the polarity of the line-of-sight field is seen just outside of the north edge of the spot. Both |B| and  $\gamma$  increase there, and we suspect that this is a signature of a "moving magnetic element." The location of minimum inclination of the field occurs about 3" S toward disk center from the maximum in |B|, or the minimum in intensity. This is to be expected for a sunspot at nearly 30° from disk center. The Evershed motion is prominent in the penumbral areas, and it reaches  $\pm 1.5$  km/sec in the outer regions of the penumbra.

Observed profiles and their least-squares fits are shown in Figures 4 and 5 for the spatial positions a and b indicated in Figures 3 and 6. From the Q and U profiles of Figure 4 we estimate the random noise level to be of the order of  $\pm 0.005 I_c^{(umbra)}$ . Systematic effects are still present in the profiles, probably resulting from remaining errors in the calibration and a slowly varying electronic pattern noise that is visible in the Stokes Q, U, V images at the level of  $1-3\times 10^{-3}I_c$ . The fits to the profiles are satisfactory, but it should be noted that no satisfactory simultaneous fit to the Stokes I profiles of both lines could be obtained without invoking the scattered light correction for the inversion. It should also be noted that the ad hoc recalibration for  $U \leftrightarrow V$  crosstalk improves the symmetry of the observed

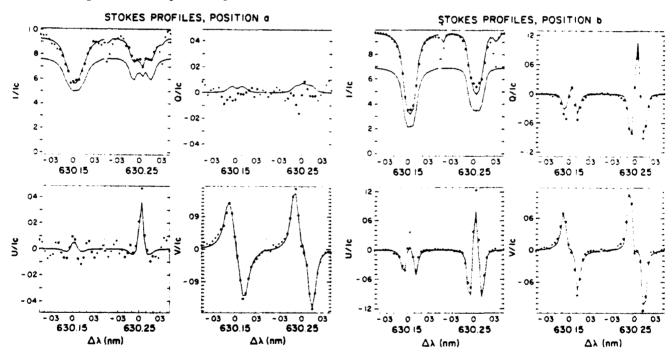


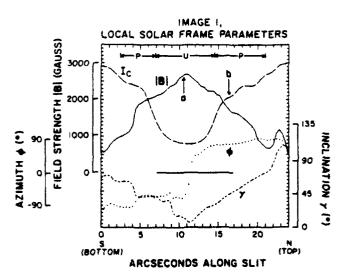
Fig. 4. Individual observed Stokes profiles for a spatial position near the center of the umbra are shown (dots): see location 'a' in Figures 3 and 6. The large dots represent wavelength positions used in the least-squares fit. The solid curves are the theoretical profiles fit to the observations. The lower Stokes I curve shows the intensity of the theoretical profile for the magnetized component of the fit only; i.e., it is the upper solid curve minus the scattered light.

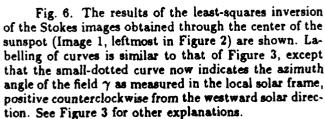
Fig. 5. Same as Figure 4, except the profiles represent location 'b' in the penumbra of the sunspot.

U Stokes profiles. However, comparison of inversion of these data both with and without the ad hoc recalibration shows that, for these specific sunspot observations, the suspected  $V \leftrightarrow U$  crosstalk causes only insignificant errors in the inferred vector magnetic field. The random noise in the observations is equally insignificant for determination of the vector field. We demonstrate this through a comparison of the results of the inversion of two sequential frames of Stokes observations.

It is fairly easy in the case of a sunspot to resolve the 180° ambiguity in the field azimuth  $\phi$ . The wrong choice leads to physically unreasonable vector magnetic fields when the field is transformed to the local solar frame where the X-Y plane is tangent to the solar surface at the location of the sunspot. Results for the selected azimuths are shown in the local frame in Figures 6 and 7 for, respectively, the slit positions in the left and right images of Figure 2. The results are quite reasonable from the standpoint of a symmetric sunspot:

- The azimuth  $\phi$  passes through zero at the location of minimum  $\gamma$ , which corresponds very closely with the maximum in |B| and the minimum in  $I_c$ .
- The variation of  $\phi$  is much smoother for the slit position displaced from the center of the sunspot (Figure 7).
- The minimum inclination of the field is substantially larger for the observation displaced from the center of the sunspot.
- The maximum inferred field strength reaches 2400 G at the displaced location.
- The sunspot is unipolar in this reference frame: the value of  $\gamma$  at the outer edges of the penumbra is between 70° and 80°.
- The magnetic element just to the north of the sunspot retains its inverse polarity in the local frame, and is highly inclined to the local normal.





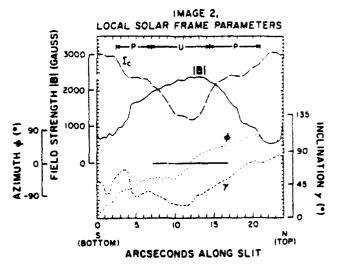


Fig. 7. Results of the least-squares inversion for the slit located to the right of the center of the sunspot (Image 2, rightmost image in Figure 2.) See Figures 3 and 6 for explanation.

The field inclination shows a much more variable behavior on the disk center (southern) side of the sunspot than on the northern side. At the present time it is unclear whether this is an artifact of calibration errors or if the inclination changes are more abrupt as viewed from the disk center side of the sunspot. From spectral observations of very high angular resolution, Bida et al. (1990) found that a stronger correlation of Doppler shifts with intensity variations exists on the limb side of a sunspot observed away from disk center. Thus, observable effects that depend on the look-angle with respect to the direction of the magnetic field do appear to be present in sunspots. This interesting effect should be investigated more thoroughly if the inclination changes indeed turn out to be real, as they may offer substantial information on the structure of sunspot penumbrae.

In Figure 8 we compare the vector field for a large symmetric sunspot derived from Stokes II data with the results for the small sunspot observed here. It is quite remarkable that the two well-developed sunspots of vastly different sizes have nearly identical values and variations of the vertical field component  $B_r$  with radius. We note that the smaller sunspot has a horizontal field component  $B_r$  which is systematically larger than that of the larger sunspot. Thus, the sunspot observed here displays a nonpotential signature, and the observations suggest the presence of a horizontal current system within the sunspot. In contrast, the larger Stokes II sunspots had most of the current defining their magnetostatic structure confined to a current sheet at their outer edges.

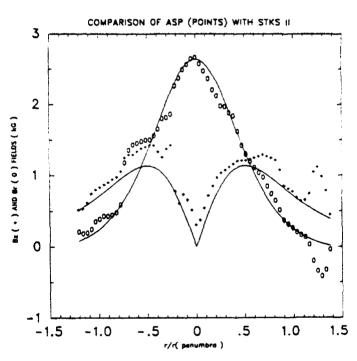


Fig. 8. A comparison is given for the variation of the radial magnetic field structure of a large symmetric sunspot observed with Stokes II on 1980 Sept. 15 (see Figure 11 of Lites and Skumanich 1990) to that of the sunspot observations presented in this paper. The solid curves are the "buried dipole" fits to the 1980 Stokes II data. The penumbral radii for the ASP and Stokes II sunspots are 6.7 and 19 Mm, respectively. The '+' symbols represent the horizontal component  $B_r$  and the '0' symbols represent the vertical component  $B_z$  of the vector field inversion shown in Figure 6.

#### V. SUMMARY AND EXPECTATIONS

The primary goals of the ASP prototype observing run were met, and in most cases exceeded. It was gratifying to have a successful installation of the prototype polarimeter at the Tower Telescope and a successful run on the first attempt. It was even more gratifying to obtain the first high-resolution full Stokes profiles of a small sunspot with a stabilized image under conditions of good seeing.

In particular, we learned a great deal about the optical system and how it needs to be modified for the final instrument. Similarly, we now recognize several problems with the polarization calibration of the system which we expect to rectify in the final instrument. One way we hope to improve the calibration is to introduce a rather well-known and large degree of circular polarization into the telescope. This should help us to identify the source of the  $U \leftrightarrow V$  crosstalk seen in the data. Other issues that must be resolved are the angular resolution of the entire system, scattering in the spectrograph and polarization optics, and the possibility of contamination of the observations by infrared light. Improvements must be achieved in the net scattered light for the final instrument. The overriding technical issue at present is the completion of the ASP cameras, including minimization of the slowly varying pattern noise. At present, none of these problems would appear to delay deployment of the full ASP instrument in mid-1991. Ultimately, the polarimeter will be capable of operation with the Lockheed/NSO Adaptive Optics System.

The radial variation of the vector magnetic field for the small sunspot observed with the ASP prototype instrument indicates a current system similar to that of the much larger sunspots observed with the Stokes II instrument. The strength of the magnetic field on the axis of the sunspot is nearly identical to that of the larger sunspots. It does have a somewhat larger horizontal field strength at all radii, suggesting a horizontal current system distributed throughout the body of the sunspot, in contrast to the nearly potential nature of the field within the larger sunspots. Such an effect might result from magnetic tension forces in the field lines as they return to locations nearby the small sunspot. Such forces could be relatively smaller for larger sunspots because of the larger dimensions involved. It is precisely these kinds of conjectures that can be tested with the spatial coverage of sunspots that will be achieved in the final ASP instrument.

The penumbrae of both large and small sunspots do not seem to have horizontal fields at their outer edges. The fields approach a maximum inclination with respect to the local normal of  $70-80^{\circ}$ . They are therefore constrained by a substantial horizontal current sheet just outside of the penumbra. It is also interesting to note the large inclination of the suspected "moving magnetic element" observed just outside of the sunspot.

### **ACKNOWLEDGMENTS**

Many people at both the High Altitude Observatory and the National Solar Observatory contributed to the success of the ASP prototype observing run. At HAO we thank C. Chambellan, H. Hull, T. Leach, C. Miller, J. Schuenke, K. Streander, and P. Stoltz for help in preparing the instrument for the observing run and for assistance during the run itself. At NSO, we thank S. Colley, S. Hegwer, R. Mann, L. November, and L. Wilkins for similar efforts. We give special thanks to F. Stauffer at NSO for preparing the software which enabled the ASP hardware to interact with the Vacuum Tower Telescope and the Universal Birefringent Filter. We also thank T. Remmle for help in incorporating the active image motion compensation into the ASP optical system. It is to the credit of all these people (and more) that the polarimeter was installed and running well within a few days of arrival at Sunspot. Finally, we thank D. Sime for commenting on the manuscript.

#### REFERENCES

- Adjabshirzadeh, A., and Koutchmy, S. 1983, Astron. Astrophys., 122, 1.
- Bida, T., Lites, B. W., Johannesson, A., and Scharmer, G. 1990, B.A.A.S., 22, 880.
- Elmore, D. F. 1988, Proc. S. P. I. E., 891, 84.
- Elmore, D. F. 1990, "A Polarization Calibration Technique for the Advanced Stokes Polarimeter," NCAR Technical Note (in preparation).
- Fisher, K. (ed.) 1989, The Advanced Stokes Polarimeter Design Review, High Altitude Observatory, National Center for Atmospheric Research, Boulder, Colo.
- Lites, B. W. 1987, Applied Optics, 26, 3838.
- Lites, B. W. 1986, "Science Objectives for a Next-Generation Solar Vector Magnetograph," (ASP preprint no. 1), National Center for Atmospheric Research, Boulder, Colo.
- Lites, B. W. and Skumanich, A. 1989, in *High Spatial Resolution Solar Observations*, (O. von der Lühe, ed), National Solar Observatory, Sunspot N.Mex., p. 389.
- Lites, B. W. and Skumanich, A. 1990, Ap. J., 348, 747.
- Lites, B. W., Skumanich, A., Rees, D. E., and Murphy, G. A. 1988, Ap. J., 330, 493.
- Lites, B. W., Bida, T. A., Johannesson, A., and Scharmer, G. B. 1990, Ap. J., (submitted).
- Murphy, G., and Skumanich, A. 1991, "Stokes Polarimeter Calibration Methodologies: Information Content, Completeness and Posedness," NCAR Technical Note, in preparation.
- Skumanich, A., and Lites, B. W. 1987, Ap. J., 322, 473.
- Tomczyk, S., Stoltz, P., and Seagraves, P. 1991, in *Solar Polarimetry*, ed. L. J. November (Sunspot, N. Mex.: National Solar Observatory, Sacramento Peak), forthcoming.

#### Discussion

- J. Stenflo: What about the 180° ambiguity?
- B. Lites: The 180° ambiguity of the field azimuth in the observer's frame is resolved in the case by choosing between the two values of magnetic field orientation in the local solar frame. Generally, the choice is simple because the "wrong" choice departs quite strongly from that which is physically reasonable for a sunspot.
- J. Staude: Did you include a fitting to thermodynamic parameters in your inversion procedure? If so, how strong is the variation of those parameters across the sunspot? How strong can uncertainties in the determination of these parameters influence the derivation of the magnetic field components?
- B. Lites: Fitting the thermodynamic parameters (line strength, Doppler width, damping, variation of source function) is an integral part of the inversion procedure. The values are never as well-determined as the magnetic field parameters, and there are frequently tradeoffs among them. I have not yet examined these variations in detail, but typical values are reasonable. The fact that we have coarse wavelength sampling of the profiles in this prototype instrument leads to larger uncertainty in the thermodynamic parameters. In the sunspot, these uncertainties seem to have little effect on the field parameters, except where the instrumental polarization crosstalk is large, or where the filling-factor is small.
- S. Koutchmy: In the case of the regular universal spot you observed outside the center of disk, you showed the variation of the azimuthal angle of the field with a large jump of almost  $\pi$  near the center of the core. Do you believe this represents the true behavior of the field inside the core of the spot?
- B. Lites: Yes, it is entirely consistent with the sunspot geometry.

# ULTRAVIOLET POLARIMETRY WITH THE UVSP

# William Henze Teledyne Brown Engineering

#### Abstract

The Ultraviolet Spectrometer and Polarimeter (UVSP) on the Solar Maximum Mission satellite has made what are probably the first polarimetric observations in the ultraviolet spectrum of the sun and stars. In this paper, a brief review is first given of various such UVSP polarimetric observations and analyses. The reduction and analysis of UVSP magnetograms of the transition region above a sunspot obtained in March 1985 are then described. Maximum values of the magnetic field of over 1200 gauss were obtained. Finally, comments and suggestions relevant to possible future ultraviolet polarimetry are discussed.

# 1. Introduction to UVSP Polarimetry

The Ultraviolet Spectrometer and Polarimeter (UVSP) was one of several instruments on the Solar Maximum Mission (SMM) satellite which was launched on 14 February 1980 and reentered the earth's atmosphere on 2 December 1989. A new feature of the UVSP was the inclusion of a polarimeter to allow the measurement of polarization in the ultraviolet which might result, for example, from the Zeeman effect in lines formed in the solar transition region. The UVSP was described by Woodgate et al. (1980); the polarimeter alone was also described by Calvert et al. (1979). Calibration measurements showing the detection of polarized emission were included in the paper by Woodgate et al.

The method used by the UVSP to measure polarization was the observation and Fourier analysis of the detected signal as a function of the angle of a rotating waveplate. The waveplate was followed in the light path by the grating, a fixed (nonrotating) partial linear polarizer which served as the analyzer.

Most of the polarimetry attempted by the UVSP was performed during the periods from February to November 1980 and from September 1984 to April 1985 when the UVSP wavelength drive was operating properly so that desired spectral features could be selected and observed. A brief review is given here of various UVSP ultraviolet polarimetric observing programs and analyses involving the sun and two stars. Some, but not all, of the results have been published previously.

• Initial detection of the magnetic field in the transition region above a sunspot (Tandberg-Hanssen et al. 1981). The first published measurement of the line-of-sight component of the magnetic field in the transition region above a sunspot was made on 24 April 1980. The measured field was 1100 gauss averaged over a field 6 arc sec square (4 pixels, each 3 arc sec square); the spectral line used was the CIV 1548 Å line.

- Spatial distribution of the magnetic field in the transition region above a sunspot compared with the surface (photospheric) field (Hagyard et al. 1981, Henze et al. 1982). The line-of-sight component of the magnetic field in the transition region above a sunspot was measured in October 1980 using the CIV 1548 Å line over a field of 21 pixels, each 10 arc sec square. The maximum field was ~1200 gauss. The transition region fields were compared with observations made by the NASA Marshall Space Flight Center of the surface (photospheric level) fields; vertical gradients were determined by Hagyard et al. (1983).
- Impact linear polarization during a flare using the SI 1437 Å line (Henoux et al. 1983). Linear polarization (maximum of 25 percent with signal-to-noise ratio of 2.9) was observed in the SI 1437 Å line during the decay phase of the soft X-ray emission and possibly at the time of impulsive hard X-ray emission in a flare on 15 July 1980. The polarized electric vector was directed toward disk center. The observations were interpreted as possibly due to the impact of energetic electrons propagating vertically downward onto the chromosphere where the neutral sulfur atoms were excited.
- Stellar polarimetry in the continuum at 1559 Å (not formally published but presented at a scientific meeting [Henze and Woodgate 1987]). Two stars were observed by the UVSP in August 1980. Although the primary purpose of the observations was a calibration of the absolute sensitivity of the UVSP at several wavelengths based on IUE measurements of the same stars, polarimetry was also performed at one wavelength (1559 Å). No polarization was detected; the upper limits at the 3- $\sigma$  level were 3 percent for  $\alpha$  Leo and 7 percent for  $\rho$  Leo. These limits are too high to be of significant astrophysical interest.
- Linear polarization across the Mg II h and k line profiles (Henze and Stenflo 1987). The linear polarization profile and its center-to-limb variation was measured across the Mg II h and k lines near 2800 Å in October 1984. Linear polarization with the electric vector oriented parallel to the solar limb was detected in the line wings on the short wavelength side of the h line and the long wavelength side of the k line with the maximum values toward the solar limb, in agreement with theoretical predictions based on coherent scattering of an anisotropic radiation field. The predicted negative polarization (electric vector oriented perpendicular to the limb) between the two lines was not detected.
- Discussion of a supposed magnetic "transient" during a flare (Henze 1986). It had been reported informally earlier by an investigator that data in the CIV 1548 Å line showed a magnetic transient of 19 kilogauss during a flare on 13 July 1980. The conclusion by Henze (1986), based on the lack of agreement of the expected signals in the two line wings and on the duration of possible significant transients (too brief for the sequential nature of the polarimetry method), was that there was no evidence of magnetic transients and that the earlier report was erroneous.
- Stokes profiles of the CIV 1548 Å line. One profile was shown by Tandberg-Hanssen et al. (1981); others are mostly not yet analyzed.
- Additional magnetometry in transition region above a sunspot (March 1985), presented here in Section 2.

Based on the experience with the UVSP, some suggestions and comments relevant to possible future ultraviolet polarimetry are offered in Section 3.

# 2. Magnetometry in Transition Region above a Sunspot

#### 2.1. Observations

The UVSP observations were made as part of a program coordinated by M. J. Hagyard. an *SMM* guest investigator. The goal was to determine the vertical distribution of the magnetic field in a sunspot. The target was a large sunspot in NOAA active region 2637 which was observed on several days in late March 1985.

The UVSP observing sequence began with rasters to find the position of minimum intensity in the sunspot and show its location in the active region to allow coalignment with ground-based observations. These rasters, shown in Figure 1 for 29 March, were made near 3100 Å so that the rasters look similar to white-light images in the visible; the pixel size and spacing was 3 arc sec square. Before the following SMM orbit, the slit was changed to one with a 10 arc sec square entrance aperture to allow observation of the C IV 1548 Å line with a higher count rate than would be obtained with a smaller entrance slit. The exit slit was wide, effectively including the entire line; the line was split into two halves (designated blue and red for the short- and long-wavelength sides, respectively) with each half sent to a separate detector. The sensitivity ratio of the red to blue detectors was 1.647.

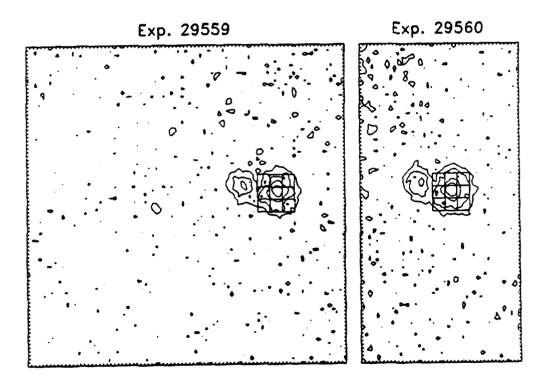


Fig. 1. Contour plots of UVSP spectroheliograms near 3100 Å showing location of UVSP magnetograms on 29 March 1985. Heliographic north is up. Left: experiment 29559 over full UVSP field of view. Right: experiment 29560 which found the position of minimum intensity in the right half of the field of view. The pixel size and spacing of both rasters was 3 arc sec. The magnetograms (experiments 29563 and 29566) were  $3 \times 3$  rasters with a pixel size of 10 arc sec and were centered at the same minimum intensity position. The magnetogram pixel positions are shown superimposed on the two contour plots.

A short spectral scan was made to find the spectral line; then repeated magnetograms were performed with every second repetition done at a shifted wavelength drive position to aid in the calibration of the line width. Each individual repetition consisted of four rasters, one at each of the equally spaced angular positions of the rotating waveplate. Each raster contained nine pixels in a  $3 \times 3$  pattern as shown in Figure 1.

A complete magnetogram experiment contained 168 repetitions and took 21 minutes. The time occupied by the motions of the raster mechanisms, the waveplate, and the wavelength drive, during which no counts were being recorded, meant that less than one third of the total time was actually used for observing  $(168 \times 4 \times 9 \times 63 \text{ ms})$  gate time = 6.35 minutes).

(Another magnetogram experiment was performed in the same orbit at the position of minimum intensity in the left side of the field of view. Because there was no sunspot at that position, the resulting magnetic fields were small and not significant. Therefore, those results are not presented here and the magnetogram positions are not shown in Figure 1.)

# 2.2. Method of Analysis

The method of analysis is basically the same as described by Henze  $et\ al.\ (1982)$  and Henze (1984). The Stokes I and V parameters were determined from the observed signals at the four waveplate positions for each repetition in each detector. A magnetic circular polarization signal was then defined as

$$R_m \equiv \frac{1}{2} \left( \frac{V_r}{I_r} - \frac{V_b}{I_b} \right) \tag{1}$$

which is related to the magnetic field through the Zeeman effect by

$$B\cos\gamma = \frac{4\pi mc^2}{e\lambda^2 g_{\text{eff}}} \Delta\lambda_D \left(\frac{\pi^{1/2}}{2}\right) R_m \left(1 - R_v^2\right) \exp\left(\left[\Delta\lambda_v/\Delta\lambda_D\right]^2\right),\tag{2}$$

where  $\gamma$  is the angle between the field and the line of sight. The Doppler shift signal  $R_v$  is defined as

$$R_v \equiv \frac{I_r - I_b}{I_r + I_b} \tag{3}$$

and is related to the Doppler shift by

$$R_{v} = \operatorname{erf}(\Delta \lambda_{v} / \Delta \lambda_{D}), \tag{4}$$

where  $\Delta \lambda_v = (\lambda_0/c) v$  and erf is the error function.

In order to determine the magnetic field or velocity, it is necessary to know the Doppler width  $\Delta\lambda_D$ . The width was determined for each pixel from a least squares straight-line fit of the observed values of the inverse error function of the observed Doppler shift signal  $R_v$  for each repetition versus velocity as shown in Figure 2. The velocity is the component along the line of sight toward the sun of the spacecraft orbital velocity at the time of the observation plus a correction for the "calibration" shift of the wavelength drive for every second observation. The unshifted points are at the lower left in the figure while the points with the velocity correction are at the upper right. The coefficients resulting from the fit

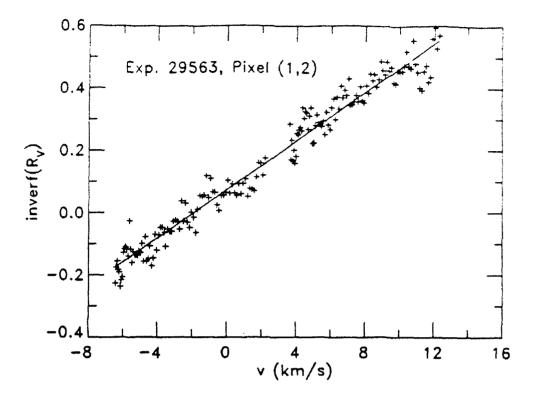


Fig. 2. Example of calibration of Doppler width for one pixel. Vertical axis is the inverse error function of the observed Doppler shift signal. Horizontal axis is the component along the line of sight toward the sun of the spacecraft orbital velocity at the time of the observation plus a correction for the "calibration" shift of the wavelength drive for every second observation. Positive velocities indicate red shifts. The points with the velocity correction are at the upper right. The straight line is a least-squares fit to the points, yielding the parameters  $\Delta\lambda_D=0.132\pm0.002~{\rm \AA}$  and  $v_{\rm off}=1.91\pm0.09~{\rm km~s}^{-1}$ .

are then converted into the Doppler width  $\Delta \lambda_D$  and an offset velocity corresponding to the orbital velocity at  $R_v = 0$ .

#### 2.3. Results

The variations with time (i.e., with repetition) of the intensity (sum of counts from two detectors weighted by ratio of sensitivities), line-of-sight velocity, and line-of-sight magnetic field for one pixel are shown in Figure 3. The top and bottom lines on each plot show the uncertainty range based on the statistical fluctuations in the counting rates (i.e., assuming that the uncertainty in an individual count rate is equal to the square root of the number of counts). The very large fluctuations in the magnetic field are due primarily to the statistical uncertainties. Therefore, we ignore the variations and take the mean of the 168 repetitions to decrease the uncertainty.

The results for the mean values of all of the parameters are given in the table. The pixels are arranged in the same pattern as shown in Figure 1 with north up. Positive velocities indicate upward (blue-shifted) motions. The uncertainties in the table are the mean values of the uncertainties for the individual repetitions divided by the square root

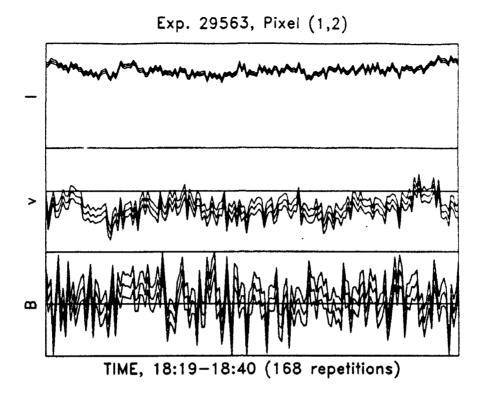


Fig. 3. Example of time variation of intensity (top), line-of-sight velocity (middle), and line-of-sight magnetic field (bottom) for one pixel. Each plot also shows the uncertainty range for each parameter introduced by statistical noise (square root of the number of counts). Vertical scale for intensity is 0 to 600 counts, for velocity is -7 to +5 km s<sup>-1</sup>, and for magnetic field is -15000 to +15000 gauss. Positive velocities indicate upward (blue-shifted) motions.

Table 1. Results (Mean Values) for Exp. 29563

$ m Pixel \ \Delta \lambda_D \ (\AA) \ Intensity (counts) \ Velocity (km s-1) \ Mag. Field (gauss)$	$(2,2)$ $0.155\pm0.003$ $581\pm0.9$ $1.07\pm0.06$ $-169\pm272$	$(2,1)$ $0.122\pm0.002$ $150\pm0.5$ $2.93\pm0.11$ $295\pm422$	(2.0) 0.112±0.002 292±0.7 1.03±0.06 1052±285
Pixel $\Delta \lambda_D$ (Å) Intensity (counts) Velocity (km s <sup>-1</sup> ) Mag. Field (gauss)	(1,2) 0.132±0.002 447±0.8 -1.90±0.06 1227±275	$(1,1)$ $0.118\pm0.003$ $453\pm0.8$ $-2.37\pm0.09$ $1348\pm254$	$(1,0)$ $0.115\pm0.002$ $531\pm0.9$ $0.04\pm0.05$ $1342\pm220$
Pixel $\Delta \lambda_D$ (Å) Intensity (counts) Velocity (km s <sup>-1</sup> ) Mag. Field (gauss)	$(0,2)$ $0.129\pm0.002$ $296\pm0.6$ $-5.54\pm0.12$ $920\pm354$	$(0,1)$ $0.119\pm0.002$ $295\pm0.6$ $-4.38\pm0.10$ $1061\pm325$	(0,0) 0.146±0.003 254±0.6 -3.79±0.12 -482±424

of 167. The peak values of the magnetic field are over 1200 gauss and are factors of 4 to 6 times the uncertainty, thus appearing to be statistically significant. The sign of the field (i.e., positive) is the same as the photospheric level field observed by ground-based magnetographs. Also, the peak fields in experiment 29566 (observed at the same position one orbit later but not tabulated here) are generally consistent with the peak fields in experiment 29563.

The results for 26 March 1985 will be published in a paper in preparation by M. J. Hagyard et al. which will contain comparisons with ground-based observations including magnetograms from the Marshall Space Flight Center.

## 3. Comments Relevant to Possible Future Ultraviolet Polarimetry

Although it is believed that the UVSP has indeed observed polarization for the first time in the ultraviolet, it has been difficult to go beyond the level of simple detection of polarization or magnetic fields because the count rates are usually so low that the uncertainties are high simply due to counting statistics. This difficulty is made more severe by the fact that the UVSP could observe only one pixel at a time and by the sequential method of polarimetry used, i.e., the analysis of the detected signal as a function of rotating-waveplate angle. It was impossible to perform polarimetry at many spatial positions during one orbit of the spacecraft and to obtain information about variations over large fields with good spatial resolution. Also, activity could easily confuse the polarization signal in situations where the brightness of the observed feature is not constant. Valuable observing time was also lost while the various mechanisms (waveplate, wavelength drive, raster) were changing position.

As an example of what an instrument like the UVSP would require to improve the statistical significance, we consider the following example involving the magnetic field. The typical UVSP uncertainty  $(1\,\sigma)$  in the magnetic field is 300 gauss in a 10 arc sec square pixel obtained in approximately 42 seconds of real observing time (but requiring a total time of 140 seconds because of overhead to allow for motion of instrument mechanisms.) This results from a typical UVSP rate of approximately 500 counts in 63 ms. (The intensities in the table are the means of the intensities measured at the four waveplate positions.) To decrease the uncertainty to 3 gauss would require an increase in the number of counts by a factor of  $10^4$ . Improving the resolution to 3 arc sec would require an increase in the observing time by a factor of 10. Thus, even if the overhead ratio were improved to a factor of only 2, the UVSP would require more than 100 days to observe one pixel:

Several methods might be used to increase the counting rate and reduce the observing time required in any possible future instrument.

- The collecting area could be increased (UVSP had 66.4 cm<sup>2</sup>), perhaps by a large factor.
- It might be possible to increase the efficiency (UVSP had  $\sim 10^{-4}$  to  $10^{-3}$ ).
- A different method of measured polarization might be employed or, at least, more efficient observing sequences which waste less time on moving mechanisms could be designed.
- Finally, array detectors should be used to allow simultaneous observation of many pixels.

#### References

- Caivert, J., Griner, D., Montenegro, J., Nola, F., Rutledge, F., Tandberg-Hanssen, E. A., Wyman, C. L., and Beckers, J. M. 1979: "An Ultraviolet Polarimeter for the Solar Maximum Mission". Optical Engineering 18, 287.
- Hagyard, M. J., West, E. A., Tandberg-Hanssen, E., Smith, J. E., Henze W., Beckers, J. M., Bruner, E. C., Hyder, C. L., Gurman, J. B., Shine, R. A., and Woodgate, B. E. 1981: "The Photospheric Vector Magnetic Field of a Sunspot and Its Vertical Gradient", in *The Physics of Sunspots* (L. E. Cram and J. H. Thomas, eds.), Sacramento Peak Observatory, pp. 213-234.
- Hagyard, M. J., Teuber, D., West, E. A., Tandberg-Hanssen, E., Henze, W., Beckers, J. M., Bruner, M., Hyder, C. L., and Woodgate, B. E. 1983: "Vertical Gradients of Sunspot Magnetic Fields", Solar Physics 84, 13.
- Henoux, J. C., Chambe, G., Semel, M., Sahal, S., Woodgate, B., Shine, D., Beckers, J., and Machado, M. 1983: "Impact Linear Polarization Observed in a UV Chromspheric Line During a Solar Flare", Astrophys. J. 265, 1066.
- Henze, W. 1984: "Analysis of UVSP Dopplergrams and Magnetograms and their Calibration Using the Orbital Velocity of the SMM Spacecraft", Solar Physics 92, 67.
- Henze, W. 1986: "Discussion of a Possible Magnetic Transient in UVSP Observations", Solar Physics 104, 359.
- Henze, W., and Stenflo, J. O. 1987: "Polarimetry in the Mg II h and k Lines", Solar Physics 111, 243.
- Henze, W., Tandberg-Hanssen, E. A., Hagyard, M. J., Woodgate, B. E., Shine, R. A., Beckers, J. M., Bruner, M., Gurman, J. B., Hyder, C. L., and West, E. A. 1982: "Observations of the Longitudinal Magnetic Field in the Transition Region and Photosphere of a Sunspot", Solar Physics 81, 231.
- Henze, W., and Woodgate, B. E. 1987: "Ultraviolet Stellar Polarimetry from the Solar Maximum Mission Satellite", presented at joint meeting of the American Astronomical Society and the Canadian Astronomical Society, Vancouver, British Columbia, June 1987, abstract published in Bull. Amer. Astron. Soc. 19, 724 (1987).
- Tandberg-Hanssen, E., Athay, R. G., Beckers, J. M., Brandt, J. C., Bruner, E. C., Chapman, R. D., Cheng, C. C., Gurman, J. B., Henze, W., Hyder, C. L., Michalitsianos, A. G., Shine, R. A., Schoolman, S. A., and Woodgate, B. E., 1981: "Preliminary Observations and Results Obtained with the Ultraviolet Spectrometer and Polarimeter", Astrophys. J. Lett. 244, L127.
- Woodgate, B. E., Tandberg-Hanssen, E. A., Bruner, E. C., Beckers, J. M., Brandt, J. C., Henze, W., Hyder, C. L., Kalet, M. W., Kenny, P. J., Knox, E. D., Michalitsianos, A. G., Rehse, R., Shine, R. A., and Tinsley, H. D. 1980: "The Ultraviolet Spectrometer and Polarimeter on the Solar Maximum Mission", Solar Physics 65, 73.

#### Discussion

- S. Koutchmy: Do you have one single simultaneous observation which has shown a change of the sign of the magnetic field in an active region?
- W. Henze: No. We attempted to find two spots with opposite polarities but were never successful.
- J. Staude: How large was the magnetic field strength at the photospheric level measured simultaneously to your measurements in the CIV line above the sunspot of March 1985? Do you plan a comparison of your measurement with the results of a force-free extrapolation of the photospheric magnetogram?
- W. Henze: The photospheric field was approximately 1000 to 2000 gauss. The exact values will be published in a paper by Hagyard et al.
- J. Jefferies: What spread in values of the Doppler width do you find? Are these values generally consistent with those found by other analyses of the profiles of this spectral line?
- W. Henze: The Doppler widths found here range from 110 to 180 mÅ. This is consistent with other observations of the Doppler width in the CIV 1548Å line. Sunspot umbral width is usually  $\sim 100$  mÅ.

# Progress on the Analysis of BBSO Vector Magnetograms

### Haimin Wang

Big Bear Solar Observatory California Institute of Technology Pasadena, CA 91125, USA

#### Abstract

This talk is divided into two parts:

- (1) I present the evidences that the BBSO vector magnetograph system is measuring correct magnetic fields: (a) comparing the BBSO magnetograms with the data simultaneously obtained at Huairou Solar Observatory, and Mees Solar Observatory; (b) comparing the measured field with the H $\alpha$  filtergrams to show that the field azimuth matches with the H $\alpha$  fibril structure; (c) measuring the vector fields of naked  $\alpha$  spots near the disk center to show that the observed transverse fields have the radial structure.
- (2) I present the prospect of the scientific application of the vector magnetograph data at BBSO. Especially, I introduce a new way to study the relationship between the flares and magnetic structure the shear map, which is defined as the  $\theta \times B_t$ , where  $\theta$  is the angle between the azimuthal of potential field and the measured transverse field, and  $B_t$  is the absolute value of the transverse field strength. Comparing the shear map and the location of flares, we found majority of flares occurred near strong shear area but there are some exceptions.

#### 1. Introduction

Observation of solar vector magnetic fields is of vital importance in understanding solar activities. Hagyard and her colleagues in Marshall Space Flight Center have lead the way in the measurements of vector magnetic field, the interpretation of the data, and the study of the relationship between vector magnetic fields and solar flares (Hagyard, 1988; Hagyard and Rabin, 1986; Hagyard et al. 1982,1984,1988). At Big Bear Solar Observatory, we have made a great effort to establish a system to measure solar vector magnetic fields with high temporal and spatial resolution. In this paper, we will compare the vector magnetograms obtained at BBSO, Huairou Station and the Mees Solar Observatory(MSO), to diagnose if the measurements of

vector fields at the three observatories agree; we will compare the measurements of the transverse fields with the  $H\alpha$  fibril structure; we will also present the observed vector fields of naked spots near the solar disk center.

Finally, we will discuss the application of the vector magnetograph system. The most important application is to study the relationship between the evolution of magnetic structure and solar flares.

#### 2. Observation

The Videomagnetograph (VMG) system at BBSO was developed by Leighton and Smithson (Mosher 1976). Its recent development was described by Zirin (1985). The system has made valuable longitudinal field observation for almost two decades. BBSO started the vector field experiment in the summer of 1988. In the first paper of this subject, Cacciani, Varsik and Zirin (1989) described the BBSO system for vector field measurements using a Magneto-Optical Filter (MOF). Normally, a 1/4 A Zeiss birefringent filter tuned to 6103A is used instead of the MOF. The time resolution of the system is one set of (I,Q,U,V) images per minute. The pixel resolution is between 0.2" to 0.6", the actual spatial resolution is about 1" to 2".

# 3. Diagnosis for BBSO Vector Magnetograph

In the end of September, 1989, active region BBSO # 1761 (Boulder # 5702) was followed by BBSO, Huairou Observatory in China, and MSO. BBSO had almost continuous observation from September 19 to 25; Huairou and MSO covered part of the period.

In Figure 1, we compare a pair of vector fields obtained by BBSO at 0020 UT. September 24, 1989 and by Huairou at 0030 UT, September 24, 1989, which is close to BBSO's end of a observing day and Huairou's beginning of a observing day. The longitudinal fields are presented by contours: solid line draws positive fields, dashed line, negative. We plotted 4 contour levels for each polarity: 100,400,1600,3200 Gauss. The transverse fields are plotted with bars. The length of the bars is proportional to the transverse field strength. The longest bars in each magnetograms are roughly 1500 Gauss. Careful comparison between the two plots of the Figure 1 shows similarity of measurements by the two stations, for both longitudinal and transverse fields.

Similarly, Figure 2 compares a pair of magnetograms obtained by BBSO at 1955UT September 22, and by MSO scanned from 1821 to 1931UT, September 22. We need to rescale the BBSO magnetogram to match with the pixel scale of MSO which is about 6 arcsecond. Again, the visual inspection of two magnetograms shows great similarity.

The longitudinal and the amplitude of transverse fields observed at different observatories can be compared quantitatively by means of correlation coefficients, which are listed in the following table:

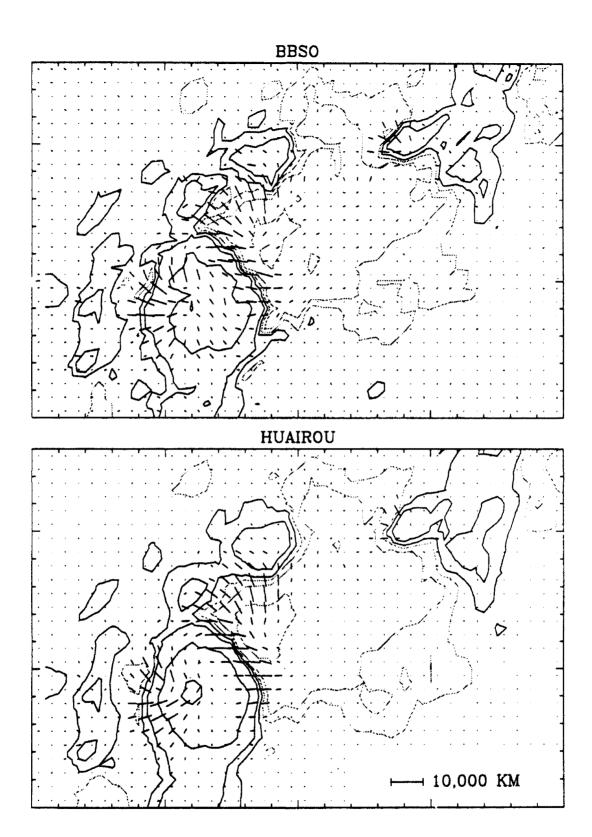


Fig. 1 Comparison between a pair of vector magnetograms obtained at BBSO and Huairou Station, at about 00:30UT, September 24, 1989.

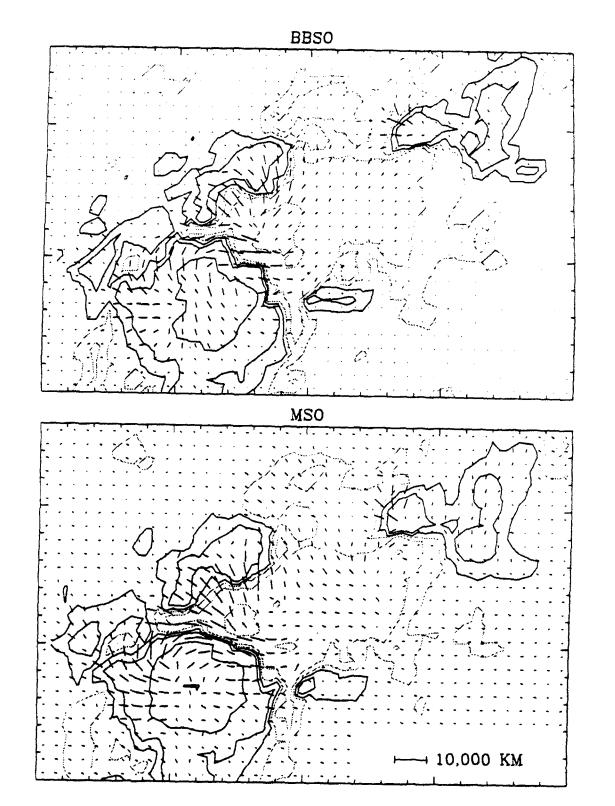


Fig. 2 Comparison between a pair of vector magnetograms obtained at BBSO and MSO, University of Hawaii, at about 1930UT, September 22, 1989.

	BBSO vs. Huairou	BBSO vs. MSO
Longitudinal Field	0.93	0.87
Transverse Field Strength	0.89	0.75

Table 1. Correlation between Magnetograms

The correlation for various comparisons are reasonably good. The longitudinal fields have better correlation than the amplitude of transverse fields; correlation between BBSO vs. Huairou is better than that of BBSO vs. MSO, probably because that BBSO and Huairou have the similar VMG systems.

The correlation method is not a practical way to compare the azimuthal angles of transverse field measurements. The transverse field strength of most pixels falls below the noise level in the observing field of view, the azimuthal angle of those pixels could not be determined correctly. The correlation coefficient between angle measurements is very much under-estimated due to the noise pixels. However, when we calculated the correlation between the measurements of the field strength, as listed in table 1, the contribution of individual pixel to the correlation coefficient is weighted by the pixel intensity. So the noise data points, which have low pixel intensity, have little effect on the correlation coefficient. In Figure 3, we show a different way to compare the measurements of azimuthal angles. We plot the mean angle differences between the measurements of BBSO and Huairou, at 0020UT, Sept 24, as a function of transverse field strength. When the field strength is close to 0 gauss, the mean angle difference is nearly 45°, meaning that the measurement is not reliable at all, since the angle difference could range from 0 to 90; when field strength decreases from 0 to about 200 Gauss, the mean angle difference drops from 45° to 20° rapidly; when the field strength is larger than 1000 Gauss, the mean angle difference is around 5°. So we could conclude that the transverse field measurement is very reliable when the strength is larger than 1000 gauss, reliable between 200 to 1000 gauss, not reliable if weaker than 200 gauss. The comparison between the measurements of BBSO and MSO shows similar results.

The similar comparisons were made for the magnetograms obtained in October 19, 1989 at BBSO and MSO. The results are consistent again.

Figure 4 shows a H $\alpha$  picture and a superimposed transverse magnetogram obtained around 2000UT, September 22. The careful comparison demonstrated that the orientation of dark fibrils are generally consistent with the transverse field bars.

Figure 5 shows the observation of a naked spot near the solar disk center. Normally, the direction of transverse field has a 180-degree ambiguity, which can not be determined by the polarization measurements only. In this plot, the 180 ambiguity has been solved using potential field as the first order approximation.

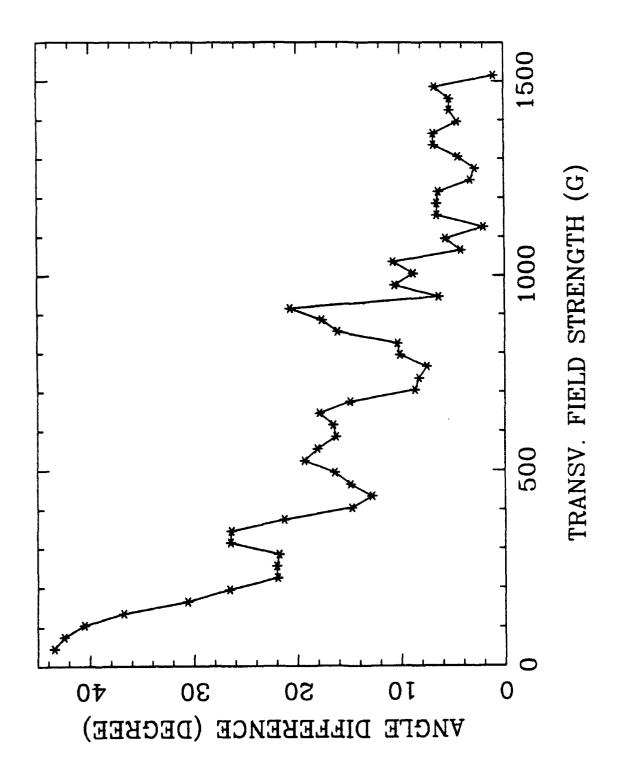


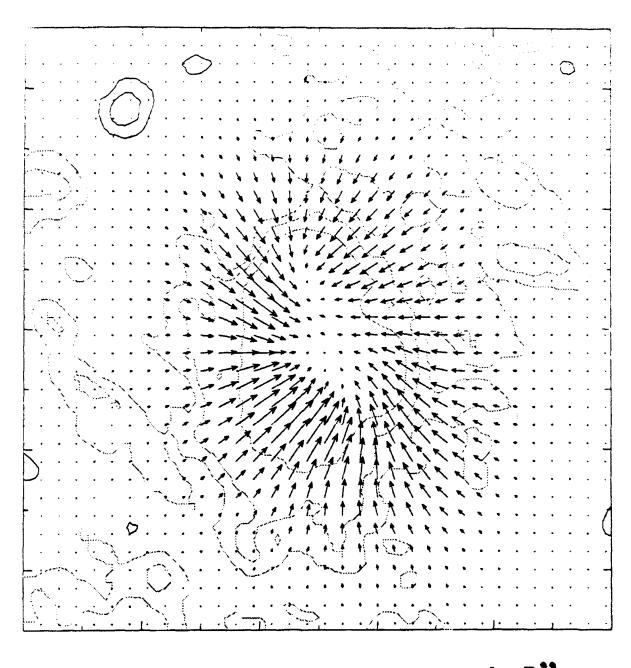
Fig. 3 The mean azimuthal angle difference between the BBSO and Huairou's transverse field measurements, as a function of transverse field strength.



# 10,000 km

Fig. 4 Comparison of the transverse magnetic fields and an H $\alpha$  filtergram. The data were obtained at BBSO, at about 2000UT, September 22.

### 8-16-90 2014UT



**-** 5"

Fig. 5 The vector magnetogram of a naked sunspot, observed on August 16, 1990 near the solar disk center.

The nice radial transverse magnetic field structure confirms that we are measuring correct vector magnetic fields.

### 4. Discussions and Future Goals

From vector magnetic field measurements, the vertical electric currents and magnetic twists could be calculated (Hagyard 1988, Hagyard et al., 1984). These information would be quite important for the flare prediction. Hagyard (1990) pointed out that flares are closely related with (1) transverse field strength, (2) shear angle and (3) size of the large shear. We hereby introduce a new way to display the magnetic structure: the shear map. In the near future, it will be developed as shear movie. The shear map is the gray scale map defined as  $B_t \times \theta$ , where  $B_t$  is the strength of transverse field and  $\theta$  is the angle between the observed transverse field azimuthal and that of potential field. In Figure 6 and 7, we show the shear maps for the active region on Oct. 19, 1989 and March 11, 1989 respectively.

In Figure 6, we marked four pairs of footpoints (a,b,c and d) of four bigger flares in this region occurred between Oct. 18 and Oct. 20. (a) The flare on 18:32UT, Oct. 18. (b) 19:43UT, Oct. 19. (c) 15:10UT, Oct. 20. (d) 21:35UT, Oct. 20. The dashed line shows the magnetic neutral line. The place where flares occurred are near the segments of neutral line with big shear. However, flares avoid the maximum shear locations, marked as M1 and M2.

The March 1989 super active region (Boulder # 5395) produced some 200 flares. Seven X class flares occurred exclusively in two sites, 'a' and 'b', as shown in Figure 7. The magnetograms used to construct the shear map are observed in Huairou. Note that, 'b' is very close to the maximum shear location; 'a' does not have strong shear at all. The further study show that, the site 'a' is the place where new fluxes were emerging continuously (Wang et al., 1990).

As the 22nd Solar cycle is rising, the successful operation of vector magnetograph systems could generate important scientific data. Especially, the BBSO system could achieve fairly high temporal and spatial resolution with good and constant seeing. That adds the power to study the evolution of magnetic fields in flare productive regions. Furthermore, we will coordinate almost round-the-clock vector field observations between BBSO and Huairou, so magnetic fields could be followed continuously. Currently, we are making vector field movies, current movies and shear movies for several flare productive active regions. Our goal is to find out (1) change of magnetic configuration immediately before and following big flares; (2) long term evolution of magnetic structure, to understand the energy built up

### Acknowledgements

for solar flares.

I am grateful to Dr. H. Zirin at BBSO, Dr. R. Canfield at MSO and Dr G.

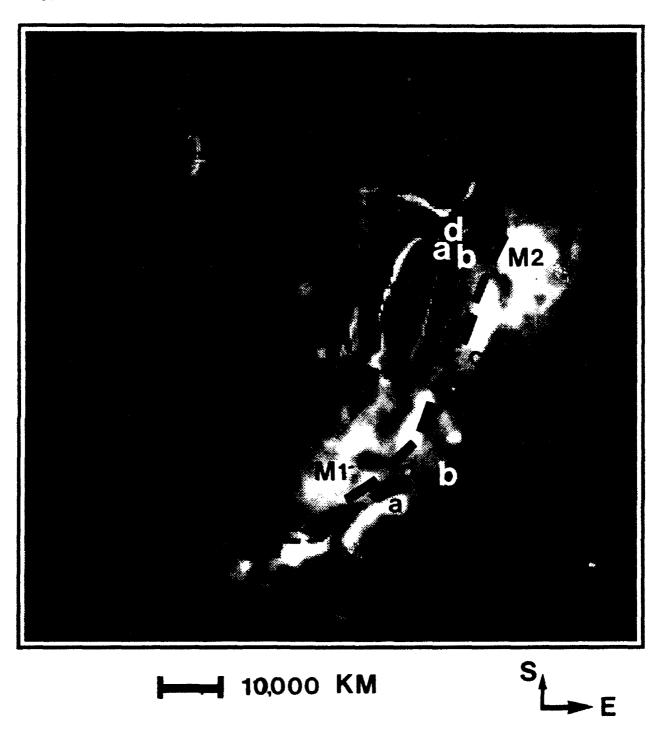


Fig. 6 Flare footpoints superimposed in the shear map of Oct. 19, 1989.

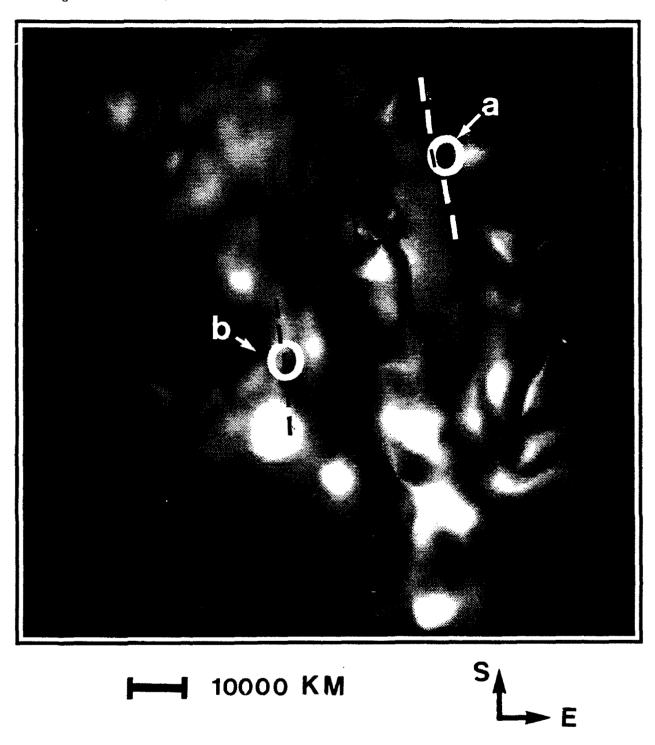


Fig. 7 Flare locations superimposed in the shear map of March 11, 1989.

Ai at Huairou Solar Observatory for their valuable suggestions. I am also grateful to Dr. A. Cacciani for providing and testing the Magneto-Optical Filter. I thank staff of all the three observatories for the supports during the observation. The operation of the BBSO magnetograph and data reduction was supported by NASA under NGL 05-002-034, the NSF under ATM-8816007.

### References

Cacciani, A., Varsik, J. and Zirin, H.: 1989, Solar Physics 125, 173.

Hagyard, M.J.: 1988, Solar Physics 115, 107.

Hagyard, M.J.: 1990, to appear in Memorie della Societa Astronomica Italiana.

Hagyard, M.J. and Rabin, D.M.: 1986, Adv. Space Rev. 6, 7.

Hagyard, M.J., Cumings, N.P., West, E.A. and Smith, J.E.: 1982, Solar Physics 80, 33.

Hagyard, M.J., Smith, J.B. Jr., Teuber, D. and West, E.A.: 1984, Solar Physics 91, 115.

Hagyard, M.J., Gary, G.A. and West, E.A.: 1988, NASA Technical Memorandum 4048.

Mosher, J.: 1976, BBSO preprint.

Wang, H., Tang, F., Zirin, H. and Ai, G.: 1990, to be submitted to Solar Physics.

Zirin, H.: 1985, Australian J. Phys. 38, 961.

### Discussion

- J. Stenflo: The most serious calibration problem is that the derived value of the transverse magnetic flux may be incorrect by a large factor outside sunspots if the magnetic filling factor is not taken into account. How have you dealt with this problem?
- H. Wang: We have not dealt with this hard problem yet. The calibration could be based on the observation only by following an  $\alpha$  spot from E to W limb.
- J. Harvey Were the maps of vertical current and shear computed in the solar normal coordinate or planeof-the-sky coordinate system?
- H. Wang: They are computed in the plane-of-the-sky coordinates system in order to avoid the transformation that mixes measured longitudinal and transverse fields.

# Recent Results from the San Fernando Observatory Video Spectra—Spectroheliograph

by

G.A. Chapman and S.R. Walton

San Fernando Observatory. Department of Physics and Astronomy California State University, Northridge Northridge, CA 91330 USA

Abstract. Results are presented from VSSHG observations of an extensive sunspot group, NOAA 5669, that transited disk center on 4 September 1989. The data are presently processed to obtain four images: a saturation-free longitudinal magnetogram, a Dopplergram, a continuum image, and a line core spectroheliogram. All images are from two-dimensional spectral data with a spectral window of about 1 Å, centered on the 6302.5 Å line of neutral iron. The images show the well-known "fringing" of sunspot fields, the "unsymmetrical" Evershed flow, as well as large-scale flow patterns within the active region. The results presented here are preliminary and will be improved by Fourier filtering of the original video spectra, after digitizing from video tape. Velocities in the Dopplergram are referred to laboratory wavelengths, using nearby telluric O<sub>2</sub> lines.

### 1. Introduction

In the past, measurements of the magnetic field intensity in the solar photosphere have been made by the "Babcock" method (or the Leighton photographic method). These methods convert Zeeman or Doppler line shifts into intensity variations in photometric detectors. However, the conversion of these intensity variations into magnetic or velocity signals becomes non-linear and saturates within sunspots. Furthermore, the shape of the solar absorption line changes in sunspots and non-spot magnetic regions, altering the calibration of these "Babcock" intensity variations.

The only way past these difficulties is to measure the entire line profile for each solar surface element in all of the desired polarizations. Such observations can be carried out in one of two ways: either by a sequence of images at different wavelengths and polarization, or a sequence of spectra at different positions and polarizations. The former is the basis of the Lockheed group's use of a rapidly tunable filter (SOUP); the latter is derived from the spectra-enregistreur (Rayrole 1967) or the Spectra-Spectroheliograph (SSHG) (Title and Andelin 1971). However, the technique at the SFO utilizes video technology, hence the designation VSSHG.

The filter scheme is clearly preferable for balloon- and space-borne instruments, due to size and weight considerations. However, at ground-based locations, the filter scheme mixes image distortions into the spectral domain. To achieve high a signal-to-noise ratio, the images at different wavelengths must have seeing distortions removed ("destretching").

We have adopted the second approach in the VSSHG. This has the advantage that all spectral elements for one line on the sun are obtained at the same time. Thus, there is no mixing of spectral and spatial information. The spatial resolution of the images may

be lower than for the filter method, although this will depend on scanning speed, image stability, and selection of raw spectra.

We obtain pairs of spectra of opposite polarization side-by-side on a single video image. In order to maximize speed in obtaining image and reduce cost of storage, we recorded the spectral image directly from our Cohu CCD camera onto 3/4 inch. U-matic VCR magnetic tape. These data are recorded at the standard NTSC rate of 30 frames per second and are later processed to produce digital images of the solar magnetic and velocity field as well as core and continuum images. The regions are scanned with an interval of  $1\frac{1}{4}$  minutes or less in order to filter out the 5-minute p-mode oscillations. (We are looking for "steady" flows associated with active region evolution.)

### 2. Observing Scheme

The vacuum spectroheliograph is scanned mechanically at a speed determined by the number of video frames to be summed during subsequent processing for noise reduction. For the images shown here, five video frames were summed. The scan speed during this period was higher than it should have been, resulting in a north-south compression of the images by a factor of about 2.4. More recently, the scan speed using the 28 cm vacuum telescope is typically 1.56 arc-sec per second; with our image scale, this results in undistorted images with a six-frame sum. This scanning speed appears to be a useful compromise between speed, to improve spatial resolution, and signal-to-noise ratio in the derived images. A higher signal-to-noise ratio would require more video frames to be summed for each line of the output images, and a correspondingly slower scanning speed.

### 3. Data Analaysis

The recorded spectra are digitized by a Matrox MVP video digitizer and processor operated in a PC-AT clone that also controls a JVC model 600 U-matic VCR. The video data are digitized from the tape while the tape is in play mode, as commanded from the PC: the tape is backed up 60 frames (two seconds) before the next desired digitization to allow the playback to stabilize. The summed video spectra are corrected for the dark and flat-field response of the CCD, and a Gaussian fit is used to remove the blend with the telluric O<sub>2</sub> line at 6302.7 Å. Finally, the desired processing schemes are applied to each line of the spectrum, and the processed data are written to magnetic disk as a set of digital images generated one line at a time. The pixel size in the digitized spectra corresponds to 0.46 arc sec in the spatial direction and 9 mÅ in the spectral direction. (The spectral resolution of about 20 mÅ is set by the entrance slit width.)

The images produced are: a continuum image, formed from an average of a few pixels at a wavelength of 6302.25 Å; a line core image, formed from the minimum intensity within several pixels of the center of the solar line—we allow for the Doppler shift of the line; and a line-of-sight magnetogram and line-of-sight velocity field map, both calculated using a center of gravity technique. That is,  $B_{\parallel}$  and  $v_{\parallel}$  are given by:

$$B_{\parallel} = k_B \times \frac{\int \lambda V(\lambda) d\lambda}{\int [I_c - I(\lambda)] d\lambda} \tag{1}$$

and

$$v_{\parallel} = k_{\rm w} \times \frac{\int \lambda [I_{\rm c} - I(\lambda)] d\lambda}{\int [I_{\rm c} - I(\lambda)] d\lambda}$$
 (2)

where  $I(\lambda)$  and  $V(\lambda)$  are the Stokes profiles,  $I_c$  is the continuum intensity, and  $k_B$  and  $k_v$  are the appropriate constants to convert from splitting in pixels to longitudinal field and velocity, respectively. That is, the ratio of the above integrals, calculated as simple sums in the digitized spectra, give essentially the line-of-sight magnetic field and the shift of the line center in pixels; the known dispersion and Landé g factor are used to convert to  $B_{\parallel}$  and  $v_{\parallel}$ .

The integrals in equations 1 and 2 are calculated only over that wavelength range for which  $I(\lambda)$  is less than 90% of  $I_c$ , as a means of reducing noise (Brants 1985). Some noise in spot umbrae, visible in these images, will be reduced in the future by Fourier smoothing the spectra before calculating the quantities indicated in equations 1 and 2.

The resulting images are both simultaneous and perfectly co-registered, essentially by definition. Seeing-induced image motion changes the spatial relationship between lines, but not within a single line of the images.

Much of the data from August, 1989 (NOAA Region 5643) have been processed, as have some of the data from September 1989 (NOAA Region 5669). An analysis of the relationship between non-spot magnetic fields and their continuum contrast has been carried out by Lawrence et. al. (1990) for the August 1989 data. The video data have been processed with a preliminary version of the software, without Fourier smoothing and without use of floating point arithmetic in the processing. Test runs of new software, which use a DSP Point-I array processor to both Fourier smooth the data and calculate the above integrals using floating-point arithmetic, produce significantly better results, with reduced streaking and random noise, particularly in sunspot umbrae. The noise outside of spots for the magnetic image is approximately 30G RMS, and for the Doppler image is about 40 m/s RMS.

### 4. Results

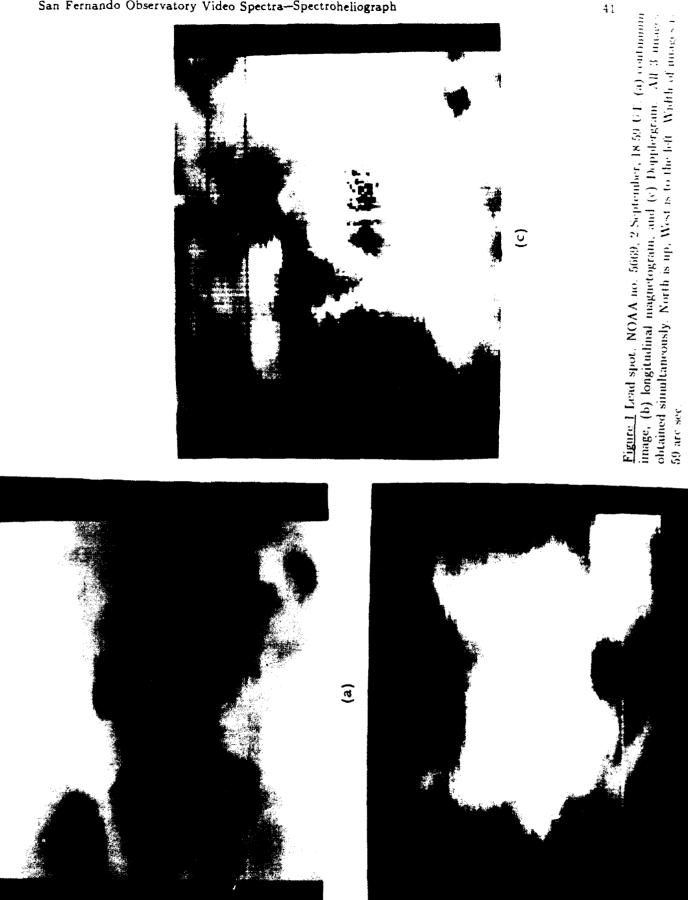
Figure 1 shows the leader spot for NOAA 5669 at 18:59UT on 2 September 1989. These images have been magnified in the computer so that individual pixels can be seen. This spot shows an interesting opposite (South, black) polarity feature in the north part of the penumbra. There is no obvious darkening in the continuum image, but there is a curious bipolar Doppler feature with a strong red-shifted feature at the same position as the black magnetic flux. There is a curved light bridge dividing the main part of the spot into two umbrae. The mean line-of-sight magnetic field for these two umbrae was 1873G. The field strength in the light bridge was 1432G, a difference of 440G or over 20 standard deviations. It is possible that there is a directional change to the magnetic fields in this region. Since each scan takes only about 1 minute, we can repeat scans at  $1\frac{1}{4}$  or  $2\frac{1}{2}$  minute intervals and sum and difference the Doppler images so as to enhance either the steady flows or the oscillatory velocities.

Figure 2 shows the entire active region from which Figure 1 was taken. Figure 2(a) shows the continuum image, 2(b) shows the sum of two Dopplergrams separated by  $2\frac{1}{2}$  minutes, and 2(c) shows the difference of these same two Dopplergrams. There are some interesting flow patterns in Figure 2(b), especially at the trailing (right) side of the main spot, where a two-pronged downflow is adjacent to a large region of upflow associated with opposite polarity magnetic fields in the penumbral region between the two large umbrae. There is some suggestion of weaker p-mode waves in 2(c) in parts of the active region with a strong magnetic field. The horizontal streaks in 2(b) and 2(c) have been found to be caused by the use of integer arithmetic, and have been eliminated in a new version of the processing software.

In Figure 3, we see NOAA 5669 on 4 September 1989 at 20:00UT (The magnetic polarities are shown reversed.) Figure 3(a) and (b) are images of the continuum and line-of-sight magnetic field, respectively. In Figure 3(c), a single Dopplergram, one can see that the northern parts of the active region are blue shifted and the southern parts are red shifted with maximum velocities of approximately -0.49 km/s and +1.48 km/s, respectively. The peak line-of-sight magnetic field in the leader spot (left side) is  $2684 \pm 59 \text{ G}$ . A small "satellite" magnetic feature to the northeast of the main spot is more closely seen in Figure 4.

In Figures 4(a) through (c), we have magnified views of the corresponding Figures 3. One of the interesting features to note is the "satellite" magnetic feature (white) near the center of the figure. The peak magnetic field strength of this feature seems to be at the right edge of the penumbra of the lead spot. The magnetic feature, which has a peak field strength of  $319 \pm 23$  G, corresponds to a strong downflow (white) to the west (left) of a large region of upflow (black) in the Dopplergram of Figure 4(c). This may correspond to a westward plasma flow in a magnetic loop rather than the loop rising or falling.

Figure 5 shows some details of NOAA 5643 on 17 August 1989 at 22:59UT. Figure 5(a) gives an overview of the region (all images are compressed by about a factor of 2 in the N-S [vertical] direction). In Figures 5(b) and (c) the leader spot is magnified. In Figure 5(b) the continuum image is shown with two squares, located off the umbra where the line-of-sight



<u>(P</u>

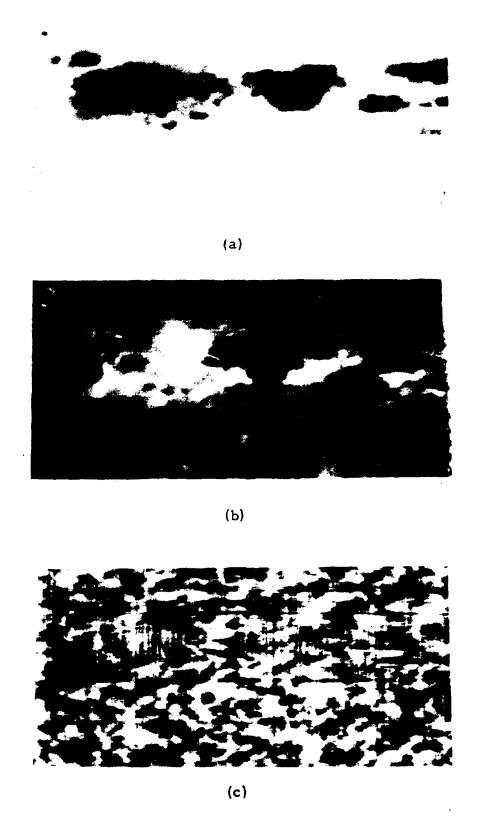
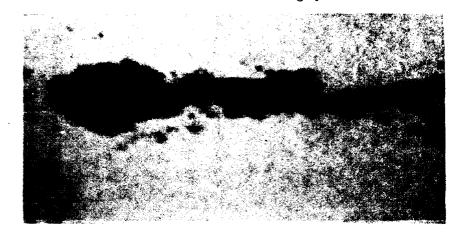


Figure 2 Complete image of data of Figure 1. (a) continuum, (b) sum of 2 Dopplergrams with  $2\frac{1}{2}$  minute time separation to eliminate most of the p-mode oscillations, and (c) difference of same 2 Dopplergrams to enhance p-mode and eliminate slowly varying velocities.



(a)



(b)



(c)

Figure 3 NOAA no. 5669 on 4 September 1989, 20:00 UT. (a) continuum image, (b) longitudinal magnetogram, and (c) Dopplergram. The northern part of the region shows preferentially blue shifts and the southern part red shifts, with maximum velocities of approximately -0.49 km/s and +1.48 km/s, respectively. The peak magnetic field strength in the leader spot is  $2684 \pm 59$ G. The small white region (arrow) has  $B = 319 \pm 23$ G. Black is positive and white is negative in this view.

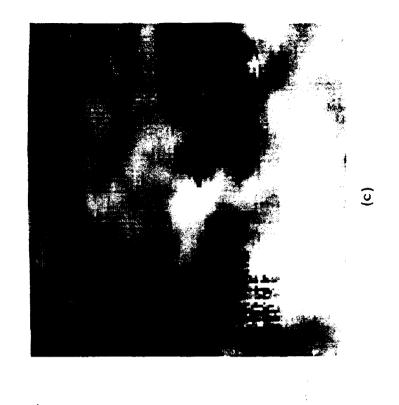
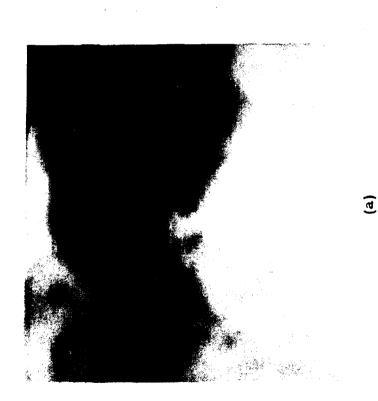


Figure 4 Magnified views of leader spot of Figure 3. (a) continuum, (b) magnetogram of white features, and (c) Dopplergram showing strong change in velocity to the right (east) of the white feature. Noise in the spot umbra can be reduced by reprocessing the original video data with Fourier noise removal





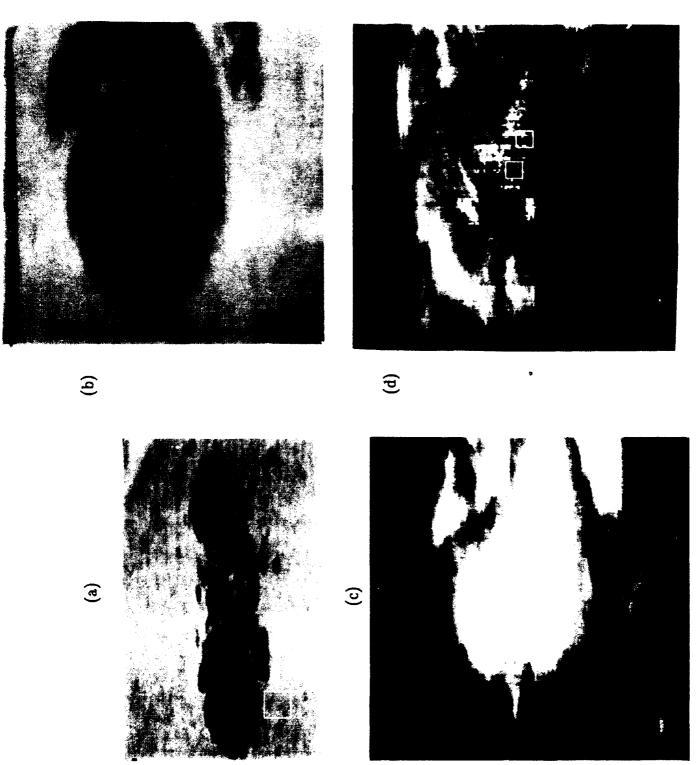


Figure 5 Images of NOAA no. 5643 on 17 August 1989 at 22:59 UT. (a) continuum image at  $\lambda = 6302.2$ Å. The contrast has been enhanced with respect to the photospheric intensity. The white square yields a photospheric intensity of 1773 in machine units, with a standard deviation of 17.8 or 1.0% per pixel. (b) Continuum image, (c) line-of-sight magnetic field, and (b) line-of-sight velocity. See text for discussion of boxed regions. West is toward the left.

field is still strong. Within the left box we find the following quantities on images above a representation of  $I/I_{ph}=0.26$ .  $B_{\parallel}=1552\pm87 G$ .  $r_{\parallel}=-280\pm110$  m/s. For the rigid box we find, for the same quantities:  $I/I_{ph}=0.32$ .  $B_{\parallel}=2406\pm57 G$ , and  $r_{\parallel}=433\pm110$  m/s. The uncertainties are the standard error. The rectangles are 8 by 8 pixels (measured in units where the N-S direction is compressed by a factor of about 2.)

For the leader sunspot of NOAA 5643 we find a peak magnetic field strength of about 2400G. Near the center of the disk, there is a faint ring of opposite polarity flux outside the penumbra, perhaps representing the outer edge of the "superpenumbra" (Figure 5(5)). We find a peak Evershed velocity of approximately 2.2 km/s near the penumbra-photosphere boundary. The spatial character of the Evershed flow is highly structured. The nature of the flow on the disk side is different than that on the limbward side. Individual elements show Doppler shifts corresponding to velocities of about 2.5 km/s, near  $\mu \approx 0.7$ . Flow patterns can be seen persisting for most of the day. Some of the larger follower magnetic elements show no Doppler signal.

### 5. Summary

We have presented preliminary results from the SFO VSSHG that show it to be a promising instrument. The data acquisition technique is relatively fast and inexpensive. Raw data are stored in analog form and can be processed by increasingly sophisticated software.

With the present software we can produce images showing interesting relationships between the magnetic, velocity, and intensity fields. For example, in NOAA 5669, over several consecutive days, we see a strong N-S asymmetry in the velocity images, suggesting opposite flow patterns in solar radius or solar longitude or a combination of the two Detailed analysis of proper motions will help resolve this ambiguity. It is important to note that this N-S Doppler asymmetry was not seen in NOAA 5643. An important question is whether these different Doppler patterns relate to any differences in the evolution of the magnetic field or intensity configurations; e.g., umbral versus penumbral areas.

We hope to address some of these fundamental questions in the near future while making incremental improvements to the processing software. In addition, we have added the ability to measure Stokes Q and U spectra. These data should help us better understand the evolution of the total magnetic field.

This work has been partoly supported by California state funds and partly by NSF grant number AST-8603009. We thank Dr. J.K. Lawrence for suggesting improvements to this paper.

### REFERENCES

Brants, J.J. 1985, Solar Phys. 98, 197.

Chapman, G.A. and Walton, S.R. 1989, in O. van der Luhe (ed.) High Spatial Resolution Observations, (Sunspot, NM: National Solar Observatory), p. 402.

Lawrence, J.K., Chapman, G.A., and Walton, S.R. 1990, Ap. J. (submitted).

Rayrole, J. 1967, Ann. Astrophys. 30, 257.

Title, A.M. and Andelin, J.P. 1971, in R. Howard (ed.), "Solar Magnetic Fields", IAU Symp. 43, 298.

### Discussion

- S. Koutchmy: Outside the core of sunspots, do you have any method to calculate the strength of the magnetic field by introducing the filling factor for example?
- G. Chapman: No, we don't yet know the filling factor in non-spot field regions.
- S. Koutchmy: What is the contrast you measure for "faint" fields at the disc center?
- G. Chapman: The contrast depends on the magnetic flux measured in the feature (to be published by Lawrence et al.).
- **E. Landi**: How is the  $\Delta_{\lambda}$  appearing in your equations defined?
- G. Chapman: The line center is determined from the nominal line position relative to the telluric  $O_2$  lines.

### THE POTSDAM VECTOR MAGNETOGRAPH: METHODICAL EXPERIENCES AND RESULTS

Jürgen Staude, Axel Hofmann, Gerhard Bachmann

Zentralinstitut für Astrophysik Sonnenobservatorium Einsteinturm 1561 Potsdam, Germany

### Abstract

After a short historical introduction the instrumentation of the double line vector magnetograph is described as it is working in connection with the tower telescope of the Solar Observatory 'Einsteinturm' at Potsdam. Subsequently we outline the calibration of the instrumental response to incident polarised light including the procedures for eliminating signal distortions (instrumental polarization, parasitic stray light). The theoretical calibration of deriving the magnetic field components from the observed Stokes profiles is the next step. Finally we give a few examples of vector magnetograms and outline some of our methods for deriving further information from the magnetograms, e.g. calculations of electric current densities, force-free magnetic field extrapolation and modeling of the microwave radio emission.

### 1. INTRODUCTION

After the pioneering work of Hale (1908) Mt. Wilson was for many years the only observatory where solar magnetic fields have been measured by visual or photographic methods. The Solar Observatory 'Einsteinturm' at Potsdam was the second institution where such measurements have been performed: Von Klüber (1947) developed and used since 1942 a well operating photographic technique with circular analyzer which has subsequently been improved and applied by Grotrian et al. (1953, 1956) over several decades. In 1970 photoelectric measurements of Stokes parameters started at Potsdam in close cooperation with colleagues from the SibIZMIR institute at Irkutsk which used the same type of vector magnetograph in the Sayan observatory. The equipment, methodical experiences, and first results obtained at Potsdam have been described in a report by Bachmann et al. (1975).

Since then our magnetograph as well as the data handling have been considerably improved. In the present paper we intend to outline the present state of our instrumentation (Section 2), our procedure of instrumental calibration including methods for reducing signal distortions (Section 3), the theoretical calibration for deriving the magnetic field components from the measured Stokes parameters (Section 4), and finally examples of resulting magnetograms and of applications of such data in further investigations of solar active regions are given (Section 5).

### 2. INSTRUMENTATION

The Potsdam double line vector magnetograph is working in connection with the solar tower telescope 'Einsteinturm'. The two coelostat mirrors with diameters of 60 cm reflect the light into vertical direction. The objective lens has a diameter of 60 cm and a focal length of 14 m, but for polarization measurements the aperture is usually restricted to 45 cm. By means of an optical enlarging system an equivalent focal length of 28.4 m can be achieved. A 45° plane mirror deflects the light from the vertical into the horizontal direction of the spectrograph installation. Photoelectric guiding and scanning systems are used to enable a scanning of a selected region on the Sun with an extent up to 6'x7' and a spatial resolution of 3"x3".

The double spectrograph consists of 2 independent auto-collimating grating spectrographs, either of them with an objective lens with a diameter of 35 cm and a focal length of 12 m, moreover, a plane grating with an area of 20 x 30 cm $^2$  or 20 x 25 cm $^2$  and 600 grooves per mm. Both spectrographs obtain their light through a common slit and polarizing modulator with subsequent beam splitting.

A rectangular modulation of the state of polarization is achieved by means of two step-modulated Pockels cells which are working with frequencies of 900 Hz and 300 Hz, followed by a quarter-wave plate and a linear polarizer. The modulation scheme is similar to that described by Stepanov et al. (1975): In 6 subsequent phases signals are obtained which are proportional to  $I\pm V$ ,  $I\pm Q$ , and  $I\pm U$ . In either of the two spectrographs photometer slits select 3 ranges (line core:  $\pm 40$  mÅ; both wings:  $\pm (40-160)$  mÅ from the line center) in the profile of the respective Fraunhofer line and fed the light to photomultipliers. That means, all 4 Stokes parameters can be measured quasi-simultaneously in 3 ranges of either of 2 independently chosen line profiles. Additional channels measure the intensity in a continuum band,  $I_c$  (used for normalization) and in the core of the H-alpha line (used for co-alignment with filtergrams of high spatial resolution. Moreover, the Doppler compensators are working independently from each other in either of the two lines in order to center the lines onto the photometer slits and to measure the line-of-sight velocities v. A sampling rate of 16 Hz is used in each of the 28 channels, the data are then stored on a magnetic tape.

The rms noise corresponds to degrees of polarization of 0.0005. Applying the calibration procedures of the following sections, threshold values of 6 G for the longitudinal component and 120 G for the transverse components of the solar magnetic field are obtained, if the line FeI 5253.5 Å is used.

Since 1982 measurements of the 4 Stokes parameters in one wing of a magnetically sensitive line, that is to say with a reduced variant of the magnetograph described above have been performed; a short description and first results have been published by Bachmann et al. (1983). In 1988 we started test measurements in two lines using the complete instrumentation.

### 3. INSTRUMENTAL CALIBRATION AND ELIMINATION OF SIGNAL DISTORTIONS

A reliable measurement of Stokes profiles requires a careful calibration of the instrumental response of the whole equipment (telescope and modulator) to incident polarized light. This calibration must include an elimination or at least a strong reduction of signal distortions originating in the atmosphere of the Earth and in the telescope.

Temporal variations of the transparency of the atmosphere are eliminated by normalizing all Stokes parameters to Unfortunately, such a simple procedure cannot exclude distortions by parasitic stray light, that is true scattering of light, for instance at dust particles, and image blurring due to air turbulence. Measurements of stray light have been performed at Potsdam for various seeing conditions, usually by scanning Ic across the solar limb and outside the limb; the results have been compared with other estimates of stray light (intensity contrasts in sunspot umbrae, measurements of Zeeman splittings in umbrae from photographic spectra and their comparison with magnetograph data). These data have shown that blurring can usually be neglected for our moderate spatial resolution of 3". A determination and correction for (unpolarised) scattered light from the quiet photosphere, however, cannot be avoided and has been applied to all measurements. Otherwise errors of factors of 2-3 can easily be achieved under moderate seeing conditions. The earlier discussed discrepancies between 'theoretical' and 'empirical' calibration curves (Severny, 1967, 1977) could largely be due to such simple origins.

Instrumental polarization is mainly due to the oblique reflections at the plane mirrors of the solar telescope. The results are depolarization and crosstalks among the different Stokes parameters, but also a miscentering of the used line within the photometer slits is possible. The latter effect was particularly dangerous for older magnetographs which made use of the symmetry properties of the ideal Stokes profiles with respect to the line center. In earlier papers (Jäger, 1972, 1974; Bachmann et al., 1975) different methods have been discussed for eliminating such distortions. These methods require the knowledge of the Mueller (instrumental response) matrix of the telescope which can be measured but also calculated by means of Fresnel's formulae, if the mirror constants and the reflection angles at the telescope mirrors are known. In each case the elements of the Mueller matrix will depend on time.

At present we are including the determination of instrumental polarization into the calibration of the whole instrumental response. For this purpose a large linear polarizer (diameter 45 cm) or a circular polarizer (diameter 30 cm) can be placed in front of the first coelostat mirror and rotated by definite angles. In this way the Mueller matrix of the whole equipment is measured before and after each scanning of a region on the Sun; interpolation is then sufficient for determining the matrix for each moment during the observation. Small residual errors can still remain due to imperfect properties of the calibration optics. Their removal is only partly possible and requires more sophisticated methods of signal corrections.

As far as no polarization-free telescope is available, each method for reducing the instrumental polarization is useful. For instance, a great part of linear polarization can be compensated by a tilted glas plate with appropriate orientation of its two axes, moreover, one can look for optimum angles of the coelostat mirrors for which instrumental polarization is diminished by partial mutual compensation (Bachmann, 1984).

### 4. THEORETICAL CALIBRATION

In principle the term 'magnetograph' is misleading because such a device measures signals which are proportional to the Stokes line profiles  $(I_i=(I,Q,U,V))$  of light emitted from a selected region on the Sun. Such a 'Stokesmeter' becomes a magnetograph only by the theoretical calibration, that is by calculating the relation between the Stokes line profiles and the magnetic field vector B. B is determined by its components  $B_{H}=B\cos\phi$ ,  $B_1=B_1\cos\phi$ ,  $B_1=B_1\cos\phi$ ,  $B_2=B_1\sin\phi$  with  $B_1=B\sin\phi$ , where B=|B|,  $B_{H}$  and  $B_1$  are the longitudinal and transverse field components, respectively, is the angle between the line-of-sight and B, and  $\phi$  is the azimuth of B. The problems of theoretical calibration have been reviewed in several papers by the present authors (Bachmann et al., 1975; Staude, 1980; Staude and Hofmann, 1988), here we will only outline those procedures which are nowadays used at Potsdam.

For calculating the required relation between  $I_i$  and B a suitable theory of line formation in the presence of a magnetic field is needed. In each case such a theory makes use of a given model atmosphere, that is of the spatial distribution (usually the height dependence) of thermodynamic quantities. This implies that the theoretical calibration becomes model dependent. Additional information on the used line (more generally, on the used atom or ion) such as quantum numbers, excitation potentials, and oscillator strengths, must be provided as well.

In our observatory a computer code BHM has been developed for performing the required calculations. A detailed description of an earlier version of this code has been given in a report (Staude, 1982). This code uses the equations of transfer for the Stokes vector I; in a form as simple as in LTE. That means, a system of 4 coupled linear ordinary differential equations with variable coefficients can be numerically integrated by a Runge-Kutta technique with automatic choice of step width. Non-LTE effects can be considered by applying coefficients bi which describe the deviations from the LTE populations of the upper and lower energy levels of the considered transition. The bi are obtained from a usual multi-level non-LTE calculation neglecting the magnetic splitting; the LINEAR code of Auer et al. (1972) and the MULTI code of Carlsson (1986) are available for this purpose. Calculations by Rees (1969) and by Domke and Staude (1973) have shown that such a 'zero field approximation' is a good approach for practical purposes. The codes LINEAR and MULTI also contain useful procedures for deriving semi-empirical model atmospheres as it has been done, e.g., by Staude (1981) for the sunspot umbra. BHM considers the height dependence of all thermodynamic quantities and hence of all line parameters such as line absorption and emission, damping, Doppler widths, continuum absorption, but also B and v can vary.

Anomalous dispersion is taken into account. Usually Russell-Saunders coupling and electric dipole transitions are assumed, but other splitting patterns can also be considered. If hyperfine structure splitting is important, the splittings and strengths of subcomponents can be calculated by the HYPER code of Landi Degl'Innocenti (1978). Blends of several magnetically split lines can be calculated as well.

The described code is used to calculate synthetic Stokes line profiles and theoretical calibration curves (integrations of the profiles over the photometer slit widths) for given values of (B,  $\gamma$ ,  $\varphi$ ) and selected model atmospheres. Comparisons between such data sets and the measured Stokes parameters yield the desired information on B. Our calculations show that the results are sensitive with respect to the proper choice of the model atmosphere for the observed point on the Sun, moreover, simple approaches such as the 'weak field approximation' can result in large errors.

Simultaneous measurements in 2 lines can provide information on unresolved fine structures in the observed pixel. Procedures for applying the line-ratio method to vector magnetograph measurements with our equipment have been developed by Bachmann (1990) applying the code described above.

The mean depths of formation of the different Stokes profiles and the range of depths which essentially contribute to the line formation are important for the interpretation of polarimetric measurements. In order to calculate these quantities a method has been proposed which is based on the probability interpretation of a scalar product of Stokes vectors (Staude, 1972).

### 5. EXAMPLES OF MAGNETOGRAMS AND OTHER DERIVED QUANTITIES

A first example of a vector magnetogram is given in Figure 1. The position of the observed region with sunspots was in the southern hemisphere of the Sun, at a distance of 450-500 from the central meridian. Therefore projection effects result in a strong asymmetry of the transverse field, we are looking into the spots from a NW direction. The simple pattern of B<sub>1</sub> azimuths of the isolated spot in the western part is only obtained after carefully performing the calibration and correction procedures described in Sections 3 and 4. In the example of Figure 2 the vector field components and the geometrical mapping of the off-center vector magnetogram were transformed from the image plane into the heliographic plane. The resulting transverse field shows a strong twist, contrary to the example of the spots in Figure 1. The be used to calculate the transverse field magnetograms can vertical current density, j<sub>z</sub>. The result is also shown in Figure 2. It is interesting to note that one ribbon of a flare in this active region was concentrated in the umbra, just at the position of the maximum of downflowing  $j_z$  in our magnetogram, while the other ribbon was located in a weak field region where it was stretched and nearly parallel to the neutral line (Hofmann et al., 1987).

Our magnetograms have also been used to calculate the force-free magnetic field structure above the photospheric region where the

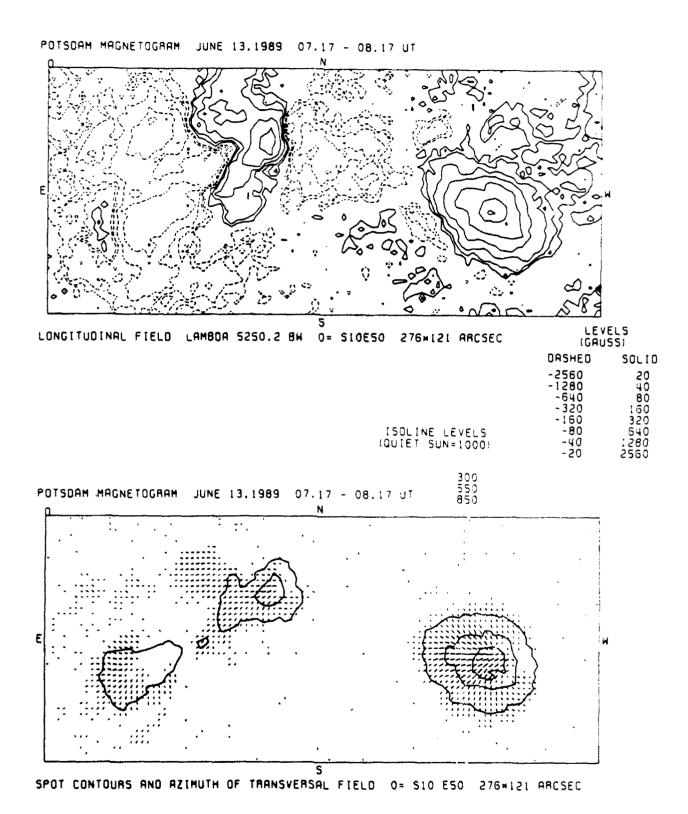
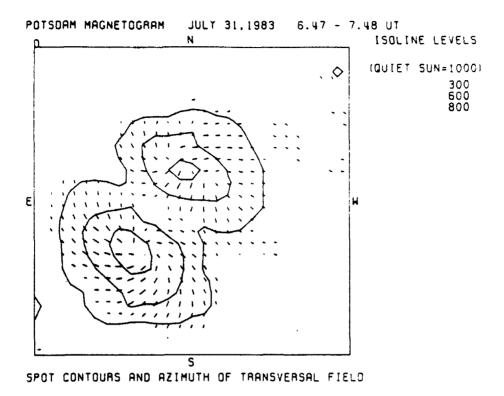


Figure 1. Maps of the longitudinal magnetic field strength and the transverse field directions of AR NOAA 5533.



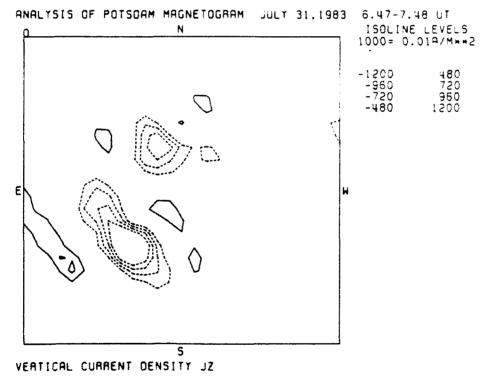


Figure 2. Maps of the transverse magnetic field directions and of electric currents in the main (double) spot of AR NOAA 4263.

measurement has been performed. A procedure for the theoretical extrapolation from a Bn magnetogram assuming a linear force-free field  $(\nabla \times B = \alpha B \text{ with } \alpha = \text{constant})$  has been developed by Seehafer (1978). The free parameter & is determined by fitting calculated lines of force of B to observed fine structures in filtergrams; Bi magnetograms can also be used to compare the observed field with the theoretical prediction from extrapolation procedure. In a first test of the method we used SacPeak magnetograms of the complex active region of August 1972 (Seehafer and Staude, 1979). Interesting results have been obtained for a small active region with a large p-spot of 4 July, 1973 (Seehafer and Staude, 1980): A moving magnetic feature pressed together opposite magnetic fluxes to form an X-type neutral sheet which could be identified in the extrapolated field; configuration was the cause of chromospheric activity such as subflares and ejections. The same magnetogram has also been used to compare the results from our extrapolation procedure with those of other authors such as Nakagawa and Raadu (1972) and Schmidt (1964), the latter only for the special case of a potential field, that is x = 0 (Seehafer, 1982; Seehafer and Staude, 1983). extrapolated magnetic field structures have also been used in model calculations of microwave radio emission (e.g., Hildebrandt et al., 1984) which could be compared with the measurements from radio telescopes such as VLA, WSRT, or RATAN with large spatial resolution.

The Potsdam magnetographs have been included into several international programs for comparing the results from quasisimultaneous measurements of the same active region. A comparison of B<sub>m</sub> magnetograms has been organized by Pflug (1980) who also proposed methods for finding a uniform zero point and scaling of the different B<sub>m</sub> maps. Recently a cooperative program included vector magnetograms from Potsdam and Sayan and B<sub>m</sub> data from Ondrejov; the comparison included methods for eliminating signal distortions and for calculating current densities (Hofmann et al., 1988a,b) as well as vertical field gradients (Hofmann and Rendtel, 1989). After applying all possible calibration and correction procedures the data show generally a good agreement, but some differences in details due to different seeing and instrumental conditions and to the use of different lines cannot completely be removed.

### 6. CONCLUSIONS

In the present paper we intended to describe the instrumentation of our double vector magnetograph as well as our procedures of instrumental and theoretical calibrations, including the methods of diminishing the systematic errors from signal distortions and model assumptions. The examples show that the resulting magnetograms provide reliable and useful data for further investigations of physical processes and structures in solar active region. Of course, analogous to other instruments of this kind our magnetograph is a compromise between different demands, determined by our scientific aims and limited by our instrumental and atmospheric conditions. For instance, we intended to scan complete active regions with moderate spatial resolution (3" is the limit determined by our seeing conditions), but to have also sufficient spectral information to reduce uncertainties from model assumptions

and unresolved fine structures. Suggestions for an improvement are straightforward: Better detectors such as CCD cameras could provide more complete information in much shorter time, e.g., more (at least 3 or 4) lines should be used to measure simultaneously the magnetic field vector at different height levels, and more measuring points in each Stokes profile would improve the theoretical calibration.

### Acknowledgement

J.S. would like to thank the staff of the Sacramento Peak Observatory for the splendid hospitality, moreover, he is grateful to the workshop organisers, particularly to Larry November and Ramona Elrod, for their efforts to provide the support and organise the travel which allowed him to attend the interesting meeting.

### References

```
Auer, L.H., Heasley, J.M., and Milkey, R.W.: 1972, Kitt Peak Nat.
   Observ. Contr. No. 555.
Bachmann, G.: 1984, Bull. Astron. Inst. Czechosl. 35, 308.
Bachmann, G.: 1990, Astron. Nachr. 311, 63.
Bachmann, G., Hofmann, A., and Staude, J.: 1983, Publ. Debrecen
   Heliophys. Observ. 5, 369.
Bachmann, G., Jäger, F.W., Künzel, H., Pflug, K., and Staude, J.:
   1975, HHI-STP Report (Berlin) No. 4, 38pp.
Carlsson, M.: 1986, Uppsala Astron. Observ. Report No. 33.
Domke, H., and Staude, J.: 1973, Solar Phys. 31, 279.
Grotrian, W., Künzel, H., Mattig, W., and Schröter, E.H.:
   1953, Publ. Astrophys. Observ. Potsdam No. 97;
   1956, Publ. Astrophys. Observ. Potsdam No. 99.
Hale, G.E.: 1908, Ap. J. <u>28</u>, 315.
Hildebrandt, J., Seehafer, N., and Krüger, A.: 1984,
   Astron. Astrophys. 134, 185.
Hofmann, A., Rendtel, J., Aurass, H., and Kalman, B.: 1987,
   Solar Phys. <u>108</u>, 151.
Hofmann, A., Grigorjev, V.M., Selivanov, V.L., and Klvana, M.:
   1988a, Astron. Nachr. 309, 331.
   1988b, Astron. Nachr. 309, 373.
Hofmann, A., and Rendtel, J.: 1989, Astron. Nachr. 310, 61.
Jäger, F.W.: 1972, Solar Phys. 27, 481.
Jäger, F.W.: 1974, Solar Phys. 39, 499.
Landi Degl'Innocenti, E.: 1978, Astron. Astrophys. Suppl. 33, 157.
Nakagawa, Y., and Raadu, M.A.: 1972, Solar Phys. <u>25</u>, 127.
Pflug, K.: 1980, Phys. Solariterr. (Potsdam) 13, 5.
Rees, D.E.: 1969, Solar Phys. 10, 268.
Schmidt, H.U.: 1964, NASA-SP 50, 107.
Seehafer, N.: 1978, Solar Phys. 58, 215.
Seehafer, N.: 1982, Solar Phys. 81, 69.
Seehafer, N., and Staude, J.: 1979, Astron. Nachr. 300, 151.
Seehafer, N., and Staude, J.: 1980, Solar Phys. 67, 121.
Seehafer, N., and Staude, J.: 1983, Phys. Solariterr. (Potsdam)
   <u>22</u>, 5.
Severny, A.B.: 1967, Izv. Krymsk. Astrofiz. Observ. 36, 22.
Severny, A.B.: 1977, Izv. Krymsk. Astrofiz. Observ. <u>56</u>, 142.
```

Staude, J.: 1972, Solar Phys. 24, 255.

Staude, J.: 1980, Phys. Solariterr. (Potsdam) 14, 58.

```
Staude, J.: 1981, Astron. Astrophys. 100, 284.

Staude, J.: 1982, HHI-STP Report (Berlin) No. 14, 24.

Staude, J., and Hofmann, A.: 1988, ESA SP-285 Vol. II, 123.

Stepanov, V.E., Grigorjev, V.M., Kobanov, N.I., and Osak, B.F.: 1975, Issled. po Geomagn., Aeron. i Fiz. Solntsa (Irkutsk) 37, 147.

von Klüber, H.: 1947, Z. Astrophys. 24, 121.
```

### Discussion

- J. Stenflo: Your double magnetograph has the capacity of recording the Stokes parameters in two spectral lines simultaneously. How do you exploit this capability?
- J. Staude: First measurements have been done applying the line-ratio method of the two lines FeI 5247.06Å and 5250.22Å from RMT No. 1. Preliminary results for facular regions and the quiet sun yield field strengths of roughly 2 kG, field directions which are nearly perpendicular to the solar surface, and filling factors which strongly vary from point to point.
- G. Simon: Which of the three models (Nakagawa, Boulder; Schmidt, Munich; or Seehafer, Potsdam) do you prefer? That is, does one seem to agree consistently better with other observed phenomena, such as directions of  $H\alpha$  fibrils or penumbral filaments, than the others?
- J. Staude: We prefer the Potsdam method developed by Seehafer because it does not require the net magnetic flux in the measured magnetogram to be zero. For the other methods the latter should be achieved by artificial manipulations at the measured data. A comparison with the Schmidt procedure is only possible for a potential field. Generally we found good agreement with the majority of observed data if we used Seehafer's method.
- L. November: What method do you use to invert Stokes line profiles to give  $\vec{B}$  and other parameters?
- J. Staude: See the answer to John Jefferies' question.
- L. November: What assumptions are used in the extrapolation of flux lines? Force-free?
- **J. Staude We assume a force-free field with constant**  $\alpha$  and determine the value of the  $\alpha$  by fitting the calculated lines-of-force to fine structures in  $H\alpha$  filtergrams.
- J. Jefferies: How do you use the polarimetric data to infer active values for the magnetic field vectors what is your calibration procedure?
- J. Staude: The "theoretical calibration" uses a grid of synthesized Stokes' profiles which are calculated for a set of values of magnetic field strength, of angles, and for a small number of atmospheric models (flux tube, sunspot umbra, quiet sun); the profiles have been integrated over the widths of the photometer slits. The analyzing procedure selects the data set for the most suitable atmospheric model (e.g., umbral model for dark features) and determines the magnetic field components by interpolation.
- K.S. Balasubramaniam: How long did it take you to make observations of a whole active region?
- J. Staude: The scanning of a large region with  $4 \times 5$  arcmins takes about one hour.
- J. Harvey: In your second vector magnetogram, one has the impression of a strong azimuthal twist of the penumbral transverse field. Do you see this nice phenomenon frequently?
- J. Staude: Azimuthal twists of the transverse field around sunspots have been frequently observed, but in most cases the twist is weaker than in the example given here. This strong twist is the result of a counterclockwise rotation of the spot with a rate of 40°/day, which could be inferred from a series of heliograms.
- S. Koutchmy: From test consistency between magnetic field mapping you did above sunspots and the radio-emissions you showed which correspond to the coronal levels, what kind of strength do you get for the coronal magnetic field?
- J. Staude: Radio microwave emission calculations based on our measured and extrapolated magnetic field magnetic field data are in agreement with the data of radio emission observed above sunspots, if the umbral transition region and lower corona are situated at low heights above the umbral photosphere, that is at 2000-3000 km where the magnetic field strength is still of the order of 1-2 kG. This is also in agreement with the SMM data of magnetic fields measured in the sunspot transition region (see W. Henze's paper).

Solar instruments for magnetic and velocity measurements in IZMIRAN.

### B. IOSHPA

Institute of Terrestrial Magnetism, Ionosphere and and Radio Have Propagation of Academia of Sciences USSR Troitsk, Hoscow Reg., USSR

I.KOGEVATOV

Radiophysical Institute, Gorky, USSR

Summary. The principles of measuring of all the Stokes parameters simultaneously by vectormagnetograph and line-sight velocity by integro-interferometric tachometer are described. These instruments are installed on Solar Tower Telescope of IZMIRAN and can be used for measuring the velocity distribution on two different heights in the solar atmosphere simultaneously

## 1. Solar magnetograph for simultaneous measurement of all magnetic field components

It is known that the measurement of the Stokes parameters of the incoming radiation is sufficient for the determination of the total magnetic vector. The method of the simultaneous determination on of all Stokes parameters has been developed in IZMIRAN in early 60 and has been described in some papers (Ioshpa and Obridko, 1962; Ioshpa and Obridko, 1964). In the same time the method of vector magnetic field measurement was supposed also in Crimean Astrophysical Observatory (Stepanov, Severny, 1962). In the following years the methods of measuring the vector magnetic fields were very intensively developed and now many Stokesmeters and vectormagnetographs are operating in different observatories throughout the world (see, for example, Hagyard, ed., 1985).

Here I want only to remind the main features of our method and our instrument.

Let the incoming sunlight described by Stokes vector Io(Io,Vo,Qo,Uo) pass the retarder  $/\delta/$ , electrooptical modulator /KDP Pockels cell/ with the variable retardation  $\delta_4$ =A sin  $\omega$ t and polaroid (fig.1).

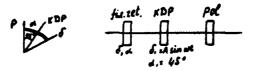


fig.1.Optical scheme to record simultaneously all Stokes parameters with a single electrooptical modulator. Here  $\alpha$  and  $\alpha$  — the position angles of the ordinary axes of the plates relative to the axis of the polaroid(see the left part of figure).

Then the output Stokes vector I may be calculated by Mueller matrix method: I = MIo , where

 $M=M(p)R(45)M_{KDP}R(45)R(\alpha)M(6)R(-\alpha)$ .

(1.1)

But we are interested mainly in the first line of the output

Mueller matrix representing intensity falling on the detector. It may be represented as

I=Io+Qo [(cos<sup>2</sup>2 $\alpha$  + sin<sup>2</sup>2 $\alpha$  cos  $\delta$ )cos  $\delta$ i-sin2 $\alpha$  sin  $\delta$  sin  $\delta$ i]+ + Uo[(sin2 $\alpha$  cos2 $\alpha$  cos $\delta$ -sin2 $\alpha$  cos2 $\alpha$ )cos $\delta$ i +cos2 $\alpha$  sin $\delta$  sin $\delta$ i]+ + Vo[ sin 2 $\alpha$  sin $\delta$  cos $\delta$ i + cos $\delta$  sin $\delta$ i]. (1.2)

From our point of view it is more conveniently to represent the result in the coordinate system in which the one axis is directed along the main axis of the polarization ellipse; in this system the parameter U=0 and the 4 Stokes parameters may be replaced by 3 Stokes parameters I,Q,V and the angle between the direction of the transversal field and some arbitrary direction

I=1/2[Io -Qo (cos2 $\phi$  sin2 $\phi$  cos $\delta$ i+sin2 $\phi$  cos $\phi$  cos $\delta$ i = - sin2 $\phi$  sin $\delta$  sin $\delta$ i) =-Vo (cos2 $\phi$  sin $\delta$  cos $\delta$ i +cos $\delta$  sin $\delta$ i) ], (1.3)

where  $\Phi$ — the angle between the direction of the great axis of the polarization ellipse and the ordinary axis of KDP plate,  $\varphi$ — angle between the axes of KDP and retarder  $\delta$  plates/fig.2/.



fig. 2. The positions of optical element axes relative to the direction of magnetic vector in the image plane.

Using  $\delta_1=$  Asino, we expand  $\cos\delta_1$  and  $\sin\delta_1$  in terms of Bessel functions

 $\cos \delta_{i} = J_{0}(A) + 2J_{2}(A) \cos 2\omega t + \dots, \sin \delta_{i} = 2J_{1}(A) \sin \omega t + \dots$  (1.4)

Then we can separate signals at various frequencies:

 $I\omega = J_1(A)Q_0 \sin 2\Phi \sin 6-J_1(A)V_0 \cos 6, \qquad (1.5)$   $I_2\omega = J_2(A)Q_0 (\cos 2\Phi \sin 2\phi + \sin 2\Phi \cos 2\phi \cos 6) - J_2(A)V_0 \cos 2\phi \sin 6,$   $I_{==1/2}(I_{-J_0}(A)Q_0 (\cos 2\Phi \sin 2\phi + \sin 2\Phi \cos 2\phi \cos 6) - V_0 \cos 2\phi \sin 6J).$ 

The last term will be unchanged it we choose  $A=2,46-(\lambda,-2,52)$  modulation ) because Jo(-2,40)=0.

In our magnetograph the radiation from both wings of the magnetic line falls alternately on the exit slit of the spectrograph and the photomultiplier by the aid of a little glass plate switching very sharply from one side to another with a frequency  $\Omega << \omega$ . So we can add or subtract the signals from two wings of the profile.

By summing and subtracting the signals we can totally separate Stokes parameters and measure them simultaneously if the they are symmetric relative to the center of the spectral line:

 $I\omega_{+} = J_{1}(A) \otimes \sin 2\Phi \sin 2\Phi,$   $I2\omega_{+}J_{2}(A)\otimes (\cos 2\Phi \sin 2\Phi + \sin 2\Phi \cos 2\Phi \cos \delta),$   $I\omega_{-}=J_{1}(A) \otimes \cos \delta,$   $I2\omega_{-}=J_{2}(A) \otimes \cos 2\Phi \sin \delta$ 

If we chose  $\delta=\pi/2$ , then

 $I\omega = J_1(A)Q_0 \sin 2\Phi$ ,  $Iz\omega = J_2(A)Q_0 \cos 2\Phi \sin 2\Phi$ , (1.7)  $Iz\omega = J_2(A)V_0 \cos \Phi$ .

When we take A=2,40, then Jo/A/=0, J1(A)=0,53, J2(A)=0,42 and by  $\varphi$ =30 we have

 $I\omega + = 0.53 \, \text{Qo sin} 2\Phi$ ,  $Iz\omega + = 0.36 \, \text{Qo cos} 2\Phi$ , (1.3)  $Iz\omega + = 0.21 \, \text{Vo}$ .

The calculation of magnetic field parameters has been based on Unno theory in the assumption of true absorption for a Milne-Eddington solar photosphere model (Unno,1956). We use the line FeI  $\lambda$  5250.2 A. The sensitivity of longitudinal component measurement is about 5 G, of transversal component 100-150 G. The instrument has only one photomultiplier and that's why we don't have any difficulties connected with the mutual nonstability of detectors. The main drawback of this scheme is the danger of the cross talk between the signals corresponding to the different Stokes parameters. This cross talk will be inevitable if the parameters V and Q are asymmetric relative to the line center. The problem of asymmetry and its influence on the results obtained by proposed scheme should be carefully investigated. We also do not consider here the calibration problem.

# 2. The method of measuring the center of gravity displacement by integral spectrometer (tachometer).

Recently some instruments for measuring velocity and magnetic field based on interferometric principles have been developed (Beckers and Brown,1978; Brown,1981; Evans,1981). We want to describe shortly the instrument that is now in operation on solar tower telescope in IZMIRAN.

First of all we want to give a short account of the idea of the method. The interferogram of quasimonochromatic radiation can be described using the conception of amplitude A(d/ and phase  $\Psi(z)$  where d+ path-length difference of the rays (Gorsky, Rogevatov, and Lebedev, 1979; Didcovsky, Rogevatov, and Stepanjan, 1986).

$$I(d) = A(d) \cos \Psi(d). \tag{2.1}$$

The single-valuedness of this relation is provided by additional relations between  $\Psi(\textbf{d})$  and A(d) :

$$A(d) = \left[ \begin{array}{ccc} I^2(d) + I_0^2(d) \end{array} \right]^{1/2},$$
 
$$\Psi(d) = \arctan t g \frac{I_0^2(d)}{I_0^2(d)}, \qquad (2.2)$$
 where 
$$I_0(d) = -\frac{1}{t} - \int\limits_{-\infty}^{\infty} \frac{I_0(t)}{t-d} dt - Gilbert conjugate.$$

We can expand A(d) and  $\Psi(d)$  in degrees of d:

$$\ln \frac{A(d)}{W} = -\chi_2 \frac{d^2}{2!} + \chi_4 \frac{d^4}{4!} + \dots + \chi_{2n} \frac{d^{2n}}{(2n!)} (-1)^{2n}$$

$$\Psi(d) = \chi_1 d - \chi_3 \frac{d^3}{3!} + \dots + \chi_{2n-1} \frac{d^{2n-1}}{(2n+1)!} (-1)^{n-2}$$
(2.3)

where {  $X_n$  } are the semi-invariants or cumulants of intensity spectrum and W is the area of the line profile (i.e.the equivalent width of the line ). The first semi-invariants coincide with the first central moments and have simple geometrical sense

$$X_{1} = \frac{\int I(x) x dx}{W} - \text{center of gravity for } I(x),$$

$$X_{2} = \frac{\int I(x) (x-xi)^{2} dx}{W} - \text{the width of } I(x),$$

$$X_{3} = \frac{\int I(x) (x-xi)^{3} dx}{W} - \text{asymmetry of } I(x),$$

$$X_{4} = \frac{\int I(x) (x-xi)^{3} dx}{W} - \text{excess.}$$

For the Gaussian profile the function I(x) is determinated by  $\chi_1$  and  $\chi_2$  totally. The next semi-invariants describe the distinction of the real profile relative to the Gaussian, and if it is small the expansion diminishes very quickly.

As seen from the above expressions, the contribution of semi-invariants of different numbers to the amplitude and phase of the interferogram depends strongly on the path-length difference d If d is small enough, the amplitude of the interferogram depends only on the equivalent width, W, whereas the phase depends only on the position of the "gravity center" of the line profile ): .Choose W and Xi are determinate from the amplitude and phase of the interferogram at d(<1 (d=1 corresponds to value  $\lambda/\Delta\lambda$   $\lambda$  and for the photospheric lines usually equal to  $40000~\lambda$ ) one can proceed to perform measurements at larger values of d and determine the width, Xz and asymmetry, Xs , of the line. These four parameters can be obtained simultaneously by using two Michelson interferometers with adequately selected path-length differences, dies and delication and delications and delications and delications and delications and delications and delications are delicated path-length differences, dies and delications and delications and delications and delications are delicated path-length differences, dies and delications and delications are delicated path-length differences, dies and delications and delications and delications are delicated path-length differences, dies and delications are delicated path-length differences.

But it is easier to measure the first 4 semi-invariants by the aid of a single Fabri-Perot interferometer which realized simultaneously an equidistant series of the path-length differences do, 2do, 3do,... The amplitude and phase shifts of interferograms corresponding to different values of disamble measured with the aid of a single interferometer by sawtooth modulation of the distance between the mirrors by about  $\lambda/2$  at time interval To. Then the output detector will yield the current containing a number of harmonics at frequencies multiple of for 1/To. The signal at frequency for will have the amplitude and the phase corresponding to the path-length difference do whereas the signals at 2fo, 3fo, etc. However, it should be noted that the line area and the first three semi-invariants (Xi, Xi, Xi) are of particular interest. Therefore the reflection coefficients of the mirrors should be calculated in such a way that the major

part of the light energy were spent to form the first harmonics of the output signal of the interferometer. In the case of measuring the shift of the spectral line gravity center—the first harmonic reaches its maximum at—the reflection—coefficient—of about 45 %. The path—length difference d was choosen equal to 3,11 mm, and the spectral line we use is  $\lambda o=5576$  A.

.This method has been suggested and realized in Radiophysical institute .Gorky.The instrument was installed on the Tower Solar Telescope of IZMIRAN in 1990 and it is operated now simultaneously with the vector-magnetograph (fig. 3).

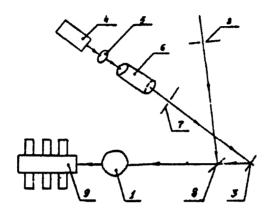


fig.3.Structural scheme of the optical-mechanical block of Fabri-Perot Tachometer. 1-interferometer Fabri-Perot,2-slit diaphragm,3-mirror,4-the source of reference radiation(laser),5-wide-field optics,6-objective,7-diaphragm,8-light divider,9-block of multipliers.

New instrument installed in place of the tachometer based on the two-rays Michelson interferometer scheme that had been used on IZMIRAN Solar Tower Telescope during some years for the measuring the velocity fields in the Har filament neighboring loshpa and Kulikova, 1989).

The FeI 5576 line is known to have the Lande factor equal to zero, which makes the radial velocities measured in this line less burdened with errors, especially when the magnetic field is nonuniform. The line is isolated with the aid of a diffraction spectrograph, which naturally decreases the potential efficienty of the instrument. On the other hand, the use of spectrograph makes the selection of lines easier than with the other optical filters.

In order to refer measurements to the frequency standards that are much more stable than the length standards, the axission of a frequency-stabilized lazer is directed to the interference together with the  $\lambda$  5576 line emission. The lazer emission from three points of the 40 mm aperture of the interferometer is detected by separate photodetectors. The phase shift of the lazer emission is used to continuously correct the position of the mirrors with the aid of three piezoceramic elements. It is easy to show that the phase stabilization in the standard emission interferogram is equivalent to replacing the length standard (d) by the frequency standard  $\nu$  of the stabilized lazer (Kogavatov and Cheragin,1983). The frequency stability of the lazer is 5.10°, which in principle enables the Doppler shifts corresponding to the radial velocity of about 1.5 m/s to be measured. However, this

is possible only if the optical paths of the solar and lazer emissions in the interferometer are absolutely identical. In fact, owing to inevitable deformation of the elements, we did not manage to get the proper instability of the instrument in the frequency band of 0-1 Hz lower than 5 m/s. Notwithstanding, we are satisfied with the stability obtained, since the errors in the above frequency range depending on the guiding precision, the image tremor at the input slit of the spectrograph, as well as the photonoise are usually much higher. The real sensitivity of the instrument is about 20 m/s. Now we plan to measure with this instrument not only the Doppler velocity but also the longitudinal magnetic field by using an additional electrooptical modulation.

### REFERENCES

Beckers, J.M., and Brown T.M., 1978, in Proceedings of the JOSO Workshop, Future Solar Optical Observations, Needs and Constrains, ed. G. Godoli, G. Noci, A. Righini (Firenze), pp. 189-203. Brown T.M. 1981, in Solar Instrumentation: What's Next?, ed. R. B. Dunn, pp. 150-154.

Hagyard, M.J., ed., 1985, Measurements of Solar Vector Magnetic Fields Evans J. 1981, in Solar Instrumentation: What's Nexto, ed.R.S. Dunn, pp. 155-169.

Gorsky, S.M., Kogevatov, I.E., and Lebedev, V.P., 1986, Izvestija Krimskoj Astrophizicheskoj observatorii, 74, 142-158.

Didcovsky, L.V., Kogevatov, I.E., and Stepanjan, N.N. 1979, Astronomicheskj journal, 56,590-594.

Ioshpa, B.A., and Kulikova E.H. 1987, in Trudi 13 Consultativnogo soveshanija po phyzike Solntsa, ed. Novosibirsk, Nauka, pp. 157-172. kogevatov, I.E., and Cheragin, N.P. 1983, Isledovanie po Geomagnetizmu, Aeronomii i Phyzike Solntsa, 64, 75-42.

Stepanov, V.E., and Severny ,A.B. 1962, Astrophizicheskoj observatorii,28,165-180.

Investija (rimsko)

Unno.W.1956, Publ. Astron. Soc. Japan, 8, 108.

### SOLAR VECTOR MAGNETIC FIELD MEASUREMENTS

G. Allen Gary, M. J. Hagyard, and E. A. West Space Science Laboratory, NASA/George C. Marshall Space Flight Center Huntsville, Alabama 35812 USA

### ABSTRACT

This paper contains a discussion of recent results with the Marshall Space Flight Center's (MSFC) filter vector magnetograph and the co-aligned  $H\alpha$  telescope. This report emphasizes total vector magnetic measurements and the co-spatial, co-temporal  $H\alpha$  observations. The observations reported include magnetic shear data along the neutral inversion line, vector field measurements below prominences, and vector magnetic field measurements associated with flares and surge activity. The importance of a large field of view and high polarimetric sensitivity in solar vector magnetic field measurements is also discussed.

### I. INTRODUCTION

The capabilities of the MSFC vector magnetograph have been extended by the addition of a co-aligned H $\alpha$  telescope. The magnetograph, itself, consists of a symmetric 30-cm Cassegrain system which has a field of view of 6 by 6 arcmin giving an effective pixel size of 2.8 by 2.8 arcsec with 2 by 2 binning for the CCD (Hagyard et al. 1982; Hagyard, Cumings, and West 1985). The iron line Fe I 5250.2 is selected by a Zeiss birefringent filter ( $\Delta\lambda = 0.125\text{Å}$ ). The polarimetry uses KD\*P electro-optical modulators in conjunction with the sheet polarizers in the Zeiss filter (West 1985). The resulting magnetic field sensitivities are  $B_i^0 \approx 5$  and  $B_i^0 \approx 125$  G with a temporal cadence of 5 min. The Zeiss filter can be tuned  $\pm 8$  Å about the Fe I 5250.2 line. This allows the three Fe I lines at 5247.0 (g=2.0, ep=0.09), 5250.2 (g=3.0, ep=0.12), and 5250.6 (g=1.5, ep=2.20) to be selected for performing flux tube analysis (cf. Solanki, Keller, and Stenflo 1987), which is just beginning to be performed. The work to date has concentrated on the Fe I 5250.2 line and the information it contains on the nonpotential field configuration. The magnetograph was developed in the early 1970's and has been operating since 1979 supporting Solar Maximum Mission, Spacelab, rocket experiments, and joint ground base observations. Some recent results of the MSFC magnetograph are contained herein which reflect the important addition of a H $\alpha$  telescope.

The H $\alpha$  telescope was added to the magnetograph in 1989. It was the engineering-backup model of the Skylab ATM H $\alpha$  1 telescope. The system is a 17-cm Cassegrain which feeds a Fabry-Perot spectral filter with a 0.7 Å bandpass (Markey and Austin 1977). The medium bandpass was selected for Skylab's pointing requirements which needed the sunspots to be resolved for positioning information. Updated with a CCD camera system, the H $\alpha$  system gives co-spatial, co-temporal images of chromospheric activity. With the H $\alpha$  telescope coaligned, the MSFC magnetograph has been observing > 30% of the days since the last quarter of 1989.

The astrophysical investigation of the solar magnetic active regions, especially magnetic shear at flare sites, is a major capability of the magnetograph. Much of the MSFC research has been on the magnetic configuration of the preflare state of the nonpotential fields. The investigations that have been carried out include magnetic morphology studies (Hagyard, West, and Cumings 1977; Hagyard and Teuber 1978; Patty 1981; Schmahl et al. 1982, Patty and Hagyard 1986; Neidig et al. 1986; Hagyard et al. 1986; Machado et al. 1988), magnetic shear programs (Hagyard et al. 1984; Hagyard, Moore, and Emslie 1984; Hagyard 1984, 1987, 1990; Hagyard and Rabin 1986; Moore, Hagyard, and Davis 1987; Hagyard and Smith 1988; Venkatakrishnan, Hagyard, and Hathaway 1989), vertical electric fields, Jz, studies (Krall et al. 1982; deLoach et al. 1984; Hagyard, West, and Smith 1985; Ding et al. 1985, 1987; Haisch et al. 1986; Lin and Gaizauskas 1987; Hagyard 1988), nonpotential analysis of active region (Strong et al. 1984a.b; Machado et al. 1986; Gary et al. 1987; Gary 1989; Hagyard, Venkatakrishnan, and Smith 1990); magnetic field submergence/emergence analysis (Rabin, Moore, and Hagyard 1984, 1985), canopy study (Adams et al.

1990), magnetic energy evaluation (Machado and Moore 1986; Gary et al. 1987), coronal field extrapolations (Teuber, Tandberg-Hanssen, and Hagyard 1977; Hagyard et al. 1981, 1983, 1985; Henze et al. 1982; Chiuderi Drago, Alissandrakis, and Hagyard 1987; Haisch et al. 1988); full line spectral analysis (Balasubramaniam and West 1990), and magneto-optical effects (West and Hagyard 1983). We present here only recent results with the MSFC vector magnetograph.

### II. SHEARED MAGNETIC FIELD

The relation of sheared magnetic fields to the degree of nonpotentiality of magnetic fields continue to play a major role in the analysis of MSFC magnetograms. The phenomenological parameter of magnetic "shear" is defined as the angular difference ( $\Delta\phi$ ) between the angle of the observed transverse magnetic field (i.e., the direction of linear polarization) and the angle of the potential transverse field calculated from the line-of-sight (longitudinal) magnetic field (Hagyard et al. 1984; Hagyard, Venkatarisknan, and Smith 1990) This is referenced along the longitudinal neutral line. This is a direct measure of the nonpotentiality of the magnetic field. Figure 1 illustrates in what manner the electric currents in the solar atmosphere induce "shear" in the observed photospheric field along the neutral line.

Analysis of shear mapped along the neutral line and correlated with flares has resulted in suggested "threshold" values for the shear  $(\Delta\phi)$  of  $\approx 80^{\circ}$  along the interval of the neutral line where the transverse field is strongest  $(>\frac{1}{2}(B_t)_{max})$  (Hagyard, Venkatakrishnan, and Smith 1990). The total length of this sheared region is important in determining the  $\Delta\phi$  threshold value for a flare (Hagyard 1990). A summary of a shear analysis for a number of active regions is given in Table 1 where the total length of the shear region along the neutral line is  $> 10^4$  km. Quick assessment of the active region sheared field is now routinely done with computer codes which allows maps of magnetic shear to be generated at the time of the observations using an online MicroVax 3500 and an array processor.

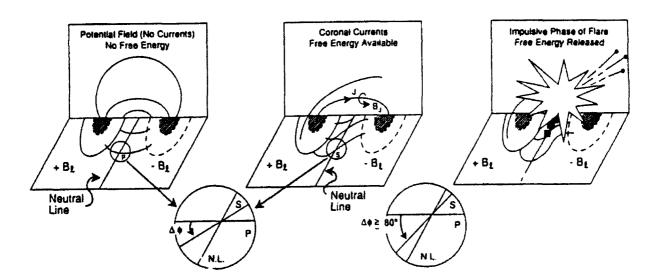
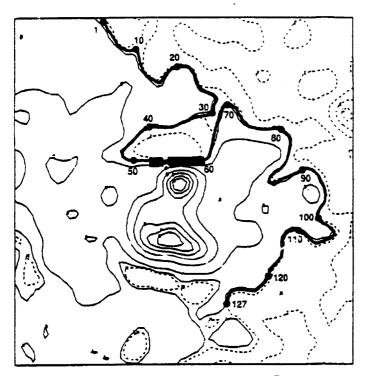


Fig.-1. Illustration of angular magnetic shear,  $\Delta\phi$ , and its role as a flare precursor. Atmospheric electric currents, J, build up, producing a change in the direction of the transverse field vectors along the neutral line. The free energy that is then contained in the magnetic field is released when the shear angle is large. The circular insert shows the transverse field direction of a shear field (S) with the corresponding potential field direction (P) along the neutral line (N.L.). When  $\Delta\phi \geq 80$  there is a high probability of a flare at this site.

Analysis of shear for the recent flare of 1989 October 15 is shown in Figure 2. The image from the  $H\alpha$  telescope is shown in Figure 2b with the neutral line. The shear mapped along the neutral line shows where the shear "threshold" values ( $\blacksquare$ 's) are exceeded and at this position the flare straddles the neutral line.



b. Flare in Ha

a. Magnetic Shear Map

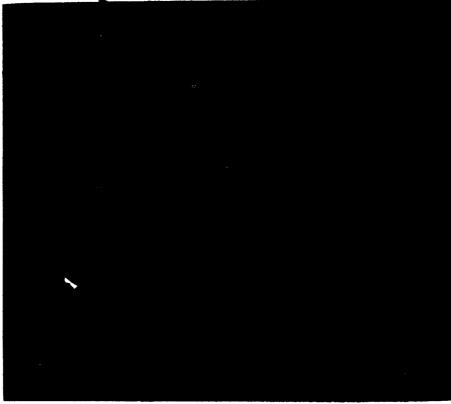


Fig. 2.-MSFC shear map (a) and Ha flare image (b). Active region AR 5740 observed on 1989 October 15. In Figure 2a the main neutral line is shown as a bold line on the contours of the line-of-sight magnetic field. Areas along the magnetic neutral line where the magnetic field is strongly nonpotential are marked by with the flare emission brackets this area of the neutral line.

68 G. A. Gary et al.

The large shear is a flare precursor because a nonpotential configuration is necessary for a pre-flare state. We believe that a further detailed analysis of the "threshold" values of the shear will lead to a better understanding of the conditions necessary for a flare.

Date	AR	Maximum Δφ	B <sub>T</sub>	No. pixels with $\Delta \phi \geq 70^{\circ}$ and $B_T \geq \frac{1}{2}B_T^{n_2}$	Flare class
April 1980	2372	85°	1005 G	8	1B/X2 1B/M4
Nov. 1980	2776	88°	1035 G	8	1B/M2 1B/M4
April 1984	4474	90°	1725 G	15	3B/X13
Feb. 1986	4711	90°	1105 G	11	1B/M2
Oct. 1989	5740	90°	700 G	7	1N/M1
Nov. 1989	5776	88°	870 G	10	1B/M9
Feb. 1990	5947	89°	700 G	9	SF/C4

TABLE 1. Summary of Nonpotential Characteristics at Flare Sites

#### III. FILAMENT FIELDS AND COALIGNED IMAGES

The importance of having coaligned co-temporal vector magnetograms and H $\alpha$  ("chromospheric magnetograms") is borne out from the observations of a filament on 1990 June 12. Shown in Figure 3 are the MSFC magnetographic and H $\alpha$  observations at  $\approx$  1630 UT, at the end of a C1 sub-flare which started at 1522 UT. The analysis shows the configuration of the H $\alpha$  filament going hand in hand with the magnetic structure of this active region. A portion (A) of the filamentary feature was observed to run parallel to the measured transverse field. The transverse field is dominated by the normal field component and hence shows the distinctive limb directed orientation. The region is centered around N54 E79. Further analysis of the sheared region (A) using heliographic transformations (Gary and Hagyard 1990) is needed due to the large distance from disk center, but coaligned H $\alpha$  images do allow analysis of magnetic field associated filaments. The H $\alpha$  images, in general, provide the location and the means to establish magnetic fields of features not seen in the magnetograph intensity maps.

The phenomena associated with flare and pre-flare activity must be studied, under a synergistic approach, for it is clear there are a multitude of interacting areas of research (e.g., sunspot morphology, current-carrying field topology, evolution of emerging fields, kinematics of photospheric bulk motion, pre-flare heating, and flux tube interaction). H $\alpha$  imagery has added greatly to the MSFC magnetograph operation studying such interconnecting phenomena by providing locations of H $\alpha$  features and analysis of various phenomena, such as the surge analysis given in the next section.

#### IV. FIELDS ASSOCIATED WITH AN Ha SURGE

A sub-flare and associated surge of AR 6100 on 1990 June 13 was observed with the H $\alpha$  telescope. A series of H $\alpha$  observations on June 13 are shown in Figure 4c: 1514 UT (A), 1636 UT (B), 1638 UT (C), 1643 UT (D), 1646 UT (E), and 2033 UT (F). A sub-flare occurred at 1636 UT and the associated surge was observed at 1643 UT. An analysis of the associated magnetograms is being performed. The photospheric magnetic field associated with the surge changed from June 12 to June 13. The enlargements of the transverse field (Figs. 4a and 4b) show a change from a nearly potential field to a strongly nonpotential field with the shear on the neutral line  $\Delta\phi\approx90^{\circ}$ . While the reconfiguration was rather subtle, its coincidence with the dynamic events that took place has stimulated further analysis of this event. This particular event proves the importance of coaligned H $\alpha$  images and the increase desire to improve the polarimetric resolution of existing magnetographs.

The expected uncertainties for the transverse field strength  $\delta B_t$  and for the azimuth of the transverse field  $\delta \phi$  are given by :

$$\delta B_t = \frac{1}{2}B_t^0(B_t^0/B_t)$$
 and  $\delta \phi = \frac{1}{2}(B_t^0/B_t)^2$ ,

c.

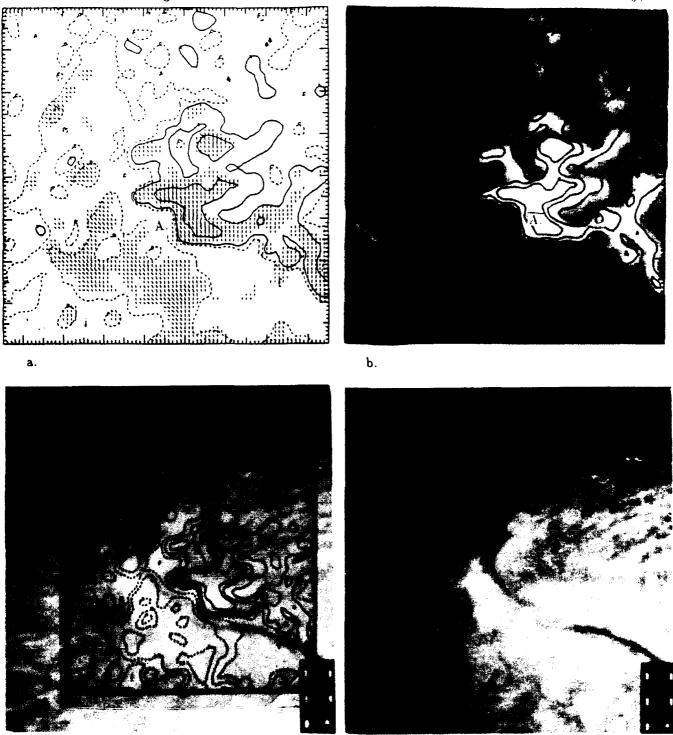


Fig. 3.-Coaligned, high-latitude H $\alpha$  filament image with the MSFC vector magnetogram. The longitudinal magnetic field of the filament is shown in Figure 3a as contours and with the transverse field shown as line segments. The gray scale of longitudinal field is shown Figure 3b with the longitudinal contours. In Figure 3c the longitudinal contours are shown overlaid on the H $\alpha$  filament shown in Figure 3d. The filament is shown overlying the neutral line. In region A the transverse field is parallel to the neutral line. The near-limb projection effect is apparent in the transverse field directions and needs to be considered in order to determine the extent of the sheared field in region A.

d.

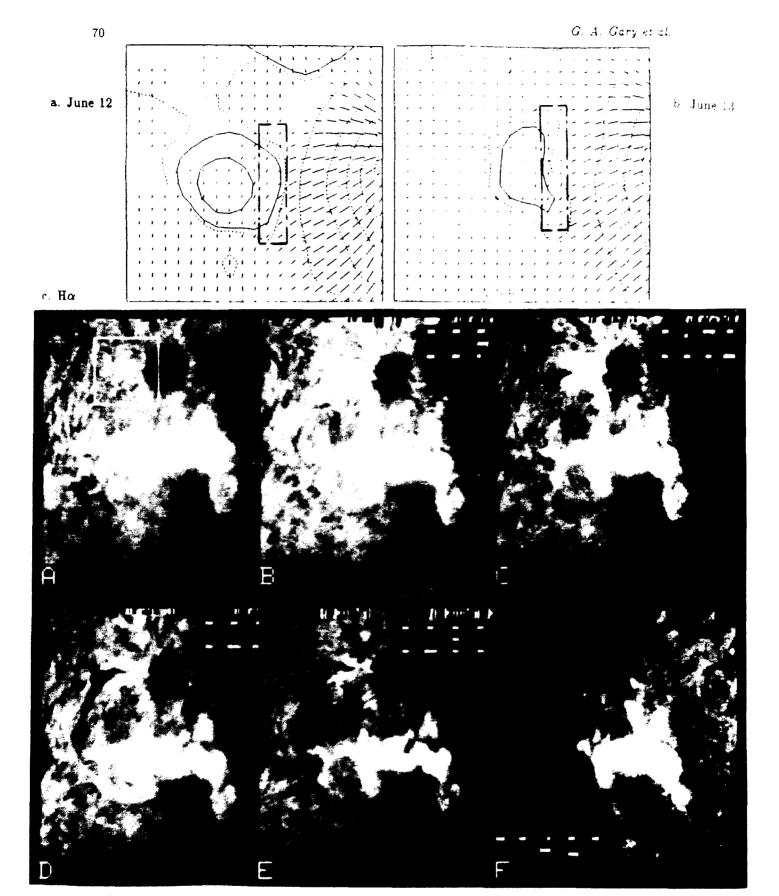


Fig. 4.-Development of shear at a site of a sub-flare and surge. Figure 4a and 4b shows enlargements of the magnetogram for the area marked by a box in the  $H\alpha$  image. The 1990 June 12 magnetogram (a) indicates that the transverse field is nearly potential. The corresponding enlargement (b) for June 13 shows that the transverse field direction alone the neutral line had rotated almost  $90^\circ$  to a sheared configuration. The dot-dashed rectangle areas indicated regions of interest. Associated with the nonpotential configuration was a series of dynamical effects seen in  $H\alpha$ , as shown in Figure 4c.

where  $B_t^0$  is the instrumental sensitivity (Hagyard, Gary, and West 1988). Hence, for  $B_t \approx 150$  G, the uncertainties are  $\delta B_t = 52$  G and  $\delta \phi = 20^\circ$ . Hence, this nonpotential field reconfiguration can be recognized above noise level of the background field. However, improvements in the sensitivity of the magnetograph are needed to detect small changes in the field.

#### V. CONCLUDING REMARKS

The polarimetric resolution, discussed above, and the general results of the magnetograph depend on the photometric conversion method. The functional relationships between the corrected bandpass integrated fractional polarizations  $(P_V, P_Q)$  and the magnetic field components  $(B_l, B_t)$  can be derived using the solutions of Kjeldseth Moe (1968) to the radiative equations in the weak field approximation. In the linear form these are given by:

$$B_i = c_1 k P_V$$
 and  $B_i = c_2 [k P_Q]^{1/2}$ , where  $P_V = \overline{V}_{\tau=0} / \overline{I}_{\tau=0}$  and  $P_Q = \overline{Q}_{\tau=0} / \overline{I}_{\tau=0}$ ,

where the constants  $c_1$  and  $c_2$  are dependent on the solar atmospheric models used. The bar over the Stokes parameters I, U, and V indicates the average over the filter profile with  $\tau=0$  indicating the exiting state of polarization for the solar atmosphere. The detailed nonlinear results using the Kjeldseth-Moe analysis can be found in Hagyard, Gary, and West (1988). The k-factor is a correction factor for internal instrumental depolarization and corrects for the difference between the MSFC field magnitude and the Mount Wilson sunspot data. The MSFC correlation between the polarimetric values and the derived magnetic field measurements currently uses the nonlinear equations. However, model-independent conversion relations can be derived using the filter magnetograph in a Stokes mode of operation (Balasubramaniam and West 1990; Balasubramaniam, Hagyard, and West 1990).

These linear conversion relations given above also show what is to be expected from the polarimetry of a space-borne magnetograph. Using the West polarimeter design (West 1985), the degree of polarization can improved from the  $10^{-3}$  range for ground-based observation to  $10^{-4}$  range or below for space-borne instruments. For typical values of  $c_1$ ,  $c_2$ , and k (4500, 3300, and 4), the space-borne instrument can improve the magnetic field resolution from 5 and 125 G, for the longitudinal and transverse fields, respectively, to 0.2 and 15 G for a space-borne magnetograph. In addition to the high-polarimetric accuracy, a wide field of view (e.g., 4x8 arcmin) is necessary in order to: (1) calculate the total energy, (2) determine total field and topology, (3) capture the flare sites and associated activity, (4) measure total flux change in the active region, and (5) delete the problem of rastering a number of smaller fields of view. The need for a wide field of view is often overlooked in considering a space-borne magnetograph (Hagyard, Gary and West 1988). An instrument needs at least a 4x8 arcmin field of view to contain 90% of all bipolar active regions (Tang, Howard, and Adkins 1984). A large field of view is critical for research programs, such as the one presented above, where the total active region or a large prominence needs to be studied.

#### **ACKNOWLEDGEMENTS**

This work was supported by NASA through its Office of Solar and Heliospheric Physics and by the MSFC under the Center Director's Discretionary Fund Project.

#### REFERENCES

Adams, M., Moore, R. L., Gary, G. A., and Hagyard, M. J. 1990, "Three-Dimensional Structure of Penumbral Magnetic Fields," in preparation.

Balasubramaniam, K.S., and West, E. A. 1990, "Polarization Studies of Zeeman Affected Spectral Lines Using the MSFC Magnetograph" SPIE Conference on Polarimetry-Visible, Infrared, Ultraviolet, and X-Rays, San Diego, CA.

Balasubramaniam, K.S., Hagyard, M. J., and West, E. A. 1990, "Stokes Profile Analysis of a Sunspot Using the MSFC Magnetograph," in these proceedings.

Chiuderi Drago, F., Alissandrakis, C., and Hagyard, M. J. 1987, "Microwave Radio Emission Above Steady and Moving Sunspots," Solar Phys., 112, 89.

72 G. A. Gary et al.

deLoach, A. C., Hagyard, M. J., Rabin, D., Moore, R. L., Smith, J. B., West, E. A., and Tandberg-Hanssen, E. 1984, "Photospheric Electric Current and Transition Region Brightness within an Active Region," Solar Phys., 91, 235.

- Ding, Y. J., Hong, Q. F., Hagyard, M. J., and deLoach, A. C. 1985, "Inferred Flows of Electric Currents in Solar Active Regions," in Measurements of Solar Vector Magnetic Fields, ed. M. J. Hagyard, NASA CP-2374, p. 379.
- Ding, Y. J., Hagyard, M. J., deLoach, A. C., Hong, Q. F. and Liu, X. P. 1987, "Explorations of Electric Current Systems in Solar Active Regions. I. Empirical Inferences of the Current Flows," Solar Phys., 109, 307.
- Gary, G. A. 1989, "Linear Force-Free Magnetic Fields for Solar Extrapolation and Interpretation," Ap. J. Suppl., 69, 323.
- Gary, G. A., and Hagyard, M. J. 1990, "Transformation of Vector Magnetograms and the Problems Associated with the Effects of Perspective and the Azimuthal Ambiguity," Solar Phys., 126, 21.
- Gary, G. A., Moore, R. L., Hagyard, M. J., and Haisch, B. M. 1987, "Non-Potential Features Observed in the Magnetic Field of an Active Region," Ap. J., 314, 786.
- Hagyard, M. J. 1984, "Studies of Solar Magnetic Fields during the Solar Maximum Year," NASA TM-86469 (1984).
  Hagyard, M. J. 1987, "The Relation of Sheared Magnetic Fields to the Occurrence of Flares," Artificial Satellites, 22, 69.
- Hagyard, M. J. 1988, "Observed Nonpotential Magnetic Fields and the Inferred Flow of Electric Currents at a Location of Repeated Flaring," Solar Phys., 115, 107.
- Hagyard, M. J. 1990, "The Significance of Vector Magnetic Field Measurements," Memorie della Societa Astronomica Italiana, in press.
- Hagyard, M. J., and Teuber, D. 1978, "Comparisons of Measured and Calculated Potential Magnetic Fields," Solar Phys., 57, 267.
- Hagyard, M. J. and Rabin, D. M. 1986, "The Measurement and Interpretation of Magnetic Shear in Solar Active Regions," Adv. Space Res., 6(6), 7.
- Hagyard ,M. J., and Smith, J. B. 1988, "Flare Onset at Sites of Maximum Magnetic Shear," Bull. AAS, 20(2), 711.
   Hagyard, M. J., West, E. A., and Cumings, N. P. 1977, "The Spiral Configuration of Sunspot Magnetic Fields," Solar Phys., 53, 3.
- Hagyard, M. J., Moore, R. L., and Emslie, A. G. 1984, "The Role of Magnetic Field Shear in Solar Flares." Adv. Space Res., 4, 71.
- Hagyard, M. J., West, E. A., and Smith, J. B. 1985, "Electric Currents in Active Regions," in Proc. of Kunming Workshop on Solar Physics and Interplanetary Travelling Phenomena, ed. C. DeJager and Chen Biao (Beijing: Science Press), p. 179.
- Hagyard, M. J., Cumings, N. P., and West, E. A. 1985, "The New MSFC Solar Vector Magnetograph." in Proc. of Kunming Workshop on Solar Physics and Interplanetary Travelling Phenomena, ed. C. DeJager and Chen Biao (Beijing: Science Press), p. 1216.
- Hagyard, M. J., Gary, G. A., and West, E. A. 1988, "The SAMEX Vector Magnetograph: A Design Study for a Space-Based Solar Vector Magnetograph," NASA TM-4048.
- Hagyard, M. J., Venkatakrishnan, P., and Smith, J. B., Jr. 1990, "Nonpotential Magnetic Fields at Sites of Gamma-Ray Flares," Ap. J. Suppl., 73, 159.
- Hagyard, M. J., Cumings, N. P., West, E. A., and Smith, J. E. 1982, "The MSFC Vector Magnetograph," Solar Phys., 80, 33.
- Hagyard, M. J., Smith, J. B., Teuber, D., and West, E. A. 1984, "A Quantitative Study Relating Observed Shear in Photospheric Magnetic Fields to Repeated Flaring," Solar Phys., 91, 115.
- Hagyard, M. J., Teuber, D., West, E. A., Tandberg-Hanssen, E., and Henze, W. 1985 "The Vertical Gradient of Sunspot Magnetic Fields," in *Proc. of Kunming Workshop on Solar Physics and Interplanetary Travelling Phenomena*, ed. C. DeJager and Chen Biao (Beijing: Science Press), p. 204.
- Hagyard, M. J., West, E. A., Tandberg-Hanssen, E., Smith, J. E., Henze, W., Beckers, J. M., Bruner, E. C., Hyder, C. L., Gurman, J. B., Shine, R. A., and Woodgate, B. E. 1981, "The Photospheric Vector Magnetic Field of a Sunspot and Its Vertical Gradient," in *Physics of Sunspots*, ed. L. Cram and J. Thomas, Sacramento Peak Observatory, p. 213.
- Hagyard, M. J., Teuber, D., West, E. A., Tandberg-Hanssen, E., Henze, W., Beckers, J. M., Bruner, M., Hyder, C. L., and Woodgate, B. E. 1983, "Vertical Gradients of Sunspot Magnetic Fields," Solar Phys., 84, 13.
- Hagyard, M. J., Gaizauskas, V., Chapman, G. A., deLoach, A. C., Gary, G. A., Jones, H. P., Martres, M. J., Porter, J. G., Schmieder, B., Smith, J. B., and Toomre, J. 1986, "Preflare Magnetic and Velocity Fields," in *Energetic Phenomena on the Sun*, ed. M. Kundu and B. Woodgate, NASA CP-2439, p. I-16.
- Haisch, B. M., Bruner, M. E., Hagyard, M. J., and Bonnet, R. M. 1986, "A Comparison of Photospheric Electric Current and Ultraviolet and X-Ray Emission in an Active Region," Ap. J., 300, 428.

- Haisch, B. M., Strong, K. T., Harrison, R. A., and Gary, G. A. 1988, "Active Region Coronal Loops: Structure and Variability," Ap. J. Suppl., 68, 371.
- Henze, W., Tandberg-Hanssen, E., Hagyard, M. J., Woodgate, B. E., Shine, R. A., Beckers, J. M., Bruner, M., Gurman, J. B., Hyder, C. L., and West E. A. 1982, "Observations of the Longitudinal Magnetic Field in the Transition Region and Photosphere of a Sunspot," Solar Phys., 81, 231.
- Kjeldseth Moe, O. 1968, "A Generalized Theory for Line Formation in a Homogeneous Magnetic Field," Solar Phys., 4, 267.
- Krall, K. R., Smith, J. B., Hagyard, M. J., West, E. A., and Cumings, N. P. 1982, "Vector Magnetic Field Evolution and Associated Photospheric Velocity Shear Within a Flare-Productive Active Region," Solar Phys., 79, 59.
- Lin ,Y. and Gaizauskas, V. 1987, "Coincidence Between Hα Flare Kernels and Peaks of Observed Longitudinal Electric Current Densities," Solar Phys., 109, 81.
- Machado, M. E., and Moore, R. L. 1986, "Observed Form and Action of the Magnetic Energy Release in Flares." Adv. Space Res., 6 (6), 217.
- Machado, M. E., Gary, G. A., Hagyard, M. J., Smith, J. B., Hernandez, A., and Rovira, M. G. 1986, "Characteristics, Location and Origin of Flare Activity in a Complex Active Region," Adv. Space Res., 6 (6), 33.
- Machado, M.E., Moore, R. L., Hernandez, A. M., Rovira, M. G., Hagyard, M. J., and Smith, J. B., Jr. 1988, "The Observed Characteristics of Flare Energy Release. I. Magnetic Structure at the Energy Release Site," Ap. J., 326, 425.
- Markey, J. F., and Austin, R. R. 1977, "High Resolution Solar Observations: The Hydrogen-Alpha Telescope on Skylab," Appl. Opt., 16, 917.
- Moore, R. L., Hagyard, M. J., and Davis, J. M. 1987, "Flare Research with the MSFC Vector Magnetograph: Observed Characteristics of Sheared Fields that Produce Flares," Solar Phys., 113, 347.
- Neidig, D. N., Smith, J. B., Hagyard, M. J., and Machado, M. E. 1986, "Flare Activity, Sunspot Motions and the Evolution of Vector Magnetic Fields in Hale Region 17244," Adv. Space Res., 6(6), 25.
- Patty, S. R. 1981, "Analysis of the Vector Magnetic Fields of Complex Sunspots," in *Physics of Sunspots*, ed. L. Cram and J. Thomas, Sacramento Peak Observatory, p. 64.
- Patty, S. R., and Hagyard, M. J. 1986, "Delta Configurations: Flare Activity and Magnetic Field Structure," Solar Phys., 103, 111.
- Rabin, D. M., Moore, R. L., and Hagyard, M. J. 1984, "A Case for Submergence of Magnetic Flux in a Solar Active Region," Ap. J., 287, 404.
- Rabin, D. M., Moore, R. L., and Hagyard, M. J. 1985, "Evidence for Submergence of Magnetic Flux in a Growing Active Region," in Measurements of Solar Vector Magnetic Fields, ed. M. J. Hagyard, NASA CP-2374, p. 437.
- Schmahl, E. J., Kunde, M. R., Strong, K. T., Bentley, R. D., Smith, J. B., and Krall, K. R. 1982, "Active Region Magnetic Fields Inferred from Simultaneous VLA Microwave Maps, X-Ray Spectroheliograms and Magnetograms," Solar Phys., 80, 233.
- Solanki, S., Keller, C., and Stenflo, J. O. 1987, "Properties of Solar Magnetic Flux Tubes from Only Two Spectral Lines," Astr. Ap., 188, 183.
- Strong, K. T., Benz, A. O., Dennis, B. R., Leibacher, J. W., Mewe, R., Poland, A. I., Schrijver, J., Simnett, G., Smith, J. B., and Sylwester, J. 1984a, "A Multiwavelength Study of a Double Impulsive Flare," Solar Phys., 91, 325.
- Strong, K. T., Smith, J. B., Jr., McCabe, M. K., Machado, M. E., Saba, J. L. R., and Simnett, G. M. 1984b, "Homologous Flares and the Evolution of NOAA Active Region 2372," Adv. Space Res., 4(7), 23.
- Tang, F., Howard, R., and Adkins, J.M. 1984, "A Statistical Study of Active Regions 1967-1981," Solar Phys., 91, 75.
- Teuber, D., Tandberg-Hanssen, E., and Hagyard, M. J. 1977, "Computer Solutions for Studying Correlations between Solar Magnetic Fields and Skylab X-Ray Observations," Solar Phys., 53, 97.
- Venkatakrishnan, P., Hagyard, M. J., and Hathaway, D. H. 1989, "Evaluation of Magnetic Shear in Off-Disk Center Active Regions," Solar Phys., 122, 215.
- West, E. A. 1985, "Analysis of the New Polarimeter for the Marshall Space Flight Center Vector Magnetograph," in Measurements of Solar Vector Magnetic Fields, ed. M. J. Hagyard, NASA CP-2374, p. 160.
- West, E. A., and Hagyard, M. J. 1983, "Interpretation of Vector Magnetograph Data Including Magneto-Optic Effects: I. Azimuth Angle of the Transverse Field," Solar Phys., 88, 51.

#### **VECTOR MAGNETOGRAPHY**

David M. Rust and John W. O'Byrne\*

The Johns Hopkins University Applied Physics Laboratory Laurel, Maryland 20723

Summary: Development of the JHU/APL vector magnetograph (VMG) at the National Solar Observatory gives insight into the advantages and drawbacks of trying to infer solar active region magnetic fields from filtergram measurements with 0.8 - 3.0 arcsec spatial resolution, several-minute temporal resolution and 120 - 180 mÅ spectral resolution. The use of a narrow-band filter and the weak-field approximation (WFA) of the Stokes profiles gives good temporal and spatial data on magnetic fields, but sacrifices information on the thermodynamic parameters. A model of the VMG's response in the wings of the Ca I line at 6122 Å shows that the range of validity of the WFA can be extended to 4000 G. It also shows that the response of the VMG is insensitive to the Doppler shifts due to the motions (< 1 km/s) exhibited by most solar features. The role of vector magnetography with a narrow-band filter in flare research is emphasized and several examples of early observations with the VMG are given.

#### 1. Introduction

To understand the origins of solar flares in magnetic fields is one of the most difficult challenges in astrophysics today. Although a great deal of progress was made during the past decade in characterizing flare emissions and emission processes (e.g., Chupp, 1990), almost no progress was made towards understanding the association between flares and magnetic fields. That flares draw their energy from magnetic fields has been known for about half a century. There is no other plausible energy source. That some sort of explosive instability is involved is widely accepted. It has been the impetus for a substantial body of theoretical work (Priest, 1981). But, observations with the spatial and temporal resolution and the polarization sensitivity needed to bring new insight into flare research have rarely been obtained. The basic problem was dramatically limned by Harvey (1985) at the last major polarimetry workshop. His list of requirements for ideal Zeeman-effect observations is shown in Table 1. The production of such observations will require a meter-class telescope, 0.05 arcsec spatial samples, 20 mÅ spectral resolution, a 10-s frame rate, and at least a Gigabyte/s data rate.

Existing vector magnetographs fall far short of the ideal since they rely on 0.25 m telescopes, 0.5 - 5.0 arcsec spatial samples, 120 - 250 mÅ spectral resolution and 20 s - 1000 s frame rates. Nevertheless, sufficiently promising results have been obtained with such instruments, by the Huntsville group in particular, that new magnetographs are under construction in Hawaii, Beijing, and Huntsville, and a new vector magnetograph has just been installed here at Sacramento Peak. The new instruments, as well as established instruments in Okayama, Irkutsk, Huntsville, and Big Bear Lake aim to man vector fields on time scales appropriate for flare research, hence they all attempt vector magnetography, the art of learning important physics from imperfect measurements. This is to be distinguished from Stokes polarimetry, which is characterized by an emphasis on high spectral and polarimetric precision and by the use of a spectrograph rather than a filter for spectral discrimination. There is generally a sacrifice of spatial and

<sup>\*</sup> Present address: School of Physics, University of Sydney, N. S. W. 2006, Australia

temporal resolution in Stokes polarimetry compared to vector magnetography, where spatial resolution of 0.5 arcsec can possibly be realized and where the temporal resolution over a field of view large enough for effective flare research may approach Harvey's 10-s ideal. Not until a meter-class telescope is flown in space or under a balloon will a vector magnetograph simultaneously achieve 0.1-arcsec spatial resolution with a 10-s frame rate, although the proposed Large Earth-Based Solar Telescope (Stenflo, 1989) and the THEMIS (Mein, 1989) telescope on the Canary Islands will represent major advances toward the goals of Table 1.

Table 1. Requirements for observation of  $I(x,y,\lambda,t)$ .

Parameter	Element	Ratio: ale	Number	Rationale	Implication
$\begin{array}{c} \text{Angular} \\ (z,y) \end{array}$	0.05 arc sec	scale heigh: in photosphere	4000x3000	cover an active region	>1m aperture telescope
Spectral (λ)	0.02Å @ 6000Å	resolve spectral structure	20 per line × 6 lines	cover a line cover a height range	large wavelength range spectrometer
Temporal (t)	10 sec	sound travel time across Δz or Δy	1	resolve oscillations and activity of active region	high data rate
Sensitivity for I, Q/I, U/I, V/I	~10 <sup>-4</sup>	define B adoquately	~10 <sup>4</sup> or 2 bytes	adequate dynamic range	very high data rate

At The Johns Hopkins University, our objective is to try to infer enough information from vector magnetograms at 1 - 3 arcsec resolution to give useful physical insight into the structure and evolution of the magnetic fields in active regions. Flux emergence, flux cancellation and regions with sheared magnetic fields need to be better understood if we are to make any progress in understanding solar flares. A central problem is how to identify the build-up of energy in an active region. Are sheared magnetic fields the reservoirs of flare energy? And how are strong horizontal fields outside a normal penumbra to be understood? Vector magnetograph observations should help answer these questions, even though the available instruments do not have sufficient spatial resolution to resolve the finest solar magnetic features.

Early detection of the structure of emerging or stressed magnetic fields might give several hours notice of a major flare and great insight into its physical nature. The new vector magnetographs are all to be located at sites with plenty of clear weather, although variable and sometimes quite poor seeing conditions will remain  $\varepsilon$  problem. Long runs with a vector magnetograph can be used to try to locate stored magnetic energy in active regions before and after a flare. This has been attempted in a few cases, with considerable uncertainties (e.g., Rust and Bar, 1973; Tanaka and Nakagawa, 1973; Rust, Nakagawa and Neupert, 1975; Krall et al., 1982; Sakurai, 1987; Yang, Hong and Ding, 1988). In most published studies, only line-of-sight photospheric magnetic field data were available. Now, the accuracy of basic magnetic energy accounting can be increased by including the transverse field components.



Figure 1. The APL Solar Vector Magnetograph on the spar in the Hilltop Dome, Sacramento Peak Observatory, Sunspot, New Mexico. The upper part is the evacuated 25-cm Cassegrain telescope. The lower part is the magnetograph optics housing.

In this paper, we describe the JHU/APL vector magnetograph, including the calibration technique, and then discuss how the data can be interpreted in physical terms and how some of the limitations traditionally associated with vector magnetography can be overcome. Finally, observations of two active regions are discussed.

#### 2. Instrumentation

The JHU/APL vector magnetograph (VMG), shown in Figure 1, is installed in the Hilltop Dome at the National Solar Observatory at Sacramento Peak, for the joint use of APL, Air Force Geophysics Lab and National Solar Observatory staff. First light was achieved in May, 1989, and the VMG began production of vector magnetograms in October. The instrument was described in detail at the Tenth Sacramento Peak Workshop (Rust and O'Byrne, 1989).

# 3. Polarization Measurement Technique

In order to achieve useful sensitivity in a vector magnetograph, instrumental polarization should be below  $10^{-3}$  or even  $10^{-4}$ . In the APL/JHU instrument, polarization-producing reflections are avoided by using a straight-through optical train from the telescope, which is a 25-cm Ritchey-Crétien reflector. Because of the radial symmetry of the telescope and the small, 2.4 x 3.6 arcmin, field of view, polarization aberration should be less than  $10^{-3}$ . Measurements are planned to establish the actual level of polarization aberration.

The polarization analyzer itself (Figure 2) was designed to eliminate crosstalk between the relatively strong line-of-sight magnetic field signal, which is encoded in circularly polarized light, and the much weaker transverse field signal, encoded in the linearly polarized component. The major potential source of circular-to-linear crosstalk is avoided by removing the quarterwave plate from the beam when the linear measurements are made. The linear measurements are made with a Glan-Taylor prism, whose polarization purity is better than  $10^5$ :1. It has no residual retardation. However, the prism causes  $\sim 2$  arcmin of beam deviation, which could produce spurious polarization signals. Two optical wedges, mated to the prism as shown in Figure 2, reduce the beam deviation to < 2 arcsec. The image motion compensator described below removes this residual deviation. A second quarterwave plate converts the beam polarization state

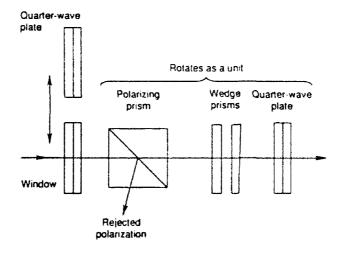


Figure 2. VMG polarization analyzer assembly. The window moves into the beam for linear polarization measurements; the first quarter-wave plate replaces it in the beam for circular polarization measurements.

to circular. This step minimizes intensity variations at the down-stream folding mirrors when the prism rotates. The time required to change the prism angle is  $\sim 300$  ms. The prism zero is automatically checked and reset, if necessary, to within  $0.3^{\circ}$  of the waveplate optic axis at the beginning of each observing session. An error in prism orientation even of this small degree would produce a serious error in the linear

polarization measurements due to crosstalk from the circular component if the quarterwave plate were simply rotated and not removed from the beam for the linear measurements.

Vector magnetic fields are derived from images obtained at six sequential settings of the prism and V aveplate:  $0^{\circ}$ ,  $90^{\circ}$ ,  $45^{\circ}$  and  $135^{\circ}$ , with the waveplate out, and  $0^{\circ}$  and  $90^{\circ}$ , with the waveplate in. Thus, the images correspond to measurements of I+Q, I-Q, I+U, I-U, I+V and I-V. They are obtained at a rate of about 30 images/min. Up to 50 six-image sequences are taken for each vector magnetogram. The scheme has the disadvantage that the seeing will vary from image to image, and in the VMG, one may expect some crosstalk into Q, U, and V from I. Estimating the effect of the crosstalk is difficult because it depends on the spatial gradients in I and on the quality of the seeing. No detailed study of the tolerable levels of crosstalk in filter magnetograms has been undertaken, and the approach used in practice is to examine successive magnetograms for consistency. Seeing effects could be alleviated by use of a beamsplitter (e.g., Rust and Keil, 1991; Lites and Skumanich, 1989) or by a fast modulation technique such as the one described by Povel (1991), or by observing from a platform outside the atmosphere. These alternatives have yet to be implemented in vector magnetography.

The deleterious effects of poor seeing can be further alleviated with the image motion compensator (IMC) described by Strohbehn (1990). The IMC in the VMG stores a  $32 \times 32$ -pixel image from a 6-arcsec segment of a reference image, and each subsequent image is cross-correlated against it. An offset is thus established for each image. Offsets may be due to seeing, prism rotation, or tracking errors. The IMC tilts a relay mirror as necessary to remove each offset. The bandwidth of the IMC is  $\sim 80 \text{ Hz}$ , which is sufficient to remove most translational motion. Of course, defocus and scintillation will still degrade the images. Our IMC is derived from the fast Fourier transform IMC developed recently at the National Solar Observatory (Rimmele and von der Lühe, 1989).

# 4. Spectral Selection Technique

In order to provide the VMG with a large-aperture, narrow-band filter that can eventually be used in a balloon-borne instrument or in space, JHU/APL and the Division of Applied Physics at the Commonwealth Scientific and Industrial Research Organization (CSIRO) in Australia developed a lithium niobate (LiNbO<sub>3</sub>) Fabry-Perot etalon (Burton, Leistner and Rust, 1987). It has a spectral bandwidth of 167 mÅ and 50% peak transmission. The etalon is made from a 75-mm diameter wafer of crystalline, Z-cut lithium niobate polished to a thickness of 220 µm and 1/400<sup>th</sup> wave rms flatness. The finesse, i.e., the ratio of free spectral range to passband width, is 21, and the contrast between transmission at the peak and at the minima between peaks is 180. Dielectric coatings on the surfaces are 93% reflecting over a 6000 - 8000 Å band. Figure 3 shows the comb profile of the etalon.

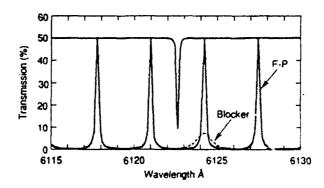


Figure 3. Comb spectrum of the Fabry-Perot etalon. For clarity, the etalon and the blocker (dashed line) are drawn as though tuned ~ 2 Å redward of the Ca I line at 6122.2 Å. Peak transmission of the etalon is 50%; peak transmission of the 1.1 Å blocker is 7%. (A 28% transmitting blocker was installed recently.)

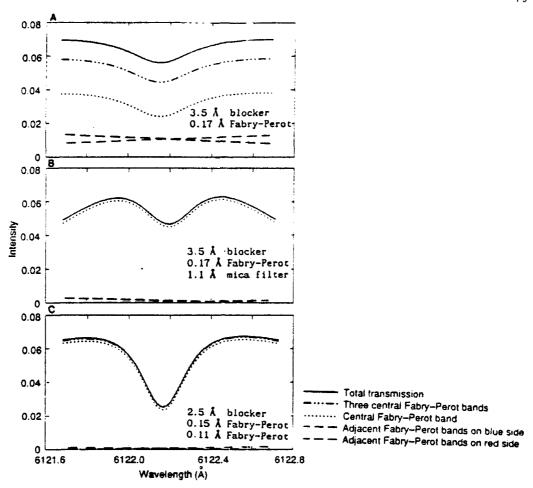


Figure 4. (a) Comparison of 6122 Å line profiles after passage through the 0.17 Å F-P filter and a 3.5-Å blocking filter; (b) profile with the 1.1 Å cleaved mica blocker as predicted and measured, and (c) expected profile with two lithium niobate filters in series with a 2.5 Å blocker.

The refractive index of lithium niobate changes upon application of an electric field. Thus, voltage applied across a conductive indium tin oxide layer on the etalon faces will change the optical length of the resonant cavity and allow passband tuning. The tuning constant is 0.4 mÅ/volt. The thermal tuning constant is 32 mÅ/ $^{\circ}$ C. The temperature of the etalon in the VMG is controlled to within  $\pm$  0.1 $^{\circ}$  C, and the voltage is controlled to < 1 volt, so the tuned, relative passband wavelength is known to  $\pm$  4 mÅ. VMG measurements are not sensitive to <  $\pm$  20 mÅ errors in placement of the passband (Sect. 5).

While the etalon has performed well, we had considerable difficulty finding a filter to block the unwanted Fabry-Perot orders. The best commercial thin-film blockers have too broad a profile at full aperture to suppress the adjacent passbands, which are at  $\pm$  3.25 Å. The VMG now incorporates a 1 Å Daystar<sup>TM</sup> mica etalon. Figure 4(a) shows the washed-out profile of the magnetically-sensitive Ca I line at 6122.2 Å (Landé g factor = 1.75) before we replaced a 3.5 Å thin-film blocker by the mica etalon. Figure 4(b) shows the profile in the instrument as now configured.

Eventually, we hope to further improve the definition of the profile by using two LiNbO<sub>3</sub> etalons. Hernandez (1986) predicts that two nearly identical etalons operated in series will have a combined passband 38% narrower than that for one etalon. Our preliminary measurements of two etalons in series showed a passband reduction of 30%, i.e., to 120 mÅ. The predicted effect of using two etalons on the Ca I line can be seen in Figure 4(c). We estimate the present sensitivity threshold of the VMG at 400

Gauss for transverse fields and 60 G for longitudinal fields. The sensitivity should improve by a factor of two when the two-etalon scheme is implemented.

# 5. Magnetographic Response

The output signal from a vector magnetograph is usually a series of measurements of the Stokes polarization vectors at several wavelengths in an absorption line. In relating these measurements to the magnetic fields on the Sun, one must consider how the line radiation is formed and how ideal measurements are degraded by the limited spectral resolution of a filter magnetograph. Poor seeing also degrades the measurements (Lites 1987).

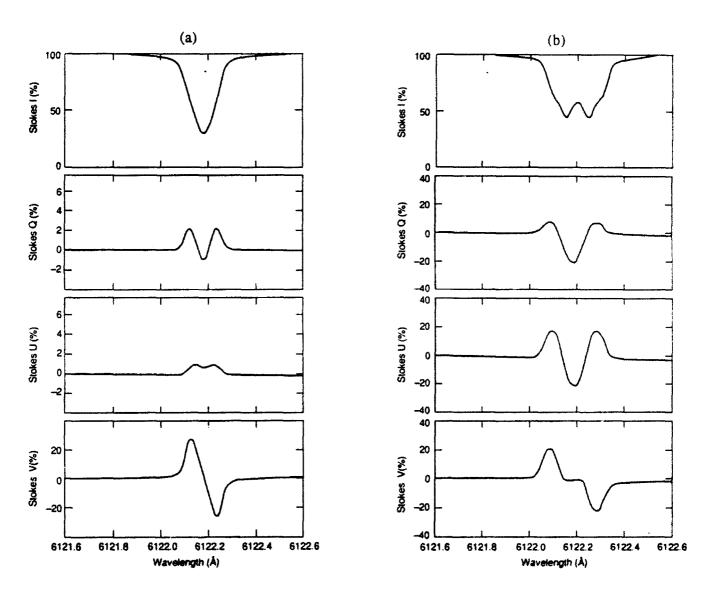


Figure 5. (a) Simulated profiles of the Stokes parameters, I, Q, U, and V, which represent intensity (I), linear polarization (Q and U) and circular polarization (V) as a function of wavelength through the Ca I line (courtesy of B. Lites). The profiles show the response of a perfect spectrograph to a 1000 Gauss magnetic field at  $\gamma = 30^{\circ}$  and  $\chi = 0^{\circ}$ . For the profiles in 5(b), B = 3000 G,  $\gamma = 67^{\circ}$  and  $\chi = 30^{\circ}$ .

Dr. Bruce Lites provided Stokes input profiles (shown in Figures 5(a) and 5(b)), which were computed for the Ca I 6122 Å line according to the Unno-Rachkovsky radiative transfer equations. Lites assumed a Milne-Eddington atmosphere threaded by a constant magnetic field. Using Lites idealized Stokes profiles and taking into account the VMG's spectral resolving power,  $\lambda/\Delta\lambda = 40000$ , and the fact that the pixels may sample regions not uniformly filled with magnetic structures, we simulated the expected response of the VMG. For an assumed filling factor of unity, we computed output Stokes profiles for 1000 G and 3000 G fields. They are shown as Figures 6(a) and 6(b), respectively. At 1000 G the principal features of the input profiles are preserved by the VMG except that the Stokes U signal fails to show the small central bump. Ideally, Stokes U should be zero in the example, but in Lites' profiles there is a small U component which is due to Faraday rotation (Landolfi and Landi Degl'Innocenti, 1982). The convolved profiles for a 3000 G field (Figure 6(b)) reproduce Stokes V very poorly at line center, but the amplitude of the signal in the wings is proportional to the input amplitude. Q and U are recorded in proportion to their amplitudes in the simulated input profiles, but details of the Zeeman splitting in the I signal are washed out.

As a result of the simulations, we have not tried to extract magnetic field parameters from measurements of the Stokes profiles at several wavelengths, e.g., by using a multi-parameter least-squares fitting routine (Skumanich and Lites, 1987). Earlier, Lites and Skumanich (1985) concluded that extraction of magnetic and thermodynamic parameters from filtergram observations with moderate spectral resolution and with noise levels characteristic of the CCD used in the VMG could not be done reliably for fields of less than 1000 G.

Jefferies, Lites and Skumanich (1989), following on the work of Ronan, Mickey and Orrall (1987), showed that, for spectral lines with a Landé g-factor of  $\sim 2.5$  and Doppler width of  $\sim 40$  mÅ, reliable values of strength and direction for magnetic fields up to  $\sim 1000$  G can be obtained by integrating the Stokes parameters over wavelength:

$$B \cos \gamma = \frac{1}{\mu_{\lambda}} \left( \frac{\tilde{V}}{2D(0)} \right) \tag{1}$$

B sin 
$$\gamma = \frac{1}{\mu_{\lambda}} \sqrt{\frac{4\Delta\lambda_D}{D(0)X(\eta_o, a)}} \tilde{Q}^{\frac{1}{2}}$$
 (2)

where B is the magnetic field intensity, which was assumed uniform with depth in the atmosphere,  $\gamma$  is the zenith angle,  $\mu_{\lambda}$  is the magnetic moment for the atomic transition, D(0) is the depth at line center in the magnetic feature,  $\tilde{V}$  and  $\tilde{Q}$  are the integrals of the V and  $Q^2 + U^2$  Stokes parameters, respectively, across the line profile, and  $X(\eta_{O},a)$  is a thermodynamic factor  $\sim 3$ , in most cases. Assuming that D(0) can be measured or inferred from high resolution data, then the longitudinal field  $B\cos\gamma$  and transverse field  $B\sin\gamma$  can be obtained using VMG measurements from at least three positions in the spectral line.

At first, we used the relations given above, but the measurements in the line center always gave confusing results. This should have been expected because of the Faraday rotation and because the etalon's passband is too wide to allow a clean separation between measurements in the line wings and in the core, as the method of Jefferies Lites and Skumanich requires. We have since concentrated on measuring I, Q, U and V in one line wing only.

We interpret our VMG measurements by appeal to the so-called weak field approximation (WFA). Jefferies and Mickey (1990) recently put the use of the WFA on a firmer footing than heretofore in

ŧ

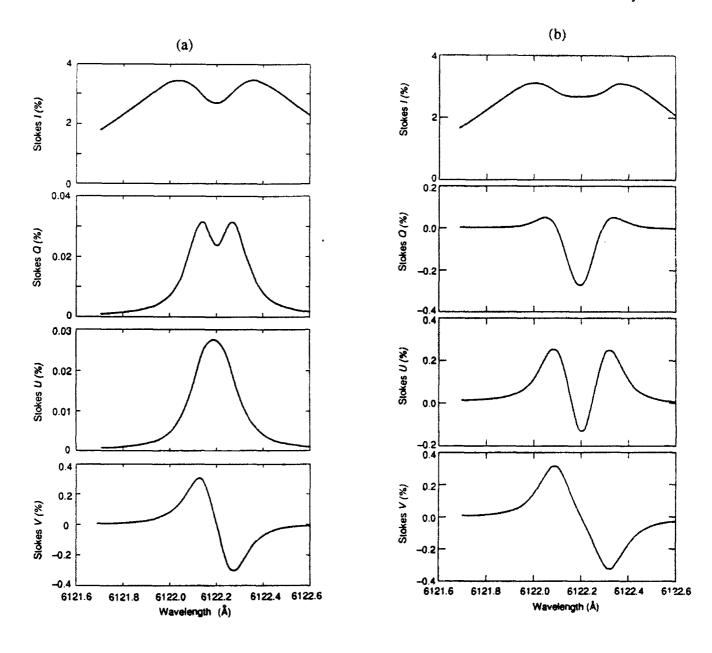


Figure 6. Simulated instrumental profiles, for the same field parameters as in Figure 5. The VMG spectral smoothing has been taken into account. The indicated signal levels are much lower than in Figure 5 because the instrument transmission losses were included, i.e., all values are referenced to the unfiltered solar continuum.

virtually all applications with sufficiently broad spectral lines. The "weak-field" approximation has in the past been applied only when the ratio of the magnetic splitting  $\Delta\lambda_B$  (=  $\mu_\lambda B$ ) to the Doppler width  $\Delta\lambda_D$  of the spectral line is small. Jefferies and Mickey greatly extended the range of the WFA by carefully examining the errors entailed in letting this ratio approach and even exceed unity. They concluded that the range of validity for the WFA can be larger than previously thought, when magnetograph measurements are made sufficiently far into the line wings. Hagyard et al. (1988) arrived at the same conclusion.

Jefferies and Mickey (1990) showed that the relative errors in the inferred field parameters, B,  $\gamma$  and  $\chi$ , will be small provided that measurements are made at least two Doppler widths from line center. The limitations of this approach are that nothing can be learned about the thermodynamic state of the atmosphere and that the "filling factor" f, which is the proportion of a resolution element permeated by magnetic field, cannot be determined without additional assumptions or measurements in two or more spectral lines. They also assumed negligible line weakening, and we have yet to establish whether this assumption is valid for Ca I 6122.

With the WFA, unwieldy differences and sums of Voigt profiles in expressions for the Stokes profiles can be replaced by simple relations convenient for vector magnetography. Figure 7 shows the relative error made in replacing the Stokes profile expressions developed in the Unno-Rachkovsky radiative transfer analysis with the first terms in the respective Taylor series expansions. For a splitting factor  $v_b$  (=  $\Delta \lambda_B / \Delta \lambda_D$ ) up to unity, Figure 7a shows that the relative error in determining V is less than 25% whenever V is measured at least two Doppler widths from line center. Figure 7b shows a similar result for Q and U. In the case of the 6122 Å line, for which  $\Delta \lambda_D = 116$  mÅ,  $v_b$  is less than unity for magnetic fields < 3800 G, so we can apply the WFA to interpret all our measurements.

To calibrate the VMG, we use the simple relation,

$$V = -\mu_{\lambda} B \cos \gamma \left(\frac{dI}{d\lambda}\right) \tag{3}$$

where  $dI/d\lambda$  is the slope of the line at the offset position  $\Delta\lambda_{off}$  of the passband from line center. It is obvious that V will always be largest where the slope is steepest, and therefore, we position the filter on the blue wing of the line, which is steeper than the red wing.

In calibrating the VMG, we assume that the telescope and polarization analyzer introduce no unwanted retardation or polarization. Eventually another series of measurements will be performed to determine the polarization matrix of the telescope under operating conditions. Until then, we assume that an accurate Stokes V calibration is obtained by application of a voltage  $\mathcal{E}_{cal}$  to the etalon. (For the Ca I line,  $(B\cos\gamma)_{cal}$  (Gauss) = 13  $\mathcal{E}_{cal}$ , where  $\mathcal{E}_{cal}$  is expressed in volts.)

In order to get  $(B\cos\gamma)_{measured}$  from  $(B\cos\gamma)_{cal}$   $(V_{measured}/V_{cal})$ , the slope,  $dI/d\lambda$ , of the line should be the same for both calibration and observation. This means that the calibration should be performed on the same solar scene as the observations. Thus, calibration and observation sequences are interleaved on the VMG with no change in field of view. Because spectral line profiles vary from quiet sun to plage to sunspot, data from vector magnetographs that calibrate with the lineshift signal from solar rotation may not be reliable for quantitive studies.

The Huntsville group has taken another approach to calibration, relying on simulation of the instrument response (Gary et al., 1987) coupled with an empirical correction factor determined by comparison with the Mt. Wilson visual measurements. The correction factor is large (k = 8.1), and it indicates how scattered light and poor seeing can significantly degrade vector magnetograph measurements. We intend to compare our VMG results with visual field determinations with and without the IMC operating to try to determine the degree to which the seeing effects are being removed by the IMC.

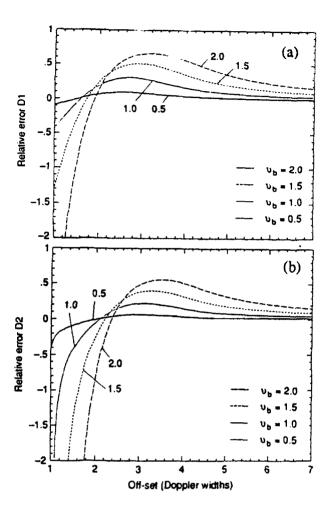


Figure 7. (a) Relative error  $D_1$  in Stokes V measurements as a function of the offset of the filter profile from line center and the splitting factor  $v_b$ . (b) Relative error  $D_2$  in Stokes Q measurements.

Calibration of the Q and U signals is similar to the V calibration. According to Jefferies and Mickey (1990), the Stokes Q vector is given in the WFA by where, again,  $\Delta \lambda_{off}$  is the offset of the

$$Q = \left(\frac{\mu_{\lambda} B \sin \gamma}{2}\right)^{2} \left(\frac{dI}{d\lambda}\right) \left(\frac{3}{\Delta \lambda_{off}}\right) \tag{4}$$

filter passband from spectral line center and the azimuthal factor has been suppressed. As shown below, Q is proportional to the square of a simulated Zeeman shift over a wide-range, for appropriate choice of  $\Delta \lambda_{off}$ . For calibration of the Q and U signals, then, one again introduces a passband shift in the etalon, now to simulate the apparent shift  $\mu_{\lambda} B \sin \gamma$ . The calibration of Q (and U) is done with the same  $\Delta \lambda_{off}$  and  $dI/d\lambda$  as the measurements.

Jefferies and Mickey are silent about the effect of spectral smearing, but it is clear in Figures 8b and 9b that the VMG signals will be proportional to V and to  $Q^2$ , respectively. The VMG response is the convolution of the instrument profile P and the Stokes signal:

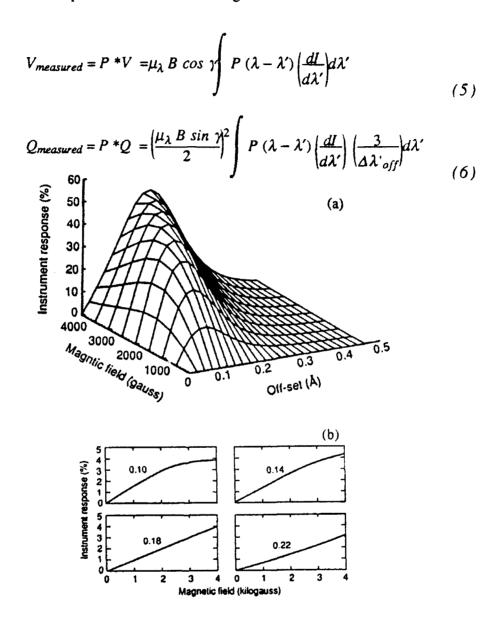


Figure 8. (a) Response of the VMG to Stokes V as a function of filter offset  $\Delta \lambda_{off}$  and magnetic field. (b) Comparison of response curves at values of  $\Delta \lambda_{off}$  from 0.10 Å to 0.22 Å. The VMG is operated at  $\Delta \lambda_{off} = 0.18$  Å.

Figure 8a shows the VMG's expected Stokes V response to spectral shifts simulating magnetic fields up to 4000 G for a range of  $\Delta\lambda_{off}$ . The simulation takes into account the smoothing effect of the instrument profile. Figure 8b shows the response at selected values of  $\Delta\lambda_{off}$ . It shows that the VMG response is linear to 4000 G at  $\Delta\lambda_{off} = 0.2$  Å, but the slope of the response curve is about three times steeper for fields under 2000 G when  $\Delta\lambda_{off} = 0.12$  Å. For higher fields, the response is not linear at this

offset. The VMG response to weak fields is best at  $\Delta\lambda_{off}=0.1$  Å, but this is less than one Doppler width from line center, so we sacrifice sensitivity to stay in the range where the weak field approximation is valid for most fields. We run with the filter passband offset from line center by 450 volts, i.e.,  $\Delta\lambda_{off}=0.18$  Å, which is about 1.5 Doppler linewidths.

Figure 8 shows that the response of the VMG is not very sensitive to  $\Delta\lambda_{off}$ . This has the practical consequence that the mesurements are not strongly degraded by local Doppler shifts. For example, a Doppler shift of 20 mÅ, which corresponds to a velocity of 1 km/s, produces a 25% change in V response and less than 10% change in the Q and U response.

Figure 9a shows a simulation of the VMG's overall Stokes Q response, and Figure 9b shows the response at a few values of  $\Delta\lambda_{off}$ . The best response is obtained at  $\Delta\lambda_{off}=0.22$  Å, where the maximum slope represents a 1.35% change in intensity per 1000 G. This is ~ 7 times less than the Stokes V response in the same range.

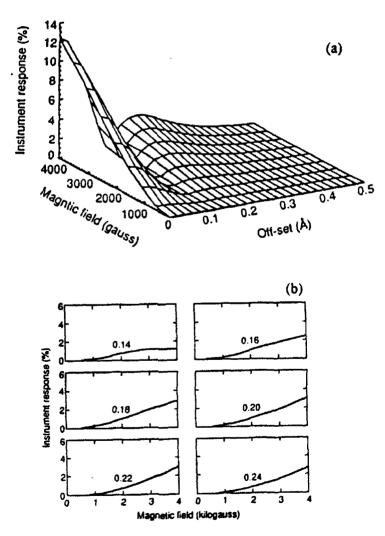


Figure 9. (a) Response of the VMG to Stokes Q as a function of filter offset  $\Delta \lambda_{off}$  and magnetic field. (b) Comparison of response curves at  $\Delta \lambda_{off} = 0.14$  Å to 0.24 Å. The VMG is operated at  $\Delta \lambda_{off} = 0.22$  Å.

# 6. Physical Interpretaion

In the above discussion, we have ignored any possible dilution of the signal due to a filling factor f < 1. In reality, only a fraction f of the area sampled by each VMG pixel is filled with magnetic elements. If all these elements were to be at different orientations and also were to display a wide range of magnetic intensities, then there would be little hope of getting any physically meaningful data from a vector magnetograph. However, by making two assumptions about the unresolved flux elements, one can estimate the energy and direction of photospheric fields from vector magnetograph measurements.

From  $H_{\alpha}$  observations, such as the one shown in Figure 10, one can reasonably surmise that the scale of directional variations in the azimuth and zenith angles,  $\chi$  and  $\gamma$ , is at least larger than the scale of the VMG pixels. That is, even though there are probably many 0.1 arcsec or smaller flux elements contributing to the signal at each pixel, it seems unlikely on the basis of the large-scale organization seen in chromospheric fibrils that the unresolved elements are oriented in a random pattern. Therefore, in interpreting the VMG signals we assume that  $\chi$  and  $\gamma$  are the same for all flux elements within any given pixel.

Another assumption about the fine-scale structure of the magnetic field is needed to obtain a meaningful interpretation of VMG measurements. We assume that the field strength B is the same in all flux elements, as suggested by the observations of Stenflo and Harvey (1985). These authors concluded that, outside sunspots,  $B \sim 1100$  G in each fluxtube. Then we may write, for the measured Stokes parameters,

$$Q \sim f B^2 \sin^2 \gamma \cos 2\chi \tag{7}$$

$$U - fB^2 \sin^2 \gamma \sin 2\chi \tag{8}$$

$$V^2 \sim f^2 B^2 \cos^2 \gamma \tag{9}$$

so that the filling factor f drops out of the equation for  $\chi$ .

$$\tan 2\chi = U/Q \tag{10}$$

It remains in the expression for  $\gamma$ .

$$\tan \gamma = \sqrt{\frac{4\sqrt{Q^2 + U^2}}{3f V^2} \left(\Delta \lambda_{off} \frac{dI}{d\lambda}\right)}$$
 (11)

Equation (11) follows from Jefferies and Mickey, except that they misplace the filling factor in their equations so that it would not appear at all in an expression for  $tan \gamma$ . Instead, the effect of the factor  $1/\sqrt{f}$  on the value of  $B \sin \gamma$  derived from Q and U measurements is this: for f << 1,  $\gamma$  is near  $90^{\circ}$  for all values of Q, U, and V. In order to remove this tendency for a vector magnetograph to overestimate the strength of the transverse field relative to the longitudinal one, one must make an estimate of f. One may consider the context of the measurements. In sunspots, f = I is probably a good assumption. Outside sunspots, the filling factor will depend on the effective aperture of the VMG, with seeing taken into account. It is well known that the average value of  $B^2$  deduced from magnetograms increases when the



Figure 10. Active region NOAA 6063 recorded at the Big Bear Solar Observatory on 17 May 1990 with a lithium niobate etalon tuned to  $H_{\alpha}$  line center. The scale is 2.2 arcsec/mm. Note that the scale of the regions of approximately uniform field direction, as outlined by the fibrils, is much greater than a VMG pixel.

seeing improves and this represents one of the most serious impediments to quantitative use of magnetograms. We hope to find a way to use the error signals from the IMC as an index for the seeing, which can then be used to remove this effect from magnetogram series.

Since  $V \sim f B \cos \gamma$ , which is the flux, it should be reasonably well-determined by VMG measurements so long as the line profile in the unresolved flux elements is not too different from that in the interstitial regions. Jefferies and Mickey (1990) concluded that expected profile variations will have little effect on flux measurements.

The magnetic energy E in the layer of the atmosphere permeated by elements of field B and cross-sectional area a is  $\sim N$  a  $B^2$   $l/8\pi$ , where l is the thickness of the layer, N = A/af, is the number of flux elements each of area a in the projected area A of one pixel. Using the estimated value of f, one can make an estimate for E. Although we haven't tried carrying this through yet, the above analysis shows that virtually all the physically meaningful quantities relating to the magnetic field may be estimated from VMG observations.

### 7. Observations

Reduction and analysis of VMG observations is still in a preliminary state. Figure 11 shows an example of the earliest VMG data, a photographic representation of longitudinal and transverse

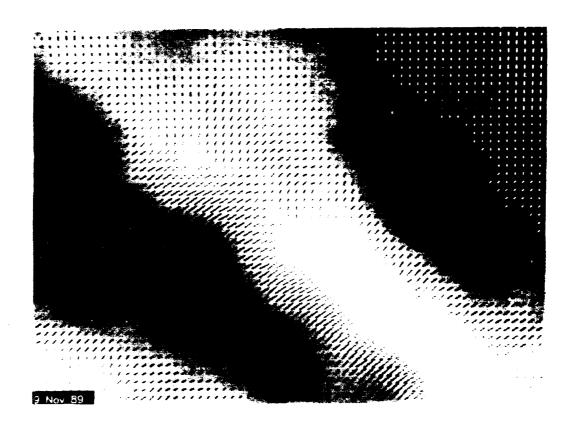


Figure 11. Early data from the VMG showing NOAA region 5783 on November 9,1989. The photo shows the fields with the scale enlarged so that a slash representing the transverse field direction can be drawn for each 0.4-arcsec pixel.

components of the magnetic fields in the leading spot of a large active region, NOAA 5783, which was near the center of the disk on November 9, 1989. The figure shows an enlarged section, 32 x 20 arcsec, of the whole 3.6 x 2.4 arcmin VMG field of view. The longitudinal magnetic component is represented by the usual gray scale, where white represents positive polarity and black represents negative polarity. The transverse field component is represented by short slashes, each one drawn at a 0.4-arcsec pixel. The slashes here are quite consistent from pixel to pixel, but some of this consistency must be due to the fact that the image definition was worse than one pixel, the observations having been obtained in ~ 4 arcsec seeing and without the benefit of the IMC.

The resolution of the magnetograms is still not up to the quality that we think can be achieved. We expect substantial improvement in image definition with routine operation of the IMC, which was brought on-line only recently. Image quality at the Hilltop Dome is frequently ~ 2 arcsec or worse, so the camera scale of 0.4 arcsec/pixel is usually reduced to 1 - 1.5 arcsec/pixel during processing. With the help of the IMC, we hope to hold the resolution at 0.4 arcsec/pixel on the days with exceptional observing conditions.

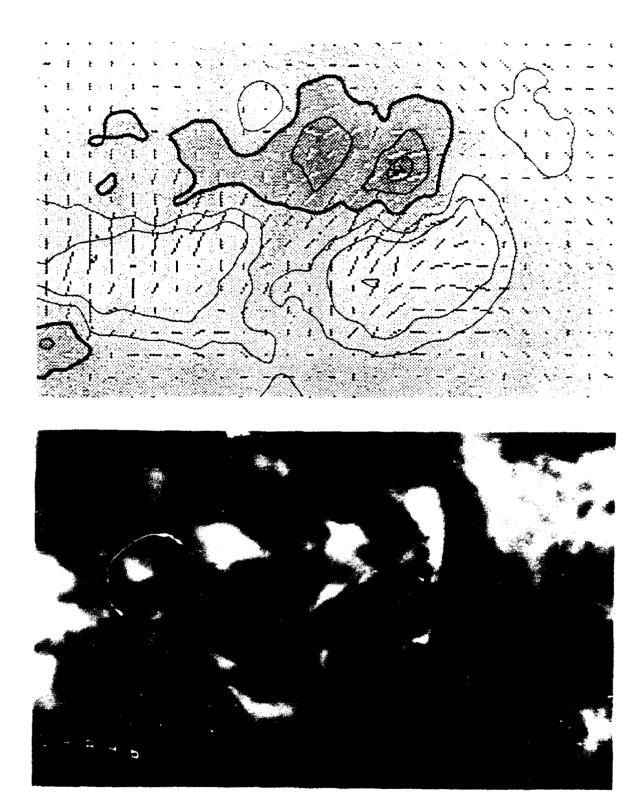


Figure 12. (Top) Vector magnetogram of NOAA region 6233 on August 30, 1990, at 1440 UT. Heavy contours outline areas of positive (upward-directed) field. Light contours show negative field regions. (Bottom)  $H_{\alpha}$  photograph at 1548 UT of the same region (BBSO photo).

According to Eq. (10), there is a 180° ambiguity in the direction of the transverse component as measured with the VMG, as there is with any vector magnetograph. There is no foolproof way to resolve it. One method of trying to determining the vector field direction is to use the Stokes V measurements, which give the magnetic flux through the photosphere, to compute the transverse components of the field under the assumption that the fields are current free. This usually gives a plausible resolution of the 180° ambiguity when the indicated field azimuth is within 45° of the measured azimuth. Unfortunately, the method fails in the most interesting cases, such as the one shown in Figure 12. The active region there is NOAA 6233, which was near the center of the disk on August 30, 1990, the fourth day of the Solar Polarimetry Workshop. Positive and negative longitudinal field components are represented in the figure by heavy and light contours, respectively. The slashes suggests that the vector fields generally behave as expected, viz., they diverge from the strong field concentrations, but this map and the others obtained that day also consistently show transverse fields parallel to the line dividing positive and negative longitudinal fields. This is the "sheared" type of field configuration that Krall et al. (1982) and others have associated with flares. The direction of the shear is not obvious from the magnetic maps, but it can probably be determined by examining the evolution of the region.

An  $H_{\alpha}$  picture (Figure 12) was obtained at the Big Bear Solar Observatory at nearly the same time as the magnetogram. Note that where the transverse field direction is parallel to the boundary between positive and negative fields, the boundary  $H_{\alpha}$  filament is narrow and sharply defined. Where the transverse field direction makes an angle closer to  $90^{\circ}$  with the boundary, the boundary filament is thicker and more diffuse. It will be interesting to find out whether this is a general trait of filaments above transverse fields.

# 8. Acknowledgements

We are grateful to Kim Strohbehn and Terry Harris, respectively, for electronic systems and optical design, and to John Townsend for software support. We thank the National Solar Observatory, which provided a home for the VMG, and the staff there who helped to install the instrument at the Hilltop Dome. We are grateful to Bruce Lites, Larry November and John Jefferies for helpful discussions. This research is supported principally by the Air Force Office of Scientific Research, grants AFOSR-87-0077 and 90-0102. Initial development of the lithium niobate filter was supported by NASA grant NAGW-522. APL Independent Research and Development funds supported the APL Solar Observatory and start-up development of the instrumentation.

#### 9. References

Burton, C. H., Leistner, A. J. and Rust, D. M., 1987, "A Solid Tunable Fabry-Perot Etalon for Solar Seismology," *Instrumentation in Astronomy VI*, SPIE Conf. Proc. 627, 39 - 49.

Chupp, E. L. (Editor), 1990, Proc. 2nd Workshop on Impulsive Solar Flares, Astrophys. J. Suppl. 73, No. 2.

Gary, G. A., Moore, R. L., Hagyard, M. J., and Haisch, B. M., 1987, "Non-Potential Features Observed in the Magnetic Field of an Active Region," Astrophys. J. 314, 786.

Hagyard, M. J., Gary, G. A., and West, E.A., 1988, The SAMEX Vector Magnetograph, NASA Tech. Memo. 4048, Marshall Space Flight Center, Huntsville, Ala.

Harvey, J. W., 1985, "Trends in Measurement of Solar Vector Magnetic Fields Using the Zeeman Effect," in *Measurements of Solar Vector Magnetic Fields*, M. Hagyard (ed.), NASA Conf. Pub. 2374, p. 109.

Hernandez, G., 1986, Fabry-Perot Interferometers, Cambridge Univ. Press, Cambridge, p. 96.

Jefferies, J., Lites, B. W., and Skumanich, A., 1989, "Transfer of Line Radiation in a Magnetic Field." Astrophys. J. 343, 920.

Jefferies, J. and Mickey, D. L., 1990, "On the Inference of Magnetic Field Vectors from Stokes Profiles," submitted to Astrophys. J.

Krall, K. R., Smith, J. B., Jr., Hagyard, M. J., West, E. A., and Cummings, N. P., 1982, "Vector Magnetic Field Evolution, Energy Storage, and Associated Photospheric Velocity Shear within a Flare-Productive Active Region," Solar Phys. 79, 59.

Landolfi, M., and Landi Degl'Innocenti, E., 1982, "Magneto-Optical Effects and the Determination of Vector Magnetic Fields from Stokes Profiles," Solar Phys. 78, 355.

Lites, B. W., 1987, "Rotating Waveplates as Polarization Modulators for Stokes Polarimetry of the Sun: Evaluation of Seeing-Induced Crosstalk Errors," Appl. Optics 26, 3838.

Lites, B. W. and Skumanich, A., 1985, "The Inference of Vector Magnetic Fields from Polarization Measurements with Limited Spectral Resolution," in *Measurements of Solar Vector Magnetic Fields*, M. Hagyard (ed.), NASA Conf. Pub. 2374, p. 342.

Lites, B. W. and Skumanich, A., 1989, "The Advanced Stokes Polarimeter," in *High Spatial Resolution Solar Observations*, D. Neidig (ed.), National Solar Observatory, Sunspot, NM, p. 389.

Mein, P., 1989, "High Resolution Observations with THEMIS Prospects in Magnetic Field Observations, in *High Spatial Resolution Solar Observations*, D. Neidig (ed.), National Solar Observatory, Sunspot, NM, p. 12.

Povel, H. P., 1991, "CCD Image Sensor as a Demodulator in a 2D Polarimeter with a Piezo-Elastic Modulator," in *Solar Polarimetry*, L. November (ed.), National Solar Observatory, Sunspot, NM (these proceedings).

Rimmele, Th. and Lühe, O. v. d., 1989, "The National Solar Observatory / Kiepenheuer Institut Solar Feature Correlation Tracker, in *High Spatial Resolution Solar Observations*, D. Neidig (ed.), National Solar Observatory, Sunspot, NM, p. 90.

Ronan, R., Mickey, D., and Orrall, F., 1987, "The Derivation of Vector Magnetic Fields from Stokes Profiles: Integral versus Least Squares Fitting Techniques", Solar Phys. 113, 353.

Rust, D. M. and Bar, V., 1973, "Magnetic Fields, Loop Prominences and the Great Flares of August, 1972," Solar Phys. 33, 445.

Rust, D. M. and O'Byrne, J. W., 1989, "High Resolution Vector Magnetograph," in *High Spatial Resolution Solar Observations*, D. Neidig (ed.), National Solar Observatory, Sunspot, NM, p. 378.

Rust, D. M. and Keil, S., 1991, "A Search for Polarization in Ellerman Bombs," submitted to Solar Phys.

Rust, D. M., Nakagawa, Y., and Neupert, W., 1975, "EUV Emission, Filament Activation and Magnetic Fields in a Slow-Rise Flare," Solar Phys. 41, 397.

Sakurai, T., 1987, "A Study of Magnetic Energy Build-up Based on Vector Magnetograms," Solar Phys. 113, 137.

Skumanich, A., and Lites, B. W., 1987, "Stokes Profile Analysis and Vector Magnetic Fields. I. Inversion of Photospheric Lines," Astrophys. J. 322, 473.

Stenflo, J. O., 1989, "LEST Update," in High Spatial Resolution Solar Observations, D. Neidig (ed.), National Solar Observatory, Sunspot, NM, p. 27.

Stenflo, J. O. and Harvey, J. W., 1985, "Dependence of the Properties of Magnetic Fluxtubes on Area Factor or Amount of Flux," Solar Phys. 95, 99.

Strohbehn, K., 1990, "Solar Vector Magnetograph Fine Guider," JHU/APL Tech. Memo. S1A-67-90, JHU Applied Physics Laboratory, Laurel.

Tanaka, K. and Nakagawa, Y., 1973, "Force-Free Magnetic Fields and Flares of August 1972," Solar Phys. 33, 187.

Yang, H-S., Hong, Q. F. and Ding, Y. J., 1988, "A Constant-alpha Force-Free Analysis of the Active Region AR 4711 of February, 1986," Solar Phys. 117, 57.

#### Speaker: Rust

#### Discussion

- J. Stenflo: A major problem is that the derivation of the vector field from the polarimetric observations is strongly affected by the magnetic filling factor and temperature line weakening. This cannot be accounted for by your calibration procedure, in particular because the flux elements are not resolved.
- D. Rust: The magnetograph accurately measures the flux through the photosphere and in most cases, it should give an accurate measurement of the azimuth angle. For the purpose of eventually characterizing the overall structure and development of an active region these data may be enough.
- J. Harvey: A partial correction from line profile variability could be made by doing the offset calibration of  $dI/d\lambda$  in the actual region being studied rather than using disk center. This would be incomplete for areas with dilute filling factors but is better than assumption of a constant  $dI/d\lambda$ .
- S. Koutchmy: Do you see the magnetic field of the core of the sunspot and if yes, do you see also the "blue/red" asymmetry? If not, then why is the magnetic field measured above the core of a sunspot on your map not randomly distributed, as we might presume for the scattering of radiation around the sunspot.
- D. Rust: We believe that the signal in sunspot umbrae is due to scattered light, mostly, but it has not been quantitatively measured yet. We have measured the magnetograph response on the blue wing and on the red wing. The blue wing gives a much stronger response to a simulated magnetic field and this must be due to a steeper profile there than in the red wing.
- B. Lites: Preliminary non-LTE synthesis of 6122Å line shows it to strengthen enormously in sunspot umbrae. As it has such a strong temperature dependence, it may not be the ideal line to use: much of the polarization signal in active regions arises from spots and pores, yet the calibration is based upon quiet-sun profiles.
- D. Rust: The instrument can be calibrated better in inducing artificial line shifts over the same field of view as used for the measurements. Until now, we haven't done this because of the added data analysis effort.
- Ai G.: Do you find any Faraday rotation effect in the line you use?
- D. Rust: We have been measuring both wings and the line center. The line center results are where the Faraday effect should be more important. We do not always agree with the line wing results. I suppose that part of this could be due to Faraday rotation.

Speaker: O'Byrne

#### Discussion

- J. Jefferies: Many years ago Giovanelli was using a combination of Fabry Perot to observe in a narrow band near  $H\alpha$ . I think he had some problems with interference fringes between the étalons do you anticipate such problems?
- J. O'Byrne: We are aware of possible problems with interference and reflection between the two étalons. Currently we slightly tilt ( $\sim 0.1^{\circ}$ ) our single Fabry-Perot to guard against problems with on-axis reflections. Similar small tilts in a dual Fabry Perot mounting should average fringe problems. Also, we probably have fewer surfaces than Giovanelli because of our use of solid Fabry Perots.
- S. Koutchmy: Could you envisage to remove or change the prefilter of the Fabry Perot étalon and work with many orders to have a better S/N ratio and look at net polarization effects on the disk? Maybe this could be used for calibration purposes.
- J. O'Byrne: Allowing adjacent Fabry Perot orders through will clearly increase the light level as it rapidly reduces contrast in the spectral line and looses all polarization information. This may be useful for calibration purposes perhaps. While not too difficult a change, it could not be done routinely. As to the corona, we are interested in using an Fabry Perot in a coronagraph.
- D. Rust: Can one use linear polarizers only to calibrate matrix of telescope, or is the use of circular polarization necessary, too?
- L. November: The Jones matrix of a system is uniquely determined by multiple linear polarization sources only.
- A. Skumanich: This is a comment on D. Rust's statement of the use of only a linear polarizer to calibrate the telescope. It is necessary but not sufficient, one also needs to introduce circular polarization to determine V, Q, U cross talk.
- J. O'Byrne: Although most of our calibration runs to date have been with linear polarizers, we have run with a circular polarizer also.
- E. West: Can you tune the prefilter into the continuum and what kind of polarization signal do you get?
- J. O'Byrne: We can certainly tune both filters out into the continuum. With our current tuning range of 3000 volts on the Fabry Perot, we can reach over 1Å to the blue of the line. In principle we can go further with high voltages. The polarization "signal" in the continuum is very low, but I cannot guaranty it at this point.
- A. Skumanich: We also need B maps in the local solar frame.
- J. O'Byrne: We are well aware of this need, especially because of the tendency to produce apparently strong transverse fields directed radially when observing away from disk center. This makes the vector maps much more difficult to interpret.
- Ai G.: Why is the transverse field, outside of the sunspot so strong? Maybe the vertical lines are noise or systematic error.
- J. O'Byrne: When you zoom in on the image and display more vectors in any region (the maps I showed display vectors for only 1 in 10) the vectors remain coherent over small patches of the map i.e. the vectors are certainly not noise dominated. As I mentioned in my talk, the solar oscillations and drift of the blocker profile during an observing sequence are being investigated as sources of systematic error leading to the field outside the spots. The vector map does however emphasize the effect because of its scaling of vector lengths.

- H. Wang: Why the transverse fields are so strong in the umbra of the spot?
- J. O'Byrne: The orientation of the vectors is often quite consistent with projection effects caused by observing regions away from disk center. Whilst this effect is clearly present I do not believe it is the primary explanation. We are investigating the effect of oscillations and blocker profile mentioned earlier. We expect our "fast" mode to reduce this effect substantially.
- J. Harvey: In order to obey Skumanich's plea for solar as well as observer's reference frame plots of vector fields, the 180° ambiguity has to be resolved at every pixel. Which of the many suggested schemes should be used to do this?
- A. Skumanich: That's correct but one ultimately needs to go to the solar frame to do physics. Perhaps we can start at the spots and work outward. This may not be unique and perhaps several solar maps may be necessary to explore the consequences of the ambiguity.

# A BRIEF INTRODUCTION TO THE MULTICHANNEL SOLAR MAGNETIC FIELD TELESCOPE

# Ai Guoxiang

Beijing Astronomical Observatory, Chinese Academy of Sciences

#### I. Introduction

The construction of the Multichannel Solar Magnetic Field Telescope is granted by the Astronomical Committee. Bureau of Mathematics. Physics and Chemistry, Chinese Academy of Sciences for the project of the Seventh Five-year Plan. The design of the telescope is based on the principle of the multichannel filter invented during the end of 1983 to early 1984. After selecting several themes and studying various plans during the period of 1984 to 1986, the Beijing Astronomical Observatory and the Nanjing Astronomical Instrument Factory signed an agreement in 1986 and began to construct the telescope. The construction of the telescope has been supported by the committee and the bureau mentioned above. Now we have begun the optical, mechanical and electrical combined testing. The telescope will be completed in September and installed at Huairou Solar Observatory in October. 1990.

As we all know the 22th solar cycle is coming. With the view to make full use of the above telescope by solar physicists working in China and all other countries of the world and to help their working plans or selecting themes for further studies, we give here a short description of the telescope and its astronomical capabilities.

#### II. Telescope

The telescope system contains four seperate telescopes installed on a unified driving system. (See Fig. 1)

## 1. 600 mm Vacuum 9-channel Telescope

This telescope consists of a primary mirror with an aperture of 600 mm, a reflection-type Gregorian vaccum system and a reflection grating at the first focal plane. The solar region of  $4' \times 5.5'$  is retained for observing. In front of the colliminated light is placed the panchromatic KD\*P magnetic field analyser. In the head of the multichannel filter, the beam of light is by passing through the polarizing beam splitter split into 5 rays of different wavelengths of the spectrum. These rays, after passing through the 5 respective colliminated system, enter the body of the 9-channel filter, forming 9 solar local images in the end with the help of 9 image lens systems. The two sizes of the solar images can be used: 120 mm or 60 mm. These images are followed up by 9 sets of PULNiX TM 860 CCD used as receivers. 800 (H)× 590 (V) pixel, each being

11.5  $\mu \times 11.0\mu$  in size, corresponds respectively with the solar details of 0."38  $\times$  0."37 or 0."19  $\times$  0."185 and the field of view of 3.'6  $\times$  5.'1 or 1.'8  $\times$  2.'55. Following these CCDs, six parallel videorecorders are used in recording the real time data and three series 151 image processing systems are used in obtaining digital data. The analog signal on the video tape also can, according to the need of users, be used afterwards in obtaining digital data with series 151 image processing system.

Every channel of the 9-channel filters is a wavestrip-adjustable universal filter. The central wavelengths have adjustable range of  $1500\ \text{\AA}$  to  $2000\ \text{Å}$ . Almost all the solar spectral lines in the visible range of  $3800\ \text{A}$  to  $7000\ \text{Å}$  can be used as observing lines. The spectral lines firstly selected on the basis of the opinions and the themes selections before the design are shown in Fig. 2. Additional wellknown, useful spectral lines, as listed in Table 1, can be selected and used as observing lines by the interested.

Because the spectral resolution of some channels is as high as 0.048 Å, it is possible to obtain, by spectral scanning with a wavelength adjusting apparatus, the profile of the spectral line with a time resolution 10 of the two-dimensional field of view over the solar region. The most characteristic feature, also the unique capability of this system is the following. One can obtain real time 3-dimensional (the sunface of the sun and the different levels of the sun) data for the vectorial magnetic field, the component of the velocity field in the direction of the line of sight and monochromatic images. One can also observe, by spectral scanning, the profiles of the Stokes parameters. It is estimated that the sensitivity of the magnetic field is about  $\pm 1$  G for the longitudinal component and ± 10 G for the transverse component. The velocity field (obtained from the profile of spectral lines by scanning) of the range from  $\pm$  10 M/S to  $\pm$  1000 KM/S can be observed. In addition the coronal vector fields can be obtainted, through the Handle effect by using the related line pairs. The time resolution is usually about 1 minute. It can be made shorter or longer, if necessary, as short as 10. or as long as 5 minutes.

# 2. 350 mm Solar Magnetic Field Telescope

This is the present system we are familiar with. It will be installed on the new telescope so that the continuous data and regular active regional data can be obtained. FeI  $\lambda$  5324.19 Å and H<sub> $\beta$ </sub> 4861 Å are used in observing the vector magnetic field and the line of sight velocity field. The field of view is 4' × 6'. Each CCD pixel corresponds to the solar details of 0."5 × 0."7. The time resolution is one minute. (This can be made shorter or longer.) The sensitivity are:  $\pm$  1 G ( $\pm$  15 G) for the longitudinal (transverse) magnetic fields and  $\pm$  5 M/S for the velocity field.

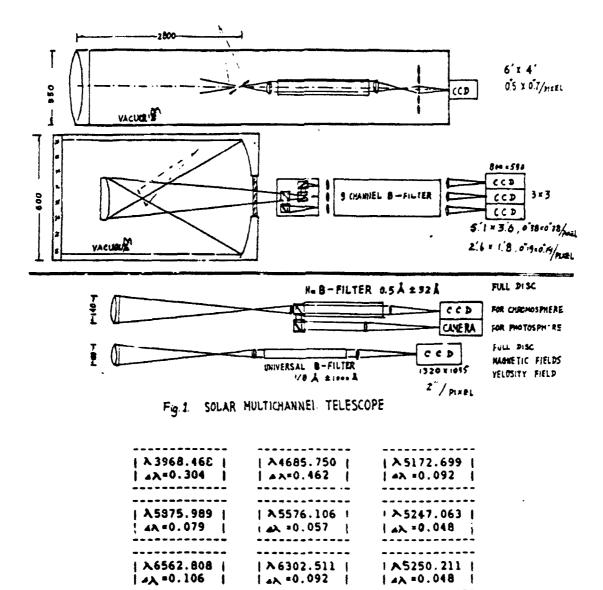


Fig 2. Parameters of 9 channels for the highest priority lines.

- 3. 100 mm Full Disk Magnetic and Velocity Field Telescope The aperture of the objective lens is only 100 mm. The two sizes of solar images can be selected: 6 mm and 9 mm. Various spectral lines can be selected by using a universal filter of band width  $\frac{1}{8}$  Å. The present selected spectral lines are  $\lambda$  5324 Å for observing the vector magnetic field, and  $\lambda$  5576 Å for observing the velocity field. A new design of double passband mode is adopted in this filter. It has a high comprehensive S/N. The KO 1521 Megaplus corresponds to 2" solar details CCD, involving 1320×1035 pixels, is used in the receiving system. Each pixel corresponds to 2" solar details. The resolution of 2" being so appropriate, the S/N of the 100 mm telescope will be one time higher than the original magnetic field telescope. In case of 5 minutes of integrate time the sensitivity of the longitudinal magnetic field is estimated to be  $\pm 1$  G, that of the transerve field,  $\pm 15$ , and that of the velocity field,  $\pm 1 \text{M/S}$ . The integrated time can be made shorter or longer, if necessary. The magnetic field and the velocity field can not be observed at the same time with the system. About 1 minute of time is needed in exchanging the observations.
- 4. 140 mm Full Disk Chromosphere and Photosphere Telescope This is a 2-channel simultaneous observing system, both using the same 140 mm objective lens and collimating system. The light is split into two beams of which one beam, after passing the 0.5 H $_{\alpha}$  universal filter ( $\pm$  32 Å adjustable), forms the full disk chromospheric or photospheric image (when used as a side band), the other one after passing the  $\lambda$  5500  $\pm$  50 Å filter, forms the white light photospheric image. (Solar images are 200 mm.) These images are monitored with CCD or observed with camera, giving background material.

If one feels necessary, the small telescope attached to the present magnetic field telescope can further be used. It has a 80 mm objective lens and a daystar filter of a band width of 1.5 Å. Ca 3933 Å is used in observing. The full disk Ca monochromatic image is formed and monitored with CCD. The weight of this small telescope is only 5 kg.

By means of the photoelectric guiding and the deviating apparatus, it is possible to arrange the 600 mm and 350 mm telescopes to observe the selected local regions of the sun, while the 100 mm and the 140 mm telescopes monitor the full disk all the time.

III. Real Time Receiving and Follow-up Processing System This system cotains 13 CCDs for receiving the simultaneous video solar images through the various channels. These images can be recorded continuously at the frame period 40 ms (field period of 20 ms). Because the S/N caused by the atmospheric vibration usually is about 100:1 under the video conditions, while the S/N of a good recorder is as high as 47 db, about 224:1, i.e. The video recorded analog signal do

not reduce the S/N of the data, when digitized. Therefore, the video recorders are mainly used in the terminal system. To save money, the cost of a recorder being 1/30 of that of an image processor, we use only 3 series 151 image processors in the 9-channel system to obtain the most urgently needed real time digital data. If the observers are not satisfied with the analog data, series 151 image processing system can be used in data processing afterwards. In addition, the video recorded data are continuous and the time resolution can be selected freely for various analyses.

The block diagram of the receiving operating and follow-up system is shown in Fig. 3. The real time digital data can be memoried in the IPAIO-D erasable laser disk system (650 MB/piece) through 80486 computer. The data can be read afterwards for processing on the IDUIO-D erasable laser disk which is connected with the VAX-11/750 computer. These two sets of laser disks are for real time recording the large amount of digital data and for the convenience of using the data. The waste of time caused by transforming the data is avoided. The digital data is often used. So it is restored in the disk for daily usage.

A lot of analog data obtained with the video recorder is memoried in the tapes. These data can be replayed for searching for the needed characteristics. These data can also be digitized and used. The observers have to keep the data in their own tapes, for we will not provide the daily usage. Either digital data or analog data can be changed into photographs with the screen camera system for intuitive usage.

The photographs of  $H_{\alpha}$  and white-light full disk image and local sunspot image can be taken with 135 camera.

There are AMT-8300-16 large capacity real time tapes with a storage of 3000 digital maps for editing the digital data into a continuous telefilm. A number of analog video tapes can also be edited into concentrated telefilm by the editing machine.

Besides the magnetograms and the Dopplergrams obtained with VAX-11/750 computer and Sun4 workstation we have collected some program libraries edited by the solar physicists for general use.

For the better use of the computers at Huairou Observatory, we shall build through E-MAIL working terminals at Zhong Guan Cun for the convenience of users there.

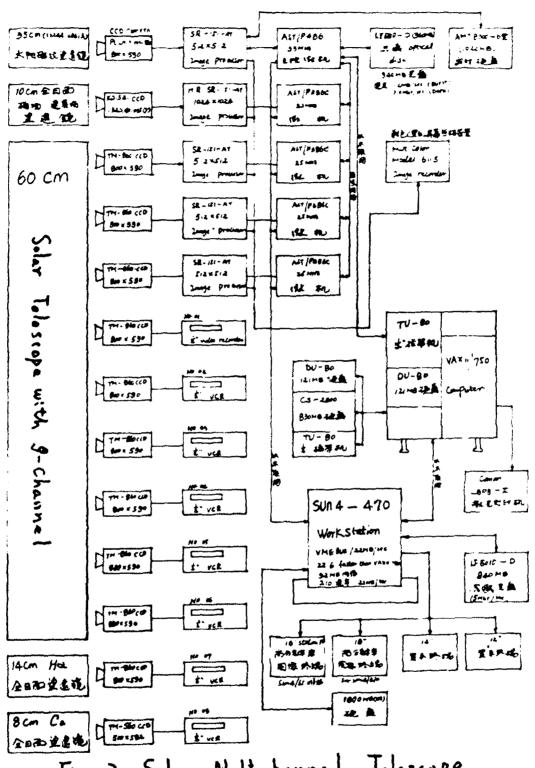


Fig. 3. Solar Multichannel Telescope

# Two-dimensional polarimeter with CCD image sensors and piezo-elastic modulators

H.P. Povel, C.U. Keller, J.O. Stenflo

Institute of Astronomy, ETH-Zentrum, CH-8092 Zurich

Summary. A new type of polarimeter for application in solar physics is described, which combines fast polarization modulation and high spatial resolution using piezoelastic modulators and charge coupled device (CCD) image sensors. The problem of incompatibility between the slow read-out of CCD sensors and fast modulation has been solved. First two-dimensional Stokes Q and V images, free from gain-table noise, and with an rms noise level of about  $10^{-3}$  have been obtained

#### 1. Introduction

Two-dimensional Stokes polarimetry with subarcsecond resolution and a polarimetric accuracy beyond  $10^{-3}$  requires

- (1) modulation frequencies of the Stokes parameters Q, U and V well above some 100 Hz, where the noise introduced by seeing fluctuations becomes negligible,
- (2) strictly simultaneous images of all four Stokes parameters,
- (3) elimination of gain-table noise (errors in the flat field),
- (4) high spatial resolution,
- (5) low instrumental polarization,
- (6) fast image acquisition and real-time processing for image selection and control.

The fulfillment of these requirements can be achiveded with modern equipment like fast electro-optical modulators (1,3), CCD image sensors (2,4), large, polarization-free telescopes at appropriate sites (4.5), and modern high-speed real-time image processing systems (6).

However, there remains one serious problem to be solved: How can the evident incompatibility between fast intensity modulation (kHz), comparably long integration times (typically 0.1 s) and slow CCD read-out frequencies (typically 50 Hz) be overcome? A solution is now offered by the ETH polarimetry system.

The polarimetric system designed and presently tested at ETH Zürich uses two piezo-elastic modulators (Kemp, 1969) and three CCD imaging sensors to measure simultaneously I, Q, U and V (Stenflo. 1984). The problem of demodulating the high 50 kHz intensity modulation produced by the modulators has been solved by controlling the photo charges in the CCD detectors (Povel et al., 1990), as will be described in the following sections.

#### 2. The Polarization Modulator

The principle of the piezo-elastic modulator (PEM) is outlined in the following. By resonant excitation of a longitudinal standing acoustic wave in a slab of optical material like fused silica with a piezo transducer, strain induced birefringence results. This leads to a modulated retardation  $\Phi(t)$  given by

$$\Phi(t) = A\sin(\Omega t)\sin(\pi x/L), \tag{1}$$

where A is the maximum retardation,  $\Omega$  the characteristic frequency, and L the length of the slab in the direction x of the acoustic wave. For L=57 mm one gets  $\Omega/2\pi=v_s/2L=50$  kHz in fixed silical where  $v_s$  is the speed of sound. According to (1) in the middle of the slab (x=L/2) the retardation is approximately flat. Consequently the useful spatial  $(\Delta x)$  and angular aperture  $(\Theta)$  of the retarder are rather large. If one accepts a phase deviation  $\epsilon = \Delta \Phi/\Phi = 1\%$  one gets  $\Delta x \approx 2L\sqrt{2\epsilon} = 5$  mm and  $\Theta \approx \sqrt{2\epsilon} \approx 8^\circ$  and (1) can be replaced by

$$\Phi(t) = A\sin(\Omega t),\tag{2}$$

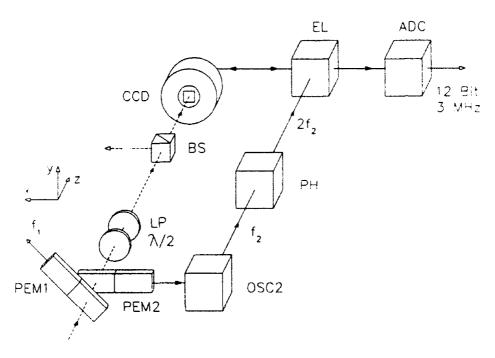


Fig. 1. Principle of the polarimeter with CCD sensors and piezo-elastic modulators (details are described in the text).

With two piezo-elastic modulators (PEM1, PEM2), a  $\lambda/2$  retarder, and a linear polarizer (LP), as arranged in Fig. 1, a compact polarization modulator can be built. This setup has been analyzed in detail by Stenflo (1984). The optical components are oriented in the following way: PEM1 at 45°. PEM2 and LP at 0°, and the  $\lambda/2$  retarder at 11.25° with respect to the y-axis, as indicated in Fig. 1. A light beam with polarization described by the Stokes vector (I,Q,U,V) is, after passing the modulator package, transformed into a 100% linearly polarized beam with the Stokes vector (I',I',0,0), where

$$I'(t) = \frac{1}{2} [I + x_q Q \cos(2\Omega_1 t) + x_u U \cos(2\Omega_2 t) + x_v V \sin(\Omega_1 t)]. \tag{3}$$

104 H. P. Povel et al.

 $\Omega_1$  and  $\Omega_2$  are the frequencies of PEM1 and PEM2, respectively. The coefficients  $x_{q,u,v}$  depend on the optical parameters chosen. For the setup described above, with  $A_1 = A_2 = 2.40$  one gets  $x_q = x_u = 0.61$  and  $x_v = -0.74$ .

According to (3), besides the DC component  $I_i$ , the output I'(t) so the modulator contains three AC components with frequencies  $2\Omega_1$ ,  $2\Omega_2$ , and  $\Omega_1$ , having amplitudes proportional to the polarization parameters Q, U, and V, which can be measured by synchronous demodulation techniques. A single channel system of this type which uses three lock-in detectors is presently under test at Arosa Astrophysical Observatory of the ETH Zürich. Two beam splitters are positioned behind the modulator package, if three CCD array sensors are used for the Q, U, and V images. In Fig. 1 only the first beam splitter (BS) is shown.

#### 3. The Demodulator

A small modulation  $a\sin(\Omega t)$  with known frequency  $\Omega$  buried in a noisy background with a frequency spectrum  $f(\omega)$  can be detected by synchronous demodulation as will be explained below. The input signal I(t) is multiplied by a periodic demodulator function  $D(\Omega t)$ . The product  $D(\Omega t) \times I(t)$  is passed through an integrator (low pass filter) with a time constant T. If  $D(\Omega t)$  is performed by periodic switching between +1 and -1 polarity, the output of the integrator as a function of the frequency  $\omega$  of the input signal is given by

$$S(\omega) \sim \sum_{k=1,3,5,...} \operatorname{sinc}[(k\Omega - \omega)T],$$
 (4)

This expression shows, that a very strong supression of noise at  $\omega = \Omega$  can be achieved, if the integration time T is made much longer than the modulation period  $2\pi/\Omega$ .

With an integrating photo detector synchronous demodulation can be performed easily by periodically reading out and summing the photo charges  $q_+$  and  $q_-$  generated during the first and second half of the modulation period. The normalized difference (fractional polarization) of the sums  $Q_+ = \sum q_+$  and  $Q_- = \sum q_-$ ,

$$P = \frac{Q_{+} - Q_{-}}{Q_{+} + Q_{-}},\tag{5}$$

is independent of the signal amplitude, which depends on the responsivity of the photo detector and on the photon flux. P is proportional to the Stokes parameter selected by the demodulation frequency  $\Omega = \Omega_1$ ,  $2\Omega_1$ , or  $2\Omega_2$ .

In CCD image sensors the read-out frequency of one pixel is limited by the maximum frame rate, which is usually 60 Hz (or two or four times larger if arrays with multiple output registers are available). Therefore the modulation frequency is restricted to 30 Hz, completely incompatible with the 50 kHz modulation frequency of the PEM, and much too low as compared with the limit imposed by the seeing fluctuations.

A solution to this problem has been found and successfully tested by Povel et al. (1990). The basic idea is to integrate the two images  $I_+$  and  $I_-$  corresponding to the two modulation phases (half periods) directly on the chip without reading them out after each modulation half-cycle. For this purpose a storage area protected from light must be provided on the chip, where the two images can be stored alternatingly during the two modulation phases. During a phase transition the image charges are rapidly transferred from the storage area to the light sensitive zone and vice versa. This cycle is repeated many times, until the summed charges nearly fill the CCD potential wells and the frame is read out.

The principle is illustrated in Fig. 2. The storage zone is formed by covering every second CCD row by an opaque mask. During integration the charge packets are shifted up and down by one row

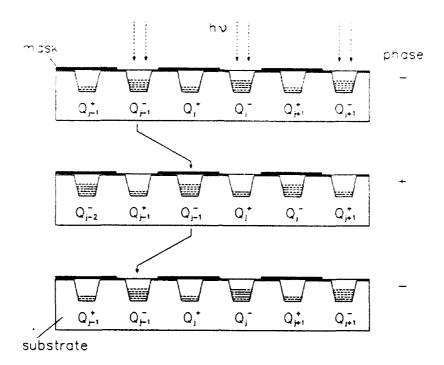


Fig. 2. Principle of demodulation with a three-phase CCD-image sensor. Shown are the potential wells along a column and the position of the charge packets during the two modulation half periods (indicated as + and -).

in synchrony with the modulation. After read-out of the frame the image of the fractional polarization  $P = (I_+ - I_-)/(I_+ + I_-)$  is calculated by combining corresponding rows.

The finite transfer time needed to shift the rows by one position leads to a mixing of  $I_+$  and  $I_-$ , thus reducing P. Another mixing effect which is due to transport losses during the charge transfer, limits the useful number of modulation cycles over which can be integrated.

The P86000 frame transfer sensor made by EEV was chosen for this project, because its three-phase buried channel structure allows fast bi-directional charge transfer and promises a very high transfer efficiency. The sensor has 385 pixels/line, 285 lines/half-frame and a pixel size of  $22 \mu m \times 22 \mu m$ .

The setup is depicted in Fig. 1. It shows the above described modulator package together with a block diagram of the electronics. The reference signal  $f_2$  from the PEM2 oscillator driver (OSC2) is passed through a phase shifter (PH), which also doubles the frequency. The signal  $2f_2$  is fed into the CCD electronics block (EL), where it is used by the clock sequencer during demodulation. The analog signal from the CCD sensor is amplified and processed (EL) and finally digitized into a 12 bit/3MHz video data stream by a fast analog-digital converter (ADC).

The first test to demonstrate the feasibility of the method (Povel, et al. 1990) was made with a slit imaged on one CCD row. It showed that the transfer time could be made sufficiently small not to cause a noticeable smearing effect on P. Furthermore no significant degradation of the polarization signal could be observed for a modulation frequency as high as 100 kHz, even at 1 s integration time, i.e., after  $2 \times 10^{-5}$  shifts. To avoid a significant parasitic signal in the screened storage rows, the width of the slit imaged on the sensor surface may not be larger than 18  $\mu$ m.

After it was shown that the new demodulation principle works well for one row, the next natural step would have been to put a slit mask directly on the CCD chip. However, because this has to be done during the manufacturing process, where the costs are rather high, we decided to project in scale 1:1 a mask with  $18~\mu m$  slits on the sensor. With this setup two-dimensional polarization images have

been obtained. Yet some critical restrictions became apparent. The 1:1 scale, which has to be accurately maintained, requires very fine positioning and high mechanical stability within 1  $\mu$ m. Furthermore the setup proved to be sensitive to small optical aberrations, leading to an incomplete masking at the outer part of the field of view. The use of a high quality optical system can certainly solve these problems, but the setup would still remain rather cumbersome and difficult to adjust.

For this reason we finally decided to place the mask directly on the sensor. EEV agreed to manufacture some modified chips according to our specifications. The geometry is shown in Fig. 3. The aluminium mask is isolated from the electrodes by a thin oxide layer. In order to have a better charge collection and separation, the potential well is extended over two electrodes  $\Phi_1$  and  $\Phi_2$  during integration, whereas during charge transport only one electrode is kept at high potential. The transmission of the mask turned out to be  $< 10^{-5}$ . The cross talk between screened and unscreened rows due to light scattering and charge diffusion was measured to be about 0.02. This leads to a reduction of the demodulated signal (apparent depolarization) by a factor of 0.96, which is acceptable by a wide margin.

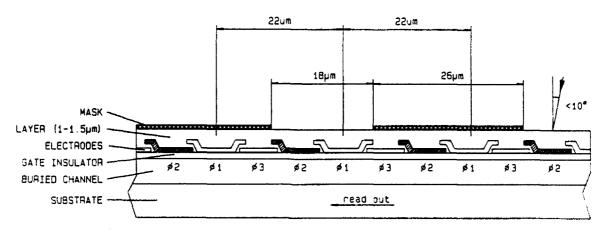


Fig. 3. Cross section through the modified EEV P86000 imager with aluminium mask.

The phase dependence  $P(\alpha)$  of the demodulated signal was found to agree well with theory. The expected function is plotted in Fig. 4 together with the measured values, which are averaged over a square of  $16 \times 16$  pixels. The theoretical curves have been multiplied by a constant calibration factor (given in Fig. 4).

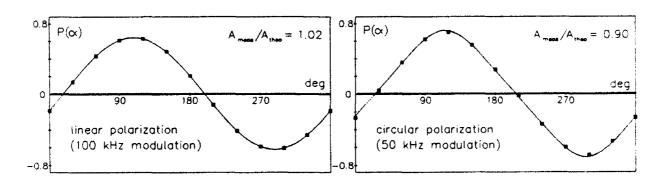


Fig. 4. Demodulated signal  $P(\alpha)$  as a function of phase shift  $\alpha$ . The measured values (black squares) have been obtained with 250 ms integration time, and have been averaged over columns 40-55 and rows 40-55.

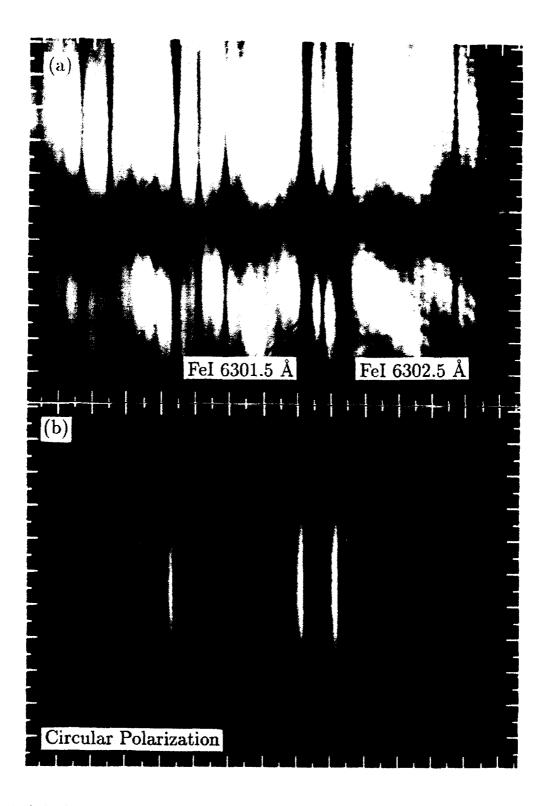


Fig. 5. (a) Stokes I, representing  $I_+ + I_-$  (raw data) and (b) Stokes V/I, representing  $(I_+ - I_-)/(I_+ + I_-)$ . The spectrum was recorded in first order, with the spectrograph slit crossing a sunspot. The exposure time was 250 ms, the chip temperature  $-5^{\circ}$ C. The field of view is approximately  $110'' \times 14.6 \text{ Å}$ .

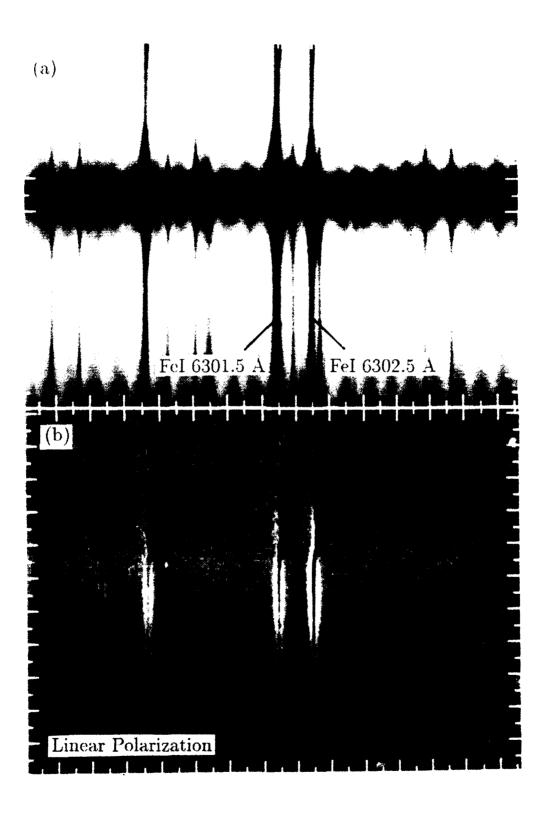


Fig. 6. As in Fig. 5, but for (a) Stokes I and (b) Stokes Q/I.

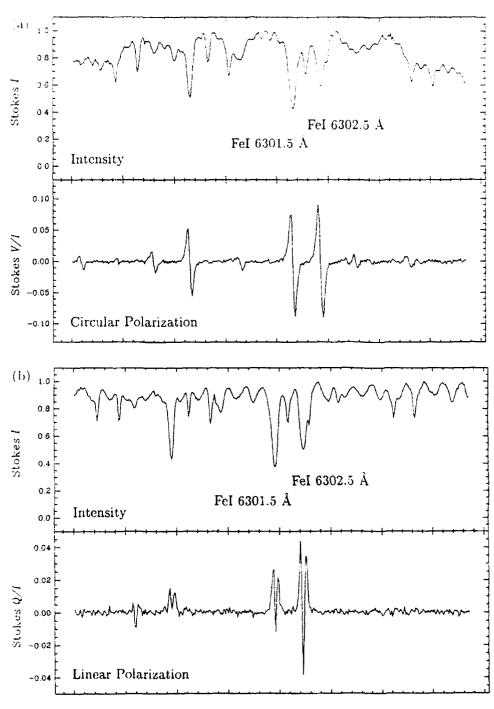
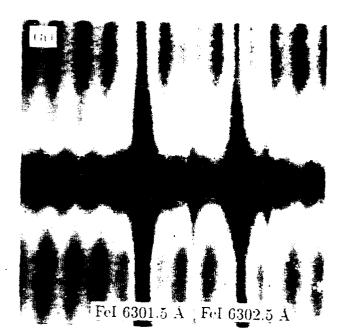
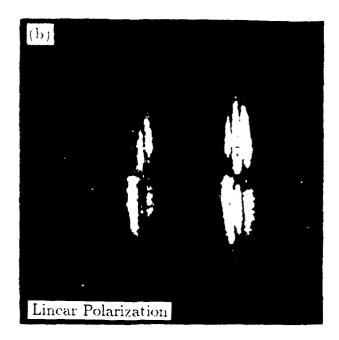


Fig. 7. Cross sections through the two-dimensional spectra shown in Figs. 5 and 6, along one pixel row through the center of the sunspot. Via the Zeeman effect the magnetic field in the sunspot generates the characteristic symmetric Q/I and anti-symmetric V/I line profiles. The rms noise is approximately  $3 \times 10^{-3}$  in the V/I spectrum and  $10^{-3}$  in the Q/I spectrum.





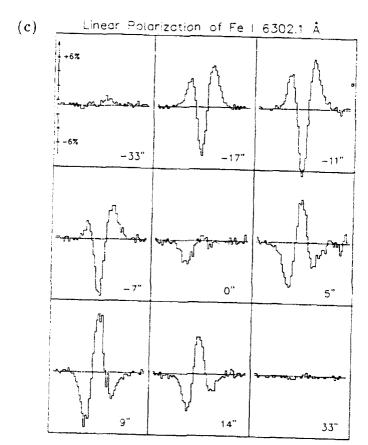


Fig. 8. (a) Stokes I (raw data), (b) Stokes Q/I, and (c) cross sections through the Q/I-image of the FeI 6302.1 Å line at different distances from the sunspot. The spectrum was recorded in the second order. The integration time was 300 ms, the chip temperature  $-8^{\circ}$ C. The field of view is approximately 95"  $\times$  3 Å.

For 100% linearly polarized light one obtaines

$$P(\alpha) = \frac{4}{\pi} J_2(A) \sin(\alpha) / [1 - J_0(A)], \tag{6}$$

for 100% circular polarization

$$P(\alpha) = \frac{4}{\pi} [J_1(A)\sin(\alpha) - \frac{1}{3}J_3(A)\sin(3\alpha)]. \tag{7}$$

First two-dimensional Stokes Q and V line profiles have been obtained with a prototype of the new polarimeter at the ETH solar tower in Zürich (f=10.7 m, D=25 cm) at the focus of a Littrow spectrograph (f=4.6 m, 1200 lines/mm). The effective pixel size corresponds to  $0.85'' \times 37$  mA in the first order, or  $0.85'' \times 14$  mÅ in the second order.

The data shown in Figs. 5-8 are raw data, not corrected for pixel-to-pixel variations of the responsivity and analyzing power. The strong fringes appearing in the I-images are probably due to interference effects in the glass windows in front of the sensor (CCD cover and vacuum window). This can be seen by the change in the fringe pattern, when the components are rearranged (see the difference between Figs. 5a and 6a). The fringes, which may be removed by flat fielding, will be reduced in an improved setup. Nevertheless, the fringe effects are entirely absent in the V/I and Q/I images, as expected. Thus the polarimetric accuracy is not dependent on the accuracy of the flat field.

Acknowledgements. H. Aebersold was responsible for the design of part of the electronics. The mechanical setup was constructed by F. Aebersold. The project is supported by the Swiss National Science Foundation under contract No. 20-26'436.89.

#### References

Kemp, J.C.: 1969, "Piezo-Optical Birefringence Modulators," J. Opt. Soc. Am. 59, 950.

Stenflo, J.O.: 1984, "Solar Magnetic and Velocity-Field Measurements: New Instrumental Concepts." Appl. Opt. 23, 1267

Povel, H.P., Aebersold, H., Stenflo J.O.: 1990, "Charge Coupled Device Image Sensor as a Demodulator in a 2-1) Polarimeter with Piezo-Elastic Modulators," Appl. Opt. 29, 1186.

#### Discussion

- D. Deming: What is the cause of the asymmetry in linear polarization, where the two sigma peaks have unequal amplitudes?
- P. Povel: It is probably due to cross-talk caused by the telescope mirror system.
- L. November: Would it be possible to manufacture a CCD with rows separately masked with alternate polarization states?
- P. Povel: No, one is restricted to a metal mask (e.g. aluminum).
- C. Keller: The difference to previous schemes lies mainly in the fact that both polarizations are measured with the same detector area. When calculating Stokes V divided by Stokes I the gain table divides out. This leads to an accuracy of  $10^{-3}$  at exposure times of 0.25 sec (with a small telescope).
- L. November: I think that a 2 polarized scheme does not preclude forms of automatic gain cancellation between the 2 polarizer channels if the output CCD rows are shifted in sign within the retarder modulator.
- S. Tomcyzk: In both your instrument, and that of D. Rust, one half of the solar image is lost. How will this affect the science you intend to do?
- D. Rust: In the scheme with a Ronchi ruling and a birefringent beam splitter, both senses of polarization are passed and detected all the time. It has a factor of 2 greater light efficiency than the modulation scheme, but the loss of spatial resolution is the same, namely, a factor of 2 in one of the two dimensions.
- P. Povel: If you mean intensity then it is just a loss in photons ( $\sqrt{2}$  loss in statistics). If you mean spatial resolution then it is a factor of 2 we loose.
- A. Gary: What was the transfer loss in the CCD array? Was this 10<sup>-5</sup>? Does this represent the S/N limit for the device?
- P. Povel: We don't see a significant degradation of the measured polarization signal (with 100% polarized input), even if we integrate for 1s. At 100 kHz modulation frequency this means  $2 \cdot 10^5$  times shifting the lines back and forth. From this we conclude that transfer losses should be much smaller than  $10^{-5}$
- T. Moran: Would you prefer to transfer rows at a slower rate than 50 kHz? If so, why?
- P. Povel: Transferring rows at a slower rate would allow longer integration, if there is a large transfer loss.
- M. Semel: What would be the total efficiency? Do you plan to observe several lines (in different wavelength ranges) simultaneously?
- P. Povel: We have not yet calibrated the total efficiency of our system, but plan to do this in the near future. Yes, the system is well suited for simultaneous observation of different lines.
- B. Lites: How can the system be as efficient as, say, a rotating wave plate, when beam splitters are required to obtain simultaneous Q, U, V signals? The separate detectors are blind to the frequencies at which the other stokes parameters are modulated, therefore the system efficiency must be much lower than a device that detects all three modulation efficiencies simultaneously.
- P. Povel: It is true that each of the three CCDs sees only one of the three modulation frequencies and we loose a factor of three in Stokes Q, U and V, but not in I. However, we believe that our system is free from the systematic errors and seeing noise, which are the major problems with a rotating wave plate system.

# 2-D REAL TIME POLARIMETRIC SPECTROGRAPH WITH

#### 64-CHANNEL

Ai Guoxiang

Beijing Astronomical Observatory Chinese Academy of Sciences Beijing 100080 P. R. China

#### ABSTRACT

The brief description of the multichannel birefringent filter and its three types is provided. 2-D real time polarimetric spectrograph with 64-channel, its achromatic KD<sup>\*</sup>P modulater, the construction with module, and automatic supplement system for temperature change, are introduced.

#### I. INTRODUCTION

At present, there are mainly two types of optical instruments for the solar physical research: the spectrograph represented by the solar grating spectrograph and the filter represented by the birefringent filter. These two types of solar instruments have a long history and both have played an important role in the research of solar physics. They are being developed and improved. Each type has its own strong points as well as weak. The grating spectrograph provides a broad spectral range with a very high spectral resolution, but it is restricted to an one-dimensional field of view along a spectrograph slit. The 2-D spectrum obtained by means of machanical scan is not simultaneous. In contrast with the spectrograph, the filter can obtain a solar monochromatic image with plane simultaneously, but it can not obtain a solar spectrum simultaneously. Recently, a universal birefringent filter (Beckers, 1975) can obtain different monochromatic images with different wavelengths, but can not yield solar spectrum simultaneously. A survey for a new instrument combining the advantages of the above two types is in urgent need in the research of solar physics, inspecially, in research of eruptive proceedure, stokes parameter profile for vector magnetic field, line profile for real velocity field. A new system, the multi-channel birefringent filter (MCBF), has been developed to achieve simultanously good spatial coverage at a number of wavelengths with high spectral purity (Ai and Hu, 1985a, 1985b, 1987a, 1987b, 1987c). The three types are introduced in section 2. A Solar Multichannel Telescope with 9-Channel is under developing at Huairou Solar Observatory of Beijing Astronomical Observatory. 2-D real time spectrograph with 64-channel, the achromatic KD\*P modulator, the construction and automatic supplement system for temparature will be introduced in section 3. 4. A discuss and proposal will be in section 5.

# II. THE PRINCIPLE OF A MULTICHANNEL BIREFRINGENT FILTER

1. Compound Polarizing Beam Splitter (CPBS)

114 Ai G.

As early as in 1947, Banning constructed the polarizing beam splitter (PBS). The principle of the polarizing beam splitter is illustrated in Figure 1a. Part of the incident light is reflected at the Brewster angle from a multi-layer, thin film surface, and the rest is transmitted. The reflected (S) and the transmitted (P) beams have mutually orthogonal linear polarization.

Over the years one has improved substantially the polarizing beam splitter (PBS), e.g. in terms of throughout, which may be as high as 95-97%, the field of view, the spectral quality, and the stability of the material. At present, the degree of polarization of a PBS is about 99.5%, and it can be used in a convergent beam with a focal ratio of 8:1. The working wavelength range in the visible is about 3,000 Å. The absorption of light is about 3-5%, which is better than 10%-15% for polaroids. Although PBS has been known for nearly fourty years, it has not yet been used in birefringent filters. The two main reasons for this are that one polarizing degree is slightly lower (usually about 99%) than required for the filter, and it is generally more expensive than the polaroid. To overcome the low degree of polarization, the compound polarizing beam splitter (CPBS) has been designed. In Figure 1b two polaroids, with polarizing degree of about 90%, are inserted immediately after the PBS, which polarize the two emergent beams to about 99%. The resulting degree of polarization then becomes

$$P = 1 - 0.5 \times (1 - 0.99) \times (1 - 0.90) = 0.9995$$

This value satisfies fully the requirements for the filter. Because the transmission of the polaroid (which has a degree of polarization of only 0.90%) is higher than 0.95, the resulting transmission of the CPBS becomes 90-92%. The transmission of the CPBS may be enhanced by improving its multi-layer thin film.

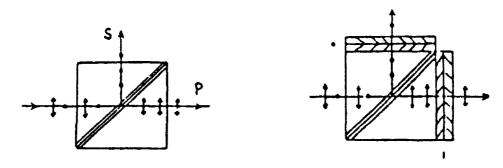


Figure 1. a. À polarzing beam splitter b. A compound polarizing beam splitter 2. The Principle of a MCBF

Figure 2 illustrates a compound element of a Lyot filter. When P2 || P1, the transmisson is  $T_{||} = cos^2(\pi\mu d/\lambda)$ . The factor  $\mu$  is the birefringent index, and d is the thickness of the birefringent crystal. When P2 $\pm$ P1, one gets  $T_{\perp} = sin^2(\pi\mu s/\lambda)$ .  $T_{||}$  and  $T_{\perp}$  supplement each other in the transmission spectrum, that is  $T_{||}+T_{\perp}\equiv 1$ . When the polaroids are used, one beam and one channel can be obtained.

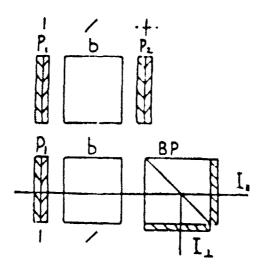


Figure 2. The figure illustrates the difference between the traditional Lyot filter and a MCBF.

The other beam is absorbed and leads to heating of the element. When a CPBS replaces the polaroid in Figure 2, two beams,  $I_{\parallel}$  and  $I_{\perp}$ , are available, and one has a multi-channel element.

A MCBF with three elements and its spectral transmission profile are shown schematically in figure 3 and Figure 4. The eight channels are equally spaced in the spectrum.

A polarizing solid Michelson interference filter has been constructed by Title and Ramsey (1980). As early as in 1949, an analogous filter was originally suggested by Evans. The spectral resolution of the filter may reach 10<sup>6</sup>, which corresponds to about 0.01 Å. A multichannel, polarizing solid Michelson interference filter (MPSMIF) is similar to a MCBF (Figure 5). It is also possible to make a MCBF with 0.01 Å spectral resolution.

Since the beam can be directed forwards, backwards, and sidewards, various geometrical arrangements can be applied to obtain suitable configurations of the MCBF. The reflected beam can either be directed up, down, left, or right relative to the incident beam. Various models of the MCBF can thus be constructed, but they can be divided into two main categories. One is the orthogonal model, for which the directions of the emergent beams from every CPBS are perpendicular to each other. This model keeps the original PBS scheme, which is simple. It is suitable for filters with only a few channels, in which case the detectors, e.g. the cameras, are placed farther apart. The second category is the parallel model, for which the orthogonal beam from the CPBS is reflected to a parallel direction using total reflecting prisms. The directions of the exit beams then become parallel with the incident beam. All channels are placed in a square matrix, for example, 2×2; 3×3; 4×4; and so on. This solution provides a compact MCBF, which may be

enclosed in the same thermostat or cooling system as the detectors (CCDs or reticons). According to the scheme of Figure 3 the following quantitative relationship in the MCBF.  $M = 2^N$  where N is the number of MCBF elements, as M is the number of channels, the number of CPBS is M-1.

## 3. 2-D Spectrograph

The first type of a MCBF that we will describe is the 2-D real time spectrograph. When the thickest crystal is located at the beginning, and thinner crystals are placed successively later along the light path, the 2-D spectrograph is obtained. When the spectral channels of the MCBF are distributed around a particular spectral line, a 2-D spectrograph is obtained.

We might be shocked at a great number of filters with narrow band for the MCBF. Fortunately, this problem can be resolved by the construction of MCBF itself. The thick crystal is required to be located in the fore part of the filter and thinner crystal in the rear along the light path. The thickest crystal is applied to all the channels so as to reduce the amount of crystal. It the thickness of the thickest element is d, the total crystal thickness of the Lyot filter is  $(2-1/2^{n-1})d=2d$ , where n is the number of elements. In the 2-channel filter, the thickest crystal is still d. The two successive filters need separate crystals with thickness d each. So the total crystal thickness is Sd. In the 4-channel filter, the thickest crystal is still d, the following less thick crystal is  $2 \times d/2 = d$ . The following next less thicker crystal is  $4 \times d/4 = d$ , so that for the 4-channel filter, the total crystal thickness is 4d. Each element in MCBF has equal crystal thickness. Table 1 gives the amount of crystal for MCBF.

Table 1

Relation between the number of channels and the amount of crystal needed for an MCBF

No. of channels	Total crystal thickness	In Comparison with Thickness of Single Lyot Filter
1	2d	1
2	3d	1.5
4	4d	2
8	5d	2.5
16	6d	3
32	7d	3.5
64	8d	4
128	9d	4.5
256	10d	5
512	11d	5.5
1024	12d	6
2048	13d	6.5
4096	14d	7

Table 1 shows that when the number of channels increases exponentially, while the amount of crystal needed increases only linearly.  $M=4^{R-1}$ , where R is the rate

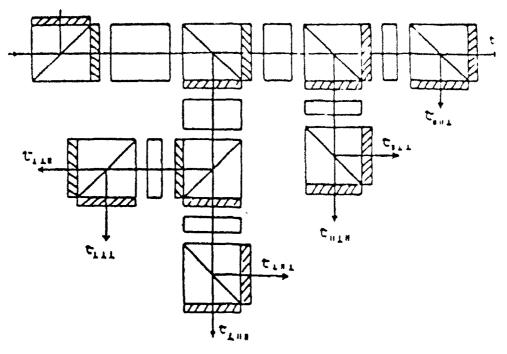


Figure 3. An eight channel scheme of MCBF

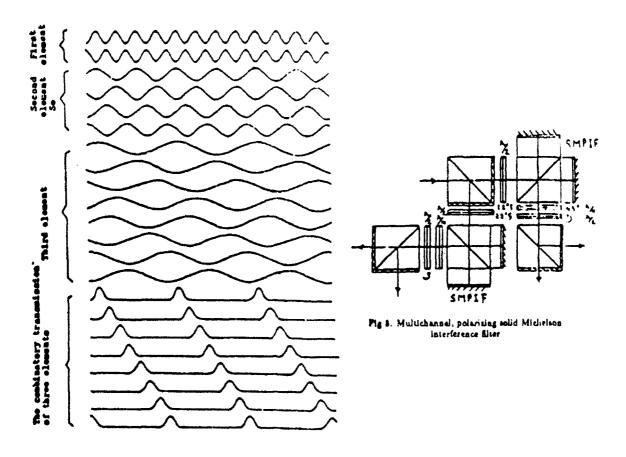


Figure 4. The spectral transmission profile of an night channel MCSF.

of total crystal thickness of MCBF to single filter. It should be emphasized that a smaller amount of calcite has been practically used than that of quarts which is cheaper and processed more easily. Quartz plates equally thick can be produced in batch. CPBSs and equipments adjusting wave lengths are used in large quantities. Though these components are not expensive, the process and adjustment need a large amount of labour indeed.

# 4. The Totally Transmitting Berefringent Filter

If two identical birefringent filters are placed in the two beams split by the first CPBS and the beams from these two filters are merged into one beam by the last CPBS, one gets a totally transmitting birefringent filter. This is so because the totally transmitting birefringent filters utilize the rest half light which is absorbed by the first polaroid in the traditional filter. Its transmission is twice that of the traditional filter. Using the same procedure for each of the split beams, one can multiply the number of channels and obtain a totally transmitting filter with any desired number of channels.

# 5. The Multichannel Head Birefringent Filter (MHBF)

In the MHBF, by selecting more primary elements of the filter, the channels transmitting the selected spectral lines are first isolated, after which the narrower elements are placed separately ine the different channels. The merits of an MHBF are the following:

- (1) The thickest crystal does not have to be located first, which reduces the heating load on it.
- (2) Every channel can have an independent bandwidth, in order to suit the need of the particular lines.
- (3) Behind the MHBF one may place Fabry-Perot filters and/or Daystar filters, which are all single channel interference filters.
- (4) Filters which are available in an observatory can be combined with the MHBF and used for simultaneous observation of monochromatic solar images.

# 6. 9-channel Birefringent Filter

A 9-channel birefringent filter is being designed and constructed for the Huairou Solar Observatory of the Beijing Astronomical Observatory (Ai and Hu, 1985e). Each filter channel is a universal filter, and all are adjustable in wavelength and have wide angular field. Since of with different wavelengths are used simultaneously to observe vector magnetic fields, a chromatic polarizing light analyser has to be used. A chromatic polarizing analyser using KDPs has been proposed by Ai and Hu (1985e).

# III. 2-D REAL TIME POLARIMETRIC SPECTROGRAPH WITH 64-CHANNEL

## 1. Optical System

The spectrograph consists of a filter with 64-channel, a prefilter, an achromatic KD\*P modulator with two pieces of achromatic  $\frac{\lambda}{4}$  wave plane, a collimator, 8 image lens and a lot of interference filters. The construction is shown in Fig. 6. In brief, the optical elements with Mark I is represent for Mark II-VIII.

#### 2. The Filter with 64-channel

The elements of the filter are shown in Table 2. The elements of No. 1-No. 6 are the multichannel elements following the polarizing beam splitters, the 64 channels are constructed. The passband of the filter are shown in Table 3. The half-widthes in 6563 Å, 5250 Å and 3933 Å are 0.05 Å, 0.03 Å and 0.014 Å respectively. Each element is universal element with achromatic compound waveplane of MgF2 and quartz or PVA. The total transmittance including KD°P, prefilter and interference filter is about 3%-5%. The elements of No. 7 and No. 8 are attachment elements which are used for match with the prefilter. It is possible to develope a 256-channel, by means of additional polarizing splitters.

## 3. Off-Axis Effect and Means of Treatment

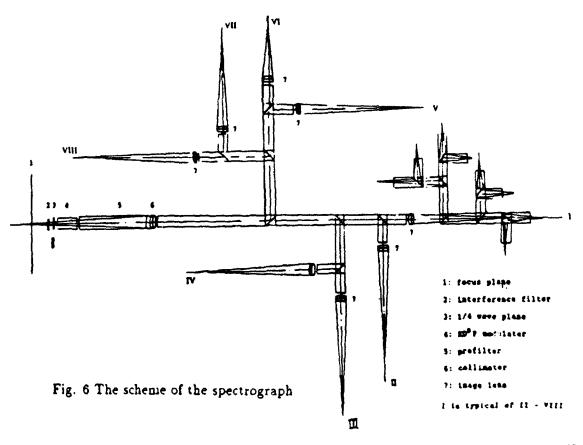
The off-axis effect of Lyot's I-type wide field of view element is as follows. (Lyot, 1944)

$$N - N_0 = N_0 \phi^2 \frac{1}{4\pi} \left( \frac{1}{a} - \frac{1}{m} \right) = N_0 \phi^2 \frac{\mu}{4m^2 \pi}$$
 (3.1)

where  $N_0$  is interference order on axis,  $\phi$  is incident angle, N is interference order on  $\phi$ . For calcite,  $\omega=1.662$ ,  $\Sigma=1.489$ ,  $\mu=0.173$  at 5576 Å,  $N_0$  of No. 1 element is about 71432.

$$N - N_0 = 751\phi^2 \tag{3.2}$$

The incident angle  $\phi$  is dependent on positions of use of the filter. At present, the commercial CCD cameras with 8.8×6.6 mm<sup>2</sup> target area and 512×512 pixels are considered. When a  $4' \times 3'$  and  $1.2' \times 0.9'$  of solar region are reciepted respectively, the sizes of solar disc are 70 mm and 235 mm, corresponding to focus distance of 752 cm and 2524 cm of the telescope, each pixel is corresponding to  $0."47 \times 0."35$ and  $0.''14 \times 0.''10$  of solar sizes. The former is corresponding to a general good seeing condition on the base-ground, the later to an excellent seeing condition or space condition. The varied apertures of the telescopes, the selected two focus distances and convergent or collimated beans are considered. The cemputed results are shown in Table 3. In convergent beam, the spectrograph is not used for large field of view  $(4' \times 3')$  in principle. However, it is able to be used for 60 cm aperture of the telescope for small field of view  $(1.2 \times 0.9)$ . If the former four elements are in collimated beam, it is able to be used for 60 cm aperture for the large field of view, and for 200 cm for the small field of view. That is direct to the present consturction of the spectrograph which the former four elements are in collimated beam.



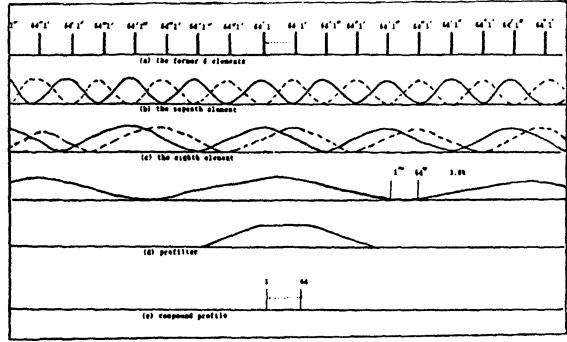


Fig. 7 The effect of the prefilter

	Table 2	
The	Elements of the	Filter

		Thick.				Interference Order	Thick of the
No	Material	(mm)	Counter	Widefield	Por C*	at 5576 Å	Element(mm)
1	Calcite	230	1	Yes	P	71432	298
2	Calcite	115	2	Yes	P	35716	174 642.25
3	Calcite	575.5	4	Yes	P	17858	116.5
4	Calcite	28.75	8	Yes	P	8929	53.75
5	Calcite	14.375	16	Yes	С	4464.5	119.38
6	Calcite	7.1875	32	Yes	С	2232.25	66.19
7	Calcite	3.5938	64	Yes	С	1116.125	27.6 233.97
8	Calcite	1.7969	64	No	C	558.0625	ار 20.8
9	Quartz	8.858	7	No	С	291	175
10	KD°P	2.0	6	Yes	С	± }	60.

P: in collimated beam C: in convergent beam

Table 3
The Passband of the Filter

_	Interference	Half-width of	Spectral	Spectral	Half-width of
Wavelength A	Order	Passband A	Resolution	Range A	Interference Filter Å
6562.808	59476	0.0500	131256	3.200	50
6302.499	62225	0.0454	138822	2.906	45
6173.341	63683	0.0433	142571	2.772	43
5889.979	67138	0.0389	151413	2.487	39
5875.650	67320	0.0386	152219	2.473	39
5576.099	71432	0.0342	163044	2.190	34
5324.191	75342	0.0306	173993	1.961	31
5250.216	76580	0.0296	177372	1.897	30
5247.060	76631	0.0296	177266	1.894	30
5183.618	77715	0.0287	180614	1.839	29
5172.699	77906	0.0286	180864	1.830	29
4861.342	83742	0.0254	191391	1.571	25
4685.682	87431	0.0224	209182	1.432	22
4340.468	95964	0.0184	235895	1.175	18
4226.728	99238	0.0171	247177	1.096	17
4101.748	103046	0.0158	259604	1.012	16
3968.470	107469	0.0144	275588	0.924	14
3933.664	108748	0.0141	278983	0.901	14

#### 4. Prefilter

Because the passbands of the spectrograph are continuous distribution along the the spectrum, the prefilter is common to all of passbands, so the prefilter has to have a square peak transmission band. If the Lyot element was used, the different transmittances and the different stray light would be appeared in the the different channels, The prefilter is a Solc filter with 7 pieces of quarts with same thickness and the tapering angle different distribution (Solc, 1965; Fredge and Hogbom, 1971). So the prefiter has a plane top of transmission band. The transmittance difference among 64 passbands are about  $\pm$  0.005. The transmission profiles of the filter are shown in Fig. 7. The prefilter is also universal filter from 3900 Å to 7500 Å.

Table 4 The Parameter to Use of the Spectrograph

		Carrie	<u>,                                     </u>		·
5.	F*	Convergent or		_	
D.		Paralle Pencil	N-N <sub>0</sub>		S/N
		of Rays			
		C 68.6'*	0.30		1:1
	752 cm	P, 11*, 27.5'	0.049	33×33	1:1
30 cm		C 20.4'	0.027	<b>⊉</b> 15	0.3:1
	2524 cm	P, 11, 8.3'	0.0044	29×29	0.3:1
		C 91.4'	0.54	Ф43	1.3:1
	752 cm	P,15, 37.5'	0.091	34×34	1.3:1
40 cm		C 27.2	0.048	Ф21	0.4:1
	2524 cm	P, 15, 11.3'	0.0082	29×	0.4:1
		C 114'	0.85	Ф51	1.7:1
	752 cm	P,18.5, 46.3'	0.139	36×36	1.7:1
50 cm		C 34.1'	0.075	Ф23	0.5:1
	2524 cm	P,185,13.9	0.013	29×29 Ф43 34×34 Ф21 29× Ф51 36×36	0.5:1
		C 137'	1.22	Ф59	2:1
	752 cm	P, 24, 60'	0.234	36×36	2:1
60 cm		C 41'	0.108	Ф25	0.6:1
	2524 cm	P. 24, 18'	0.021	29×29	0.6:1
		C 183'	2.17	₫70	2.7:1
	752 cm	P, 35, 87.5'	0.49	39×39	2.7:1
80 cm		C 55'	0.19	Ф30	0.8:1
	2524 cm	P, 35, 26.3'	0.045	28×28	0.8:1
		C 229'	3.39	Ф91	3.3:1
	752 cm	P, 40. 100'	0.65	44×44	3.3:1
100 cm		C 68'	0.30	Ф35	1:1
	2524 cm	P. 40. 30'	0.058	31×31	1:1
		C 274'	4.59	Ф107	4:1
	752 cm	P, 48, 120'	0.94	48×48	4:1
120 cm		C 82'	0.43	Φ40	1.2:1
	2524 cm	P, 48, 36'	0.084	32×32	1.2:1
		C 343'	7.63	Ф131	5:1
	752 cm	P, 60, 150'	1.46		5:1
150 cm		C 102'	0.68		1.5:1
	2524 cm	P, 60, 45'	0.13	<u> </u>	1.5:1
		C 457'	13.57	<del></del>	6.7:1
	752 cm	P, 80, 200'	2.59		6.7:1
200 cm		C 136'	1.20	<u> </u>	2:1
	2524 cm	P, 80, 60	0.23		2:1
		C 571	21.2	<del>                                     </del>	8.3:1
t	752 cm	P, 100, 250	4.06		8.3:1
250 cm		C 170	1.88		2.5:1
	2524 cm	P, 100, 75	0.37		2.5:1
L	1 2021 (111	1 - , 200, .0	1 3.01	1 22 2 2 2	2.0.1

<sup>\*</sup> D: aperture, F: focus distance \* 11: angula magnification \* Maxmum of incident angle

## 5. Achromatic KD'P Modulator

An achromatic polarimatric analyser consists of an achromatic KD\*P modulator and two pieces of achromatic quater-wave planes. The achromatic KD\*P modulator consists of three groups of KD\*P modulators. Each group has two KD\*P with crossing optical axes each other and a sandwiched achromatic half-wave plane which is compound wave-plane of magnesium fluoride (MgF2) and quarts, so it is a wide field of view. The achromatic KD\*P modulator is a Pancharatnam's achromatic electric controlled wave plane (Pancharatnam 1955). The first and the third KD\*P groups have  $\delta=\pm115^{\circ}$  phase difference, the second one has  $\pm180^{\circ}$  phase difference. In the first and third group, the optical axes are parallel. The angle difference of optical axes between the second and the first one is 70°13′, the retardation is of the modulator is  $\pm45^{\circ}$ . The modulator is able to be used from 3900 Å to 7500 Å, the modulator is same as one for the Solar Multichannel Telescope for simultaneous vector magnetic fields in the different lines on the different solar layers.

# 6. Three Types of Usage Modes

- A. The usage mode for a single line and vicinal spectrum. When a previous interference filter is selected, any solar line from 3900 Å to 7500 Å can be observed.
- B. The usage mode for simultaneous multi lines. The channes of the spectrograph can be adjused to any places in the intervals of the maxmum transmission of the prefilter, so a lot of line profiles can be simultaneously observed. In this case, a lot of interference filters following the eighth elements will be substituted for the interference filter in the front used for single line.
- C. The usage mode for simultaneous 64 lines. The 64 interference filters may be needed, one channel one line.

Because the Maxmum transmission interval of the prefilter is  $\frac{1}{4}$  of the whole width of the prefilter, so each time  $\frac{1}{4}$  of all lines from 3900 Å to 7500 Å can be selected for simultaneous observation.

# IV. Machinery Structure and Supplementation to Temperature Change

# 1. Machinery

The machinery structure consists of four components: the crystal cell, the cell of polarizing beam splitter, the rotating device and the end closure. The all components are cordwood module to change any place and direction. So the machinery struction is very simple and very convenient to assemble, adjust and modify. For example, to increase up 256 channels or to decrease down 8 channels are very simple things. The total weight of the spectrograph is about 15-20 kg.

# 2. The Mean of Supplement to Temperature Change

In traditional filter, there is thermostat with accuracy from 0.°1 C up to 0.°01 C. A thermostat with 0.°01 C for the spectrograph is very complex and very difficult, because each element of the spectrograph can be adjusted in the passband. A supplement system to temperature change is instead of the thermostat. By means of the platinum resistance thermometer with 0.°01 C of accuracy, the computer

can be used for controlling the stepping motor to ratating the half wave plane or polaroid to change the passband for supplement to the temperature change.

In general, the spectrograph is used in a room similar to room of grating spectrograph, the change of the temperature is not fast, so the supllementation is easy. If the spectrograph is needed to attach to a telescope, a preliminary thermostat with  $\pm 5^{\circ}$  C accuracy may be needed.

# V. Prospect

Design of the spectrograph has been completed, needed calcite and quarts have been obtained. The manufactory will be begun in the end of this year. It will be completed in the end of 1992 in plan. As our observatory shortages ehough CCD cameras, interference filters, TV record and image processors, it is expected that the cooperations of both manufactory and observation among our observatory and other observatories in aspects of both ground-base and space-base. It is a thought that the spectrograph will be used for a portable attachment device combined with world famous solar telescopes, for example, the Sacramento Peak solar telescope, LEST, and Hido solar telescope for observing interesting project.

This work has been supported by Chinese Academy of Sciences and NSFC. It is my pleasure to thank the support of both international travel and attending the meeting from American NSO and ONR/AFOSR/ARO-FE.

### References

Ai Guoxian and Hu Yuefeng.: 1985a. in M. J. Hagyard (ed.). "Measurements of Solar Vector Magnetic Fields". NASA Conf. Publ. 2374 p. 257.

Ai Guoxiang and Hu Yuefeng,: 1985b. LEST Technical Report No. 14.

Ai Guoxiang and Hu Yuefeng.: 1987a, Scientia Sinica Vol XXX. No. 8, 868.

Ai Guoxiang and Hu Yuefeng,: 1987b, Scientia Sinica Vol No. 8.

Ai Guoxiang and Hu Yuefeng,: 1987c Acta Astrophysics Sinica Vol. 7, No. 4, 305.

Beckers, J. M., Appl. Opt., 14 (1975). 2016.

Banning, B.: 1947, J. Opt. Soc. am. 37, 729.

Evans J. W., J. Opt. Soc. Amer., 39 (1949), 229.

Fredga. K and Hogbom, J. A. Solar Physics, 1971. 20. 204.

Lyot B., Ann Astrophys., 7 (1944), 31.

Pancharatnam, S., Proc. Indian Acad. Sci., Vol. 41 (1955), 130-137.

Solc I., J. opt. Soc. Am Vol. 55 (1965), No6. 621.

Title, A. and Ramsey, H.: 1980. Appl. Optics 19, 2046.

#### Discussion

- S. Koutchmy: I think your wonderful instrument should not be called a spectrograph because it is not looking or analyzing a spectrum; it should be called a filter or an "imaging monochrometer". Can your 64-channel instrument be designed in 3 dimensions instead of being confined to a plane?
- Ai G.: A spectrum is the distribution of the intensity of light in wavelength. Because the channels are arranged as a distribution in wavelength it is called a spectrograph. From the intensity I(x,y) in wavelength  $\lambda$ , the spectrum  $I(x,y,\lambda)$  can be obtained. In practice, the construction of the 2D spectrograph is a 3D construction; it requires 6 directions to arrange the channels.
- J. Harvey: You have been very successful in building birefringent filters in the past. But obtaining a high quality piece of calcite of length 23 cm must be a problem. Have you found a good source of such rare calcite?
- Ai G.: The thickest element is the Lyot I-type wide field element, which consists of two half parts, whose axes are vertical to each other. We just need 115 mm of calcite, 6 cm of calcite having  $37 \times 37$  mm<sup>2</sup> area have been obtained. Two pieces of about 6 cm long calcite will be combined for both halves of the thickest element.
- J. Stenflo: What kind of data handling system do you plan to use to process the data from the 64 CCDs?
- Ai G.: In some sense, the 2D real time spectrograph is a spectrograph in the computer. Indeed a very powerful image processing system is necessary at present. There are two ways to resolve the problem: One is that we first use only a few channels. The other is that a new multichannel image processor will be available. We will consider buying such a new system.

# High Spatial Resolution Polarimetry using Filtergrams

C. U. KELLER

Institute of Astronomy
ETH-Zentrum, CH-8092 Zürich, Switzerland

Summary: Using tunable filters at the Sacramento Peak Vacuum Tower Telescope Stokes V images of various solar magnetic features have been observed. Simultaneous recording of left and right circular polarization leads to high spatial resolution magnetograms. Various instrumental effects of these observations are discussed in detail. A penumbra near disk center shows small-scale features in the magnetogram which are correlated with the bright filaments. To derive the magnetic field strength Stokes V images in the wings of Fe 15247.1 Å and Fe 15250.2 Å have been analyzed in terms of the magnetic line ratio technique. Whenever a measurable amount of polarization is present, the distribution of the observed magnetic line ratio is compatible with a unique value of the magnetic field strength of about 1000 G at the level of line formation.

#### 1. Introduction

The sun provides us with a variety of small-scale structures associated with strong magnetic fields, e.g. penumbral filaments, umbral dots, and facular points. To explore their origin, morphology, and dynamics we need to know, among other parameters, their magnetic field configuration. Since their spatial scale is intrinsically small, high spatial resolution polarimetry in Zeeman sensitive spectral lines is required. Polarimetry using spectrographs has been carried out for a long time to obtain maps of the circular polarization over large areas at moderate spatial resolution. An improvement of the spatial resolution and the overall quality was achieved by using tunable filters (e.g. Harvey, 1963; Beckers, 1968; Hagyard et al., 1982; Title et al., 1987; Lundstedt et al., 1990). The polarimetric sensitivity is considerably improved by recording both polarization states simultaneously (e.g. Beckers, 1968; Lundstedt et al., 1990). In Sect. 2 high spatial resolution magnetograms are presented, which have been obtained with a similar setup as the one used by Beckers (1968).

Since magnetograms are sometimes far from being a good measure of the magnetic flux or the field strength it is indispensible to combine magnetograms at various wavelengths to obtain reliable information about the magnetic field. Previous measurements of the magnetic field strength outside sunspots had a low spatial resolution of typically a few arcsec, so that they averaged over many individual magnetic elements. It has been argued (e.g. Semel, 1986) that the almost unique value of the field strength measured by several authors may in fact be due to the averaging over a wide distribution of field strengths in the different magnetic elements, or within a single magnetic element. By using filtergrams two-dimensional maps of the magnetic field strength are obtained, so that if any reliable variation of the field strength is observed, its spatial distribution, correlation with magnetic flux or continuum intensity etc. can be derived. In Sect. 3 a method to obtain high spatial resolution magnetic field maps is described and applied to filtergrams.

#### 2. High spatial resolution magnetograms

#### 2.1. Observations

The data have been obtained with the Vacuum Tower Telescope (VTT) of the Sacramento Peak Observatory (SPO) in combination with polarization analysis optics and the Universal Birefringent Filter (UBF). The analyzer package in front of the UBF consists of an achromatic quarter-wave plate, a double calcite polarizing beam-splitter, and another quarter-wave plate to balance the intensity of the two beams leaving the UBF. The UBF provides a filter profile full

width at half maximum of 65 mÅ at 5250 Å. After the UBF the two beams are focused onto a CCD camera with a pixel size corresponding to 0'.1. It is important to note that the complete polarization analysis is performed before the beam enters the UBF, whose polarizing characteristics are thus irrelevant. The retarder and the beam splitter produce two parallel output beams, corresponding to Stokes I + V and I - V. The sum of the two beams gives Stokes I whereas the difference yields Stokes V. Since the two orthogonally polarized images are recorded strictly simultaneously seeing effects are identical in both of them and do not produce any spurious Stokes V signal. The magnetogram is represented by Stokes V divided by Stokes I and will henceforth be called Stokes V/I.

From the large number of images obtained with this set-up selected frames are presented with exposure times of 0.5 sec at -50 mÅ from the center of Fe15250.6 Å. This—avelength position has been chosen because of the Stokes V asymmetry which leads to larger Stokes V signals in the blue wing as compared with the red wing (Stenflo et al., 1984). Fe15250.6 Å has the advantage over the well-known line Fe15250.2 Å that it is less sensitive to temperature variations and shows no molecular blends in sunspots while still having a sizeable Landé-factor of 1.5. Low spatial resolution observations of plages have indeed revealed that both lines exhibit similar Stokes V amplitudes (Stenflo et al., 1984; Solanki et al., 1986). Flat field frames have been obtained by moving the telescope over the quiet sun near disk center while leaving the optical set-up unchanged. Furthermore frames with a standard USAF three bar test chart in the focal plane have been recorded for measuring the displacement vector of the two beams. The data presented in this work was recorded on 23, 24, and 25 September 1988 in active region SPO 7740, which showed a large spot, numerous pores, and extended plages.

#### 2.2. Instrumental effects

For the interpretation of the measured polarization it is important to consider possible instrumental effects and estimate their contribution and relevance. Here optical distortions, instrumental polarization and phase retardations, as well as spatial and spectral stray light are considered. The rms noise in the magnetograms is determined from the flat field image sequences and amounts to 0.7%, which corresponds to the noise expected from the photon statistics.

Residual displacements between I+V and I-V due to spatial and temporal variations are smaller than 0.01. The maximum intensity gradient is about 10% over 1" leading to a maximum error in Stokes V/I of 0.1%, which may be safely neglected. Since Stokes I to Stokes V conversion due to the polarizing properties of the instrument, instrumental depolarization, as well as polarized stray-light do not produce artificial spatial structures in Stokes V/I they are not considered any further. Because Stokes Q and Stokes U seldom exceed 20% near disk center and the cross-talk between linear and circular polarization is less than about 10% an upper limit to the influence of phase retardations of 2% in Stokes V/I is expected.

Seeing does not affect Stokes I and Stokes V/I in the same way, although Stokes I and Stokes V are affected in the same manner. This can be easily seen from Eq. (1)

$$\frac{V}{I}(\mathbf{x}) = \frac{\int V'(\mathbf{y})S(\mathbf{x} - \mathbf{y})d\mathbf{y}}{\int I'(\mathbf{y})S(\mathbf{x} - \mathbf{y})d\mathbf{y}},$$
(1)

where I and V are the observed Stokes parameters, I' and V' the intrinsic Stokes parameters, and S the instantaneous point spread function. It is easily noticed that Stokes V'/I' is not equal to V/I as long as V' and I' are not proportional. The most simple example showing the influence of seeing on V/I is unpolarized spatial stray-light (Solanki, private communication). The panel at the top in Fig. 1 shows Stokes I with and without stray-light (dashed and solid lines respectively). Since we deal with unpolarized stray-light Stokes V is not affected (middle panel). The panel at the bottom shows the resulting Stokes V/I signals. This explains how seeing can create features in a magnetogram, although it can not produce a magnetogram signal without intrinsic polarization. An upper limit for spatial stray light is obtained from the darkest parts of an umbra and amounts to 15%. Due to a damaged UBF prefilter spectral stray light amounts to about 50% in these observations. The leakage is dominated by continuum radiation which lacks significant polarization. Although the spectral stray light does not produce artificial Stokes V signals the observed Stokes V/I signal is underestimated by a factor of about two.

126 C. U. Keller

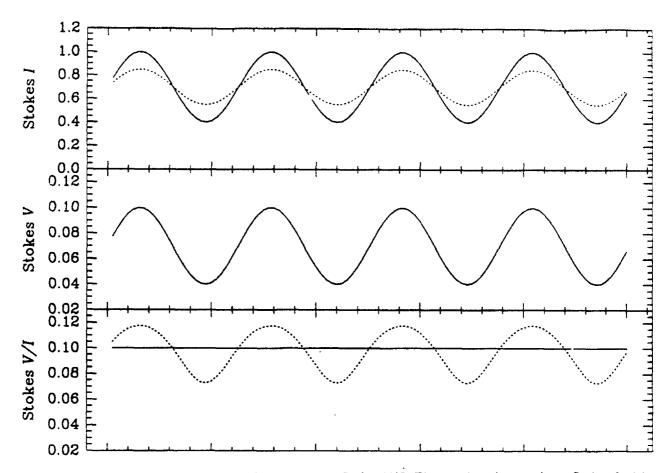


Fig. 1 The influence of unpolarized spatial stray-light on Stokes V/I. The panel at the top shows Stokes I with and without stray-light (dashed and solid lines respectively). Since stray-light is assumed to be unpolarized Stokes V is not affected (middle panel). The panel at the bottom shows the resulting Stokes V/I. This explains how stray-light can create features in a magnetogram.

#### 2.3. Results

In Fig. 2 part of the penumbra of a circular sunspot near disk center is shown. The left panel displays Stokes I while the right one displays Stokes V/I. The dark areas indicate small circular polarization while bright areas correspond to large circular polarizations. High frequencies dominated by noise as well as low spatial frequencies have been attenuated in these figures to enhance the visibility of small-scale structures. The small-scale structures in Stokes I as well as in Stokes V/I indicate the achieved high spatial resolution. A power spectrum analysis of Stokes I and Stokes V/I shows that spatial wavelengths down to about 0.5 contain signal. The most surprising feature in Stokes V/I is the filamentary structures, which are correlated with bright filaments.

Figure 3 displays a vertical cut through the images in Fig. 2. Since the variation of Stokes V/I is on the order of a few percent and even stray light of 30% cannot explain the observed variation instrumental effects can be excluded. Nevertheless this does not at all imply that these variations are associated with variations of the magnetic field. General profile changes in the filaments, which are expected from the greatly different temperature structures as well as Doppler shifts (e.g. Evershed effect), can easily produce such variations of the circular polarization at a fixed wavelength position. Since there do not exist any further observational constraints a quantitative interpretation cannot be done at the present time.

A small sunspot with light bridges (Fig. 4) shows the problems involved with the interpretation of magnetograms. Although it is well-known that the magnetic field is strongest in the umbra the polarization signal does not reach its maximum there, but in the light bridges. This is caused by the Stokes V maxima being more separated in the cool



Fig. 2 Part of a penumbra of a circular spot near disk center. The left panel shows Stokes I and the right one Stokes V/I (dark areas indicate small circular polarization while bright areas indicate large circular polarization). The large tickmarks have a separation of I''. A Fourier filter has been applied to suppress noise and enhance small-scale features. Note the filamentary structures in Stokes V/I, which are associated with bright filaments.

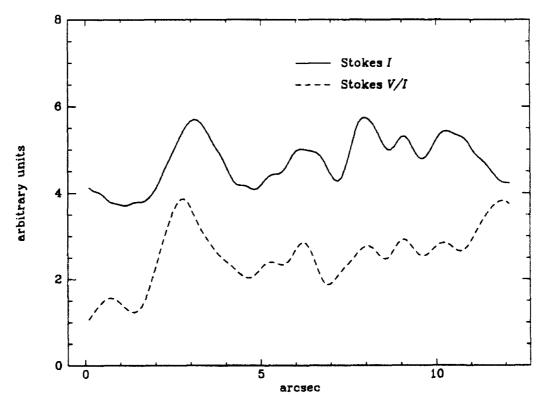


Fig. 3 Vertical cut through the penumbra shown in Fig. 2. The solid line is Stokes I, the dashed one Stokes V/I. Note the high correlation between Stokes I and Stokes V/I.

C. U. Keller

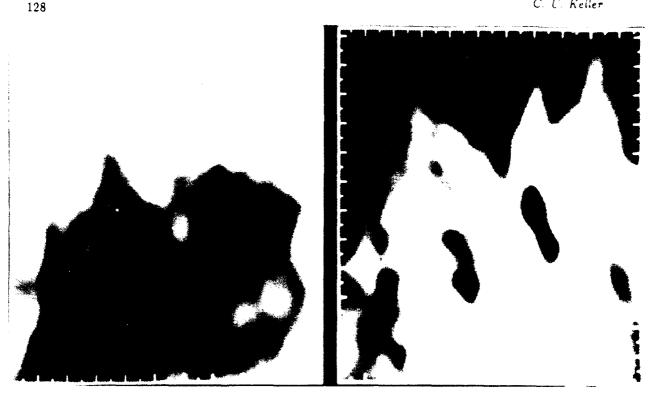


Fig. 4 Umbra and penumbra of a small sunspot near disk center. The left panel shows Stokes I while the right panel shows Stokes V/I. The applied image processing is the same as used for Fig. 2. Note the light bridges and the umbral dot showing large amounts of circular polarization.

umbra with high field strengths than in the light bridges with their hotter gas and probably lower magnetic field strength. Again the large amount of stray light needed to explain the observed variation in Stokes V/I is unrealistic Note that the upper light bridge is composed of two granule like features, which show strong polarization signals.

#### 3. Magnetic field strength determination

Numerous techniques have been developed to derive the intrinsic magnetic field strength of unresolved features, but most of them require spectrally resolved Stokes I or Stokes V profiles. A large number of filtergrams are required to obtain spectrally resolved line profiles for each spatial resolution element, which makes it very difficult to record all the filtergrams within a period within which the observed solar structure itself has not changed significantly. In contrast the magnetic line ratio technique developed by Stenflo (1973) allows magnetic field strength determinations from a small number of filtergrams. The magnetic line ratio is formed between the Stokes V signals of Fe I 5247.1 Å and Fe 15250.2 A divided by the ratio of their Landé factors

$$r_{\rm m}(\Delta\lambda_V, \Delta\lambda_F) = \frac{V\left(\lambda_I \left(\text{FeI } 5250.2 \,\text{Å}\right) - \Delta\lambda_V + \Delta\lambda_F\right)}{1.5 \, V\left(\lambda_I \left(\text{FeI } 5247.1 \,\text{Å}\right) - \Delta\lambda_V + \Delta\lambda_F\right)}. \tag{2}$$

V is the Stokes V signal as a function of wavelength,  $\lambda_I$  is the wavelength of the average Stokes I line center (averaged over the whole observed area), and  $\Delta \lambda_V$  is the Doppler shift of the Stokes V profile with respect to  $\lambda_I$  in a single resolution element.  $\Delta \lambda_F$  is the filter passband position with respect to  $\lambda_I$ . In this expression Stokes V should be thought of as having been convolved with the filter profile.

Since the two lines have nearly identical atomic parameters except for their Landé factors (g = 3 for Fe 15250.2 Å, geff = 2 for Fe i 5247.1 Å), the magnetic line ratio is almost completely insensitive to all atmospheric parameters except for the magnetic field strength (assumed to be height independent for the present analysis), the angle of inclination between the magnetic field vector and the line-of-sight, turbulent velocities, and Doppler shifts  $\Delta \lambda_V$ . All these parameters may vary from one resolution element to the next. The magnetic line ratio is unity for weak fields (Zeeman splitting much smaller than the Doppler width of the lines) and decreases for higher help strengths in the absence of noise. The magnetic line ratio is independent to a achieved spatial resolution. As defined in Eq.(2) the magnetic line ratio requires a maximum of four intergrans namely at two wavelength positions and in two polarization states each, which can be recorded in a sufficiently so or period. More details on these measurements can be found in Keller et al. (1990).

#### 3.1. Observations

The data have been obtained on August 7, 1987 by the Lockheed Group with their tunable filter at the SPO VIII. The observations consist of sequential images in left and right circular polarization in the wings of Fe 15247 1 A and Fe 15250 2 Å at  $\Delta\lambda_F = -40$  mÅ and  $\Delta\lambda_F = -80$  mÅ and in the true continuum at 5248 80 Å. The expressive time has been 400 ms, while the filter FWHM has been 55 mÅ. A pixel size of 0.177" has been chosen and a spatial resolution of better than 1" has been achieved. The observed region AR 4835 at  $\mu = 0.49$  consisted of a sunspot group the surrounding plages, and some quiet regions. The images have been corrected for the dark current and the gain table of the CCD camera, and differential geometric distortions have been removed.

A frame of about 8" by 9" has been extracted from the whole field of view for further analysis. It shows parts of a sunspot at the lower boundary as well as a small pore surrounded by a strong, unipolar plage (see Fig 6c)

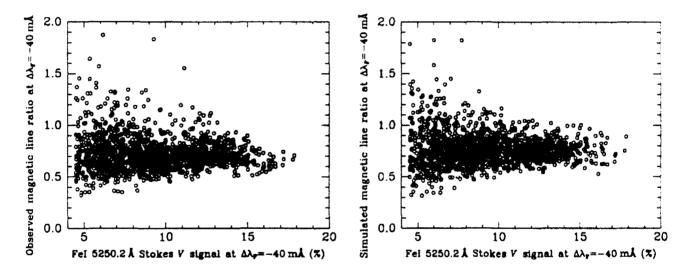


Fig. 5 a: Observed magnetic line ratio at  $-40 \,\mathrm{m}$ Å from the average Stokes I line center versus the normalized Fe 15250.2 Å Stokes V signal. Points with a Stokes V signal smaller than 4% have been omitted, since noise dominates at these low signal values. Each point in this figure corresponds to one pixel in the plage frame. b: Simulation of Fig. 5a assuming a constant magnetic line ratio of 0.75 and Gaussian noise with a standard deviation of 1.0% in the individual normalized Stokes V signals.

#### 3.2. Magnetic line ratio

Figure 5a shows the magnetic line ratio at  $\Delta\lambda_F = -40 \,\mathrm{m\AA}$  versus the modulus of the Fe 15250.2 Å Stokes V signal at  $\Delta\lambda_F = -40 \,\mathrm{mÅ}$ . Each circle in the figure represents one pixel in the frame. Pixels with a Stokes V signal smaller than 4% have been omitted because of their small signal to noise ratios. The average value of the magnetic line ratio appears to be relatively independent of the Stokes V signal while the scatter increases considerably with decreasing Stokes V signal.

Figure 6 shows maps of various parameters, i.e. the modulus of the Fe 15250.2 Å Stokes V signal at  $\Delta \lambda_F = -40 \,\text{mÅ}$  (Fig. 6a), the magnetic line ratio at  $\Delta \lambda_F = -40 \,\text{mÅ}$  (Fig. 6b), the continuum intensity at 5248.8 Å (Fig. 6c), and the ratio between the  $\Delta \lambda_F = -40 \,\text{mÅ}$  and  $\Delta \lambda_F = -80 \,\text{mÅ}$  positions of the Stokes V signal of Fe 15250 2 Å

 $C = U = K_{total}$ 

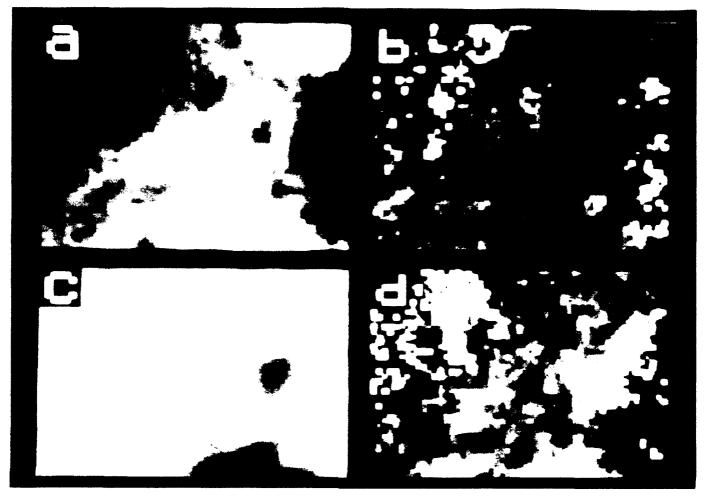


Fig. 6 Four images showing different aspects of a unipolar plage region. It includes a pore and parts of a sunspot which are surrounded by small-scale magnetic fields. The size of the frames is 8" by 9". The numbers in parentheses indicate the values of black and white in the corresponding frames. a Normalized Stokes V frame of Fe 15250.2 Å at  $\Delta\lambda_F = -40 \,\mathrm{mÅ}$  (0%, 20%), b magnetic line ratio at  $\Delta\lambda_F = -40 \,\mathrm{mÅ}$  (0, 2), c contrast in the true continuum at 5248.8 Å (-10%, 10%), d ratio between the Stokes V frames at  $\Delta\lambda_F = -80 \,\mathrm{mÅ}$  and  $\Delta\lambda_F = -40 \,\mathrm{mA}$  of the Fe 15250.2 Å line (0, 1).

(Fig. 6d). Whenever a measurable amount of magnetic flux (Fig. 6a) is present the magnetic line ratio shows no particular features that could be associated with structures in the continuum (Fig. 6c) or the Stokes V signal (Fig. 6a). However, it does show random, small-scale variations, reflecting the scatter seen in Fig. 5a.

Part of the variation of the magnetic line ratio might be due to changes in the shape of the Stokes V profiles or due to local Doppler shifts. This can be tested by looking at the ratio between the Stokes V frames of Fe15250.2 Å at  $\Delta\lambda_F=-40\,\mathrm{mÅ}$  and at  $\Delta\lambda_F=-80\,\mathrm{mÅ}$ . If the shape and the Doppler shift  $\Delta\lambda_V$  of the Stokes V profiles are the same for all individual pixels, then this ratio (i.e.  $V(\Delta\lambda_F=-80\,\mathrm{mÅ})/V(\Delta\lambda_F=-40\,\mathrm{mÅ})$ ) is expected to be constant over the whole observed area. With considerable random scatter this is basically the case, with the exception of the sunspot (Fig. 6d). The enhanced value of this ratio in the sunspot indicates that the Stokes V signal at  $\Delta\lambda_F=-80\,\mathrm{mÅ}$  is enhanced over the Stokes V signal at  $\Delta\lambda_F=-40\,\mathrm{mÅ}$  as compared with the ratio outside of the sunspot and indicates that the measured magnetic line ratio cannot be used to determine the field strength there. The main effect is due to the extreme temperature sensitivity of these two very low excitation lines. In a sunspot these lines are sufficiently strong to develop sizeable wings. Since for a given field strength the magnetic line ratio depends critically on the non-magnetic line width (Solanki et al., 1987), and the line width changes rapidly with temperature for strong lines, the magnetic line ratio cannot be considered to be a temperature insensitive diagnostic at penumbral or umbral temperatures. Another possible explanation for the enhancement of the  $\Delta\lambda_F=-80\,\mathrm{mÅ}$  to

 $\Delta \lambda_F = -40 \,\mathrm{mÅ}$  Stokes V signal is based on line shifts caused by the Evershed flow.

#### 3.3. Simulation

There are several possible sources of the scatter in the magnetic line ratio seen in Fig. 5a. These include photon and seeing noise. Doppler shifts, and a distribution of field strengths. For the present data the observed scatter can be explained in a natural way by a unique underlying magnetic line ratio which is randomly blurred by noise. To see this the observations are simulated in two steps. First synthetic Stokes V frames are created from the data without noise which lead to an intrinsic magnetic line ratio of 0.75, a value expected for  $\mu = 0.49$  and  $B = 2000\,\mathrm{G}$ . Then random noise with a position independent amplitude of 1% (corresponding to the photon and seeing noise as determined from two successive continuum frames) is added to the frames. By forming the ratio between the two synthetic, artificially rendered noisy Stokes V frames a crude simulation of the observed line ratio distribution is obtained. The similarity between the observation (Fig. 5a) and the simulation (Fig. 5b) is astonishing. The observations are, therefore, compatible with a unique value of the magnetic line ratio of 0.75, although a small dependence of the line ratio on, e.g., the Stokes V signal cannot be ruled out.

#### 3.4. Field strength determination

The observed distribution of the magnetic line ratio is compatible with a unique value. Consequently, our observations do not contradict the concept of a relatively unique magnetic field strength at the level of line formation within small-scale magnetic elements. However, to determine the value of this unique magnetic field strength, the line ratio must be calibrated. In other words, since the magnetic line ratio is not only affected by the magnetic field strength, the influence of other atmospheric and instrumental parameters on the magnetic line ratio need to be investigated to accurately determine the field strength from the observed ratio. To numerically explore these dependences fluxtube models have been used to represent the small-scale magnetic elements. Taking all influences on the magnetic line ratio into account and using the plage fluxtube model of Solanki (1986) with a field strength of 2000 G at the level of continuum formation within the fluxtube a line ratio of  $0.75 \pm 0.1$  is obtained at  $\Delta \lambda_F = -40 \,\mathrm{mÅ}$ . The uncertainty in the magnetic line ratio is due to the unknown Doppler shift  $\Delta \lambda_F$ , filter profile shape, angle between the magnetic field vector and the line of sight, and turbulent velocities which have been varied within reasonable limits. This result conforms extremely well with the observed line ratio, indicating an intrinsic magnetic field strength of about 2000 G at  $\tau_{5000} = 1$ . This is in excellent agreement with the results of Solanki et al. (1987) and Zayer et al. (1989), who obtained similar values from low spatial resolution spectra (5-10") by using the same fluxtube models.

#### 4. Discussion

Besides photon statistics, the dominant source of errors in the magnetogram observations discussed in Sect. 2 is due to the separate beams and detector areas of the two polarization states. These uncertainties restrict the present observational method to a polarimetric accuracy of about 0.2%. Magnetograms obtained from filtergrams are commonly recorded at a single wavelength position, i.e. in the wing of a Zeeman sensitive line. The observed polarization signal, however, is sometimes far from being a good measure of magnetic flux or field strength. To derive reliable information about the magnetic field from filtergrams it is indispensible to observe at various wavelength positions in various lines. Only then can influences of the magnetic field be separated from Doppler shifts and spectral line profile variations.

One example of such a multi filtergram analysis has been presented in Sect. 3. There the magnetic field strength has been derived from high spatial resolution filtergrams using the magnetic line ratio technique. Within the limits set by noise it was found that the observations are compatible with a unique value of the magnetic field strength in small-scale magnetic elements, in agreement with Stenflo (1973) and Wiehr (1978). Thus even in high spatial resolution magnetograms the signal level mainly reflects the variation of the magnetic filling factor and not the magnetic field strength. The data, however, cannot rule out the presence of a certain amount of flux in weak field

form, although it does not provide any positive evidence for such flux.

#### Acknowledgements

The present work was supported by the Swiss National Science Foundation under grants no. 2000-5.229 and 20-26436.89. The Swiss Society for Astrophysics and Astronomy provided a travel grant which is also gratefully acknowledged.

#### References

Beckers, J.M.: 1968, Solar Phys. 3, 258

Hagyard, M.J., Cumings, N.P., West, E.A., Smith, J.E.: 1982, Solar Phys. 80, 33

Harvey, J.W.: 1963, Astron. J. 68, 537

Keller, C.U., Solanki, S.K., Tarbell, T.D., Title, A.M., Stenflo, J.O.: 1990, Astron. Astrophys. 236, 250

Lundstedt, H., Johannesson, A., Scharmer, G., Stenflo, J.O., Kusoffsky, U., Larsson, B.: 1990, Solar Phys., in press

Semel, M.: 1986, in Small Scale Magnetic Flux Concentrations in the Solar Photosphere, W. Deinzer, M. Knölker,

H.H. Voigt (Eds.), Vandenhoeck and Ruprecht, Göttingen, 39

Solanki, S.K.: 1986, Astron. Astrophys. 168, 311

Solanki, S.K., Keller, C., Stenflo, J.O.: 1987, Astron. Astrophys. 188, 183

Solanki, S.K., Pantellini, F.G.E., Stenflo, J.O.: 1986, Solar Phys. 107, 57

Stenflo, J.O.: 1973, Solar Phys. 32, 41

Stenflo, J.O., Harvey, J.W., Brault, J.W., Solanki, S.K.: 1984, Astron. Astrophys. 131, 333

Title, A.M., Tarbell, T.D., Topka, K.P., Ferguson, S.H., Shine, R.A.: 1987, Astrophys. J. 336, 475

Wiehr, E: 1978, Astron. Astrophys. 69, 279

Zayer, I., Solanki, S.K., Stenflo, J.O.: 1989, Astron. Astrophys. 211, 463

## Discussion

- S. Koutchmy: I believe that unfortunately the stray light problem is indeed more complicated in case of sunspot observations; for example most stray light effects in the core is produced by light (polarized) coming from the penumbra and the spot is never axisymmetric nor at exactly the center of the disc. Further I wonder why you made your life difficult working with CCD in blue region; from our experience with the UBF we know it is better to work in red. Finally, concerning the surprising low level of polarization measured over the core of a sunspot, we use another line (629.17 nm) and we got the same result as you, even with the best spatial resolution.
- C. Keller: I fully agree that reality is much more complicated. The case of unpolarized spatial stray-light is just the most simple example you can think of. It is correct that the part of the spectrum has its advantages when working with the UBF and CCD's. However, the line used in the present work is in the green where fringes in the CCD are strongly reduced and the filter band-width is much narrower as compared to the red. Concerning the low level of polarization in the umbra see the answer to J. W. Harvey.
- **S. Koutchmy:** G. Stellmacher and I made a number of comparisons of strengths measured in 630.15 nm  $(g \sim 1.5)$  and 630.25 nm  $(g \sim 2.5)$  and easily explained the (small) difference in apparent strengths we measured by taking into account the effect of non-magnetic light scattered over the concentrated magnetic field region which means something like a filling factor of 0.6 to 0.8; typical field strength over filigree features were up to 1.5 kilogauss (Astron. Astrophys., 1978).
- C. Keller: The present method is very suited for filtergrams since it uses just one position within two lines each. This allows a large spatial coverage. Without going into the problems of the method of Koutchmy and Stellmacher and their interpretation in terms of the magnetic field strength, the method requires spectrally resolved profiles and is therefore not suited for filtergrams.

# Progress Toward an Advanced Imaging Vector Magnetograph

Alessandro Cacciani\*

Enrico Paverani
(Physics Department, University "LA SAPIENZA" - Rome, Italy)

Edward Smith
(Jet Propulsion Laboratory)

Harold Zirin

(California Institute of Technology)

#### Abstract

As part of the development phase of an imaging vector magnetograph we have tested at Big Bear Solar Observatory a simple double band imaging linear polarimeter based on a magneto-optical filter. An isolated sunspot was observed and the orientation of the field lines of the penumbra are displayed. They show an evident cyclonic aspect. If it was caused by Faraday rotation it would be consistent with the magnetic polarity (South) of the spot.

#### 1. Introduction

Due to the enormous importance of measuring the solar vector magnetic field, a great effort is being made by instrumentalists to build a suitable polarimeter able to achieve that goal. These Proceedings are evidence of the interest now being devoted to this subject. Also, refined theoretical models are necessary for a correct interpretation of the observational data.

In this short contribution we are showing a recent progress on a joint project (JPL-Caltech-Univ. of Rome) with the final aim to build a flexible, compact, easy-to-operate and inexpensive VECTOR MAGNETOGRAPH based on the combination of the magneto-optical filter (MOF; see for ex.: Cacciani, 1967; Cacciani and Fofi, 1978; Cacciani and Rhodes 1985) and the videomagnetograph. This technology is capable of spectral resolution comparable to that of a spectrograph and fair wavelength coverage (up to 5 spectral points simultaneously) along the solar line profile.

A further detailed analysis of the MOF technology is being prepared for publication, including a theoretical study of the physical and spectroscopic behavior in comparison with spectral scans made at JPL using a high resolution Tunable Laser. A preprint is almost ready and should become available soon. Interested people can send preprint requests to A. Cacciani at his home Institute using normal mail service or electronic mail through SOLAR (25000).

#### 2. Instrumentation

In order to detect and measure the vector magnetic field on the sun, the MOF can be used profitably in several ways. In this contribution we limit our discussion to the transverse component of the magnetic field, as the longitudinal component has been measured with a MOF at the 60-foot tower of Mt. Wilson Observatory and at Big Bear Solar Observatory.

<sup>\*</sup> Presently at the High Altitude Observatory, National Center for Atmospheric Research.

The simplest way to detect the Zeeman-induced linear polarization in a spectral line with an MOF is to use it as a narrow-band filter tuned to a wing of a solar line. This way has been tested at Big Bear Solar Observatory and discussed in Cacciani et al., 1989. Good results have also been obtained using a Lyot Filter, but its passband is not narrow enough to be able to isolate different parts of the U and Q profiles so that the resulting integration over the polarized profile leads to substantial cancellation of the linear polarization signal near the center of the solar line. Moreover, only one wing of a fairly strong line can be used at a time.

As already mentioned our final goal is to be able to image five wavelengths simultaneously with high spectral resolution. However limiting the spectral coverage to only two or three spectral points may provide scientifically useful observations.

In this paper we show linear polarization measurements using a simple MOF cell that gives two narrow transmission bands tuned to the far wings of the solar Potassium line at 7699 A. In other words, we observe the two sigma components simultaneously in a plane of polarization perpendicular to the field vector. This mode of operation is superior to the single-band mentioned above as it gives a better signal, and with this method one may largely compensate for solar doppler shifts. Moreover, it requires a single cell instead of two.

Figure 1 illustrates schematically the working principle of this double band linear polarimeter as used for the observations presented in Figs. 2.

A next step towards a better spectral coverage is to provide a signal from all the Zeeman ( $\pi$  - as well as  $\sigma$ -) components simultaneously. This becomes necessary for quantitative measures of the vector field, especially when the field to be measured is very low. The instrument consists of a vapor cell in a suitable transverse magnetic field that reproduces a Zeeman pattern in absorption, much the same as the one that occurs on the sun, except that the laboratory lines are much narrower. The solar U or Q profile will then be absorbed or transmitted as a whole, according to the relative orientation of the solar and instrumental magnetic azimuths. Similar considerations hold for the measurement of the longitudinal field: in this case the use of a longitudinal magnetic field (instead of a transverse one) is needed inside the MOF cell. The system is capable to measure doppler shifts as well, so that in some way their effects can be taken into account.

#### 3. Observations

The observations shown in Figure 2 have been taken at Big Bear Solar Observatory using the existing acquisition system normally used for magnetographic observations with a Lyot Filter. The MOF version discussed in Figure 1 has been installed and tested during the first two weeks of August 1990. The line used was the Potassium resonance line at 7699 A. The sunspot shown in Figure 2a was observed on August 15 and analyzed later (Figs. 2b, 2c, 2d) using computing facilities at HAO.

The very same sunspot, observed one day later, has been analyzed at Caltech by H. Wang and is shown in his contribution to these Proceedings. In comparison with his result, we find a visible counterclockwise rotation of the polarization field lines approaching the umbra (Fig. 2d). This could be simply a projection effect although the spot was close to the center of the disk (the offset, in seconds of arc, from the center was only 129 toward East and 169 toward North); or a real tilting of magnetic lines; or Faraday rotation of the linear polarization azimuth, although Lites and Skumanich's work (1990) shows that a real azimuthal twist of the magnetic field should be considered more realistic. However, the Faraday rotation cannot be excluded in our case since the observed Potassium solar line has damping wings showing significant opacity; moreover it turns out that the observed direction of rotation is in agreement with the magnetic polarity of the spot.

### 4. Scientic Objectives

At this stage of the instrument development we think we already have a proper imaging device to detect Zeeman induced linear polarization in the wings of the solar Potassium 7699 A line. In the near future we plan to address several scientific objectives. Among them we would mention the following:

- a. investigate carefully the Faraday rotation in many isolated spots as they pass across the solar disk. Sodium D lines also will be used since they have well developed wings,
- b. study the relationship between the magnetic field configurations and flares (see also H. Wang's paper in these Proceedings),
- c. study the interaction between magnetic field convection (this study is to be developed in conjunction with the SOI experiment on SOHO and headed by Dr. G. W. Simon of Sac Peak Observatory),
- d. search for weak (transverse) polar fields. This project will be headed by Dr. Roger Ulrich of UCLA.

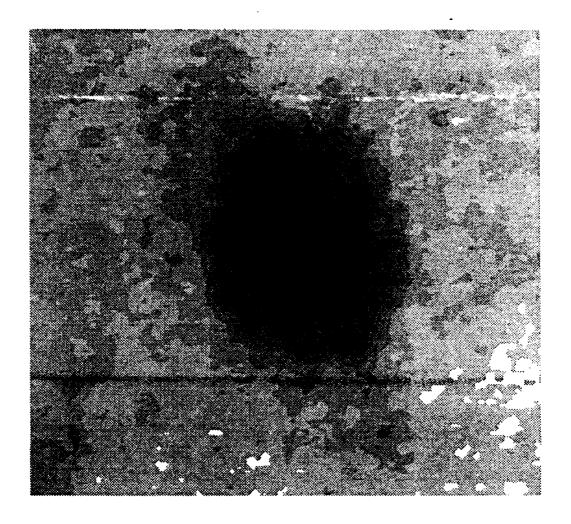


Fig. 2a. Sunspot intensity map. Aug. 15, 1990 - 18:40 UT - 129E, 168N (in seconds of arc). Shown in Figs. 2b, 2c, 2d are three different ways of displaying its linear polarization field.

....

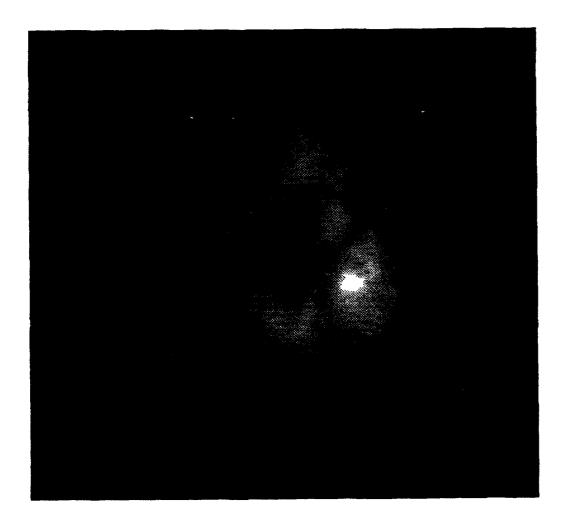


Fig. 2b. Modulus of the linear polarization field.

138



Fig. 2c. Azimuth of the linear polarization field - (black =  $-90^{\circ}$ , white =  $+90^{\circ}$  from the horizontal direction).

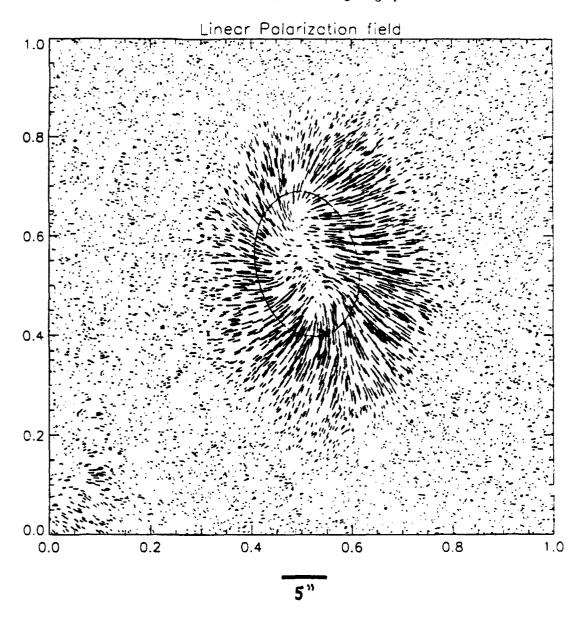


Fig. 2d. Plot of the linear polarization field lines. Inside the delimited region, close to the umbra, there is clear evidence of anticlockwise rotation of the field lines.

## Acknowledgments

This work has been carried out during the stay of A. Cacciani at Caltech and JPL in July and August 1990 (observing phase) and at HAO during the following four months (data reduction phase). We acknowledge those institutions for their support and for the facilities made available. Particularly we thank the observing staff of Big Bear Solar Observatory and Vic Tisone for the invaluable help during the computational work at HAO. Moreover, A. Cacciani acknowledges the support of his home Institute: the Consiglio Nazionale delle Richerche and the Ministero della Pubblica Istruzione. The observations at Big Bear were supported by the NSF through grant ASJ 8912982.

#### References

Cacciani, A.: 1967, Atti del Convegno della Societa, Astronomica Italiana, Vol. 1.

Cacciani, A., Fofi, M.: 1978, Solar Phys., 59, 1790.

Cacciani, A., Rhodes, E.: 1985, Solar Seismology from Space, R. Ulrich (ed.,) (UCLA).

Cacciani, A., Varsik, J., Zirin, H.: 1989, Solar Phys., 125, 173.

Lites, B. W., Skumanich, A.: 1990, Astrophys. J., 384 747.

- Ai G.: Which is stronger in longitudinal magnetic field, the bright filaments or the dark filaments in penumbra in your observing results?
- C. Keller: Since the present observations have been obtained at a single wavelength position I can only talk about polarization. In bright filaments I find larger circular polarization as compared to dark filaments. This can be due to instrumental effects, spatial stray-light, or due to different line profiles, which is the most probable. We are far away from associating the variation of circular polarization with a variation of the magnetic field strength.
- M. Semel: What is the value of the constant field strength you found?
- C. Keller: We find a field strength of about 1 kG at the level of line formation. At the level of continuum formation this corresponds to 2 kG, as deduced from a simple flux tube model which explains the observed line ratio. This takes into account the filter pass-band as well as the position on the solar disk.
- J. Harvey: Your observation of low circular polarization in a sunspot umbra is puzzling. Is it possible that telescope polarization, projection effects on the location of the filter passband could explain your observation?
- C. Keller: The major effect is due to stray-light. The stray-light (unpolarized) is about 15%, which is by a factor of 3 larger than the true intensity of the umbra. Therefore the polarization is underestimated by a factor of three. It is true that the location of the filter pass-band was chosen for small-scale magnetic fields and was therefore not optimized for the strong field of umbrae. This reduces the measured polarization again.
- J. Jefferies: How do you determine the field strength at the level of the continuum from your reference which gives its value at the height of line formation?
- C. Keller: We calculate different models of flux tubes which are parameterized by their field strength at optical depth unity inside the tube. The field strength at the level of continuum formation is obtained from the level which fits best the observed magnetic line ratio. This provides us with a value of the field strength which is nearly independent of the lines chosen for the field strength determination.
- K.S. Balasubramaniam: In calculation of the line ratio  $\sigma_n$ , and hence the magnetic field from the Stokes V of the two lines, is not there the possibility of still some scattered light since the V's of the two lines are measured separately? Also would not it be worthwhile to consider that there would be "polarized" scatter in each of Q, U, and V?
- C. Keller: Since the two polarizations are not measured simultaneously there is additional scatter in  $\sigma_n$ , but no unpolarized scattered light is present. Of course, Stokes V is affected by polarized stray-light. However, circular polarized stray-light outside of sunspots is very small and does not affect  $\sigma_n$  at the polarimetric accuracy achieved in this work, i.e. noise is much larger than polarized stray-light.

# SYSTEMATIC ERRORS IN POLARIMETER CALIBRATION DUE TO IMPERFECT CALIBRATION OPTICS

S. TOMCZYK, P. STOLTZ\*, P. SEAGRAVES

High Altitude Observatory
National Center for Atmospheric Research†
P.O. Box 3000
Boulder, Colorado U.S.A.

#### SUMMARY

We investigate systematic errors introduced in the calibration of a Stokes polarimeter when the calibration optics deviate from ideal. To accomplish this, we employ a linearized treatment of the Mueller calculus which allows for small and arbitrary imperfections in the Mueller matrices of the calibration optics, as well as a small amount of polarization in the calibration light source. We find that half of the response matrix elements contain systematic errors which can be related to imperfections in certain elements of the Mueller matrices of the calibration optics.

### I. INTRODUCTION

The response of a Stokes polarimeter to an input Stokes vector can be represented generally by the matrix equation:

$$O = XS + b$$

where O is the observed instrument vector, S is the input Stokes vector, and b is the instrumental bias vector. The matrix X, which we call the polarimeter response matrix, describes the transformation of an input Stokes vector to an instrumental vector, and is a function of the physical characteristics of the polarimeter and its electronics.

Polarimeter calibration is the process of measuring the instrumental bias vector and the response matrix of the polarimeter. This is usually done by inserting calibration optics between the light source and the polarimeter. Then the previous matrix equation is modified to:

$$O = XCS + b$$

where C is the calibration optics Mueller matrix, and S is now the Stokes vector of the calibration light source.

The instrumental bias vector can be determined straightforwardly by blocking the light beam. Then C is a dark slide with a null Mueller matrix, and measurement of O determines b. Hereafter, we will assume the instrumental vectors are corrected for bias and omit the bias term in all equations.

Determining the response matrix is not so simple. Ideally, this is accomplished by measuring the instrumental response to pure Stokes vectors formed by CS, the calibration optics and light source. For example, unpolarized light from the source with no calibration optics (C has unit Mueller matrix) produces Stokes I and determines the first column of X. Likewise, unpolarized light fed into a linear polarizer at 0 and 45 degrees produces Stokes Q and U and determines

<sup>\*</sup>Present address: Physics Department, University of Colorado, Boulder, Colorado. †The National Center for Atmospheric Research is sponsored by the National Science Foundation.

the second and third columns of X, while unpolarized light fed into a circular polarizer produces Stokes V and determines the fourth column of X.

However, it is difficult in practice to generate pure polarization states because of imperfections in polarizing optics and light sources. An imperfect optical element is defined as one with a Mueller matrix which is perturbed from the ideal representation for that element. An imperfect light source is defined as one which produces light which is slightly polarized. Calibration can be accomplished even if the generated Stokes vectors are not pure, but are known. In this case, difficulty arises because we do not know the Stokes vector of the calibration light source in the absence of a calibrated polarimeter; also, it is difficult to know the Mueller matrices of the calibration optics precisely except for the cases of dark slide and clear.

This imprecise knowledge of the polarization form of the calibrating light beam will produce systematic errors in the measured polarimeter response matrix. The purpose of this paper is to estimate the magnitude of these systematic errors as a function of the imperfections of the calibration optics and light source.

#### II. METHOD

The approach we have chosen is to start with the calibration equation:

$$O = XCS$$

and linearize the response matrix, calibration optics Mueller matrix, and light source Stokes vector. Then  $X = X_0 + dX$ ,  $C = C_0 + dC$ , and  $S = S_0 + dS$ . That is, we model these elements as the sum of an ideal term and a term representing small imperfections. The terms with the zero subscript, or zero'th order terms, are assumed known and are given by the ideal representation for these elements. The first order terms are unknown and represent small imperfections. Since we need to create nearly pure Stokes vectors to perform calibration efficiently, this approach seems reasonable. The calibration equation becomes:

$$O = (X_0 + dX)(C_0 + dC)(S_0 + dS)$$

which simplifies to:

$$O = X_0 C_0 S_0 + X_0 C_0 dS + X_0 dC S_0 + dX C_0 S_0$$

after multiplication, and neglecting second order and higher terms.

Similarly, the source Stokes vector is modeled as the sum of an unpolarized component and a first order polarization imperfection vector:

$$S_0 = I \begin{bmatrix} 1 \\ 0 \\ 0 \\ 0 \end{bmatrix} \qquad dS = I \begin{bmatrix} 0 \\ dQ \\ dU \\ dV \end{bmatrix}$$

Note that we have assumed that the intensity I is well determined, and have omitted the imperfection term dI in the source Stokes vector.

We assume that the calibration optics C are either a linear polarizer P or a linear polarizer followed by a retarder R. Also, we assume that either can be rotated in the beam, and that both are homogeneous. Then:

$$P(\theta) = P_0(\theta) + dP(\theta)$$

where  $\theta$  is the angle of the polarizer axis, and:

multiplied by the polarizer transmission  $t_p/2$ . We also assume that the polarizer transmission is well determined, allowing us to omit the 11 term in the imperfection matrix.

Likewise, the calibration retarder R can be represented by:

$$R(\phi) = R_0(\phi) + dR(\phi)$$

where  $\phi$  is the angle of the retarder fast axis, and:

$$R_0(0^{\circ}) = \begin{bmatrix} 1 & 0 & 0 & 0 \\ 0 & 1 & 0 & 0 \\ 0 & 0 & \cos \delta & \sin \delta \\ 0 & 0 & -\sin \delta & \cos \delta \end{bmatrix} \quad dR(0^{\circ}) = \begin{bmatrix} 0 & dR_{12} & dR_{13} & dR_{14} \\ dR_{21} & dR_{22} & dR_{23} & dR_{24} \\ dR_{31} & dR_{32} & dR_{33} & dR_{34} \\ dR_{41} & dR_{42} & dR_{43} & dR_{44} \end{bmatrix}$$

multiplied by the retarder transmission  $t_r$ . For efficient calibration, we know that the retardance  $\delta \approx \pi/2$ . Again the 11 term in the imperfection matrix has been omitted.

Remember that a Mueller matrix M at an arbitrary angle is given by:

$$M(\theta) = \mathcal{R}(-\theta)M(0^{\circ})\mathcal{R}(\theta)$$

where:

$$\mathcal{R}(\theta) = \begin{bmatrix} 1 & 0 & 0 & 0 \\ 0 & c2 & s2 & 0 \\ 0 & -s2 & c2 & 0 \\ 0 & 0 & 0 & 1 \end{bmatrix}$$

and  $c2 = \cos(2\theta)$  and  $s2 = \sin(2\theta)$ .

Also, we assume the response matrix is nearly diagonal:

$$X_{0} = \begin{bmatrix} X_{11} & 0 & 0 & 0 \\ 0 & X_{22} & 0 & 0 \\ 0 & 0 & X_{33} & 0 \\ 0 & 0 & 0 & X_{44} \end{bmatrix} \quad dX = \begin{bmatrix} dX_{11} & dX_{12} & dX_{13} & dX_{14} \\ dX_{21} & dX_{22} & dX_{23} & dX_{24} \\ dX_{31} & dX_{32} & dX_{33} & dX_{34} \\ dX_{41} & dX_{42} & dX_{43} & dX_{44} \end{bmatrix}$$

The results which follow pertain to the class of Stokes polarimeter with a nearly diagonal response matrix; in addition, the results from a response matrix with a significant 12 term are also presented.

### III. ANALYTIC SOLUTIONS

Given the above assumptions, we can now generate a set of hypothetical observations and solve the linearized calibration equation. It is our goal to solve for the response imperfection matrix dX. However, we would also like to solve for the light source imperfection vector dS and

the calibration optics imperfection matrices, dP and dR, as a check on our assumptions and as a test of the quality of our optics.

Note that implicit to this technique is the assumption that the calibration optics are rotated to produce polarization states. This rotation provides additional information to help us differentiate between polarimeter crosstalk and imperfections in the polarization form of the calibrating light beam. If different optics with a different set of imperfections were alternately inserted into the beam, this would not be possible.

We define the observed Stokes vector in terms of four observed quantities:

$$O = \begin{bmatrix} i \\ q \\ u \\ v \end{bmatrix}$$

We can insert and rotate hypothetical calibration optics in the beam and observe the instrument vector as a function of the angle of the calibration optics. One method of solving the equations, which is independent of the measurement angles, is to Fourier decompose the observed instrument vector in  $\theta$  and  $\phi$ . We present in Table 1 the results of the decomposition for the case of the calibration polarizer only. A factor of  $It_p$  has been omitted.

Some of the imperfections for which we can solve are apparent from inspection of Table 1. For example, the i equation for the DC component allows the solution of  $dX_{11}$ , the q and u equations for the  $\cos 4\theta$  component allow the solution of dQ and dU, the v equation of the  $\cos 2\theta$  component allows the solution of  $dX_{42}$ , etc. We can decompose the instrument vector for the case of calibration polarizer and retarder together, by positioning the retarder at various angles (eg. 0, 45, 90, degrees) and Fourier decomposing in the polarizer angle as before.

TABLE 1
Fourier Decomposition of Observed Instrument Vector
Polarizer Only

D.C.:	
$i = X_{11} + dX_{11}$	
$q = 1/2X_{22}dQ + dX_{21}$	
$u = 1/2X_{33}dU + dX_{31}$	
$v = X_{44}dP_{41} + dX_{41}$	
$\cos 2\theta$ :	$\sin 2\theta$ :
$i = X_{11}dQ + dX_{12}$	$i = X_{11}dU + dX_{13}$
•	
$q = X_{22}(1 + dP_{21}) + dX_{22}$	$q = -X_{22}dP_{31} + dX_{23}$
$u = X_{33}dP_{31} + dX_{32}$	$u = X_{33}(1 + dP_{21}) + dX_{33}$
$v=dX_{42}$	$v=dX_{43}$
$\cos 4\theta$ :	$\sin 4\theta$ :
i = 0	i = 0
$q = 1/2X_{22}dQ$	$q = 1/2X_{22}dU$
$u=-1/2X_{33}dU$	$u = -1/2X_{33}dQ$
v = 0	v = 0

146 S. Tomczyk et al.

We find that it is not possible with the above assumptions to solve for all of the imperfection terms in either the response or calibration matrices, or in the source Stokes vector. Adding observations with the retarder alone does not allow the solution of any more imperfections.

Specifically, the results for the case of polarizer alone and polarizer followed by retarder are that the equations allow for the solution of dQ and dU, but dV cannot be separated from the term  $dR_{31}/\sin\delta$ . Also, we can explicitly solve for about half of the response matrix elements, with the remainder coupled to calibration optics imperfection terms. The following is the matrix of errors to the response matrix:

$$\begin{bmatrix} 0 & 0 & 0 & -X_{11}dR_{13}/\sin\delta \\ 0 & X_{22}dP_{21} & X_{22}dP_{31} & 0 \\ 0 & X_{33}dP_{31} & X_{33}dP_{21} & 0 \\ X_{44}dP_{41} & 0 & 0 & X_{44}dP_{21} - X_{44}dR_{43}/\sin\delta \end{bmatrix}$$

The terms with 0 error are those response matrix imperfection terms for which the equations allowed explicit solution. The non-zero terms are coupled to the imperfection terms of the calibration optics. They represent systematic errors to the response matrix if these calibration optics imperfections were unknown and assumed zero. Also, the retarder imperfection terms  $dR_{12}$ ,  $dR_{21}$ ,  $dR_{22}$  and  $dR_{33}$  are the only calibration optics imperfections which could be solved for. Unfortunately, these terms do not help to decrease the systematic errors in the response matrix.

The above calculations were repeated for the case where the response matrix term  $X_{12}$  is significant, as in a single beam polarimeter. In this case the response matrix systematic errors become:

$$\begin{bmatrix} 0 & X_{12}dP_{21} & X_{12}dP_{31} & -X_{11}dR_{13}/\sin\delta \\ 0 & X_{22}dP_{21} & X_{22}dP_{31} & 0 \\ 0 & X_{33}dP_{31} & X_{33}dP_{21} & 0 \\ X_{44}dP_{41} & 0 & 0 & X_{44}dP_{21} - X_{44}dR_{43}/\sin\delta \end{bmatrix}$$

Note that now two additional terms have systematic errors.

#### IV. SIMULATIONS

Using a non-linear least squares fitting program, we investigated numerical solutions of the calibration equation:

$$O = XCS$$

Our goal was not to simulate actual calibrations of a polarimeter but rather to examine mathematical consequences of linearizing the calibration equation.

In carrying out these computer simulations, the procedure was first to pick a response matrix with which to generate mock calibration data. For this we chose the matrix for an ideal, one-channel polarimeter with an 85-degree rotating wave plate, plus cross-talk terms on the order of  $10^{-3}$ .

$$\begin{bmatrix} 1.0000 & 0.5436 & 0.0060 & 0.0090 \\ 0.0010 & 0.2906 & 0.0070 & 0.0011 \\ 0.0020 & 0.0040 & 0.2906 & 0.0012 \\ 0.0030 & 0.0050 & 0.0080 & 0.6342 \end{bmatrix}$$

This response matrix remained fixed for all data generation. We then had a random-number generator pick random imperfections for the calibration optics. These random numbers were

distributed in a Gaussian shape about 0 with a mean of around  $10^{-3}$ . Recall that we are neglecting terms in the perturbations squared and higher. In this case, these are terms of  $10^{-6}$ . Since the data we generate is rounded at  $10^{-6}$ , this validates the linear approximation. Truly random perturbations may not be entirely physical; considerations such as energy conservation and the amount of depolarization expected may give relations between the perturbations. However, as our aim was not to simulate actual calibration, but merely to investigate mathematical results, random perturbations sufficed. For simplicity, we used an unpolarized light source to generate our data and we did not include any random noise.

The computer generated a set of random imperfections for the calibration optics and then ran through a series of 25 different configurations of the retarder and polarizer. The configurations used in our simulations were clear (no calibration optics), the calibration polarizer only, at four angles (0, 45, 90, 135 degrees), the retarder only, at four angles (0, 45, 90, 135 degrees) and the 16 combinations of the two at these four angles. Introducing the retarder only measurements changes only a few terms in the error matrix given above.

After generating this mock data, we then used a non-linear least squares routine to work backwards and determine the response matrix. As a starting point, we gave the routine a guess of ideal calibration optics with no perturbations and a response matrix corresponding to an ideal rotating wave plate of 80-degrees with no cross-talk terms.

T 1.0000	0.5868	0.0000	ן 0.0000
0.0000	0.2630	0.0000	0.0000
0.0000	0.0000	0.2630	0.0000 0.0000 0.6269
0.0000	0.0000	0.0000	0.6269

The routine took this guess and fitted the entire response matrix, the input light source polariztion (not including intensity of the source), the transmissions of both the calibration retarder and polarizer, and the four calibration retarder imperfections for which we can solve theoretically. We measured the systematic errors by differencing these fitted values with the actual values. Comparison of the size of these errors to the predicted couplings allowed us test the validity of the theoretical couplings.

The results of these computer simulations verified the equations coupling the calibration perturbations to terms in the response matrix. In all cases, the least squares routine would settle on a value of the response matrix element which deviated from the actual value by the exact amount predicted by the theoretical error matrix.

### V. CONCLUSIONS

We have investigated systematic errors introduced in the calibration of a Stokes polarimeter due to imperfect calibration optics. Employing a linearized treatment of the Mueller calculus and assuming nearly ideal optics and light source, we generate a system of equations by rotating the calibration optics in the beam. We find that half of the response matrix elements contain systematic errors which can be related to imperfections in certain elements of the Mueller matrices of the calibration optics. Specifically, the systematic errors are due to only five calibration optics imperfection terms. This means that only a small number of the terms in the Mueller matrices of the calibration optics need to be determined accurately, with the required level of accuracy given by the error matrices of Section III and the desired level of polarimetric precision.

148 S. Tomczyk et al.

The simulations presented in Section IV have verified the theoretical results. In addition, simulations of this type offer the possibility of extending the theory to cases where analytic solution is difficult or impossible.

The results given here are for a restricted set of assumptions. Given additional constraints on the calibration optics it may be possible to introduce additional equations and reduce the systematic errors in the response matrix or gain additional information about the calibration light source and calibration optics imperfections. Also, the assumption of homogeneity of the calibration optics requires that uniform optics are used or that the optical system limits the sensitivity to inhomogeneities.

## **ACKNOWLEDGMENTS**

The authors would like to thank D. Elmore, G. Murphy, and A. Skumanich for many helpful discussions. We would also like to thank T. Murphy and T. Brown for reading the manuscript.

### Discussion

- A. Cacciani: My feeling is that the transfer matrix is strongly dependent on geometrical and thermal stabilities (tilt, stress, etc.). Do you have measurements and estimates about this kind of stability?
- **B. Lites:** Our initial measurements with the Advanced Stokes Polarimeter do not show strong time dependent effects in the polarization at the measured level (few  $\times$  10<sup>-3</sup>  $I_{continuum}$ ). The only time (temperature) dependent effect was noted on residual birefringence in the calibration linear polarizer, with a polarization change (if I remember correctly) of a few  $\times$  10<sup>-4</sup>  $I_{continuum}$ .

# Using the Zeeman Spectral-Polarization Symmetry for Telescope Calibration

Laurence J. November
National Solar Observatory, Sunspot NM 88349
National Optical Astronomy Observatories <sup>1</sup>

Abstract: Specific spectral symmetries exist for the polarized light components in the Zeeman radiative transfer problem for an atom that is represented by  $L \cdot S$  coupling. The two channel Lyot filter provides a natural method for making spectrally even or odd integral determinations in a single Stokes state in one measurement, not subject to seeing effects. That system is well suited for making high resolution vector magnetic field measurements because it provides a determination of the physical parameters with a minimum of observational information. If the light states are known to obey strictly the normal spectral symmetries, then it is possible to infer a Mueller matrix for the telescope from a single Stokes image obtained in this way. A matrix solution of this type is written in closed analytic form. To demonstrate the principle, a matrix is inferred for the Sacramento Peak Vacuum Tower telescope from a photographic Stokes image set obtained with the universal birefringent filter. The matrix solution is generalized to allow for the case when known and constant spectral asymmetries exist. The method may be valuable to calibrate high resolution polarimetric observations when a specific polarization calibration test was not available from the time of the observation.

#### 1. Introduction

Precise polarimetry is difficult if the telescope has a strong polarization effect. Telescopes are not usually designed to give good polarization transmission characteristics. If the optical system contains off-axis reflections or stressed elements then its polarization modification effect may be quite large, and often these features can not be avoided in long focal or evacuated systems. In the visible, the effect of an off-axis 45° reflection from aluminum produces about 15° of retardance and about 1.5% partial polarization due to asymmetric absorption; yet the Zeeman linear polarization effect due to transverse magnetic fields is characteristically less than 0.5%.

If the optical system is not polarization free, then it must be calibrated or compensated because the unpolarized signal and the strong Zeeman circular signal will produce substantial linear polarization by partial polarizing and retardance effects. A system whose polarization effect changes either over the image or over the aperture may only be represented by allowing variation of the telescope matrix over the image or within the telescope Airy disk, respectively. Dunn has shown that the spatial nonuniformity of optical windows for evacuated systems can be made small (Dunn 1984, November 1988). In that case, the optical system can be described by a one spatial component matrix model. Spatial uniformity is assumed in this paper.

A mathematical or physical model for the optical train can give an estimate of the effect or provide a correction. But models based on tabulated reflection coefficients or that rely upon the constancy of materials can not be more accurate than a few percent in the visible because material reflection parameters are a strong function of the specific surface properities: contaminants, coating purity, and thickness. In principle, direct measurement methods of the telescope matrix are more accurate (Makita 1982, Zeldin 1981, Elmore 1988, Dunn et.al. 1989, November 1989). But a model derived some time before or after the data acquisition will become inaccurate because the physical characteristics of the telescope can change in time.

A simple calibration scheme uses the fact that rotating linear polarization provides a unique determination of a following Jones matrix (Azzam and Bashara 1977, November and Elmore 1987, November 1990). Continuous monitoring of the optical system by such a method should be the best method. An alterate method is proposed here for use when no calibration was done at the time of the solar measurement: The solar Zeeman signal itself may be used to provide a limited calibration. For an atomic process describable by  $L \cdot S$  coupling, the Zeeman effect has a specific spectral symmetry (section 2). An imaging measurement

<sup>&</sup>lt;sup>1</sup> Operated by the Association of Universities for Research in Astronomy, Inc. (AURA) under cooperative agreement with the National Science Foundation.

based upon the passband features of a Lyot filter can detect the polarization state in even and odd spectral integrals to provide an intrinsically fast system (section 3). An empirical telescope Mueller matrix is derived (section 4) and discussed (section 5).

#### 2. The Spectral Symmetry of the Zeeman Effect

The radiative transfer equation for light described by the four Stokes intensities:  $I(\tau, \nu)$ ,  $Q(\tau, \nu)$ ,  $U(\tau, \nu)$ .  $V(\tau, \nu)$  in optical depth  $\tau$  and frequency  $\nu$  is written:

$$\mu \frac{d}{d\tau} \begin{pmatrix} I(\tau, \nu) \\ Q(\tau, \nu) \\ U(\tau, \nu) \\ V(\tau, \nu) \end{pmatrix} = \begin{pmatrix} 1 + \eta_I & \eta_Q & \eta_U & \eta_V \\ \eta_Q & 1 + \eta_I & \rho_V & -\rho_U \\ \eta_U & -\rho_V & 1 + \eta_I & \rho_Q \\ \eta_V & \rho_U & -\rho_Q & 1 + \eta_I \end{pmatrix} \begin{pmatrix} I(\tau, \nu) \\ Q(\tau, \nu) \\ U(\tau, \nu) \\ V(\tau, \nu) \end{pmatrix} - \begin{pmatrix} B(\tau) + \eta_I S(\tau) \\ \eta_Q S(\tau) \\ \eta_U S(\tau) \\ \eta_V S(\tau) \end{pmatrix}. \tag{1}$$

where  $\mu$  is the cosine of the incident angle in the atmosphere, and  $B(\tau)$  is the continuum source function, and  $S(\tau)$  is the line source function. This form is acceptable for radiative transfer in a spectral line in the assumption of complete redistribution.  $\eta_I$ ,  $\eta_Q$ ,  $\eta_U$ , and  $\eta_V$  are the opacity ratios and  $\rho_Q$ ,  $\rho_U$ , and  $\rho_V$  are the magneto-optical ratios. The opacity ratios and the magneto-optical ratios are functions of optical depth and frequency.

For absorption in an atom without a hyperfine effect (Fe, Ca, etc.), the  $L \cdot S$  fine structure gives the spectral distributions  $\Pi(\nu/\nu_L)$  and  $\Sigma(\nu/\nu_L)$  for the line  $\pi$  and  $\sigma$  components, respectively.  $\Pi(\nu/\nu_L)$  and  $\Sigma(\nu/\nu_L)$  are sums of weighted delta functions distributed in  $\nu/\nu_L$  according to the atomic transition where  $\nu_L \equiv \frac{|e|}{4\pi mc} |\vec{B}|$  is the Larmor frequency;  $|\vec{B}|$  is the magnetic field induction (gauss), e and m are the electron charge and mass, and e is the speed of light. By definition the sum is one, i.e.  $\int \Pi(\nu/\nu_L) d\nu = 1$  and  $\int \Sigma(\nu/\nu_L) d\nu = 1$ ; these splittings have been tabulated for all possible transitions (e.g. Beckers, 1969). The relevant opacity ratios and magneto-optical ratios have been derived in many places. Rewriting the solution derived by Landi Degl'innocenti and Landi Degl'innocenti (1972) in terms of convolutions of the fine structure distributions with a Lorentzian spectral distribution for the individual oscillators  $L(\nu, \gamma)$  and with the Gaussian thermal distribution of Doppler velocities  $G(\nu, \Delta\nu_D)$ , gives the following:

$$\eta_{I}(\nu_{0} + \nu) = \frac{\eta_{0}}{4} ((\Pi(\frac{\nu}{\nu_{L}}) + \Pi(-\frac{\nu}{\nu_{L}})) \sin^{2} \phi + (\Sigma(\frac{\nu}{\nu_{L}}) + \Sigma(-\frac{\nu}{\nu_{L}}))(1 + \cos^{2} \phi)) * L(\nu, \gamma) * G(\nu, \Delta\nu_{D}).$$

$$\eta_{Q}(\nu_{0} + \nu) = \frac{\eta_{0}}{4} ((\Pi(\frac{\nu}{\nu_{L}}) + \Pi(-\frac{\nu}{\nu_{L}}) - \Sigma(\frac{\nu}{\nu_{L}}) - \Sigma(-\frac{\nu}{\nu_{L}})) \cos 2\theta \sin^{2} \phi) * L(\nu, \gamma) * G(\nu, \Delta\nu_{D}),$$

$$\eta_{U}(\nu_{0} + \nu) = \frac{\eta_{0}}{4} ((\Pi(\frac{\nu}{\nu_{L}}) + \Pi(-\frac{\nu}{\nu_{L}}) - \Sigma(\frac{\nu}{\nu_{L}}) - \Sigma(-\frac{\nu}{\nu_{L}})) \sin 2\theta \sin^{2} \phi) * L(\nu, \gamma) * G(\nu, \Delta\nu_{D}).$$

$$\eta_{V}(\nu_{0} + \nu) = \frac{\eta_{0}}{2} ((\Pi(\frac{\nu}{\nu_{L}}) - \Pi(-\frac{\nu}{\nu_{L}})) \cos \phi) * L(\nu, \gamma) * G(\nu, \Delta\nu_{D}).$$
(2)

 $\gamma$  is the reciprocal oscillator damping time, and  $\Delta\nu_D$  is the Doppler width.  $\eta_0 = \frac{N\pi e^2 f}{\kappa_c mc}$ , N is the number density atoms in the lower level, f is the oscillator strength,  $\kappa_c$  is the continuum absorption coefficient.  $\nu_0 \equiv c/\lambda$  is the line center frequency for wavelength  $\lambda$  in the observer's frame.  $\phi$  and  $\theta$  are the field inclination and azimuth from the line of sight.  $L(\nu, \gamma)$  and  $G(\nu, \Delta\nu_D)$  are normalized to have a unit integral over frequency  $\nu$ :

$$L(\nu,\gamma) = \frac{\gamma}{\pi} \frac{1}{\nu^2 + \gamma^2},$$

$$G(\nu, \Delta \nu_D) = \frac{1}{\pi^{\frac{1}{2}} \Delta \nu_D} \exp(-(\frac{\nu}{\Delta \nu_D})^2)$$

"\*" denotes the spectral convolution. Although the convolutions are inherently dimensionless, the first convolution in every Equation (2) is with a sum of delta functions. That convolution represents a sum of components rather than an integral over frequency, and it thereby introduces units of inverse frequency.

The magneto-optical ratios  $\rho$  can be similarly written as a convolution of the fine structure distributions  $\Pi(\nu/\nu_L)$ ,  $\Sigma(\nu/\nu_L)$ , with the line refractive index function, the normalized Rachkovsky function,  $F(\nu, \gamma)$ , and

with a Gaussian:

$$\rho_{Q}(\nu_{0} + \nu) = \frac{\eta_{0}}{4} ((\Pi(\frac{\nu}{\nu_{L}}) + \Pi(-\frac{\nu}{\nu_{L}}) - \Sigma(\frac{\nu}{\nu_{L}}) - \Sigma(-\frac{\nu}{\nu_{L}})) \cos 2\theta \sin^{2} \phi) * F(\nu, \gamma) * G(\nu, \Delta\nu_{D}), 
\rho_{U}(\nu_{0} + \nu) = \frac{\eta_{0}}{4} ((\Pi(\frac{\nu}{\nu_{L}}) + \Pi(-\frac{\nu}{\nu_{L}}) - \Sigma(\frac{\nu}{\nu_{L}}) - \Sigma(-\frac{\nu}{\nu_{L}})) \sin 2\theta \sin^{2} \phi) * F(\nu, \gamma) * G(\nu, \Delta\nu_{D}), 
\rho_{V}(\nu_{0} + \nu) = \frac{\eta_{0}}{2} ((\Pi(\frac{\nu}{\nu_{L}}) - \Pi(-\frac{\nu}{\nu_{L}})) \cos \phi) * F(\nu, \gamma) * G(\nu, \Delta\nu_{D}),$$
(3)

where:

$$F(\nu,\gamma) = \frac{1}{\pi} \frac{\nu}{\nu^2 + \gamma^2}.$$

The normalization of  $F(\nu, \gamma)$  is defined to be consistent with the normalization of  $L(\nu, \gamma)$ .

The convolution of two even or two odd functions is even, but the convolution of an even and an odd function is odd. The Fourier transform of an even function is real, and the Fourier transform of an odd function is imaginary. Thus the Fourier transform of the convolution of even and odd functions is the product of real and imaginary functions which is imaginary, so the convolution is odd, etc. Since both the Lorentzian and Gaussian functions are even in frequency,  $L(\nu, \gamma) = L(-\nu, \gamma)$  and  $G(\nu, \Delta\nu_D) = G(-\nu, \Delta\nu_D)$ , the symmetry of the opacity ratios is simply given by substitution of  $-\nu$  for  $\nu$  in Equations (2):

$$\begin{cases} \eta_{I}(\nu_{0} + \nu) = \eta_{I}(\nu_{0} - \nu), \\ \eta_{Q}(\nu_{0} + \nu) = \eta_{Q}(\nu_{0} - \nu), \\ \eta_{U}(\nu_{0} + \nu) = \eta_{U}(\nu_{0} - \nu), \\ \eta_{V}(\nu_{0} + \nu) = -\eta_{V}(\nu_{0} - \nu) \end{cases}$$
(4)

The Rachkovsky function is odd in frequency,  $F(\nu, \gamma) = -F(-\nu, \gamma)$ , and this reverses the inherent symmetry of a function with the convolution; from Equations (3):

$$\begin{cases} \rho_{Q}(\nu_{0} + \nu) = -\rho_{Q}(\nu_{0} - \nu), \\ \rho_{U}(\nu_{0} + \nu) = -\rho_{U}(\nu_{0} - \nu), \\ \rho_{V}(\nu_{0} + \nu) = \rho_{V}(\nu_{0} - \nu) \end{cases}$$
(5)

The spectral symmetry of  $\eta(\nu)$  and  $\rho(\nu)$ , Equations (4) and (5), show that the transfer matrix on the right of Equation (1) has even transpose symmetry around the diagonal in its first three elements, and odd transpose symmetry in its fourth element with the substitution of  $\nu_0 - \nu$  for  $\nu_0 + \nu$ . At each optical depth  $\tau$  only one symmetry is allowed in the particular solution of Equation (1) consistent with the symmetry of the source functions. Since the source functions  $B(\tau)$  and  $S(\tau)$  are even in  $\nu$  (as constant functions), the Stokes intensities particular solutions must obey the following symmetry conditions:

$$\begin{cases} I(\tau, \nu_0 + \nu) = I(\tau, \nu_0 - \nu), \\ Q(\tau, \nu_0 + \nu) = Q(\tau, \nu_0 - \nu), \\ U(\tau, \nu_0 + \nu) = U(\tau, \nu_0 - \nu), \\ V(\tau, \nu_0 + \nu) = -V(\tau, \nu_0 - \nu) \end{cases}$$
(6)

Whereas, the homogeneous solution to Equation (1) may satisfy any symmetry permitted in the eigenvectors of the opacity matrix, these solutions give zero contribution by the usual choice of boundary condition that the intensities vanish with zero source function. The emergent Stokes intensity vector for  $\tau = 0$ ,  $(I(\nu), Q(\nu), U(\nu), V(\nu))$ , will preserve the symmetry of Equation (6) if  $\nu_0$  remains constant over the line forming region. We can expect this to be an observable property of the Stokes intensities if further there is no variation of  $\nu_0$  within a resolution element. Spectral symmetries of this type have been pointed out before (Landi Degl'innocenti and Landi Degl'innocenti 1970).

A useful limiting form for the transfer equation is the weak field approximation. For the limit  $|\nu_L|/(\gamma^2 + \Delta\nu_D^2)^{\frac{1}{2}}$  small, the fine structure distributions take the form:

$$\lim_{|\nu_{L}| \to 0} \Pi(\frac{\nu}{\nu_{L}}) + \Pi(-\frac{\nu}{\nu_{L}}) = 2\delta(\nu),$$

$$\lim_{|\nu_{L}| \to 0} \Sigma(\frac{\nu}{\nu_{L}}) + \Sigma(-\frac{\nu}{\nu_{L}}) = 2\delta(\nu),$$

$$\lim_{|\nu_{L}| \to 0} (\Pi(\frac{\nu}{\nu_{L}}) + \Pi(-\frac{\nu}{\nu_{L}}) - \Sigma(\frac{\nu}{\nu_{L}}) - \Sigma(-\frac{\nu}{\nu_{L}})) * f(\nu) = g_{QU}\nu_{L}^{2} \frac{d^{2}}{d\nu^{2}} f(\nu),$$

$$\lim_{|\nu_{L}| \to 0} (\Pi(\frac{\nu}{\nu_{L}}) - \Pi(-\frac{\nu}{\nu_{L}})) * f(\nu) = g_{V}\nu_{L} \frac{d}{d\nu} f(\nu).$$
(7)

 $\delta(\nu)$  is the Dirac delta function. The opacity ratios can then be written:

$$\eta_{I}(\nu_{0} + \nu) = \eta_{0}L(\nu, \gamma) * G(\nu, \Delta\nu_{D}),$$

$$\eta_{Q}(\nu_{0} + \nu) = g_{QU}\nu_{L}^{2}\cos 2\theta \sin^{2}\phi \frac{d^{2}\eta_{I}}{d\nu^{2}},$$

$$\eta_{U}(\nu_{0} + \nu) = g_{QU}\nu_{L}^{2}\sin 2\theta \sin^{2}\phi \frac{d^{2}\eta_{I}}{d\nu^{2}},$$

$$\eta_{V}(\nu_{0} + \nu) = g_{V}\nu_{L}\cos^{2}\phi \frac{d\eta_{I}}{d\nu},$$
(8)

where the constants  $g_{QU}$  and  $g_V$  are Landé g factors which can be defined from the fine structure distributions. Thus  $\eta_I \sim o(\nu_L^0)$ ,  $\eta_Q \sim o(\nu_L^0)$ ,  $\eta_U \sim o(\nu_L^0)$ ,  $\eta_V \sim o(\nu_L^0)$ ,  $\rho_Q \sim o(\nu_L^0)$ ,  $\rho_U \sim o(\nu_L^0)$ , and  $\rho_V \sim o(\nu_L^0)$ . Since the source functions:  $B(\tau) \sim o(\nu_L^0)$  and  $S(\tau) \sim o(\nu_L^0)$  it follows for the Stokes intensity solutions that:  $I(\nu,\tau) \sim o(\nu_L^0)$ ,  $Q(\nu,\tau) \sim o(\nu_L^0)$ ,  $U(\nu,\tau) \sim o(\nu_L^0)$ , and  $V(\nu,\tau) \sim o(\nu_L^0)$ . Retaining terms only to a single order in  $\nu_L$  in each component of Equation (1) we have the four differential equations:

$$(\mu \frac{d}{d\tau} - (1 + \eta_I))I(\nu, \tau) = -B(\tau) - \eta_I S(\tau),$$

$$(\mu \frac{d}{d\tau} - (1 + \eta_I))Q(\nu, \tau) = \eta_Q(I(\nu, \tau) - S(\tau)),$$

$$(\mu \frac{d}{d\tau} - (1 + \eta_I))U(\nu, \tau) = \eta_U(I(\nu, \tau) - S(\tau)),$$

$$(\mu \frac{d}{d\tau} - (1 + \eta_I))V(\nu, \tau) = \eta_V(I(\nu, \tau) - S(\tau)).$$
(9)

Applying the boundary condition, the integral solutions can be written in the following form for  $\tau = 0$ :

$$\vec{s}(\nu_0 + \nu) = \begin{pmatrix} I(\nu) \\ Q(\nu) \\ U(\nu) \\ V(\nu) \end{pmatrix} = \begin{pmatrix} I_c - D_I P_I(\nu) \\ D_Q P_{QU}(\nu) \\ D_U P_{QU}(\nu) \\ D_V P_V(\nu) \end{pmatrix}$$
(10)

This solution assumes that the magnetic field orientation and inclination,  $\theta$  and  $\phi$ , are constant over the line forming region. The coefficients  $D_I$ ,  $D_Q$ ,  $D_U$ ,  $D_V$  can be interpreted as the line strengths. Following Jefferies et.al. (1989), differentiating the first Equation (9) gives:

$$\left(\mu \frac{d}{d\tau} - (1 + \eta_I)\right) \frac{dI(\nu, \tau)}{d\nu} = \frac{d\eta_I}{d\nu} (I(\nu, \tau) - S(\tau)). \tag{11}$$

This form can be used to eliminate  $(I(\nu,\tau)-S(\tau))$  from the other three Equations (9). Thus, it follows for  $\nu_L$  and  $\gamma$  constant over the line forming region:  $V(\nu,\tau) \propto \frac{d}{d\nu}I(\nu,\tau)$ . For the vector field constant over the line forming region  $P_V = \frac{d}{d\nu}P_I$ . Although the analogous relation  $P_{QU} \sim \frac{d^2}{d\nu^2}P_I$  is suggested by the limiting form for the opacity ratios, Equation (8), this relation is not justified rigorously.

## 3. Measurement of the Stokes Even and Odd Components with a Birefringent Filter

Beckers (1975) developed a simple system for measuring even or odd Stokes components in a spectral line using the natural properties of a Lyot filter. The two channel Lyot arrangement is shown schematically in Figure 1 and operates at the Sacramento Peak Vacuum Tower Telescope with the universal birefringent filter (UBF). The last Lyot element in the UBF was left without an exit linear polarizer so that two different spectral channels A and B are simultaneously transmitted by the polarizing beam splitter. The element remains fixed in orientation with respect to the following optics.

The two channel Lyot design normally transmits a spectral integral of the Stokes polarization state  $\vec{s}(\nu)$  that is selected by the polarization analyzer before the UBF:

$$\vec{s}_{\alpha} = \int \vec{s}(\nu) \operatorname{sinc}^{2}(\nu) \cos^{2}(\nu + \alpha) d\nu = \int \vec{s}(\nu) T_{\alpha}(\nu) d\nu. \tag{12}$$

 $\alpha$  is the orientation of the exit polarizer, and the scale of frequency  $\nu$  is the phase of the retardance of the  $\frac{1}{4}$ Å final Lyot element. The  $\mathrm{sinc}^2(\nu)$  is the serial product of the transmission of all the Lyot elements except the final one, the  $\frac{1}{2}$ Å, 1Å, 2Å, etc.:  $\mathrm{sinc}^2(\nu) = \cos^2(\frac{\nu}{2})\cos^2(\frac{\nu}{4})\cos^2(\frac{\nu}{8})\dots$ 

Four specific exit polarizer orientations  $\alpha$  are of interest:  $T_{+}(\nu) \equiv T_{\alpha=0}(\nu)$ ,  $T_{-}(\nu) \equiv T_{\frac{\pi}{2}}(\nu)$ ,  $T_{R}(\nu) \equiv T_{-\frac{\pi}{4}}(\nu)$ , and  $T_{B}(\nu) \equiv T_{\frac{\pi}{4}}(\nu)$ . In the arrangement of Figure 1, the exit polarizing beam splitter simultaneously transmits the spectrally even pair,  $\vec{s}_{+} \equiv \vec{s}_{\alpha=0}$  and  $\vec{s}_{-} \equiv \vec{s}_{\frac{\pi}{4}}$  in the two channels A and B. With the  $\lambda/4$  wave retarder inserted after the UBF, the exit system transmits the spectrally odd pair  $\vec{s}_{R} \equiv \vec{s}_{-\frac{\pi}{4}}$  and  $\vec{s}_{B} \equiv \vec{s}_{\frac{\pi}{4}}$ . Differences of images in A and B define the transmission functions  $T_{even}(\nu) \equiv T_{+}(\nu) - T_{-}(\nu)$  and  $T_{odd}(\nu) \equiv T_{R}(\nu) - T_{B}(\nu)$ :

$$\vec{s}_{even} \equiv \vec{s}_{+} - \vec{s}_{-} = \int \vec{s}(\nu) T_{even}(\nu) d\nu = \int \vec{s}(\nu) \operatorname{sinc}^{2}(\nu) \cos(2\nu) d\nu,$$

$$\vec{s}_{odd} \equiv \vec{s}_{R} - \vec{s}_{B} = \int \vec{s}(\nu) T_{odd}(\nu) d\nu = \int \vec{s}(\nu) \operatorname{sinc}^{2}(\nu) \sin(2\nu) d\nu,$$

$$\vec{s}_{\Sigma} \equiv \vec{s}_{+} + \vec{s}_{-} = \vec{s}_{R} + \vec{s}_{B} = \int \vec{s}(\nu) T_{\Sigma}(\nu) d\nu = \int \vec{s}(\nu) \operatorname{sinc}^{2}(\nu) d\nu.$$
(13)

No additional intensity measurements made at other orientations  $\alpha$  can add information to the measurement defined by  $\vec{s}_+$ ,  $\vec{s}_-$ ,  $\vec{s}_R$ , and  $\vec{s}_B$ . The measurement made with a Lyot filter in this way is inherently restricted to give one Fourier component in  $\nu$  and DC spectral integrals. The Lyot transmission functions are plotted in Figure 2.

Measurement of the I component of the Stokes vectors  $\vec{s}_{even}$ ,  $\vec{s}_{odd}$ , and  $\vec{s}_{\Sigma}$  requires that unpolarized light enter the filter. An unpolarized state can be obtained by rapidly cycling between two orthogonal entrance states with the KD\*P before the UBF. Then, with the exit KD\*P removed from the beam, the image difference A-B gives  $I_{even}=I_+-I_-$  in the spectrally even configuration and  $I_{odd}=I_R-I_B$  in the odd configuration (with the  $\lambda/4$  inserted after the UBF). The sum  $I_++I_-=I_R+I_B=I_{\Sigma}$ . The unpolarized experiment alone is useful in defining the velocity v, continuum intensity, and line strength parameters as described in Appendix A.

Analysis of the polarized components is more difficult since an analyzer does not transmit  $\pm Q$ , but rather  $I\pm Q$ ! Analysis of the individual Stokes intensities is affected by cycling the light state before it enters the UBF while synchronously switching the sense of the spectral states in the two image planes A and B. The KD\*P following the UBF cycles between 0 and  $\lambda/2$  waves retardance to switch the two states exiting the last Lyot element. The switching time can be made to be sufficiently rapid so that little seeing difference can be expected between the successive polarization states, and also so that the temporal sum feels an approximately equal contribution from both intensity states (for this work we use 250 Hz).

Analog sums are formed in the output channels with the synchronous transmission of two polarized intensities, i.e.  $I(\nu) \pm Q(\nu)$ , and two spectral states,  $T_{\pm}(\nu)$  or  $T_{\beta}(\nu)$ . Let  $A_{Q,even}$  and  $B_{Q,even}$  refer to the measured intensity with the spectrally even exit configuration for the Stokes state Q:

$$\begin{cases} A_{Q,even} = (I_+ + Q_+) + (I_- - Q_-), \\ B_{Q,even} = (I_- + Q_-) + (I_+ - Q_+), \end{cases}$$

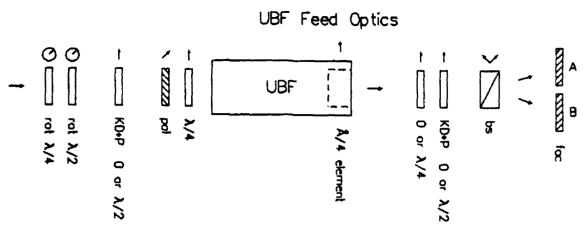


Figure 1 UBF feed optics: The light entering the UBF rapidly chops by means of the first KD\*P between two orthogonal polarization states selectable by two rotating wave plates. The light exiting forms two simultaneous spectral images A and B which are switched in sense by the exit KD\*P.

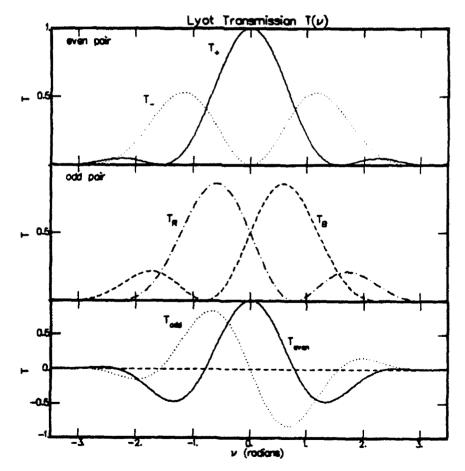


Figure 2 Spectral transmission of a two channel Lyot: In one optical arrangement the filter simultaneously transmits the even spectral pair  $T_+$  and  $T_-$ , and in another optical arrangement the odd spectral pair  $T_R$  and  $T_B$ . The horizontal axis  $\nu$  is in the retardance phase of the final Lyot element. The difference functions,  $T_{even} = T_+ - T_-$  and  $T_{odd} = T_R - T_B$ , are shown in the last panel.

155

and similarly for the odd spectral pair:

$$\begin{cases}
A_{Q,odd} = (I_R + Q_R) + (I_B - Q_B), \\
B_{Q,odd} = (I_B + Q_B) + (I_R - Q_R),
\end{cases}$$
(14)

Substituting the integral definitions Equation (13), gives:

$$Q_{even} \equiv \frac{1}{2} (A_{Q,even} - B_{Q,even}) = \int Q(\nu) T_{even}(\nu) d\nu,$$

$$Q_{odd} \equiv \frac{1}{2} (A_{Q,odd} - B_{Q,odd}) = \int Q(\nu) T_{odd}(\nu) d\nu,$$

$$Q_{\Sigma} \equiv A_{Q,even} + B_{Q,even} = A_{Q,odd} + B_{Q,odd} = \int I(\nu) T_{\Sigma}(\nu) d\nu = I_{\Sigma}.$$
(15)

Similar expressions can be written for the other Stokes states U and V to give  $U_{even}$ ,  $U_{odd}$ ,  $V_{even}$ , and  $V_{odd}$  also. The sums  $A_{Q,even} + B_{Q,even}$  are the same for all the Stokes states and in both the spectrally even and odd experiments:  $\bar{s}_{\Sigma} = (I_{\Sigma}, I_{\Sigma}, I_{\Sigma}, I_{\Sigma})^{T}$ .



Figure 3 A high resolution  $V_{odd}/I_{\Sigma}$  image. The intensity sum  $I_{\Sigma}$  is shown on the left and the difference divided by the sum  $V_{odd}/I_{\Sigma}$  or magnetic flux on the right in Ball 6142Å from a single photographic pair in the two channel Lyot UBF made of a quiet region at sun center. The center 10 arcsec field of view is magnified in the lower pair. Though the seeing was very good in this image, the granulation structure that appears in the intensity sum is naturally blurry at height in the solar atmosphere. The magnetic flux image shows much fine structure in the chromospheric network that is right of center in the upper field of view and upper right in the lower magnified field of view.

156 L. J. November

Figure 3 shows a high resolution  $V_{odd}/I_{\Sigma}$  image defined according to Equation (15). The images were recorded on film in BaII 6142Å with the UBF with its 0.22Å passband with Wollaston beam splitter with an exposure time of about 100 msec while switching the KD\*Ps at 250 Hz; thus about 25 states were photographically added in each output channel. The sum of the two channels is shown on the left.  $I_R + I_B = I_{\Sigma}$ , and the difference divided by the sum on the right in the figure,  $V_{odd}/I_{\Sigma}$ , after correction for the film response (November 1983). The sum is equivalent to the intensity integrated in a 0.44Å passband. Equation (13). The sum shows a blurry granulation structure which is characteristic of images made in strong lines. The  $V_{odd}/I_{\Sigma}$  images on the right, which are taken as a proxy for the longitudinal magnetic flux, shows the chromospheric network right of center in the upper  $V_{odd}/I_{\Sigma}$  image. The lower images are magnifications of part of the field of view from the upper pair. The images show interesting magnetic fine structure and indicates the high spatial resolution of the observation; the finest chromospheric network magnetic structure is about 0.3 arcsec.

## 4. Recovery of the Telescope Matrix

The optical arrangement of a telescope with reflecting optics is represented by the polarization transformation rule:  $\vec{s}' = \mathcal{M}\vec{s}$  where  $\mathcal{M}$  is the 4x4 real Mueller matrix,  $\vec{s}$  is an entering Stokes polarization vector and  $\vec{s}'$  is the corresponding exiting polarization vector.

If the polarization properties of the solar light obey the simplest rule, that  $I(\nu)$ ,  $Q(\nu)$ , and  $U(\nu)$  are even and  $V(\nu)$  is odd, then the solar light itself may be applied as a reference in the determination of  $\mathcal{M}$ . Under this assumption the exit spectrally odd component  $\vec{s}'_{odd}$  can occur only with a unique entrance state, and  $\vec{s}'_{even}$  obeys a conjugate constraint. Corresponding to the observed  $\vec{s}'$  there is a unique  $\vec{s}$ , where  $\vec{s} = \mathcal{M}^{-1} \vec{s}'$ , as presumably the telescope does not contain a complete polarizer and  $\mathcal{M}$  is nonsingular. In addition it is probably a good assumption that quiet regions outside the chromospheric network are not polarized so that  $\mathcal{M}^{-1} \vec{s}'_{quiet}$  should not be polarized.

The determination of  $\mathcal{M}$  is an optimization problem because the number of measurements, corresponding to pixels in the image, may be quite large, thus providing redundant information. At the same time, the conditions do not span the degrees of  $\mathcal{M}$  in two ways, as we shall see. To define  $\mathcal{M}$  correctly by a general least squares approach, the formulation must include proper Lagrange constraints because of the underdetermination; this general form is difficult. We therefore make use of the following theorem and ordering properties of the problem to invert the system for  $\mathcal{M}$  simply. The system of vector equations  $\vec{s}_{m}' = \mathcal{M} \vec{s}_{m}$  counted by the index m can also be written as an equation in matrices of vertical column vectors:

$$(\vec{s}_1' \vec{s}_2' \vec{s}_3' \cdots) = \mathcal{M}(\vec{s}_1 \vec{s}_2 \vec{s}_3 \cdots).$$

Then, the matrix  $\mathcal{M}$  for which the sum of squared residuals,  $\sum_{m} |\vec{s}'_{m} - \mathcal{M}\vec{s}_{m}|^{2}$ , is a minimum is written:

$$\mathcal{M} = (\vec{s}_1' \quad \vec{s}_2' \quad \vec{s}_3' \quad \cdots)(\vec{s}_1 \quad \vec{s}_2 \quad \vec{s}_3 \quad \cdots)^I, \tag{16}$$

where the notation  $S^I$  refers to the pseudo-inverse defined for the matrix S square or having more columns than rows:

$$\mathcal{S}^I = \mathcal{S}^T (\mathcal{S}\mathcal{S}^T)^{-1}.$$

 $S^T$  denotes the matrix transpose, and  $(SS^T)^{-1}$  the square matrix inverse. The theorem is given in a number of texts on orthogonal projections and least squares (Strong and Gilbert).

In the ideal case of spectral symmetry,  $\tilde{I}_{odd} = \tilde{U}_{odd} = 0$ , all the odd Stokes states must originate in the  $\tilde{V}_{odd}$  state before the telescope; we have:

$$\vec{s}'_{odd} = \tilde{\mathcal{M}} \begin{pmatrix} 0 \\ 0 \\ 0 \\ \tilde{V}_{odd} \end{pmatrix}. \tag{17}$$

The notation  $\vec{s}$  or  $\tilde{I}$ , etc. refers to the Stokes states in the ideal case, and  $\tilde{\mathcal{M}}$  is the optimum telescope matrix derived using the ideal conditions. Thus  $I'_{odd} \propto Q'_{odd} \propto U'_{odd} \propto V'_{odd} \propto \tilde{V}_{odd}$ . Since the amplitude of  $V'_{odd}$  is usually the largest of the exit states it is most reliable to take  $\tilde{V}_{odd} \equiv \beta_V V'_{odd}$  for some constant  $\beta_V$  as a definition for  $\tilde{V}_{odd}$ .

Using the Zeeman Spectral-Polarization Symmetry

We denote the Stokes states for the quiet regions by the subscript q. Unpolarized states  $I_{q \text{ scen}}$  entering the telescope can be modified to become polarized at the exit, thus:

$$\vec{s}'_{q,even} = \tilde{\mathcal{M}} \begin{pmatrix} \hat{I}_{q,even} \\ 0 \\ 0 \\ 0 \end{pmatrix}. \tag{18}$$

Then,  $\tilde{I}_{q,even} \equiv \beta_I I'_{q,even}$ . In the ideal case of spectral symmetry  $\tilde{I}_{q,odd} = 0$  at the sun, we have  $I'_{q,odd} = Q'_{q,odd} = U'_{q,odd} = V'_{q,odd} = 0$ .

Also, for spectral symmetry  $\tilde{V}_{even} = 0$ :

$$\tilde{s}'_{even} = \tilde{\mathcal{M}} \begin{pmatrix} \tilde{I}_{even} \\ \tilde{Q}_{even} \\ \tilde{U}_{even} \\ 0 \end{pmatrix}. \tag{19}$$

It is useful to simplify this relation by combining Equation (18):

$$\tilde{\mathcal{M}}\begin{pmatrix} 0 \\ \tilde{Q}_{even} \\ \tilde{U}_{even} \end{pmatrix} = \tilde{\mathcal{M}}\begin{pmatrix} \tilde{I}_{even} \\ \tilde{Q}_{even} \\ 0 \end{pmatrix} - \frac{\tilde{I}_{even}}{\langle \tilde{I}_{q,even} \rangle} \begin{pmatrix} \langle \tilde{I}_{q,even} \rangle \\ 0 \\ 0 \end{pmatrix} \\
= \begin{pmatrix} I'_{even} - \langle I'_{q,even} \rangle \\ Q'_{even} - \langle Q'_{q,even} \rangle \\ U'_{even} - \langle U'_{q,even} \rangle \\ V'_{even} - \langle V'_{q,even} \rangle \end{pmatrix} - \frac{\tilde{I}_{even} - \langle \tilde{I}_{q,even} \rangle}{\langle \tilde{I}_{q,even} \rangle} \begin{pmatrix} \langle I'_{q,even} \rangle \\ \langle Q'_{q,even} \rangle \\ \langle U'_{q,even} \rangle \\ \langle V'_{q,even} \rangle \end{pmatrix}, \tag{20}$$

where  $\langle \rangle$  denotes the average over the image. In solar images without sunspots the contrast is low (< 04) and  $|(\tilde{I}_{even} - \langle \tilde{I}_{q,even} \rangle)/\langle \tilde{I}_{q,even} \rangle| \ll 1$ . In the present approximation the last term was dropped giving the limiting form:

$$\vec{s}'_{even} - \langle \vec{s}'_{q,even} \rangle = \tilde{\mathcal{M}} \begin{pmatrix} 0 \\ \tilde{Q}_{even} \\ \tilde{U}_{even} \\ 0 \end{pmatrix}. \tag{21}$$

The small effect of intensity contrast cross-talk into the polarized components could be better approximated by using an estimate for the contrast, e.g.  $(\tilde{I}_{even} - (\tilde{I}_{q,even}))/(\tilde{I}_{q,even}) = I'_{even} - (I'_{q,even})/(I'_{q,even})$ .

The rotation of the linear polarization states  $\tilde{Q}_{even}$  and  $\tilde{U}_{even}$  by the telescope can not be determined from the spectral information; this is the first way in which the problem is underdetermined. In the case of the Sacramento Peak Vacuum Tower Telescope this effect is less than 2° by actual measurement (November 1989, Figure 3). It is convenient to adopt the condition that the polarization state is not rotated for the ideal formulation, i.e.  $\tilde{Q}_{even} \equiv \beta_Q(Q'_{even} - \langle Q'_{q,even} \rangle)$  and  $\tilde{U}_{even} \equiv \beta_U(U'_{even} - \langle U'_{q,even} \rangle)$ . This limitation is not fundamental; in section 5 we extend the method to allow any rotation angle.

Writing the three vector relations, Equations (17), (18), and (21), in one matrix equation gives:

$$S' = \tilde{\mathcal{M}}\tilde{S}, \tag{22}$$

where:

$$\begin{split} \mathcal{S}' &= \left( \begin{array}{c} \vec{s}'_{even,i} - \left( \vec{s}'_{q,even} \right), & \vec{s}'_{odd,j}, & \vec{s}'_{q,even,k} \right), \\ \vec{\mathcal{S}} &= \left( \begin{pmatrix} 0 \\ \tilde{Q}_{even,i} \\ \tilde{U}_{even,i} \\ 0 \end{pmatrix}, & \begin{pmatrix} 0 \\ 0 \\ 0 \\ \tilde{V}_{odd,j} \end{pmatrix}, & \begin{pmatrix} \tilde{I}_{q,even,k} \\ 0 \\ 0 \\ 0 \end{pmatrix} \right), \end{split}$$

and the indices i, j, k count the vectors corresponding to pixels in the image. Substituting,  $\tilde{Q}_{even} = \beta_Q Q'_{even}$ ,  $\tilde{U}_{even} = \beta_U U'_{even}$ ,  $\tilde{V}_{odd} = \beta_V V'_{odd}$ , and  $\tilde{I}_{q,even} = \beta_I I'_{q,even}$ , gives:

$$\begin{split} \mathcal{S}'\tilde{\mathcal{S}}^T = \\ & \begin{pmatrix} s_{l}(l_{q,\text{even}}^{2}) & s_{Q}((l_{\text{even}}^{\prime} - (l_{q,\text{even}}^{\prime}))(Q_{\text{even}}^{\prime} - (Q_{q,\text{even}}^{\prime}))) & s_{U}((l_{\text{even}}^{\prime} - (l_{q,\text{even}}^{\prime}))(P_{\text{even}}^{\prime} - (l_{q,\text{even}}^{\prime}))) & s_{U}((l_{\text{even}}^{\prime} - (l_{q,\text{even}}^{\prime}))(P_{\text{even}}^{\prime} - (l_{q,\text{even}}^{\prime}))(P_{\text{even}}^{\prime} - (l_{q,\text{even}}^{\prime}))) & s_{U}((l_{\text{even}$$

For convenience, I represent the sums over elements in the form of image averages  $\langle \rangle$  and have assume it that an equal number of spatial elements n contribute to each of the vectors counted by the indices i,j,k. Applying the theorem, Equation (16), gives the optimum  $\mathcal{M}$  explicitly:

The conditions, Equations (17), (18), and (21), will be satisfied for any choice of the constants  $\beta_I$ ,  $\beta_Q$ ,  $\beta_U$ ; it is convenient to choose  $\beta_I = \beta_Q = \beta_U = \beta_V$  such that  $\det(\tilde{\mathcal{M}}) = 1$ . This is the second incompleteness in the system. The relative absorption in the four Stokes states might be included from a representative model for the optical system.

An observation of  $Q'_{odd}$ ,  $U'_{odd}$ ,  $V'_{odd}$ ,  $Q'_{even}$ ,  $U'_{even}$ , and  $V'_{even}$  is shown in Figure 4 with each image normalized by  $I'_{\Sigma}$  and plotted on the same scale of contrast. The observation region was an emerging bipolar



Figure 4 Stokes spectrally even and odd measurement of an emerging bipolar flux region. Spectrally even and odd images taken with the two channel Lyot for the Stokes Q, U, V states at the exit of the telescope. All of the images were normalized by the intensity sum using the formula (A-B)/(A+B), and were printed with the same scale of contrast. All of the odd images should be correlated because the spectrally odd signal at the sun is mainly Stokes V which is changed in its polarization state by the telescope.

flux region without spots near the center of the sun. The incoming polarization state was selected by setting the rotating retarders before the entrance KD\*P of Figure 1. Even though the figure was formed from the average of six sets of photographic pairs it is still much noisier in  $V'_{odd}$  than the example Figure 3 which was made in the same way. Though the seeing was fairly good, the voltage on the KD\*P may have been incorrectly adjusted. Still, the correlation between different observables seems apparent: Note the similarity between the images  $V'_{odd}$  and  $Q'_{odd}$ ; the correlation coefficient between these is 0.36 which is statistically significant for the large number of points in the image ( $\approx 10^4$ ). Though the noise in  $U'_{odd}$  is larger due to the smaller signal, still the main features appear to be correlated in  $V'_{odd}$ .

After subtracting a common background field from the images, the averages in the non-magnetic portions verify the quiet-odd relation:  $\langle Q'_{q,odd} \rangle = \langle U'_{q,odd} \rangle = \langle V'_{q,odd} \rangle = 0$  within 3% of the dynamic range. Applying the formula Equation (24) gives a matrix  $\tilde{\mathcal{M}}$ . Then  $\tilde{\vec{s}} = \tilde{\mathcal{M}}^{-1} \vec{s}'$  gives  $\tilde{\vec{s}}_{odd}$ ,  $\tilde{\vec{s}}_{even}$ , and  $\tilde{\vec{s}}_{q,even}$  with most power in the expected components, verifying the process.

#### 5. Discussion

In actual practice the solar profile functions are not precisely symmetric. The deviations from symmetry may occur because of height variation of the central frequency along a line of sight or due to spatial effects within a resolution element.

The well known property of the convective red shift is alone able to produce rather large spectral asymmetries. The property that granular up flow is bright at the center of the sun leads to a stronger line that is blue shifted on the average. This property leads to spectral asymmetries in the polarized Stokes components even in the weak field approximation, Equations (7)-(10). Figures 5 and 6 show an example taken from the Kitt Peak Solar Atlas (Kurucz et.al. 1984) for the center of the disk,  $\mu = 1.0$  and for near the limb  $\mu = 0.2$ , respectively. The spectral profile in the vicinity of FeI 5250.2Å is shown in the upper panel: the first derivative (solid) and its negative (dashed) is shown in the second panel; the second derivative is shown in the lower panel. Though the line profile is almost symmetric in the first panel of Figure 5, the derivative profile in the second panel shows about 10% red over blue excess. A similar excess is apparent in the third panel for the second derivative. The property is considerably lessened near the limb in Figure 6. This spectral asymmetry is apparent in nearly all examples. If the spatial distribution of magnetic flux were not strongly correlated with the granulation field than such asymmetry should be expected in the nominal Stokes profile functions.

If the spectral asymmetry is constant then both spectral components for each Stokes state must be proportional, i.e.  $Q_{even} = D_Q \int P_{QU} T_{even} dv$ ,  $Q_{odd} = D_Q \int P_{QU} T_{odd} dv$ , so  $Q_{even} \propto D_Q$  and  $Q_{odd} \propto D_Q$ . One linear combination of the spectral pairs is zero, and the ideal Stokes states  $\vec{s}_{even}$  and  $\vec{s}_{odd}$  can always be formed by a linear combination of the actual Stokes states  $\vec{s}_{even}$  and  $\vec{s}_{odd}$ . Also, the effect of velocity variation v over the field introduces a systematic variation of the spectral asymmetry, see Appendix A. Equations (A8) and (A9). The effect of velocity is removed by applying a linear operator that is a function of the velocity to the actual Stokes states. Also the effect of rotating the linear polarization state by a known amount  $\chi$  is represented by a linear operator. We can represent all of these effects by one linear operator  $\mathcal A$  that acts on a single vector containing the idealized Stokes states from section 4 to give the actual Stokes states:

$$\begin{pmatrix} \vec{s}_{even,i} \\ \vec{s}_{odd,i} \end{pmatrix} = \mathcal{A}(v_i, \chi) \begin{pmatrix} \vec{\tilde{s}}_{even,i} \\ \vec{\tilde{s}}_{odd,i} \end{pmatrix}. \tag{25}$$

A different transformation must be applied to each pixel in the image counted by the index i. The actual telescope matrix transformation  $\mathcal{M}$  can be represented as  $\mathcal{S}' = \mathcal{MS}$ , where:

$$S' = (\vec{s}'_{even,i}, \vec{s}'_{odd,j}, \vec{s}'_{q,even,k}, \vec{s}'_{q,odd,l}),$$

$$S = (\vec{s}_{even,i}, \vec{s}_{odd,i}, \vec{s}_{q,even,k}, \vec{s}_{q,odd,l})$$

The indices i, j, k, l count pixels in the image. A determination of  $\mathcal{M}$  follows using the theorem Equation (16), but now the formulation correctly includes the systematic asymmetries and velocity effects. The solution must still include a priori information: the rotation of the linear polarization state  $\chi$ , and the

λ5250 KPO μ=.2 Atlos

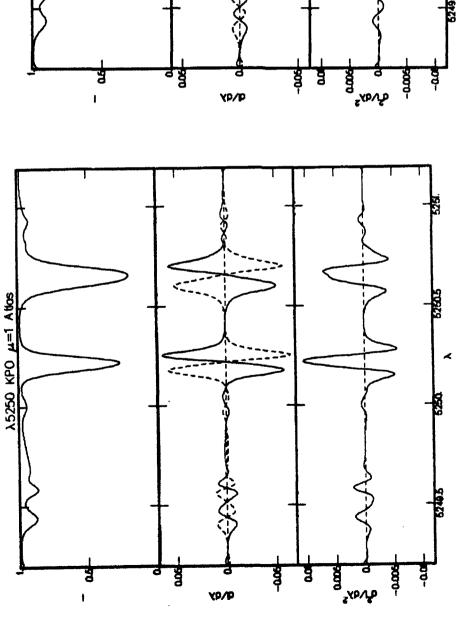


Figure 5 Kitt Peak Solar Atlas around FeI 5250.2A for the center of the sun. A portion of the Kitt Peak Solar Atlas is shown in the top panel with the first derivative (solid) and minus the first derivative (dashed) in the second panel. The second derivative is shown in the third panel. The first derivative is an approximation for the Stokes V profile.

Figure 6 Kitt Peak Solar Atlas around Fe1 5250.2Å for near the limb. The same Fe1 5250Å portion of the Kitt Peak Solar Atlas as in Figure 5 is shown but for near the limb. The atlas is shown in the top panel; the first derivative (solid) and minus the first derivative (dashed) in the second panel; the second derivative is shown in the third panel. The normal asymmetric effect due to the distribution of granulation brightness with velocity disappears near the limb.

relative absorption coefficients  $\beta_I$ ,  $\beta_Q$ ,  $\beta_U$ , and  $\beta_V$  of Equation (24), which can be taken from a nominal model for the optical train.

#### 6. Conclusions

Although this work has shown the viability of using the data itself to form a calibration for the telescope polarization effect, its usefulness must be limited to post facto analysis where a calibration was not available. Some of the most interesting questions regarding the nature of the field at high spatial resolution could be precluded by assuming spectral profile shapes a priori.

Matrix determinations that rely on calibration optics can be as accurate as those elements are known. Geometrically defined calibration methods may give a much higher absolute accuracy (November 1991). For example, a Jones matrix is uniquely determined by a rotating linear polarizer; linear polarizers based upon reflection or refraction effects, Brewster angle reflectors, or Wollaston prisms, can be very accurate ( $< 10^{-4}$  not pure linear polarization).

#### Appendix A. Lyot Velocity Measurements and Effects on Polarized Components

The line center position  $\nu_0 - v$  can vary with position over the field of view due to the Doppler effect in the line of sight velocity v.  $\nu_0$  is taken as the average line position corresponding to the filter center tune position. With a proper interpretation of the unpolarized observations,  $I_{even}$ ,  $I_{odd}$ , and  $I_{\Sigma}$ , v can be determined reliably. The symmetry of the polarized components is affected in a systematic way by the variation of the velocity over the field of view.

Equation (10) represents the profile functions in the weak field approximation. Including the velocity v which may vary from pixel to pixel we have:

$$\vec{s}(\nu_0 + \nu) = \begin{pmatrix} I_c - D_I P_I(\nu - \mathbf{v}) \\ D_Q P_{QU}(\nu - \mathbf{v}) \\ D_U P_{QU}(\nu - \mathbf{v}) \\ D_V P_V(\nu - \mathbf{v}) \end{pmatrix}. \tag{A1}$$

 $I_c$  is the continuum intensity,  $D_I$  is a unpolarized line depth, and v the Doppler red shift.  $D_Q$ ,  $D_U$ , and  $D_V$  are the strengths of the polarized components. The profile functions  $P_I(\nu)$ ,  $P_{QU}(\nu)$ , and  $P_V(\nu)$  are assumed to be known.

For small v:

$$I_{even} = I_c \int T_{even}(\nu) d\nu - D_I \int P_I(\nu) T_{even}(\nu) d\nu + v D_I \int \frac{dP_I(\nu)}{d\nu} T_{even}(\nu) d\nu,$$

$$I_{odd} = -D_I \int P_I(\nu) T_{odd}(\nu) d\nu + v D_I \int \frac{dP_I(\nu)}{d\nu} T_{odd}(\nu) d\nu,$$

$$I_{\Sigma} = I_c \int T_{\Sigma}(\nu) d\nu + v D_I \int \frac{dP_I(\nu)}{d\nu} T_{\Sigma}(\nu) d\nu.$$
(A2)

The system of three Equations (A2) is linear in  $I_c$ ,  $D_I$ , and v  $D_I$ , and gives their unique determination with the constant spectral profile integrals:

$$\zeta_{k,Ieven} = \int \frac{d^k P_I(\nu)}{d\nu^k} T_{even}(\nu) d\nu,$$

$$\zeta_{k,Iodd} = \int \frac{d^k P_I(\nu)}{d\nu^k} T_{odd}(\nu) d\nu,$$

$$\zeta_{k,I\Sigma} = \int \frac{d^k P_I(\nu)}{d\nu^k} T_{\Sigma}(\nu) d\nu.$$
(A3)

Rewriting Equation (A2) in vector form, we have:

$$\begin{pmatrix} I_{even} \\ I_{odd} \\ I_{\Sigma} \end{pmatrix} = \mathcal{V} \begin{pmatrix} I_c \\ D_I \\ v D_I \end{pmatrix}. \tag{A4}$$

where:

$$\mathcal{V} = \begin{pmatrix} \frac{\pi}{2} & -\zeta_{0,Ieven} & \zeta_{1,Ieven} \\ 0 & -\zeta_{0,Iodd} & \zeta_{1,Iodd} \\ \pi & 0 & \zeta_{1,I\Sigma} \end{pmatrix}.$$

For  $P_I(\nu)$  strictly even,  $\zeta_{1,Ieven} = \zeta_{0,Iodd} = \zeta_{1,I\Sigma} = 0$ , and Equation (A4) has the inverse:

$$\begin{pmatrix} I_c \\ D_I \\ v D_I \end{pmatrix} = \frac{1}{\pi \zeta_{0,Ieven} \zeta_{1,Iodd}} \begin{pmatrix} 0 & 0 & \zeta_{0,Ieven} \zeta_{1,Iodd} \\ -\pi \zeta_{1,Iodd} & 0 & \frac{\pi}{2} \zeta_{1,Iodd} \\ 0 & \frac{\pi}{2} \zeta_{0,Ieven} & 0 \end{pmatrix} \begin{pmatrix} I_{even} \\ I_{odd} \\ I_{\Sigma} \end{pmatrix}. \tag{A5}$$

Thus,  $vD_I \propto I_{odd}$ . The line strength variation  $D_I$  over the field of view must be small (November 1983), so when  $P_I(\nu)$  is approximately even,  $v \propto I_{odd}$  approximately. Since  $I_{odd}$  comes from one simultaneous image pair without seeing differences between the images, v defined using Equation (A4) should be mostly unaffected by the seeing.

Nonlinear corrective terms in v can be included in the expansion of Equation (A2) to give:

$$\begin{pmatrix} I_{even} \\ I_{odd} \\ I_{\Sigma} \end{pmatrix} = \mathcal{V}(\begin{pmatrix} I_c \\ D_I \\ v D_I \end{pmatrix} - v^2 D_I \begin{pmatrix} \zeta_{2,Ieven} \\ \zeta_{2,Iodd} \\ \zeta_{2,I\Sigma} \end{pmatrix}). \tag{A6}$$

The inverse relation can be used to define an iteration procedure for v:

$$\begin{pmatrix} I_c \\ D_I \\ v D_I \end{pmatrix} = \mathcal{V}^{-1} \begin{pmatrix} I_{even} \\ I_{odd} \\ I_{\Sigma} \end{pmatrix} + v^2 D_I \begin{pmatrix} \zeta_{2,Ieven} \\ \zeta_{2,Iodd} \\ \zeta_{2,I\Sigma} \end{pmatrix}), \tag{A7}$$

where the velocity on the right side is taken from the previous iteration.

This formulation is applicable to the Fourier tachometer velocity measurement but it considers the effects caused by a relatively narrow blocking function  $\int |T_{\Sigma}|^2 d\nu \gg \int |T_{even}|^2 d\nu$  (Brown 1981, Evans 1981, November 1983). The narrow blocker design has an advantage because it gives an intrinsically better signal to noise, but a disadvantage that a nominal profile function,  $P_I(\nu)$ , must be assumed.

The Doppler velocity changes the measured spectral symmetry due to the offset of the filter passband from the line center. Since the polarized components shift with the unpolarized profile, v must be the same as that found from the unpolarized signal, Equations (A1) and (A2) (without considering the effects of a changing atmospheric seeing between observations of the different polarized components). Using  $\zeta_{k,V}$  to denote the spectral integrals over the polarized profile function  $P_V(\nu)$  as in Equation (A3), the polarized observables  $V_{even}$  and  $V_{odd}$  can be written:

$$V_{even} = D_V \zeta_{0,Veven} - v D_V \zeta_{1,Veven},$$

$$V_{odd} = D_V \zeta_{0,Vodd} - v D_V \zeta_{1,Vodd}.$$
(A8)

We can define  $\tilde{V}_{even} \equiv D_V \zeta_{0,Veven}$  and  $\tilde{V}_{odd} \equiv D_V \zeta_{0,Vodd}$ ; these are the polarized components shifted by v in the filter passband. Then, eliminating  $D_V$  from the definition gives:

$$\begin{pmatrix} V_{even} \\ V_{odd} \end{pmatrix} = \begin{pmatrix} 1 & -v \frac{\zeta_{1,Veven}}{\zeta_{0,Veven}} \\ -v \frac{\zeta_{1,Veven}}{\zeta_{0,Veven}} & 1 \end{pmatrix} \begin{pmatrix} \tilde{V}_{even} \\ \tilde{V}_{odd} \end{pmatrix}. \tag{A9}$$

 $D_V$  is eliminated to give a useful formula for affecting the velocity correction by a linear operator. Similar equations can be written for the other Stokes states to give  $\tilde{Q}_{even}$ ,  $\tilde{Q}_{odd}$ ,  $\tilde{U}_{even}$ , and  $\tilde{U}_{odd}$ .

If the profile functions have ideal symmetry then half of the spectral integrals will be zero. The relation Equation (A9), then assumes a trivial form. For example, in V,  $\zeta_{0,Veven} = \zeta_{1,Vodd} = 0$ . In this case, the effect of v is always second order and  $\tilde{V}_{odd} = V_{odd}$ . With ideal symmetry  $V_{odd}$  is a measure of field strength that is correctly defined with reference to the spectral line center not with reference to the filter tune position. It is usual to use  $V_{odd}/I_{\Sigma}$  as a proxy for the longitude magnetic flux, independent of the velocity.

#### References

Azzam, R.M.A, and Bashara, N.M., 1977, Ellipsometry and Polarized Light, North-Holland, Amsterdam.

Beckers, J.M., 1969, A Table of Zeeman Multiplets, AFCRL-TR-69-0115, Air Force Cambridge Research Lab., Office of Aerospace Research, United States Air Force.

Beckers, J.M., Dickson, L., and Joyce, R.S., 1975, A Fully Tunable Lyot-Ohman Filter, AFCRL-TR-75-0090. Air Force Cambridge Research Lab., Office of Aerospace Research, United States Air Force.

Brown, T.M. 1980, "The Fourier Tachometer: Principles of Operation and Current Status", Solar Instrumentation: What's Next?, R.B. Dunn ed., National Solar Observatory Publication, p. 150.

Dunn, R.B., 1984, "Window Considerations for LEST", Lest Foundation Technical Report 3, Univ. of Oslo Inst. Theoretical Astron.

Dunn, R.B., November, L.J., Colley, S.A, Streander, G.W., 1989, "The National Solar Observatory polarimeter", Optical Engineering 28

Elmore, D.F., 1988, "Measurement of the polarization properties of the NSO Vacuum Tower Telescope: physically constrained approach", *Polarization Considerations for Optical Systems*, R.A Chipman, ed., Proc. SPIE 891, 84-90.

Evans, J.W., 1980, "The Fourier Tachometer: The Solid Polarizing Interferometer", Solar Instrumentation: What's Next?, R.B. Dunn ed., National Solar Observatory Publication, p. 151.

Jefferies, J., Lites, B.W., Skumanich, A, 1989, "Transfer of line radiation in a magnetic field", Astrophys. J. 343, 920-935.

Kurucz, R.L., Furenlid, I., Brault, J., Testerman, L., June 1984, Solar Flux Atlas from 296 to 1300 nm, National Solar Observatory Atlas 1, Harvard University Publisher, available from the National Solar Observatory, Sunspot, NM 88349 USA.

Landi Degl'innocenti, E., and Landi Degl'innocenti, M., 1970, "Radiative transfer for polarized radiation: symmetry properties and geometrical interpretation", Il Nuovo Cimento 62B, 1-16.

Landi Degl'innocenti, E., and Landi Degl'innocenti, M., 1972, "Quantum theory of line formation in a magnetic field", Solar Phys 27, 319-329.

Makita, M., Hamana, S., Kawakami, H., 1982, "High Accuracy Measurement of the Instrumental Polarization of the Solar Coude Telescope at the Okayama Astrophysical Observatory", Ann. Tokyo Astron. Obs. 12, 493-499.

November, L.J., Elmore, D.E., 1987, "Measurement of the polarization properties of the NSO/Sunspot Vacuum Tower Telescope", B.A.A.S..

November, L.J., 1988, "Measurement of a multiple component serial device of partial polarizing and retarding elements", Polarization Considerations for Optical Systems, R.A Chipman, ed., Proc. SPIE 891, 91-102.

November, L.J., 1989, "Determination of the Jones Matrix for the Sacramento Peak Vacuum Tower Telescope", Optical Engineering 28, 107-113.

November, L.J., 1991, "Absolute Polarimetry: Geometrically Defined Calibration", in prep.

Strong, Gilbert, Linear Algebra and its Applications, ISBN 015551005.

Zeldin, L.K., 1981, "A design study for a video Stokes polarimeter", MS thesis, Cal. State Univ., Northridge, Dept of Physics and Astronomy.

#### Acknowledgements

The data used for Figures 3 and 4 were obtained with the Sacramento Peak Vacuum Tower Telescope with the help of the National Solar Observatory observing staff. Marc M. Pic digitized and analyzed the frames that were used in Figure 4.

#### Discussion

- J. Stenflo: The circumstance that the Stokes V profile is not entirely antisymmetric due to velocity field gradients will enter into your analysis as a fictitious V to Q cross-talk. This effect may however be sorted out by a multi-line analysis, since the Stokes V asymmetry is different in different spectral lines. Also your self-calibration method may help sort it out, since the V to Q cross-talk varies over the day, whereas the statistical properties of the Stokes V asymmetry do not.
- L. November: If the effect is systematic, i.e. proportional in strength to the  $V_{odd}$  component then it should be possible to subtract the effect.
- S. Solanki: Although the Stokes V asymmetry may be a problem at solar disk center, it varies across the solar disk and even changes sign near the limb. Therefore, it should be possible from radial scan to determine the position on the solar disk at which the V asymmetry disappears (with depends on the line used) and to carry out the analysis at that point.
- B. Lites: High resolution spectra of umbra taken at La Palma contain telluric reference lines which give an absolute wavelength reference. These spectra show that umbra are nearly at rest within  $\pm$  200 m/s or so a result found at lower resolution by Beckers a number of years ago. Thus, one might expect the Stokes V profile to be symmetric in umbrae.
- B. Lites: How well do the lobes of the UBF spectral profile match the 3 lobes of the Stokes Q-profile, for example?
- L. November: The filter passband ( $\frac{1}{4}$ Å at 6563Å) was chosen to be close to the width of many spectral lines of interest for velocity or magnetic studies. It is this parameter that is relevant, I think, in deciding the inherent sensitivity of the system to measure the line shift, Doppler effect, or to measure a difference in line positions, Zeeman Q, U or V effects.

# FRINGES IN POLARIZING OPTICAL ELEMENTS

## BRUCE W. LITES

High Altitude Observatory
National Center for Atmospheric Research\*
P.O. Box 3000
Boulder, Colorado, USA

## **ABSTRACT**

A Muller Matrix description is developed for expressing the effects of spectral fringes (channel spectra) arising from polarizing optical elements in astronomical polarimeters. This description allows one to derive the effects of fringes in a straightforward manner. The formalism is applied to the case of the rotating linear retarder that will be used in the Advanced Stokes Polarimeter (ASP). It is shown that, through proper calibration of the ASP polarimeter on a pixel-by-pixel basis, the effects of spectral fringing should not be troublesome, but these effects may be more troublesome in polarimeters which demand higher polarization accuracy.

### I. BACKGROUND

In the Advanced Stokes Polarimeter we will have a number of polarizing optical elements with nearly parallel optical surfaces. These surfaces will produce spectral fringes, just as the multiple reflections from the parallel surfaces cause fringes in a Fabry-Perot interferometer.

In the ASP we will minimize the problems caused by fringes through the use of anti-reflection coatings. Even with these coatings, we expect that the amplitudes of the fringes will be in the range 0.4 - 1%, so that the fringes cannot be neglected relative to our design goal of  $10^{-3}$  in the polarization accuracy. It is therefore important to understand the nature of the optical effects that these fringes will produce, and the expected magnitude of such effects. In particular, fringes in the retarding optical elements will produce perturbations of the polarization as well as the intensity, and all of these effects vary rapidly with wavelength.

The target for polarization accuracy for the ASP is 0.1% of the continuum intensity  $I_c$ . This accuracy guides the design of the instrument with regard to the crosstalk among the four Stokes parameters. One should adhere to the 0.1% goal for the crosstalk terms  $I \rightarrow Q, U, V$ , but requirements on the crosstalk terms among Q, U, V may be relaxed somewhat, for the following reasons. When the magnetic field is very strong, in sunspots for example, the polarization may be large for either the circular or linear states. Typically in a sunspot umbra one may find a maximum polarization in any of the Stokes parameters  $Q/I_c$ ,  $U/I_c$ ,  $V/I_c$  of 0.2 - 0.3. Crosstalk errors of the order of 1% among these terms usually will be smaller than the errors either in the fit to the observed profiles due to inadequacies of the analytic model used in the least-squares inversion or due to noise. Spatial averaging of the profiles due to seeing and the ASP resolution element of 0.4" will further add to the deviations of the real profiles from those of our theoretical model. If we relax the requirement for crosstalk accuracy among Q, U, V to 1%, then the maximum error of the profiles due to crosstalk is  $.002 - .003 I_c$ , which is close to the noise level we expect to achieve in normal scans of active regions. We target a signal to noise (S/N) of 300:1 for much of our work, with the hope of getting 1000:1 when we concentrate on analysis of the chromospheric field. Note that we will use the higher S/N when we expect weak polarization signals from the Mg b-lines, for example, outside of sunspots. In these cases we can certainly tolerate a crosstalk

<sup>\*</sup>The National Center for Atmospheric Research is sponsored by the National Science Foundation.

among Q, U, V of 1%, as the *net* polarization will be very small. A target crosstalk tolerance of 1% among Q, U, V now appears to be adequate for most of the scientific analyses we we attempt with the ASP.

In the following I develop a description of the effects of fringes in optical elements and I estimate the effect of fringes arising from the ASP rotating waveplate modulator.

## II. GROSS PROPERTIES OF THE FRINGES

Before embarking on the details of the fringe effects, I will give some estimates of the fringe amplitudes and spacings so that one may gauge the importance of the fringes in what follows.

# a) Fringe Amplitudes

Anti-reflection coatings optimized for the specific wavelengths used in ASP will leave a residual reflection at the surfaces of 0.1 - 0.3%, and broadband coatings may result in reflection coefficients closer to 1%. The peak-to-peak range of the fringes will be four times these values of reflectivity.

# b) Fringe Spacing in Wavelength

Most of the ASP optical elements will have thicknesses of the order of 1 cm. The fringe spacing will be of the order of 0.1 A at 5500 A for a 1 cm thick element. The fringe spacing varies inversely with the thickness of the device and directly with the wavelength. The width of the fringes in wavelength (50 mA) is comparable to the widths of the spectral lines being observed, further emphasizing the need to minimize their influence.

# c) Polarization Fringes

When describing spectral fringes, one normally considers only their signature in intensity. When the fringes are created by a device that retards one state of polarization relative to another, I will show in what follows that the fringe pattern will differ with differing states of polarization of both the beams incident upon and exiting from the element.

# III. A MULLER MATRIX REPRESENTATION OF FRINGE EFFECTS IN A LINEAR RETARDER

As fringing is an effect of wave interference, a development of the fringing properties of a polarizing element must start from a description of phases and amplitudes of the electromagnetic wave. Thus, one cannot use the intensity information only (i.e., the Muller matrix formalism) to derive the effects of fringes on polarized radiation. However, once one derives the correct behavior of the modification of the wave using the amplitudes an phases, one may describe the effects of fringing using the Muller algebra.

## a) The Incident Wave

Following Jefferies, Lites and Skumanich (1989), I describe the wave incident upon the retarder by the two orthogonal components of the electric vector:

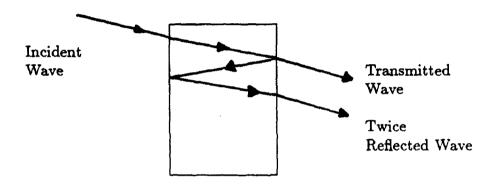
$$\tilde{a}_x = A_x e^{i\omega t} 
\tilde{a}_y = A_y e^{i\omega t}$$
(1)

Here the amplitudes  $A_x$  and  $A_y$  are complex in order to describe any incident state of linear or circular polarization.

## b) Some Assumptions and Pefinitions

- 1. The retarder is such that the fast and slow axes are perpendicular to the propagation direction of the incident radiation.
- 2. The coordinate system is chosen such that the fast axis is along the x-direction.
- 3. The reflection coefficients for the wave (NOT the intensity!) along the fast and slow axes are given by  $r_f$  and  $r_s$ , respectively.
- 4. The phase retardance of the fast and slow waves upon one traversal of the retarder is given by  $\phi_f$  and  $\phi_s = \phi_f + \delta$ , respectively. Thus  $\delta$  is the relative retardance of the slow beam with respect to the fast beam.
- 5. The absorption of the fast and slow beams is given by  $\eta_f$  and  $\eta_s$ , respectively.

## c) Expressions for the Wave on Exit from the Retarder



Note the geometry in the above figure. As the reflection from the coated surfaces is so small, I need only consider the transmitted wave and the wave which suffers two reflections, then interferes with the transmitted wave.

For the transmitted wave, the polarization components of the wave may be described as:

$$\tilde{a}_{x}^{t} = A_{x}e^{i\omega t}[(1-r_{f})(1-\eta_{f})e^{-i\phi_{f}}], 
\tilde{a}_{y}^{t} = A_{y}e^{i\omega t}[(1-r_{s})(1-\eta_{s})e^{-i(\phi_{f}+\delta)}].$$
(2)

Similarly, for the twice-reflected wave, I have:

$$\tilde{a}_{y}^{r} = A_{x}e^{i\omega t}[r_{f}(1-\eta_{f})e^{-i\phi_{f}}r_{f}(1-\eta_{f})e^{-i\phi_{f}}(1-r_{f})(1-\eta_{f})e^{-i\phi_{f}}],$$

$$\tilde{a}_{y}^{r} = A_{y}e^{-i\omega t}[r_{s}(1-\eta_{s})e^{-i(\phi_{f}+\delta)}r_{s}(1-\eta_{s})e^{-i(\phi_{f}+\delta)}(1-r_{s})(1-\eta_{s})e^{-i(\phi_{f}+\delta)}].$$
(3)

The resultant wave amplitude upon exit of the retarder is the sum of the transmitted and twice-reflected components:

$$\tilde{a}'_{x} = A_{x}(1 - \eta_{f})e^{i(\omega t - \phi_{f})}[(1 - r_{f}) + r_{f}^{2}(1 - r_{f})(1 - \eta_{f})^{2}e^{-2i\phi_{f}}], 
\tilde{a}'_{y} = A_{y}(1 - \eta_{s})e^{i(\omega t - \phi_{f})}[(1 - r_{s})e^{-i\delta} + r_{s}^{2}(1 - r_{s})(1 - \eta_{s})^{2}e^{-i(2\phi_{f} + 3\delta)}].$$
(4)

I now assume that  $\eta_f = \eta_s = 0$ , as most research quality PVA waveplates are highly transmitting. Any imbalance of the absorption for the fast and slow waves will result in a slight linear polarization from the device. Furthermore, I assume that  $r_f = r_s = r$ . This also is a good approximation for ASP, as the transmitting optical elements potentially having significant retardance are all near normal incidence. Under these assumptions, equations (4) reduce to:

$$\tilde{a}'_{x} = A_{x}e^{i(\omega t - \phi_{f})}[(1 - r) + r^{2}(1 - r)e^{-2i\phi_{f}}], 
\tilde{a}'_{y} = A_{y}e^{i(\omega t - \phi_{f})}[(1 - r)e^{-i\delta} + r^{2}(1 - r)e^{-i(2\phi_{f} + 3\delta)}].$$
(5)

Since  $r \ll 1$ , I may neglect terms of higher order than  $r^2$ . I also ignore the overall phase factor  $\phi_f$  common to both  $\tilde{a}'_x$  and  $\tilde{a}'_y$ . The amplitudes of the polarized components of the emergent waves may be expressed in terms of the incident amplitudes (eq. 1):

$$\tilde{a}_{x} = \tilde{a}_{x}[(1-r) + r^{2}e^{-i\phi}] = H_{11}\tilde{a}_{x} 
\tilde{a}'_{y} = \tilde{a}_{y}[(1-r)e^{-i\delta} + r^{2}e^{-i(\phi+3\delta)}] = H_{22}\tilde{a}_{y}$$
(6)

where I have defined  $\phi = 2\phi_f$ .

## d) The Coherency Matrix Formulation

The coherency matrix formalism (see Appendix C of Jefferies et al. 1989) most easily allows one to determine the Muller Matrix from the matrix expressing the modification of the wave amplitudes upon traversal of the retarder. If one describes the modification of the complex amplitudes of the wave by a  $2 \times 2$  complex matrix H:

$$\mathbf{A'} = \mathbf{H} \cdot \mathbf{A} \tag{7}$$

where the matrices A, A' are given by

$$\mathbf{A} = \begin{bmatrix} a_{\mathbf{x}} & 0 \\ a_{\mathbf{y}} & 0 \end{bmatrix} , \quad \mathbf{A'} = \begin{bmatrix} \tilde{a}'_{\mathbf{x}} & 0 \\ \tilde{a}'_{\mathbf{y}} & 0 \end{bmatrix}$$
 (8)

and H is the diagonal interaction matrix whose components are given by  $H_{11}$  and  $H_{22}$  in eq. 6. Then using the results of Jefferies *et al.*, the Stokes vectors upon input (S) and exit (S') of the retarder may be expressed as:

$$\mathbf{S}_{k}' = \sum_{j=0}^{3} \operatorname{trace} \left\{ \sigma_{k} \left[ \mathbf{H} \frac{\sigma_{j}}{2} \mathbf{H}^{\dagger} \right] \right\} \mathbf{S}_{j} = \sum_{j=0}^{3} \mathbf{M}_{kj} \mathbf{S}_{j}$$
 (9)

where  $\sigma_k$  are components of the Pauli matrices, and M is the Muller matrix which we seek.

# e) An Expression for the Muller Matrix of a Fringing Retarder

Performing the matrix algebra, ignoring terms of order greater than  $r^2$ , and defining the transmission fraction t = 1 - r, I have:

$$\mathbf{M} = \begin{bmatrix} a' & b' & 0 & 0 \\ b' & a' & 0 & 0 \\ 0 & 0 & c' & d' \\ 0 & 0 & -d' & c' \end{bmatrix}$$
(10)

where

$$a' = \frac{1}{2}(H_{11}H_{11}^* + H_{22}H_{22}^*) = t^2 + tr^2[\cos\phi + \cos(\phi + 2\delta)]$$

$$b' = \frac{1}{2}(H_{11}H_{11}^* - H_{22}H_{22}^*) = tr^2[\cos\phi - \cos(\phi + 2\delta)]$$

$$c' = \frac{i}{2}(H_{22}H_{11}^* + H_{11}H_{22}^*) = t^2\cos\delta + tr^2[\cos(\phi + 3\delta) + \cos(\phi - \delta)]$$

$$d' = \frac{i}{2}(H_{22}H_{11}^* - H_{11}H_{22}^*) = t^2\sin\delta + tr^2[\sin(\phi + 3\delta) - \sin(\phi - \delta)].$$
(11)

It is easily seen that the expression (10) may be broken into a sum of Muller matrices describing an ideal retarder  $(M_s)$  and the perturbation due to the fringing effects  $(M_p)$ :

$$\mathbf{M} = \mathbf{M}_{s} + \mathbf{M}_{p} = t^{2} \begin{bmatrix} 1 & 0 & 0 & 0 \\ 0 & 1 & 0 & 0 \\ 0 & 0 & \cos \delta & \sin \delta \\ 0 & 0 & -\sin \delta & \cos \delta \end{bmatrix} + tr^{2} \begin{bmatrix} a & b & 0 & 0 \\ b & a & 0 & 0 \\ 0 & 0 & c & d \\ 0 & 0 & -d & c \end{bmatrix}$$
(12)

where I have the following coefficients of the perturbation matrix:

$$a = [\cos \phi + \cos(\phi + 2\delta)]$$

$$b = [\cos \phi - \cos(\phi + 2\delta)]$$

$$c = [\cos(\phi + 3\delta) + \cos(\phi - \delta)]$$

$$d = [\sin(\phi + 3\delta) - \sin(\phi - \delta)]$$
(13)

# IV. WHAT WILL THE FRINGES FROM THE ROTATING WAVEPLATE DO TO THE ASP SIGNAL?

### a) The Perturbation Matrix for a Rotating Waveplate

The rotating waveplate modulator in ASP is located very near an image of the aperture, so that any fringes introduced by it will appear at the focal plane of the spectrograph as pure spectral features, with no variation along the spatial dimension, i.e., along the slit. As the waveplate rotates, the polarization character of the fringes will cause a modulation of this fringe pattern. I now ask if this modulation will affect the inferred Stokes signal of the polarimeter.

We understand what to expect from an ideal rotating waveplate described by  $M_s$ . In order to understand the influence of the perturbation matrix,  $M_p$ , we must subject it to the rotation:

$$\mathbf{M}_{p}' = \mathbf{R}^{-1} \mathbf{M}_{p} \mathbf{R} \tag{14}$$

where R is the rotation matrix

$$\mathbf{R} = \begin{bmatrix} 1 & 0 & 0 & 0 \\ 0 & \cos 2\alpha & \sin 2\alpha & 0 \\ 0 & -\sin 2\alpha & \cos 2\alpha & 0 \\ 0 & 0 & 0 & 1 \end{bmatrix}$$
 (15)

and  $\alpha$  is the time-dependent angle of rotation. The rotated perturbation matrix  $\mathbf{M}_p'$  has the form:

$$\mathbf{M}_{p}' = tr^{2} \begin{bmatrix} a & bc_{2} & bs_{2} & 0\\ bc_{2} & (ac_{2}^{2} + cs_{2}^{2}) & c_{2}s_{2}(a - c) & -ds_{2}\\ bs_{2} & c_{2}s_{2}(a - c) & (as_{2}^{2} + cc_{2}^{2}) & dc_{2}\\ 0 & ds_{2} & -dc_{2} & c \end{bmatrix}$$
(16)

where  $c_n = \cos n\alpha$  and  $s_n = \sin n\alpha$ .

# b) The ASP "Dual-Beam" Polarimeter

The final demodulation scheme separates out the two polarizations corresponding to  $I' \pm Q'$  and differences these two signals. The difference signal resulting from the fringes is given by:

$$D = bc_2I + (ac_2^2 + cs_2^2)Q + (a - c)c_2s_2U - ds_2V .$$
  
=  $bc_2I + \{0.5(a + c) + 0.5(a - c)c_4\}Q + 0.5(a - c)s_4U - ds_2V$  (17)

This form has the following consequences:

- 1. The fringes change only the amplitudes of the Q', U', V' signals as detected by the polarimeter. No frequency or phase change of the modulation of these quantities results from fringes.
- 2. The "DC" term in the demodulated Q' signal is altered. This is of no consequence for our measurement, except for an insignificant increase in some seeing-induced crosstalk among the Stokes parameters which result from such offset terms (Lites 1988).
- 3. The fringes introduce a modulated Stokes I signal into D that has the same frequency as the modulation of V. But this is not of concern since the phase is  $\pi/2$  different than the modulation of V (in the absence of fringes). Careful calibration of the phase of the demodulation should then remove the influence of this form.

In summary, fringes in the rotating waveplate should not affect observations if the polarimeter is properly calibrated on a pixel-by-pixel basis, i.e., both along the slit and the dispersion. The net fringe amplitude from the rotating waveplate should be less than the theoretical values of 0.5 – 1%, due to irregularity of the surfaces of the modulator waveplate. In addition, rays passing through the modulator at differing angles in the f/36 beam will produce a range of phases  $\phi$ . The detector will average over this range.

# c) The ASP Prototype "Single-Beam" Polarimeter

The single-beam polarimeter detects the signal from only one orientation of linear polarization emerging from the rotating waveplate: for example, the I' + Q' signal. In this case, the demodulation signal for the fringe perturbation is given by:

$$D = (a + bc_2)I + [bc_2 + (ac_2^2 + cs_2^2)]Q + [bs_2 + c_2s_2(a - c)]U - ds_2 V$$
  
=  $(a + bc_2)I + [0.5(a + c) + bc_2 + 0.5(a - c)c_4]Q + [bs_2 + 0.5(a - c)s_4]U - ds_2 V$  (18)

Comparing eq. 18 with the signal for the dual-beam detector scheme (eq. 17), one finds several new sources of crosstalk:

- 1. Stokes Q is now modulated at the same frequency as V, but  $\frac{\pi}{2}$  out of phase.
- 2. Stokes U experiences a modulation at the same frequency and phase as Stokes V. The fringing in the waveplate thus produces a  $U \to V$  crosstalk.

## V. SUMMARY

The formalism of Jefferies et al. (1989) provides a prescription for expressing the effects of wave interference in optical elements of a polarimeter in terms of Muller matrices. This prescription is simple and straightforward to apply.

Under the assumptions made in Section III.B, I find that the amplitudes of the fringes from the rotating waveplate should be of small amplitude, and the net result of such fringes will be the necessity of calibration of the polarimeter at each wavelength. The fact that the waveplate sits in a divergent f/36 beam and is known to have a slight optical wedge probably reduces the effects of fringes in this optical element to a level comparable to or smaller than the  $10^{-3}$  precision needed for ASP. It should be noted that no fringes of this type were observed at the level of a few tenths of a percent in the recent ASP prototype polarimeter run.

Other optical devices may show large effects of polarizing fringes. As pointed out by Makita et al. (1982), optically active elements such as crystalline quartz (where a linearly polarized beam traveling along the optical axis will rotate its plane of polarization) may show much more dramatic fringing effects resulting from the optical activity. Such behavior may be easily described through the application of the prescription given above.

### **ACKNOWLEDGMENTS**

I wish to thank S. Tomczyk and A. Skumanich for several helpful discussions and suggestions. I also thank J. Harvey for pointing out several references on related topics, as listed in the discussion of this paper.

#### REFERENCES

Jefferies, J. T., Lites, B. W., and Skumanich, A. 1989, Astrophys. J., 343, 920.

Lites, B. W. 1987, Applied Optics, 26, 3838.

Makita, M., Hamana, S., Kawakami, H., and Nishi, K. 1982, Ann. Tokyo Ast. Obs., 19, 24.

#### Discussion

- J. Harvey: The effect of multiple reflections in wave plates in not trivial in some precise polarization applications. The exact theory is given by Holmes (J. Opt. Soc. Amer. 54, 1115, 1964). This shows for example, that a simple quarter wave plate may have a retardation of a quarter wave at several different wavelengths rather than just one. A good discussion of these effects is in the Makita solar polarimeter is given by Makita et al. Ann. Tokyo Ast. Obs. 19, 24, 1982).
- Ai G.: Do you find any fringes in measurements of Dopplergram as used different wavelengths?
- B. Lites: Fringes do not seem to be apparent at the few  $\times 10^{-3}$  I continuum level in our Stokes images, which are differences of 128 images taken over an interval of about 2 seconds. Since we do not produce "Dopplergrams", but spectra, and we derive velocities from the line profiles, we cannot at present assign a velocity error to optical fringes which we do not see.

# SENSITIVITY TO POLARIZATION: HOW CAN WE MEASURE WEAK VECTOR MAGNETIC FIELDS AT HIGH ANGULAR RESOLUTION?

## BRUCE W. LITES

High Altitude Observatory
National Center for Atmospheric Research\*
P.O. Box 3000
Boulder, Colorado, U.S.A.

#### ABSTRACT

The difficulties of using ground-based instrumentation to measure weak vector magnetic fields in the photosphere through polarization measurements of high precision in the visible spectrum are discussed. Integration times sufficient to attain the needed precision are so long that both seeing and the intrinsic evolution of the solar photosphere present the extremely difficult task of eliminating the influence of strong-field regions. A much more reasonable approach to this observational problem is to use the very high Zeeman sensitivity of lines in the thermal infrared. The polarization in these lines remains large even for magnetic field strengths less than 100 G, and it should be possible to identify weak field regions coexisting in an observing element with the strong field signature of flux tubes.

#### I. INTRODUCTION

Recently there has been some discussion concerning ground-based measurement of visible wavelengths with high polarimetric precision. Two of the most important reasons cited for attempting high-precision measurements of the visible solar spectrum are to measure weak fields in the photosphere and to measure chromospheric fields. Other applications of high-precision plarimetry include depolarization due to the Hanle effect, specifically in prominences (Leroy et al. 1983), and resonance polarization near the limb of the Sun. these latter two effects are interesting applications of precision polarimetry, but they will not be considered further here.

The question is still open whether a weak component of the solar magnetic field coexists in the photosphere along with the dominant component, i.e., strong fields which are highly localized in sunspots and flux tubes. If indeed a diffuse, weak magnetic field is present in the photosphere, then its existence raises a very interesting scientific question: how does this field resist being swept to the loci of strong downflows in the intergranular lanes? Both numerical simulations (Nordlund 1986; Nordlund and Stein 1989, 1990) and theory (see Schüssler 1990 for review) suggest that a diffuse, weak magnetic field would rapidly be transformed into isolated flux tubes. Yet some observations (Zirin 1987) using longitudinal magnetographs suggest a weak field component does indeed exist with a strength of < 100 G. Spruit et al. (1987) argued the theoretical case for a weak, mixed polarity background field.

Magnetic fields with strengths of one to a few hundred G may exist in the upper photosphere above active regions. Evidence for these weaker fields comes from infrared measurements (Deming et al. 1988). Higher up in the chromosphere, the field is known to become very much more diffuse than in the photosphere. It forms the chromospheric canopy (Jones 1985), where kilogauss field strengths may be the exception (directly over sunspots) rather than the rule. The problem of measurement of vector magnetic fields in the chromosphere is then more difficult than in the photosphere both because of the much weaker field strengths and because of the paucity of chromospheric lines with appropriate Zeeman splitting (Lites et al. 1988). At present, it appears

<sup>\*</sup>The National Center for Atmospheric Research is sponsored by the National Science Foundation.

174 B. W. Lites

that only those chromospheric lines between 390 - 1100 nm are viable candidates for measurement of chromospheric vector magnetic fields.

These are two of the most important reasons to attempt high precision measurements of the visible solar spectrum. Other applications of high precision polarimetry include depolarization due to the Hanle effect, specifically in prominences (Leroy et al. 1983), and resonance polarization near the limb of the Sun. These are interesting applications of precision polarimetry, but they will not be considered further here.

In the case of measurement of chromospheric fields one expects the field strength to vary with position on the disk much more slowly than in the photosphere due to the expansion of the field resulting from the large drop in gas pressure with height. Extreme angular resolution may not be needed for these measurements: with moderate resolution (0.3", for example), the filling factor for the field may be very large; that is, at most locations in the chromosphere the scale of horizontal variation of the field may be large compared with this dimension. In view of all of the interesting physics connected with the measurement of vector magnetic fields in the chromosphere (c.f. Lites et al. 1988), it is entirely appropriate to consider ground-based measurements of the chromospheric vector field using lines in the visible spectrum. The challenges provided by the low intrinsic polarization signals of the chromospheric magnetic fields may be met by new facilities such as THEMIS and LEST.

The case for measurement of weak magnetic fields in the photosphere using the visible spectrum is much more clouded. In Section II I will first give some justification for moderate polarization accuracy when measuring strong fields in the photosphere. Section III outlines the polarization and angular resolution requirements for measurement of weak fields using lines in the visible. I summarize the difficulties of achieving the signal-to-noise ratio necessary to measure such weak fields in Section IV. Another problem associated with measurement of weak fields, the photon flux requirement, is summarized in Section V. In Section VI I suggest a possibility for a new type of detector which would eliminate all of the the polarization crosstalk due to seeing, maintain a highly efficient use of the available photons, and greatly reduce the problems associated with the variation of detector sensitivity from pixel to pixel. The possibility of measurement of weak fields using Zeeman-sensitive lines in the thermal infrared is discussed in Section VII.

# II. IS HIGH POLARIMETRIC ACCURACY NEEDED FOR QUANTITATIVE MEASUREMENT OF STRONG PHOTOSPHERIC MAGNETIC FIELDS?

At photospheric heights it is believed that most of the solar flux resides either in sunspots, pores, or in small flux tubes with field strengths of the order of 1000 G or greater (Stenflo 1973). The diagnostics developed for simultaneous measurements of several spectral lines in the visible suggest that, outside of sunspots, roughly 90% of the flux resides in these strong-field concentrations (Howard and Stenflo 1972). Measurements by Rabin (in these proceedings) using lines at 1.5 microns confirm that the fields are strong in plages. Interpretation of polarization measurements of photospheric lines must be constrained by this reality: the fine structure of the field away from sunspots demands very high angular resolution, but at visible wavelengths the intrinsic (i.e., resolved) line polarization will be large.

Polarimeters designed for modest sensitivity to polarization ( $10^{-3}$  relative to the continuum intensity  $I_c$ ), but with nearly complete resolution of both the line profile and the small scale features, will provide a level of polarization accuracy that is adequate to reveal the polarization signatures of the magnetic fields in Zeeman-sensitive lines of the visible spectrum. This polarization accuracy would cause only a few percent distortion of typical strong-field Stokes profiles

(Figure 1). Departures of the real solar atmosphere from the idealized atmospheric models that form the basis for inversion of the profiles will generally produce distortions of the profiles of this order or larger. Distortions of this magnitude will not cause appreciable errors in the inferred magnetic field (Skumanich, et al. 1985).

Lower spectral resolution or spatial averaging of the magnetic features will hide essential physics of the line formation and magnetic fields. Nonetheless, much may be learned from polarization measurements of somewhat degraded angular resolution, provided full Stokes profiles of several spectral lines with similar formation properties but differing Zeeman sensitivities are obtained simultaneously. Suppose that one flux tube could be isolated within one 0.6" square pixel of a polarimeter. If the flux tube is of the order of 0.2" in diameter, one could accept a polarization accuracy of  $5 \times 10^{-4}$  for this pixel yet still obtain an accuracy of 10% in the Stokes Q profile averaged over the flux tube. Such accuracy may be sufficient to determine the mean orientation of the flux tube relative to the local solar normal with an accuracy of the order of 5-10 degrees.

Thus, polarimeters designed for good ( $\sim 10^{-3}$ ) but not extreme polarization accuracy and high angular resolution will be able to address a wide range of important scientific questions regarding magnetic fields in the photosphere including: the structure of sunspots; the emergence of flux and its subsequent dispersal, recombination, and submergence; and the buildup of magnetic shear induced by large scale motions in the photosphere and below.

# III. POLARIZATION AND ANGULAR RESOLUTION REQUIREMENTS FOR MEASUREMENT OF WEAK PHOTOSPHERIC FIELDS

Figure 2 shows the simulated Stokes profiles for a magnetic field of strength 100 G. If the field is reduced to 10 G, the Stokes I,Q,V profiles have nearly identical shapes, but the Q profile is reduced by a factor of  $10^{-2}$  and the V profile is reduced by a factor of  $10^{-1}$  relative to the 100 G case, as expected from the weak-field limit (Stenflo 1985; Jefferies et al. 1989). The magneto-optical effects are nearly eliminated in the 10 G case, so that Stokes U is never greater than  $10^{-7}I_c$ . This figure demonstrates that it will be necessary to attain a polarization accuracy of  $10^{-4}I_c$  or better if one desires to measure the vector field with modest precision for field strengths of 100 G or smaller. This requirement is even more stringent if significant spectral degradation is imposed (i.e., filtergraph polarimetry with bandpass  $\gtrsim 0.01$  nm.)

A further requirement for weak field measurements is imposed by the confinement of much of the magnetic flux to small flux tubes: one must achieve very high angular resolution along with low scattered light in order to avoid contamination of the weak field regions by polarized radiation from the flux tubes. The nonlinear behavior of linear polarization with field strength guarantees that a small contamination of the weak field region by a neighboring flux tube would lead to a completely erroneous measured polarization signal. Rabin et al. (1990) have measured the average magnetic flux density outside active regions to be  $1.8 \times 10^{23}$  and  $6.1 \times 10^{23}$  Mx for, respectively, solar minimum and solar maximum. The mean field strength implied by these fluxes is 3.1 and 6.1 G, respectively. If much of this flux is confined to flux tubes of strength about 1000 G, then the mean separation between such flux tubes is 3.7 and 2.6", respectively. These estimates are upper limits for the mean separation, as the flux measurements of Rabin et al. (1990) do not fully resolve all of the structure in the magnetic field so that some cancellation of polarization must occur. Very high angular resolution is thus imperative to isolate weak field regions in between such a distribution of flux tubes.

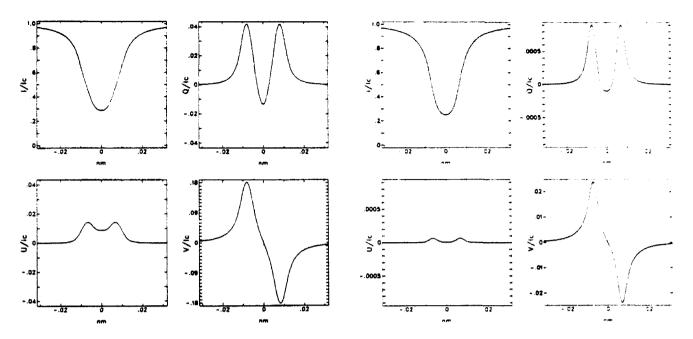


Fig. 1. Synthetic Stokes Profiles of Fe I 525.02 nm are shown as computed from a Milne-Eddington model atmosphere with the following parameters:  $|\mathbf{B}| = 1000$  G,  $\gamma = 45^{\circ}$ ,  $\chi = 0^{\circ}$ ,  $\Delta\lambda_D = 3.5$  pm, a (damping) = 1 pm,  $\eta_0 = 20$ ,  $\mu b_1 = 0.8$ ,  $b_0 = 0.2$ .

Fig. 2. Profiles computed the same as those in Figure 1, except with  $|\mathbf{B}| = 100 \text{ G}$ .

Such measurements must also be carried out in a way that places the weak field regions in the context of the surrounding magnetic structure of the atmosphere, in order to avoid contamination by magnetic signal from the strong field flux tubes. This requirement demands the use of two-dimensional detectors.

# IV. HOW COULD A POLARIZATION ACCURACY OF 10<sup>-4</sup> BE ACHIEVED?

If two-dimensional detectors are a practical requirement for measurement of weak magnetic fields, then one must ask how a polarization accuracy of  $10^{-4}$  may be achieved with such detectors. The signal-to-noise ratio (S/N) attained by the measurement must be compatible with the polarization accuracy, and it sets the minimum number of photoelectrons that must be sampled to reach a polarization accuracy of  $10^{-4}$ . This constraint sets a fundamental limitation upon the integration time for weak-field measurements which is independent of the size of the telescope or the efficiency of the optical system.

If the efficiency of the device which modulates the polarization were 100%, then one would need a minimum of  $10^8$  sampled photoelectrons to attain a S/N of  $10^4$ . Most modulation schemes are not this efficient. Typically, the efficiency is about 50%. In this case  $4 \times 10^8$  photoelectrons must be measured. The well size of the array detectors being used determine the number of expose/read cycles that must be carried out in order to build up the desired S/N. In practice, it is undesirable to approach the nominal full-well state of a CCD detector, due to nonlinearity near saturation. Using half-full-well accumulation as a guideline, one may place the typical number of photoelectrons in the continuum per expose/read cycle at  $5 \times 10^4$  (for the ASP cameras which operate at 60 Hz readout) to  $2 \times 10^5$  (for CCD cameras with pixels roughly  $20 \mu$  on a side). Thus, one will need between 2,000 and 10,000 expose/read cycles to attain a S/N of  $10^4$  in the Stokes parameters.

A medium-sized format CCD (400 pixels on a side) may be read at about 60Hz at room temperature without having the read noise dominate the photon sampling noise, provided the number of photoelectrons is a reasonably large fraction of the full well. At this read rate, between 30 and 170 seconds are necessary to accumulate enough photoelectrons for a S/N of 10<sup>4</sup>, even if the read noise is negligible. This sample time is unacceptable for two reasons: 1) seeing fluctuations during such long periods virtually guarantee an unacceptable degradation of the image quality, and 2) even if the seeing were perfect, the small-scale structure of the solar scene will evolve radically during this period.

# V. IS THERE ENOUGH LIGHT?

Even if one could somehow overcome the difficulties outlined in Section IV, one is still faced with limitations imposed by photon flux. The demands for high precision in Stokes polarimetry lead to the high photon flux requirement shown above. This difficulty is compounded by the reduced efficiency of the total optical system due to the polarizing optics and the dispersing elements (a spectrograph or a filter). The needs for high angular resolution and low intrinsic polarization of ground-based telescopes increases the complexity of optical systems – LEST being a good example. The result is that the net efficiency of the optical system for Stokes polarimetry is only a few percent.

If one takes the HAO/NSO Advanced Stokes Polarimeter as a typical example (Lites et al., in these proceedings), one finds that, with 0.4" pixels and 3 pm wavelength resolution, the ASP attains 1/4 to 1/2 the full-well limit in the 1/60 sec exposure time using the 76 cm Tower Telescope as a light feed. A pixel size of 0.1" is more appropriate for the needed angular resolution. For this pixel size the amount of light falling upon the detectors is reduced by a factor of 0.06. A factor of 10 enhancement of flux from a larger telescope such as the LEST could make up for much of this deficit, and more efficient dispersing elements (such as a Fabry-Perot interferometer) might replace the rest of the flux.

There are several other gains that are possible when one is searching for weak fields. The weak field approximation (WFA: Jefferies et al. 1989) for the line formation shows that the shapes of the Stokes profiles are set by the shapes of the Stokes I profile for weak fields. Two advantages are then possible: 1) a simplified analysis for the extraction of magnetic fields is appropriate, and 2) the full spectral resolution is not needed as the shapes of the Stokes Q, U, V profiles do not enter into the analysis\*. Filter measurements with roughly 10 pm bandpass should be adequate for this task. This gain in photon flux from the wider bandpass will allow one to fill the wells of CCDs with larger pixels, thereby considerably reducing the number of expose/read cycles. With LEST, the 30-second integration time could be possible for this kind of measurement.

Thus, even with the largest telescopes that will become available during the coming decade, the light flux will not be sufficient to achieve the 10<sup>4</sup> S/N with reasonably short exposure times.

# VI. AN EFFICIENT DETECTION SCHEME FOR STOKES POLARIMETRY

The Stokes V signature decreases linearly with field strength, whereas Stokes Q and U decreases quadratically. Figures 1 and 2 show that such measurements must not only achieve the appropriate S/N, but crosstalk, particularly between Stokes I and V to Q and U, must also be minimized. Therefore, very rapid modulation/demodulation of the polarization signal will be essential to reduce the seeing-induced crosstalk for weak field regions (Lites 1987). In the fu-

<sup>\*</sup>Note that the WFA also indicates that the only utility of a multi-line analysis would be to determine if any strong-field signal is scattered into the resolution element.

178 B. W. Lites

ture, modulation schemes such as the one described by Povel (in these proceedings) in which the modulation is carried out much faster than typical seeing fluctuations, must be used.

The particular device suggested by Povel, and as applied to simultaneous measurement of all Stokes parameters (Stenflo and Povel 1985), accomplishes very well the elimination of seeing-induced crosstalk but it is inefficient in its use of the available photons. More than half of the image plane at the detector is masked from the incoming light. In addition, the Q, U, and V signals are modulated at different frequencies/phases, so three separate beams with three separate detectors would be needed to make simultaneous measurements. Thus, the system is about a factor of 6 less efficient than theoretically possible, and it uses only one of the possible two linearly polarized states available. Therefore, a gain of a factor of 12 in efficiency is possible. If light flux is the limiting factor (as is usually the case in Stokes polarimetry), then it is theoretically possible to have a more efficient system on a telescope the size of the NSO/Sunspot Vacuum Tower Telescope than would be the Povel/Stenflo system on LEST.

How could such an efficient demodulation system be constructed? An elegant scheme would be one in which a CCD-like device that would have several identical planes stacked vertically one upon another (Figure 3). The subsurface planes would be blind to the incoming radiation, and thus could be used for on-chip charge storage. For such a device to work, it must cycle the charge gathered on the surface plane of the CCD downward through the lower planes, then from the lowest plane back up to the surface, in a rapid sequence. With such a device it would be possible to demodulate the Q, U, and V signals simultaneously with no loss of efficiency either at the surface of the detector or through beamsplitting.

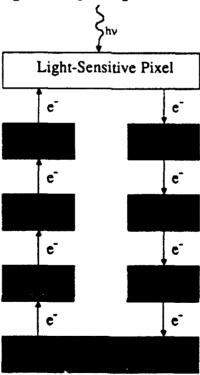


Fig. 3. Shown is one possible arrangement for an on-chip demodulation device, conceptualized by G. Murphy. Light is detected by the top element as in an ordinary CCD. The photoelectrons are then circulated below the active surface of the chip in the direction of the arrows. The eight charge wells would allow rapid demodulation of the full Stokes polarization signal.

# VII. THE THERMAL INFRARED

The problems associated with measurement of weak vector fields using lines in the visible spectrum seem insurmountable with present or foreseeable instrumentation. Even if one were to operate a polarimeter in space, the angular resolution/scattering problem would be formidable, and the evolution of the solar scene would have to be resolved.

Elsewhere in these proceedings Deming has summarized the advantages of the high "magnetic sensitivity" of lines in the thermal infrared. Most of the problems associated with the measurement of weak magnetic fields using visible lines vanish at these wavelengths. Even if the telescope does not resolve individual flux tubes, the polarization signature of the weak fields may be distinguished from those of strong fields in the unresolved profiles themselves. The profile splitting is considerable at  $12\mu$  even for 100 G fields. Thus, the linear and circular polarization signatures remain roughly the same strength, and comparable to the Stokes I signature, for weak fields. The direct measurement of the wavelength splitting of the Zeeman components will indicate the field strength for fields down to about 100 G. For weaker fields one would assume a large filling factor and determine the vector field using the WFA.

It should be noted that the problem of detection of weak fields using lines in the visible is greatly eased if one is satisfied with measurements of the longitudinal field component only. The linear dependence of Stokes V upon field strength allows one to relax considerably the requirements on polarization accuracy for weak field measurement. However, the stringent angular resolution requirements are still needed to isolate flux tubes, and the uncertainty associated with resolution/scattered light problem will always cast those inferences of weak fields in doubt.

# **ACKNOWLEDGMENTS**

I wish to thank R. Dunn, D. Elmore, S. Martin, G. Murphy, and D. Rabin for helpful discussions.

## REFERENCES

Deming, D., Boyle, R. J., Jennings, D. E., and Wiedemann, G. 1988, Ap. J., 333, 978.

Howard, R., and Stenflo, J. O. 1972, Solar Phys., 22, 402.

Jefferies, J., Lites, B. W., and Skumanich, A. 1989, Ap. J., 343, 920.

Jones, H. P. 1985, in *Chromospheric Diagnostics and Modelling*, (B. Lites, ed.), National Solar Observatory, Sunspot, N.Mex., p. 175.

Leroy, J. L., Bommier, V., and Sahal-Bréchot, S. 1983, Solar Phys., 83, 135.

Lites, B. W. 1987, Applied Optics, 26, 3838.

Lites, B. W., Skumanich, A., Rees, D. E., and Murphy, G. A. 1988, Ap. J., 330, 493.

Nordlund, A. 1986, in Small Scale Magnetic Flux Concentrations in the Solar Photosphere, (W. Deinzer, M. Knölker, and H. H. Voigt, eds.). Abh. Akad. D. Wiss. Göttingen No. 38, Vandenhoeck & Ruprecht, Göttingen, p. 83.

Nordlund, A., and Stein, R. F. 1989, in *Solar and Stellar Granulation*, (R. J. Rutten and G. Severino, eds.), NATO ASI Series C, Vol. 263, Kluwer, Dordrecht, p. 453.

Nordlund, A., and Stein, R. F. 1990, in Solar Photosphere: Structure, Convection and Magnetic Fields, (J. O. Stenflo, ed.), Proceedings, 138th Symposium of the IAU, Kluwer, Dordrecht, p. 191.

Rabin, D, DeVore, C. R., Harvey, K. L., and Hoeksema, J. T. 1990, in *The Solar Interior and Atmosphere*, (A. N. Cox, W. C. Livingston, and M. S. Matthews, eds.), in press. Schüssler, M. 1990, in *Solar Photosphere: Structure, Convection and Magnetic Fields*, (J. O. Stenflo, ed.), Proceedings, 138th Symposium of the IAU, Kluwer, Dordrecht, p. 161.

- Skumanich, A., Rees, D. E., and Lites, B. W. 1985, in Measurements of Solar Vector Magnetic Fields, (M. J. Hagyard, ed.) NASA Conference Publication 2374, p. 306.
- Spruit, H. C., Title, A. M., and van Ballegooijen, A. A. 1987, Solar Phys., 110, 115.
- Stenflo, J. O. 1973, Solar Phys., 32, 41.
- Stenflo, J.). 1985, in Measurements of Solar Vector Magnetic Fields, (M. J. Hagyard, ed.) NASA Conference Publication 2374, p. 263.
- Stenflo, J. O., and Povel, H. 1985, Applied Optics, 24, 3893.
- Zirin, H. 1987, Solar Phys., 10, 101.

### Discussion

- S. Koutchmy: I am not quite as pessimistic as you are concerning the threshold of detection for the "weak" fields. From our experience we find out that a  $10^{-3}$  precision seems already reached on a single video-magnetograph when automatic subtraction of the darkest level is done properly; then 400 magnetograms (100 sec integration time) for example can be "add and or" processed, improving the precision by a factor 20 at least, which means a precision of  $5 \cdot 10^{-5}$ . However, we are indeed very limited when doing integration by intrinsic changes (amplitude variations; proper motion) of the faint magnetic element; with the current resolution we have now at the VTT/SP we saw definite changes in a small flux point  $(4 \cdot 10^{16} \text{ Mx})$  in less than 50 sec.
- **B.** Lites: I seriously doubt that you achieve a signal to noise of  $10^{-3}$  from single frames of a video camera, for reasons discussed in this paper. If you add N frames to make a "single video-magnetogram", then you must demonstrate that the individual frames have a noise level of  $\sqrt{N} \cdot 10^{-3}$ .
- C. Keller: The polarimeter described by Povel in this meeting reaches an accuracy of about  $2 \cdot 10^{-3}$  in a single exposure. By improving the electronics it seems to be feasible to read  $1 \cdot 10^{-3}$ , without having a full well depth of  $10^6$  electrons. A video-magnetograph as mentioned by Koutchmy will never obtain such a low noise level in a single exposure.
- **B.** Lites: I do not understand how one can exceed the statistical limitations of signal to noise imposed by the number of photons actually sampled (and as represented by the number of photoelectrons). Thus, I do not believe that a signal to noise of 10<sup>3</sup> is possible with fewer than 10<sup>6</sup> photoelectrons.
- J. Harvey: One of the difficulties you pointed out is the limited ability to make a high S/N measurement quickly. One way this could be improved, given a large telescope, is to beam split excess light onto many CCD's simultaneously. One might also use many spectrum lines simultaneously to improve S/N.
- G. Chapman: A serious limitation to doing all magnetic studies using the  $12\mu$  lines is that they are formed in the low chromosphere and thus it would not be possible to study the magnetic fields in the photosphere.
- B. Lites: It is not clear that they are formed in the low chromosphere, or even at the temperature minimum. They are certainly formed above the deep photosphere, however. Several groups including Rutten and Carlsson in Utrecht are studying this problem. There are likely to be other lines in the thermal infrared which are in absorption.
- J. Stenflo: I think your theoretical estimates of measurement errors based in Poisson statistics are not correct, since they disagree in the experimental results. We obtain a polarization accuracy of close to  $10^{-3}$  in a single CCD frame, although our CCD does not have a deep well structure. When determining the relative error as  $1/\sqrt{N}$ , it appears that N should be represented by the number of incoming photons rather than the number of accumulated electrons in the detector.
- B. Lites: The number of detected photons set the statistical properties of the measured signal. The number of photoelectrons in the CCD well represents the number of detected photons. Otherwise, you would be creating measured information from photons which do not interact with the experiment, a situation that seemingly defies fundamental laws of physics. I suggest that there must be something wrong with the noise measurement in your CCD images.

- A. Gary: MSFC have a detail analysis of a space-borne magnetograph (SAMEX) based on a 0.25 arc sec pixel which shows possibility at 10<sup>-4</sup> polarization measurements with a filter magnetograph. Is this spatial resolution enough or what would you suggest, knowing that data rates must be considered?
- **B.** Lites: A resolution of 0.25" should be sufficient for weak field measurement, provided it is a true 0.25". Even a small amount of scattering could allow contamination by nearby kilogauss field regions. The measurements must be taken during a time interval short compared to the migration time of flux tubes.
- S. Solanki: Even if it may appear almost hopeless to find very weak fields in the visible or near IR, we will still have to try, since we cannot resolve weak fields with polarities mixed over short distances with the  $12\mu$  lines without building HUGE telescopes.
- B. Lites: However, huge telescopes are considerably easier to make for IR wavelengths.
- **D. Rabin:** The near infrared may be the ideal place to search for weak fields. To take the example of Fel 6389 cm<sup>-1</sup>, g = 3.0, application of radiative transfer models to its Stokes profiles should allow fields as small as 200 gauss to be extracted with confidence. Additionally, the flux per Doppler width is comparable to visible-wavelength lines, and high angular resolution can be obtained with meter-class telescopes.
- Ai G.: Which is main source of the noise, a count of the electrons or the seeing?
- B. Lites: Seeing is the fundamental limitation in present measurements. If the images can be improved, then I suspect that we will feel the limitations of light flux and the detector more strongly.
- L. November: I think that qualitatively the Stokes maps derived in active regions look rather good with single CCD images (i.e. Topka). Clearly, if the polarized signal is .06 and the signal/noise in a CCD readout 600 then the polarized signal to noise is 10. Maybe this is not too bad as a practical possibility. Of course Q,  $U \propto B^2$  and  $V \propto B$  so a limitation in S/N must occur with reduced field strength.

# Using KD\*P Modulators to Measure the Stokes Vector on the Sun

### E. A. West

NASA/Marshall Space Flight Center

## ABSTRACT

Longitudinal KD\*P modulators are used in ground-based solar magnetographs to eliminate seeing effects. Although these modulators can be used as variable retarders, their optical properties when zero voltage is applied will influence their performance in instruments requiring very accurate polarization measurements. This paper will discuss measurements that are being made at the Marshall Space Flight Center (MSFC) on the optical properties of different KD\*P modulators when zero voltage is applied and how these properties affect their performance in the Marshall vector magnetograph. The temperature dependence, field of view errors, polarization fringing and the dc bias problems will also be discussed.

## I. INTRODUCTION

Longitudinal KD\*P modulators have always been a part of the polarimeter of the MSFC vector magnetograph (West, 1985). Although these devices allow the magnetograph to rapidly modulate between polarization states to minimize seeing effects, understanding the systematic errors associated with these devices, and how to minimize those errors, is essential for an instrument that is trying to make very accurate polarization measurements ( $< 10^{-3}$ ). Some of the systematic errors have been described in other articles, and a more detailed discussion of those errors can be found in the referenced articles. When reading this paper (and many of the referenced articles), the reader must keep in mind that, in vector magnetic field measurements, the circular [V] and linear [Q, U] polarizations are not created equal. Linear polarization created by active regions near the center of the solar disk is inherently weak when compared to the circular polarization signal, and the transverse field,  $B_T$ , is related to the square root of the total linear polarization signal  $(B_T \approx \sqrt{P_L})$  while the longitudinal field,  $B_L$ , is directly related to the circular polarization signal  $(B_L \approx P_V)$ . Therefore, to improve the resolution of the vector magnetic field measurements, the accuracy of the linear polarization measurement is usually emphasized.

## II. SYSTEMATIC ERRORS

The systematic errors that the instrumentalist must be aware of when using longitudinal KD\*P modulators are: (1) the temperature characteristics, (2) the optical properties, and (3) the electrical characteristics.

# A) Temperature Characteristics

The following equation gives the relationship between the halfwave voltage  $(V_1)$  of a KD\*P modulator and its temperature  $(T_1)$ :

$$V_1 = V_{RT}(\frac{T_1 - T_c}{T_{RT} - T_c})$$

where  $V_1$  is the halfwave voltage at temperature  $T_1$ ,  $V_{RT}$  is the halfwave voltage at room temperature,  $T_c$  is the Curie temperature (222 °K),  $T_{RT}$  is room temperature (298 °K), and  $T_1$  is the temperature of KD\*P.

The room temperature halfwave voltage is usually dependent on the deuteration level of the KD\*P crystal; the higher the deuteration level the lower the halfwave voltage. Figure 1 shows the temperature dependence of two KD\*P modulators that have been used in the MSFC vector magnetograph. To minimize any systematic errors due to temperature drifts, the MSFC KD\*P modulator has a temperature controller whose temperature is set to 10 °F above the expected maximum ambient temperature. Since there was limited space in the MSFC polarimeter section of the optics box, the controller had to be set up in this way to minimize distortion from thermal convection. The temperature is then monitored by the data acquisition computer and will warn the observer when the KD\*P temperature is out of range. Large thermal transients must also be controlled or the modulator may be damaged since the windows and KD\*Ps expand (or contract) at different rates.

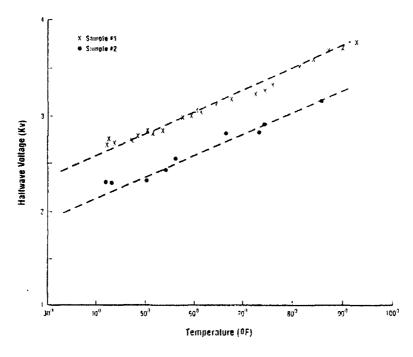


FIG. 1. Temperature characteristics of KD\*P modulators

# B) Optical Properties

Figure 2 shows the optical (and electrical) elements that make up a longitudinal KD\*P modulator. Transparent, indium tin oxide (ITO) electrodes are placed on both sides of a KD\*P crystal with a gold electrode at the outer edge of the aperture. The aperture size is  $\geq 25$  mm and the thickness of the KD\*P crystal is approximately 3 mm.

The optical errors that must be minimized when using longitudinal KD\*Ps in vector magnetic field measurements are: (1) stress induced birefringence, (2) field of view errors and (3) polarization fringing.

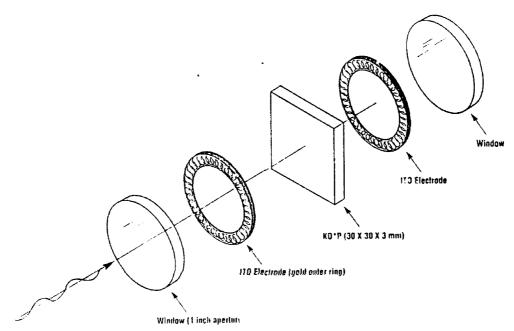


FIG. 2. Schematic of longitudinal KD\*P modulator

# i) Stress-Induced Birefringence

A recent study (West and Bhatia, 1990) at MSFC implied that the bi-axial properties that have been seen in some of the longitudinal KD\*P modulators used in the MSFC vector magnetograph were stress induced. Table 1 is for the unmounted KD\*P samples while Table 2 is the KD\*P modulators obtained commercially. The data suggest that KD\*P crystals can be grown with zero birefringence along the "optic" axis ( $\Delta n_z$  should be zero for a uniaxial crystal) and that the biaxial properties that have been observed are stress induced. This stress-induced property is usually minimum at the center of the modulator and maximum at the outer edge. Depending on the stress pattern, the result can be an integrated, non-zero retardance over the aperture when zero voltage is applied. In the past a bias voltage had been applied to the KD\*P modulators to obtain a "zero" retardation (see electrical characteristics section).

Table 1. Unmounted KD\*P crystals: cross separation and distance to the first circular intensity minimum. The thickness and the z direction birefringence  $(\Delta n_z)$  were determined assuming a distance of 91 cm between the focal point in the KD\*P sample and the detector

KD*P Sample no.	Cross separation (mm)	Estimated $\Delta n_z$	Distance to first minimum (cm)	Estimated thickness (mm)	Measured thickness (mm)
0-3	0	0.0	8.4	4.14	4.17
0-7	3	5.25E-7	9.4	3.30	3.10
0-8	2	3.50E-7	8.5	4.04	4.10
0-9	0	0.0	8.4	4.14	4.10
0-11	0	0.0	8.4	4.14	4.10
5-2	0	0.0	8.5	4.04	4.10
5-4		0.0	9.7	3.10	3.40
9-2	0 2 3	0.0	8.4	4.14	3.95
9-3		3.50E-7	8.4	4.14	3.91
9-4		5.25E-7	9.6	3.16	3.10

Table 2. Mounted KD\*P modulators: cross separation distance and distance to the first circular minimum. The thickness and the z direction birefringence  $(\Delta n_z)$  were determined assuming a distance of 91 cm between the focal point in the KD\*P sample and the detector.

KD*P Sample no.	Cross separation (mm)	Estimated $\Delta n_z$	Diameter of first fringe (cm)	Estimated thickness (mm)
H87131	20	3.70E-6	10.0	2.91
M-6	6	1.05E-6	10.0	2.91
1919 <b>B</b>	2	3.50E-7	10.2	2.80
103	4	7.00E-7	10.1	2.85
21684	3	5.25E-7	9.6	3.17
M-7	2	3.50E-7	9.6	3.17

# ii) Field of View Errors

The field of view errors associated with KD\*P crystals (which is a negative uniaxial crystal with zero applied voltage) are well known and are natural properties on any birefringent crystal. Two techniques have been developed to minimize the field of view errors in longitudinal KD\*Ps: adding a positive uniaxial crystal (West, 1978) and a crossed KD\*P design with halfwave plates between the KD\*Ps (Guo-xiang and Yue-feng, 1981). A recent paper has discussed the possibility of extending the the field of view even further by combining the two techniques (West, 1990).

# iii) Polarization Fringing

At different times the MSFC vector magnetograph has had fringing in its polarization data. The fringing pattern is usually the same in the three polarization measurements  $\left[\frac{Q}{I}, \frac{U}{I}, \frac{V}{I}\right]$  (Figure 3) although the peak to peak magnitude may vary. This polarization pattern is similar to the ring pattern produced by a uniaxial crystal when mounted between two circular polarizers. The diameter of the rings in this polarization pattern changes with the wavelength position of the Zeiss birefringent filter. Since this is an instrumental error, it can be removed with the proper calibration (Figure 4).



FIG. 3. Fringe pattern seen in polarization maps created by the MSFC vector magnetograph. The image on the left is the  $\frac{V}{I}$  map, on the right the  $\frac{Q}{I}$ . The peak to peak polarization signal for the fringe pattern is  $\pm 0.001$ .

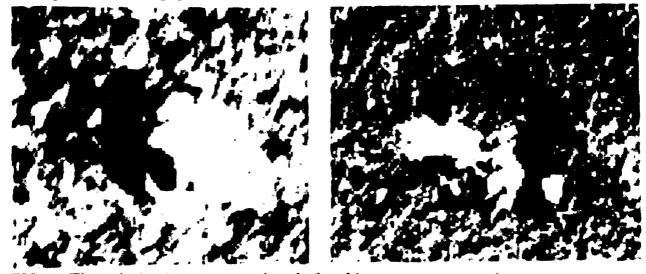


FIG. 4. The polarization maps produced after fringe pattern correction.

Understanding how this fringing pattern is produced is more difficult. Since this filter acts as the analyzer for the magnetograph, it is assumed that reflected light from the Zeiss filter is partially polarized with its major axis at 90° to the transmission axis of the filter. Since the fast axis of the KD\*P is at 45° to the transmission axis of the filter, the reflected light from the Zeiss filter will travel through the KD\*P and will receive a quarterwave retardance. Light that is reflected at the front surface of the KD\*P back toward the Zeiss filter will undergo another quarterwave retardance but the apparent fast axis seen by this polarized light will be rotated 90°. Therefore in the ideal world, the light will return to its original state and the polarization pattern would not exist. But a uniaxial crystal that is mounted between crossed circular polarizers and whose optic axis is parallel to the incident light will create circular polarization patterns. Since the reflections between the KD\*P and the Zeiss filter would create a crossed circular polarizer system, the source of the fringe pattern is the unknown. The following are three possibilities that are being studied: (1) large field of view errors for reflected light that passes through the crystal more than once. (2) changes in the KD\*P thickness with applied voltage, or (3) stress-induced birefringence creating ± quarterwave fast axes that are not 90° apart. Although the author is leaning toward the field of view errors, experiments are being developed that should clarify solve this problem.

# C) Electrical Characteristics

Modulation characteristics that have repeatable, time-varying changes are considered systematic errors and will be discussed here. In order to synchronize the polarimeter with the CCD camera (in 1980, a SEC vidicon), a dc modulation scheme is applied to the KD\*P modulator. Typical exposure times are 70 ms and the transition from one polarization state to the next is approximately 2 ms.

There are three problems that have been identified when applying dc voltages to the KD\*P modulators. The first problem is related to the retardation changes at the beginning of the modulation sequence and the next two problems are related to modulator failures created by dc bias voltages.

Initially there is some delay in the response of the modulator to the applied voltage (Figure 5). Although this stabilization time ( $\Delta t_I$ ) does vary among the KD\*P modulators (and is probably related to the RC time constant of the KD\*P crystal), the response normally stabilizes after the first four cycles and the data acquisition system starts acquiring data at this point.

One of the main problems associated with the original MSFC polarimeter (Figure 6) was the zero to halfwave modulation sequence (2A/2B). Although the dc voltage problems did not show up in the modulators used in the early magnetograph, electrode discoloration and disintegration were problems. If the zero/halfwave modulation failure existed in the early magnetograph (before 1980), recognition of the problem did not occur until a new vendor was selected to supply our KD\*Ps in 1980. Although the modulators that were obtained showed a significant improvement in the electrode quality and lifetime, the zero/halfwave (2A2B sequence in Figure 6) modulation became a major problem.

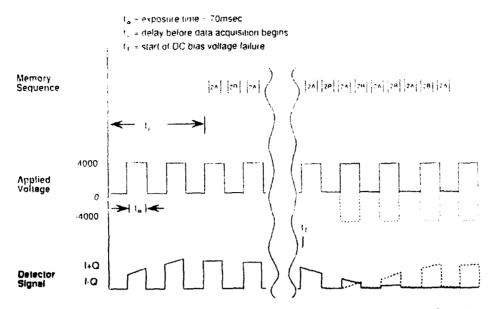
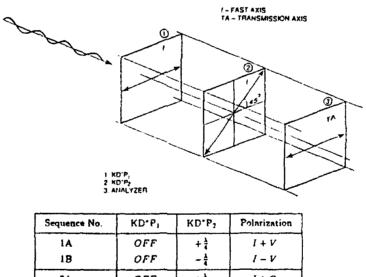


Figure 5. Modulation characteristics of a longitudinal KD\*P when a dc voltage is applied. In the initial cycles the modulator response varies with time. Many of the KD\*Ps used at MSFC would fail if the applied voltage was not symmetric (ex. 2A2B sequence (Figure 6) which would modulated the KD\*P between 0 and 4000 volts).

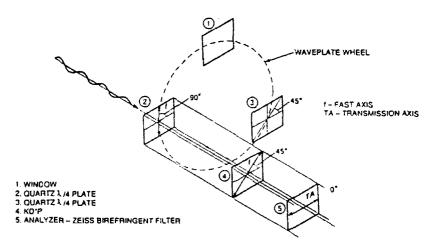


Sequence No.	KD-P,	KD-P2	Polarization
1A	OFF	+ 1/4	I + V
18	OFF	- <del>1</del>	1 – V
2A	OFF	+ 1/2	I+Q
28	OFF	OFF	I-Q
3A	+ 1/4	+ 1	I + U
38	+ 1/4	- <del>\frac{\lambda}{\tau}</del>	1 - U

Figure 6. Polarimeter used in the original MSFC vector magnetograph (1975-1982) consisted of two KD\*Ps whose fast axes were 45° apart.

Figure 5 shows the electrical response of a KD\*P modulator when a zero/halfwave voltage is applied. Although the time that it took for the failure to become obvious  $(\Delta t_f)$  would vary, all of the new KD\*P modulators in 1980 failed the zero/halfwave modulation sequence (2A2B). When observing the modulator between crossed polarizers, the failure would usually start in the center of the modulator and spread to the outer edge. The interesting point about this failure was that a reverse modulation scheme (zero/minus halfwave voltage - dashed line in Figure 5) would cause the modulator to start working again. Therefore, in 1981 the MSFC polarimeter was redesigned (Figure 7) to eliminate any zero/halfwave or zero/quarterwave modulation schemes.

The MSFC vector magnetograph began observations using the new polarimeter (Figure 7) in 1984. At that time bias voltages were used to correct for small retardation errors in the polarimeter. The retardation errors are from two sources, the stress induced birefringence (which will vary with each KD\*P modulator) and the retardation errors in the quartz quarterwave plates used in the waveplate wheel to select the measured polarization (Figure 7). Even though the bias voltages have been small (200-300 volts), these dc biases can still create stability problems in some of our KD\*P modulators. Until the failure mechanism can be corrected, the dc biases have been eliminated and the instrumental errors are corrected in the data analysis software.



Sequence No.	Waveplate Position	KD.b	Polarization
1A	Window	+ 1/4	I+V
1B	Window	$-\frac{\lambda}{4}$	I-V
2A	½(FA@45°)	+ 1/4	I+Q
2B	$\frac{\lambda}{4}(FA@45^\circ)$	$-\frac{\lambda}{4}$	I-Q
3A	À(FA@90°)	+ 1/4	I+U
3B	$\frac{\lambda}{4}(FA@90^\circ)$	- ½	1 - U

FIG. 7. Polarimeter in existing MSFC vector magnetograph (1983-present) consisting of a single KD\*P and a rotating waveplate wheel.

### III. SUMMARY

Although longitudinal KD\*P modulators have many systematic errors that the instrumentalist must be aware of and must minimize, they have been used successfully in the MSFC vector magnetograph. Research into the systematic errors of other modulators, such as liquid crystal devices, is underway at MSFC to determine their modulation characteristics, no candidates have been found with improved modulation characteristics and a simple interface to imaging systems. Therefore, KD\*Ps will continue to be the active element used to minimize seeing effects in the MSFC polarimeter until the "perfect" modulator can be found.

# REFERENCES

Guo-xiang, A., Yue-feng, H.: 1981, "The KD\*P Modulator in the Solar Magnetic Field Telescope," *Tianti Wuli Xuebao*, 1, 273.

West, E. A.: 1978, "Extending the Field-of-View of KD\*P Electro-optic Modulators," Applied Optics, 17, 3010.

West, E. A.: 1985, "Analysis of the new polarimeter for the Marshall Space Flight Center vector magnetograph," in Measurements of Solar Vector Magnetic Fields, NASA Conf. Publ. 2374, 160.

West, E. A., and Bhatia, S. S.: 1990, "Optical Properties of KD\*P Modulators," Polarimetry: Radar, Infrared, Visible, Ultraviolet, and X - Ray, SPIE proceedings.in press.

West, E. A.: 1990, "Large field-of-view KD\*P Modulator," Polarimetry: Radar. Infrared, Visible, Ultraviolet, and X - Ray, SPIE proceedings, in press.

# Performance of the IAC Stokes I and V Analyzer

J. Sánchez Almeida; V. Martínez Pillet

Instituto de Astrofísica de Canarias, E-38200 La Laguna, Tenerife, Spain

Abstract: The chromatic behaviour of the IAC analyzer, commonly used at the German Vacuum Gregory-Coude Telescope at the Spanish Observatorio del Teide (Canary Islands), is investigated. It is shown that, through careful alignment of the optical components, a nearly perfect circular analysis can be obtained at wavelengths of 4000 Å and 6000 Å. For other visible regions the crosstalk between linear and circular polarization can be always made lower than 10 %.

# 1 Introduction

Laboratory measurements have been performed in order to test the instrumental polarization of the IAC Stokes I and V polarimeter. It mainly consists of an achromatic quarter-wave plate ahead of two crossed (turned by  $90^{\circ}$ ) linear polarizers. Complete descriptions of the device have been given elsewhere (Semel, 1980; del Toro Iniesta, 1987; Sánchez Almeida, 1988; del Toro Iniesta, Martínez Pillet, and Vázquez, 1990). The analizer produces two simultaneous images. Ideally, the intensities of these two images,  $I_1$  and  $I_2$ , should be related to the Stokes I and V parameters of the incoming light as:

$$I_1 \propto I + V,$$
 (1a)

$$I_2 \propto I - V.$$
 (1b)

To this end, the angle between one of the axes of the  $\lambda/4$  and one of the polarization directions of the linear analyzers must be 45° and the retardance of the  $\lambda/4$  exactly 90°. However, the lack of achromaticity of the quarter-wave plate and/or

misalignments between the latter and the polarizers will produce an output depending on the four Stokes parameters. Our aim is to measure the importance of these crosstalk terms and to show that, by selecting particular wavelengths regions, the ideal case represented by equations 1 can be achieved. It is shown that, in the visible region of the spectrum, the crosstalk between linear and circular polarization signals is always lower than 10 % assuming a perfect alignment between the  $\lambda/4$  and the linear polarizers.

# 2 Description of the measurements

In the coordinate system where the x-axis coincides with the fast axis of the  $\lambda/4$ , the two outputs of the analyzer will be:

$$I_1 = \frac{1}{2}(I - M_q Q - M_u U + M_v V), \qquad (2a)$$

$$I_2 = \frac{1}{2}(I + M_q Q + M_u U - M_v V), \qquad (2b)$$

where  $I = (I, Q, U, V)^{\dagger}$  is the input Stokes vector and:

$$M_q = -\sin(2\Delta\phi),\tag{3a}$$

$$M_{u} = -\sin(\Delta\delta)\cos(2\Delta\phi), \tag{3b}$$

$$M_{v} = \cos(\Delta \delta) \cos(2\Delta \phi).$$
 (3c)

In equations (3a-3c), the angle between the fast axis of the  $\lambda/4$  and the directions of transmission of the polarizers are  $45^{\circ} + \Delta \phi$  (I<sub>2</sub>) and  $135^{\circ} + \Delta \phi$  (I<sub>1</sub>). On the other hand, the retardance of the  $\lambda/4$  is  $90^{\circ} + \Delta \delta$ . Note that in an ideal case  $\Delta \delta = \Delta \phi = 0$ . In principle,  $\Delta \delta$  is a wavelength dependent quantity. Once  $\Delta \delta$  and  $\Delta \phi$  have been obtained, the weights of the different Stokes parameters (the M's) are given by equations (3a-3c).

The measurements were made by introducing linearly polarized light through the analyzer at an angle  $\theta$  relative to the x-axis (measured counterclockwise). Thus, the input Stokes vector is  $\mathbf{I}(\theta) \propto (1,\cos 2\theta,\sin 2\theta,0)^{\dagger}$ , which, once substituted in equations (2a-2b), makes the outputs,  $I_1$  and  $I_2$ ,  $\theta$ -dependent quantities. An example of the modulation of both intensities can be seen in Figure 1. The solid lines represent least square fits to functional forms like:

$$I_1 = a_1 - a_2 \sin 2\theta - a_3 \cos 2\theta, \tag{4a}$$

$$I_2 = b_1 + b_2 \sin 2\theta + b_3 \cos 2\theta. \tag{4b}$$

The a's and b's obtained from these fits are related to  $\Delta \delta$  and  $\Delta \phi$  through the equations:

$$\frac{a_2}{a_1} = \frac{b_2}{b_1} \simeq -\Delta \delta,\tag{5a}$$

$$\frac{a_3}{a_1} = \frac{b_3}{b_1} \simeq -2\Delta\phi. \tag{5b}$$

These relations are easily obtained from equations (2), (3), (4) and the input Stokes vector  $\mathbf{I}(\theta)$  given above. They are valid to first order in  $\Delta\delta$  and  $\Delta\phi$  (i.e.,  $\Delta\delta$ ,  $\Delta\phi\ll 1$  rad).

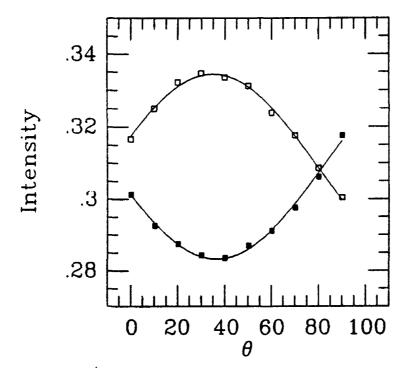


Fig. 1. The modulation of the two outputs,  $I_1$  (solid squares) and  $I_2$  (open squares), of the analyzer when linearly polarized light ( $\lambda = 5600 \text{ Å}$ ) is introduced. In the ideal case no modulation at all should be discerned. The least square fits (solid lines) provide the neccesary information to derive the crosstalk terms between Stokes V and Stokes Q and U.

The measurements described above were made at seven wavelengths. We select the spectral regions using interference filters with a typical band-pass of 100 Å.

For the 4000 Å region, where the amount of light of our unpolarized lamp falls abruptly, a colour filter was needed.

# 3 Discussion of the results

The results obtained from the measurements are presented in Figures 2 and 3. Figure 2 shows the variation of  $\Delta\delta$  with wavelength (the ideal case is  $\Delta\delta=0^{\circ}$ ). In the laboratory we did not make any distinction between the fast axis of the quarter-wave plate and the slow axis. This means that we can not determine the true sign of  $\Delta\delta$ . The negative sign assigned to the great majority of the measurements in Figure 2 has, then, no real significance. A remarkable fact about Figure 2 is the good agreement between the values obtained with both images  $I_1$  (black squares) and  $I_2$  (white squares). Figure 2 tells us that the best spectral regions to use our analyzer are around 4000 Å and 6000 Å.

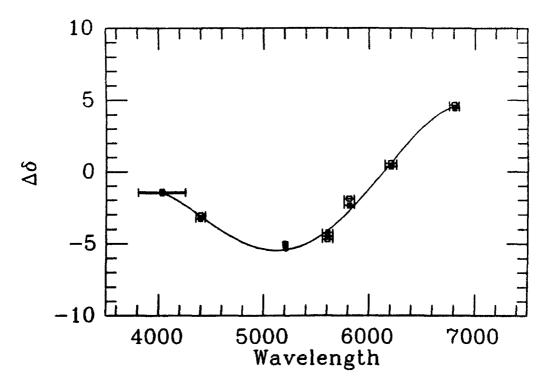


Fig. 2. The wavelength dependence of the deviations from a 90° degrees retardance of the quarter-wave plate. Solid squares are obtained from image  $I_1$ ; open squares from image  $I_2$ . The ideal case would be  $\Delta \delta = 0$ . The error-bars give the FWHM of the filters used to select the spectral region.

As a proof of the reliability of the measurements, we show in Figure 3 the excellent agreement obtained for  $\Delta\phi$  measured at different wavelengths in both images. The mean value obtained was  $3^{\circ} \pm 0.3^{\circ}$ .

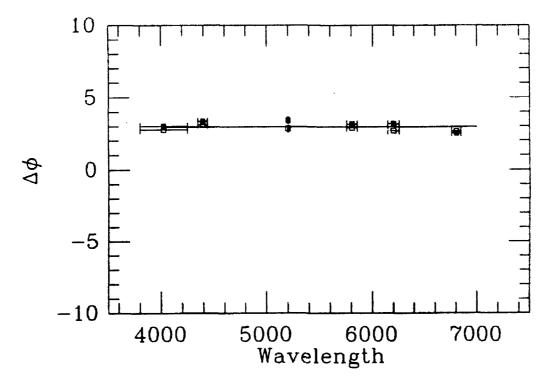


Fig. 3. Self-consistency of our measurements. A wavelength independent angle  $\Delta\phi$  of  $3^{\circ} \pm 0.3^{\circ}$  is found.

Probably the most interesting quantity for the potential user of the IAC polarimeter is given in Figure 4. The relative weight between the linear and circular polarization, i.e., the amount of crosstalk from Q and U to V, is shown as a function of wavelength. The solid line corresponds to perfect alignment between the optical components ( $\Delta \phi = 0^{\circ}$ ) and gives the minimum crosstalk possible. The ideal conditions ( $\Delta \delta = 0^{\circ}$ ) are then reached at 6100 Å and near the blue part of the 4000 Å region. On the other hand, at 5000 Å our analyzer introduces a 10 % crosstalk between the linear and circular polarization signals. The dotted and dashed lines correspond to  $\Delta \phi = 1^{\circ}$  and  $\Delta \phi = 2^{\circ}$  respectively. For these values the ratio between the weights of the linear and circular polarization becomes a less wavelength-dependent quantity, ranging from 5 to 10 %. In order to illustrate the effects produced by the crosstalk terms of our analizer, we show in Figure 5 a synthetic Stokes V profile as if it were observed with and without the crosstalk terms. We chose a line (FeI 5250Å) which lies in a spectral region where the quarter-wave plate behaves especially badly. The profile has been synthesized using a sunspot model atmosphere (Maltby et al., 1986, with a constant radial

magnetic field of 3000 G). The sunspot is assumed to be located at an heliocentric angle  $\sim 60^{\circ}$ . One can see that the effects are not too pronounced, except that one is interested in the symmetries of the profile.

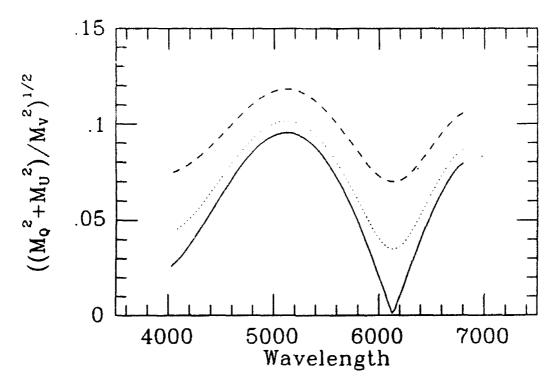


Fig. 4. The wavelength dependence of the crosstalk between linear and circular polarization. Solid line is for perfect alignment of the optics ( $\Delta \phi = 0$ ). Dotted and dashed lines are for  $\Delta \phi = 1^{\circ}, 2^{\circ}$  respectively. The ideal case of a perfect circular analyzer is reached for perfect alignment (solid line) at wavelengths of 4000 Å and 6100 Å.

It should be taken into account that the crosstalk originated in the telescope could increase these values to intolerable levels, preventing any attempt to measure circular polarization signals. On the other hand, the use of this analyzer at the German Gregory Coude Telescope located at Izaña (Canary Islands) during epochs of zero Sun declination, when no telescopic crosstalk is produced (Wiehr 1971, Sánchez Almeida, 1988), and in the wavelength regions we have already mentioned (where many interesting magnetic lines are present), the contamination of the circular polarization by linear polarization could be as low as 1-2% without needing any compensation to the system.

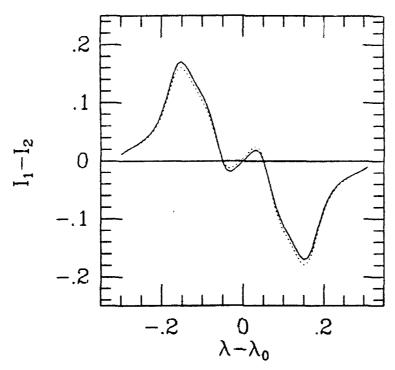


Fig. 5. Numerical simulation of the instrumental polarization produced by the analizer. Using a Stokes V profile of FeI 5250 Å synthesized using a sunspot model atmosphere (see text), we have computed the *circular polarization signal* produced by the instrument  $(I_1 - I_2)$ . This signal is represented versus wavelength (in Å and referred to the central wavelength of the line  $\lambda_0$ ). The solid line corresponds to an analizer with vanishing instrumental polarization ( $\Delta \delta = \Delta \phi = 0$ ) while the dotted line represents the real analizer ( $\Delta \delta = -5.2^{\circ}$ ,  $\Delta \phi = 0^{\circ}$ ).

# References

Maltby, P., Avrett, E.H., Carlsson, M., Kjeldseth-Moe, O., Kurucz, R.L., Loeser, R.: 1986, Astrophys. J. 306, 184

Sánchez Almeida, J.: 1988, Ph. D. thesis, University of La Laguna

Semel, M.: 1980, Astron. Astrophys. 91, 369.

del Toro Iniesta, J.C.: 1987, Ph. D. thesis, University of La Laguna

del Toro Iniesta, J.C., Martínez Pillet, V., and Vázquez, M.: 1990, this proceedings

Whier, E.: 1971, Solar Phys. 18, 226

# POLARIZATION OF THE DOMELESS SOLAR TELESCOPE OF THE HIDA OBSERVATORY (Preliminary Report)

Mitsugu MAKITA<sup>1</sup>, Yasuhiro FUNAKOSHI<sup>2</sup> and Yoichiro HANAOKA<sup>2</sup>\*

<sup>1</sup> Kwasan Observatory, Kyoto University, Yamashina, Kyoto 607, Japan and <sup>2</sup> Hida Observatory, Kyoto University, Kamitakara, Gifu 508-13, Japan

Abstract. Instrumental polarizations of the Domeless Solar Telescope (DST) are measured with an accuracy of 1 per cent. The variation of the Stokes parameters from sunrise to sunset is reproduced by adopting probable optical constants for the two oblique reflection mirrors in the telescope. The entrance and exit vacuum windows affect the polarization less than the measured accuracy.

#### 1. Introduction

The measurement of instrumental polarizations is necessary before the measurement of magnetic fields in non on-axis optical systems. This can tell us an accuracy of magnetic field measurements, or, if the instrumental polarization varies in some regular manner, this will make us devise some sophisticated compensators to increase the accuracy.

The Domeless Solar Telescope (DST) of the Hida Observatory involves two oblique mirrors in its optical path. In such system the instrumental polarization is inevitable. Farther more, it has entrance and exit vacuum windows. Therefore, this experiment aims at clarifying if the instrumental polarization can be described with the two oblique mirror system (e.g., Makita et al. 1982), or, if it is additionally modified by the distorted windows.

## 2. Measurement — Polarimeter and Dete or

Figure 2.1 shows the optical layout of the DST system. Details on the DST is given elsewhere(e.g. Nakai and Hattori(1980)). In relation to the present study we repeat some features on the concerning elements briefly. The optics of the telescope on the alt-azimuth mounting is the Gregorian system with additional two windows and two flat mirrors. The system focal length is 32.2 m with F/53.7, that is, 300 mm solar disk image on the working focus. The entrance window made of BK7 is 660 mm in blank diameter (608 mm in aperture), 40 mm in thickness. As shown in Figure 2.2, it is mounted in the cell isolated thermally. The measured deflection of the window was  $91\mu\text{m}/500$  mm under the operating pressure (1-5 Torr). The exit window of UBK7 is 418 mm in diameter (346 mm free), 40 mm in thickness, supported similar to the entrance window. Two flat mirrors, the Newtonian in front of the prime focus and the Coudé at the crossing point of the azimuth and elevation axes, fold the beam 90° respectively and introduce the instrumental polarization obviously. All mirror surfaces are aluminized and, except for the primary, overcoated to increase the reflectivity with Zeiss H-08 coating. Windows and slits are coated with MgF2 to increase the UV transmissivity.

The slit assembly at the center of the working table of the vertical vacuum spectrograph is a stack piling-up the entrance slit, filters, some analysing devices, etc.. For the present polarimetoric work, it consists of a slit with  $50\mu$ m-width  $\times$  0.5 mm-length, a rotatable quarter-wave plate and a Wollaston prism as the polarimeter, and a narrow band filter for the order separation of the grating as shown in Figure 2.3. The Wollaston prism, made of quarz, splits the incidence beam into mutually orthogonally polarized ones with the angle of  $0.1017^{\circ}$ ; the doubling direction and the azimuth of the ordinary ray are accordant to the direction of the slit length. By restricting the slit length to 0.2 mm(=1.3" of the sun), a pair of well separated spectral strips are obtained on the detector. The slit length and the separation angle are so small that the collimated beams illuminate the grating with no vignetting. To calibrate the orientation of the Wollaston

<sup>\*</sup> Present address: Nobeyama Radio Observatory of the National Astronomical Observatory. Nobeyama, Minamimaki, Minamisaku, Nagano 384-13, Japan

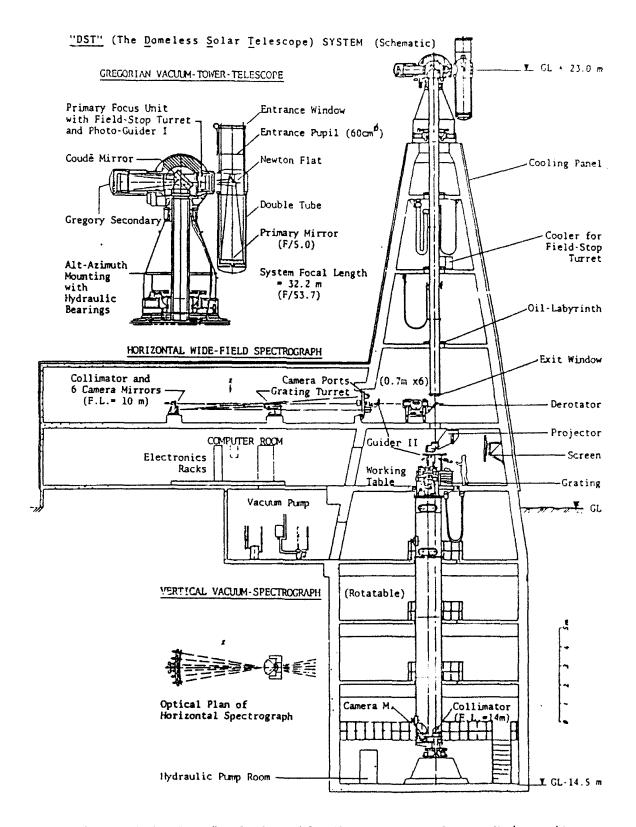


Figure 2.1 "DST" of the Hida Observatory, Kyoto University

From Telescope

Interference Filter Quarter-wave Plate (with Field Lense) Wollaston Prism Entrance Slit (rotatable) To Collimator Mirror Segment Vacuum Sealings, Heat Insulators'

Figure 2.2 Entrance Window Suport

Figure 2.3 Stack-up of Slit Assembly

prism, the wave plate is replaced to a linear polarizer with the axis direction known. The linear dispersion of the 14 m spectrograph is  $0.176\text{\AA}\text{mm}^{-1}$  at  $\lambda = 6303 \text{\AA}$ .

As the detecting device we are using an SIT camera system set on the outlet port of the spectrograph. A personal computer controls the system via GPIB. The 1"-SIT(TH9659) accepts the pair of spectra including Fe I 6302.5 and neighboring atmospheric lines across its TV scanning direction. The host computer generates a sampling line on one of the pair and records its intensity profile digitized with the 8-bit A/D converter and then on another alternatively. The number of sampling points along the spectrum is identical to that of the TV scanning lines, i.e. the spectral resolution of  $\Delta\lambda$ =3.44 mÅ for 512 lines. The cycle time to get a set of 512 data points is 75 msec. The effective width of the sampling line defined by the horizontal TV resolution of 10 mm/500 TVL corresponds to 0.13" of the sky blurred by the seeing.

For an axis angle of the quarter wave plate, 120-pair scan data are stored on the RAM successively within 18 sec and then sent to the 5.25" floppy diskette. This data transfer requires about 42 sec and meantime the wave plate is rotated to the next angle in sequence of 0°, +45°, -45° and +22.5° in respect of the Wollaston separation direction. One sequence of observation needs less than 3.5 min including fine adjustment and then the "telescope position" is reversed by turning the azimuth axis with 180°; this procedure is useful to make clear the azimuth- and elevation-dependences of the instrumental polarization because the orientation changes of the two flat mirrors cause different instrumental effects relative to the fixed working focal plane. To evaluate the instrumental polarization of the DST, the time-series observations of the solar disc center were done assuming quiet and unpolarized through the above mentioned scheme on April, May and July 1990.

#### 3. Calculation of the Instrumental Polarization

### 3.1. Conventions of Expressions

### (1) Expression of a Vector Rotation

We consider righthanded coordinates as shown in Figure 3.1. The vector **A** and **B** are in the x-y plane, and the vector **A** becomes the vector **B** when it is rotated by an angle  $\alpha$  around the x-axis; such a relation is symbolically described as

$$\mathbf{B} = r(\alpha)\mathbf{A} \quad . \tag{3.1.1}$$

### (2) Vector Rotation at a Reflection

In Figure 3.2, the reference system of an incident ray to a plane mirror is  $(\mathbf{x}, \mathbf{y}, \mathbf{z})$  and that of the reflected ray is  $(\mathbf{x}', \mathbf{y}', \mathbf{z}')$ . The vector  $\mathbf{z}$  and  $\mathbf{z}'$  are set along the propagation direction of rays, and the vector  $\mathbf{x}$  and  $\mathbf{x}'$  are set in the reflection plane, or the plane which includes both the incident and the reflected rays, and the vector  $\mathbf{x}'$  is the reflected image of the vector  $\mathbf{x}$ . Then we consider a vector  $\mathbf{x}_0$  of which the relation with  $\mathbf{x}$  is given as

$$\mathbf{x} = r(\alpha)\mathbf{x}_0 \quad . \tag{3.1.2}$$

The relation between the vector  $\mathbf{x}'$  and the vector  $\mathbf{x}_0'$ , which is the reflected image of the vector  $\mathbf{x}_0$ , is expressed as

$$\mathbf{x}' = r(-\alpha)\mathbf{x}_0' \quad , \tag{3.1.3}$$

or

$$\mathbf{x}_0' = r(\alpha)\mathbf{x}' \quad , \tag{3.1.4}$$

because the reference system is reversed after the reflection.

#### (3) Image Vector passing through the Pupil of an Optical System

An image is turned over after the pupil of an optical system as shown in Figure 3.3. Let a vector  $\mathbf{x}_0$  given as

$$\mathbf{x} = r(\alpha)\mathbf{x}_0 \quad , \tag{3.1.5}$$

in the object image system (x, y, z), then the vector  $x_0'$ , which is the image of  $x_0$ , is given as

$$\mathbf{x}' = r(\alpha)\mathbf{x}_0' \quad , \tag{3.1.6}$$

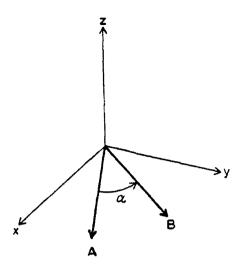


Fig. 3.1. Rotation of a vector. On the x-y plane the vector **A** becomes the vector **B** with the rotation of an angle  $\alpha$ , and such a relation is described as **B** =  $r(\alpha)$ **A**.

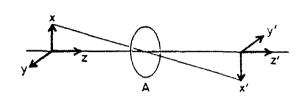


Fig. 3.3. Direction vectors through the pupil of the optical system. The vectors x', y' and z' are the images of the vectors x, y and z, respectively.

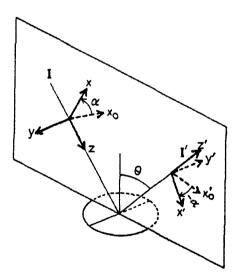


Fig. 3.2. Reflection of light by a mirror. The vectors x' and  $x_0'$  are reflected images of the vectors x and  $x_0$ , respectively. The angle  $\theta$  is the reflection angle.

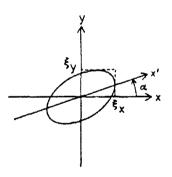


Fig. 3.4. A polarization ellipse.

in the reference system of the passing light  $(\mathbf{x}', \mathbf{y}', \mathbf{z}')$ . Therefore the rotation relation between the vectors does not change by passing an pupil.

## (4) The Muller matrix for a reflection

Stokes parameters of a polarized light are defined as

$$\begin{pmatrix} I \\ Q \\ U \\ V \end{pmatrix} = \begin{pmatrix} \xi_x^2 + \xi_y^2 \\ \xi_x^2 - \xi_y^2 \\ 2\xi_x \xi_y \cos(\epsilon_x - \epsilon_y) \\ 2\xi_x \xi_y \sin(\epsilon_x - \epsilon_y) \end{pmatrix} , \qquad (3.1.7)$$

where  $\xi_x$  and  $\xi_y$  are amplitudes of electric oscillations along x- axis and y-axis respectively, and  $\epsilon_x$  and  $\epsilon_y$  are phases; see Figure 3.4 in the case of a perfect polarized light. We take the vector  $\mathbf{x}$  parallel to the x-axis as the reference vector for the Stokes parameters.

Then we consider the Stokes parameter change through a reflection. When the reflection angle is  $\theta$  as in Figure 3.2, the Stokes vector  $\mathbf{I}'$  referred to the vector  $\mathbf{x}'$  is given as

$$\mathbf{I'} = \mathbf{L}(\theta)\mathbf{I} \quad , \tag{3.1.8}$$

where  $L(\theta)$  is the Muller matrix for a reflection, which is described as

$$\mathbf{L}(\theta) = \frac{R_{\mathbf{y}}^2}{2} \begin{pmatrix} X^2 + 1 & X^2 - 1 & 0 & 0 \\ X^2 - 1 & X^2 + 1 & 0 & 0 \\ 0 & 0 & 2X \cos \tau & 2X \sin \tau \\ 0 & 0 & -2X \sin \tau & 2X \cos \tau \end{pmatrix} . \tag{3.1.9}$$

In these equations  $R_x$  and  $R_y$  are the reflection coefficient of the electric vibration parallel to the x- and y-axes, and  $X=R_x/R_y$ , and  $\tau$  is the phase difference  $(\epsilon_x-\epsilon_y)$  due to the reflection. The parameters X and  $\tau$  are the function of  $\theta$  and described with refraction index n and absorption coefficient k of the material of the mirror surface as follows:

$$X^{2} = \frac{f^{2} + g^{2} - 2f\sin\theta\tan\theta + \sin^{2}\theta\tan^{2}\theta}{f^{2} + g^{2} + 2f\sin\theta\tan\theta + \sin^{2}\theta\tan^{2}\theta} , \qquad (3.1.10)$$

$$\tan \tau = \frac{2g\sin\theta\tan\theta}{\sin^2\theta\tan^2\theta - (f^2 + g^2)} \quad . \tag{3.1.11}$$

where

$$f^{2} = \frac{1}{2} \left[ n^{2} - k^{2} - \sin^{2}\theta + \sqrt{(n^{2} - k^{2} - \sin^{2}\theta)^{2} + 4n^{2}k^{2}} \right] , \qquad (3.1.12)$$

$$g^{2} = \frac{1}{2} \left[ -n^{2} + k^{2} + \sin^{2}\theta + \sqrt{(n^{2} - k^{2} - \sin^{2}\theta)^{2} + 4n^{2}k^{2}} \right]$$
 (3.1.13)

When the angle  $\theta$  is not so large, the phase difference  $\tau$  is somewhat smaller than  $\pi$ . We adopt the values n = 1.13 and k = 6.39 for an aluminum mirror at the wavelength 6300 Å(Schulz 1954, Schulz and Tangherlini 1954).

### (5) The Muller matrix for a rotation of the reference coordinates

The reference vector of a Stokes vector can be taken in any direction. If the reference vector is rotated in the  $\mathbf{x}$ - $\mathbf{y}$  plane by an angle  $\alpha$  (see Fig. 3.4), the Stokes vector referred to the vector  $\mathbf{x}'$  is given as

$$\mathbf{I'} = \mathbf{R}(\alpha)\mathbf{I} \quad , \tag{3.1.14}$$

where R is the Muller matrix for a rotation described as

$$\mathbf{R}(\alpha) = \begin{pmatrix} 1 & 0 & 0 & 0 \\ 0 & \cos 2\alpha & \sin 2\alpha & 0 \\ 0 & -\sin 2\alpha & \cos 2\alpha & 0 \\ 0 & 0 & 0 & 1 \end{pmatrix} . \tag{3.1.15}$$

(6) Stokes vector passing through the pupil

An image is rotated by  $\pi$  after the pupil. This rotation does not affect the Stokes vector by the equation (3.1.15).

### (7) Stokes vector at a reflection

Now we consider the change of the Stokes vector  $\mathbf{I}_0$  referred to the vector  $\mathbf{x}_0$  in Figure 3.2 by a reflection. At first the reference vector of the Stokes vector is changed to  $\mathbf{x}$ , and from the equation (3.1.14) the new Stokes vector is described as

$$\mathbf{I}_1 = \mathbf{R}(\alpha)\mathbf{I}_0 \quad . \tag{3.1.16}$$

Next, from the equation (3.1.8) the Stokes vector after the reflection is given as

$$\mathbf{I}_{1}' = \mathbf{L}(\theta)\mathbf{I}_{1} \quad . \tag{3.1.17}$$

Finally, the Stokes vector referred to the vector  $\mathbf{x_0}'$ , which is the reflected image of  $\mathbf{x_0}$ , is written as

$$\mathbf{I}_0' = \mathbf{R}(\alpha)\mathbf{I}_1' \quad . \tag{3.1.18}$$

Therefore, equations (3.1.16), (3.1.17) and (3.1.18) give

$$\mathbf{I}_0' = \mathbf{R}(\alpha)\mathbf{L}(\theta)\mathbf{R}(\alpha)\mathbf{I}_0 \quad . \tag{3.1.19}$$

### (8) Coordinates of the Sun

The necessary values for calculating instrumental polarizations are the azimuth  $\psi$ , the altitude  $\varphi$ , and the parallactic angle p of the Sun. These values are measured as Figure 3.5.

## 3.2. Muller matrices of the optical system of the DST

The optical path of the DST is shown in Figure 3.6 (also see Figure 2.1). This configuration is called the west position, because the telescope tube is set westward to the rotation axis of the azimuth. We consider through the optical path the change of the west direction vector  $\mathbf{W}$  of the Sun's disk, and the modification of the Stokes vectors by each optical element. The initial Stokes vector is referred to the vector  $\mathbf{W}$ , which is rotated by  $p - \pi/2$  from the zenith direction vector  $\mathbf{Z}$ .

At first the light passes through the entrance pupil  $A_1$ , and the west direction vector is rotated by  $\pi$  and corresponds to the vector  $\mathbf{x}_1$  in Figure 3.6, but the Stokes vector is not changed because of the equation (3.1.15) with  $\theta = \pi$ . We ignore the effect of the entrance window.

Next, the light reflected by  $S_1$  or the primary mirror; the reflection angle at the  $S_1$  is 0, therefore the west direction vector is not changed through the reflection. Therefore, if we take the reference vector  $\mathbf{x}_1$  and  $\mathbf{x}'$  of the  $S_1$  to be identical with the west direction vector, the Stokes parameters of the reflected light  $\mathbf{I}_1'$ , which is also referred to the west direction, is written as

$$\mathbf{I}_1' = \mathbf{L}(0)\mathbf{I}_0 \tag{3.2.1}$$

from the equation (3.1.8).

Next, we consider the reflection by the Newtonian mirror  $S_2$ . The vector  $\mathbf{x}_2$  of the reference system of the incident light to the  $S_2$  is horizontal and perpendicular to the vector  $\mathbf{Z}$  as shown in Figure 3.6. Therefore this vector is expressed referred to the images of the west direction vector (or the vector  $\mathbf{x}_1$ ) as

$$\mathbf{x}_2 = r(p)\mathbf{W} \quad . \tag{3.2.2}$$

Therefore the vector  $\mathbf{x_2}'$  of the reflected light, which points the Sun, is expressed as

$$\mathbf{x}_2' = r(-p)\mathbf{W} \quad . \tag{3.2.3}$$

The Stokes vector referred to  $\mathbf{x}_2$  is written as

$$\mathbf{I}_2 = \mathbf{R}(p)\mathbf{I}_1' \quad . \tag{3.2.4}$$

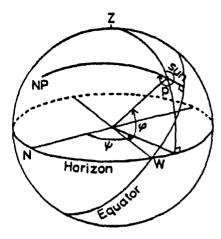


Fig. 3.5. Coordinates of the Sun. The angle p is a pallaractic angle,  $\psi$  is an azumuth, and  $\varphi$  is an altitude of the Sun. These angles are positive along the arrow directions in this Figure.

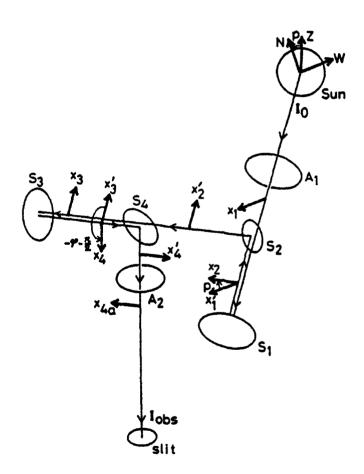


Fig. 3.6. The optical path of the Domeless Solar Telescope.  $S_1 - S_4$  are the mirrors.  $A_1$  is the entrance aperture and  $A_2$  is its image. The vector  $\mathbf{x}_n$  and  $\mathbf{x}_n$  are the reference vectors of the incident and reflected Stokes parameters to the mirror  $S_n$ .

206 M. Makita et al.

The reflection angle on the  $S_2$  is always  $\pi/4$ , then the Stokes vector referred to  $\mathbf{x}_2$  is written as

$$\mathbf{I}_2' = \mathbf{L}(\pi/4)\mathbf{I}_2 \quad . \tag{3.2.5}$$

The reflection angle of the Gregory mirror  $S_3$  is 0, then we take the vector  $\mathbf{x}_3$  and  $\mathbf{x}_3$  to be identical with  $\mathbf{x}_2$ . Therefore the direction referred to the west direction after the reflection by the  $S_3$  is written as

$$\mathbf{x}_3' = r(p)\mathbf{W} \quad . \tag{3.2.6}$$

The Stokes parameters after the  $S_3$  is

$$\mathbf{I}_3' = \mathbf{L}(0)\mathbf{I}_2' \quad . \tag{3.2.7}$$

The vector  $\mathbf{x_4}$  or the reference vector of the incident light to the Coudé mirror  $S_4$  points to the nadir. Therefore  $\mathbf{x_4}$  is expressed as

$$\mathbf{x_4} = r(-\varphi - \pi/2)\mathbf{x}_3'$$
 (3.2.8)

or

$$\mathbf{x}_4 = r(-\varphi + p - \pi/2)\mathbf{W} \quad . \tag{3.2.9}$$

Therefore

$$\mathbf{x}_{4}' = r(\varphi - p + \pi/2)\mathbf{W}$$
 (3.2.10)

The Stokes parameters referred to x3' is described as

$$\mathbf{I}_4 = \mathbf{R}(-\varphi - \pi/2)\mathbf{I}_3' \quad . \tag{3.2.11}$$

The reflection angle of the  $S_4$  is  $\pi/4$ ; then the Stokes parameters referred to  $\pi_4$  is

$$\mathbf{I}_{4}' = \mathbf{L}(\pi/4)\mathbf{I}_{4} \quad . \tag{3.2.12}$$

Then the light passes the aperture  $A_2$ , which is the image of  $A_1$  made by  $S_1 - S_4$ . The reference vector of the light is rotated by  $\pi$  through  $A_2$ . We take the new reference vector  $\mathbf{x}_{4a}$  rotated by  $\pi$  from  $\mathbf{x}_4$ , of which the relation to the west direction is identical to that of  $\mathbf{x}_4$ , because the west direction is also rotated by  $\pi$  after  $A_2$ . The Stokes parameters are not changed by  $A_2$ , namely,

$$\mathbf{I}_{4\alpha}' = \mathbf{I}_4' \quad . \tag{3.2.13}$$

We ignore the effect of the exit window between the mirror  $S_4$  and the spectrograph slit.

Finally the light reaches the slit of the spectrograph. From the equation (3.2.10) the direction of  $x_{4a}$  referred to the west direction is expressed as

$$\mathbf{x}'_{40} = r(\varphi - p + \pi/2)\mathbf{W}$$
 (3.2.14)

When the spectrograph is rotated to cancel the rotation of the solar image on the spectrograph slit, the Stokes parameters measured by the polarimeter on the spectrograph are the values referred to the west direction. The Stokes vector expressed in equation (3.2.13) must be rotated by  $-\varphi + p - \pi/2$  by the equation (3.2.14) and the observed Stokes vector is

$$\mathbf{I}_{obs} = \mathbf{R}(-\varphi + p - \pi/2)\mathbf{I}_{4a}^{\prime} \quad , \tag{3.2.15}$$

or from the equations (3.2.1), (3.2.4), (3.2.5), (3.2.7), (3.2.11), (3.2.12) and (3.2.15),

$$\mathbf{I}_{obs} = \mathbf{R}(-\varphi + p - \pi/2)\mathbf{L}(\pi/4)\mathbf{R}(-\varphi - \pi/2)\mathbf{L}(0)\mathbf{L}(\pi/4)\mathbf{R}(p)\mathbf{L}(0)\mathbf{I}_0 \qquad (3.2.16)$$

If the telescope is at east position or the telescope tube is set eastward to the rotation axis of the azimuth, the observed Stokes vector is written as

$$\mathbf{I}_{obs} = \mathbf{R}(\varphi + p + \pi/2)\mathbf{L}(\pi/4)\mathbf{R}(\varphi + \pi/2)\mathbf{L}(0)\mathbf{L}(\pi/4)\mathbf{R}(p)\mathbf{L}(0)\mathbf{I}_{0} . \tag{3.2.17}$$

When the spectrograph is fixed, the measured Stokes parameters are the values referred to the west direction on the ground. In this case  $I_{obs}$  for the west position is written as

$$\mathbf{I}_{abs} = \mathbf{R}(\psi)\mathbf{L}(\pi/4)\mathbf{R}(-\varphi - \pi/2)\mathbf{L}(0)\mathbf{L}(\pi/4)\mathbf{R}(p)\mathbf{L}(0)\mathbf{I}_{0} , \qquad (3.2.18)$$

and for the east position

$$\mathbf{I}_{obs} = \mathbf{R}(\psi + \pi)\mathbf{L}(\pi/4)\mathbf{R}(\varphi + \pi/2)\mathbf{L}(0)\mathbf{L}(\pi/4)\mathbf{R}(p)\mathbf{L}(0)\mathbf{I}_0 \quad , \tag{3.2.19}$$

where  $\psi$  is the azimuth of the sun.

We calculate  $I_{ob}$ , for  $I_0 = (1..0.,0.,0.)$  or unpolarized light and compare it with measured Stokes parameters in the next section.

### 4. Analysis

The obtained intensities of the polarization spectra split by the Wollaston prism are given as

$$\begin{cases} I_{\perp} = a(I+P)/2 \\ I_{\parallel} = b(I-P)/2 \end{cases} \tag{4.1}$$

where

 $I_{\perp}$ ,  $I_{\parallel}$ : intensities of the light beams split by the Wollaston prism which have perpendicular and parallel polarizations against the split plane (see Fig. 2.3).

I, P: incident total intensity and polarization component to the analyzing device.

a, b: effective transmission factors of the spectrograph for the two split beams.

The analysis is made to determine the ratio m, which satisfy the following null condition,

$$\frac{a}{2}(I+P) - m\frac{b}{2}(I-P) = 0 \tag{4.2}$$

An example of this analysis is shown in figure 4.1. Upper two curves are intensity profiles of the spectra and the bottom shows the residual of formula (4.2). Horizontal lines are separated by 25 digits.

The transmission factors, a and b, are obtained from the measurements made at the wave plate angles of 45° and -45°. At these position angles the polarization component is V Stokes parameter. Let  $m=m_+$  for 45° and  $m=m_-$  for -45°, formula (4.2) becomes

$$\frac{a}{2}(I+V) - m_{+}\frac{b}{2}(I-V) = 0$$

$$\frac{a}{2}(I-V) - m_{-}\frac{b}{2}(I+V) = 0$$

These formulae give

$$a/b = \sqrt{m_+ m_-} \tag{4.3}$$

Therefore the degree of polarization is calculated from formula (4.2) as

$$\frac{P}{I} = \frac{m - (a/b)}{m + (a/b)} \tag{4.4}$$

The polarization component is the following for each position angles of the wave plate (ref. Makita et al. 1985; Makita et al. 1986);

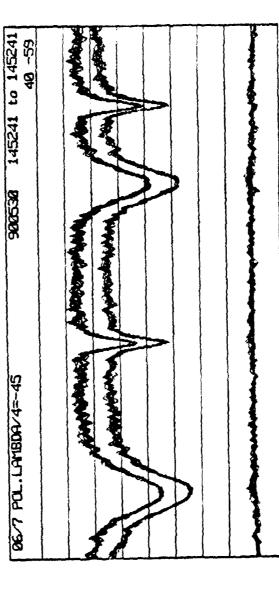
$$P = \begin{cases} Q & \text{at } 0^{\circ} \\ \pm V & \text{at } \pm 45^{\circ} \\ Q/2 + U/2 + V/\sqrt{2} & \text{at } 22.5^{\circ} \end{cases}$$
(4.5)

With the use of formulae (4.3), (4.5) and (4.4), a set of the observations made at the position angles, 0°, 45°, -45°, and 22.5°, give the degree of polarization as shown in Figure 4.2. Upper diagrams for July 21 are

Fig. 4.1. Intensity Profiles of the Polarization Spectra and Their Difference.

\*\*\* READ C-1888 SIT 2-CHANNEL SCANNING DATA \*\*\*

တမှာ Ø Max level = Min level = 300530 145241 to 145241 to Level = 152 224 Ref. levels: Max Level = 152 224 Min Level = 38 57 Mean Level = 114 178 OG√7 POL.LAMBDA/4≈-45 Scan Mode: Double No. of points/scan: 512 Sampling: 0 to 15



22.5 (E) 0° (E) ±45° (E) +5 EAST POSITION 0 -5 22°.5 (W) 0° (W) ±45° (W) +5 HEST POSITION 0 -5 16 10 10 12 14 LOCAL TIME 8 10 14 12 16 16 12 14 LOCAL TIME LOCAL TIME on July 24, 1990 0° (E) ±45°(E) 22°5 (E) +5 EAST POSITION 0 -5 0° (W) 22°5 (W) ±45° (W) +5 0 -5 10 12 14 LOCAL TIME 14 16 8 10 12 14 16 local time 16 LOCAL TIME

Fig. 4.2. Diurnal Variation of the Instrumental Polarization (in unit of per cent) on July 21, 1990.

210 M. Makita et al.

obtained with the rotating spectrograph to which the solar image is fixed relatively (ref. equations (3.2.16) and (3.2.17)), and lower diagrams for July 24 are obtained with the fixed spectrograph to which the solar image rotates relatively (ref. equations (3.2.18) and (3.2.19)).

#### 5. Result and Discussion

The time variation of the polarization components is compared with the calculation described in Section 3 (ref. Makita and Nishi 1970). The calculated values are shown as the dashed curves in Figure 4.2. The discrepancy from the observed values is remarkable, especially, for V Stokes parameter. This is probably due to the coating of the mirrors which modifies the original optical constant of the aluminum mirrors. The parameter in the Muller matrix (3.1.9) is revised from the original value, so as to give a bette, fit to the observed V parameter, as

$$\tau = \pi - 12.2^{\circ} \quad \to \quad \pi - 36.6^{\circ} \tag{5.1}$$

Solid curves in Figure 4.2 show the better fit with the revised value in (5.1). Observations made at the west position on April 25 and May 30 lead to the same result.

Still sometimes large deviations from the calculated values are seen in Figure 4.2. They might occur due to some erroneous observing process, or due to the following facts;

- (1) clouds which inequally changed the intensities of the pair spectra, because they are measured not simultaneously but with a time separation of a fraction of a second.
- (2) a drift of the spectrum which is resulted from a relaxation of the distortion of the spectrograph tank caused at the change of the telescope position. The sample lines of the SIT camera move perpendicularly to the spectrum dispersion and the spectrum intensity was not uniform. This effect is excluded in the case of the fixed spectrograph.
- (3) a thermal spatial shift of the SIT detector. This deteriorates the data by the same reason as in the case (2).

The instrumental polarization of the DST, thus, can be interpreted, within an accuracy of 1 per cent, as the two oblique mirror system, unnecessary to be taken into account the effect of the vacuum windows. The windows seem to be well supported (see Figure 2.2) and to receive uniform stress and strain, which lead to no modification of the incident polarization. The rather regular variation of the instrumental polarization suggests a possibility to develop polarization compensators which will increase the accuracy of the measurements. However higher accuracy measurements will be necessary in order to observe the magnetic fields which in most cases produces the polarization of 1 per cent or less.

The authors express their thanks to young colleagues for stimulating discussions on the polarization measurements.

#### References

Makita, M. and Nishi, K., 1970, Ann. Tokyo Astron. Obs. 12, 121-138.

Makita, M., Hamana, S., Kawakami, H. and Nishi, K., 1982, Ann. Tokyo Astron. Obs. 19, 24-37.

Makita, M., Hamana, S., Nishi, K., Shimizu, M., Koyano, H., Sakurai, T. and Komatsu, H., 1985, Publ. Astron. Soc. Japan 37, 561-574.

Makita, M., Hamana, S., Nishi, K., Shimizu, M., Sakurai, T. and Shibasaki, K., 1986, Astrophys. Space Sci. 118, 163-167.

Nakai, Y. and Hattori, A., 1985, Mem. Faculty of Sci. Kyoto Univ. 36, 385-399.

Schulz, L. G., 1954, J. Opt. Soc. America 44, 357-362.

Schulz, L. G. and Tangherlini, F. R., 1954, J. Opt. Soc. America 44, 362-368.

# Section 2 Polarimetric Observations chair: S.L. Keil

# STOKES PROFILE ANALYSIS OF A SUNSPOT USING THE MSFC MAGNETOGRAPH

K. S. Balasubramaniam,\* E. A. West, and M. J. Hagyard Space Science Laboratory, NASA/George C. Marshall Space Flight Center Huntsville, Alabama 35812 USA

#### **ABSTRACT**

Stokes filtergrams of a sunspot (AR 4662: June 9, 1985) have been observed using the MSFC magnetograph. We present here the analysis of the resulting Stokes profiles to recover the vector magnetic field and other physical parameters of the sunspot using the nonlinear least square inversion. An inter comparison of the results with the MSFC vector magnetograms will be presented.

#### I. INTRODUCTION

Filter magnetographs, such as Marshall Space Flight Center (MSFC) vector magnetograph, have conventionally used polarization measurements from the wings of the Zeeman broadened spectral lines to infer the vector magnetic field configuration of active regions. In spite of the fact that the spectral bandpass of the MSFC filter magnetograph is large (125 mÅ), its excellent spatial coverage offers the advantage of observing the vector magnetic field configuration of an entire active region. However, the filter can also be tuned to various portions of the spectral line, like a conventional spectrograph but with low resolution. This study aims to compare the results from a Stokes profile measurement of the entire line with that of the wing measurement of the filter magnetogram. Presently the MSFC vector magnetograph records all four Stokes polarization signals about the FeI 5250.2 Å spectral line.

#### II. THE INSTRUMENT

The MSFC vector magnetograph consists of a 30 cm cassegrain telescope with a 6x6 arcminute field of view (Hagyard, Cumings, and West 1985). The polarization optics consist of a wheel containing two quarter-wave plates and a window, followed by a KD\*P crystal (West 1985, 1989). The entrance window of the Zeiss filter acts as the polarization analyzer. The Zeiss filter has a bandpass of 125 mÅ which is tunable to ±8 Å about 5250.2 Å, in steps of 10 mÅ. The detector is a CCD camera with 1.4 square arcsecond pixels.

The sequence of acquiring the filtergrams in all four Stokes polarization is as follows. At any given filter position, the orthogonal circular polarization images (I+V) and I-V are acquired. Next, the linear polarization I+Q and I-Q images are acquired. Here the +Q direction is defined as the direction along the transmission axis of the Zeiss filter. The final set of linear polarization images are I+U and I-U, with their polarization directions at  $\pm 45^{\circ}$  to the  $\pm Q$  directions.

#### III. OBSERVATIONS

The measurements reported here (Balasubramaniam and West 1990) were made on a simple sunspot, (AR 4662) observed on June 9, 1985, shown in Figure 1. The sunspot was located in the south-eastern hemisphere of the Sun, about 4 arcmin away from the disc center. The sunspot had a size of about 45 arcsec in diameter, was circular in shape, and had a negative magnetic polarity.

<sup>\*</sup> National Research Council Resident Research Associate

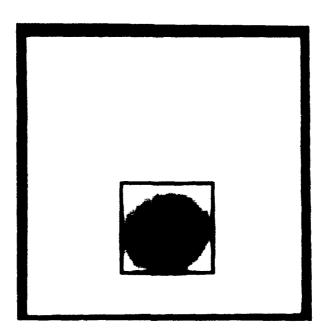


Fig. 1.- AR 4662 of June 9, 1985. The area within the box surrounding the sunspot is about 42x42 square arcsec. In the figure, Earth's north is toward the top and east is toward the left. This intensity picture has been acquired at the line center of the FeI 5250.2 mÅ spectral line, with the Zeiss filter.

For purposes of clarity, the observations can be divided into two categories: Filter scan data and monitoring data. The filter scan data were complete Stokes filtergrams obtained about the Fe I 5250.2 Å spectral line extending from +170 mÅ in the red wing of the spectral line to - 170 mÅ in the blue wing of the spectral line in steps of 10 mÅ. The monitoring data were taken in order to monitor the circular-to-linear polarization cross-talk introduced by the polarimeter. The entire observations were performed between 1300 UT to 1800 UT on June 9, 1985.

#### IV. DATA REDUCTIONS

#### a) Monitoring Data

The monitoring data were Stokes filtergrams obtained at +60 mÅ and -60 mÅ of the spectral line center, in succession (called a monitoring set). Six such data sets were observed, interlaced with the filter scan data, to monitor the polarization cross-talk as a function of time.

The monitoring data have been corrected for image motion, in excess of that uncompensated for by the limb tracker, using the intensity minimum in the sunspot. The monitoring data have also been corrected for the linear polarization bias introduced by a tilted glass plate, which is used by the limb tracker to correct for image motion. Following these corrections, the polarization cross-talk introduced by the polarization optics was measured. The polarization cross-talk is a circular-to-linear cross-talk introduced by the KD\*P crystals. Scatter plots of the linear polarization signals (Q, U) versus the circular polarization signals (V) were used to determine the relationship between the circular and the linear polarization signals and to estimate the polarization cross-talk. The cross-talk is known to vary with time, and is due to a drift in the KD\*P voltages

and the temperature. Using the six data sets at  $\pm 60$  mÅ, the change in circular-to-linear cross-talk has been measured as a function of time.

After six data sets of the monitoring data were corrected for cross-talk, the resultant data were used to derive the standard deviation  $(\sigma_Q, \sigma_U, \sigma_V)$  in Q, U and V as a function of Q, U and V respectively. This was separately derived for the sunspot umbra, penumbra and photosphere.

#### (b) Filter Scan Data

The filter scan data extended from +170 mÅ in the red wing to - 170 mÅ in the blue wing of the Fel 5250.2 Å absorption line, in steps of 10 mÅ. These data have also been corrected for image motion using the line center filtergram as the reference, for linear polarization bias introduced by the tilted glass plate of the limb tracker, and for instrumental cross-talk derived from the monitoring data.

The reduced filtergrams were then used to extract the Stokes profiles. Sample Stokes profiles Q, U and V in the umbra of the sunspot are shown in Figure 2 (dashed lines). These Q, U and V spectra have been normalised to the intensity spectrum. Also, the observed spectrum is convolved with the Zeiss filter spectral transmission function.

# V. DERIVATION OF THE MAGNETIC FIELD USING NONLINEAR LEAST SQUARE INVERSION

In order to derive the vector magnetic field parameters (the magnetic field strength, its inclination and azimuth) and other physical parameters from the observed Stokes Q, U and V polarized spectral line profiles, such as the line-of-sight component of the velocity, the Doppler width, the damping constant, the ratio of line-center to continuum opacity and slope of the source function, we need to compare the observed polarization profiles with the analytical solutions of these profiles from the polarized radiative transfer equations. This comparison can be achieved by the nonlinear least square inversion.

The nonlinear least square inversion technique was first developed by Auer, Heasley, and House (1977) to compare the observed Stokes profiles with that of the theory of polarized radiative transfer. This technique has been improved by Landolfi and Landi Degl'Innocenti (1982) to include magneto-optic effects. Further modifications to include additional parameters to the fit (line-of-sight velocities, slope of the source function, scattered light, etc.) have been made and applied to the study of sunspots (Skumanich, Rees, and Lites 1984; Skumanich and Lites 1987; Balasubramaniam 1989; Lites and Skumanich 1990). Theoretical analysis of the inversion technique using low spectral resolution Stokes profiles has been performed by Lites and Skumanich (1984). This study is an extension of an earlier work (Balasubramaniam and West 1990) using Stokes profiles observed with the MSFC magnetograph.

Since the observed profiles are convolved with the Zeiss filter transmission function, we must take the convolution into account while comparing the analytical profiles with the observed profiles. Convolution of the analytical profiles was chosen over the deconvolution of the instrument profile from the observed profile, because the Fourier deconvolution process would introduce additional frequencies. Moreover the observed standard deviations, which are to be used in the fitting process, are in the "convolved" domain. Hence we compare the profiles in the "convolved" domain. We also do not consider the observed intensity profile as it is contaminated by both scattered light as well as light from non-magnetic component of the observing element (Skumanich and Lites 1987; Balasubramaniam 1989; Arena, Landi Degl'Innocenti, and Nochi 1990). Since the standard deviations (inverse of signal-to-noise, S/N) for each of the Q,U,V profiles have been separately derived for the umbra, penumbra, and photosphere, we would have effectively taken into account the scatter on Q, U, and V, separately, for the umbra, penumbra, and photosphere. It is worthwhile to note that the gradient of the S/N in Q vs. Q, S/N in U vs. U, S/N in V vs. V functions become steeper as we move from the photosphere, through the penumbra to the umbra, in accordance with the known fall-off in scattered light as we move from the photosphere to the umbra.

The transfer of polarized radiation has been well studied, and an analytical solution of the transfer in terms of the Stokes profiles has been derived (Landolfi and Landi Degl'Innocenti 1982). The analytical

Stokes profiles are derived under the assumption of a plane-parallel Milne-Eddington model atmosphere, where all quantities entering the spectral line-forming process are assumed to be constant within the depth of formation of the spectral line. A local thermodynamic equilibrium is assumed in the spectral line-forming region and the source function  $B(\tau) = B_0 + B_1(\tau)$  is assumed to vary linearly with optical depth. The analytical solutions (using the notations of Land Degl'Innocenti 1976) are

$$I = B_0 + \frac{\mu B_1}{\Delta} [(1 + \eta_I)((1 + \eta_I)^2 + \rho_Q^2 + \rho_U^2 + \rho_V^2)]$$

$$Q = \frac{-\mu B_1}{\Delta} [(1 + \eta_I)^2 \eta_Q + (1 + \eta_I)(\eta_V \rho_U - \eta_U \rho_V) + \rho_Q R]$$

$$U = \frac{-\mu B_1}{\Delta} [(1 + \eta_I)^2 \eta_U + (1 + \eta_I)(\eta_Q \rho_V - \eta_V \rho_Q) + \rho_U R]$$

$$V = \frac{-\mu B_1}{\Delta} [(1 + \eta_I)^2 \eta_V + \rho_V R].$$

where

$$\Delta = (1+\eta_I)^2[(1+\eta_I)^2 - \eta_Q^2 - \eta_U^2 - \eta_V^2 + \rho_Q^2 + \rho_U^2 + \rho_V^2] - R^2$$

and

$$R = \eta_0 \rho_0 + \eta_U \rho_U + \eta_V \rho_V$$

Here  $\mu = \cos \theta$  where  $\theta$  is the angle between the line of sight and the normal to solar surface. The quantities  $\eta_{I,Q,U,V}$  and  $\rho_{Q,U,V}$  are given by:

$$\eta_{I} = 0.5[\eta_{p}sin^{2}\psi + 0.5(\eta_{b} + \eta_{r})(1 + cos^{2}\psi)] 
\eta_{Q} = 0.5[\eta_{p} - 0.5(\eta_{b} + \eta_{r})]sin^{2}\psi cos(2\phi) 
\eta_{U} = 0.5[\eta_{p} - 0.5(\eta_{b} + \eta_{r})]sin^{2}\psi sin(2\phi) 
\eta_{V} = 0.5(\eta_{r} - \eta_{b})cOS\psi$$

and

$$\rho_Q = 0.5[\rho_p - 0.5(\rho_b + \rho_r)] sin^2 \psi cos(2\phi) 
\rho_U = 0.5[\rho_p - 0.5(\rho_b + \rho_r)] sin^2 \psi sin(2\phi) 
\rho_V = 0.5(\rho_r - \rho_b) cos \psi.$$

where  $\psi$  is the inclination and  $\phi$  is the azimuth of the magnetic field vector. For a normal Zeeman triplet (e.g., FeI 5250.2Å line), the absorption profiles ( $\eta$ 's) and the anomalous dispersion profiles ( $\rho$ 's) are

$$\eta_p = \eta_0 H(a, v) \qquad \qquad \rho_p = 2\eta_0 F(a, v)$$

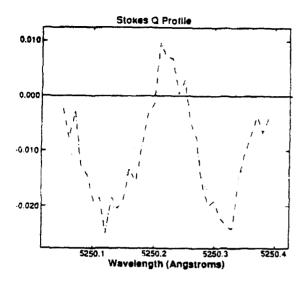
$$\eta_{b,r} = \eta_0 H(a, v \pm v_H) \qquad \qquad \rho_{b,r} = 2\eta_0 F(a, v \pm v_H).$$

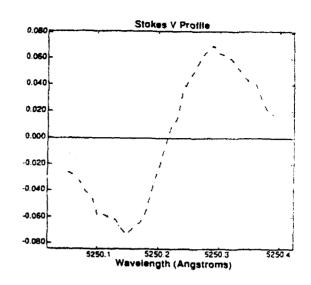
Here a is the damping parameter of the spectral line,  $\eta_0$  is the ratio of the line center to the continuum opacity, and

$$v = \frac{\lambda - \lambda_0}{\Delta \lambda_D}$$

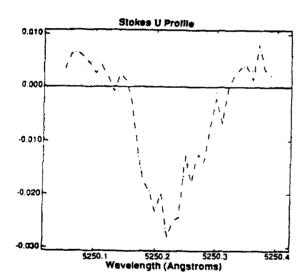
is the wavelength separation of any point on the spectral line at wavelength  $\lambda$ , from the line-center wavelength  $\lambda_0$ , in units of the Doppler width  $\Delta \lambda_D$ . The Zeeman splitting  $v_H$ , resulting from a magnetic field of intensity H, is in units of the Doppler width

$$v_H = \frac{(4.67^{-13} \lambda^2 g_J H)}{\Delta \lambda p}$$





Fitted Profile



# Observed Profile Derived Parameters B = 1320 G $\psi = 51^{\circ}$ $\emptyset = -25^{\circ}$ $\eta_o = 10$ $\Delta \lambda_D = 22 \text{ mA}$ $\alpha = .031$ $\lambda = 5250.212$

 $\mu B = -1.160$ 

Fig. 2.- Stokes polarization profiles Q, U, and V acquired with the MSFC vector magnetograph (dot-dashed lines) in the sunspot umbra, compared with the fitted profiles resulting from the non-linear least square inversion (dotted lines). The values of the derived parameters resulting from the fit are shown in the bottom right.

where gj is the Lande' factor.

The Faraday and Faraday-Voigt functions are explicitly given by

$$H(a, v) = \frac{a}{\pi} \int_{-\infty}^{+\infty} \frac{e^{-y^2}}{(v - y)^2 + a^2} dy$$

$$F(a,v) = \frac{1}{2\pi} \int_{-\infty}^{+\infty} \frac{(v-y)e^{-y^2}}{(v-y)^2 + a^2} dy.$$

A detailed explanation of these quantities is given by Landi Degl'Innocenti (1976).

The nonlinear least square optimization uses the simultaneous minimization of the residuals, namely the sum of the squares of the differences between the observed and the fitted profiles (the chi-squared fit) (Bevington 1967; Fletcher 1971). There are several parameters to the fit that are constantly upgraded at every iteration until a reasonably good fit is achieved (the residuals are minimized). These parameters are the magnetic field strength, its inclination and azimuth, and the thermodynamic parameters of the spectral line forming region such as the line center wavelength, the Doppler width, the ratio of the line-center to continuum opacity, the slope of the source function and the damping constant of the spectral line. The idea is to look for gradients in chi-squared with respect to each one these parameters, at every step of the iteration, and proceed in a direction until chi-squared reaches a global minimum. For our purposes, the chi-square is defined as

$$\chi^{2} = \sum_{i} \frac{1}{\sigma_{Q_{i}}^{2}} \left( Q_{i}(obs) - Q_{i}(a_{j}; fit) \right)^{2}$$

$$+ \sum_{i} \frac{1}{\sigma_{U_{i}}^{2}} \left( U_{i}(obs) - U_{i}(a_{j}; fit) \right)^{2}$$

$$+ \sum_{i} \frac{1}{\sigma_{V_{i}}^{2}} \left( V_{i}(obs) - V_{i}(a_{j}; fit) \right)^{2}.$$

The summation over all the wavelength points is taken care of by the i index. The  $a_j$  refers to all the parameters that enter the Stokes Q, U, and V profiles. The  $\sigma$ 's refer to the standard deviation (see Section IV) of each one of the Stokes parameters. In our fitting process we use only the Stokes Q, U and V profiles. We do not include the Stokes I profile in the fitting process.

We have derived all the eight parameters mentioned above for the whole sunspot. A typical example of the simultaneous fitting of the Stokes Q, U and V profiles is also shown in Figure 2. The dotted lines represent the best fit derived from the analytical solutions convolved with the Zeiss filter profile and the dashed lines represent the observed curves for a point in the sunspot umbra.

The magnetic field strength, its inclination and azimuth derived for the sunspot, using the nonlinear least square fitting process, have been converted to the longitudinal and transverse magnetic field components, respectively, to the line-of-sight. They are shown for the sunspot (inside boxed area of Figure 1) in Figures 3a and 3b respectively. We now wish to compare these results with those derived from the wing measurements alone.

#### VI. DERIVATION OF THE MAGNETIC FIELD USING WING MEASUREMENTS

The MSFC vector magnetograms are calculated from the observed polarization in the wings of the Fe I 5250.2 Å spectral line using calibration curves of the circular polarization versus the longitudinal field strength  $(B_L)$  and the linear polarization versus the transverse field strength  $(B_T)$  (for a detailed explanation see Hagyard, Gary, and West 1988). These calibration curves are constructed based on the Kjeldseth Moe (1968) solutions to the radiative transfer equation neglecting magnetooptical effects, for a penumbral model atmosphere. The convolution of the Zeiss filter transmission profile is taken into account in the calculations,

since the observed profile is the integral of the spectral line polarization across the passband of the Zeiss filter.

If  $P_Q$  and  $P_U$  are the fractional linear polarization and,  $P_V$  the fractional circular polarization, measured at any given location on the spectral line wing (say, 90 mÅ in the blue wing of the spectral line), then the field strengths are calculated by the following relations.

$$B_L = f_1 (G_k P_V)$$
  
 $B_T = f_2 (G_k P_L)^{1/2}$ 

where the functions  $f_1$  and  $f_2$  represent polynomial fits to the calibration curve and depend on spectral line profile parameters (atmospheric model, damping, Doppler width), the Zeiss filter transmission profile, and the position of the filter, v, at the wing of the spectral line relative to the line center. Here  $P_L = (P_Q^2 + P_U^2)^{1/2}$  and  $G_k$  is a gain constant to compensate for partial loss of contrast due to scattered light effects. The inclination and azimuth angles are, respectively, given by

$$\psi = \arctan(B_T/B_L)$$
$$2\phi = \arctan(P_U/P_Q)$$

The vector magnetic field contour maps of the sunspot for the Zeiss filter tuned at 90 mÅ in the blue wing of the spectral line are shown (boxed area of Figure 1) in Figures 4a and 4b.

#### VII. COMPARISON

Figures 3 and 4 show the comparison of the vector magnetic field parameters derived by two separate methods. The longitudinal magnetic field strengths derived using the two methods are represented in Figures 3a and 4a. We notice that each of the fitted contour levels in Figure 3a have a smaller area compared to the contour levels of the wing measurements in Figure 4a. Also, at about the geometric centre of the sunspot. the contour level L (-1600 G), in Figure 4a (wing measurement), skirt about center. The wing measurements used observations at 90 mÅ; the calibration curve  $(B_L \text{ vs. } P_V)$  for this spectral location "saturates" at about -2300 G. (The "saturation" field strengths would have been stronger had the wing measurements been farther out in the wing). Thus for the wing measurements, we would expect some effects of saturation. However, these should occur at the location at the location of the maximum field strength lying north of the geometric center.

The maximum longitudinal field strength in Figure 3a is about -2300 G, whereas, from the wing analysis the maximum longitudinal magnetic field strength is about -2500 G. In both cases, the maximum lies north of the geometric center. About the periphery of the sunspot, in Figure 3a, the lower longitudinal contours of the fitted field may deviate from the actual field due to a limitation of the fitting process (that uses the simultaneous minimization of all the three Stokes profiles Q, U, and V), in the presence of low S/N.

A comparison of the transverse magnetic field strengths is shown in Figure 3b and 4b. The azimuths are represented by ticked lines and the transverse field strengths by continuous contours. The azimuth values agree very well with each other. The good agreement in azimuths is additional proof that azimuths derived from the measurements in the far wings of the spectral line can neglect magneto-optical effects (West and Hagyard 1982). The overall structure of the transverse field contours appear qualitatively similar with the two methods as seen in Figures 3b and 4b. However, differences in the contour levels exist, for example, the maximum of the fitted contour level is 1200 G (Figure 3b), and the maximum contour level from the wing measurements is 1400 G (Figure 4b). The calibration curve for transverse field based on the wing measurement ( $B_T$  vs.  $P_L$ ) is good for up to 1800 G. Since the value of the maximum transverse field is about 1400 G, no saturation effects should appear. Also, the maximum contour level of Figure 3b (fitted method) lies within the umbra, whereas the maximum for the wing measurement (Figure 4b) lies in the penumbra.

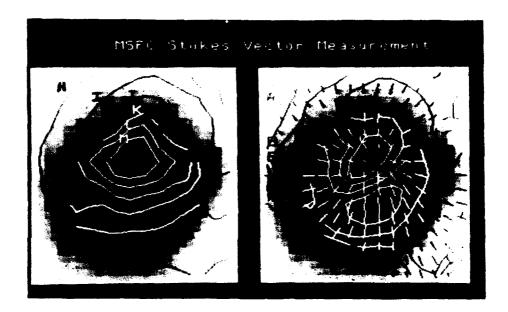


Fig. 3.- Vector magnetic field maps derived using nonlinear least square inversion of the full line Stokes profiles. Fig. 3a.- The derived longitudinal magnetic field strength contours superimposed on the intensity are shown in frame on the left. Note that contours change contrast with the changing background. Contour levels for the longitudinal magnetic field strength, in Gauss, are H = -100, I = -400, J = -800, K = -1200, L = -1600, M = -2000, N = -2400. Fig. 3b.- The derived transverse magnetic field strength is shown on the right. Continuous contours represented by the transverse field strengths, in Gauss, are A = 200, B = 400, C = 600, D = 800, E = 1000, F = 1200, G = 1400. Tick marks are the azimuths (with the  $180^{\circ}$  ambiguity).

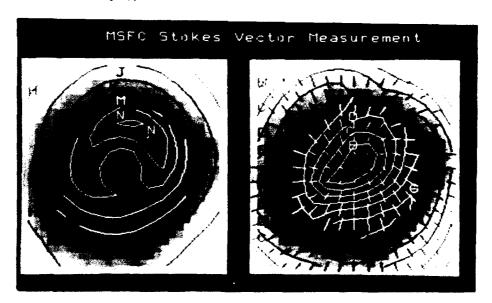


Fig. 4.- Maps of the vector magnetic field using the 90 mÅ blue wing polarization measurements.

Fig. 4a.- The longitudinal field maps are shown on the left. Contour levels are same as that of Figure 3a.

Fig. 4b.- The transverse magnetic field contours are shown on the right. Contour levels are same as those in Figure 3b. Tick marks are the azimuth.

We now comment on one other parameter derived from the nonlinear least square fitting process, namely the line center wavelength. The velocities for each spatial position (Figure 5) have been derived from the fitted wavelengths to the line center with reference to the fitted wavelength obtained at the center of the umbra (5250.209 Å) and are defined by

 $v_r = \frac{\Delta \lambda}{\lambda} c$ 

where  $\Delta\lambda$  is the difference between the fitted wavelength at any position and the fitted wavelength  $\lambda$  at the center of the umbra, and c is the velocity of light. We have noticed that the velocities derived in this manner largely coincide with the velocities derived from the zero-crossing of the Stokes V profile implying that, in a fitting process that involves the polarization profiles Q, U, and V only, the line center wavelength determination is largely weighted by the Stokes V profile. From these observations we have found that, apart from the radial outward motion of material in the sunspot penumbra (up to a maximum of about 1.6 km s<sup>-1</sup>), there are also material motions inside the umbra (inflows).

Although we are still studying the accuracy and significance of the thermodynamic parameters derived from the nonlinear least square inversion process, the changes in temperature and pressure would significantly affect the line formation of the FeI 5250.2 Å line in the presence of umbral fields. In general, the thermodynamic parameters are less accurately determined in the inversion process than the vector magnetic field parameters (Lites and Skumanich 1984; Skumanich and Lites 1987; Balasubramaniam 1989; Lites and Skumanich 1990). There is some amount of non-uniqueness in the thermodynamic parameters. For example, physically the opacity ratio is proportional to the number density of atoms and inversely proportional to the Doppler widths. Similarly, the damping constant is inversely proportional to the Doppler width. However, in the inversion process, these parameters are treated separately and their inter-relationship has not been considered. Hence, we are still studying the variation of the thermodynamic parameters across the active region, and their influence on the magnetic field parameters.



Fig. 5.- Line-of-sight component of the velocity contours, computed from the fitted line center wavelengths, using the sunspot center as the zero reference velocity. The background grey is the intensity picture. White contour levels are positive velocities and dark contour levels are negative velocities. White contour levels, in m/s, are A=100, B=350, C=100

600, D = 850, E = 1100, F = 1350, G = 1600, and dark contour levels are H = -100, I = -350, J = -600, K = -850, L = -1100, M = -1600.

#### VIII. CONCLUSIONS

We have shown comparisons that vector magnetic field parameters of a sunspot from the MSFC instrument, derived using complete line profile analysis and from the wing measurements alone. The azimuth of the transverse magnetic field agree well. The longitudinal and magnetic field does not agree well in the umbra. This may be due to scattered light at the source, scattered light in the instrument, weakening of the line due to changes in the thermodynamic conditions or projection effects. Some of the thermodynamic parameters could possibly provide clues to these departures. This study establishes that filter magnetographs can also be used for low spectral resolution studies with an added advantage of a good spatial coverage. Some further studies using the full line profile analysis could include anomalies in the structure of sunspots as suggested by the interpretation of vector magnetograph observations (West and Hagyard 1982), inclusion of the Stokes I profile to derive filling factors, development of sunspot model, and multi-spectral line analysis etc.

#### **ACKNOWLEDGEMENTS**

We thank Allen Gary for critical comments and suggestions. James Smith helped us with the figures. This work was done while one of us (K.S.B) held a National Research Council-NASA/MSFC Research Associateship.

#### REFERENCES

- Arena, P., Landi Degl'Innocenti, E., and Nochi, G. 1990, "Velocities and Magnetic Fields Observed in a Sunspot," to appear in Aston. Ap.
- Auer, L.H., Heasley, J.N., and House, L.L. 1977, "Determination of Vector Magnetic Fields from Stokes Profiles," Solar Phys., 55, 47.
- Balasubramaniam, K.S. 1989, "Stokes Polarimetry and the Measurement of Vector Magnetic Fields in Solar Active Regions," Ph.D. Thesis, Indian Institute of Science, Bangalore, India.
- Balasubramaniam, K.S., and West, E. A. 1990, "Polarization Studies of Zeeman Affected Spectral Lines Using the MSFC Magnetograph", Proc. SPIE Conference on Polarimetry-Visible, Infrared, Ultraviolet. and X-Rays, Huntsville, AL.
- Bevington, P.R. 1967. Data Analysis and Error Analysis for the Physical Sciences, Chapter 11, McGraw-Hill, New York.
- Fletcher, R. 1971, U.K. Atomic Energy Estbl. Tech. Rep. AREE 6799.
- Kjeldseth Moe, O. 1968, "A Generalized Theory for Line Formation in a Homogenous Magnetic Field," Solar Phys., 4, 267.
- Landolfi, M., and Landi Degl'Innocenti, E. 1932, "Magneto-Optical Effects and the Determination of Vector Magnetic Fields from Stokes Profiles," Solar Phys., 78, 355.
- Landi Degl'Innocenti, E. 1976, "MALIP A Programme to Calculate the Stokes Parameters Profiles of Magnetoactive Fraunhoffer Lines," Astron. Astrophys. Suppl., 25, 379.
- Lites, B.W. and Skumanich, A. 1984, "The Inference of Vector Magnetic Fields with Limited Spectral Resolution," Measurement of Solar Vector Magnetic Fields, NASA CP-2374, ed.M.J. Hagyard, p.342.
- Lites, B.W. and Skumanich, A. 1990, "Stokes Profiles and Vector Magnetic Fields. V. The Magnetic Field Structure of Large Sunspots Observed with Stokes. II," Ap. J., 348, 747.
- Hagyard, M. J., Curnings, N. P., and West, E. A. 1985, "The New MSFC Solar Vector Magnetograph," in *Proc. of Kunming Workshop on Solar Physics and Interplanetary Travelling Phenomena*, ed. C. DeJager and Chen Biao (Beijing: Science Press), p. 1216.
- Hagyard, M. J., Gary, G. A., and West, E. A. 1988, "The SAMEX Vector Magnetograph: A Design Study for a Space-Based Solar Vector Magnetograph," NASA TM-4048.

- Skumanich, A., Rees, D.E., and Lites B.W., 1984. "Least Square Inversion of Stokes Profiles in the Presence of Velocity Gradients," in Measurement of Solar Vector Magnetic Fields, NASA CP- 2374, ed. M.J.Hagyard, p.306.
- Skumanich, A. and Lites, B.W. 1987, "Stokes Profile Analysis and Vector Magnetic Fields. I. Inversion of Photospheric Lines," Ap. J., 322, 473.
- West, E.A. 1985, "Analysis of the New Polarimeter for the Marshall Space Flight Center Vector Magnetograph," Measurement of Solar Vector Magnetic Fields, NASA CP-2374, ed. M.J. Hagyard, p.160.
- West, E.A. 1989. "Using KD\*P Modulators for Polarization Measurements of the Sun," Proceedings of the SPIE Meeting on Polarization Considerations for Optical Systems, SPIE 1166, p. 434.
- West, E. A., and Hagyard, M. J. 1983, "Interpretation of Vector Magnetograph Data Including Magneto-Optic Effects: I. Azimuth Angle of the Transverse Field," Solar Phys., 88, 51.

#### Discussion

- H. Wang: Your bandpass is 125 mÅ and scan step is 10 mÅ. That means a very smoothed profile. How does that affect your results?
- K.S. Balasubramaniam: We take the analytical profiles at every step of the iteration, convolve the analytical profiles with the Zeiss filter transmission function, and then compare it with the observed profiles. So in principle we would have taken the convolution into account by oversampling within the instrumental resolution width. From the RMS errors in the values of the vector magnetic field parameters calculated by Lites and Skumanich (1986) we will be well within the 5% errors.
- J. Stenflo: Because of the spectral smoothing with your filter I think your inversion system is ill conditioned. For instance, the magnetic field effects distinguished themselves from the magnetic flux effects through a subtle deformation of the shape of the Stokes profiles. As this effect is smoothed out, your inversion will tend to zoom in on a solution corresponding to a filling factor of unity, which results in serious underestimates of the field strengths and overestimates of the inclination angles.
- **J. Harvey**: Since the subject of blends has come up, in the umbra of sunspots the  $5250.2\text{\AA}$  line is blended with a TiO line. This distorts V, Q and U measurements. Do you correct for this in your analysis?
- K.S. Balasubramaniam: We have not taken blends into account. Since the spectral width of the Zeiss filter is large, the blends may be "absorbed" by the smearing process. We have not quantitatively estimated the influence of blends.
- S. Koutchmy: Did you try to integrate the V Stokes profiles over the whole region to look at the net circular polarization?
- K.S. Balasubramaniam: No.
- S. Koutchmy: On the interpretation of your data: do you have any idea what parts of the core of the spot (bright umbral dots or the dark parts) is contributing to the radiation you analyzed? The line you use is temperature sensitive.
- K.S. Balasubramaniam: We are not able to spatially resolve the umbral dots as our seeing was about 2-3 arcseconds or sometimes even greater.
- B. Lites: The problem mentioned regarding the two-dimensional spatial continuity of spectral observations (versus filter observations) may be largely alleviated through the use of good-quality slit-jaw images. Such images may be "destretched", as is done with filter images, in order to place the spectral information into its precise two-dimensional context. Such a procedure, now being used on high-resolution spectral scans from La Palma, reduce considerably this drawback of spectral verses filter observations.

## Spectropolarimetry of active regions:

Jose Carlos del Toro Iniesta, Valentín Martínez Pillet.

and Manuel Vázquez

Instituto de Astrofísica de Canarias E-38200 La Laguna, Tenerife, SPAIN

#### Abstract

A circular analyzer has been used at the focal plane of a telescope in days of absence of instrumental polarization to simultaneously record  $I \pm V$  spectrograms at two different wavelength ranges:  $\sim 6300$  Å and  $\sim 3930$  - 3970 Å. The observations have been analyzed within two, also different, frames: on the one hand, an empirical relationship between brightness temperature and the magnetic field strength has been found for sunspot umbrae, which allows a determination of the Wilson depression; on the other, estimates of the chromospheric longitudinal component of the magnetic field (magnetic flux if the filling factor is not unity) in two umbrae, in a penumbra, and in a plage have been found by using profiles of the resonance lines H and K of CaII. A ratio of order 2-3 between the longitudinal components of the field at the chromospheric height of formation of the CaII lines and the photospheric height of formation of the 6302.5 Å Fei line is also found in umbrae.

#### 1 Introduction: Common features of the observations

Several active regions have recently (September 1989) been observed by our group, and some preliminary results are presented in this communication. Despite the fact that two distinct scientific objectives are intended, an observational link is present between them: circular analysis has been performed before the light is dispersed by the spectrograph.

The polarimeter we employed is a circular one and was designed by M. Semel, who kindly lent it to us in 1985. Since this year, it has become property of the I.A.C. The optical design and main characteristics were already published by Semel (1980). Technical details and laboratory calibration of the instrument may be found in these proceedings in a poster communication by Sánchez Almeida and Martínez Pillet. Here, we will concentrate on the most important property of the analyzer: it provides strictly simultaneous  $I \pm V$  imaging of a given zone of the Sun; thus, when placed immediately behind the spectrograph slit, simultaneous  $I \pm V$  spectrograms can be recorded at the focal plane.

<sup>†</sup> Based on observations made with the Grégory-coudé Teleskop (G.C.T.) operated on the island of Tenerife by the Universitäts- Sternwarte (Götingen) in the Spanish Observatorio del Teide of the Instituto de Astrofísica de Canarias

Instrumental polarization is as important as the optical quality of the polarimeter itself, as far as the accuracy of the analysis is concerned. Fortunately, the observations were carried out at the German Grégory-coudé telescope which allows two periods a year (around the equinoxes) with zero instrumental polarization (see Wiehr, 1971 and Sánchez Almeida, 1988). The spectrograph itself does not introduce as polarizing effect because the analysis is performed before the light enters it. Only small residual effects appear in the spectrograms which can easily be removed during the data reduction. The circular analysis is especially good in two spectral regions (see Sánchez Almeida and Martínez Pillet, these proceedings): one around 6100 Å and another around 4000 Å. It is in these two wavelength ranges where the observations we are dealing with have been carried out. In particular, we have analyzed the Fe 1 6302.5 Å line in the first range and the Ca 11 H and K resonance lines in the second range. Photographic Kodak 2415 film was used as detector.

#### 2 On the search for magnetohydrostatic signatures in sunspots

#### 2.1 The temperature-magnetic field strength relationship

Sunspots are in magnetostatic equilibrium as long as the Alfvén travel time is much shorter than their lifetime (Meyer et al. 1974). Hence gravity, pressure and magnetic forces have to balance each other. In other words, thermodynamics and magnetic field are coupled.

After analyzing the horizontal component of the magnetostatic equation, Martínez Pillet and Vázquez (1990) found the following equation, which relates the inner temperature, T. and the magnetic field, B, of the spot:

$$\frac{T(r, z_{\text{WD}})}{T_0(0)} = \frac{m(r, z_{\text{WD}})}{m_0(0)} \frac{T_0(z_{\text{WD}})}{T_0(0)} \frac{\rho_0(z_{\text{WD}})}{\rho(r, z_{\text{WD}})} \left[ 1 - \frac{1 + f_{\text{T}}}{2\mu P_0(z_{\text{WD}})} B^2(r, z_{\text{WD}}) \right]$$
(1)

Equation (1) holds for each point in the umbra at any given depth. In this case,  $z_{\rm WD}$  stands for the Wilson depression depth in a scale in which 0 corresponds to  $\tau_{5000}=1$  in the external atmosphere; r is the radial distance of the point from the axis of the tube which constitutes the spot; index 0 indicates that the corresponding parameter is measured in the external atmosphere; m's are mean molecular weights,  $\rho$ 's are densities,  $\mu$  is the magnetic permeability, and P is the pressure.  $f_{\rm T}$  is a parameter which includes all the magnetic tension terms and whose value can be calculated depending on the assumed configuration for the spot. For example, in a Schlüter & Temesváry's (1958) spot,  $f_{\rm T}=0.5$ ; if there is no magnetic tension,  $f_{\rm T}=0$ . In general we can stay that  $f_{\rm T}<1$  because higher values would imply too strong magnetic tensions.

Equation (1) can be seen as a linear relationship between the internal temperature and square of the magnetic field strength for different points in the umbra. Despite the fact that emperatures are not directly observable, Eq. (1) should have an empirical translation: continuum intensities are straightforwardly related with brightness temperatures. If this linear relationship is achieved with observational data, one can easily deduce a value for  $P_0(z_{\rm WD})/(1+f_{\rm T})$  from the ratio of the coefficients of a least squares fit. Note that no previous knowledge is needed of the factors outside the brackets in the right hand term of the equation. Once this ratio is known and assuming values for the magnetic tension parameter,  $f_{\rm T}$ , the external pressure at the Wilson lepression depth,  $P_0(z_{\rm WD})$ , is obtained.  $z_{\rm WD}$  can be inferred from this and using, for instance, the convection zone model by Spruit (1977).

#### 2.2 The observed ~ 6302 Å spectrograms

The first spectral zone mentioned in §1 has been, for many reasons, one of the most used for magnetic field studies. In our case, and apart from the already mentioned special characteristics of our polarimeter, it is important to use a line with a high effective Landé factor like Fe1 6302.5  $\hat{A}$  ( $g_{\rm eff}=2.5$ ). This is so because we need, in fact, magnetic field strengths in order to look for the linear relationship predicted in Eq.(1). This will only be possible if the  $\sigma$ -components are near complete separation when only circular analysis of the light has been carried out. The distance between the V-peaks yields a good measurement of B provided this strength is higher than  $\sim 1400\,\mathrm{G}$  (Lites & Skumanich 1990). To be conservative we shall only take into account measurements of B higher than 2000 G. In doing so we also avoid problems which could appear in the outer umbral parts, i.e., in the umbra-penumbra boundary. The observations are illustrated in Fig.1. I- and

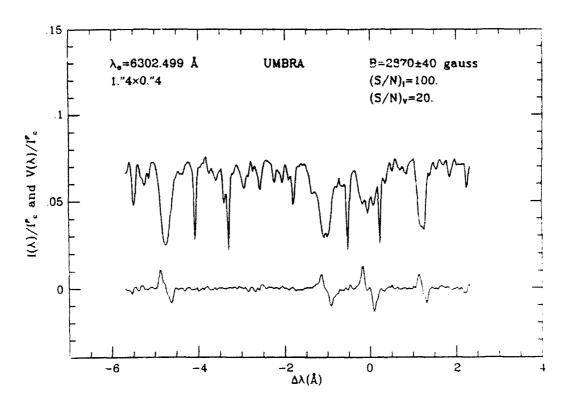


Fig. 1: Example of I- and V-profiles observed in an umbra. Raw data

V-profiles observed in an umbral core are shown. The maximum field strength found in this umbra was 3100 G; these profiles correspond to a point with 2870 G. Moreover, we have estimated the inclination of the field with respect to the solar surface normal ( $\gamma \simeq 20^{\circ}$ ) by using the relative intensities of the  $\pi$ - and  $\sigma$ -components (the heliocentric angle of the spot was  $\theta \simeq 35^{\circ}$ ).

In the V-spectrum, a conspicuous signature of magnetooptical effects is seen in the  $\lambda 6302.5$  line. The signal to noise ratios are labelled in the figure; they seem fairly high if the photographic detector used is taken into account. Low levels of stray-light are found in the spectrograms as is apparent in the I-spectrum. The intensity scale is in units of the quiet continuum intensity; one can clearly appreciate how the umbral continuum intensity of these raw data is near that obtained by other authors after correcting for stray-light effects (see, e.g., Maltby et al. 1986). Moreover, we are sure that the  $\pi$ -component of the  $\lambda 6302.5$  line is mainly due to inclination with respect to the line of sight and not to stray-light. In fact, the Fe II 6149 Å line was also recorded during the observations.

Due to its temperature sensitivity, this line can only be seen in the outer parts of umbrae and in penumbrae, but it is in these zones where the stray-light effects could be more important. Rather, no central " $\pi$ -component" is discerned from the noise as corresponds to its Zeeman pattern. After these arguments we can conclude that stray-light effects are small and easily removable during the data reduction.

#### 2.3 Wilson depression determination

In §2.1 we drew a scheme for semiempirical evaluation of the Wilson depression depth. It basically consists in looking for a linear relationship between brightness temperatures and squares of the magnetic field strength. First of all, we show in Fig.2 what the continuum intensity-magnetic field strength diagram looks like. Data from two different roundish and stable spots are shown.

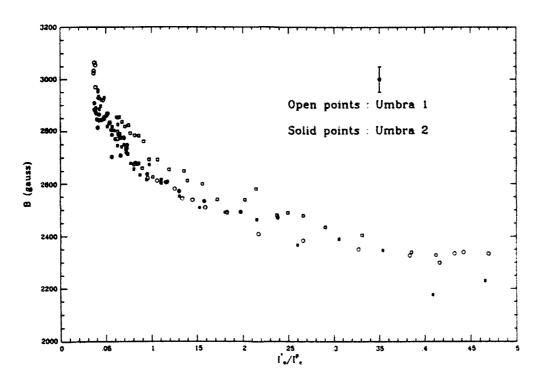


Fig. 2: Magnetic field strength vs. continuum intensity. Circles and squares correspond to two different slit positions along the spots

Continuum intensities are in units of the quiet Sun value and have already been corrected for stray-light effects (Martínez Pillet & Vázquez 1991). Magnetic field strengths have been determined by measuring the distance between the well separated V-peaks of the Fe1  $\lambda$ 6302.5. Once this diagram is translated to that between squares of the magnetic field strength,  $B^2$ , versus brightness temperatures,  $T_{\rm b}$ , a relationship much closer to linearity appears (see Fig. 3).

Following the procedure described in § 2.1 and for different values of the magnetic tension parameter,  $f_{\rm T}$ , we have determined values between 380 and 630 km for the Wilson depression depth. These values are in agreement with those obtained by other authors (see for instance, Gokhale & Zwaan 1972) on actually different bases. A statistical study analyzing data from several spots at different stages of evolution should be pursued and this is our aim for the near future. This

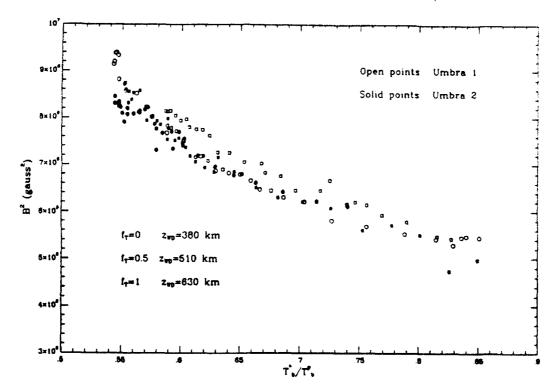


Fig. 3: Square of the magnetic field strength vs. brightness temperature. Symbols are the same as in Fig. 2

kind of study can provide important clues about the evolution of sunspot stability and structure.

#### 3 Chromospheric magnetic field

#### 3.1 The observed Call H and K Stokes-profiles

Among the lines of the solar visible spectrum, the resonance H and K lines of ionized calcium have been one the most important sources of information, over the last two decades, about the state of the chromosphere (Linsky 1970). In particular, their emission cores are actually indirect indicators of magnetic activity in the Sun and in stars (Skumanich, Smythe, and Frazier 1975; Schrijver et al. 1989). Call filtergrams of the solar surface show a zoo of brightness structures which are mostly thought to be related with magnetic photospheric structures. In spite of this, the considerably well-known distribution and hierarchy of magnetic fields in the photosphere is still lacking at higher layers where the H and K lines are formed. From an observational point of view, the chromospheric counterparts of the photospheric network and active regions are virtually unexplored as far as their magnetic properties are concerned.

Several problems of the chromosphere like its own thermodynamic stratification (Ayres 1981) or the merging height of magnetic flux tubes (Solanki and Steiner 1990) will remain unsolved without looking at the polarization state of lines like Catt H and K. NLTE transfer of polarized radiation is hard to understand, but there are simple effects like the reversals in the V-profiles which are just a consequence of the non-monotonic dependence of the source function on optical depth as the H<sub>2</sub>,

 $K_2$ ,  $H_3$ , and  $K_3$  peaks are. These reversals were predicted by Auer, Heasley, and House (1977) and by Rees, Murphy, and Durrant (1989), but they have not been observed until recently by our group (Martínez Pillet *et al.* 1990).

As commented in § 1, only circular analysis was performed. Moreover, our observations have a rather modest spatial resolution mainly due to the long exposure times ( $\sim 70\,\mathrm{s}$ ) imposed by both the photographic detector and the low transmission of the prefilter used. With such exposure times, three minute oscillations may have left their fingermarks in the spectra and they have not been taken into account. Nevertheless, with the state of the art as depicted in the preceeding paragraphs it is not difficult to conceive that even non-ideal observations as ours may provide important information. In fact, many interesting features have been observed in the V-profiles: among them are worth mentioning the strong asymmetries –in area and in peaks– apparent in practically all the profiles.

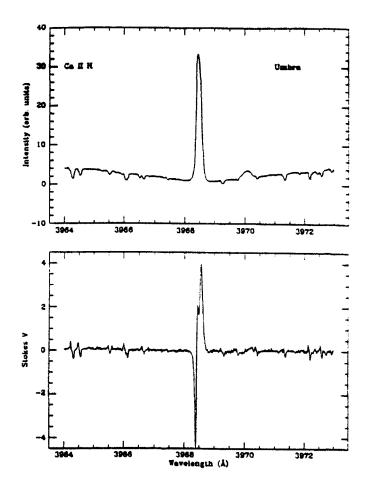


Fig. 4: Call H I- and V-profiles observed in an umbra

Fig. 4 shows I- and V-profiles of the CaII H line observed in an umbra. The reader can appreciate the asymmetric emission core with no  $H_3$  reversal. V shows clear asymmetries in peaks and areas and a reversal in the middle of the core-profile is apparent; the change of sign on this core-profile with respect to that of the photospheric lines corresponds to the fact that this core is in emission. These profiles look much more complicated when observed in a plage as is seen in Fig. 5. The noisier V-signal can be attributed both to the higher optical densities in the photographic film and to the lower magnetic flux present in the plage.

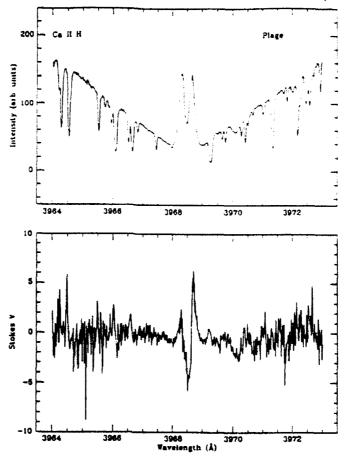


Fig. 5: Call H I- and V-profiles observed in a plage

#### 3.2 Magnetic field estimates: the weak field approximation

As far as the magnetic field is concerned, we can only refer to longitudinal components,  $B_{||}$ , due to the circular analysis of the radiation made. This is not exactly true if the filling factor is not unity; in this case we can only determine magnetic fluxes. However, it is fairly unlikely that this case will arise, even in plages, when analyzing lines like the Ca || H- and K-cores which are formed so high in the atmosphere. In what follows no distinction between strengths or fluxes will be made, but that remark should be borne in mind.

Before applying any sophisticated method of spectral synthesis or inversion using NLTE radiative transfer codes like the one proposed by Rees, Murphy, and Durrant (1989), we believe it is interesting to estimate a single value directly from the profiles. Such measurement does not provide information about the stratification of magnetic fields along the atmosphere. Variations are indeed expected both from the theoretical and the observational (asymmetries) points of view. Single measurements, however, are easier to achieve and provide preliminary ideas about what is happening.

The weak field approximation (studied in depth in these proceedings by Jefferies and Mickey) is perhaps the most adequate to apply to the Call H and K lines because:

• They are at blue wavelengths (3933, 3969 Å),

- Their effective Landé factors are small (1.333, 1.167 in LS coupling)
- They are very broad, and
- They are formed in high levels of the atmosphere where B should be below photospheric values.

As already known, the weak field approximation establishes a linear relationship between the V-profile and the derivative of I with respect to  $\lambda$ . We are mainly interested in the cores of the lines which are formed above the temperature minimum, i.e. in the chromosphere. Let us, however, remark that this proportionality between V and  $dI/d\lambda$  does indeed avoid any observation of non-zero V-signal in the photospheric wings of the lines within our error limits (S/N is not higher than 100 in I). For comparison, a rough estimate of the ratio between the expected signals in the wings of MgI b line at 5172 Å and CaII H is of the order 14 for the same B.

If V and  $\mathrm{d}I/\mathrm{d}\lambda$  have to be proportional, a superposition of the two functions of  $\lambda$  should illustrate the physics. Left pannels of Figs. 6, 7, and 8 show that superposition for penumbral (6), umbral (7), and plage (8) observations. A complementary illustration is in the right pannels of these figures, where point-to-point V vs.  $-\mathrm{d}I/\mathrm{d}\lambda$  diagrams are shown. In the left pannels,  $-\mathrm{d}I/\mathrm{d}\lambda$ 

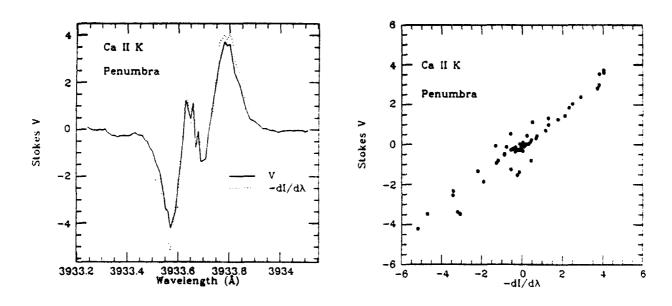


Fig. 6: K line core observed in a penumbra. V and  $-\mathrm{d}I/\mathrm{d}\lambda$  superposed (left pannel); point-to-point comparison between both fuctions of  $\lambda$  (right pannel)

is scaled so as to correspond to  $B_{\parallel}=1000\,\mathrm{G}$ . In Fig.6 a fairly well-established proportionality is seen, the slope of a linear fit to the points in the right-hand side diagram corresponding to  $B_{\parallel}=800\pm20\,\mathrm{G}$ . This is not the case in Fig.7, nor in Fig.8, where even when a proportionality is seen in one of the V-lobes it is not seen in the other. Note that the ellipse-like diagram of Fig.7 does not seem to be an scatter effect; in fact, it is seen in the two umbrae observed.

In view that the only symmetric profile observed behaves as expected, we asked ourselves whether the asymmetries are the reason for the break-down of the weak field approximation relationship. In fact, magnetic field gradients are implicitly avoided in the weak field approxima-

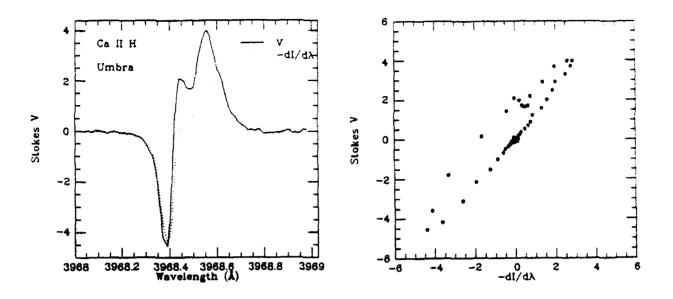


Fig. 7: H line core observed in an umbra. V and  $-\mathrm{d}I/\mathrm{d}\lambda$  superposed (left pannel); point-to-point comparison between both fuctions of  $\lambda$  (right pannel)

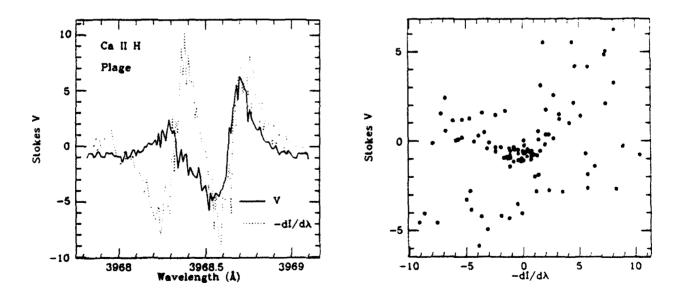


Fig. 8: H line core observed in a plage. V and  $-dI/d\lambda$  superposed (left pannel); point-to-point comparison between both fuctions of  $\lambda$  (right pannel)

tion scheme. This approximation has to hold between symmetric I-profiles and antisymmetric V-profiles.

Provided an origin of wavelengths and that they are real functions, each I and V can be considered as a sum of two functions of  $\lambda$ : one even and another odd, which will be referred to, in what follows, as their symmetric and antisymmetric parts, respectively. In order to calculate them we have used the parity properties of the Fourier transform after choicing as  $\lambda$ -origin the center of gravity of the I-profile. The derivatives of the symmetric part of I have also been calculated using Fourier transform properties. Fig. 9 shows the same point to point diagrams of Figs. 7 and 8, but between the antisymmetric part of V and the derivative of the symmetric part of I. The clearly

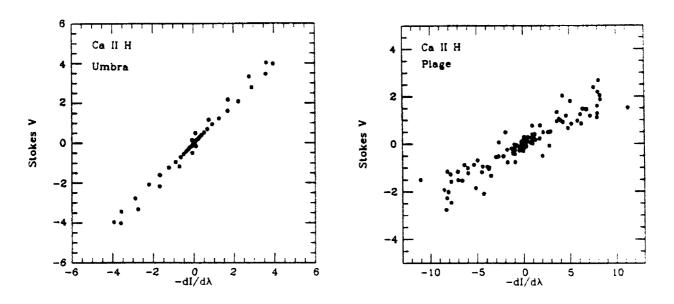


Fig. 9: Antisymmetric part of V vs. derivative of symmetric part of I. Same observantions than in Figs. 7 and 8

better agreement with proportionality between both functions allows us to evaluate the longitudinal component of the magnetic field (the magnetic flux if the filling factor is not unity). For the umbral observation,  $B_{||} = 1100$  G; for the plage observation,  $B_{||} = 260$  G. Another possibility of obtaining estimates of  $B_{||}$  is to use the center of gravity method (Semel 1967; Rees & Semel 1979) just on the original profiles. Table 1 shows a comparison between both kind of measurements. A fairly good agreement is found.

#### 4 Concluding remarks

The good accuracy of the I.A.C. polarimeter as a circular analyzer at two wavelength regions (around 6100 Å and 4000 Å) have been used to study two different problems. Namely, the attainment of magnetostatic signatures in sunspots, deriving values for the Wilson depression depth, and preliminary estimates of the chromospheric magnetic field as measured in the Call H and K resonance lines via the weak field approximation in several active regions.

A linear relationship has been found between brightness temperatures and magnetic field strengths in the core of two umbrae. This relationship allows us to determine the Wilson de-

Zone	$B_{\parallel}$ Weak field appr. (G)			$B_{  }$ Center of gravity (G)		
Umbra	1117	±	12	1109	±	6
Umbra	1520	±	20	1050	土	40
Penumbra (K)	800	±	20	600	±	20
Plage	260	±	100	350	±	90

Table 1: Magnetic field measurements

pression depth depending on the assumed configuration for the spot. Values of this parameter, ranging from 400 to 600 km, have been found and are comparable with those obtained by other authors on strictly different bases. A further implicit hypothesis underlying this analysis is the fact that both continuum intensities and magnetic field strengths are assumed to be measured at a narrow vertical region around  $\tau = 1$  in the umbra, i.e. at the Wilson depression. This does not seem to be too strong given the low degree of sophistication of the semiempirical method used. We consider, in fact, this easy handling as one of the most powerful characteristics of the procedure.

On the other hand, the weak field approximation appears to break-down for asymmetric profiles. Instead, it has been applied to the symmetric and antisymmetric parts of I and V, respectively. This has been shown to be successful in estimating values of the longitudinal component of the magnetic field (values proportional to the magnetic flux if the filling factor is not unity). The values found are in fair agreement with those obtained via the center of gravity method which reinforces their reliability. Moreover, an estimate of the ratio between photospheric and chromospheric magnetic field is possible because the umbrae observed have been the same in both wavelength regions. A ratio of 2-3 has been found as measured in the photospheric formation region of the Fe I 6302 Å line and in the chromospheric formation region of the Ca II H and K lines.

The last analysis has been conducted prior to any sophisticated use of spectral synthesis or inversion technique, but the possibility of their application is currently open and should be pursued in the near future.

Finally, we do not want to conclude without stating our hope of valuable improvements on the observations (and, consequently, on the analysis) by using CCD cameras instead of photographic films in our observing campaign next year. Both spatial resolution and S/N ratio will be reasonably improved.

#### Acknowledgements:

The Ca II observations are part of a broader program carried out in collaboration with R.J. García López, R. Rebolo, J.E. Beckman, and S. Char. This work has been partially supported by the Spanish DGICYT under project no. PB87-0521.

#### References

Auer, L.H., Heasley, J.N., and House, L.L. 1977, ApJ, 216, 531

Jefferies, J., Mickey, D.L. 1990, These proceedings

Linsky, J.L. 1970, Solar Phys., 11, 355

Lites, B.W., Skumanich, A., Rees, D.E., Murphy, G.A. 1988, ApJ, 330, 493

Maltby, P., Avrett, E.H., Carlsson, M., Kjeldseth-Moe, O., Kurucz, R.L., and Loeser, R. 1986, ApJ, 306, 284.

Martínez Pillet, V. and Vázquez, M. 1991, Solar Phys. (submitted)

Martínez Pillet, V. and Vázquez, M. 1990, Ap&SS, 170, 75

Martínez Pillet, V., García López, R.J., del Toro Iniesta, J.C., Rebolo, R., Vázquez, M., Beckman, J.E., and Char, S. 1990, ApJ, 361, L81

Meyer, F., Schmidt, H.U., Weiss, N.O., and Wilson, P.R. 1974, MNRAS, 169, 35

Rees, D.E., Semel, M. 1979, A&A, 74, 1

Rees, D.E., Murphy, G.A., and Durrant, C.J. 1989. ApJ, 339, 1093

Sánchez Almeida, J. 1988, Ph. D. Thesis, Universidad de La Laguna

Sánchez Almeida, J., Martínez Pillet, V. 1990, These proceedings

Schrijver, C.J., Coté, J., Zwaan, C., and Saar, S.H. 1989, ApJ, 337, 964

Schlüter, A., Temesváry, S. 1958, in: I.A.U. Symp. 6, Electromagnetic Phenomena in Cosmical Physics, ed. B. Lehnert, Cambridge, Cambridge University Press, p. 263.

Semel, M. 1967, Ann. Astrophys., T. 30, No. 3

Semel, M. 1980, A&A, 91, 369

Skumanich, A., Smythe, C., and Frazier, E.N. 1975, ApJ, 200, 747

Solanki, S.K., Steiner, O. 1990, A&A, 234, 519

Spruit, H.C. 1977, Ph. D. Thesis, University of Utrecht

Wiehr, E. 1971, Solar Phys., 18, 226

#### Discussion

- **S. Koutchmy**: You are dealing only with the emission line profile of Call in the spot; what about the absorbed (reversed) part?
- **J.C.** del Toro Iniesta: The wings are so broad that no measurable V signal is obtained, within the signal to noise. Non-zero V signals have already been observed in MgIB lines by other authors, but in this case V signal should be much smaller due to their lower Landé factor and broader wings.
- S. Koutchmy: Do you see 3 min oscillations in the CallK line, and how do you take care of effects produced by these oscillations?
- J.C. del Toro Iniesta: We have not taken any oscillations into account. It is true that they can influence the observed profiles, but a proper consideration for the oscillation can not be made with the present instrumentation.
- A. Skumanich: The  $K_{2V}$  part of CaII is often perturbed in plage regions by transient emission, and may be the cause of the breakdown on the violet side of  $K_2$  in your  $\bar{V}$  verses  $dI/d\lambda$  relations.
- J.C. del Toro Iniesta: It may perhaps have some influence on the whole problem, but it is also found in umbral observations and not only in plage.
- A. Skumanich: I commend you on your effort to obtain observational signatures, as you called it, of lateral force balance. How invariant is your field-intensity relative to the size of the spots? How different are the penumbral areas or radii?
- J.C. del Toro Iniesta: I am sorry but we have not any statistical result. These are just preliminary results with these two spots. It is our aim to extend this kind of study to as many spots as possible.
- S. Solanki: In the first part of your talk you presented a relationship between brightness (or temperature) and field strength in sunspots. Since the brightness jumps at the boundary between the umbra and the penumbra, does the field strength in your model also jump at that point in your model?
- J.C. del Toro Iniesta: No, it does not. The spot is just considered as a vertical flux tube embedded in a nonmagnetic atmosphere, but no considerations on the model atmosphere have been taken into account. This relation only comes from the horizontal component of the magnetostatic equation. The problem you mention is in the boundaries of the tube and perhaps correspond to the upper part of the diagram where some saturation begins to occur. In any case our spatial resolution is not good enough to observe strong jumps in brightness in the boundary.
- J. Stenflo: I would advise you not to use the terminology "field strength" for your observational results, since your weak-field approximation of course provides no information on the magnetic filling factor and this only gives you values of the magnetic flux. Your use of the term "field strength" may mislead some people to believe that you have really determined the intrinsic field strength in the plage chromosphere. Instead, your flux densities provide a lower limit to the chromospheric field strength (assuming that the different thermodynamic properties of the magnetic and non-magnetic chromospheres have properly been accounted for).
- J.C. del Toro Iniesta: Thank you for your precision. In fact, any unknown filling factor different from unity should be taken into account.

# HIGH SPATIAL RESOLUTION OBSERVATIONS OF MAGNETIC FLUX ELEMENTS

#### Serge KOUTCHMY

Institut d'Astrophysique de Paris, CNRS 98bis, Bld Arago, F-75014 Paris, France and NSO-S.P.O., Sunspot, NM 88349, USA

Summary. We shortly review works done at the VTT of SPO during the last 15 years, on both high spatial resolution spectroscopy using polarization analysis and magnetography with a polarization modulator inside the UBF. Respective merits and noticeable results are discussed. We stress the importance of using high-speed measurements to track the magnetic signal and avoid losses due to image motion; the efficiency in improving the resolution using the 2-D Wiener filtering is also demonstrated. Subarcsec resolution magnetic maps are discussed, to show not only the dominant-polarity magnetic-elements, but also the mixed minor-polarity and the weak field outside.

#### 1. Introduction

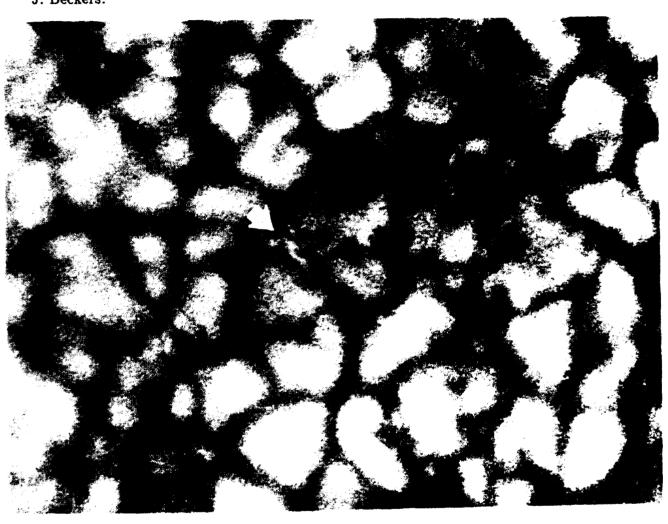
There is no need to introduce the subject as several recent reviews, Zwaan, 1987, Stenflo, 1989 for ex., and several conferences have been devoted to it in the last years: Schröter et al. 1988, Deinzer et al. 1986, for example.

However, from the observational point of view, not very much has been written on high spatial resolution measurements of non-spot magnetic-fields, although a considerable progress has been made possible thanks to the use of CCD cameras and fast processors. The "old" review papers by J. Harvey, 1976 and J. Beckers, 1976 are still a reference on the subject; a considerable effort has been produced by the H. Ziringroup at Big Bear Observatory, see Martin, 1988 for example and the A. Tittle-group of Lockheed at Sac. Peak and now at La Palma, see Title et al. 1987, for example.

Results obtained using IR techniques or adaptative optics systems are not considered here, as they still are in a stade of development. At the Vacuum Tower Telescope (VTT) of N.S.O. Sacramento Peak Observatory, several attempts have recently been made with both the Echelle Spectrograph (ESP) and the Universal Bi-Refringent Filter (UBF), to measure polarized line profiles or polarized filtergrams, by G. Simon, L. November and others. In this report, a short account of past and recent observations made by our group at NSO-SPO, Koutchmy et al. 1978-1988, will be given in an attempt to justify the search for very-high-spatial-resolution flux-tubes studies, although this approach has been largely contested in the literature. We however believe that other methods, for example those based on the use of 2 or more magnetic lines simultaneously

S. Koutchmy

interpreted, especially in the case of low spatial resolution FTS data, are not less subject to arbitrary interpretations; even if the precise physical parameters are not ultimately measured, the high spatial resolution methods have brought very much for the analysis of thermodynamical parameters in concentrated magnetic fields regions (temperature; velocities) and appear more straightforward for the analysis of the dynamical and the morphological characteristics of a flux-tubes region. Indeed, one of the best pieces of evidence for the existence of very concentrated magnetic fields outside of spots comes from the famous "filigree" pictures of R.B. Dunn, P. Mehltretter and the filtergrams of J. Beckers.



4860 A 4 arcsec. 100 km

Figure 1. Small part of an early photographic frame obtained at the prime focus of the VTT of SPO, from high speed bursts. The resolution reaches 0.15 arcsec (see Koutchmy 1977) on the filigree structure shown by the arrow.

The beautiful magnetograms obtained at Kitt-Peak and Big Bear, although of very high sensitivity, are of lower spatial resolution (3 or more arcsec), making their calibra-

tion a very tedious work. To give here a more perspective definition of what should be the today aim of high spatial resolution magnetographic (polarimetric) observations, consider figure 1 which shows the typical and best resolution (ultimate at NSO-SP) "picture" of a flux tube region (a small network element observed at the photospheric level).

Extremely bright features of  $\lesssim 0.2$  arcsec cross-section are seen, apparently embedded in an intergranular lane (examples with the same structure overlapping a granule can be also found...). This obviously magnetic feature is of very complicated morphology (nothing like a model-flux-tube) and more importantly, rapidly changing (with a time scale of 1 to 10 sec!). The question we address here is: where is the magnetic field? Clearly: do we "see" the dissipating current sheets associated to a concentration of magnetic fields with amplitudes up to 1 to 2 Kgauss inside, and of smaller amplitude around or, alternatively, do we see the "walls" of a Wilson depression of a more static concentrated field of unique amplitude producing a set of evacuated tubes, as theoretical works seem to predict?

#### 2. Observing constraints

In high spatial resolution observations, a magnetic signal is clearly extracted from a polarization analysis resulting in a differential modulation effect over the f.o.v., due to the Zeeman longitudinal effect when Left Circular Polarization (LCP) and Right Circular Polarization (RCP) light is measured (the transverse Zeeman effect, producing a considerably smaller modulation and accordingly, a far smaller signal-noise ratio, is not considered here in the context of very small scale structures). Ground-based observations are permanently disturbed by Earth-atmospheric effects and, correspondingly, the spatial resolution, characterized by the resulting Modulation Transfert Function (MTF) see figure 2, will strongly depend of the exposure time and, accordingly, the resulting ultimate resolution will drastically change. Additionally, very-small-scale structures are changing rapidly, so the first constraint is to perform observations strictly simultaneously or, at least, switch the measurements from one channel to the other one at a rate fast enough to reduce the differential effects produced by image motion, and changing blur and distorsion to a value comparable with the achieved resolution. To clear up this point, let us consider the simple case of a single magnetic element of size  $\Delta x$  and  $\Delta y$  with a unique value of field  $B(x,y) \equiv B_o = cte$  over its whole area  $\Sigma = \Delta x.\Delta y$  and with a zero value outside.

Consider B given by measurements in LCP and RCP lights performed alternatively with a time laps  $\Delta t$ ; correspondingly, the magnetic element has moved, in  $\Delta t$ , over the pixels of the detectors, in the image plan, by an amount of  $\delta x$  and  $\delta y$  from the initial values  $x_o$ ,  $y_o$ . Without entering into the details of the method used to deduce B from the magnetic signal, in both the weak and the strong field approximation, we have for each single magnetogram:

$$B_i = \int_{\Delta t} f(x_o, x_o + \delta x, y_o, y_o + \delta y) dt$$
 (1)

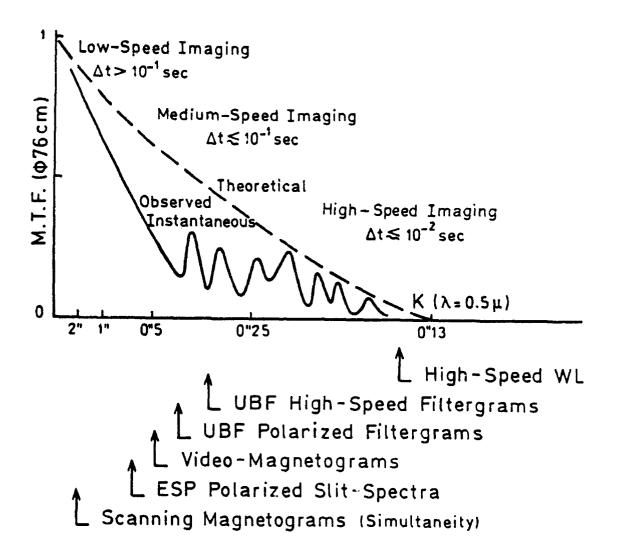


Figure 2. The MTF at the VTT of SPO, with the resulting resolution reached using different methods of observation.

Considering, in a first approximation, only linear "seeing" effects, we have  $\delta x = v_x.\Delta t$  and  $\delta y = v_y.\Delta t$ ,  $v_x \simeq v_y$  being constant during  $\Delta t$  and obviously being related to the quality of the seeing. In case we have  $\delta x \ll \Delta x$  and  $\delta y \ll \Delta y$ , equation (1) reduces to  $B_i \approx B_o$ ; this case includes the case of simultaneous measurements, when  $\Delta t \equiv 0$ . Unfortunately, the conditions are difficult to satisfy in case of magnetographic measurements performed using the switching between 2 polarization states, especially when the reading time of the CCD is  $\Delta t_r \gg \delta t$ , with  $\delta t \lesssim \Delta x/v_x$ ;  $\delta t \lesssim \Delta y/v_y$ ; this is critical if, as one believes,  $\Delta x$  and  $\Delta y$  (flux tube size) are very small! With the assumption made before, eq.(1) can be rewritten also this way:

$$F_{i} \approx B_{o} \left[ \int \int_{to}^{to+\delta t} f_{L} . dxdy - \int \int_{to+\Delta t}^{to+\Delta t+\delta t} f_{R} . dxdy \right]$$
 (2)

where  $f_L$  and  $f_R$  describe the response of the magnetograph in LCP or RCP lights and  $F_i$  is the magnetic flux.

In case the region which is analyzed contains many flux tubes with different signs, the apparent flux measured  $F_i$  will be drastically reduced and can even reach a zero value! It is clear that the only way to perform a more or less correct measurement is to have  $\Delta t \leq \delta t$  or better  $\Delta t \ll \delta t$ . It means also that the exposure time should always be short. Let us put numbers: for a very good seeing,  $v \leq 0.5$  arcsec.sec<sup>-1</sup>; assuming  $\Delta x \sim 0$ .2 and  $\Delta y \sim 0$ .2, we get  $\Delta t \leq 0.4$  sec, so the switching between measurements should be made in less than 1/3 sec. Now, such switching assumes an exposure time  $\tau < \Delta t$  which is rather small, so integration should be performed to improve the signal-noise ratio; accordingly, the measurements described by eq.(2) and the corresponding frames are repeated in a "cycling" time  $\Delta t \geq \Delta t$ ; image motion (and blurring) is such that a random smearing is then produced during the whole sequence, the resulting measured flux being:

$$\bar{F} \approx \int F_i dt = \int \int F_i(x,y).S(x-x_o, y-y_o)dxdy$$
 (3)

 $x_o$  and  $y_o$  being the coordinates in a reference frame corresponding to the average. It is important to note that S is a smearing function, so no magnetic signal is lost during the integration, eq.(3); then, the mapping of  $F_i$  can be considerably improved in resolution, in case the signal-noise permits (!), using a deconvolution of eq.(3) or, better, a Wiener filter, see Koutchmy 1977, for example. This technique is of course limited by the noise and even, sometimes, by undeterminations occurring when the pattern is complicated; recent success has however been obtained in image restauration as dramatically shown in the case of Hubble Space Telescope pictures, giving more confidence in these techniques.

Finally, we note that subtracting afterward LCP and RCP pictures which have been smeared out due to a long integration time (> 0.3 sec), even when a destreching is performed to remove the differential distorsion, irremediably produces a loss of magnetic signal.

#### 3. Results coming from the high-spatial-resolution spectroscopy

This method is well-known from the works of J. Beckers at S.P.O., for example. The set-up (quater-wave plate and Wollastone) is used in conjunction with the Echelle Spectrograph of the VTT to obtain splitted spectra near 630.2 nm, see Koutchmy and Stellmacher, 1978. Simultaneous unpolarized spectra are also obtained in a non-magnetic line (557.6 nm) and in  $H\alpha$ , as well as slit-jaw pictures. With the skill assistance of H. Mauters, we tried to obtain the best possible spatial resolution along the slit, by taking many spectra during moments of good stability of the image, optimizing the exposure time (1.5 sec) and the slit-width (0.75 arcsec) to obtain a good signal-noise ratio in the

S. Koutchmy

core of the splitted magnetic lines 630.15 and 630.25 nm. This last line with g=2.5gives the best chance to resolve flux tube magnetic fields; many spectra show a splitting in the core of the line corresponding to 1 Kgauss and more, so the field seems almost resolved; the field in the wings (half depth) could also be measured with a method similar to the so-called center-of-gravity method promoted by M. Semel. No doubt that to-day, using a large CCD chip, a better resolution could be achieved, although it is still hard to imagine how spectra of 100×70 mm size could be read out fast enough to take advantage of moments of best seeing and scan a large enough region. Figure 3 obtained by Dara and Koutchmy, 1983 shows how the distribution of the field looks like when a typical rosette or network patch is analyzed by using this method, without making any correction for the loss of polarization due to the telescope nor for the smearing! Already a 1 KG field is directly measured at the location of highest strength. Note that the region overlies the quiet sun (minimum of activity) and of course, no traces of a pore is seen, as evidenced from the inspection of the spectra between the lines, in the continuum, or the simultaneous spectrum of the non-magnetic line at 557.6 nm and. evidently, of the slit-jaw pictures taken in the continuum, see also Koutchmy and

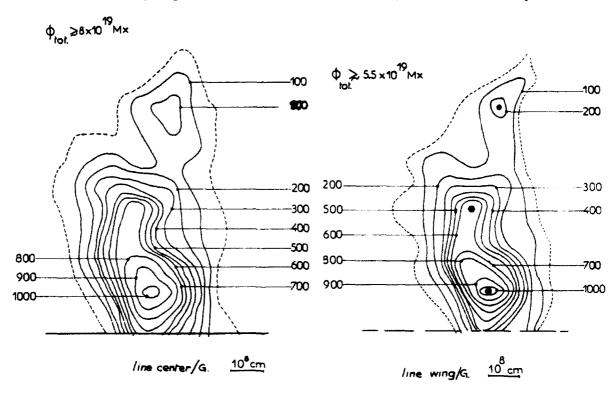


Figure 3. Isogauss maps in a rosette of the chromospheric network obtained by scanning the region and performing a high spatial resolution analysis of polarized spectra of the 630.25 nm line of FeI. A similar map is obtained using the simultaneously observed 630.15 nm line (see Dara and Koutchmy, 1983).

Note that the field seems more concentrated in the deepest layers measured in the wings of the line, compared to result obtained at line center. No corrections are introduced to remove effects of telescope polarization nor effects of the spatial smearing. Numbers are given in gauss.

Stellmacher, 1978. The velocity field was deduced from the 557.6 nm spectra and it has been clear, since that time, that no large downward velocities were observed in the magnetic region, a result largely confirmed by latter results coming from the analysis of FTS polarized spectra. However, the line is wider in the magnetic region and several effects could be responsible for that: turbulent velocities (unresolved) or magnetic effects due to the presence of unresolved fields of parasitic polarity (see further). We first tried to improve these results, by removing effects of 5-min oscillations, see Dara et al., 1987. Nothing really special or conspicuous can be concluded at this point, as a better resolution is needed to investigate the distribution of velocities in the magnetic feature; note that on spectra the continuum brightening, see figure 1, of the magnetic feature is completely washed out by the smearing and a rather lower than the average intensity is observed! Further, few indications can be obtained by trying to correct in

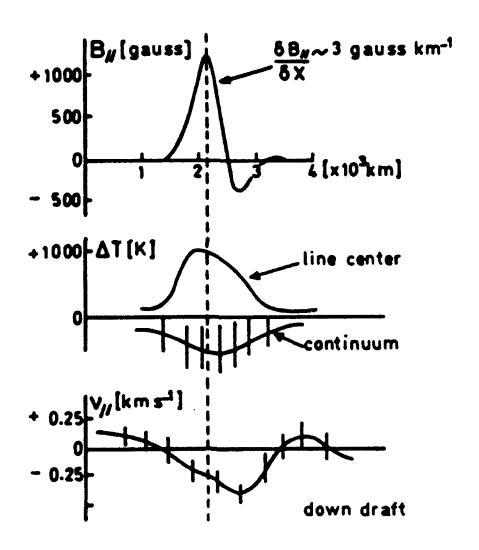


Figure 4. Cross-section obtained when the best resolution polarized spectra, through the maximum of the magnetic-field pattern of figure 3, is deconvolved in the spatial direction. Note that the distance between the opposite polarities is less than 1 arcsec and that a large undetermination appear for the continuum contrast.

S. Koutchmy

the spatial direction the spectrum, as the signal-noise is very high on these polarized spectra. A solution was suggested in Koutchmy and Stellmacher, 1988, with the first indication of a surprising result: a parasitic polarity seems to be present in the concentrated magnetic field region, see figure 4. This is a direct consequence of the non-symmetric distribution of the magnetic signal, of the very high gradient appearing in one wing only and of the effect of the non-magnetic regions on the profiles or, equivalently, of the filling factor. The use of an independent method was needed to confirm this unexpected result.

#### 4. Results coming from the high spatial resolution magnetograms

Several methods can be used to obtain a magnetogram with the UBF, at the VTT. A carefull analysis has been made by L. November (see the present Workshop Proceedings) with the "2-wings" method and by the A. Title group with their own filter, see Title

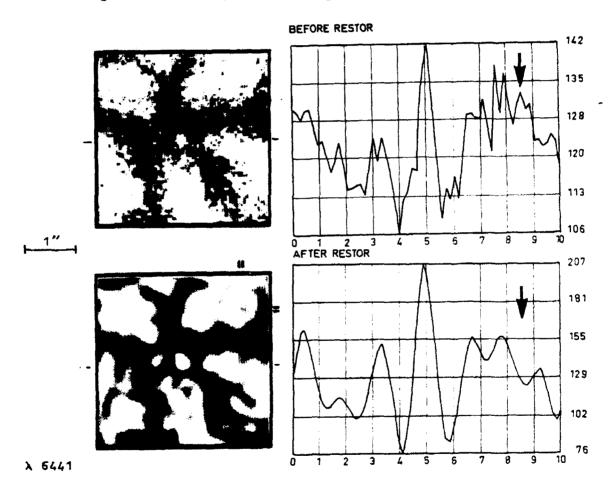


Figure 5. Illustration of how the 2D-Wiener filter works on a noisy picture taken from the observation of filigrees in the true continuum, upper left; results are shown at the bottom left. Quantitative results are presented at right by a scan in intensity performed horizontally through the center of the filigree. The central intensity is almost 2 times higher than in intergranular space.

et al., 1987 for example, using the CCD-imaging method. In order to follow the lines sketched in part 2, we tried the fastest methods, both photographically and with CCDs. Dara et al., 1990, see also the present Proceedings (more results will be published in a forthcoming paper in A.A.) have used the photographic method in taking simultaneously 2 polarized images in the 610.2 nm line of CaI which best fits the spectral width of the UBF filter. The achieved spatial resolution is again limited, due to the difficulties inherent to microdensitometry work and also, to the differential distorsion effects by the Wollastone prism, when images are splitted; finally, the exposure time is not as short as it is needed although few sequences easily reach the subarcsec resolution. More work could be done on them.

One way to improve the resolution, as stated several times here, see formula (3), is to deconvolve integrated pictures. In case of a magnetogram maps of the V-stokes parameter in one wing only, and presumably in the blue wing (see further), will be considered. The first works done on the I-stokes parameter have shown how this technique works and it is worthwhile to illustrate the result namely on this example. Figure 5 shows a region with concentrated magnetic field, following the technique used originally by Dunn and Zirker, to discover the filigrees (scanning the Ha line); it is obtained in the true continuum with granules surrounding it; in this case, the magnetic feature looks roundish and embedded at the crossing of several dark lanes. A 2 D-Wiener filter was used to deconvolve and smooth the noise, see Koutchmy, 1977, with quantitative result shown on the side of figure 5. Note that a tiny feature like a filigree observed in the continuum, see also figure 1, is not only becoming brighter and narrower, but also, new features appear: for example ring-like brightening over a granule (see tick marks) was rather flat (the reality of the feature is confirmed thanks to results obtained using independent pictures); note also that only a 2-D processing brings "new" features : the deconvolution/filtering of the 1-D scan shown at right of figure 5 would have never shown the result as evidenced by the feature appearing under the arrow (a relative minimum appearing at the location of a relative maximum on the original noisy scan). Finally, note the total absence of any Gibbs effect in the final picture. Accordingly, the 2D-Wiener filtering is well suitable for improving noisy pictures or mapping of the magnetic field, provided the smearing can be described with a shift-invariant isotropic real function; as a rule this function possesses extended wings which describe effects often attributed to the scattering light, considerably reducing the contrast.

The last results we want now to discuss come from a recent observation (Feb. 90) done with a CCD-camera and the CHIRP-system, see also Koutchmy et al. in the present proceedings. All conditions discussed in part 2 are satisfied in these observations: magnetograms are obtained at a rate of 4 subtracted full video-CCD frames; the KDP being switched at a frequency of 15 Hz, only 1/15 sec, or 67 msec of time is spent between 2 frames used to build a single magnetogram which is quite fair for 0.16 arcsec pixel size when the seeing is good at SPO (no fast image motion, of course!); then the magnetic signal can be integrated on successive differential frames (single magnetograms) although a spatial smearing occured. On lines 610.2727 nm of CaI with a 7.7 pm shift in blue or red wings successively, and 517.2698 nm b2 of MgI with 5.0 pm shifts, 20 single magnetograms are integrated to form a set of 20 "second generation"

### YEAR MEDICAL

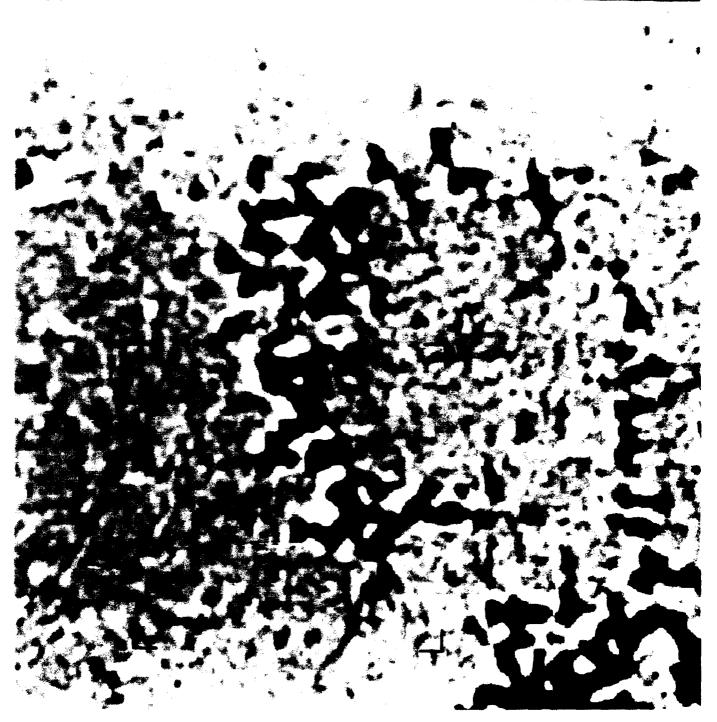


Figure 6. High contrast magnetic map of a moderately plage area outside active regions, to show the distribution of different polarities of magnetic flux elements. The magnetic signal is measured in to the blue wing of 610.2 at 7.5 pm or roughly at the 200-300 km levels above the photosphere. Note the weak field appearing almost everywhere.

magnetograms used to obtain, after integrating again and 2D-Wiener filtering, the best signal-noise ratio magnetogram in the blue or in the red wing of the corresponding line. These 2 spectral lines have shown a quite comparable distribution of the small-scale magnetic features, with ultimate size of order of 0.5 arcsec and smaller and strength (preliminary calibration without removing effects due to the instrumental loss of polarization) in the 1 KG range. A third line was used to show even higher the magnetic field in  $H\alpha$ , with 50 pm shifts; there, the signal is definitely smaller, so a 100 single magnetograms integration rate is used instead of 20. Magnetograms in  $H\alpha$  are very sensitive to the quality of the seeing, suggesting flux tube in fibrils are of very small scale; the field seen at deeper levels appears also on  $H\alpha$  magnetograms, but the distribution is smooth or "diffuse".

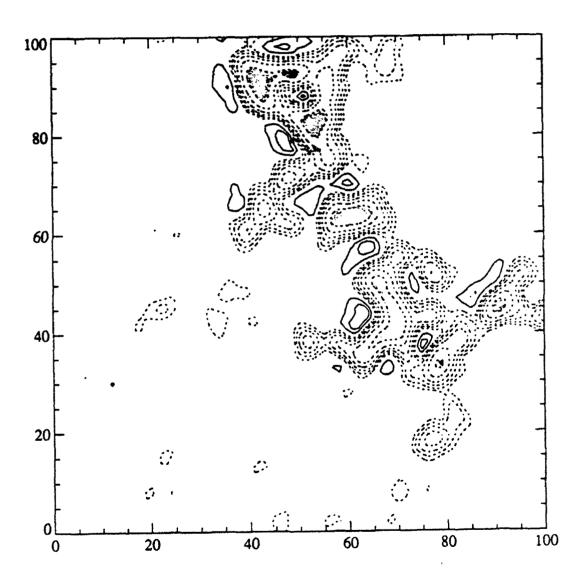


Figure 7. A magnified portion of figure 6;  $16 \times 16$  arcsec size with curves of isogauss, using a threshold level of  $\pm 50$  gauss. Note the distribution of the minor polarities compared to the positions of the dominant polarities.

Many new features appear on the set of filtered magnetograms we obtained with this method, mainly shown on our poster paper (see the present proceedings). One of the main result has been to definitely show the importance of the minor or parasitic polarity occuring almost everywhere close to the dominant concentrated field. This is illustrated on figure 6 which is a well contrasted print of our best photospheric magnetogram in the blue wing of 610.2. Note that the corresponding red-wing magnetogram gives essentially the same result but it shows a more noisy weak field, presumably due to the influence of the red-shifted intensities of intergranular lanes superposed to the magnetic signal. The weak field is also present, in both polarities, almost everywhere. We checked the reality of these features by analyzing sub-sets formed: 1) of the odd and of the even numbers of single magnetograms (presumably uncorrelated), and 2) of the first 10 and of the last 10 magnetograms. Results are consistant and we determined that the smallest flux detected for sure on the resulting magnetogram of figure 6 is certainly less than  $3 \times 10^{16}$  Mx. Many weak bi-poles separated by only 1 arcsec or less are seen. The effective resolution is better than 0.5 arcsec (the resolution corresponding to the Nyquist frequency is 0.32 arcsec). On the last figure 7, we show an enlargement of  $16 \times 16$  arcsec<sup>2</sup> when a threshold is put to make the isogauss map "clear". It shows clearly the location of the minor polarities "inserted" close to the dominant magnetic flux concentration. More results are coming from the comparison of different magnetograms with filtergrams obtained during the same run in the true continuum, in b1+40 pm and in  $H\alpha$ , but this is beyond the scope of this paper.

#### 5. Conclusions

Sub-arcsec magnetography seems to show what could be the start of a new approach to the modeling of flux-tube regions:

- Occurrence of 2 polarities, with one largely dominating polarity which seems to be open toward the chromosphere and possibly the corona;
- Field lines coming from the minor polarity confined to low levels, possibly the canopies;
- Essentially no-downdraft in the dominant polarity, but possibly a downdraft in the minor polarity.

We notice that mixing 2 polarities in a "resolution" element, when low resolution observations are considered, could explain the famous Blue/Red asymmetries of this V-stokes parameter quite simply.

We also show rapidly changing small magnetic flux, especially when weak fields are considered. These fields correspond to fields smaller by at least one order of magnitude; they cannot be detected with the spectroscopic method which uses exposure times exceeding what is required from consideration exposed in part 2. A whole area of new results can be expected when the right methods will be at work.

#### Acknowledgements.

All observations reported here are coming from the VTT of NSO-S.P.O. and the staff of the VTT should be credited from them. During the course of the analysis, which

spends more than 13 years (!), many people have contributed. Among them, I benefited from the skill work and critical approach of G. Stellmacher (IAP) and H. Dara (Athens) and many others, including several students: Fr. Déon, Ch. LePicard, Fr. Lignères, Ali Adjabshirizadeh, Tr. Darvann and Ch. Keller. Finally, Jack Zirker, C. Alissandrakis and O. Koutchmy also brought very much in the course of these works, but I want to stress that in no case one of these persons could be considered responsible for the possible misinterpretation(s) of observations reported here.

#### References

Beckers, J.M. 1976, in "Physics of Solar Planetary Environments", Proc. ISTP, Boulder, vol.1, 89-113

Daras-Papamargaritis, H. and Koutchmy, S. 1983, Astron. Astrophys., 125, 280

Dara, H.C., Alissandrakis, C.E. and Koutchmy, S. 1987 Solar Phys., 109, 19

Dara, H.C., Alissandrakis, C.E. and Koutchmy, S. 1990 Solar Phys., 126, 403

Deinzer, W., Knölker, M. and Voigt, H.H. 1986, "Small-scale Magnetic Flux Concentrations in the Solar Atmosphere", Vandenhoeck and Ruprecht, Göttingen

Dunn, R.B. and Zirker, J.B. 1973, Solar Phys., 33, 281

Harvey, J. 1977, in High lights in Astronomy, vol.4, part II, 223

Koutchmy, S. 1977, Astron. Astrophys., 61, 397

Koutchmy, S. and Stellmacher, G. 1978, Astron. Astrophys., 67, 93

Koutchmy, S. and Stellmacher, G. 1988 in "The role of Fine-Scale Magnetic Fields on the Structure of the solar atmosphere", Schröter et al., Cambridge Univ. Press, 103-109

Martin, S.F. 1988, Solar Physics, 117, 243-259

Schröter, E.H., Wyller, A. and Vasquez, M. 1988, "The role of Fine-Scale Magnetic Fields on the Structure of the Solar Atmosphere", Cambridge University Press, Cambridge

Stenflo, J.O. 1989, Astron. Astrophys. Review, 1

Title, A.M., Tarbell, T.D. and Topka, K.P. 1987, Ap.J., 317, 892

Zwaan, C. 1987, Ann. Rev. Astr. Ap., 25, 83

#### Discussion

Wang: I am worried about the bright ring around the dark magnetic elements. We never see this structure in BBSO magnetograms although we can see intra-network fields better.

Koutchmy: There is no bright around the large amplitude (strength) magnetic elements! The minor polarities are not distributed randomly over this limited field; it seems that they are more numerous on one side (possibly related to their dominant proper motion direction?). The use of the Wiener filter, when the noise is properly taken into account, seems to avoid effects you mentioned (Gibbs effect, etc.). I could have presented a less noisy final results which would have never suggested any "bright ring" effect (not to be confounded with the random noise) but I think it is fair to show also what is our noise.

Harvey: The opposite polarities surrounding the strong magnetic features in your magnetogram resemble ringing (Gibbs phenomenon) associated with Fourier filtering. Did you use such filtering and, if so, did you run tests to determine the amount of the ringing?

Koutchmy: Again, we have nothing like a ringing around strong magnetic features; a minor polarity is seen only on one side. Using the Wiener filter in 2D image restoration does not produce this effect, provided the spectral distribution of the noise is taken into account (see Astron. Astrophys. 61, 1967, 397). Of course this limits the resolution reached; there is no miracle. Using the procedure, many test runs are made with several subsets of the data and the ringing phenomenon is avoided whatever the signal. An additional and convincing check is given by the same filter processing of the  $Mgb_2$  magnetogram: there almost no "new" minor field appears and, of course, no traces of a ringing effect, although the field is not less concentrated.

Solanki: Since visible spectral lines are not completely split outside of spots and pores, a line weakening (i.e. a change of line shape) can also affect the apparent splitting of a line. Therefore, I suggest that in order to make your conclusion that magnetic field and line weakening are not well correlated more reliable, you first combine  $I \pm V$  spectra to a stokes V spectrum and compare this to synthetic V profiles calculated for different temperatures and field strengths.

Koutchmy: Line weakening and magnetic field are well correlated up to a resolution of 0.2 arcsec. There are suggestions that in cases when the minor polarity is close to the dominant magnetic concentration, the line weakening is displayed by an amount  $\leq 0.2$  arcsec; this result seems reliable because it is coming from the comparison of the shape of both magnetic and non-magnetic lines observed strictly simultaneously at the same location of the Sun.

Lites: Can you estimate the lower limit on average field strength within a resolution limit!? If so, do you see any evidence for weak (diffuse) magnetic fields in the photosphere?

Koutchmy: The estimate of the smallest flux we see gives few  $10^{16} Mx$ , which corresponds to a quiet weak field. After restoration, the strength (amplitude) of the field in these very small flux elements is of order of few tens of gauss; polarity are mixed, although even at a distance of 5 to 10 arcsec of the dominant field pattern, the strength seems higher when the polarity corresponds to the dominant field. This effect is more pronounced when the  $Mgb_2$  magnetograms are considered; there, only the dominant polarity seems to exist.

# High Resolution Spectropolarimetry of an Active Region

D. Bonaccini
Arcetri Astrophysical Observatory, Florence (Italy)

E. Landi Degl'Innocenti
Astronomy Department, University of Florence (Italy)

L.A. Smaldone
Physical Sciences Department, University of Naples (Italy)

P. Tamblyn
National Solar Observatory/Sacramento Peak, Sunspot, NM, USA

Abstract: Some spectropolarimetric observations at moderately high spatial resolution are presented. The observations, obtained through a Fabry-Perot interferometer in cascade of an Universal Birefringent Filter, show the high potentiality of this spectroscopic technique for the detailed analysis of solar active regions.

#### Introduction

A new technique is devised to obtain spectropolarimetric observations of photospheric lines in solar active regions. The technique involves the use of an Universal Birefringent Filter (UBF) in combination with a Fabry-Perot Interferometer (FPI) to obtain filtergrams with a spectral resolution of the order of  $3 \times 10^5$  (Bonaccini et al., 1989; Bonaccini and Stauffer, 1990). The polarimetric analysis is performed before the spectral analysis by means of a quarter-wave plate followed by a linear polarizer. The solar radiation collected by the telescope feeds the polarization analyzer, then the UBF and FPI, and is finally collected on a CCD camera which produces a monochromatic image, in right or left circular polarization, of the field of view (see Fig. 1).

The various images, corresponding to different polarization directions and to several wavelengths across a given spectral line, are obtained sequentially in time; by means of a beam-splitter feeding a second CCD camera, a white-light image of the same field of view is also collected simultaneously with each monochromatic image, to give the possibility of carefully removing the seeing induced distortions, via a de-stretching algorithm.

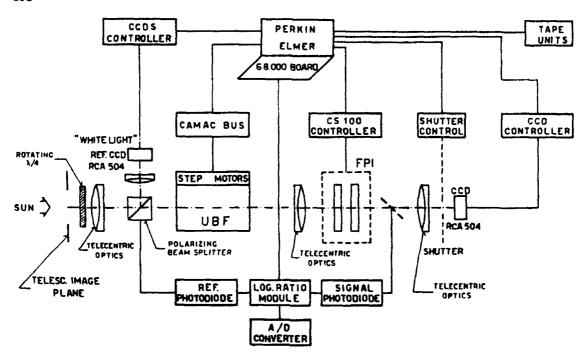


Figure 1: Schematic configuration, at the NSO/SP Vacuum Tower Telescope, of the Universal Birefringent Filter and the Fabry-Perot Interferometer. The telecentric configuration for the UBF and FPI assures the uniformity of the passband on the whole FOV.

The observations have been obtained at the Vacuum Tower Telescope of the National Solar Observatory / Sacramento Peak on August 6, 1988, UT 15:10. They refer to an active region at heliographic latitude 19°.8 N and longitude 0°.6 E (Boulder Number 5101); the observed field of view ( $30 \times 30 \text{ arcsec}^2$ ) partially covers a large pore (or, more probably, an emerging sunspot). The spectral line observed is FeI  $\lambda$  5247.05, with 15 wavelength points across the profile, plus 1 continuum point. The exposure time is 0.5 s for each wavelength and polarization state for a total of 30 s to cover the full line.

First, the filtergrams have been processed to remove systematic errors introduced by the transfer optics and detector response, transparency modulations in the UBF and FPI, and quarter-waveplates retardation changes with wavelength or polarization direction. The monochromatic images have then been "de-stretched" by means of a numerical algorithm due to L. November (November, 1986) and the line profiles corresponding to each pixel (covering an area of  $0.2 \times 0.25$  arcsec<sup>2</sup>) have been recovered through standard techniques. Finally, from the line profiles a set of parameters has been obtained for each pixel in the field of view, such as equivalent width, velocity, magnetic field, and moments of various order. In particular the longitudinal magnetic field has been deduced through the center of gravity method (Rees and Semel, 1979).

#### Results

The spatial resolution achieved, for the velocity and magnetic field, is of the order of 0.8 arcseconds. Looking to the magnetic and velocity maps, we can notice that strong magnetic fields are mainly concentrated in pores and that structures characterized by upward velocities are well correlated with bright features.

The various correlations between different parameters are shown in the form of scatter-plots

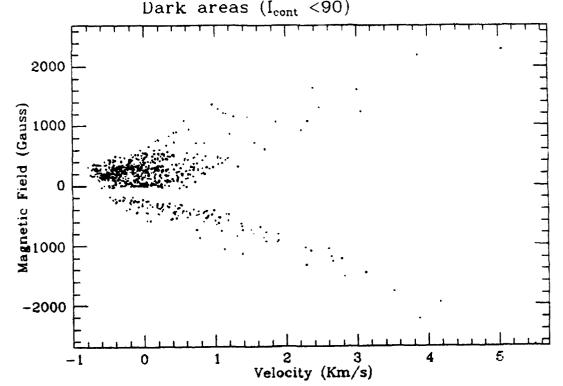


Figure 2: Correlation between magnetic field and velocity for areas having a continuum intensity smaller than 90% of the mean quiet contunuum intensity (dark areas).

(Figures 2-6). As our observed region contained several pore-like structures, we have analyzed separately the regions having a continuum intensity smaller or larger than a threshold value (arbitrarily set to 90% of the mean quiet continuum intensity). For convenience, we refer to these regions with the name of dark areas and bright areas, respectively.

In dark areas, we notice that strong magnetic fields are well correlated with high downdraft velocities, suggesting a linear relationship of the form: B = 500 V, where B is in Gauss and V in Km/s (see Fig. 2). Also, there is a less definite correlation between magnetic field and continuum intensity, the data showing that strong magnetic fields are always found in regions of low  $I_c$ . However, a low value of  $I_c$  does not necessarily imply that B is strong (Fig. 3).

For bright areas, we find a definite correlation between velocity and continuum intensity, the brighter regions being characterized by upward velocities and the darker regions by downward velocities (Fig. 4). This correlation obviously reflects the granular structure of the quiet atmosphere. Where the magnetic field is present, we find that relatively large values of B are associated with lower values of the continuum intensity, thus suggesting a concentration of the magnetic field in intergranular lanes (Fig. 5). However, a definite lack of correlation between B and downdraft velocities (Fig. 6) suggests that the intergranular lanes where the magnetic field is present have a different dynamical behavior from the non-magnetic ones.

Due to the poor seeing conditions at the moment of the observations, these results have to be considered of an exploratory and preliminary nature. They show however the high potentiality of this spectroscopic technique for the detailed analysis of solar active regions.

#### Acknowledgments

We are deeply indebted to the director of the Sacramento Peak Observatory and to the members

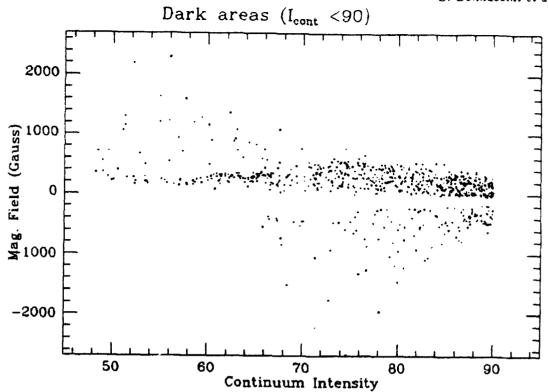


Figure 3: Magnetic field versus continuum intensity for dark areas

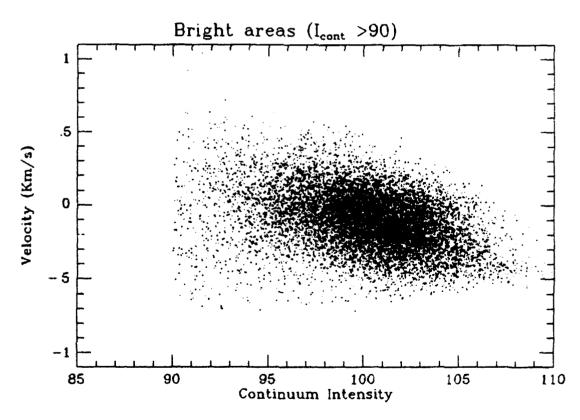


Figure 4: Correlation between velocity field and continuum intensity for pixels having a continuum intensity larger than 90% of the mean quiet continuum intensity (bright areas). Most of the spread in the velocity is due to the 5 minutes oscillations.

many spectra during moments of good stability of the image, optimizing the exposure time (1.5 sec) and the slit-width (0.75 arcsec) to obtain a good signal-noise ratio in the

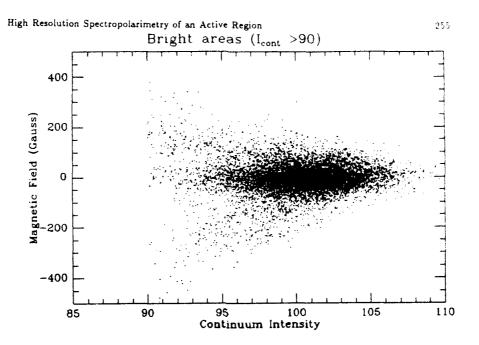


Figure 5: Magnetic field versus continuum intensity for bright areas. The large values of B associated with lower values of the continuum intensity suggest a concentration of B in the intergranular lanes.

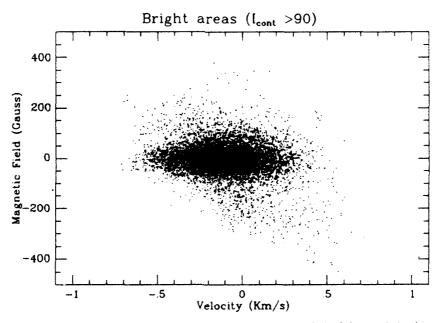


Figure 6: Magnetic field versus velocity for bright areas. One can notice the lack of the correlation between B and V existing in dark areas.

of the VTT staff for the help provided during the observations. Many thanks are due to the Dr. J. Zirker for useful suggestions and to the Dr. L. November for the use of his destretching algorithms.

#### References

Bonaccini D., Cavallini F., Ceppatelli G. and Righini A.: 1989, Astron. Astrophys. 217, 368

Bonaccini D. and Stauffer F.: 1990, Astron. Astrophys. 229, 272

November L.: 1986, Applied Optics 25, 392

Rees D. E. and Semel M. D.: 1979, Astron. Astrophys. 74, 1

#### Discussion

- S. Solanki: Have you also studied the velocity as derived from the Stokes V zero-crossing wavelengths?
- E. Landi: No, but we intend to do it in the following. The zero-crossing of the V Stokes parameter is however more affected by noise than the center of gravity of the intensity profile. Moreover, these two quantities are obviously related to different parameters. The first gives an indication on the line of sight velocity of the magnetic concentrations, while the second rather gives an indication on the average velocity of the area covered by the pixel.
- B. Lites: What is the approximate angular resolution of your profiles?
- E. Landi: The angular resolution is of the order of 1 arcsec.
- L. November: Were the data averaged over the 5 minute oscillations? This must produce noise in any real correlation.
- E. Landi: The data were not averaged over the 5 minutes oscillations. As the scanning time for the whole profile is 30 s, we think that the presence of oscillations is not capable of altering the mean conclusions of this work. However, it is true that the effect of oscillations will show up as an additional source of noise in the scatter-plots.
- A. Cacciani: Can you show us the overall transmission profile of your UBF + FP filter? In particular: 1) What is the wing behavior of this transmission profile? 2) What is its variation from the center to the edge of of the field of view?
- E. Landi: 1) The transmission profile of the UBF with the Fabry Perot interferometer filter has very reduced side lobes, whose detailed behavior and amplitudes depend on the wavelength on which the filter is centered. A quantitative description of the transmission profile at different wavelengths can be found in Bonaccini et al. (1989), Astron. Astrophys 217, 368. 2) Due to the telecentric configuration of the system there are not variations of the transmission profile from the center to the edges of the field of view.
- C. Keller: Could the extremely high temperature sensitivity of Fel 5247.1Å together with different temperatures in the magnetic fields explain the correlation between continuum intensity and flux for the bright areas?
- E. Landi: We think that the correlation between magnetic field and continuum intensity has its most natural explanation in the presence of magnetic fields in intergranular lanes.
- S. Koutchmy: Do you have a plot of magnetic field strength as a function of the central line intensity?
- E. Landi: The only parameters that we have extracted from the data are continuum intensity, center of the line and magnetic field. The last parameters, being deduced from the full line profile, are better determined than the central intensity of the line.

## SMALL SCALE MAGNETIC FIELD MAPPING WITH HIGH TEMPORAL RESOLUTION

H.C. DARA<sup>1</sup>, C.E. ALISSANDRAKIS<sup>2</sup>, and S. KOUTCHMY<sup>3</sup>

- <sup>1</sup> Research Center for Astronomy and Applied Mathematics, Academy of Athens, 14, Anagnostopoulou St., GR-10673, Athens, GREECE.
- <sup>2</sup> Section of Astrophysics, Astronomy and Mechanics Department of Physics, University of Athens, GR-15783, Athens, GREECE.
  - <sup>3</sup> Institut d'Astrophysique, CNRS, 75014 Paris, FRANCE and AFGL, NSO-Sacramento Peak, Sunspot, 88349 NM, USA

ABSTRACT. Two dimensional maps of the longitudinal magnetic field can be readily calculated for small-scale magnetic regions. Here we use an one-hour time sequence of high spatial resolution (0.75 arc sec) filtergrams, obtained at the Sacramento Peak Vacuum Tower Telescope with the universal filter (UBF) in the wings of the magnetically sensitive  $\lambda$  6103 CaI line. The time difference between two magnetic maps is 32 sec. The measurements of the magnetic field in the blue wing are about 40% higher than in the red wing.

#### 1.-INTRODUCTION

Small-scale magnetic fields far from active regions have been the subject of many publications in the last two decades (Frazier and Stenflo, 1972; Howard and Stenflo 1972; Koutchmy and Stellmacher 1978; Stenflo and Harvey, 1985; Title et al, 1987; Grossmann-Doerth et al, 1989). Efforts have been made for high spatial resolution observations, but the question of whether small-scale magnetic fields are unresolved and thus quite strong, even when they appear weak, is still open. If the spatial resolution is poor, it is not easy to evaluate the contribution of each of the fine structures seen in a high resolution observation; still, even in high resolution observations there may be unresolved "flux tubes" as Stenflo (1973) has inferred.

In a previous publication we presented maps of small-scale magnetic fields obtained from high resolution spectra (Dara and Koutchmy, 1983); these were constructed from one dimensional measurements, therefore were not instantaneous. In this paper we present two dimensional magnetic maps using high resolution filtergrams and we discuss the blue-red asymmetry and the limitations of the observations.

#### 2.- OBSERVATIONS

High resolution (0.75 arc sec) filtergrams were obtained with the Tower telescope and the universal filter (UBF) of the Sacramento Peak Observatory. Each wing of 6103 Ca I was simultaneously observed in right and left circularly polarized light, consequently the atmospheric

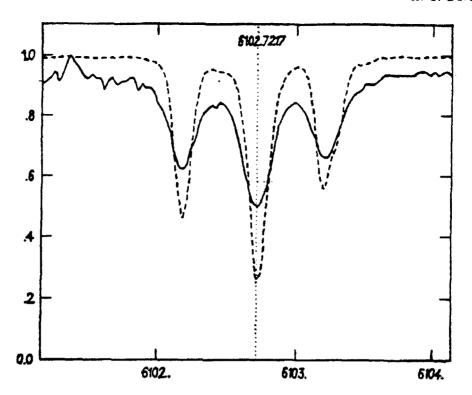


Figure 1: The dashed curve shows the line profile from the AFGL Atlas, while the solid curve is the scan of the line profile obtained with the UBF over an out of focus image of the sun at the center of the disk.

distortion was the same for both polarizations. A Wollastone prism was used for the separation of the two polarizations. The positions where we centered the filter in the blue and the red wing were those which gave the best signal to noise ratio for the magnetic field and were determined empirically; the shift from the line center was  $\pm 70$  mÅ. The UBF was carefully checked before the run and the small line shift due to the solar rotation was taken into account.

The filter bandwidth at 6103 Å was 186 mÅ, while the scale of the image on the film was 10 arc sec/mm. The field of view was 100 by 200 arc sec and the telescope was pointed in a quiet region near the center of the disk, at N18 W12.

The vignetting effect was important, therefore flat-field pictures, with the solar image outfocused, were used for the correction. A step wedge was used for the photometric calibration.

We digitized the best frames at each wavelength with the fast microphotometer of Sac Peak and got an equivalent matrix of 700 by 780 pixels. The spot size was 0.7 arc sec and the sampling step 0.3 arc sec. We selected two regions for mapping of the magnetic field; one region was bipolar, while the other was unipolar with two separate components.

#### 3.- DATA REDUCTION AND RESULTS

Magnetograms were obtained using the "weak field" approximation. Under this assumption, the subtraction of the two opposite polarity images in each wing gives a signal proportional to

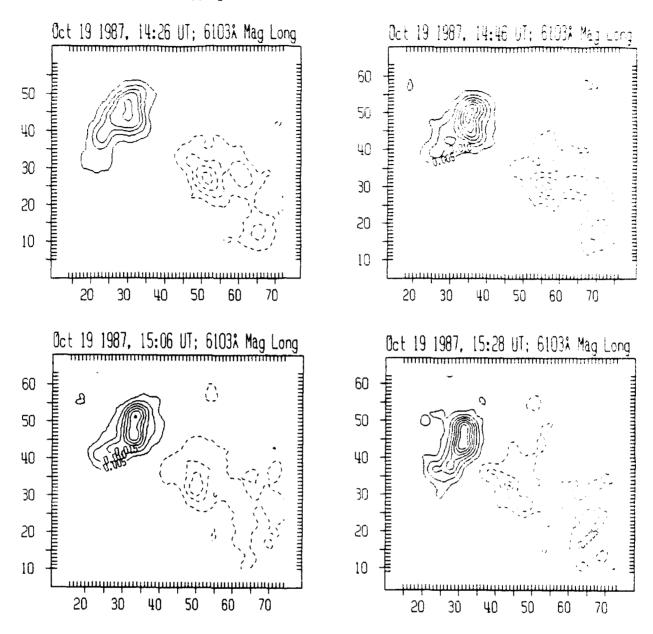


Figure 2: Magnetic field maps of the measured longitudinal component for a bipolar region. Each map is the result of averaging of 5 min of observations. Solid and dashed contours indicate positive and negative polarities; contours are in steps of 0.3% contrast (~30 Gauss). Tickmarks are every 0.3 arc sec.

the Zeeman shift and the derivative of the line profile; the reference profile was obtained with the UBF at the center of the disk, with the solar image outfocused (Figure 1).

For each wing the superposition of the two opposite circular polarization pictures was carried out on the computer screen, by moving one picture with respect to the other, until a uniform background away form the magnetic regions was obtained on the subtracted image. The final magnetic map is the average of the maps in the two wings, which were superposed using the same method.

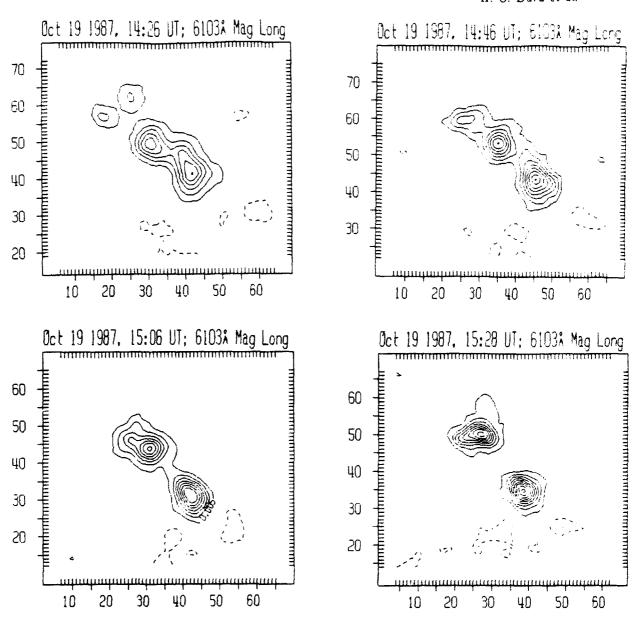


Figure 3: Magnetic field maps similar to those of figure 2, but for the unipolar region.

Figures 2 and 3 give the maps of both regions, averaged further over a five minute interval in order to reduce the effect of the five-minute oscillations and to improve the signal to noise ratio, at the expense of a slightly degraded spatial resolution. The total flux in both regions is of the order of 10<sup>19</sup> Mx. The maximum magnetic field in both regions is 330 Gauss.

Choosing the best filtergrams of the sequence we compared the measurements of the longitudinal magnetic field in the red and in the blue wing (Figure 4). In both regions the measurements of the magnetic field were higher in the blue than in the red wing, which is a manifestation of the well-known blue-red asymmetry of the line profile. The slope of the red-blue regression lines is 0.7, that is the values measured in the blue wing were 40% higher than those of the red.

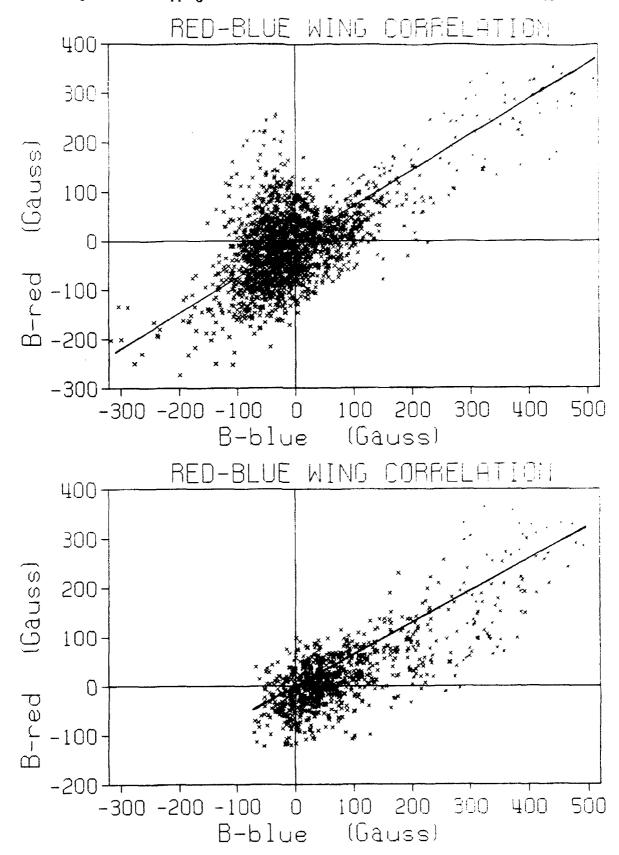


Figure 4: Correlation diagram between the values of the longitudinal magnetic field in the red wing and those in the blue wing, for the two regions: (a) bipolar and (b) unipolar.

#### 4.- DISCUSSION

The values of the magnetic field intensity that we obtained using the "weak field" approximation are lower than the true peak intensity because we used a non-magnetic Stokes I profile as reference. The I profile in a magnetic region would be less deep and the slope in the wings would be smaller, leading to an underestimation of the magnetic field intensity. The observed values are reduced further due to loss of circular polarization by the telescope optics and the entrance window (the loss because of the window is about 20%). It is also possible that mixed polarities which cannot be resolved might be present inside the dominant polarity region, reducing even further the values of the intensity of this dominant polarity.

These two factors, together with the effect of spatial resolution which is still insufficient to show the elementary flux-tubes can reduce a kG field to the observed values. Moreover the presence of unresolved mixed polarity field may have an important effect on the red-blue asymmetry.

However, although the magnetic field is underestimated, these magnetograms have the advantage of a satisfactory spatial resolution; moreover, since a map can be obtained every 32 sec, changes of the magnetic features can be closely followed.

#### **REFERENCES**

Dara, H. C. and Koutchmy, S.: 1983, Astron. Astrophys., 125, 280.

Frazier, E. N. and Stenflo, J. O.: 1972, Solar Phys., 27, 330.

Grossmann-Doerth, U., Schüssler, U. and Solanki, S. K.: 1989, Astron. Astrophys., 221, 338.

Howard, R. and Stenflo, J. O.: 1972, Solar Phys., 22, 402.

Koutchmy, S. and Stellmacher, G.: 1978, Astron. Astrophys., 67, 93.

Stenflo, J. O.: 1973, Solar Phys., 32, 41.

Stenflo, J. O. and Harvey, J. M.: 1985, Solar Phys., 95, 99.

Title, A.M., Tarbell, T.D. and Topka, K.P.: 1987, Astrophys. J., 317, 892.

Acknowledgements

The analysis presented here was taken during the stay of two of us (H.D. and S.K.) at SPO. We are grateful to the staff, and especially to Dr. Larry November for their valuable assistance. The authors who stayed at SPO would like to thank the director Dr. Ray Smartt for his kind hospitality and financial support. Travel funds between Greece and France have been covered by the Greek Secretariat for Research and Technology.

# HIGH SPATIAL RESOLUTION V-STOKES POLARIMETRY TO MEASURE THE ZEEMAN EFFECT IN FLUX TUBES AND PROMINENCE FILAMENT THREADS

Serge Koutchmy<sup>1</sup>, Jack B. Zirker<sup>2</sup>, Tron Darvann<sup>3</sup>, Olga Koutchmy<sup>4</sup>, Fritz Stauffer<sup>2</sup>, Richard Mann<sup>1</sup>, Roy Coulter<sup>1</sup>, and Steve Hegwer<sup>1</sup>

Paris Institut d'Astrophysique, CNRS, France

<sup>2</sup>National Solar Observatory/Sacramento Peak, Sunspot, NM USA<sup>1</sup>

<sup>3</sup>Oslo Institut of Astronomy, Norway

<sup>4</sup>Paris University P & M Curie, France

The "CHIRP"\* real-time video processor has been used in conjunction with an RCA-504 CCD-camera at the exit of the UBF filter of the VTT of NSO/SP. Video-magnetograms were obtained consecutively in the blue and in the red wings by integrating short sequences of subtracted images in left and right circular polarized light. A 42x42 arcsec region situated close to the disc-center, in the vicinity of the "feet" of a large filament, has been chosen for the analysis of "plagettes" and flux-tube regions, see Figure 1 and 2. Magnetograms were obtained using 3 different lines corresponding to 3 levels of the low solar atmosphere: 610.27nm line of CaI to measure magnetic fluxes at the photospheric level; the 517.27nm b2 line of MgI (core of the line is used) for the

Operated by the Association of Universities for Research in Astronomy, Inc. (AURA) under cooperative agreement with the National Science Foundation.

low-chromosphere level and the 656.28nm H $\alpha$  line (medium wings are used) for the typical chromosphere level. Single magnetograms and preliminary results have been already presented at the last SPD-AAS Meeting.

On figures 3a to c, we show samples of our best magnetograms, processed in order to increase as much as possible the visibility of the smallest magnetic fluxes and to illustrate the statistically significant contribution in flux—tube regions of the subordinate polarity in mixing polarities at the <u>sub—arcsec scales</u>. The phenomenon is clearly demonstrated on the photospheric magnetograms; it is completely absent in the low—chromosphere magnetograms, although the same field strengths are observed over the dominant polarity and exactly the same data—processing has been applied to the data—set.

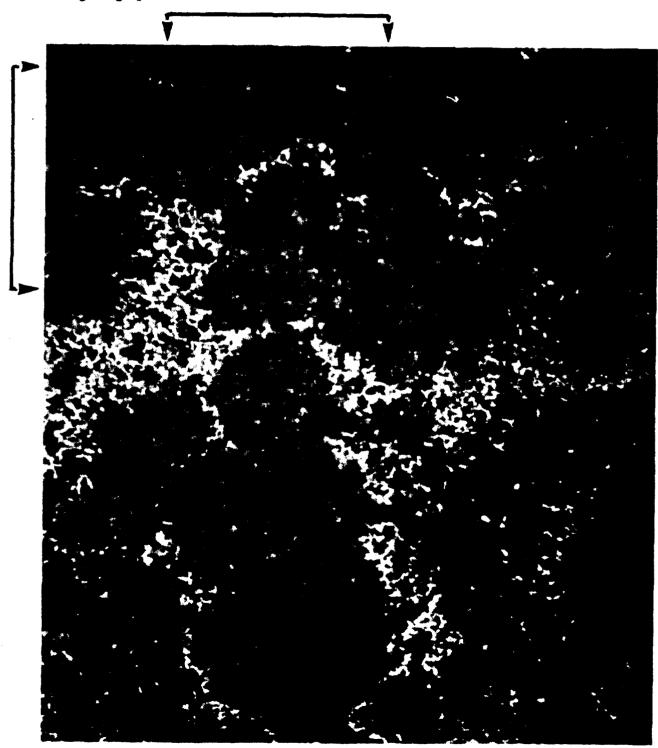
Absolute calibration of magnetic fluxes has been attempted using two methods: a) using simultaneous observations performed with the Echelle spectrograph to visually measure the Zeeman splitting in 1 KG field regions and b) by measuring the absolute value of the circular polarization degrees. Typical field strengths are indeed at their maximum of order of 1 KG for both the photospheric and the low chromosphere magnetograms.

Figure 4 shows the relation between the strengths of the field as measured in the blue and in the red wings: at this resolution only a small asymmetry is observed for the weakest fields in the photospheric line and a reversed effect seems to be observed in the chromospheric line.

The spatial correlation is excellent between filtergrams in  $b_1$ — 40 pm and both photospheric and low chromosphere magnetograms. The H $\alpha$  magnetograms clearly show the plagette which seems surprising, in view of the conventional picture of field lines spreading with height onto the middle chromosphere. H $\alpha$  fibrils are also seen but their footpoints are not clearly apparent.

#### FIGURE 2

Filtergram observed in the wing of the b1 line of MgI, to show regions of temperature excess co-spatial with the concentrated magnetic fields (the bright network). Note that at this scale, flux tubes are confined to regions forming a filigree pattern and sometimes to single knots. The same region, observed simultaneously, is shown in Figure 2', in the deepest layers of the true green continuum and on Figure 2'', in the highest layers at the H $\alpha$  line center. The part of the field analyzed in great detail with the new SPO video-magnetograph is shown.



#### FIGURE 1

Full solar disc picture in H $\alpha$  taken at the Hilltop facility of SPO on February 25, 1990, 16:00 U.T. The region corresponding to the b<sub>1</sub>-40pm filtergram of Figure 2 is shown with yellow contours.

N

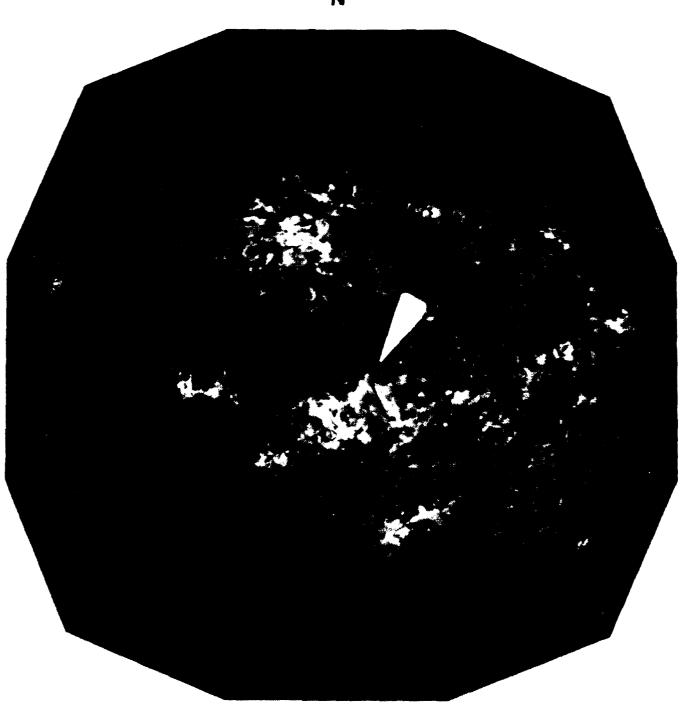
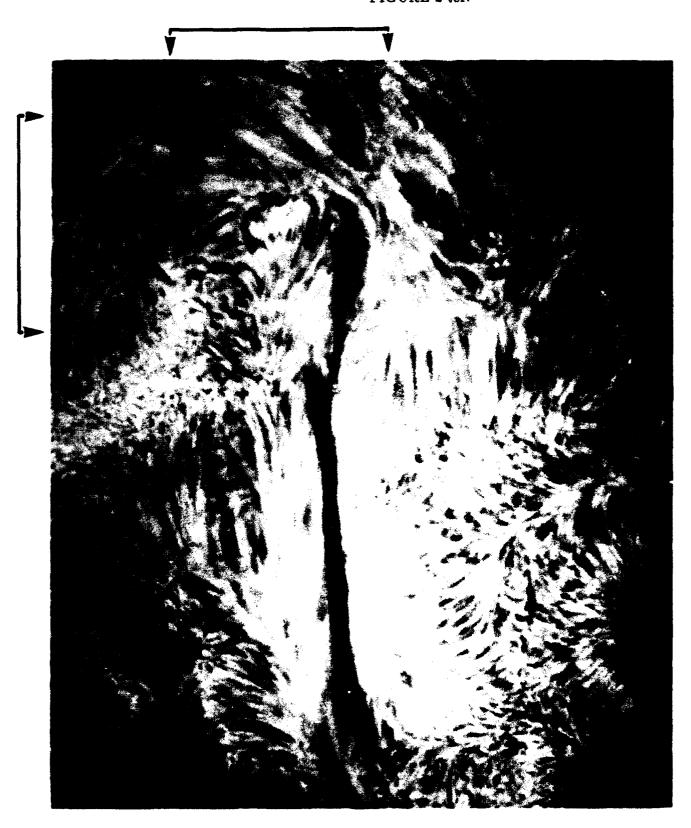
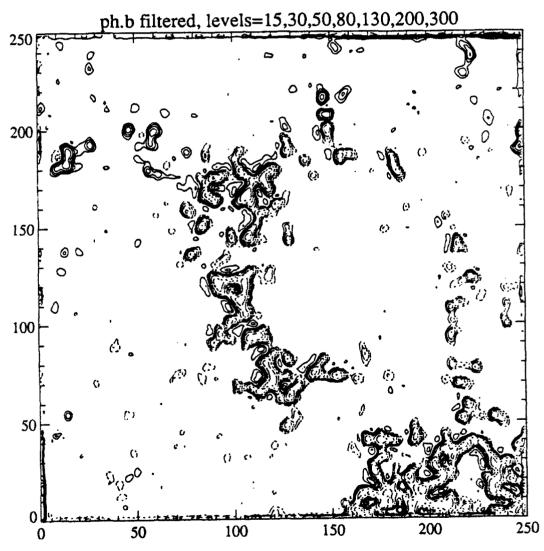


FIGURE 2 ter.



Photospheric magnetogram obtained in the blue wing of the 612.27 nm line of CaI, at -7.5 pm. Levels are shown in relative units (typically 1 unit  $\approx$  2 gauss, without making corrections for the loss of polarisation due to the telescope) in dashed or continuum lines, depending on the polarity. Note the scale: 1 px is 0.16 arcsec, so the resolution achieved after using the Wiener filter is of order of 0.4 arcsec or better; the full frame shown has a size of  $40 \times 40$  arcsec<sup>2</sup>, and 400 single magnetograms are superposed to improve the signal to noise ratio before processing the frame (100 sec integration time). The orientation of the magnetogram corresponds to a  $90^{\circ}$  clockwise rotation when compared to figures 2 and the distorsion present in the original magnetograms has been corrected. The correlation between flux concentration and MgI b1 + 40 pm is excellent.



ph.b filtered, levels=-15,-30,-50,-80,-130,-200,-300,-500

Figure 6: Magnetic field versus velocity for bright areas. One can notice the lack of the correlation between B and V existing in dark areas.

High Spatial Resolution V-Stokes Polarimetry

#### 2-73

#### FIGURE 3b

Chromospheric magnetogram obtained in the blue wing of the 517.27 nm b2 line of MgI at -5.0 pm. The scale is slightly different from the scale of figure 3-a but the resolution is the same. Note that the size of fluxules of the dominant polarity are typically the same as those of figure 3a corresponding to photospheric levels, but the mixed polarity is almost absent (compare also with figure 3-c). The magnetogram corresponds to a 100 sec integration, as on figure 3-a, but it has been obtained 2.5 min later.

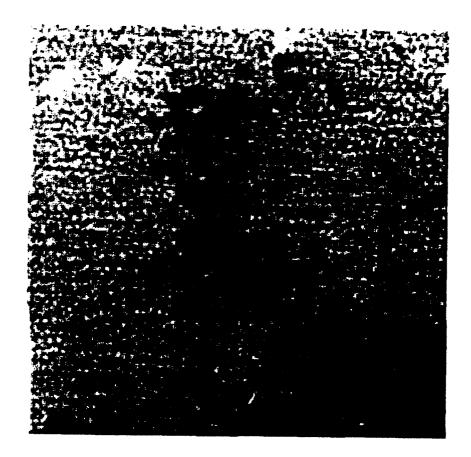


#### FIGURE 3c

The mixed-po'arity contribution is dramatically illustrated on a display with white-dashed lines for the minor polarity and in weakly dark for the dominant polarity (see also figure 3-a), the average background level being grey. Note that the minor polarities close to the dominant field concentrations are not distributed around it but seem to occur on the side turned to the upper corner where concentrations of reversed polarity occur. Tick marks point to a fluxule element consistently observed during 100 sec with a value corresponding to  $4 \times 10^{16}$  Mx and a 40 gauss amplitude.

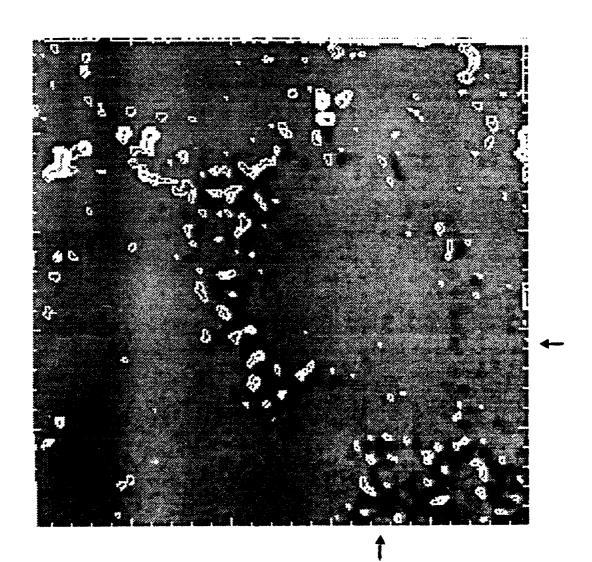
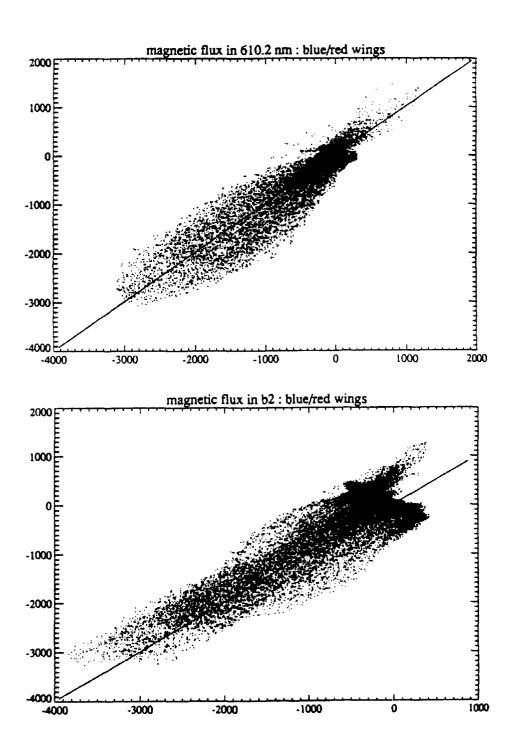


#### FIGURE 4

Diagram illustrating the relation between magnetic fluxes per pixel observed in the blue wing, as compared to what is observed in the red wing of the line. A rather very small blue/red asymmetry is observed in the photospheric line and a reversed effect in the low-chromospheric line.



## Visualization of Intergranular Magnetic Fields

H.Lundstedt A.Johannesson Lund Observatory, Box 43, S-221 00 Lund, Sweden

Birgitta Larsson
Institute of Mathematical and Physical Sciences
University of Tromsö, P.O.Box 953, N-9001 Tromsö, Norway

#### Abstract

A new method of displaying white light images and corresponding simultaneous magnetograms was presented. The method made it possible to identify intergranular magnetic fields. The magnetograms were recorded with the Swedish Solar Telescope on La Palma, Canary Islands.

### 1 Introduction

The purpose of this paper was to introduce a new method of visualizing intergranular fields. The method uses colors and since color images were not reproducible in this proceeding we will only discuss the method. Interested may receive copies of the color slide which was presented at the meeting.

## 2 Simultaneous Stokes I-, and Stokes V/I-images

The Stokes I-, and Stokes V/I-images shown in Figure 1, were recorded in the blue wing of the FeI-spectral line at wavelength 525.022 nm. We used a polarizing beamsplitter and obtained herewith strictly simultaneous images of Stokes I and V/I (Lundstedt, 1987; 1989; Lundstedt et al., 1990; Lundstedt and Johannesson, 1990). The images cover a very small area of the sun, about 20 square arcseconds. The two sets of Stokes I-, and V/I-images, were separated by 11 minutes.

The upper and lower left images illustrate Stokes I images produced by a burst of 40 oppositely polarized images recorded on May 21, 1989. Images upper and lower right



Figure 1: Stokes I- (left images), and Stokes V/I-images obtained with the Swedish solar telescope on La Palma, Canary Islands. The smallest magnetic elements are in the order of 0.3 - 0.4 arcseconds.

illustrate Stokes V/I images produced out of the same burst of oppositely polarized images. The upper magnetogram was recorded in the long wavelength wing of the iron line, while the lower magnetogram, recorded some II minutes later, was done in the shortwavelength wing of iron. In the lower magnetogram light areas represent magnetic fields directed outward while the dark areas are magnetic fields directed inwards. The smallest magnetic elements are in the order of 0.3 - 0.4 arcseconds. The Stokes V/I-signal in the images peaks at about 6%.

## 3 New Representation of Magnetograms

The strictly simultaneous measurements of Stokes I and V calls for a proper representation. The classical way of displaying white light images and magnetograms in a gray scale is not sufficient for detailed studies. Instead we suggest the use of colors and gray scale simultaneously. This gives the possibility to show both intensity and polarization in the same image.

274 H. Lundstedt et al.

In practice such an RGB image consists of three planes and is formed as follows:

```
r_{ij} = \text{STOKES I} + (\text{STOKES V} + | \text{STOKES V} |)/2
```

 $g_{ij} = STOKESI$ 

 $b_{ij} = \text{STOKES I} + (-\text{STOKES V} + |\text{STOKES V}|)/2$ 

The color and intensity for each pixel are then a linear combination of RGB.

## 4 Magnetic Features

By superimposing the magnetic flux structures, colored, on images of the photosphere the position of the flux relative the photosphere structure were easily studied.

In the first superimposed image (left in hama viewer, shown at the meeting) the magnetic flux outlines, as expected, areas of pores. The positive (blue) polarity clearly dominates. Very little of negative (red) polarity is visible. In the second colored image (right in hama viewer) (11 minutes later) an area of negative polarity, of non-pores has moved in. This flux area outlines an area of disturbed granulation. It may also be noticed that the granules have totally changed between the two images. In the two images there is no flux in the inner part of any granule. On the other hand the magnetic flux outlines the borders of granules, i.e. the flux appears as intergranular (Title et.al.,1987) magnetic fields. The flux is also highly fragmented and nowhere is the flux smooth over areas.

## 5 References

Lundstedt, H.: 1987, Magnetic Field Measurements with the Swed ish Solar Telescope on La Palma, in Proc. of Inaugural Workshop and Round Table Discussion for the D-E-S Telescope Installation on Canary Islands, eds. E.-H. Schröter, M. Vázquez and Arne Wyller, p.343.

Lundstedt, H.: 1989, A High Resolution Magnetograph for the Swedish Solar Telescope on La Palma, in "High Spatial Resolution Solar Observatiosn", 10:th Sacramento Peak Summer Workshop, Sunspot, New Mexico, ed. O. von der Lühe.

Lundstedt, H., Johannesson, A., Scharmer, G., Stenflo, J.O., Kusoffsky, U. and Larsson, B.: 1990, Magnetograph Observations with The Swedish Solar Telescope on La Palma, Solar Physics (in press).

Lundstedt, H. and Johannesson, A.: 1990, CCD-Magnetograms observed with the

Swedish Solar Telescope on La Palma, in Proc. of Astrophysical Processes and Structures in the Universe, Nordic-Baltic Meeting, Uppsala 18-21 June 1990, Sweden.

Title, A.M., Tarbell, T.D. and Topka., K.P.: 1987, On the relation between magnetic field structures and granulation, Astrophysical Journal, 317, 892-899.

## ON THE COMPLEXITY AND REACTIVITY OF MAGNETIC FEATURES IN SOLAR ACTIVE REGIONS

J. LINKE \*

Institute of Terrestrial Magnetism, Ionosphere and Radiowave Propagation - Troitsk, Moscow region, USSR

SUMMARY. In this paper an empirical method of a semi quantitative analysis of the complexity and of the reactivity of ensembles of magnetic features in the solar photosphere in the considered active regions is proposed and briefly discussed. For this analysis we use photospheric photo heliograms and vector magnetograms as material of observations and the possibilities of the two-dimensional topology as theoretical tool.

#### 1. INTRODUCTION

We know that the understanding of the processes in the solar atmosphere, like reconnection, flares and other effects appears to be found in the MHD processes in the basic magnetic elements ('micro scale'); see e.g. Stenflo (1989), and references in this. The investigation of an ensemble of flux tubes in the frame of non-symmetry magnetic hydrodynamic (MHD) -approximation is yet impossible. Several studies of the characteristic of the magnetic field of active regions in the 'macro scale' have been published ( e.g. Klimchuk, 1987; Schrijver, 1987, 1989; Chumac, 1989; Howard, and references in this, 1989). In our paper one method of a semi quantitative analysis of the complexity and of the reactivity of magnetic features in the 'macro scale' of a solar active region will be proposed and discussed.

#### 2. METHOD OF ANALYSIS

Many of magnetograms and other observation materials appear to show that the distribution of the longitudinal magnetic field  $B_{\rm Z}$  at and in the vicinnity of sunspots/pores in the photosphere has discretely concentrated structures. In connection with this fact, these magnetic features of different magnetic polarities at the photosphere may be considered as local sources by which the whole magnetic field on the photosphere is formed.

To characterize the magnetic complexity of active regions we propose to use the number of magnetic saddle points NSP in the frame of a two-dimensional system (photospheric sphere) of the considered region. Molodensky and Syrovatsky (1977) applied successfuly the mathematical tool of the Poincaré index to

<sup>\*</sup> On leave from Central Institute of Astrophysics, Potsdam, Sonnenobservatorium Einsteinturm, GDR

magnetic fields. Sources and sinks of the magnetic field like sunspots or pores have in this frame the Poincaré index of +1. But the magnetic saddle points have the index of -1. If we suppose that the magnetic flux in the region considered is balanced, and that the net 'dipole moment is non-zero than this region is regarded as an dipole when his seen from large distances, when its Poincaré index is 2. This is equivalent to the Theorem of Euler for the characteristic X(Q) of a surface Q, with X(Q) = 2). Therefore, NN + NS - NSF = X(Q), where NN and NS are the numbers of sources/sinks, and NSP is the number of saddle points. But the observers get in general only information on a part of the whole magnetic field structures at the photosphere. In order to eliminate the disbalance of magnetic flux of opposite signs we use the modified form of the theorem of Euler for the case of a sphere with holes. That means, X(Q) is reduced by the difference of the numbers of the observed magnetic features of opposite polarities. Hence we get the following equation for the number of saddle points as the empirical parameter of the complexity of the considered active region, dependent from the observation time to, the spatial resolution, and temporal resolution of the used materials of observation :

$$NSP(to) = NN(to) + NS(to) - X(Q,to)$$
 (1)

with 
$$X(Q,t_0) = 2 + / NN(t_0) - NS(t_0) /$$
 (2).

The numbers of the magnetic features NN(to) and NS(to) can be detected by means of different ways. We can use photo heliograms of the considered active region together with maps of the longitudinal magnetic field component (Bz) or the Bz - maps together with the maps of the signal - intensity and the maps of the transverse magnetic field in the frame of interactive image processing routines (see e.g. Kazmierzak, 1980). For the evaluation of the reactivity REC(to) of the interacting resolved magnetic features of the considered active region we introduce the following empirical equation:

$$REC(to) = Cqp (NSP(to)+1) (NN(to) NS(to))/(\pi r(to)^{2})$$
 (3)

where the parameters NSP(to), NN(to), and NS(to) come from above equations (1) and (2). The parameter r(to) is the minimal distance among the magnetic features of different signs at the considered active region at the time to. The parameter Cqp is the inverse reactivity parameter for the case of the ideal quadrupol configuration with the value of r(to) = 10 arc sec. The physical dominant 'micro scale' mechanisms for the empirical parameter REC(to) may be the local electric current loop coalescence and the local nonlinear kink instability. For the case NSP = 0 only the second mechanism is working in the first order.

#### 3. EXAMPLES AND DISCUSSION

A general illustration of the idea of the parameters introduced

above gives the 'Sea serpent' process model for the emergence and the disappearance of flux through the surface (Spruit et al., 1987): . The parameters of complexity and reactivity are crowing in the time where the emergence take place. After the reconnection the values of the parameters are lower then at the moment before the emergence took place. The application of the method introduced above to an analytical force-free magnetic field model (Low, 1982, 1989) gives the following result. Using the value 2 (apparent quadrupol model) for the parameter of complexity NSP, the reactivity parameter is crowing with the smaller distance between the centers of the magnetic features of opposite polarities in the considered region, generated by the simulated crowing of the magnetic shear. For the application of the method described above to observation data, we have checked about 30 examples. Our resulting material shows that the eruptive processes as reconnection, flares and others appear to take place in the regions of two neighbouring magnetic opposite polarities if the distances between their centers r(t) decrease with the time t. But we could not detect such effect if the value of r(t) is nearly constant and greater than r(t) of the model parameter Cqp in time or is growing with time. This result continous the earlier results, by Martres et al. (1974). Let us demonstrate briefly the significant case of comparison between two moments of the active region AR 4201 June 1983 (see Ruzdjak et al., 1986. At June 3 in this region were some large flares. But at the June 7 this region was without significant eruptive effects. The NSP - parameter for the active region June 3 is lower as for this region at June 7. But the REC parameter shows the inverse behavior. The distribution of the magnetic feature for the first day was more compact (has a higher 'symmetry') as the distribution of the magnetic feature for the second considered day.

Our first results show that the empirical parameters NSP(to) and REC(to) appear to be useful for a semi quantitative analysis of the degree of complexity and of the reactivity of solar active regions in the frame of spatial and temporal resolution of the used photo heliograms and vector magnetograms.

#### **ACKNOWLEDGEMENT**

This work was granted by USSR Academy of Sciences through project 'ENERGY'. For the helpful discussions the author would like to thank especially Dr. V.L. Selivanov, Dr. V.N. Obridko, and Dr.G.V. Kuklin.

#### REFERENCES

Chumac, O.V.: 1989, (private communication, preprint). Howard, R.F.: 1989, Solar Physics 123, 271. Kazmierzak, H.: 1980, in 'Erfassung und maschinelle Verarbeitung von Bilddaten', Akademie Verlag, Berl. S. 145. Klimchuk, J.A.: 1987, Astrophys. J. 323, 368.

Klimchuk, J.A.: 1987, Astrophys. J. 323, 368.
Low, B.C.: 1982, Solar Physics 77, 43.

1988, Solar Physics 115, 269.

Martres, M.J.,:: 1974, in 'Flare Related Field Dynamics 'Rayrole, J., Ribes, E. Proceedings of the Conference held in Semel, M. Sou-Escout I. Boulder, Colorado, 23-25 September.

Molodensky, M.M.: 1977, Astron. J. (USSR) 54, 1293.

and Syrovatsky S.I.

Ruzdjak, V. Vrsnak, N.: 1986, Contribution Astron. Observatory Hofmann, A., Krivsky, L., Skalnate Pleso 15, 55.

Markova, E., and Kalman, B.

Schrijver, C.J.: 1987, Astron. Astrophys. 180, 241. 1989, Solar Physics 122, 193. Spruit, H.C.: 1987, Solar Physics 110, 115.

Titel, A.M., and van Ballegooijen, A.A.
Stenflo, J.O.: 1989, in 'The Astronomy & Astrophysics
Review' 1, 3.

## THE CHARACTER OF VELOCITY FIELD DISTRIBUTION IN THE QUIESCENT FILAMENT REGION

Ioshpa B.A.

Institute of Terrestrial Magnetism, Ionosphere and Radio Wave Propagation of Academia of Sciences of USSR Troitsk, Moscow Region, USSR

KogevatovI.E. and Kulikova E.H. Radiophysical Institute, Gorky, USSR

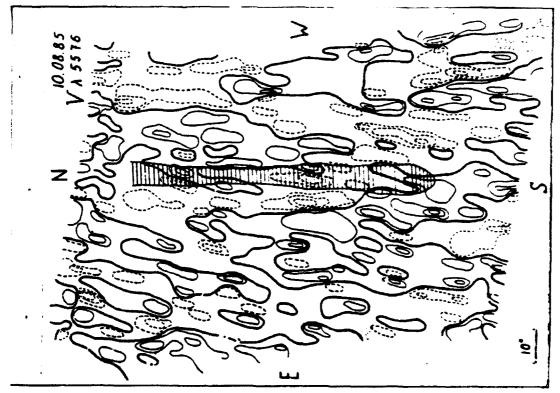
Summary. The results of the investigation of the velocity field in the photosphere under the quiescent filaments are discussed. The measurements were carried simultaneously in two lines with the help of the magnetograph and the integro-interference spectrometer. The method of determination the horizontal velocity structure from the measured vertical velocities is proposed. The calculated velocity distribution shows the rapid change of the direction of the horizontal flows near the filament.

The investigation of velocity distribution in regions under H $\alpha$ -filaments is very important because it may give a clue to the understanding of the processes leading to energy storage, the character of the prominence stability and so on. Many papers were devoted to this problem recently ( see the survey of Schmieder, 1988), but the results of different authors are controversial and the problem is far from clearness.

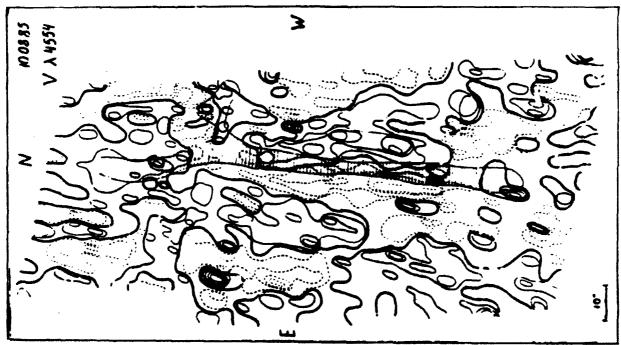
Here we give some results of the investigation of the velocity fields near a quiescent filament in the photosphere observed during 1984-1985 with the magnetograph (Ioshpa, 1962) and integro-interference spectrometer IIS(Kogevatov, 1983). Observations on both instruments were carried out simultaneously in two lines: Ba II  $\lambda$  4554 A (magnetograph) and  $\lambda$  Fe 5576 A, g=0 (IIS). We chose for an analysis the most stable parts of the quiescent filaments far from active regions. Simultaneously, we obtained Ha-filtergrams using the solar light reflected from the mirror entrance slit of the spectrograph. Besides we used Ha-filtergrams obtained with the Opton Ha -filter obtained several hours before and after the velocity observations. During the analysis we account for 5-min oscillations. A part of our data was analyzed and described by Ioshpa and Kulikova, 1988, 1989.

Here, we sum up the results of analysis of the data obtained in three observational periods (September 1984; the end of August - beginning of September 1985; August 9-14, 1985).

- 1 The stable parts of filaments lie near the boundary between the sinking and the rising plasma regions. These regions have a tendency to be stretched along the filament axis. The line V=0 and the neutral magnetic line often lie very close to each other (see fig. 1).
- 2. The analysis of one and the same region during some days (27 Aug.-1 Sept. 1985) has shown that several hours before the destruction of the filament or some part of it the velocity structure changes substantially, the velocity channels being stretched in the direction normal to the filament axis than parallel with it; the neighboring parts of the filament became intersected by regions of opposite velocity direction. May be some



simultaneously. Right map(in line) specifial lines part of the filament. His solid lines-lines of zero radial velocity, thin solid lines-isolines of the rising plasma (100,200,300 m/s,...), dashed lines-the same for the sinking matter. fig.1.The Doppler velocity distribution near the filament (shaded),obtained 10 Aug.1985 in two spectral lines



B. A. Ioshpa et al.

contradiction between the results concerning the velocity distribution near the filaments can be explained if we assume that the velocity structure depends on the evolution character of the filament analyzed, in particular, on its stability (Ioshpa and Kulikova, 1988).

3. We have made an attempt to use the measured distribution of radial velocities near the center of the solar disk to calculate the orientation of horizontal velocities under the filaments.

The physical aspect of the problem is as follows. It is supposed that the vertical flow of matter decreases rapidly with the height due to a sharp vertical density gradient. Therefore we have a thin layer with the lower boundary where the matter rises or sinks (sources or drains) and the upper boundary where the vertical flow is nearly zero. In this layer the balance between vertical flows is provided by narizontal flows. We assume that in the whole layer the matter density  $\rho$  is constant and on the height hold the sharply diminishes to zero. Of course lit is a very crude idealization of the real situation on the Sun but it gives us the possibility to solve a potential type problem. For a symmetrical divergent source (in the assumption that not V=0) we can write the following local relation

$$V_z dx dy = 2\pi rh V_{tang}$$
, (1)

where h is the height of the layer.

It can be shown that the integral link between the horizontal and the vertical flows of matter may be represented as follows

$$V_{X}(X,y) = \frac{1}{2\pi h} \int \int \frac{V(X,y)\cos\varphi}{r} dx^*dy^*,$$

$$\forall y (x,y) = \frac{1}{2\pi h} \int \int \frac{V(x,y) \sin \varphi}{f} dx dy^*,$$

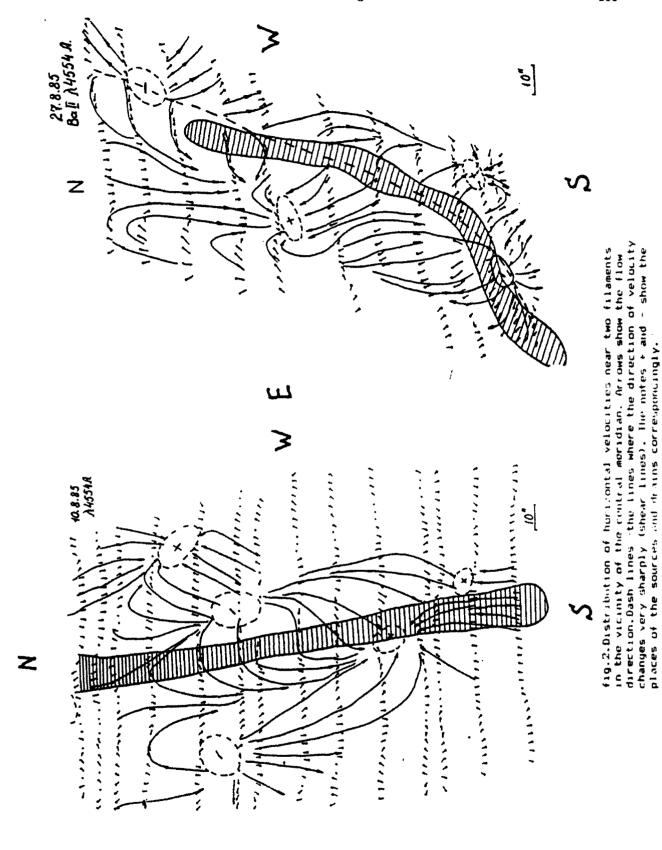
$$V(x,y) = \sqrt{|Vx|^2 + |Vy|^2}$$

$$\varphi = \operatorname{arctg} \left[ \frac{y - y}{x - x} \right]$$
 ,

where Vz is the velocity of the vertical flows.

In fact, this is the solution of a Foisson type potential problem with inner sources for the velocity. The necessary integration region depends on the scale of the velocities under investigation. Thanging the integration interval we have found out that the character of flows weakly depends on it at distances 4 times as large as the characteristic scale of the velocity field under investigation. The real value of h is not important for our problem if we want to know only the direction of transversal velocity.

Fig. 2 illustrates the orientation of horizontal velocities calculated using the above formulas for two filaments near the center of the disk discussed in detail by Ioshpa and Kulikova, 1988,1989. One can note a sharp change in velocity direction as the filament is crossed. The character of velocity distribution similar to one of the shear variants discussed by Rompolt and Bogdan, 1986.



u

#### REFERENCES

Ioshpa, B.A.1962, Geomagnetizm i Aeronomija, 2, 172-176. Ioshpa, B. A., and Kulikova E. H. 1988, in Phizica Solnechnoj Aktivnosti Moscow, ed. Nauka, pp. 168-175.

in Trudi 3 Consultativnogo Edveshanija. ------- 1989,

November, Nauka

Mogevatov.I.E., 1983 , Issledovvanija po Georagnatizmu, Aeronomii i Prizike Scintsa,64,pp.42-45.

Rompolt D., and Bogram Th. 1986, in Compna and Prominence Plausas, ed. Polanc,pp.31-88.

Schmieder B., 1988, in Dynamics and Structures of Quiescent Frominences, ed. Priest, pp. 15-46.

## OBSERVATION AND INTERPRETATION OF $H\alpha$ POLARIZATION

#### IN SOLAR FLARES

#### J.C. Hénoux

URA 326 - Dasop, Observatoire de Paris 92195 Meudon France

Summary. Impact linear polarization of the H\$\alpha\$ chromospheric line has been observed in some flares and reported (Hénoux et al., 1990). A new observation made on July 17th 1982 is presented. The characteristics of the 10 minutes time integrated polarization are similar to the characteristics of the polarization observed in other flares, i.e. the main direction of the polarization is close to the radial direction and the polarization degree reaches 5 %. However, in a few locations, an higher polarization fraction as high as 15 % is observed in the one minute time integrated data. The observational method is described and the origin of the observed polarization is discussed. Zeeman and Stark polarization are excluded. Ly\$\alpha\$ resonance and X-ray irradiation could contribute. The most probable cause is impact polarization produced by protons or neutral beams. We cannot discriminate between a local and a non-local origin of these beams. In the assumption of a coronal origin, the characteristics required from these protons to explain the observations have been derived and already published. Depending on the absence or existence of wave scattering, the minimum individual proton energy varies from 200 keV to a few MeV. Whatever the initial distribution, transport effects in the chromosphere generate an anisotropic velocity distribution for protons. The predicted polarization fraction is conspatible with the observed 10 minutes time integrated polarization fraction.

## 1. Introduction

In 1981, using the ultraviolet spectro-polarimeter on SMM, linear polarization in the integrated profile of the 1437 ÅS I line was detected during a solar flare, (Hénoux et al. 1983a). At that time we also started measurements of the linear polarization in the Hα line. The detection of line linear polarization in three flares, in July 7th 1982, has been reported and the interpretation of these observations has been published (Hénoux and Chambe, 1990; Hénoux et al., 1990; Smith et al., 1990). The observed polarization integrated over ≈ 10 minutes was close to 3 % and radial, i.e. directed in the flare-to-disk-center direction. In this paper a new observation is presented that confirms the existence of a privileged radial direction of the polarization. However one minute time integrated polarization maps show a dispersion around this direction that could be due to deviation of the magnetic field from the vertical direction. As discussed below, the most probable cause of the observed polarization is impact on the chromosphere of a proton beam or of a neutral beam.

The instrumentation and the method used to measure the linear polarization are described in section 2 and some characteristics of the polarization observed in the 1982 July 17th flares are reported. The interpretation of the available  $H\alpha$  polarization observations as impact polarization resulting from the collisional excitation of hydrogen by protons is discussed in section 3. In this section the required characteristics of the protons are recalled. A general discussion and a conclusion are given in section 4.

## 2. Observations

## Instrumentation and method

Observations were made with a filter tuned at the center of the H $\alpha$  line. The choice of this line made possible to use a flare patrol instrument and to benefit of the support available for flare patrol. Moreover even if H $\alpha$  may not be ultimatly the best line to study impact polarization, its large turbulent width strongly reduces the polarization by the Zeeman and Stark effects. We estimated (Hénoux and Semel, 1981) that the contribution to the polarization fraction of these two effects does not exceed 0.5 %.

The instrument used was an H $\alpha$  flare patrol heliograph. The telescope was a 15 cm refractor. The axial symmetry of the optics makes our measurements not to be affected by instrumental polarization. The monochromatic Lyot filter had a 0.75 Å bandpass. A rotating half-wave plate was inserted in front of the linear polarizor at the entrance of the filter. The half-wave plate was rotated through  $22^{\circ}.5$  per step; and one set of 16 H $\alpha$  filtergrams was obtained per minute on film. The time delay between two successive images was 2 s. The rotation of the half-wave plate introduces a modulation of the intensity  $\mathcal{I}$  of the radiation that has travelled through the linear polarizor that follows it, i.e.:

$$\mathcal{J} = \frac{1}{2}(I - U\cos 4\alpha - Q\sin 4\alpha),\tag{1}$$

where Q and U are the linear Stokes parameters and  $\alpha$  is the angle between the direction of transmission of the polarizor and any axis of the half-wave plate. The Stokes parameter V is not measured.

The two entrance and exit sides of the half-wave plate are not strictly parallel. Therefore the wave-plate rotation introduces a motion of the image. Consequently a cross-correlation technics have to be used to compensate for these motions. Cross-correlation was made, on digitized data, using an area not affected by the flares. Then, by substraction of the appropriate digitized images, the Stokes parameters were obtained. In order to reduce the effect of the temporal variation of the flare intensity I, we used a set of three consecutive images. This gives

$$U_{2i+1} = (-1)^{i} [(\mathcal{J}_{2i} + \mathcal{J}_{2i+2}) - 2\mathcal{J}_{2i+1}], \tag{2}$$

$$Q_{2i} = -(-1)^{i} [(\mathcal{J}_{2i} + \mathcal{J}_{2i+2}) - 2\mathcal{J}_{2i+1}], \tag{3}$$

with

$$\alpha = \frac{\pi}{8} \times i, \tag{4}$$

where i varies from one to seven. The polarization fraction and the azimuth of the polarization are easily derived from the Stokes parameters.

## Observation of the 17 July 1982 flares

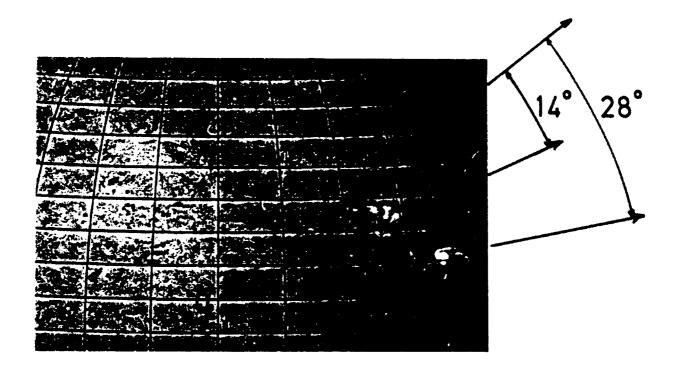


Fig.1 - Positions of the observed flares on the solar disk. The angles between a reference axis OZ and the two flare-to-disk-center directions are shown.

The limits of the digitized image are plotted in dashed lines.

Two chromospheric Hα flares were observed on the 17th of July 1982 at respectively 11N, 38W and 17N, 29W, with respective starting and ending times 10:25, 11:05 and 10:32, 11:02. Intense soft X-ray emission was observed reaching  $3\,10^{-4}$  and  $8\,10^{-5}$  Watts m<sup>-2</sup> in the energy bands 1-8 Å and 0.5-4 Å. At the time where we write this paper we do not have any hard X-ray data available (No hard X-ray burst is recorded on the SMM Hard X-Ray Burst Spectrometer events list). The position on the solar disk of the two flares relatively to the disk center is shown in Figure 1.

The H $\alpha$  line appears to be linearly polarized during the flares. The time development of the mean H $\alpha$  intensity in a 60 000  $\times$  60 000 km<sup>2</sup> area including the flare on the western part of the field of view is plotted in Figure 2. On this figure we have reported also the time dependence of the relative number of pixels in the selected area with a polarization fraction higher than 2%. This relative number varies from 10 % before the flare to nearly 50 % at maximum. Strong fluctuations occur around a mean value that appears to be significantly correlated with the time

evolution of the Ha brightness integrated over the area.

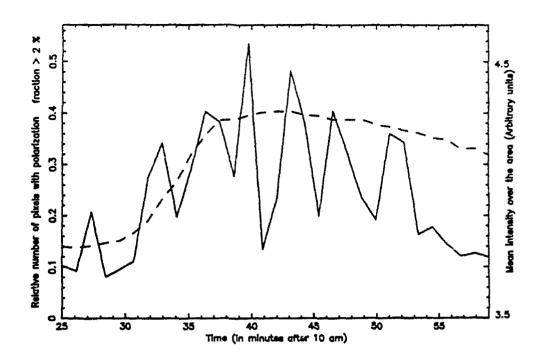


Fig.2- Time dependence of the mean  $H\alpha$  brightness and of the relative number of pixels with a polarization fraction higher than 2% on the western 17th July 1982 flare area. Dashed lines are for the mean  $H\alpha$  intensity. Full lines are for the relative number of pixels.

An image of the spatial distribution of the polarization in amplitude and direction in the western flare of July 17th at 10:40 near the maximum of  $H\alpha$  emission, is presented in Figure 3. In the brightest  $H\alpha$  patch the direction of the polarization is close to the flare-to-disk-center direction. However the polarization is not restricted to the brightest regions, that are presumably at the feet of hot loops, but is also present in cooler regions. A great variety of orientations of the direction of polarization is seen.

Three different origins of the observed polarization are possible. They are respectively 1) impact polarization due to particles moving, with some pitch-angle, along magnetic field loops; 2) resonance polarization in regions surrounding a bright Ly $\alpha$  emitting patch; 3) impact polarization due to photoelectrons generated by soft X-ray irradiation. Linear impact polarization by particles moving around lines of force would be parallel to the projection of the magnetic field on the solar disk. Resonance polarization or impact polarization by photoelectrons would produce a circular structure, that would appear elliptical in projection, and which is centered on the projection on the solar disk of the irradiating source. The polarized electric field would be tangent to it. A complete detailed study would require additional data, as photospheric magnetic field map, soft X-ray and UV images, and is not possible at that time. However information on the origin of the polarization can be obtained by considering the angular distribution of the polarization azimuth both in the set of many one minute integrated polarization maps and in the map of the 4 to 15

minutes integrated polarization.

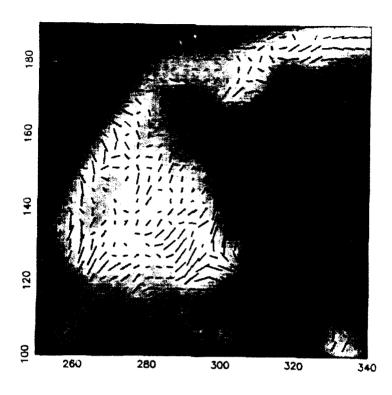


Fig.3 - Orientation of the polarized electric vector in the western H $\alpha$  flare at 10:40 for polarization fractions  $\geq 2\%$ . One pixel of the H $\alpha$  intensity image is 1 arc second. The polarization has been integrated over 3  $\times$  3 pixels. On the left an arrow indicates the radial direction for the brightest H $\alpha$  patch.

The Stokes parameters have been integrated around the maximum of  $H\alpha$  emission, i.e. from 10:38 to 10:51. Histograms of the azimuthal distribution of the fourteen minutes time integrated polarization that exceeds 2% are shown in Figure 4. Three histograms have been made for the full field of view and for the two separate flaring regions in this field. All three histograms are clearly peaked. For the regions at the east and west part of the field of view, for which the azimuth of the flare-to-disk-center direction are respectively  $14^0 \pm 2$  and  $28^0 \pm 3$ , the maxima of the histograms are at azimuthal angles respectively equal to  $20^{\circ} \pm 5$  and  $35^{\circ} \pm 5$ . Clearly the most frequent azimuth of the linear polarization integrated during the maximum of  $H\alpha$  emission differs from the azimuth of the flare-to-disk-center direction by less than 7°. Resonance polarization alone would lead to a direction of the net polarization perpendicular to the radial direction on the solar disk. Impact polarization by photoelectrons created by XUV radiation would have characteristics similar to resonance polarization. The radial direction of the net polarization can be understood as due to impact polarization produced by particles spiralling around the magnetic field lines. In each point on a H\alpha emitting loop the resulting direction of the polarization vector is the projection on the solar disk of the magnetic field direction. Integration over time live a radial direction of polarization due to a dominant contribution of the vertical component of the field.

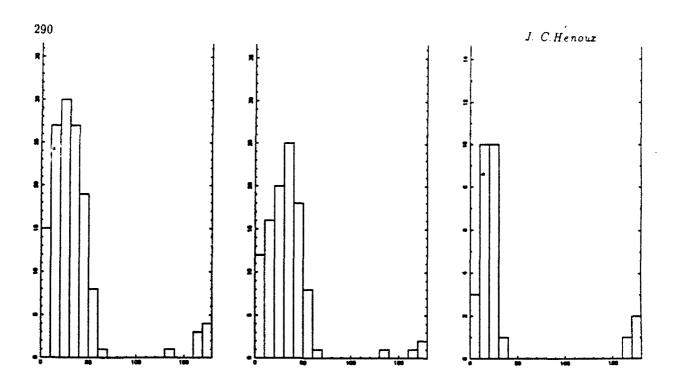


Fig.4 - Histograms of the azimuthal distribution of the polarization fraction, integrated from 10:38 to 10:51, that exceeds 2% in the full field of view (left) and in the two flaring regions on the west (center) and on the east (right). The reference axis for the definition of the azimuth is defined in Figure 1.

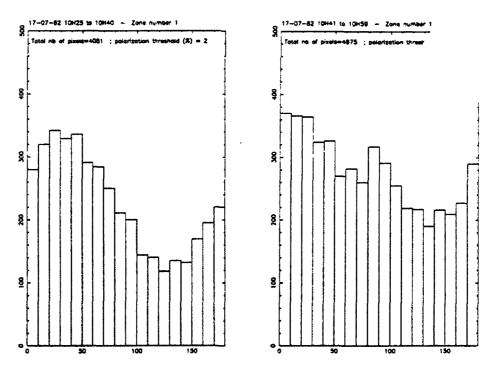


Fig.5 - Histograms of the azimuthal distribution of the one minute time integrated polarization that exceeds 2% in the western flare area during the rise (from 10:25 to 10:40) and after the maximum (from 10:41 to 10:59) of  $H\alpha$  emission.

Histograms of the azimuthal distribution of the one minute time integrated polarization that exceeds 2% in the western flare area during some period of time  $\Delta t$  have also been drawn. The

histograms that cover respectively the rise of  $H\alpha$  emission from 10:25 to 10:40 and the decay phase in the western flare are shown in Figure 5. They peak at an azimuth angle of  $25^{\circ} \pm 5$ , to be compared with the azimuth of the flare-to-disk-center direction which is equal to  $28^{\circ} \pm 3$ . The peak is more pronounced during the rise of  $H\alpha$  emission. The position of the peak suggests that we observe impact polarization at the feet of flaring loops where the distribution of magnetic lines of force there is presumably more or less symmetrical around the solar vertical.

# 3. Polarization as diagnostic of the nature and anisotropy of particles bombarding the solar chromosphere

## Impact polarization

The radiation emitted by an atom collisionally excited by a beam of particles - electrons or ions - may be linearly polarized (Skinner, 1926; Percival and Seaton, 1959; Kleinpoppen, 1969; Heddle, 1979). The maximum polarization fraction is observed at 90° of the direction of propagation of the beam and is defined as

$$P(90^{\circ}, v) = (I_{||} - I_{\perp})/(I_{||} + I_{\perp}), \tag{5}$$

where  $I_{\parallel}$  and  $I_{\perp}$  are the intensities of the vibrations parallel and perpendicular to the beam propagation direction and v is the particle velocity.

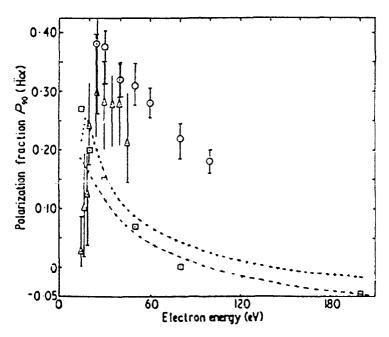


Fig.6 - Measured and computed values of the polarization fraction at  $90^{\circ}$  ( $P(90^{\circ}, v)$ ) of an electron beam as a function of the energy of the electrons as published by Syms et al. (1975). Plus and alternate plus and minus signs represent respectively DWPO II and Born theoretical values. Circles and triangles are experimental values (Kleinpoppen et al., 1962; Kleinpoppen and Kraiss, 1968). Squares are theoritical values calibrated with measured integrated cross sections (Mahan, 1974).

For a dipolar transition the angular dependence of the polarization fraction is given by

$$P(\beta, v) = P(90^{\circ}, v) \sin^2 \beta / (1 - P(90^{\circ}, v) \cos^2 \beta), \tag{6}$$

J. C. Henoux

where  $\beta$  is the angle between the line of sight and the particles beam travel direction. The Figure 6 shows computed and observed values of  $P(90^0, v)$  for the H $\alpha$  line collisionally excited by a monoenergetic electron beam (Syms et al., 1975). Notice the change of the sign of the polarization fraction for increasing energy. The energy dependence of the polarization fraction for proton excitation is similar to the one corresponding to excitation by electrons but is not yet accuratly known. At high energy the polarization fraction computed in the Born approximation is independent of the particle mass and depends only of its velocity (Scharmann and Schartner, 1969). The amplitude of the polarization fraction at threshold is maximum (100%) for a singlet transition between a ground state <sup>1</sup>S and an excited state <sup>1</sup>P. Fine and hyperfine structure splitting reduce the polarization of the emitted radiation.

Nature and origin of the bombarding particles in the Sun

Polarization observations alone do not give information on the nature of the particles that produce the observed polarization. These particles could be either deca eV electrons or deca eV to deca keV protons.

Our first interpretation of  $H\alpha$  and S I 1437 Å line polarization was excitation by deca eV electrons associated with a significant heat flux at the base of the transition zone (Hénoux et al., 1983b). An analytical ad-hoc representation of the velocity distribution function was used. A more exact traitement would require to solve the Fokker-Plank equation for low energy electrons. As a matter of fact at chromospheric densities deca eV electrons are quickly scattered by Coulomb collisions. That presumably excludes any significant anisotropy of the velocity distribution of low energy electrons formed higher in the atmosphere. However deca eV electrons, either accelerated locally or forming together with protons a neutral beam, could have an anisotropic velocity distribution in the chromosphere leading to polarized line emission. Contrary to electrons, heavy protons keep a more or less straight line path while loosing energy. Low energy protons are less affected by Coulomb scattering and are therefore better candidates to explain the observed polarization, even if originating in the corona. Protons of a few hundred keV, accelerated there, reach the chromosphere with a much smaller energy and still have kept their directivity. Indeed protons accelerated locally could also have an anisotropic velocity distribution.

## Anisotropy diagnostic

On the sun, energetic particles bombarding the solar atmosphere have a velocity distribution function  $f(v,\alpha)$ , with a pitch angle  $\alpha$ , that we can assume to be symmetrical around an uniform magnetic field direction. Expressing the particle velocity distribution function as a sum of Legendre polynomials,

$$f(v,\alpha) = \sum_{l} a_{l}(v) P_{l}(\cos \alpha), \tag{7}$$

and defining an anisotropy factor b(v) as  $a_2(v)/5a_0(v)$ , we obtained (Hénoux et Chambe, 1990; Hénoux et al.,1990) the following expression for the maximum polarization that could be observed at  $90^{\circ}$  to the solar vertical

$$\mathcal{P}(90^{\circ}) \simeq \left[ \int_{v_0}^{\infty} P(90^{\circ}, v)b(v)J_0v\sigma(v)dv \right] / \left[ \int_{v_0}^{\infty} J_0v\sigma(v)dv \right]. \tag{8}$$

Here  $\sigma(v)$  is the excitation cross-section,  $v_0$  is the particle velocity at threshold and

$$J_0 = \int_0^\infty f(v, \alpha) \sin \alpha d\alpha. \tag{9}$$

In practice the main confront to the line intensity and polarization comes from the particles at velocity close to the threshold velocity  $v_0$ . Therefore the equation (8) can be rewritten as

$$\mathcal{P}(90^{\circ}) \simeq b(v_{0})P(90^{\circ}, v_{0}). \tag{10}$$

For a dipolar transition

$$\mathcal{P}(\theta) = \mathcal{P}(90^{\circ})\sin^2\theta/(1 - \mathcal{P}(90^{\circ})\cos^2\theta), \tag{11}$$

where  $\theta$  is the angle between the line of sight and the magnetic field direction. For a vertical magnetic field  $\theta$  is the heliocentric angle. Consequently the anisotropy factor  $b(v_0)$  can be derived from the measurement of the linear polarization fraction once we know  $P(90^0, v_0)$ .

Energy and anisotropy requirements for protons beams.

In the assumption that the protons are accelerated higher in the atmosphere, transport effects have to be taken into account in order to derive the minimum individual proton energy and the minimum proton energy flux. The proton energy is affected mainly by Coulomb collisions and the proton pitch angle can be modified in scattering by waves.

The effect of Coulomb collisions alone was computed in Hénoux et al. (1990). The minimum individual energy  $E_p$  required from a proton to reach the H $\alpha$  forming layers depends on the coronal temperature and column density. For temperatures higher than  $10^7$  K and a coronal column density  $N_c = 1.5 \, 10^{20} cm^{-2}$ ,  $E_p$  has to be higher than about 160 keV. The minimum energy flux was found by equating the collisional excitation rate of hydrogen level 3 by the proton beam to the thermal excitation rate by background electrons. At the preceeding coronal temperature and column density the minimum flux is equal to  $3.10^8$  ergs cm<sup>-2</sup> above 160 keV.

If Alfvèn or magnetoacoustic waves are generated, they could scatter the beam and increase the energy requirements by increasing significantly the particle path. Wave generation depends on the ratio of the beam to background electron number density, on the ratio of proton velocity to Alfvèn velocity and on the anisotropy of the proton velocity distribution function. No self-consistent computation of the interaction between protons and waves does exist. In the limit of strong scattering, Smith et al. (1990) have computed the required proton energy and proton flux. In a loop of length  $10^9$  cm, the diffusive propagation increases the particle path by a factor hundred and much higher energy protons (2-20 MeV) are required to explain  $H\alpha$  polarization.

By transport effects, the anisotropy of the proton velocity distribution function may vary from the corona to the chromosphere. Even if at the top of the transition region the proton velocity distribution is isotropic, atmospheric stratification would make this distribution anisotropic in the H $\alpha$  forming layers. Because protons arriving in the chromosphere with a higher inclination on the solar vertical suffer more collisions than protons travelling vertically, the final velocity distribution function in the chromophere would be anisotropic with a maximum in the vertical direction. The resulting anisotropy factor would give informations on the power index  $\delta$  of the distribution

J. C. Henoux

with energy of the proton flux ( $\propto E^{-\delta}$ ). The higher the slope of the distribution, the higher the anisotropy factor would be. As computed in Hénoux et al. (1990),  $b(v_0) = (\delta + 1)/(\delta + 7)$ . For  $\delta = 4$  the anisotropy factor  $b(v_0) = 0.45$ . Consequently the polarization fraction would be as high as  $\approx 11\%$  for a limb flare and close to 5% for a flare at heliocentric angle  $40^{\circ}$ . The observed polarization fraction depends on the integration time. The polarization fractions resulting from an integration over more than four minutes are lower than this value. However the maximum for a one minute integrated observation reaches 15% in a few pixels in the July 17th 1982 western flare. Such a high value is not in contradiction with the hypothesis of impact polarization as long as it does not exceed the polarization fraction observable at  $90^{\circ}$  from a proton beam travel direction ( $P(90^{\circ}, v_{th})$ ), which is in the 20 to 30 % range.

## 4. Concluding Remarks

On a pure observational basis, we rule out Zeeman effect as the origin of the observed polarization because of the temporal association between the mean H $\alpha$  brightness and the number of polarized pixels during the flare. Moreover no systematic steady polarization is observed above sunspots penumbrae. Estimation of the net polarization produced by Stark effect leads to values that are much lower than the observed ones. If, in some limited area, the possibility to detect resonance polarization or polarization resulting from X-ray irradiation is not completly ruled out, but we do not have yet any evidence for it. The most probable cause of the observed polarization is still proton impact on neutral hydrogen in loops, with a dominant effect at their feet. Indeed a neutral beam carrying protons and electrons with equal velocities would be even more efficient. The main argument in favor of protons comes from the possibility of generating a significant anisotropy in the proton velocity distribution in dense loops.

The new polarization observations in the July 17th 1982 flares presented this paper confirms the existence of a privileged radial direction of the polarization. The angular distribution of the polarization azimuth both for one minute and for about ten minutes time integrated data show a peak within 5 to 10 degrees of the radial direction. The width of the peak in the one minute integrated data is smaller during the rise of  $H\alpha$  emission that during the decay phase. The most pronounced peak is obtained around  $H\alpha$  maximum emission in the fourteen minutes time integrated data. However one minute time integrated polarization maps show a greater dispersion around this direction. The observed dispersion could be due to deviation from the vertical of the magnetic field direction.

A detailed study of all one minute time integrated polarization maps have to be done to understand 1) the strong variation within 2 to 3 minutes time of the number of pixels that exhibit polarization (see Figure 2); 2) the loop shaped structures observed in various maps. The picture of chromospheric bombardment by protons works well for bright  $H\alpha$  patches but polarization is not limitated to the brightest  $H\alpha$  regions and a plane parallel atmospheric model is not sufficient.

## Acknowledgments

I thank G. Gelugne, P. Micheneau, X. Bringue and T. Schuld for assistance.

#### References

- Heddle, D.W.O. 1979, Advances in Atomic and Molecular Physics, pp. 381-421, D.R. Bates and B. Bederson eds., Academic Press, N.Y.
- Hénoux, J.C., Chambe, G., Semel, M., Sahal, S., Woodgate, B., Shine, R., Beckers, J. 1983a, Astrophys. J., 265, 1066
- Hénoux, J.C., Heristchi, D., Chambe, G., Machado, M., Woodgate, B., Shine, R., Beckers, J. 1983b, Astron. Astrophys. 233, 238
- Hénoux, J.C., Chambe, G. 1990, J.Q.S.R.T., Vol.44, 193.
- Hénoux, J.C., Chambe, G., Smith, D., Tamres, D., Feautrier, N., Rovira, M., Sahal-Brechot, S. 1990, Astrophys. J. Supplt., 73, 303
- Kleinpoppen, H. 1969, Advances in Atomic and Molecular Physics, pp. 612-631, F. Bopp and Kleinpoppen eds., North Holland, Amsterdam.
- Kleinpoppen, H., Kruger, H. and Ulmer R. 1962, Phys. Letters, 2, 78
- Kleinpoppen, H. and Kraiss, E. 1968, Phys. Rev. Letters, 20, 361
- Mahan, A.H. 1974, Ph.D. Thesis, University of Colorado
- Percival, I.C. and Seaton, M.J. 1959, Phil. Trans. R. Soc. Lond. A, 251, 113
- Scharmann, A. and Schartner, K.H. 1969, Advances in Atomic and Molecular Physics, pp. 632-635, F. Bopp and Kleinpoppen eds., North Holland, Amsterdam.
- Skinner, H.W.B. 1926, Proc. R. Soc. Lond. A, 112, 642
- Smith, D.F., Chambe, G., Hénoux, J.C. and Tamres, D. 1990, Astrophys. J., 358, 674
- Syms, R.F., McDowell, M.R.C., Morgan, L.A. and Myerscough, V.P. 1975, J. Phys. B. Atom. Molec. Phys., Vol. 8, No. 17, 2817

#### Discussion

- J. Jefferies: One of the values of  $Ly\alpha$  was the simple structure of the 2 levels this is not so for  $H\alpha$ , and I wonder whether you have looked for other strong solar lines with simple level structure (and higher maximum polarization) as candidates for observing. I think e.g. of  $NaD_1$ , or  $NaD_2$ , or perhaps some Ca or Mg lines.
- J.C. Henoux: I agree that the  $H\alpha$  line is presumably not the best line to measure impact polarization. One reason to choose this line was that we could share a flare patrol instrument. We will have soon a dedicated polarimeter. That will allow us to use other lines like the  $NaD_1$  or  $NaD_2$  lines (as you suggested) or some He line present mainly during solar flares.
- On the other hand we would like also to make observations in the red wing of the  $H\alpha$  line in order to look for polarization due to charge exchange, which could also be present, as Dr. Zirker pointed out.

## Currents and Flares in a Highly Nonpotential Active Region

RICHARD C. CANFIELD, YUHONG FAN, K.D. LEKA.
A.N. MCCLYMONT, AND JEAN-PIERRE WUELSER

Institute for Astronomy, University of Hawaii 2680 Woodlawn Drive, Honolulu, HI 96822, USA

#### **BRUCE W. LITES**

High Altitude Observatory, National Center for Atmospheric Research P. O. Box 3000, Boulder, CO 80307, USA

#### HAROLD ZIRIN

Big Bear Solar Observatory, California Institute of Technology Caltech 264-33, Pasadena, CA 91125, USA

Summary. NOAA Active region 5747, during its October 1989 transit across the solar disk, showed highly nonpotential photospheric vector magnetic field structure and produced many solar flares, three of which we observed at Mees Solar Observatory. We invert our Haleakala Stokes Polarimeter data with the Lites and Skumanich (1987) code; both adequate spectral sampling and correction for unresolved magnetic structures are essential to the subsequent analysis. After resolution of the  $180^{\circ}$  ambiguity, we determine the photospheric distribution of the vertical current density. We apply a novel test to see whether the magnetic fields in the corona above this region are force free; we find that the observed fields and currents depart from a force-free relationship by amounts significantly exceeding statistical fluctuations or the total flux imbalance. We compare the locations of the major current systems to sites of nonthermal electron precipitation inferred from H $\alpha$  profiles of three flares observed using the Mees CCD Imaging Spectrograph. We find that the sites of energetic electron precipitation are at the edges of these currents, not at their peaks.

#### 1. Introduction

Early work in the Soviet Union (see, e.g., Moreton and Severny 1968) and recent work in the United States and Canada (see, e.g., Lin and Gaizauskas 1987, Hagyard 1988) shows that there exists a close morphological relationship between vertical electrical currents in the photosphere (inferred from vector magnetograms) and solar flares seen in Ha. However, the relationship of these currents to heating and particle acceleration in flares is documented in only a very ambiguous manner. Among the questions of present interest are the two that are addressed (for a single active region) in this paper, viz.: (1) are the observed currents and fields that are related to the flare process force free; (2) what is the morphology of nonthermal electron acceleration (and, therefore, precipitation)? The study of currents and flares is a major topic in solar physics, and has too long a history to summarize in these proceedings. Practical considerations force us to limit ourselves to a summary of just a few aspects of the active region of interest; more complete analyses will be published at a later time.

## 2. Observations

NOAA active region 5747 was observed at the Mees Solar Observatory of the University of Hawaii and the Big Bear Solar Observatory of the California Institute of Technology.

Using the Haleakala Stokes Polarimeter at Mees Solar Observatory (Mickey, 1975), we sampled Stokes I, Q, U, and V profiles of the Fe I  $\lambda$ 6302.5 line and nearby lines and continuum with 128 spectral channels, each

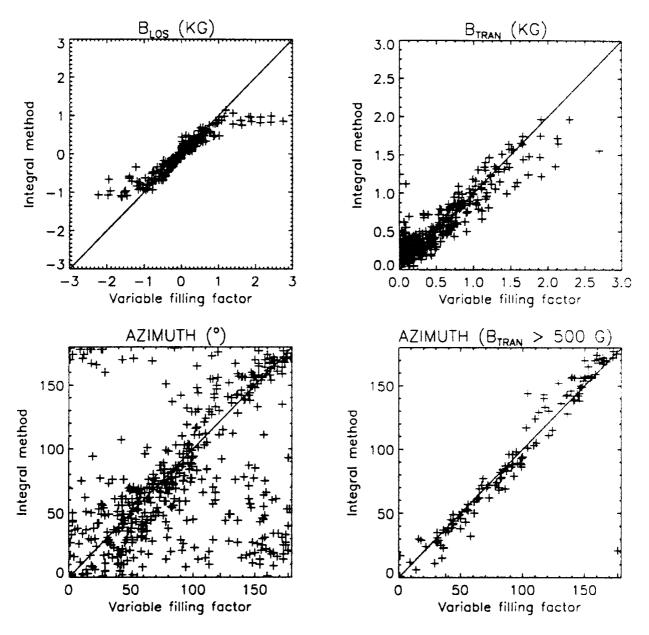


Fig. 1 - Scatter-plot comparison of inferred parameters of the average magnetic field (KiloGauss) for the MSO magnetogram of October 20, for the RMO method (Integral method) and the LS method (Variable filling factor). The quantities plotted are those of the inferred average field for each pixel, i.e. (1-f) B. All pixels in the October 20 polarimeter scan whose observed polarization was greater than 1% were inverted using the LS code and included in the figure.

having a width ~25 mÅ, while scanning a 6" aperture in a 30 x 30 spatial raster with a 5.6" sampling interval. These data form the basis for daily vector magnetograms for each of the five days from 18 through 22 October 1989. Using the Mees CCD Imaging Spectrograph (MCCD; Penn et al. 1990) we observed the I profiles of the Hα line with 50 spectral channels, each 380 mÅ in width, and 90 spectroheliogram pixels, each 2.4" on a side. The solar image was scanned to generate 90 x 90 pixel spectroheliograms with a temporal sampling interval of approximately 10 seconds. Four-dimensional MCCD datasets were obtained throughout three flares: 1N/C5 at 2134UT October 20; SN/C5 at 2005UT October 21; 2B/X3 at 1805UT October 22 1989. The latter

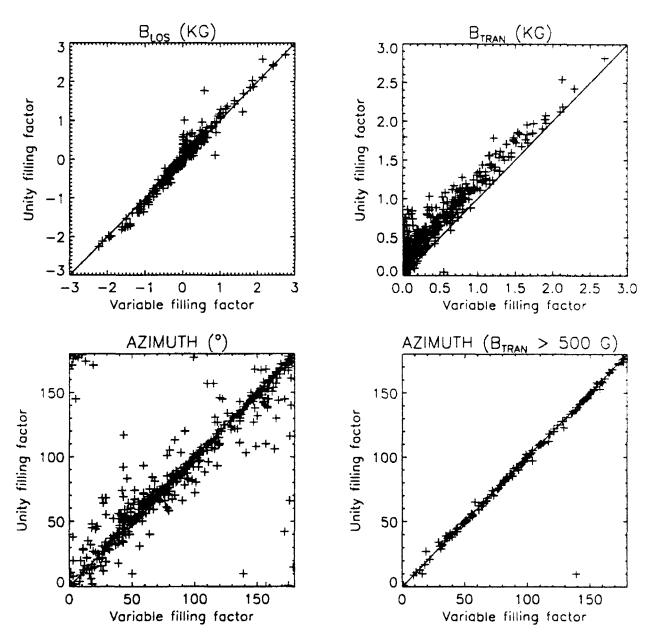


Fig. 2 - Comparison of inferred parameters of the average magnetic field for the MSO magnetogram of October 20, with and without correction for filamentary magnetic fields. The quantities plotted are for the inferred average field for each pixel, i.e. (1-f) B. Only pixels whose observed polarization is greater than 1% were inverted using the LS code. "Variable filling factor" means f is a least-squares determined parameter of the LS inversion; "Unity filling factor" means that the LS fit is constrained by the assumption f = 0.

flare occurred in a region in which a much larger flare had taken place shortly before.

From Big Bear Solar Observatory we have three days of high-resolution H $\alpha$  movies (18 - 20 October 1989), including both line center images and  $\lambda$  scans. As well, we have Stokes V magnetograms in  $\lambda$ 6103 for these same three days from the Video Magnetograph (Zirin, 1985).

In this brief paper we have enough space to show only one day's magnetogram and a related flare; we have chosen October 20, for which the data are representative.

## 3. Magnetogram Inversion Procedure

For our inversion of the observed Stokes profiles of  $\lambda$ 6302.5 we used the nonlinear least-squares code of Lites and Skumanich (1987, hereafter LS), which fits analytical (Unno/Rachkovsky) LTE Stokes profiles to the Haleakala Stokes Polarimeter data, taking into account all major magneto-optic effects. We did not use both  $\lambda$ 6302.5 and  $\lambda$ 6301.5, although both profiles are included in the observations. The best-fit parameters of the theoretical profiles determined in a least-squares sense by the LS code include the line center wavelength  $\lambda_0$ , the Doppler width  $\Delta\lambda_D$ , the Voigt wing damping constant a, the ratio of line to continuum opacity  $\eta_0$ , the gradient of source function  $B_1$ , the strength of the magnetic field B, the inclination of the magnetic field  $\psi$ , the azimuth of the magnetic field  $\chi$ , the fraction of unpolarized light f, and the wavelength offset of unpolarized light  $\lambda_{QS}$ .

For the inference of magnetic field parameters, an essential feature of any inversion of polarimetric measurements is that it does not have problems (such as signal saturation at high magnetic field strengths) that are avoidable with adequate spectral sampling of the Stokes profiles. The simple inversion method (Ronan, Mickey, and Orrall 1987, hereafter RMO) that we routinely use for quick-look magnetograms (because it is fast) integrates over the line profile, effectively throwing away all spectroscopic information; its inversion is based on the weak field approximation. It is known that this approximation breaks down for kiloGauss fields, for Fe I  $\lambda$ 6302.5. This effect can been seen in Figure 1, in which we compare the parameters of average field per pixel, i.e. (1-f) B, inferred by the RMD method to those inferred using the most sophisticated inversion method available to us, i.e. the LS code with variable magnetic filling factor (1-f). Note that the RMO method does not include the scattered light fraction as a variable of the analysis; it assumes f = 0. Clear evidence of magnetic signal saturation in the RMO method can be seen in  $B_{LOS}$  and  $B_{TRAN}$ .

Another important aspect of any inversion scheme is its ability to account for unresolved magnetic fine structure. In Figure 2 we compare inversions with magnetic filling factor fixed at unity (i.e., f = 0) and variable (determined by the LS code). As in Figure 1, the quantity plotted is the inferred average field per pixel, i.e. (1-f) B, for the indicated components of B. Stenflo (1971) showed that in the presence of filamentary fields one should expect to get the correct average value of  $B_{LOS}$  but to overestimate the average value of  $B_{TRAN}$  by a factor of order <1-f>-1/2. Figure 2 shows departures that imply (1-f) values in the range 0.1-1, but further analysis (not given here) shows that this simple explanation does not fully account for the effect.

## 4. Resolving the 180° Ambiguity and Vertical Currents

We followed a multi-step procedure in which our first approximation was to adopt the choice of directions closest to that of the potential field fitted to the line of sight component of the observed magnetic field (Sakurai, Makita and Shibasaki, 1985). This works well at most points but it fails in the most interesting regions. In strongly non-potential regions (e.g. departures of more than  $45^{\circ}$  from the azimuth of the potential field) we took into account the requirement of continuous change of direction between adjacent pixels (Aly, 1989). If ambiguity still existed we chose the direction that minimized the amplitude and small-scale variation of the vertical current density implied by  $\nabla \times B$ . As well, we chose the direction that minimized vertical

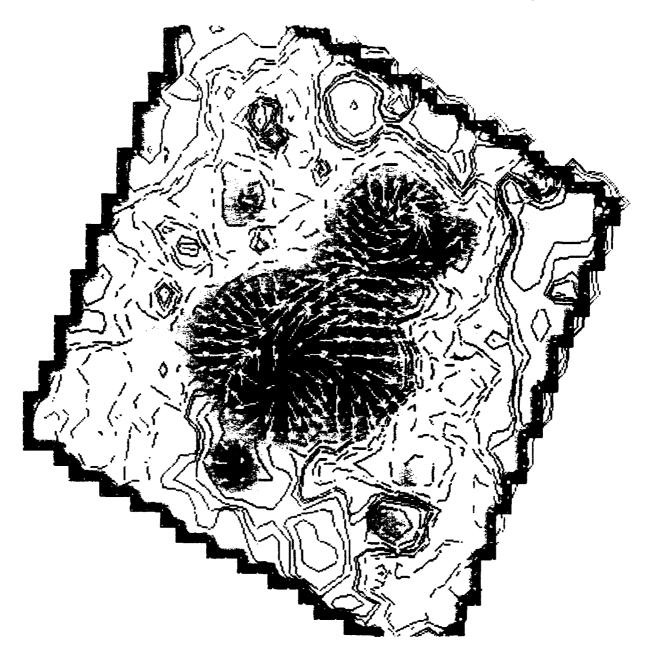


Fig. 3 - Ambiguity-resolved vector magnetogram October 20, 1989, scanned from 17:41 to 18:33 U.T., transformed from image plane to heliographic coordinates. The gray-scale image shows the sunspot structure of the active region seen in the continuum near the  $\lambda 6302.5$  line. The contours indicate the vertical magnetic field distribution averaged over each pixel, (1-f) B  $\cos \psi$ . Radial field contours are shown at 25, 50, 100, 200, 400, 800, 1600, and 3200 Gauss levels (dashed contours indicate negative fields). The arrows show the strength and direction of the transverse field; a length equal to the sampling interval indicates a field of strength ~700 Gauss. Solar North is up, East to the left.

currents in regions of horizontal fields (e.g. inversion lines in the line of sight field). Finally, we used the  $H\alpha$  fibrils and filaments shown in the BBSO movies to establish the large-scale connectivity.

Figure 3 shows an ambiguity-resolved vector magnetogram transformed from the original image plane (the region was at solar longitude ~5 W and latitude ~25 S) to heliographic coordinates. The vector magnetogram is derived from a Stokes polarimeter scan of NOAA AR 5747 made from 17:41 to 18:33 UT on October 20.

Figure 4 shows the corresponding map of vertical current density derived from  $\nabla \times B$  for the magnetogram shown in Figure 3. Although it is impossible to be certain that the magnetic field directions chosen are correct at all points, we find that such vertical currents inferred from  $\nabla \times B$  cannot be made to disappear by different choices of resolution of the 180° ambiguity. The amplitude of the uncertainty in the location of these currents

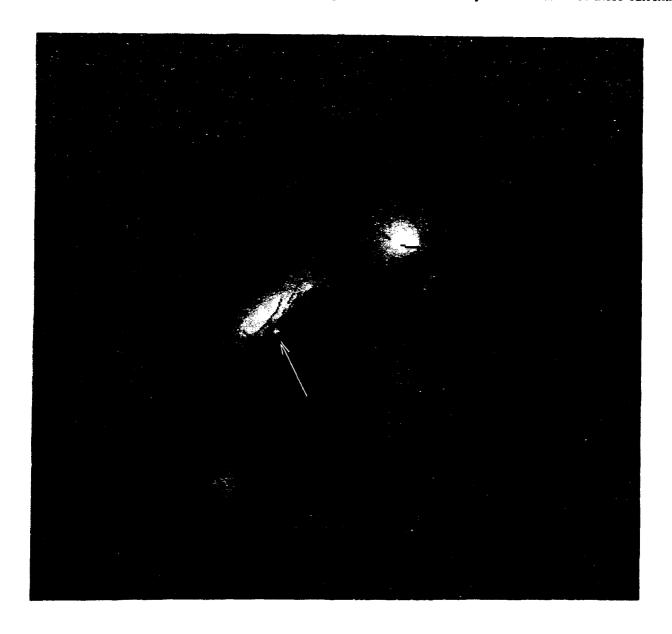


Fig. 4 - Vertical current density map (grey scale), vertical magnetic field (contours), and H $\alpha$  blue-wing difference spectroheliogram (also grey scale), in heliographic coordinates. The vertical-field contours and orientation are the same as Figure 3. The co-registered and superimposed H $\alpha$  blue-wing difference spectroheliogram shows the flare of 2134 UT October 20 about 3 minutes before H $\alpha$  flare maximum. One can easily distinguish between the co-registered current density map and the blue-wing difference spectroheliogram, even though both are shown by grey-scale images. The only feature in the difference spectroheliogram is the brightening indicated by the arrow, located on the inversion line, which identifies the site of strong nonthermal electron precipitation.

is about  $\pm$  5", which is sufficiently small that it has no effect on our conclusions below.

Making the assumption that the currents close within the magnetogram (which is justified at the ~1% uncertainty level), it is clear that two strong currents flow, which we will call the eastern and western currents. The eastern current spans the most highly non-potential section of the polarity inversion line; its southern intersection with the photosphere is very close to that of the western current. Each current carries about  $3-4\times10^{12}$  Amp.

## 5. A Necessary Condition for Force-Free Fields

It is interesting to investigate the extent to which the magnetic fields shown in Figure 3 are force free. Clearly the photospheric magnetic field of active regions is generally not force free, even on easily observed scales; horizontal currents must circulate around sunspots to confine the magnetic flux within them. However, we are not concerned with these static, purely horizontal, current systems, but only with those currents which flow through the corona, in response to stresses between photospheric footpoints. One might think of estimating the Maxwell stresses integrated over the active region (see, e.g., Low, 1985). However, this requires observations of the whole active region, and we know from comparison of the MSO vector magnetogram to the

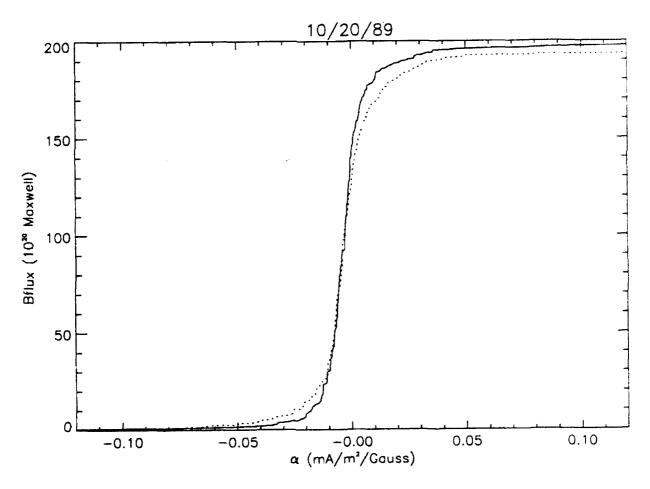


Fig. 5 - The flux integral  $\int_{-\infty}^{0} d\alpha' \Phi(\alpha')$  for regions of positive (solid) and negative (dotted) vertical magnetic field, as a function of  $\alpha = J_z/B_z$ .

simultaneous BBSO video magnetograms that some small, but not negligible, part of this active region falls outside the range of the Stokes Polarimeter scan on which the vector magnetogram is based. It is therefore not surprising that, as we shall show below, the total flux imbalance in the vector magnetogram is observed to be ~2%. Since such flux imbalance makes it impossible to meaningfully consider the integrated Maxwell stresses, we have developed a new test for force-free fields that emphasizes observationally significant vertical currents.

This suggests that one should examine the distribution of vertical current density. Figure 4 shows  $J_z$  (grey scale) and  $B_z$  (contours). These two quantities allow us to compute for each pixel the value of the magnetic flux  $\Phi$  and  $\alpha = J_z/B_z$ . If the current is force free, i.e. all currents flow parallel to the magnetic field, then  $\alpha$  must be conserved along all field lines. Except for the effects of imperfect observations, the same amount of magnetic flux of each polarity should be observed in any chosen increment of  $\alpha$ . This is more stringent than the integral test of the Maxwell stresses and may be more useful because of its more local nature.

We want to determine the distribution function  $\Phi(\alpha)$  for positive and negative fields for all pixels of Figure 3, but we want to avoid the problems associated with binning in  $\alpha$ . We have therefore plotted the flux integral  $\int_{-\infty}^{\alpha} d\alpha' \Phi(\alpha')$  separately for positive and negative magnetic fields. Figure 5 shows the distribution for regions of positive magnetic polarity as a solid curve, and for negative regions, as a dashed curve. The difference between these two curves at the right margin of this figure is a measure of the flux imbalance in this magnetogram, which is -2%; currents balance to better than -1%. Clearly the positive and negative distributions differ by more than both statistical fluctuations and the total flux imbalance at many values of  $\alpha$ , leading us to the conclusion that the coronal magnetic fields above this active region are not force free.

## 6. Co-Registration of Magnetograms and Spectroheliograms

Both the Stokes Polarimeter and the MCCD Imaging Spectrograph record a range of wavelengths that extends to the continuum; from the Polarimeter scan we make a Stokes-I map in the continuum near  $\lambda$ 6302.5; from the MCCD datacube we make a spectroheliogram in the continuum near H $\alpha$ . These images contain many sunspot features that we can use to co-register these two images in a least-squares best-fit sense. The residuals of the fit indicate that the co-registration of each individual spectroheliogram with the vector magnetogram is good to better than 2.9".

## 7. Flare Nonthermal Electron Precipitation Sites

Sites of nonthermal electron precipitation into the chromosphere can be identified unambiguously only by using a combination of blue-wing spectroheliograms and line profiles. Canfield, Gunkler, and Ricchiazzi (1984) have theoretically modeled the formation of the H $\alpha$  line in static atmospheres heated by nonthermal electrons, subject to varying levels of pressure and thermal conduction from the overlying corona. They showed that the only signature of strong nonthermal electron heating that allows one to rule out thermal conduction or high coronal pressure as a factor in line broadening is the combination of broad bright wings and central reversal. We used blue-wing difference spectroheliograms to locate sites of broad bright wings; we found that spectroheliograms made by differencing continuum (5 Å) and wing (2.5 Å) spectroheliograms were optimally sensitive (see Figure 6). Once we located the initial flare brightening in such blue-wing difference spectroheliograms we inspected the H $\alpha$  profiles at such points for evidence of self-reversal. Figure 6 shows the H $\alpha$  spectrum of a pixel that combines both broad bright wings and an obvious central reversal, allowing us to rule out both thermal conduction and high coronal pressure (P  $\sim 10^3$  dyne cm<sup>-2</sup>) as causal mechanisms.

In all three flares we found evidence for particle precipitation very early in the events. Precipitation sites were located along the vertical-field inversion line where strong observed shear and large field strength obtained along a considerable length of the inversion line, in agreement with the criteria for flare occurrence established

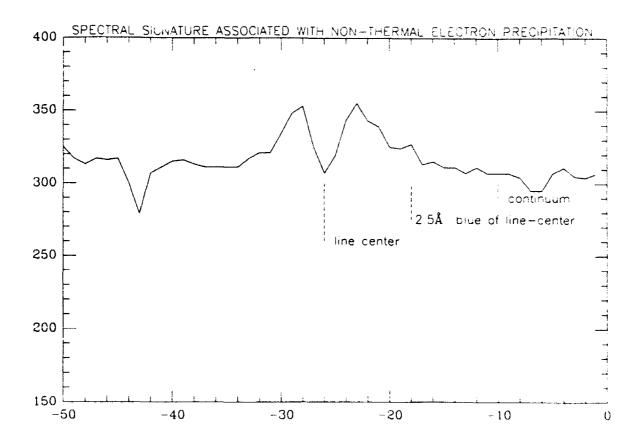


Fig. 6 - The observed spectrum of a pixel in the region indicated by the arrow in Figure 4 that shows the spectral signature associated with nonthermal electron precipitation into the chromosphere. The abscissa indicates the index number of the spectral channels, each 380 mÅ in width (blue to the right). The difference spectroheliograms (such as Figure 4) were made from spectroheliograms at  $\Delta\lambda = 2.5$  and 5in the spectral channels indicated.

by the group at MSFC (Moore et al., 1987). This is confirmation of the applicability of their result, since the particle precipitation site is obviously part of the  $H\alpha$  flare as a whole. Interestingly, to within the resolution afforded by the 2.2" pixels of the MCCD Imaging Spectrograph observations, only a single precipitation site was found.

It appears to us that a physically-motivated relationship that we should examine is that between the nonthermal electron precipitation sites and the current system of the active region. It is interesting that, in all three observed flares, the precipitation sites were at the edges of the major vertical currents, not in their centers, suggesting that acceleration occurs at sites of interaction, not interruption, of the major currents. Figure 4 shows the result for the flare of October 20th. In this event the precipitation site is not only at the edges of the major vertical currents, it is between them. The former is a common property of all three events; the latter is not.

The two major vertical current systems (the eastern and western currents identified above) existed on all five days for which we have vector magnetograms. Furthermore, the two currents were very close to one another at their southern intersection with the photosphere. This, in combination with the result that the electrons precipitate at the edges of the currents and not their centers, suggests that the electrons might have been

accelerated at a region of interaction of these two currents.

The work in Hawaii has been supported by NASA grants NAGW 864 and 1542, Lockheed Solar-A subcontract SE80D785OR, and NSF grants AST-8900716 and ATM8822366. The National Center for Atmospheric Research is sponsored by the National Science Foundation. The work at Caltech has been supported by NASA grant NAGW-1972.

#### References

Aly, J.J. 1989, Solar Phys., 120, 19.

Canfield, R.C., Gunkler, T.A., and Ricchiazzi, P.J. 1984, Ap.J., 282, 296.

Hagyard, M.J. 1988, Solar Phys., 115, 1.

Lites, B.W., and Skumanich, A. 1987, Ap. J., 322, 473. (LS)

Lin, Y., and Gaizauskas, V. 1987, Solar Phys., 109, 81.

Low, B.C. 1985, in *Measurements of Solar Vector Magnetic Fields*, ed. M.J. Hagyard, NASA CP2374 (NASA: Scientific and Technical Information Branch, 49.

Mickey, D.L. 1975, Solar Physics, 97, 223.

Moore, R.L., Hagyard, M.J., and Davis, J.M. 1987, Solar Phys., 113, 347.

Ronan, R.S., Mickey, D.L., and Orrall, F.Q. 19871 Solar Phys., 113, 353. (RMO)

Penn, M.J., Mickey, D.L., Canfield, R.C., and LaBonte, B.J. 1990, in preparation.

Sakurai, T., Makita, M. and Shibasaki, K. 1985, in Theoretical Problems in High-Resolution Solar Physics, MPA 212, 313.

Stenflo, J. 1971, in Solar Magnetic Fields, I.A.U symposium No. 43, ed. R. Howard, (Dordrecht: D. Reidel), 101.

Zirin, H. 1985, Ap. J., 291, 858.

#### Discussion

- A. Skumanich: It may be a matter of similar scales and similar azimuthal fields that explains the fact that Lites and I have observed similar teraamp currents in one particular sunspot (September 1980). The energy in the field due to these currents were a small perturbation on the basic poloidal sunspot field.
- J.C. Henoux: What is the mean current density in the currents system?
- R. Canfield: If we concentrate our attention on the two major currents, then (at our  $\sim 6'' \times 6''$  spatial resolution) the mean current density is  $\sim 5 10 \text{ mA/m}^2$ .
- M. Semel: If the integral method were so bad, one should be able to show it by applying the method to Stokes profiles obtained through the Unno equations.
- J. Stenflo: In the Gold-Hoyle flare model that you favored there are two parallel current loops, and the flare occurs through reconnection between the loops. The presence of such a current morphology was not obvious to me from your current and flare maps.
- R. Canfield: The current map shows two major regions of upward currents and only one major region of downward currents, lending credence to our interacting-loop suggestion. The Gold-Hoyle model is favored only in a very narrow (geometric) sense, i.e. it invokes interacting current-carrying loops.
- A. Gary: How many pixel points were used in calculating  $J_z$ ? How persistent were the  $J_z$  contours from day to day? If the  $J_z$  contours were constant over several days in which flares occurred, does this mean the reconnection in flare activity may not be as important as previously believed?
- R. Canfield:  $J_z$  was calculated using the four points forming a square surrounding the pixel of interest. The day to day change of  $J_z$  was sufficiently large that it is not possible to reach such a strong conclusion regarding reconnection.
- A. Gary: How are the currents calculated?
- R. Canfield: In the maps showing vertical currents and corresponding magnetic fields the values of the currents were calculated at all points where four pixel corners come together, using the values of the transverse field in only those four pixels to compute  $\nabla \times \vec{B}$ . In the overlays of the current maps on the blue-wing  $H\alpha$  images, interpolation has to be done in order to co-register them. This interpolation introduces some additional smoothing in the current maps co-registered with the  $H\alpha$  data that is not present in the original maps.

## VELOCITY GRADIENTS ACROSS A FLARING NEUTRAL LINE FROM STOKES II MEASUREMENTS

## A. SKUMANICH and B. LITES

High Altitude Observatory
National Center for Atmospheric Research\*
P.O. Box 3000
Boulder, Colorado, USA

#### SUMMARY

The pattern of profile reversals formed due to incomplete cancellation of the Stokes net circular polarization parameter, V, when the resolution element contains the magnetic neutral line (in the observer's frame) represents a sensitive diagnostic of the line-of-sight velocity difference between the opposite polarity regions. Typical V profile patterns found in such circumstances with the HAO/SPO Stokes II polarimeter are illustrated. Resulting velocity differences are estimated both by analytic decomposition of a specific neutral line profile and by composition of profiles from elements on opposite sides of the neutral line. Pre- and post-flare Stokes II observations of Hale Active Region #16604 are under such analysis. Preliminary results show that just before the flare the neutral line had a large scale "rotation" with east and west end segments moving oppositely towards the nearest neighboring spots. The relationship of this flow to the flare and its status after the flare is under study.

#### I. INTRODUCTION

I think we all agree that there is a continuing need to quantify the state of vector fields along a magnetic neutral line and to determine what changes occur after a two-ribbon flare. Of equal interest is the nature of the pre-flare velocity field associated with the neutral line and its role in stressing the field and/or participating in the initiation of the flare.

btokes II profiles obtained over a region containing a flaring neutral line allow one to address just these issues. We consider in this report a description and preliminary analysis for Stokes profiles observed just before a flare.

#### II. OBSERVATIONS

Hale active region #16604 (NOAA 2247), which had frequent weak  $H\alpha$  flares, experienced a two-ribbon flare accompanied by a class C X-ray event with peak emission at  $\approx$ 18:40 UT on 1990 January 23. This flare occurred after the 2nd and before the 3rd raster of the flaring site of a 5-raster Stokes profile sequence of this region. A raster consisted of  $20 \times 20$  positions in right ascension and declination respectively (62 Mm (EW)  $\times$  68 Mm (NS) on the Sun) at 5" intervals and had an integration aperture of 1."2  $\times$  6" and an integration time of 3 sec. It was executed in flyback mode and was completed in 45 min. Stokes profiles of the  $\lambda$ 630.25 nm Fe I line were obtained with a spectral purity of  $\approx$ 1 pm and  $10^{-3} - 10^{-4}$  polarimetric noise, refer Bauer et al. (1981) for more detail.

Figure 1 presents a "circular" polarization map observed just before the flare for #16604 which was centered at 16° S latitude and 10° W of central meridian (heliocentric). Represented in gray scale is the mean one-sided wavelength integral of the Stokes  $V/I_c$  parameter, i.e., the average of the absolute values of the one-sided integrals from line center to blue and red wings with the sign of the blue extremum in V being assigned to this average. This quantity is approximately proportional to the line-of-sight field (which is inclined  $\simeq 15$ ° to the solar normal). White polarity

<sup>\*</sup>The National Center for Atmospheric Research is sponsored by the National Science Foundation.

is a positive average or outward field and black, negative. White lines indicate neutral or polarity reversal lines. The first raster point, RP 1, is at the top north-west corner (row 1, column 20), RP 20 is at the top north-east corner (1,1), and the last, RP 400, at the south-east corner (20,1). The flare occurred at the lower E-W neutral line from  $\simeq$  RP 234 at (11,7) to  $\simeq$  RP 301 at (15,20). Note that heliocentric North is at position angle  $P = -8^{\circ}$  (i.e., NNW). A white-light (E-W reversed) image of this region is illustrated by Bauer et al. (1981).

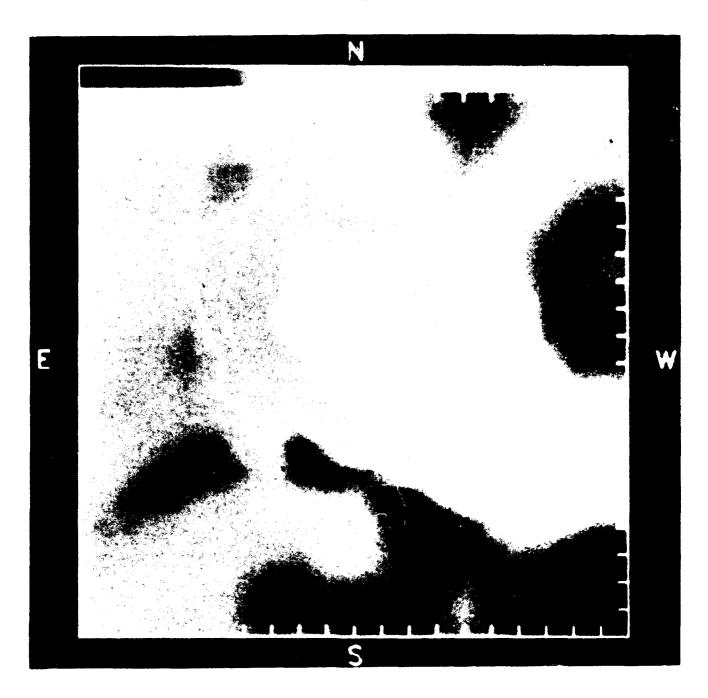


Fig. 1. A "circular" polarization map of Hale #16604 centered on 16°S and 10°W. White is a positive or outward line-of-sight field and black is negative. A '+' spot appears in the center and a '-' spot at the SW corner. The flare occurred along the southern neutral line. Geocentric directions are indicated.

## III. STOKES PROFILES

An examination of the Stokes profiles for positions about the neutral line indicated that the V profiles were "disturbed" and showed multiple reversals rather than the canonical single reversal given (approximately) by the intensity derivative of a symmetric absorption line. This is illustrated by the V profile in Figure 2 (lower right panel) for RP 251 at (12,10), a point in the neutral line just above the '+' polarity island in the lower central part of Figure 1. The dots represent the data while the solid curve represents a reference profile obtained by an Unno-Rachkovsky fit, by least squares, refer Skumanich and Lites (1987), to the (I, Q, U) parameters with a fixed estimate for the field inclination to the line of sight, viz. 75°. Only the large-size dots were used in the fit. The transverse field, which is insensitive to the assumed inclination, implied by the fit is  $B_t = 1050$  G and has a position angle of 278°. We note that the (Q, U) parameters are referred to a coordinate frame with the positive X axis (in the plane of the sky) along terrestrial W (negative right ascension) and positive Y axis along terrestrial N, i.e, polarization (and field) position angles are measured counterclockwise from West  $(0^\circ)$  to North  $(90^\circ)$ .

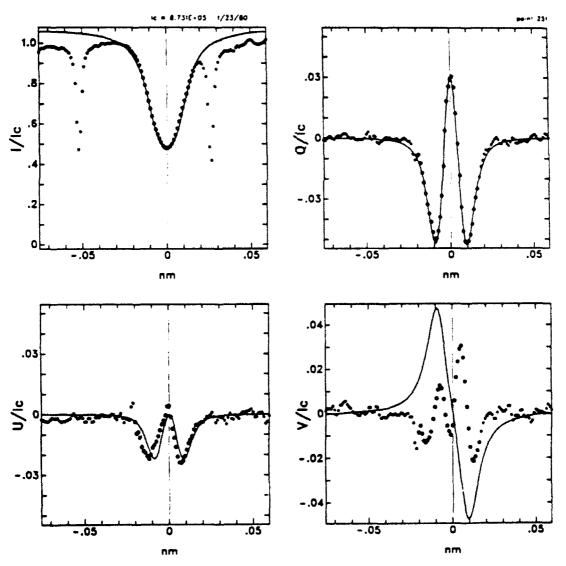


Fig. 2. Stokes parameters for the Fe I  $\lambda 630.25$  nm line at RP 251. The feature at pixel  $\simeq -0.02$  nm is an instrumental spike. Solid line is an analytic fit with fixed inclination.

As this conference is also devoted to instrumental issues we would like to comment briefly about calibration difficulties. In spite of the care involved, the Stokes II instrument response (or calibration) matrix X, for each raster was found to contain errors. X is such that if  $s_{adu}$  is the instrumental Stokes vector and s is the physical vector entering the polarimeter, then  $s_{adu} = Xs$  (refer Tomczyk, Stoltz, and Seagraves (1991) in these proceedings).

The displaced dashed polarization curves in Figure 3 represent the Stokes profiles for RP 251 that result from the use of the measured response matrix. They indicate a polarization not only in the continuum but also in the two telluric lines, i.e., they indicate  $I \rightarrow (Q, U, V)$  crosstalk. This results from errors in the first column,  $X_{j1}$ , of the response matrix. Removing this error after the fact one finds the solid curves in Figure 3. The second set of dashed curves are the initial polarization profiles but shifted by a constant amount for a more direct visualization of the corrections in shape. In addition, a 10%  $V \rightarrow U$  crosstalk, i.e., an error in the  $X_{34}$  term was also discovered. This term is a difficult element to determine (Murphy and Skumanich 1991; refer also to Lites et al. 1991, in these proceedings).

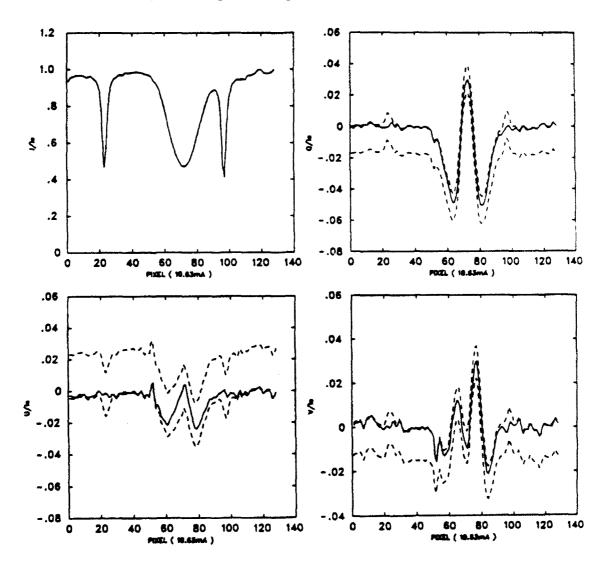


Fig. 3. The solid curves give the corrected Stokes profiles for RP 251 while the displaced dashed curves are the uncorrected profiles which show the effect of errors in the polarimeter response (calibration) matrix.

Two additional "disturbed" profiles typical of the west end of the neutral line are shown in Figure 4. In the case of the left group of four panels, RP 282 at (14,19), the reference fit yielded a transverse field  $B_t = 390$  G with a position angle of 345°. The V profile appears to have a central reversal due to the negative polarity component that might be erroneously classified as a magneto-optic effect albeit exaggerated. In the case of the right four panels, RP 286 at (14,15), the reference fit yields  $B_t = 620$  G with position angle of 333°. Here the negative polarity component produces a distinct asymmetric effect.

## IV. VELOCITY COMPOSITION OF RP 251

Using the transverse fit values as a guide and taking typical thermodynamic values for active regions as observed by Lites and Skumanich (1990), we determine by trial and error a two-component field vector that approximates the RP 251 data. Such a decomposition is given in Table I. The composite profile is compared to the data in the left four panels of Figure 5. The position angle of the transverse field was held at 278°. The Q, U parameters in Figure 5 are described in the canonical frame whose X-axis is along this fixed azimuth. The right side of Figure 5 shows the effect of changing the inclination of the negative field ( $V_b^-$  component) to 115°.

Component	Field		Line	Thermodynamics*				
	B G	$INCL\ (\psi)$	Center (pix)	$\mathrm{f}\mu B_1$	${ m f} B_0$	$\eta_0$	<b>a</b> (mA)	$\Delta \lambda_D$
$V_b^+$	1400	75°	74	.25	.14	5	0.1	45
$V_{\star}^{-}$	1000	105°	70	.30	.17	5	0.3	45

Table I: Decomposition of RP 251

These results show that the  $V_b^-$  component is blue shifted relative to the  $V_b^+$  component by 4 pixels or 2 km/sec. With the inclinations to the line of sight given in Table I, one finds that a field aligned flow towards the '+' spot of  $\simeq 4$  km/s results in both components if one presumes it lies close to the plane passing through the center of the disk. If the flow is that of the  $V_b^-$  component alone then it is along the photosphere and towards the '+' spot at  $\simeq 8$  km/sec. Our decomposition is tentative and a more careful analysis is needed to determine the correct interpretation.

## V. "DISTURBED" PROFILE GALLERY

A useful exercise that allows one to classify the types of disturbed profiles is to construct a gallery of composite profiles by superposing two V profiles from opposite sides of our neutral line with different fill factors and relative velocity shifts. We consider the two points, RP 266 ( $V_b^+$ ) at (13,15) and RP 306 ( $V_b^-$ ) at (15,15), which are neighbors of RP 286, which was illustrated in Figure 4. Their Stokes parameters are illustrated in Figure 6. In the case of RP 266 the least squares fit to all four Stokes parameters yields a transverse field of 720 G with position angle 334°. For RP 306 one finds 220 G at 339°. The field inclinations are 79° for RP 266 and 128° for RP 306. One also finds that RP 306 is redshifted by 0.3 pixels (0.15 km/s) relative to RP 266.

<sup>\*</sup>These parameters are as normally defined (refer Skumanich and Lites 1987).

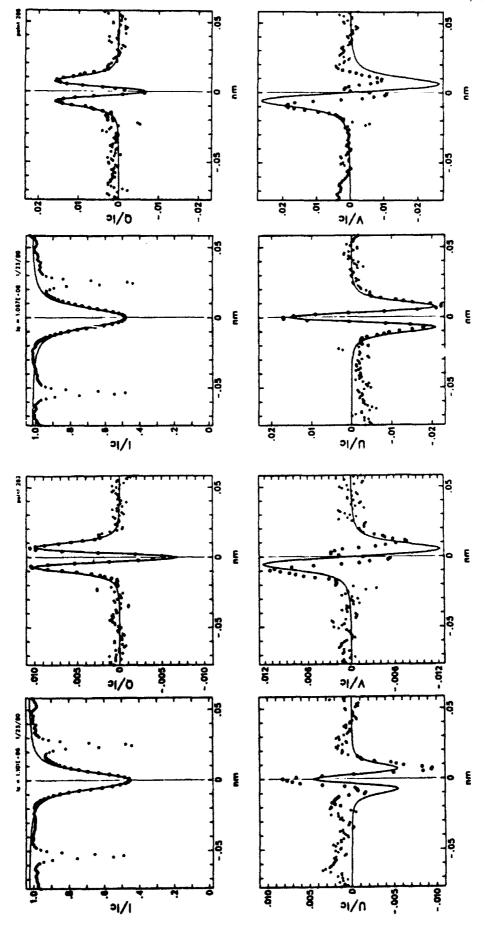


Fig. 4. Left (right) four-panel presents the Stokes profiles for RP 282 (RP 286). The solid curves are a fit to the linear polarization and intensity with fixed value for the inclination of the field. Only the large circle points were used in the fit (i.e., -20 pm to +15.7 pm about line center).

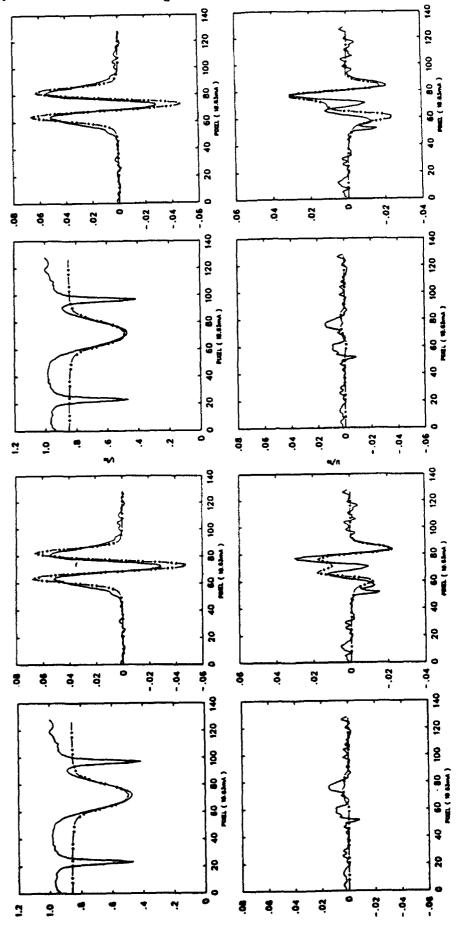


Fig. 5. A possible decomposition of RP 251. Here the data is given by the solid curves while the analytic two-component composite is given by the broken curves. Parameters Q, U are in the canonical frame whose X-axis is at position angle 278°. The left (right) four-panel has the negative polarity at 105° (115°) inclination. Note that I pixel = 10.63 mA = 1.063 pm.

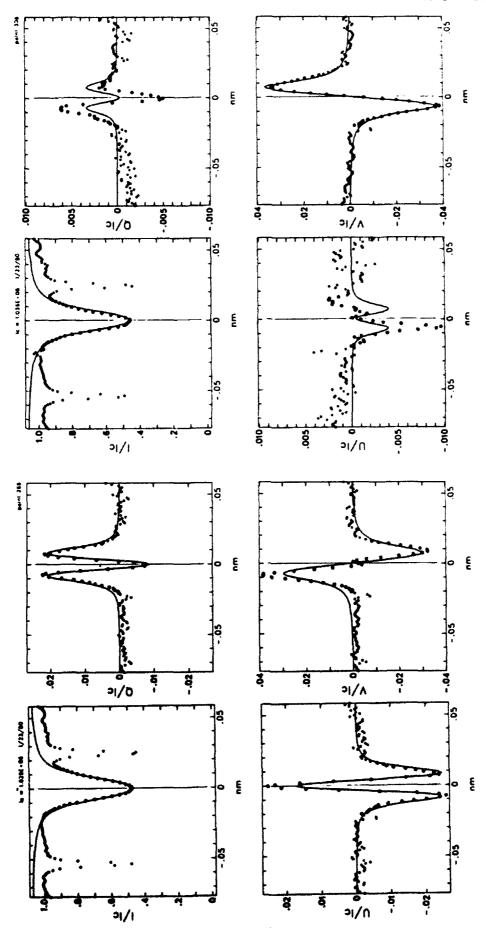


Fig. 6. Stokes parameters for two points neighboring RP 286 (refer Fig. 4). RP 266 (306) is on the left (right). Solid curves represent an analytic fit. Note the  $V \rightarrow (Q, U)$  cross-talk for RP 306.

We now construct composite profiles using the expression

$$\mathbf{s}(\Delta\lambda) = (1-f)\mathbf{s}_{266}(\Delta\lambda) + f\mathbf{s}_{306}(\Delta\lambda - v\lambda_0/C)$$

where f is the negative polarity's fill factor and v is its velocity relative to the positive polarity. The results for the V parameter are presented in Figure 7 where each row, top to bottom, has the value f = 0.2, 0.3, 0.4, 0.45 and each column, left to right, has the velocity shift v = -2, -1, 0, 1 km/sec respectively. Note that the 0.15 km/sec shift must be added. The resulting profiles are representative of most of the observed profiles. We also note that this is true for the 'abnormal' V profiles presented by Livingston (1991), refer to his panels (10) through (13).

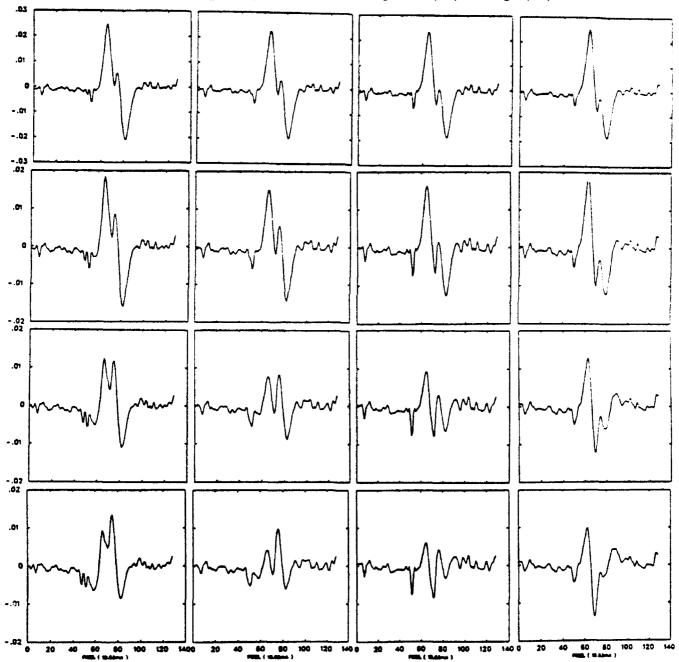


Fig. 7. Composite V profiles from the superposition of RP 266 and RP 306. The absorption spikes at pixel  $\approx$  50 are instrumental. Increasing fill factor for  $V_b^-$  is downward with increasing velocity left to right, left (right) two columns are blue (red) shifts.

A comparison of the V profile for RP 286 with those in Figure 7 indicates that  $f \simeq 0.4$  and  $v \simeq 0.5-1$  km/s. With this fill factor one finds that  $\bar{B}_t^2 = (1-f)B_{t266}^2 + fB_{t306}^2 = (570\text{G})^2$  while the analytic fit to RP 286 gave  $(620\text{ G})^2$ . For this portion of the neutral line one finds that the motion is towards the '-' polarity sunspot.

## VI. CONCLUSION

It appears that lack of spatial resolution and the presence of relative motions among magnetic elements in the resolution window are responsible for the appearance of multiple reversals in the Stokes V profile. These are sensitive to fill factor and velocity amplitudes and provide a diagnostic of the unresolved structures. Our preliminary results for the 1980 January 23 observations indicate preflare motions at the neutral line which appear to be directed towards the nearest spots related to the neutral line. The persistence of this flow and its relation to the flare are under further study.

#### ACKNOWLEDGMENTS

The authors appreciate the comments and careful reading of the manuscript by Dr. G. Murphy and thank L. Croom for composing the final figures and camera-ready copy.

## REFERENCES

- Bauer, T. G., Elmore, D. E., Lee, R. H., Querfield, C. W., and Rogers, S. R. 1981, Solar Phys., 70, 395.
- Lites, B. W., Elmore, D., Murphy, G., Skumanich, A., Tomczyk, S., and Dunn, R. B. 1991, in *Solar Polarimetry*, ed. L. J. November (Sunspot, N. Mex.: National Solar Observatory, Sacramento Peak), forthcoming.
- Lites, B. W., and Skumanich, A. 1990, Ap. J., 348, 747.
- Livingston, W. 1991, in *Solar Polarimetry*, ed. L. J. November (Sunspot, N. Mex.: National Solar Observatory, Sacramento Peak), forthcoming.
- Murphy, G., and Skumanich, A. 1991, "Stokes Polarimeter Calibration Methodologies: Information Content, Completeness and Posedness," NCAR Technical Note, in preparation.
- Skumanich, A., and Lites, B. W. 1987, Ap. J., 322, 473.
- Tomczyk, S., Stoltz, P., and Seagraves, P. 1991, in *Solar Polarimetry*, ed. L. J. November (Sunspot, N. Mex.: National Solar Observatory, Sacramento Peak), forthcoming.

#### Discussion

- A. Cacciani: I would comment that because of magneto-optical effects it is possible to get circular polarization even if the magnetic field is purely transverse provided its azimuth is variable with depth in the sun. Do you think this effect can help explaining the particular Stokes V you have found on the neutral line dividing regions with positive and negative longitudinal field)?
- A. Skumamich: Since the magnitude of V is comparable to (Q, U), I do not think azimuthal twist and its variation with height is important. In addition the optical thickness appears not to be high to enough for this to be effective. On the other hand this is an interesting suggestion and merits further study.
- K.S. Balasubramaniam: Although it may be possible to tune the various parameters to finally fit the profile, would it be possible to get "unique" solutions and physically how realistic would they be?
- A. Skumamich: How unique are the thermodynamic parameters is unclear as they, except for the Doppler width variations, play a weak role in the formation of the polarization parameters. I have tried 22 mÅ instead of 45 mÅ and the magnetic field fits are not significantly affected. However further study is needed.
- **L. November:** Have you tried combining  $\vec{B}$  information from adjacent points on the side of the neutral line where the profiles are uncontaminated?
- A. Skumanich: We intend to use such adjacent points as initial values for a least-square two component fit.

## PROPERTIES OF THE WHITE-LIGHT CORONA POLARIZATION DURING MAXIMUM OF THE SOLAR CYCLE

JÚLIUS SÝKORA Astronomical Institute of the Slovak Academy of Sciences 059 60 Tatranská Lomnica, Czech and Slovak Federal Republic

#### ABSTRACT

The results of measuring the polarization of the white-light corona, carried out during the February 16, 1980 solar eclipse, are presented. The degree of polarization was observed to be relatively high all round the sun, with the exception of a coronal hole near the south pole. Together with the well-expressed streamers, the high degrees of polarization were observed in the narrow ray at P =  $210^{\circ}$  and also in the broad region P =  $310^{\circ}$  -  $350^{\circ}$ . The general increase of coronal density characteristic for solar cycle maximum and accidental concentration of the coronal structures to the plane of sky could be responsible for such peculiarities.

#### 1. INTRODUCTION

The measurement of polarization of the corona belongs to the standard experiments carried out during total solar eclipses. Nevertheless, with respect to surviving discrepancies between the observations and the theory, and even among the results obtained by different observers during the same eclipse, it seems still valuable to deal with this problem. Namely, for example, in order to fit the theory as much as possible to variety of the forms and structures of the corona observed at different phases of the solar cycle, including, of course, differences in activity around the sun at a given eclipse.

I don't wish to summarize here the previous and very numerous achievements in the field. Perhaps, at least, the detailed papers of Van de Hulst (1950), Saito (1970) and Dürst (1973) should be mentioned. An interesting inverse approach to the problem was described by Badalyan (1986), where on the basis of physical considerations a coronal model was suggested, from which the distribution of coronal brightness was calculated and compared with the real observations. Doing so, namely the use of the polarization data showed to be highly promising because they are not spoiled by the F-component of the corona.

## 2. CONSIDERATIONS

Numerous structures can be seen on the images of the corona, taken during period of the solar maximum: streamers, narrow rays, coronal loop systems, etc. However, the contrast of these details is rather low and the isophotes, obtained from the corresponding images, are almost circular in shape (Figure 1). In the other words, while the flattening of the isophotes is clearly visible during the period of the solar cycle minimum and of lower solar activity, it is practically non-existent during the solar maximum. Since the brightness of the corona depends firstly on the density  $n_0$  at its base, the absence of flattening of the corona during the solar maximum period is thus connected with the very small variability of  $n_0$  around the sun's limb.

On the contrary, the measurement of polarization has proved to be more informative when investigating the distribution of coronal matter, namely in the period of

the maximum of the solar cycle. This simply follows from the fact that degree of polarization differs greatly in coronal holes and in streamers, while these features are practically undistinguishable when their white-light brightness is measured at distances up to  $\mathbf{q} \approx 2 R_{\Theta}$ .

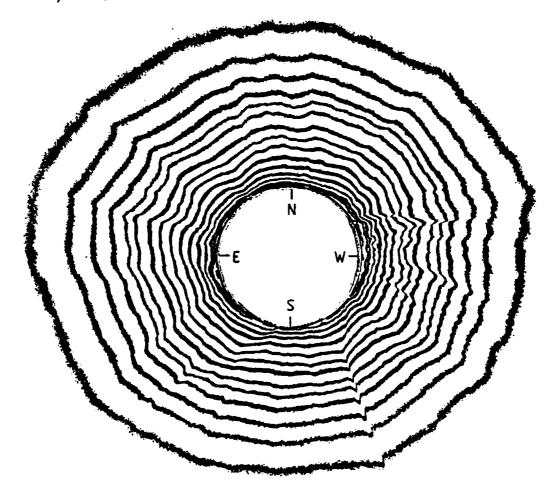


Fig. 1. Solar maximum type corona of 16 February 1990 with its "almost circular in shape" isophotes.

From the theoretical point of view the high degree of polarization should be expected practically all around the sun (at all position angles P) in period of the solar maximum. It follows from two circumstances. The first is connected with a well-known general increase of the coronal density, i.e. of the parameter  $n_0$  of the hydrostatic distribution of the density. The value of the observed degree of polarization of all the coronal radiation is given by the ratio

$$p = \frac{K_t - K_r}{K_{t} + K_r + F}$$
 (1),

where  $K_{t}$ ,  $K_{r}$  are the intensities of the tangential and radial components of the K-corona and F represents the brightness of the dust component. Because the intensities of the electron components  $K_{t}$  and  $K_{r}$  are proportional to the density, it implies, that with increase of the coronal density the F-component is relatively smaller and the observed degree of polarization increases (a numerical experiment demonstrating this is given at the end of this paper).

The second effect which we would like to pick out is connected with the possible influence of the non-homogeneities of the corona on the measured polarization. Suppo-

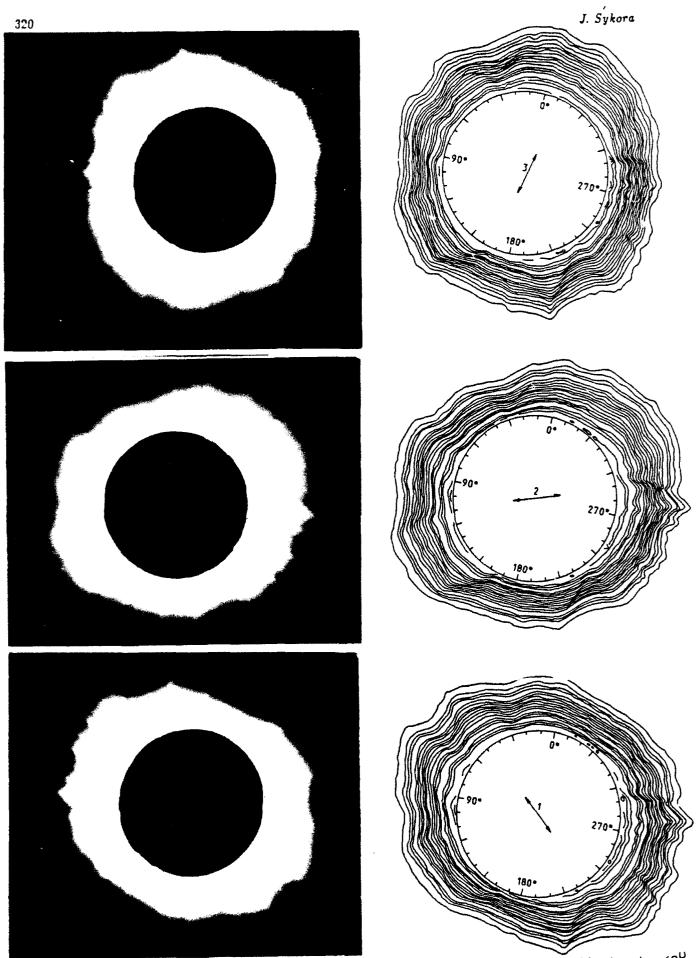
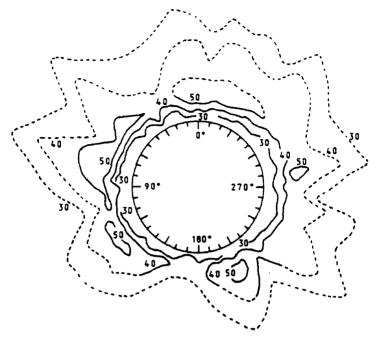


Fig. 2. The solar corona taken in three positions of polaroid differing by  $60^{\circ}$  and the corresponding systems of isophotes.



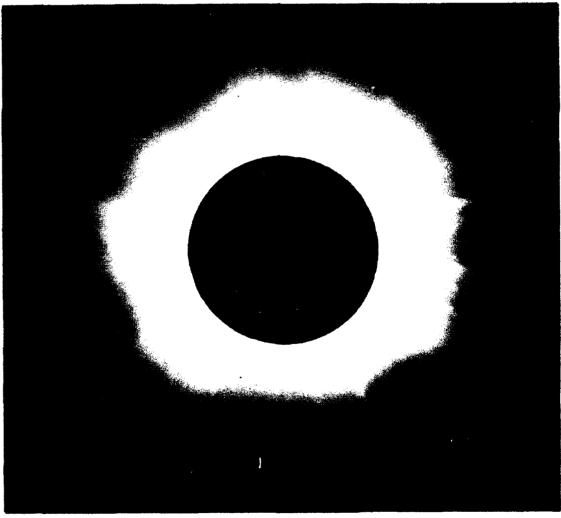


Fig. 3. The isolines of the degree of polarization, combined from two sets of the polarized pictures (the full and dashed lines) and the image of the corona taken in white-light without polaroid.

322 J. Sykor

sing that the coronal matter at heliocentric distances larger than  $1.3P_{\Theta}$  is closed exclusively in discrete coronal structures and supposing that there exists a certain concentration of these structures to the plane of the sky owing, of course, to the real distribution of the active regions on the solar surface, it also results in increase of the degree of polarization at proper segments of position angles. The corresponding polarization in such a regions can even to exceed the maximum values calculated for a dense spherically symmetrical corona. Namely, this fact seems to be prospective for investigation of the density distribution or, if you wish, for identification of the separate coronal structures.

#### 3. OBSERVATION AND THE RESULTS

Of course, I hoped to say here a few words about measurement of polarization during July 22, 1990 solar eclipse. I observed at Cherskiy (far east of the USSR), but unfortunately, the rainy weather spoiled the observation. That is why I should restrict myself to the polarization measurements carried out during the last solar maximum, namely on February 16, 1980 (Rušin and Sýkora 1981).

The images of the white-light corona were taken in three positions of the polaroid, differing by  $60^{\circ}$  from one another, with exposures of 1/250, 1/60, 1/15, 1, 4 and 16 seconds. The NP-27 ORWO emulsion has been used, allowing, together with the polaroid, observations in the range of 410-670 nm. As an example, one triplet of the images (1/15 of a second) is shown in Figure 2, together with the corresponding equidensities.

In upper part of Figure 3 the isolines of the degree of polarization, calculated according to the formula

$$\rho = \frac{2 \left[ I_{1} (I_{1} - I_{2}) + I_{2} (I_{2} - I_{3}) + I_{3} (I_{3} - I_{1}) \right]^{1/2}}{I_{1} + I_{2} + I_{3}}$$
(2),

are plotted. The comparison with the image of the corona taken in white-light without polaroid (lower part of Figure 3) indicates that the regions of increased polarization  $p \sim 50$ % relate to the isolated coronal streamers or to their superimpositions at position angles  $P = 50^{\circ}$ ,  $73^{\circ}$ ,  $203^{\circ}$  - very narrow streamer,  $235^{\circ}$  and  $280^{\circ}$ .

In comparing the above data with the positions of the boundaries of the background magnetic fields at the E and W limbs (Livshits and Sýkora 1983), determined immediately from magnetic field measurements (Kitt Peak, Stanford) as well as synoptic H<sub>C</sub>-charts, one can see that the big streamers and a number of small rays are spread out just above those boundaries. On the green line 530.3 nm coronal pictures it is usually possible to find systems of rather high loops at the base of the streamers (see for example P =  $72^{\circ}$  –  $96^{\circ}$  in Figure 1 of Livshits and Sýkora 1983), but generally the correlation between the degree of white-light polarization and the brightness of the 530.3 nm corona is poor. For example, 'the bright coronal condensations around P ~97° and others (Badalyan et al. 1984) are practically not visible in polarization data.

The low degree of polarization near  $P \sim 165^{\circ}$  is due to evident coronal hole present there. Further, in case of this near maximum 1980 corona the regions without streamers are often characterized by so high degree of polarization (at P =  $320^{\circ}$  –  $350^{\circ}$ , P =  $120^{\circ}$  –  $140^{\circ}$ ) which in other phases of the solar cycle are typical only for the well-developed streamers. This is demonstrated in Figure 4, where the polarization is well above 50 % and, except of that, the characteristic dependence of the degree of polarization on distance from the sun is shown.

#### 4. NUMERICAL EXPERIMENT AND CONCLUSION

Consequently, our analysis as well as the results of Dürst (1982) show that the polarization of the corona during the solar maximum is characterized by at least two peculiarities. The first of the effects mentioned above, i.e. the increase of the degree of polarization with the increase of density at the base of the spherically

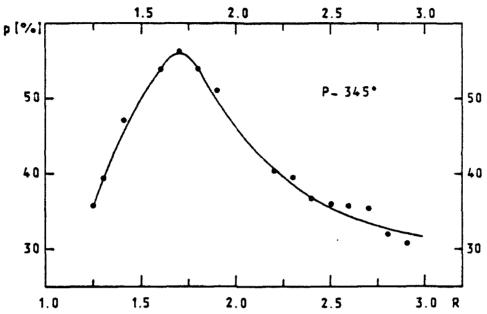


Fig. 4. An example of the dependence of the degree of polarization on the distance from the sun in a region near the north pole  $(P = 345^{\circ})$  without any evident coronal streamers.

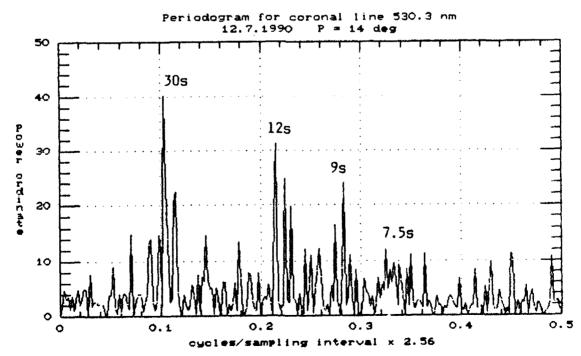


Fig. 5. The periodogram of the oscillations in 530.3 nm coronal line as detected on July 12, 1990 near the north pole ( $P = 14^{\circ}$ ).

symmetrical corona, is manifested very distinctly and seems to be without discussion. To illustrate the second effect, i.e. the increase of the degree of polarization with the increase of the number of coronal structures in the plane of the sky, we can present the following numerical experiment. At the heliocentric distance of 1.5 Re we adopt the characteristic values given by Badalyan (1986):  $n_0$  = 2.5x108 cm  $^3$ ,  $k_{\rm t}$ =600 (all the brightness are expressed in  $10^{-10}$  of the mean brightness of the centre of the solar disk) and,  $K_{\rm r}/K_{\rm t}$ =1/4. Taking F = 260 and using equation (1) we obtain p = 44.6 %. Supposing now that the spherically symmetrical corona contribute to the total brightness of the corona by  $K_{\rm t}$ =300 with the same ratio  $K_{\rm r}/K_{\rm t}$ =1/4 and the structural elements by  $K_{\rm t}$ =400, but owing to a certain concentration of them to the plane of the sky with the ratio  $K_{\rm r}/K_{\rm t}$ =1/5, then, adopting the same intensity of F-corona, p = 48.9% is obtained. This evokes that the increase of the observed degree of polarization for a few procents in comparison with the dense spherically symmetrical corona can undoubtedly result from the non-homogeneous structure of the corona.

The full analysis of the white-light corona polarization, the comparison of the coronal structures identified in the polarized light with the active features of the lower solar atmosphere and some theoretical considerations on non-homogeneous model of the corona will be published in a short time.

#### 5. CONCLUDING REMARK

In the end, I take opportunity to say a few words about solar physics performed in our institution and related to the topic of the present workshop. At the top of Mt. Lomnický Štít (2632 m) the double C. Zeiss coronagraph (D = 20 cm) is located to observe coronal emissions and prominences. Lately, measurement of polarization in FeXIV 530.3 nm coronal emission line and measurement of oscillations in that line (see example in Figure 5) have been put into operation (Rušin and Minarovjech 1990). Except of that, there are, of course, the plans to continue in measuring the polarization in 530.3 nm and 637.4 nm emission lines and in the white-light corona during solar eclipses. At the foot of the hill a new Stará Lesná Observatory (810 m) is operated. The horizontal solar telescope (D = 0.5 m, f = 35 m) and the double solar telescope to observe the photosphere and chromosphere of the sun have been just installed. We undertake the first steps to apply the physical methods of solar polarimetry in these instruments, as well.

#### REFERENCES

- Badalyan, O.G. 1986, Polarization of white-light corona under hydrostatic density distribution, Astron. Astrophys. 169, 305.
- Badalyan, O.G., Livshits, M.A., and Sýkora, J. 1984, Structure of the inner corona derived from observations of the eclipse of 16 February 1980, Solar Phys. 93, 143.
- Dürst, J. 1973, Helligkeit, polarisationsgrad und elektronendichte der Sonnenkorona, Astron. Mitt. Zürich No. 320.
- Dürst, J. 1982, Two colour photometry and polarimetry of the solar corona of 16 February 1980, Astron. Astrophys. 112, 241.
- Livshits, M.A., and Sýkora, J. 1983, Struktura korony v zelenoj linii i granici poliarnostej fonovych magnitnych polej, Astron. Zh. 60, 340.
- Rušin, V., and Minarovjech, M. 1990, Short-term oscillations in green and red coronal lines, presented at June 1990 Heidelberg Meeting "Mechanisms of Chromospheric and Coronal Heating", ed. P. Ulmschneider, in press.
- Rušin, V., and Sýkora, J. 1981, Report on the solar eclipse expedition of February 16, 1980, Bull. Astron. Inst. Czecho-Slovakia 32. 59.

Saito, K. 1970, A non-spherical axisymmetric model of the solar K corona of the minimum type, Ann. Tokyo Astron. Obs. 12, 53.

Van de Hulst, H.C. 1950, The electron density of the solar corona, Bull. Astron. Inst. Netherlands 11, 135.

J. SÝKORA: Astronomical Institute, 059 60 Tatranská Lomnica, Czech and Slovak Federal Republic.

#### Discussion

- S. Koutchmy: To improve models of coronal hole, precise measurements of the radial variation of the linear polarization ratio is very much needed; do you have such results?
- J. Sykora: We are just ready with such measurements on coronal hole observed near the south pole during the February 16, 1980 solar eclipse. We need to finish the physical analysis of them.
- S. Koutchmy: I wonder if you took into account the Earth atmosphere induced effects in your "oscillation" data analysis of the green line intensities; for example 5 minute oscillation can be nicely recorded using the scattered light outside the solar disc.
- J. Sykora: Our results are very preliminary. We need to analyze all the possible influences on the measurements. At present, we believe that most of the atmospheric and instrumental influences on our measurements are removed by subtracting the "oscillation of the continuum", measured close to the 530.3 nm coronal line simultaneously, from the oscillation of the intensity measured in this line.
- R. Altrock: What type of detector was used to record 5303Å oscillations?
- J. Sykora: A high sensitivity TV camera.

### INTERPRETATION OF POLARIZATION MEASUREMENTS OF CORONAL Fe XIII (10747Å) EMISSION

Raymond N. Smartt
National Solar Observatory/Sacramento Peak
National Optical Astronomy Observatories
Sunspot, NM 88349, U.S.A.

and

Charles W. Querfeld
Ball Aerospace Systems Group
P. O. Box 1062
Boulder, CO 80306, U.S.A.

#### Abstract

Measurements of the linear polarization of Fe XIII (10747Å) coronal emission are discussed. Uncertainties arise because of the unknown magnitude of certain depolarizing effects and reductions in the magnitude of the measured polarization because of line-of-sight and field-of-view integrations through an inhomogeneous medium. Nevertheless, polarization maps appear to be consistent with the general form of the expected magnetic field distribution in the corona as projected in the plane of the sky. Further, well-defined, large-scale coronal structures are found to be mapped well by corresponding polarization measurements. Interpretation of polarization Stokes components to determine the vector direction of the magnetic field is probably more uncertain because of fundamental uncertainties in some of the parameters that enter into the inversion procedure, especially so since the derived vectors depend very sensitively on the values of such parameters.

#### 1. Introduction

Coronal emission lines display partial linear polarization due primarily to resonance fluorescence of the incident anisotropic photospheric radiation field. The presence of a magnetic field produces an axis of quantization for the ions and the orientation of the polarization vector at any field point is parallel (or perpendicular) to the local magnetic field direction, projected on the plane of the sky. The 10747Å (Fe XIII) line transition has only one magnetic quantum state in its lower level, and hence its asymptotic limit of polarization for radiative excitation is unity. Observations in 10747Å therefore have the advantage of high intrinsic polarization. Moreover, it has a relatively high line strength and the sky brightness ( $\sim \lambda^{-2}$ ) is low relative to that for the visible. However, for any

Operated by the Association of Universities for Research in Astronomy, Inc. (AURA) under cooperative agreement with the National Science Foundation.

coronal line, the degree of polarization is reduced by such processes as isotropic collisional excitation, cascade effects, depolarizing collisions between magnetic sublevels, density inhomogeneities, the van Vleck effect, as well as line—of—sight (LOS) and field—of—view (FOV) integrations and density inhomogeneities (Sahal—Bréchot, 1974a, b, 1977; House, 1977; House et al., 1982; Querfeld, 1982). In general, the magnitude of the polarization is greatest when the magnetic field is radial — and half this value when the field is tangential and normal to the line—of—sight.

Although the theory of forbidden-line polarization is now well established (Sahal-Bréchot, 1974a, b, 1977; House, 1974, 1977; House et al., 1982), interpretation of the data involves significant uncertainties that are elaborated below. Nevertheless, the general theoretical interpretation appears to be soundly based — a systematic comparison of high-quality images recorded in the 5303Å (Fe XIV) line and corresponding polarization maps derived from 10747Å (Fe XIII) observational data, shows that the vector elements are aligned with the coronal structures where such structures provide the dominant contribution in the FOV and LOS. The van Vleck signature is clearly evident towards the top of large loop systems, as is to be expected if the observed loops trace the local magnetic field direction (Querfeld and Smartt, 1984).

#### 2. Observations

The polarimeter used to obtain measurements of the 10747Å (Fe XIII) line, as discussed here, has been described by Querfeld (1977). It is a two-channel design in which the incoming light is modulated in intensity, followed by a linear polarization sensor comprised of a rotating quartz half-wave plate and a Wollaston prism. The result of the modulation is to produce 25-Hz intensity, and 100-Hz polarization, signals. The detectors are cooled (194K) GaAsSb heterojunction photo-diodes with a quantum efficiency of 0.9. This system measures the intensity, I, and the linear polarization elements, Q and U, of the combined 10747A coronal emission line, K-corona, and sky in a 5.6 A passband centered on the emission line. Similar measurements are made simultaneously in an adjacent continuum passband. Subtraction of the two signals gives the polarization, pc and Ic for the line, and pk and Ik for the K-corona. About 130,000 polarization measurements have been obtained at heights of 1.1 R<sub>a</sub> to 1.8 R<sub>a</sub>, sampled sequentially at 128 points around the limb with a 5s integration time per point. Most measurements used a 1-arcmin field aperture, but values of 0.7 to 2.0 arc minutes were also used, depending on height and sky brightness. The measurements are dominated by noise only in the case of an exceptionally bright sky  $(> 2 \times 10^{-4} I_0)$  and a weak corona.

#### 3. Results and Discussion

Data from the above instrument have been presented elsewhere (see, for example, Querfeld and Smartt, 1984; Arnaud and Newkirk, 1987; Smartt and Arnaud, 1988). Here we are concerned with the problem of trying to extract the vector direction of the magnetic field from the Stokes components for each measurement.

Uncertainties arise in the derived values of the Stokes components I, Q, and U simply due to unknown contributions of depolarizing effects, as outlined above, and also to

the averaging effect of LOS and FOV integrations. Nevertheless, polarization values obtained with this instrument are, statistically, not inconsistent with calculated values that are based on idealized geometry and that neglect depolarizing effects — that is, the observed values are systematically and without exception less than the calculated values, and, with few exceptions, by a significant amount (Querfeld and Smartt, 1984).

The direction of the magnetic field vector is defined relative to the local radius passing through the observational point by polar and azimuthal angles  $(\theta, \phi)$  (House et al., 1982). Specifically, the interpretation aims primarily at obtaining magnetic field angles  $\theta$ ,  $\phi$  from measurements of I, Q, and U at some position angle and height in the corona. To obtain these angles requires either that the  $^3P_1$  sublevel populations be known or, equivalently, that  $N_e$  and the product of the abundance and ionization equilibrium  $N_i(T)$  is known. The coronal abundance is uncertain to at least a factor of two. Moreover the ionization equilibrium  $N_i$  is probably uncertain by a factor of two in magnitude and up to perhaps one—half million degrees in the temperature that maximizes  $N_i$ . For a confident interpretation, it is likely that the ionization and statistical equilibrium must be solved simultaneously and consistently since present calculations apply only to specific density regimes.

To provide a realistic method to carry out the inversion of the Stokes polarization Querfeld (1982) recast the statistical equilibrium equations for Fe XIII (Sahal-Bréchot, 1977; House, 1977) into a simple analytical form to obtain a zeroth order plane-of-the-sky solution. With synthetic data and without LOS integration, the inversion produces correct density and approximately correct (within  $\approx 0.1^{\circ}$ ) values for the field angles. Applied to real data, field angles that cluster in the  $\theta \approx 30^{\circ} \pm 15^{\circ}$  regime are produced. This is inconsistent with the assumption that field angles in the corona, although internally organized, should have more or less random orientation with respect to the observer. These values instead imply that real coronal emission-line data are less polarized than assumed in a simple model — reduced polarization due to FOV and LOS integrations is not accounted for in the inversion. Some additional depolarization is surely present and indeed is expected since depolarization can be caused by a variety of agencies. The interpreter infers N<sub>e</sub> from the observed intensity. If the coronal temperature differs by ten percent or so from the assumed value, the value of N<sub>1</sub> used in the inversion will be too large, the inferred value of Ne will be too small, and both the integration length, A, and the polarization will be too large. Similarly, if the assumed coronal abundance, Are or A are too large, large polarization will also result. Smaller values AFe, Ni and Ay all have the effect of requiring larger values of Ne to produce a constant intensity while diminishing the polarization.

Further preliminary work suggests that the abundance of iron in the corona might be significantly less than the value usually used and closer to the accepted photospheric value. The Fe XIII 10747Å data clearly require a reduction of the numerical values of either or both the ionization equilibrium or the abundance. We prefer the Jacobs et al. (1977) ionization equilibrium values that are smaller than the corresponding Jain and Narain (1978) values and that still require a further factor of about three reduction in the product ionization equilibrium and the abundance. To resolve such uncertainties, more accurate values for the coronal abundance are required.

#### References

Arnaud, J. and Newkirk, G.: 1987, Astron. Astrophys. 178, 263.

House, L. L.: 1974, Astron. Soc. Pacific 86, 490.

House, L. L.: 1977, Astrophys. J. 214, 632.

House, L. L, Querfeld, C.W., and Rees, D. E.: 1982, Astrophys. J. 255, 753.

Jacobs, V. L., Davis, J., Kepple, P. C., and Blake, M.: 1977, Astrophys. J. 211, 605.

Jain, N. K. and Narain, V.: 1978, Astron. Astrophys. Suppl. 31, 1. Querfeld, C. W.: 1977, Soc. Photo-Opt. Instrum. Eng. 112, 200.

Querfeld, C. W.: 1982, Astrophys. J. 255, 764.

Querfeld, C.W. and Smartt, R. N.: 1984, Solar Phys. 91, 299.

Sahal-Bréchot, S.: 1974a, Astron. Astrophys. 32, 147. Sahal-Bréchot, S.: 1974b, Astron. Astrophys. 36, 355.

Sahal-Bréchot, S.: 1977, Astrophys. J. 213, 887.

Smartt, R. N. and Arnaud, J. 1988, in Solar and Stellar Coronal Structure and Dynamics: a Festschrift in Honor of Dr. John W. Evans. Proceedings of the Ninth Sacramento Peak Summer Symosium, Sunspot, NM, 17-21 August, 1987, R. C.Altrock, ed., 451-457: Coronal Emission-Line Polarization.

#### BROADBAND LINEAR POLARIZATION MEASUREMENTS: THE SUN AND F - G - K DWARF STARS

#### J.L. LEROY

Observatoire du Pic du Midi et de Toulouse 14, Avenue Edouard Belin, 31400 Toulouse, France

Summary. The interpretation of polarization measurements performed within a broad spectral band ( $\Delta\lambda \sim 100~\text{Å}$ ) has to take into account:

- The polarization of the continuum, which is observed near the solar (or stellar) limb, strongly increasing towards the shorter wavelengths. Although it has been detected in eclipsing binaries, this phenomenon has been investigated in detail on the Sun only and there, one finds a very good agreement between the observations and the theory.
- The existence of a net polarization emerging from an absorption line results essentially from differential saturation of the Zeeman components in a transverse magnetic field. This phenomenon has been well documented in the solar case but practical applications to the magnetic vector diagnostic are more likely in the stellar case, when the lack of light prevents making the polarization analysis with a high spectral resolution. Computations as well as comparisons with solar active regions suggest a polarization degree of some units of 10<sup>-4</sup>, in the B standard band, for late-type dwarfs with large magnetic spots. At the present time, the detection of such an effect is still controversial in the case of solar type stars, but magnetic broadband polarization is clearly observed in magnetic Ap variables.

#### 1. Introduction

Throughout this paper we refer to "broadband" measurements when observations are performed within a spectral band wider than  $10\ \mathring{A}$  but narrower than  $1000\ \mathring{A}$ . According to this definition, the spectral region under study generally contains, in addition to the continuum, several spectral lines. The line contribution may be almost negligible (in the infrared solar spectrum) or overwhelming (ultraviolet solar spectrum and visible spectrum of late K-stars). Mixing together the polarization signals coming from different spectral lines and from the continuum looks to be a primitive approach and, for most purposes, one tries to treat separately the continuum and individual lines, or, even better, to scan the different parts of a line profile. Therefore, measurements obtained in a broad spectral band are not used for solar studies, since so much light is available. The situation is different, however, for stellar studies: accurate polarization measurements require a large number of photons, and the next task is to find out whether useful information can be derived from broadband measurements. In particular, it would be very interesting to obtain magnetic field determinations from polarization measurements within wide spectral bands. As usually, solar data come also into this type of investigation as a calibration of the method which is supposed

to be aimed at F - G - K stars, and thus, we begin this review with a short summary of the polarization properties of the continuum solar spectrum.

#### 2. Polarization of the continuum

#### 2.1. Polarization near the solar limb

It is a well known effect which has been investigated in detail, both by observation and theory. A synthesis of the results was presented twelve years ago at the time of the Lund workshop devoted to solar polarimetry (Leroy, 1977) and we summarize now only the main trends of this phenomenon:

- The polarization increases very steeply towards the limb: for the continuum near 5850  $\mathring{A}$ , the polarization degre is  $10^{-5}$  at 5 arc min.  $10^{-4}$  at 25 arc sec. and  $10^{-3}$  at about 2 arc sec. from the limb. The polarization vector is always parallel to the limb.
- The polarization increases very steeply towards short wavelengths: at a distance of 25 arc sec. from the limb ( $\mu = 0.226$ ) the polarization degree is  $10^{-5}$  at 9000 Å,  $10^{-4}$  at 6000 Å,  $10^{-3}$  at 4000 Å,  $10^{-2}$  at 2500 Å.

At the time of the Lund meeting, I mentioned some interesting points which gave reason for additional measurements: one of them was the apparent discrepancy between the observations obtained very close to the limb (5 arc sec.) and the theory developed by Dumont and Pecker (1971) which, once applied to the H.S.R.A. model atmosphere, forecasted smaller polarizations. For such observations near the limb, the best solution was to make measurements during an eclipse: taking advantage of the annular eclipse of April 1976, Arnaud (1987) was able to measure the continuum polarization around 4490 Å, at 1 arc sec. from the limb. The observed polarization degree (0.5 %) turns out to be well consistent with the Dumont and Pecker calculation. This last experiment gives one more reason to believe that the Sun's limb polarization is well understood and does not require additional efforts.

#### 2.2. Polarization near stellar limbs

It is often quoted that it was the search for limb polarization in eclipsing binaries which led to the unexpected discovery of interstellar polarization. Not so often is mentioned the fact that the polarization variability with the orbital period of a binary star, which was observed later, arises mainly from such phenomena as light scattering by extra-stellar material or light reflection from the component stars (Koch et al., 1989). Only in the last decade Kemp et al. (1983) were able to show the signature of limb polarization during the eclipses of Algol. Note that it is a small effect, the extra polarization to be measured being only about  $2 \times 10^{-4}$ .

As already stated, it is necessary, to reach such a level of accuracy, to perform the measurements within a rather broad passband ( $4000 - 5500 \ \mathring{A}$  in the latter case) so that one observes simultaneously the continuum and a lot of spectral lines. Now, coherent scattering in atomic lines submitted to an anisotropic excitation results also in linear polarization noticeable near the limb in some well known cases (the line of Ca I at 4227 A); the number of lines which show a similar behaviour is not negligible, as can be seen in the survey by Stenflo et al. (1983) and, eventually, the interpretation of broadband limb polarization in terms of only continuum polarization, may be inadequate. Given the extreme difficulty of the measurements, it is not sure that much additional work on this topics is worthwhile, unless new, important, applications are in view.

#### 3. The net polarization of spectral lines due to the Zeeman effect

#### 3.1. The net polarization within one spectral line

In several occasions, the net values of the Stokes parameters integrated over a line profile have been investigated to help magnetic field diagnostic (Skumanich and Lites, 1987; Ronan et al., 1987; Landolfi et al., 1989). We concentrate now on a partial aspect of this problem dealing with the case of transverse magnetic fields. As it is well known, the difference of saturation between the  $\sigma$  and the  $\pi$  components of a Zeeman triplet results in a small amount of polarization over the line profile (Leroy, 1962; 1989; Huovelin and Saar, 1991; Saar and Huovelin, 1991). The effect peaks in medium intensity lines (central absorption coefficient  $\eta_{\sigma} = 10$ ; for very faint lines there is no saturation at all; for stronger lines the saturations in reduced by the damping profile). The net polarization degree is proportional to the square of the field strength, a general feature of the linear polarization in lines with incomplete splitting. The polarization reaches an asymptotic value, of course, when the line is completely split. The more complex phenomena which happen when the field vector is not purely transverse (in particular, the magneto-optical rotation) have been studied in detail by Calamai et al. (1975), Landi Degl'Innocenti and Calamai (1982) and Calamai and Landi Degl'Innocenti (1983).

#### 3.3. The net polarization within a broad spectral interval

When the magneto-optical rotation is negligible, the polarization direction is the same for any line in the pass-band and one can simply add up the contributions of the lines in the spectral interval. This was the basis of former work devoted to the study of solar magnetic fields and, later, of stellar studies (Demkina and Obridko, 1973; Mullan and Bell, 1976). Actually, broadband linear polarization was found early in solar active regions (Dollfus, 1958) and was studied in detail by Leroy (1962), Illing et al. (1974a, 1974b, 1975), Makita (1981) and Makita and Ohki (1986).

An important feature of magnetic field measurement methods is their ability to give a significant signal after the surface integration over an unresolved stellar disc; for instance, the classical longitudinal field diagnostic based on circular polarization measurements in line wings is not very useful if one observes an unresolved set of magnetic spots with opposite polarities. Measuring the extra broadening of lines due to the magnetic field overcomes this difficulty (Robinson, 1980) and the linear polarization analysis has actually a behaviour similar to the Robinson method: in both cases the signal is proportional to the square of the field strength and to the filling factor. The linear polarization analysis has, of course, its own advantages (polarization is the unambiguous signature of a magnetic field while line broadening can result from many physical mechanisms) and drawbacks (a magnetic spot with circular symmetry, like a unipolar spot at the centre of the stellar disc, yields zero linear polarization). Anyway, the model calculations by Landi Degl'Innocenti (1982) showed that spotted stars could give a sizeable polarized signal and actual measurements were obviously needed.

In view of stellar studies, a question of major interest is the wavelength dependence of broadband polarization. Recent studies have provided some knowledge on this variation in various spectral types (Saar and Huovelin, 1990, 1991) and in the solar case (Leroy, 1989). It turns out that, for a G2 V star, the polarization increases towards short wavelengths, following roughly a  $\lambda^{-6}$  law in the strong field case (B  $\geq$  10000 Gauss) and a  $\lambda^{-4}$  law for small field strengths (B  $\leq$  1000 Gauss). The difference results from the fact that, in the case of incomplete Zeeman splitting, the polarization depends on the factor  $v_H^2$  (where  $v_H$  is the ratio of the Zeeman splitting to the Doppler width) which is proportional to  $\lambda^2$ . Both theoretical investigations (Leroy, 1989; Saar

and Huovelin, 1991) are in very good agreement for the solar spectrum and have detected some interesting spectral features (e.g. a local minimum of polarization at 5800 Å) which could help to distinguish broadband polarization of magnetic origin from other polarizing effects if filters as narrow as  $\Delta\lambda \simeq 100$  Å can be used.

#### 3.3. Polarization profiles of blended lines

In the past years, it was generally thought that broadband linear polarization would grow larger and larger towards the ultraviolet and towards cooler spectral types, both trends being due to the increasing density of metallic lines. But, in crowded spectra, most of the lines are blended and it was necessary to see the effect of blending on the net polarization: in contrast with the great amount of work devoted to the intensity profile of blends (Rauer, 1955), these was almost nothing in the literature about the Stokes profiles of blended lines, although some work is now in progress (Solanki, 1990; Saar and Huovelin, 1991). I have made recently very simple calculations based on the Unno's equations which have resulted in the unexpected conclusion that blending lines is a very effective way to decrease the net polarization (Leroy, 1990). In the solar spectrum, the effect becomes quite noticeable shortwards of 4200 Å and my conclusion was that the polarization expected in the U spectral band is not larger than in the B band. For K-type stars, I obtained even stronger decrease of the polarization due to the blends. More recently, Saar and Huovelin (1991) investigated the same problem in detail and obtained qualitatively similar, but considerable weaker reduction of polarization in blended spectral regions. Their conclusion is that even with blends, the linear polarization increases from B to U. In any case, prospects for the detection of magnetic fields in late K or M stars are less favourable than it was first believed.

We should not speak about cool stars without giving a short comment on the polarization of molecular bands: a magnetic field diagnostic based on molecular lines would be specially interesting in solar-type stars since molecules are tracers of the cool sunspots. Unfortunately, the polarization of molecular bands is weak as has been demonstrated for the CH band by Illing (1981).

#### 4. Broadband polarization measurements and magnetic field diagnostic

#### 4.1. The Sun

In the stellar case we are always measuring the integrated polarized light emitted by one or several active regions with an unknown magnetic structure and it is helpful to begin with the easier case of the Sun. As a first step, we have investigated the integrated polarization emerging from a whole active region: in the B spectral band, the polarization measured in a 1 arc min. field is about  $2 \times 10^{-4}$  (Leroy and LeBorgne, 1989). It means also that if we measure the polarization of the total Sun's light we should find about  $2 \times 10^{-7}$  when one active region is present. For several active regions the polarization grows only slightly because we have to add vectorially the various contributions corresponding to non parallel polarizations and we cannot reach more than  $5 \times 10^{-7}$ . This is a very small effect indeed and it has never been observed although the outstanding measurements by Kemp et al. (1987a) have established an upper limit of  $8 \times 10^{-7}$  for the net polarization of the Sun observed at a time of low solar activity.

334 J.-L. Leroy

#### 4.2 Expected polarization from magnetic origin in solar-type stars

The observational data on the magnetism of solar-type stars are sometimes conflicting (Gondoin et al., 1985; Toner and Gray, 1988; Marcy and Basri, 1989; Mathys and Solanki, 1989). One simple approach is to extrapolate the results obtained for the Sun to a star with the same type of magnetic activity, at a higher level. We have checked that the model by Landi Degl'Innocenti et al. (1982) successfully explains the polarizations measured in integrated solar active regions and I have applied the same analysis to a late G V star, with a spot covering 25 % of the star surface, and a field strength similar to sunspots. I found a polarization, in the B band, of about  $1 \times 10^{-4}$  which is a small effect but not beyond the measurement capabilities. Similar estimates resulting from a more detailed investigation were made by Saar and Huovelin (1991) for several spectral types. They established the maximum polarization of  $5 \times 10^{-4}$  for a G5 V star, and smaller values for earlier spectral types. Thus, measurements have to be considered seriously.

#### 4.3. Polarization measurements on F - G - K dwarfs

Among modern polarization measurements on nearby stars (not contaminated by the interstellar polarization) the most accurate are those published by Piirola (1977) and Tinbergen (1982). Tinbergen and Zwaan (1981) have noted that, for a significant number of F, G and K stars, the observed polarization is above the threshold which can be anticipated given the noise of measurements. The excess polarization is of the order of  $1 - 2 \times 10^{-4}$ , not far from the polarization computed in the previous section for heavily spotted stars.

More recent data concerning the polarization of late-type dwarfs have been published by Huovelin et al. (1985), Huovelin, Saar and Tuominen (1988) and Huovelin et al. (1989). These authors found in several cases a variable linear polarization reaching, in the U band, the  $10^{-3}$  polarization level, that they assign tentatively to a magnetic effect or to a Rayleigh scattering phenomenon. However, Leroy and LeBorgne (1989) have observed a large sample ( $\simeq 35$ ) of late type dwarfs, including several of the Huovelin et al. objects, and they have not found any significant polarization at the level of sensitivity of  $1 - 2 \times 10^{-4}$ . In this last investigation, the number of measurements on a given star ranged from 1 to 5 and it is possible that the phases of enhanced stellar activity had occured between the observations (although I feel it hard to explain in such a way the discrepancies). More probably, one has to discuss the discrepancy between these different investigations at two levels: what is the true reliability of polarization measurements at the  $10^{-4}$  level? Are there non magnetic mechanisms able to give polarizations of  $10^{-3}$  in solar type stars? (see Huovelin and Saar, 1991 and Saar and Huovelin, 1991, for Thomson and Rayleigh scattering phenomena). Additional, joint observations are under way and one can hope some progress in this field of research within one or two years.

#### 5. Conclusion

We have not mentioned in this paper the broadband circular polarization although it has been actually measured as well on the active Sun as in some stars (e.g. in  $\lambda$  AND; see Kemp et al., 1987b). The problem is that the interpretation of circular polarization is rather complex (Mürset et al., 1988): this effect results from the occurence of both magnetic fields and specific mass motions in active regions and thus, broadband circular polarization cannot yield a magnetic field diagnostic as simply as broadband linear polarization.

The new coordinated observations which are in progress will show whether broadband linear polarization is a powerfull tool for studying the magnetism of solar type stars. But, there is, in any

case, a class of stars where such measurements do yield interesting results: in some Ap stars (e.g. 53 CAM) very significant polarizations have been measured by Kemp and Wolstencroft (1974) and the theoretical interpretation by Landi Degl'Innocenti et al. (1981) proves that it is possible through this approach to refine our knowledge on these objects (some parameters escape the classical analysis via circular polarization measurements). One can also point out that interesting phenomena on stellar activity are observed in FK Comae stars (e.g. HD 199178; see Jetsu et al., 1990) and can be explored by polarimetry. Keeping in mind that there is no ideal way of measuring stellar magnetic fields, we think that broadband polarization still deserves some work, including new observations.

#### 6. Acknowledgments

The author is much indebted to Dr J. Huovelin for stimulating discussions and significant improvements on this paper.

#### References

Arnaud, J.: 1987, Private communication

Calamai, G., Landi Degl'Innocenti, E., Landi Degl'Innocenti, M.: 1975, Astron. Astrophys. 45, 297

Calamai, G., Landi Degl'Innocenti, E.: 1983, Astron. Astrophys. Suppl. Ser. 53, 311

Demkina, L.B., Obridko, V.N.: 1973, Sov. Astron. 16, 853

Dollfus, A., 1958: C.R. Acad. Sci. 246, 3590

Dumont, S., Pecker, J.C.: 1971, Astron. Astrophys. 10, 118

Gondoin, P., Giampapa, M.S., Bookbinder, J.A.: 1985, Astrophys. J. 297, 710

Huovelin, J., Linnaluoto, S., Piirola, V., Tuominen, I., Virtanen, H.: 1985, Astron. Astrophys. 152, 357

Huovelin, J., Saar, S.H., Tuominen, I.: 1988, Astrophys. J. 329, 882

Huovelin, J., Linnaluoto, S., Tuominen, I., Virtanen, H.: 1989, Astron. Astrophys. Suppl. Ser. 78, 129

Huovelin, J., Saar, S.N.: 1991, Astrophys. J., in press

Illing, R.M.E., Landman, D.A., Mickey, D.L.: 1974a, Astron. Astrophys. 35, 327

Illing, R.M.E., Landman, D.A., Mickey, D.L.: 1974b, Astron. Astrophys. 37, 97

Illing, R.M.E., Landman, D.A., Mickey, D.L.: 1975, Astron. Astrophys. 41, 183

Illing, R.M.E.: 1981, Astrophys. J. 248, 358

Jetsu, L., Huovelin, J., Tuominen, I., Bopp, B.W., Efimov, Yu.S., Linnaluoto, S., Nations, H.L., Piirola, V., Shakhovskoy, N.M., Virtanen, H.: 1990, Astron. Astrophys. Suppl. Ser. 85, 813

Kemp, J.C., Wolstencroft, R.D.: 1974, Monthly Notices Roy. Astron. Soc. 166, 1

Kemp, J.C., Henson, G.D., Barbour, M.S., Kraus, D.J., Collins II, G.W.: 1983, Astrophys. J. 273, L85

Kemp, J.C., Henson, G.D., Steiner, C.T., Powell, E.R.: 1987a, Nature 326, 270

Kemp, J.C., Henson, G.D., Kraus, D.J., Dunaway, M.H., Hall, D.S., Boyd, L.J., Genet, R.M., Guinan, E.F., Wacker, S.W., McCook, G.P.: 1987b, Astrophys. J. 317, L29

336 J.-L. Leroy

Koch, R.H., Elias, N.M., Corcoran, M.F., Holenstein, B.D.: 1989, Space Sci. Rev. 50, 63

Landi Degl'Innocenti, E.: 1982, Astron. Astrophys. 110, 25

Landi Degl'Innocenti, E., Calamai, G.: 1982, Astron. Astrophys. Suppl. Seri. 49, 677

Landi Degl'Innocenti, M., Calamai, G., Landi Degl'Innocenti, E.: 1981, Astrophys. J. 249, 228

Landolfi, M., Landi Degl'Innocenti, M., Landi Degl'Innocenti, E.: 1989, Astron. Astrophys. 216, 113

Leroy, J.L.: 1962, Ann. Astrophys. 25, 127

Leroy, J.L.: 1977, Reports from the Observatory of Lund n° 12, 161

Lercy, J.L.: 1989, Astron. Astrophys. 215, 360

Leroy, J.L.: 1990, Astron. Astrophys. 237, 237

Leroy, J.L., LeBorgne, J.F.: 1989, Astron. Astrophys. 223, 336

Makita, M.: 1981, Proc. Japan-France seminar on Solar Physics ed. by F. Moriyama and J.C. Henoux, 99

Makita, M., Ohki, Y.: 1986, Annals Tokyo Astron. Obs. 2nd Ser., XXI, n° 1

Marcy, G.W., Basri, G.: 1989, Astrophys. J. 345, 480

Mathys, G., Solanki, S.K.: 1989, Astron. Astrophys. 208, 189

Mullan, D.J., Bell, R.A.: 1976, Astrophys. J. 204, 818

Mürset, U., Solanki, S.K., Stenflo, J.O.: 1988, Astron. Astrophys. 204, 279

Piirola, V.: 1977, Astron. Astrophys. Suppl. 30, 213

Rauer, W.: 1955, Zeits. f. Astrof. 37, 1

Robinson, R.D.: 1980, Astrophys. J. 239, 961

Ronan, R.S., Mickey, D.L., Orrall, F.Q.: 1987, Solar Physics 113, 353

Saar, S.H., Huovelin, J.: 1990. Sixth Cambridge Workshop on cool stars, stellar systems and the Sun, in press

Saar, S.H., Huovelin, J.: 1991, Astrophys. J. in press

Skumanich, A., Lites, B.W.: 1987, Astrophys. J. 322, 483

Solanki, S.K.: 1990, Private communication

Stenflo, J.O., Twerenbold, D., Harvey, J.W.: 1983, Astron. Astrophys. Suppl. Ser. 52, 161

Tinbergen, J.: 1982, Astron. Astrophys. 105, 53

Tinbergen, J., Zwaan, C.: 1981, Astron. Astrophys. 101, 223

Toner, C.G., Gray, D.F.: 1988, Astrophys. J. 334, 1008

#### Discussion

- D. Rust: Do you and Huovelin measure polarization in the same way? Do you use a photoelastic modulator as Kemp did?
- J.-L. Leroy: The Pic du Midi polarimeter is a Lyot type polarimeter with a rotatable half-wave. The Huovelin instrument, designed by Pèirola, is still of a different type it is a dual channel instrument designed to cancel the harmful effect of a bright polarized background (the sky illuminated by the moon! In the case of Pic du Midi measurements have been made always with no moon in the sky.)
- S. Koutchmy: Could you please comment on the origin of the discrepancy you have for the solar-type stars you showed on your last graph?
- J.-L. Leroy: The Huovelin measurements do not display high polarization at any time. Rather they are variable as could be expected for an effect linked to a stellar activity process. Therefore, it could be that my measurements have always met a phase of quietness of the stars. I don't think that this explanation is very probable but at least it must be considered.
- J. Stenflo: The effect of the image wobble due to the mechanical modulation will be different for the different Stokes parameters (in addition to the smearing of the spatial resolution). How and with what accuracy do you correct for this wobble?
- B. Lites: The residual wobble in the image after stabilization by the fast mirror is negligible. It is far smaller than the differential stretching of the image due to seeing. The effect of crosstalk due to the residual seeing has been estimated by Lites (1987, Applied Optics, 26, 3838).

# Section 3 Polarimetry in the IR chair: J.B. Zirker

#### Polarimetry in the Infrared

Drake Deming, Tilak Hewagama<sup>1</sup>, Donald E. Jennings and Gunter Wiedemann Planetary Systems Branch, Code 693 Goddard Space Flight Center, Greenbelt MD 20771

Abstract: Polarimetry at infrared (IR) wavelengths is advantageous because the larger Zeeman splitting of IR lines results in larger net solar polarization signal. Also, oblique reflections at telescope mirror surfaces have less effect, due to the increase in the index of refraction for Aluminum films at IR wavelengths. Recent developments in IR detector arrays, and the availability of lines formed at altitudes from the deep photosphere (e.g. 1.56  $\mu m$  FeI) to the base of the chromosphere (12  $\mu m$ ) represent additional motivation to pursue polarimetry in the IR. Techniques used for IR polarimetry are still under development, especially at 12  $\mu m$ . However, recent measurements using a CdS quarterwave plate and Ge thin-film linear polarizer successfully obtained Stokes I,Q,U and V profiles of the 12.32  $\mu m$  MgI line at high spectral resolution. A significant result from these measurements is the finding that the 12  $\mu m$  line is essentially 100% polarized in sunspots. This implies that the sunspot magnetic field, at the 12  $\mu m$  altitude, is not filamentary in the sense of being a collection of small scale flux tubes, separated by field-free regions. Rather, the sunspot represents a single large flux tube, wherein the field fills all space.

#### I. Motivations for Infrared (IR) Polarimetry

Although the vast majority of solar polarimetry has been conducted in the visible spectral region, there are many advantages to doing polarimetry in the IR. The larger Zeeman splitting relative to line widths means that there is less overlap of orthogonal polarizations for IR lines, leading to a The polarization effects induced by greater net polarization signal. oblique reflections at telescope mirror surfaces are smaller in the IR. New IR array detectors are available, and IR lines are now known in the solar spectrum which are formed over a substantial range in altitudes in the solar atmosphere. Simultaneous observations of lines formed at two well-separated altitudes would give us a good basis for making 3dimensional vector magnetograms, and would doubtless improve our understanding of how magnetic energy is stored and released in solar active regions. Finally, atmospheric seeing is generally improved at IR wavelengths. This means that, at least in the near-IR near 1.6 µm, high spatial resolution observations may be more easily attained. follows, we elaborate on some of these motivations in more detail.

<sup>&</sup>lt;sup>1</sup> Also affiliated with the Astronomy Program, University of Maryland at College Park.

#### a) Solar polarization

The net polarization in a spectral line, resulting from the Zeeman effect, depends on the magnitude of the Zeeman splitting relative to the line width. The magnitude of Zeeman splitting in physical units, i.e. in energy, is independent of the line frequency, and is given as:

$$\Delta v_z = 4.67 \times 10^{-5} \text{ g } |\mathbf{B}| \text{ cm}^{-1}$$

where g is the Lande g-factor, and  $|\mathbf{B}|$  is the field strength in Gauss. The Doppler width of the line, however, is proportional to the line frequency. Consequently, IR lines are more narrow than visible lines when measured in energy units. The ratio of Zeeman splitting to line width is therefore inversely proportional to frequency, i.e. proportional to wavelength. Table 1 shows the ratio of Zeeman splitting to Doppler width for  $\lambda 6302$  in the visible, and two IR wavelengths, assuming a line broadening velocity of 1.5 km sec<sup>-1</sup> and a field strength of 1000 Gauss. For field strengths typical of solar active regions, visible-region lines are often in the regime where the line width exceeds the Zeeman splitting, whereas IR lines often show line widths which are substantially smaller than the splitting. In order to maximize the Zeeman effects relative to the Doppler effects, we want to use these narrow IR lines, i.e. we want to do "low energy solar physics!"

In the limit when the line width greatly exceeds the Zeeman splitting, the so-called weak-splitting regime, the net polarization, especially the linear polarization, can be quite small. In this regime, adequate measurement of linear polarization in the presence of telescope and instrumental polarization effects is very difficult (Harvey 1985). Moreover, net linear polarization is proportional to  $|\mathbf{B}|^2$ , whereas net circular polarization remains linear in |B|. When |B| varies within a single spatial resolution element, this mix of quadratic and linear dependences causes the mean vector field to be distorted (Stenflo 1985). One solution to this problem is to obtain very high spatial resolution using a very low polarization telescope such as LEST. In this situation, the small scale field elements will be largely resolved, and |B| should not vary significantly within a resolution element. However, another solution to this problem is to use IR lines, which are completely split. In the strong-splitting regime, the linear polarization can be just as large as the circular polarization, and has the same linear dependence on |B|. Consequently, the mean field will not be distorted, and cross-talk between circular and linear polarizations is less of a problem when they are of comparable magnitudes. An example of a strongly split IR line, the 12.32 µm emission line of MgI,

is shown in Figure 1.

Table 1. Ratio of Zeeman Splitting to Doppler Width.

λ (μm)	Lande g	$\Delta v_z/\Delta v_D$	
0.6	2.5	1.4	
1.6	3.0	4.5	
12.3	1.0	11.5	

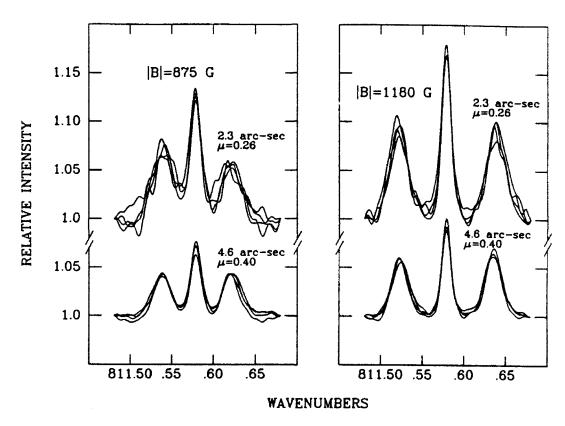


Figure 1. Example of a strongly split IR line, the 12.32 μm line of MgI observed in a sunspot penumbra at two disk positions and two values of the field strength (from Deming et al. 1988).

#### b) Telescope polarization

The problem of polarization induced by oblique reflections at telescope mirrors is well known. Harvey (1985) describes this effect for the McMath telescope. As an example, he gives the McMath Mueller matrix for a solar declination of  $+20^{\circ}$  and an hour angle of  $45^{\circ}$  as:

$$\mathbf{M_{VIS}} = \begin{bmatrix} 0.775 & 0.035 & 0.008 & 0.003 \\ 0.035 & 0.771 & 0.028 & -0.069 \\ 0.009 & 0.001 & 0.715 & 0.297 \\ 0.003 & 0.075 & -0.295 & 0.712 \end{bmatrix}$$

As wavelength increases, the real and imaginary components of the index of refraction for Aluminum films both increase. These values can be calculated using Drude-Zener theory (Bennett, Silver and Ashley 1963), or taken from the tabulations of Gray (1972). For example, we obtain n=34.2 and k=79.6 for the 12.32  $\mu m$  MgI line, from a slight extrapolation of Gray's values. Using these values, the McMath Mueller matrix for the same declination and hour angle becomes:

$$\mathbf{M}_{12\mu m} = \begin{bmatrix} 0.944 & 0.008 & 0.001 & 0.000 \\ 0.008 & 0.944 & 0.000 & -0.003 \\ 0.001 & 0.000 & 0.944 & 0.018 \\ 0.000 & 0.003 & -0.018 & 0.944 \end{bmatrix}$$

The off-diagonal elements in the 12  $\mu m$  matrix are about an order of magnitude smaller than the visible matrix. Moreover, since the linear and circular polarizations in the 12  $\mu m$  line are of the same order of magnitude, the cross-talk induced by the telescope will have no significant effect on vector field determinations using this line. Measurements which support these conclusions were made by Hewagama (1991), who determined the polarimetric properties of one of the oblique reflections in the McMath telescope.

#### c) New detectors

In recent years there have been stunning advances in the technology of IR array detectors (see Wynn-Williams and Becklin 1987). Arrays of several thousand pixels are now available, each pixel exceeding the performance of the individual detectors of a decade ago. The existing arrays (circa 1991) are summarized in Table 2 (updated from Deming et al. 1991). In the 1 to 2.5  $\mu m$  region, PtSi arrays have relatively large formats. These arrays have been used to image solar faculae at 1.6  $\mu m$  (Foukal, Little and Mooney 1989), and have other important applications in IR astronomy (Fowler et al. 1990). Although they have limited sensitivity, their large format makes them attractive for use in solar polarimeters. More sensitive InSb detectors are available in 58 x 62 format, and an array of this type is being used by Rabin et al. (1991) to do polarimetry of the 1.56  $\mu m$  line. At longer wavelengths, very sensitive Si:As arrays exist in 58 x 62 format.

One limitation in using the Si:As arrays is the high level of thermal background, which prevails at wavelengths exceeding 2  $\mu m$ , due to warm telescope and instrument optics. When used with broad optical bandpasses, the thermal background can saturate these arrays in times which are short in comparison to the 33 msec read time. In this respect, use of these arrays in solar physics is easier than in other areas of astronomy, because the solar application dictates high spectral resolution, which results in much reduced background levels if cold, narrow band, filters are used. An array of this type is being utilized at Goddard Space Flight Center to form the detector in a 12  $\mu m$  Stokes polarimeter (Deming et al. 1989), operating at 0.007 cm $^{-1}$  resolution using a Fabry-Perot etalon.

Table 2. INFRARED DETECTOR ARRAYS

Material	Format	λ-Range (microns)	Type/ Multiplexer	Manufacturer
PtSi	640 x 488	1 - 5.4	PE/DRO-CCD	Kodak, Hughes, RCA, etc.
Ge diodes	32 x 32	1 - 1.6	PV/JFET	Ford Aerospace
HgCdTe	256 x 256	1 - 2.5	PV/DRO	Rockwell
InSb	256 x 256	1 - 5.5	PV/CCD	SBRC
Si:In	32 x 32	1 - 7.5	PC/CCD	Rockwell
Si:Ga	58 x 62	5 - 17.5	PC/DRO	SBRC
Si:As	10 x 50 20 x 64 58 x 62	5 - 24	BIB/SWIFET BIB/DRO	Rockwell Rockwell, HC HC

PE=Photoemissive, PV=Photovoltaic, PC=Photoconductive, DRO=Direct Readout, BIB=Blocked Impurity Band, SWIFET=Switched MOSFET, SBRC=Santa Barbara Research Center, HC=Hughes(Carlsbad)

#### d) Lines formed over a range in height

The IR spectral region includes lines formed over a substantial range of heights in the solar atmosphere. A number of Zeeman-sensitive lines in the solar IR spectrum were observed and identified by Hall (1974). The Fel line at 1.5648 µm is especially interesting, because it has a Lande g-factor of 3, and it is formed relatively deep in the solar photosphere. Pioneering observations of this line were reported by Harvey and Hall (1975), and the line has been the subject of more recent studies by Stenflo, Solanki and Harvey (1987a), Zayer, Solanki and Stenflo (1989), Rabin and Graves (1989), Rabin et al. (1991), and Livingston (1991). The NSO near-IR magnetograph will be designed to make use of this line (Rabin et al. 1991).

At still longer wavelengths, the 12  $\mu m$  emission lines (Brault and Noyes 1983) are believed to be formed in the upper photosphere or low chromosphere (for an extended discussion, see Deming et al. 1991). The mechanism and altitude of line formation is still unresolved, but it is relatively certain that the emission occurs from an altitude higher than the most Zeeman-sensitive lines in the visible. Deming, Jennings and Noyes are planning to observe the formation altitude of the 12.32  $\mu m$  Mgl emission at the limb during the July 1991 total eclipse over Mauna Kea. If this observation is successful, Zeeman measurements using the 12.32  $\mu m$  line can be unambiguously referred to a known height. Simultaneous 1.56  $\mu m$  and 12.32  $\mu m$  polarimetry would be very desirable, since this would give three dimensional vector field information.

#### II. Techniques for IR Polarimetry

Nearly all solar IR polarimetry to date has utilized the McMath Fourier transform spectrometer (FTS). The usual technique is to modulate the polarization state of the FTS input at kHz frequencies, which produces sidebands in the transformed spectrum (Brault 1978). This technique has been widely used to obtain simultaneous Stokes profile measurements over a wide spectral range, including both the visible and the 1.56  $\mu$ m Fel line (Stenflo and Harvey 1985, Stenflo, Solanki and Harvey 1987a,b). The high quality of the data results largely from the rapid (kHz) modulation of the input beam using a photoelastic modulator. These modulators operate by producing a variable strain birefringence using an acoustic transducer (Kemp 1970, 1981). The result of these measurements has been a wealth of new knowledge concerning the structure of small scale flux tubes (Solanki 1987).

At thermal IR wavelengths, somewhat different polarimetric techniques must be used. The presence of significant thermal background emission at 12 µm means that cold, narrow band, filters must be used to limit the bandwidth of fluctuations in the thermal background. The Planck function at 5000K (the 12 µm solar brightness temperature) is larger than the 300K Planck function by a factor of only 180, because at this long wavelength the Planck function is closer to being linear in temperature (the Rayleigh-Jeans limit). This means that solar polarimetry at 0.005 cm<sup>-1</sup> (the FTS resolution) must use a cold filter, of approximately 1 cm<sup>-1</sup> bandwidth, in order to keep the background emission below the level of the 0.005 cm<sup>-1</sup> solar signal. Deming et al. (1988) used a LHe-cooled grating monochromator (Wiedemann et al. 1989) on the McMath FTS for this purpose. The use of a cold narrow-band filter on the FTS means that modulation of the input beam could take place at relatively low frequencies, since no other signal will interfere with the sidebands containing the Stokes information. Although kHz-frequency modulation may be desirable at shorter wavelengths in order to reduce atmospheric noise, it is not clear that this is necessary in the IR, where sky-chopping in IR astronomy typically utilizes chop frequencies of some tens of Hz. Polarization modulation at low frequencies can be conveniently accomplished using a rotating Fresnel rhomb or waveplate. (1991) explored techniques to measure 12.32 µm Mgl Stokes profiles. The first attempt involved a rotating ZnSe Fresnel rhomb. This was unsuccessful, because the beam deviation produced by the rhomb could not be corrected so as to keep the beam sufficiently close to the FTS optic Deviation of the beam during the FTS scan causes large levels of noise in the spectra. Rotation of a waveplate might be more successful. However, Hewagama found that good quality 12.32 µm Stokes profiles could be produced simply by making successive measurements using different orientations of the rhomb (or CdS quarterwave plate) and Ge thin-film linear polarizer. Because the FTS detects all wavelengths simultaneously, changes in atmospheric transparency during these measurements do not enter as first-order effects on the Stokes profiles. Figure 2 shows the equipment used to make 12 µm Stokes observations with the FTS. Measurement of I, Q, U and V with this method requires six successive interferograms, each of approximately 2 minute duration. example of the Stokes profiles obtained in a sunspot penumbra is shown in Figure 3.

Improvements in the technique of measuring 12  $\mu$ m Stokes profiles are certainly desirable. Incorporating array detectors into these measurements will probably necessitate using a spectrometer other than

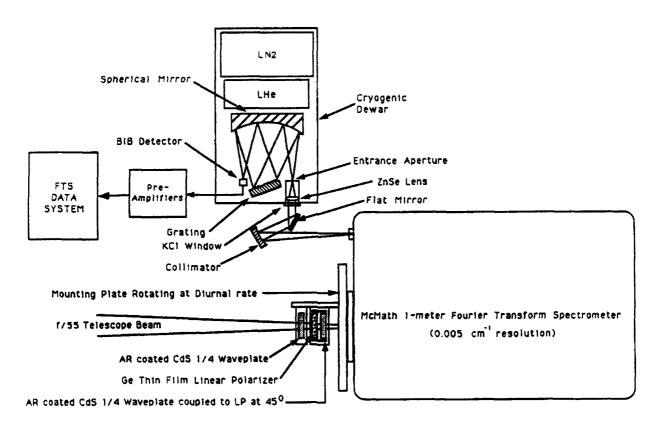


Figure 2. Equipment used to make 12 µm Stokes profile measurements with the McMath FTS.

an FTS, e.g. a Fabry-Perot. Such instruments remove the thermal background emission by chopping. Both removal of the background, and improvements in the Stokes profiles, could be accomplished simultaneously by chopping between polarization states, e.g. between I+V and I-V, etc. One naturally thinks of techniques such as photoelastic modulation to accomplish this purpose. Although photoelastic modulation in ZnSe has been used at thermal IR wavelengths (Lipp, Zimba and Nafie 1982), it is our understanding that ZnSe devices cannot attain sufficient retardation at wavelengths as long as 12.3  $\mu$ m. Instead, Si photoelastic modulators may be more suitable, or variable retardation could be achieved with an electro-optic modulator of the type which is commonly used with 10  $\mu$ m CO<sub>2</sub> lasers. A CdTe electro-optic modulator, which uses an applied electric field to achieve retardance, is being tested at Goddard for its suitability as a 12.32  $\mu$ m solar polarization analyzer.

#### III. Limitations and complementary aspects

The principal limitation of polarimetry in the IR is the limit on spatial resolution set by diffraction. At 12  $\mu$ m, the diffraction limit of the McMath telescope (1.22 $\lambda$ /D) is 2 arc-sec. Atmospheric seeing is generally

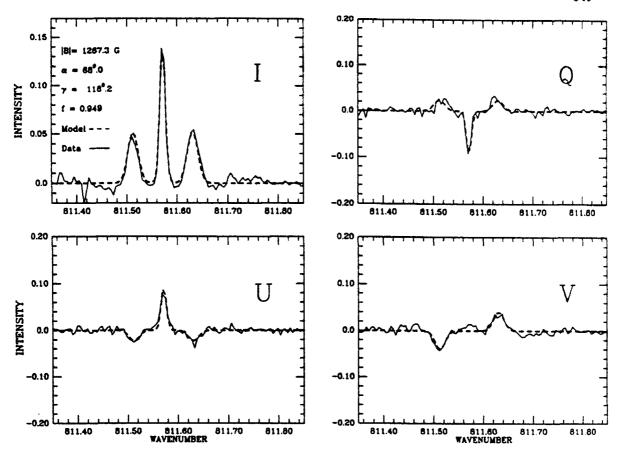


Figure 3. Example of 12  $\mu$ m Stokes I, Q, U and V profiles obtained in a sunspot penumbra with the McMath FTS by Hewagama (1991).

better at longer wavelengths, and Boyd (1978) measured the  $10~\mu m$  seeing at the McMath telescope, using an IR-upconverter to image the solar limb. Boyd found that the  $10~\mu m$  seeing was about a factor of two better than in the visible, which is in approximate agreement with the theory of astronomical seeing (Fried 1966). This implies that  $12~\mu m$  observations with the McMath will be diffraction-limited, not seeing-limited, whenever the visible seeing is 4 arc-sec or better, which is most of the time. Significant improvements in spatial resolution should be possible by increasing the telescope aperture. The recently proposed upgrade of the McMath telescope to 4-meter aperture (Giampapa, Livingston and Rabin 1990) would be highly beneficial to  $12~\mu m$  observations, either by increasing the spatial resolution at fixed throughput, or by increasing the signal level with the spatial resolution fixed.

The limitation imposed by diffraction implies that it will be very difficult for 12  $\mu$ m polarimetric observations to achieve the 0.1 arc-sec resolution which telescopes such as LEST may achieve in the visible. While this level of spatial resolution is not achieved directly by 12  $\mu$ m

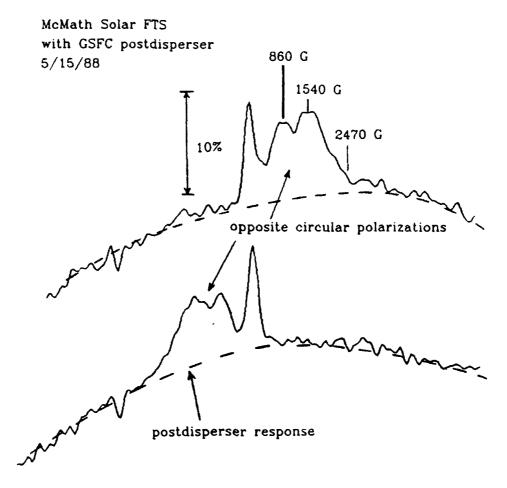


Figure 4. Unprocessed 12.32  $\mu$ m I+V and I-V profiles observed in a sunspot-forming region, where the great breadth of the  $\sigma$ -components indicates a large range of field strengths present in the 5 arc-sec field of view.

observations, the very high "magnetic resolution" obtainable using IR polarimetry at both 1.6 and 12 µm complements the high spatial resolution achieved in the visible. As an example, Figure 4 illustrates 12.32 µm Mgl profiles taken in an emerging flux region, where a sunspot was forming. The region included in the 5 arc-sec diameter FTS entrance aperture contained a dark pore and surrounding plage. The data are unprocessed, i.e. they include the response of the postdisperser. The two spectra shown are I+V and I-V. The  $\sigma$ -components of the line are very broad, indicating that this 5 arc-sec region contained fields ranging in strength from a few hundred to nearly 2500 Gauss. There is also some indication that the  $\sigma$ -components are double-peaked, and that the predominant field strengths are near 860 and 1540 Gauss. instance, because the Zeeman-spreading in the  $\sigma$ -components exceeds their intrinsic width, 12 µm Stokes profile observations can measure field strengths and obtain some vector information for these fields, irregardless of whether they are spatially resolved. If observations of a sunspot-forming region such as this could be made with an array detector,

we could obtain a very clear picture of how the field elements coalesce to form a sunspot. The "magnetically resolved" features in such observations might correspond to structures seen in high resolution visible images, or they might be of even smaller scale, since there is theoretically no lower limit to the size of features which can be "magnetically resolved" using an emission line such as 12.32  $\mu m$  MgI.

#### IV. Results from IR Polarimetry

While IR polarimetry has shown promise since the pioneering investigation of Hall (1974), very little work was done in this area for a number of years. However, new results are now beginning to appear. Hewagama et al. (1991) performed polarimetry of the 12.32  $\mu m$  Mgl line in sunspots, and obtained interesting new information relevant to the small-scale structure of the sunspot field. As is well known, sunspot penumbrae exhibit a small-scale filamentary structure which is visible in high spatial resolution images (Moore 1981). It has often been speculated that the magnetic field is concentrated into similar filaments, which may correspond to either the dark or light structures seen in the penumbra. If the penumbral field is concentrated to this degree, then intervening field-free regions may also exist in the penumbra. Unless such regions were as cool as the umbra (which is unlikely), then we would expect them to emit unpolarized radiation in the 12.32  $\mu m$  line, because the line is ubiquitous in all solar features except the umbrae of moderate and large sunspots.

Since the penumbral Zeeman splitting of this line is so large, unpolarized emission in the  $\pi-$ component must result from actual field-free regions on the Sun, instead of cancellation of orthogonal polarizations, as occurs in a weakly-split visible line. Figure 5 shows the degree of polarization in the 12.32  $\mu m$  line, plotted versus distance from the sunspot center (from Hewagama et al. 1991). It can be seen that within the sunspot the line is essentially 100% polarized, the degree of polarization dropping to perhaps 90% at the penumbra/quiet Sun boundary. This means that the field at the 12  $\mu m$  altitude (estimated to be the temperature minimum to low chromosphere region) is not filamentary in the sense of containing field-free regions interspersed with small scale flux ropes. Rather, the sunspot represents a single large flux tube, with the field filling all of the space. This conclusion is independent of the spatial scale of any filamentation in the field; it depends only on the argument that field-free regions cannot avoid emitting in the 12  $\mu m$  line.

This result concerning small scale magnetic field structure in sunspots is representative of the manner in which the high "magnetic resolution"

available using IR polarimetry can give information which is highly complementary to high spatial resolution observations in the visible.

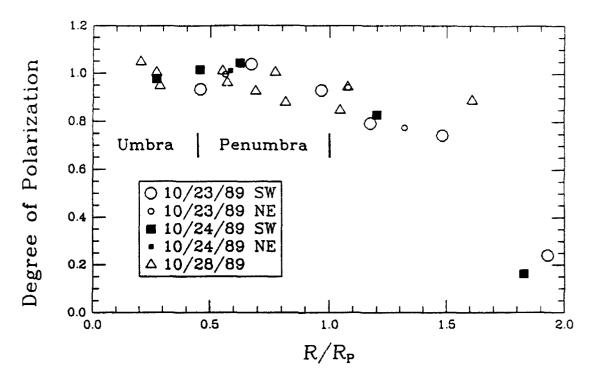


Figure 5. Degree of polarization in the 12.32  $\mu m$  line, versus distance from sunspot center, from Hewagama (1991).

#### V. Acknowledgements

We thank Dr. John W. Harvey for allowing us to use his McMath Mueller matrix calculation program. Infrared polarimetry at Goddard is supported by the NASA Solar Physics Branch, under RTOP 170-38-53-10. The National Solar Observatory is a division of the National Optical Astronomy Observatories, operated by the Association of Universities for Research in Astronomy, under contract with the National Science Foundation.

#### VI. References

Bennett, H.E., Silver, M., and Ashley, E.J. 1963, <u>J. Opt. Soc. Am.</u>, **53**, 1089. Boyd, R.W. 1978, <u>J. Opt. Soc. Am.</u>, **68**, 877. Brault, J.W. 1978, <u>Oss. Mem. Astrofis. Arcetri</u>, **106**, 33.

- Brault, J.W. and Noyes, R.W. 1983, Ap. J. Letters, 269, L61.
- Deming, D., Boyle, R.J., Jennings, D.E. and Wiedemann, G. 1988, Ap. J., 333, 978.
- Deming, D., Jennings, D.E., Hewagama, T. and Zipoy, D. 1989, <u>B.A.A.S.</u>, **21**, 848.
- Deming, D., Jennings, D.E., Jefferies, J., and Lindsey, C. 1991, in <u>The Solar Interior and Atmosphere</u>, eds. A. Cox, W. Livingston and M. Matthews, (Tucson: Univ. of Arizona Press.), in press.
- Foukal, P., Little, R., and Mooney, J. 1989 Ap. J. Letters, 336, 33.
- Fowler, A.M., Gatley, I., Merrill, K.M. and Herring, J. 1990, N.O.A.O. Preprint No. 344.
- Fried, D.L. 1966, J. Opt. Soc. Am., 56, 1372.
- Giampapa, M.S., Livingston, W.C. and Rabin, D. M. 1990, N.O.A.O. Preprint No. 345.
- Gray, D.E. 1972, American Institute of Physics Handbook, Third Edition, (New York: McGraw-Hill).
- Hall, D.N.B. 1974, <u>An Atlas of Infrared Spectra of the Solar Photosphere and of Sunspot Umbrae</u>, (Tucson: Kitt Peak National Observatory).
- Harvey, J.W. 1985, in <u>Measurements of Solar Vector Magnetic Fields</u>, ed. M. Hagyard (Huntsville: NASA/Marshall Space Flight Center), p. 109.
- Harvey, J.W. and Hall, D.N.B. 1975, B.A.A.S., 7, 459.
- Hewagama, T. 1991, Ph.D. Thesis, University of Maryland.
- Hewagama, T., Deming, D., Jennings, D.E., Osherovich, V., Wiedemann, G., Zipoy, D. and Mickey, D. 1991, submitted to Ap.J.
- Kemp, J.C. 1970, J. Opt. Soc. Am., 59, 950.
- Kemp, J.C. 1981, Proc. S.P.I.E., 307, 83.
- Livingston, W.C. 1991, this proceedings.
- Lipp, E.D., Zimba, C.G. and Nafie, L.A. 1982, Chem. Phys. Letters, 90, 1.
- Moore, R.L. 1981, Ap. J., 249, 390.
- Rabin, D.M. and Graves, J.E. 1989, <u>B.A.A.S.</u>, 21, 854.
- Rabin, D.M., Jaksha, D., Wagner, J. and Iwata, K. 1991, this proceedings.
- Solanki, S.K. 1987, Invited Review given at the <u>Tenth European Regional</u>
  <u>Astronomy Meeting of the IAU</u>, Prague, 24-29 August 1987.
- Stenflo, J.O. 1985, in <u>Measurements of Solar Vector Magnetic Fields</u>, ed. M. Hagyard (Huntsville: NASA/Marshall Space Flight Center), p. 263.
- Stenflo, J.O. and Harvey, J.W. 1985, Solar Physics, 95, 99.
- Stenflo, J.O., Solanki, S.K. and Harvey, J.W. 1987a, <u>Astron. Astrophys.</u>,173, 167.

- Stenflo, J.O., Solanki, S.K. and Harvey, J.W. 1987b, <u>Astron. Astrophys.</u>, 171, 305.
- Wiedemann, G., Jennings, D.E., Moseley, H., Lamb, G., Hanel, R., Kunde, V., Stapelbrock, M.G. and Petroff, M.D. 1989, Appl. Optics, 28, 139.
- Wynn-Williams, C.G. and Becklin, E. E. (eds.) 1987, <u>Infrared Astronomy with</u>
  <u>Arrays</u>, (Honolulu: University of Hawaii, Institute for Astronomy).
- Zayer, I., Solanki, S.K. and Stenflo, J.O. 1989, Astron. Astrophys., 211, 463.

#### Discussion

- B. Lites: 1) I think that there would be a very small height gradient of the field in sunspots over the small height difference of the formation of lines. 2) High resolution spectra from La Palma show that the penumbra field is indeed quite uniform (near unity filling factor). 3) Stokes II results for large sunspots give field strength and inclination consistent with those you measure.
- **D. Deming:** As regards 1), most estimates above sunspots are of order 0.5 G/km. Hence the  $\pm 200$  G width of the  $12\mu$ m  $\sigma$  components, if due to the height gradient, would require that the line emission originate over a  $\sim 800$  km region. I agree that this seems unlikely. As regards 2) and 3), I am please to hear this.
- J. Harvey: Have you complemented these beautiful emission line polarimetry observations by using absorption lines?
- **D. Deming:** In the 12  $\mu$ m region the only absorption lines of which I am aware are the molecular OH features and the atomic lines discussed by Glenar et al. (1988, Ap.~J Lett 335, L35). I am not familiar with the Zeeman properties of the former, and the latter are heavily blended with telluric lines. I think the most complementary observations using absorption lines would be simultaneous polarimetry at 12  $\mu$ m and 1.6  $\mu$ m. We hope to do this in the future.
- S. Koutchmy: A few brief comments: We know from the classical theories of Earth atmospheric turbulence (Tatarski, etc.) that in the case of a Kolmogorov spectrum, the Fried parameter is increasing as a power 6/5 of the wavelength. This has been checked to be nearly true for the night sky seeing (recent works in France, Chili and Hawaii) but nothing is known on the day-time seeing. Also of importance is that the size or extent of the isoplanatic patch which could dramatically increase in the IR. Measurements should be done to determine more about that and define the optimum parameters of a for future large IR solar telescopes. Another interesting aspect is that the scattered light levels both in the instrument and in the Earth's Atmosphere are considerably reduced, probably as a power 2 of the inverse wavelength. Concerning the gain in Zeeman sensitivity, this is especially interesting to measure the chromosphere and probably the coronal magnetic field which has been impossible up to now to make in the optical part of the coronal spectrum. In connection with this existing possibility, it would be important to produce a full IR spectrum of the solar corona as new lines are expected there.

In connection with the problem of the influence of 5 min oscillation, did you also look at effects produced by the temperature variations? This seems especially important in the case of the core of spot where very large temperature inhomogeneities are known to occur.

D. Deming: I agree with your comments, except that I would like to see measurements of the scattered light levels in the IR, since the situation may not be favorable as theory may predict. I especially agree with your comment about a coronal IR spectrum, especially at wavelengths long ward of  $12\mu m$  where the terrestrial atmospheric absorption has prevented observations. We looked for  $12 \mu m$  line intensity observations in "paper I" (1988, Ap. J. 333, 978) and established an upper limit which means that 5 min intensity variations will not affect our Stokes observations.

Zirker: What filling factors are seen in plage regions?

- T. Hewagama: Lower than unity: 0.8, 0.7 and less. Since the sigma components are closer together, the degree of polarization is smaller than unity. It is difficult to estimate the true filling factor uniquely.
- J.C. Henoux: Did you really find that the line width is less in the  $\sigma$  components than in the center of the  $12\mu m$  line? Could it be explained by a distribution of magnetic field strength inside umbra?
- **D.** Deming Yes, the  $\sigma$  components are invariably wider than the  $\pi$  component. In paper I (1988, Ap. J. 333, 978), we concluded that small scale variations of order  $\pm 200$  gauss were responsible.

## Sampling V-Stokes on the Solar Disk with Fe I 15648 $\mathring{A}$ and H Paschen $\beta$

William Livingston

National Solar Observatory
National Optical Astronomy Observatories†
P.O. Box 26732, Tucson, AZ 85726

Summary. From exploratory observations made with a scanning spectrometer we demonstrate that V-Stokes profiles exhibit a variety of forms. We confirm earlier work that shows the Zeeman splitting of Fe 15648Å is complete in the magnetic fields of plage regions where field strengths of between 1000 and 2000 G can be measured. In sunspot umbrae, however, molecular blends limit the line's usefulness. Some preliminary observations with chromospheric HPB 12818Å are given.

#### 1. Introduction

A number of programs utilize the all-reflecting McMath Telescope to study solar magnetic fields in the infrared where the Zeeman splitting is favorable. Harvey and Hall demonstrated 15 years ago (1975) that the Fe 15648Å line can yield directly the strengths of magnetic fields in plage. Harvey, Stenflo, and their Zurich collaborators made observations with the 1-m FTS outfitted with a polarizing modulator which yielded magnetic information from H-band lines (represented at this conference by Solanki, 1990). Rabin et al. (1990) are currently exploring the capability of a 2-D IR imager, while Deming (1990), Jennings, and Hewagama (1990) successfully are tackling polarization in the Mg I 12 micron lines.

We have resumed the work of Harvey and Hall; in fact Hall's original dewar is employed. What is new to report here concerns a sampling of the V-Stokes profiles derived from several hundred observations of a variety of active regions. Not surprisingly, different regions yield different profiles. Some at present are inexplicable.

#### 2. The Instrument

Don Hall's dewar Baboquivari\* was discovered languishing in the comer of the now defunct horizontal IR spectrograph on Kitt Peak. There it had been for over a decade, and it was now covered with cobwebs. This was in fact the detector used for his thesis and his Sunspot Atlas (Hall 1974). Plugged in it was dead, but Dick Joyce found a spare Cincinnati Electronics InSb photovoltaic diode detector which he graciously installed; it came to life and we were in business.

Babo's optical train consists of a window followed by a 200µ slit contacted to a LN<sub>2</sub> cooled copper box. Just behind the slit is an RG1000 filter. A concave mirror images the slit onto the InSb diode which has an active area 1 mm in diameter. Babo itself is fed by the camera mirror of the 13.5 m double-pass grating spectrometer (Pierce 1964). A 2.5x2.5 arc-sec Bowen image slicer serves as the entrance aperture, with an effective slit width of 140µm. This slicer, plus seeing smear, defines the size of the area sensed on the solar disk. For the observations reported here, the spatial resolution is 3 to 5 arc-sec. Polarimetry is achieved with a rotatable quarter-wave plate preceding the slicer and an HR polaroid following. Basically the setup is thus very simple.

Data is logged by the standard rapid-scan photometry system. Detector output signal is averaged during repeated scans of the grating, with the time per scan being about 1 sec. An observation consists of 10 grating

<sup>(\*)</sup> Baboquivari is a prominent mountain summit south of Kitt Peak, a site held sacred by the Tohono O'Odham Indian Nation. I'm told that permission was sought from the Nation to inscribe this name on the dewar. By so doing the detector was endowed with exceptional powers.

<sup>(†)</sup> Operated by the Association of Universities for Research in Astronomy, Inc. under cooperative agreement with the National Science Foundation.

cycles and takes about 30 seconds, including time for taping. The waveplate is then rotated 90° and the process repeated. A complete pair of observations, consisting of right- and left-circular records, requires about a minute plus the time to rotate the waveplate.

#### 3. Observations

With the solar image fixed and under guider control, samples were taken in proximity to active regions, i.e. sunspots. One procedure was to search randomly for image positions where the line profiles, as displayed on the photometry CRT screen, departed in a noticable way from the quiet Sun. Another plan involved stepping along a straight line, taking observations every 3.2 arc-sec. This was a scheme advocated by a visiting astronomer S. Vainstein who was interested in the spatial statistics of the fields. In all 400 areas were sampled.

(Obviously the non-simultaneity of the right- and left-circular analysis is a major weakness. We now have a scheme for interleaving the polarization states by switching a liquid crystal retarder synchronous with the grating cycles. This technique has been tried and works, but was not employed for the results presented here. However, preliminary results obtained by this improved method show many of the variations in V-Stokes described below and lend confidence that these 'abnormalities' are not just a consequence of seeing.)

# 4. Discussion

In figures 1 and 2 we show 16 examples of V-Stokes profiles from different areas on the Sun. Displayed full scale, 0 to 100%, are the superimposed right- and left-circular records. To left of scan center is Fe I 15<sup>4</sup>8.518, g = 3, and to the right is Fe I 15652.889, g = 1.53 (Solanki, Biémont, and Mürset 1990). The difference of these two scans (multiplied by a factor of 5 except in sunspot umbrae), is the V-Stokes profile. Measured field strength is derived from the distance between V-Stokes maxima. We arbitrarily always use the maxima and not, for example, the profile 'center of gravity'.

Panel 1 represents the quiet Sun with no detectable field. A small residual blip in the V-Stokes is probably caused by granular evolution during the course of the observation. Panels 2 through 5 show typical V-Stokes profiles for plage in order of increasing filling factors. Note that the deduced field strength is not particularly sensitive to filling factor. In panel 6 the V-Stokes profiles are relatively broad, perhaps as a consequence of a mixture of field strengths or velocities.

Panels 7, 8, and 9 are from sunspot umbrae of increasing size and darkness. As a rule, the darker the spot the stronger the magnetic field. The darker the spot the stronger also are numerous umbral molecular lines. There are two prominent umbral lines on either side of Fe 15652 but weaker umbral molecular lines are found throughout the wavelength interval. Many of these, perhaps all, display Zeeman splitting. When the molecular lines become quite intense, as in panel 9, weak molecular blends confuse Fe 15648 and the stronger ones obliterate the Fe 15652 profile. These blends limit the utility of Fe 15648 for umbral polarimetry.

Panels 10 through 14 display 'abnormal' V-Stokes profiles. Such profiles are neither common nor rare. Our experience is that they are region specific; i.e. if a region has one area of unusual profiles it tends to have others. Panels 10 and 11 indicate areas that may have opposite polarities within the observing aperture (see comments of Skumanich 1990). We have no ready explanation for the contents of panels 12, 13, and 14.

Panels 15 and 16 show how the H Paschen  $\beta$  line at 12818Å appears over a sunspot. Chromospheric H $\alpha$  and H $\beta$  have been used in the past to infer vertical field gradients over spots (e.g. Severny and Bumba 1958). HP $\beta$  is seen to produce a clear V-Stokes profile and should be more free of scattered light than the visible-light lines. At the time of writing we do not have an accurate Landé g value for HP $\beta$ . The nearby line of Ca I 12816, with a g = 1.25, allows simultaneous field measurement at the photospheric level. In addition, HP $\beta$  ought to be a good field diagnostic in prominences.

# 5. Acknowledgements

We are grateful to Dick Joyce for restoring Babo's health. Without excess incrimination, he also repaired the physical damage after I accidently dropped it. Doug Rabin supplied the IR waveplates and polarizers, together with advice on their use. Claude Plymate refreshed us on the necessary cryogenic techniques. Finally we thank both Doug Rabin and Sami Solanki for helpful discussions regarding the profiles.

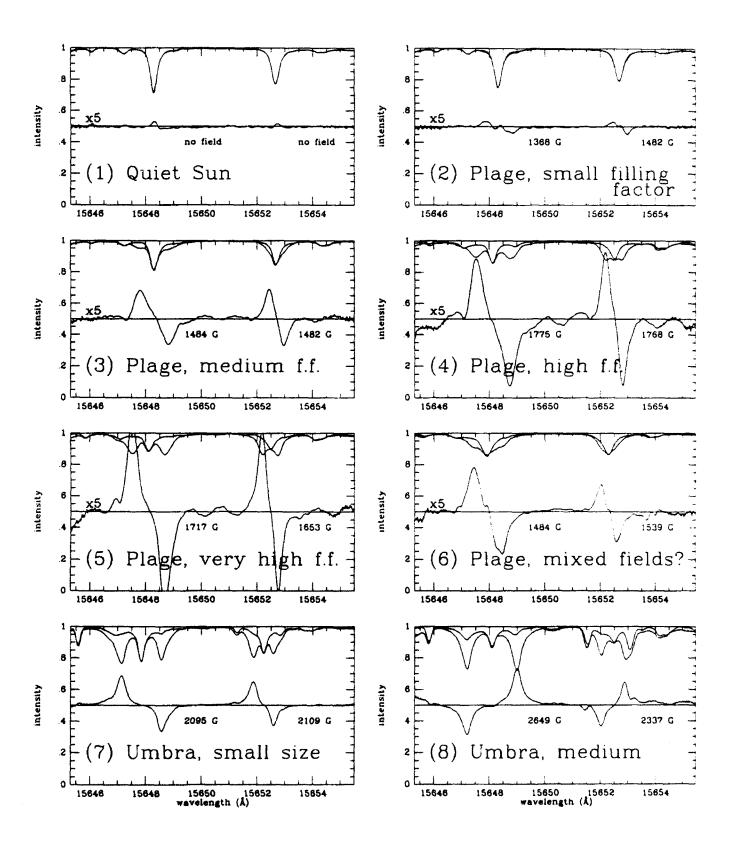


Fig. 1 Samples of I and V Stokes profiles. Actually I is represented here as the superimposed right- and left-circular recordings. V has not been divided by I.

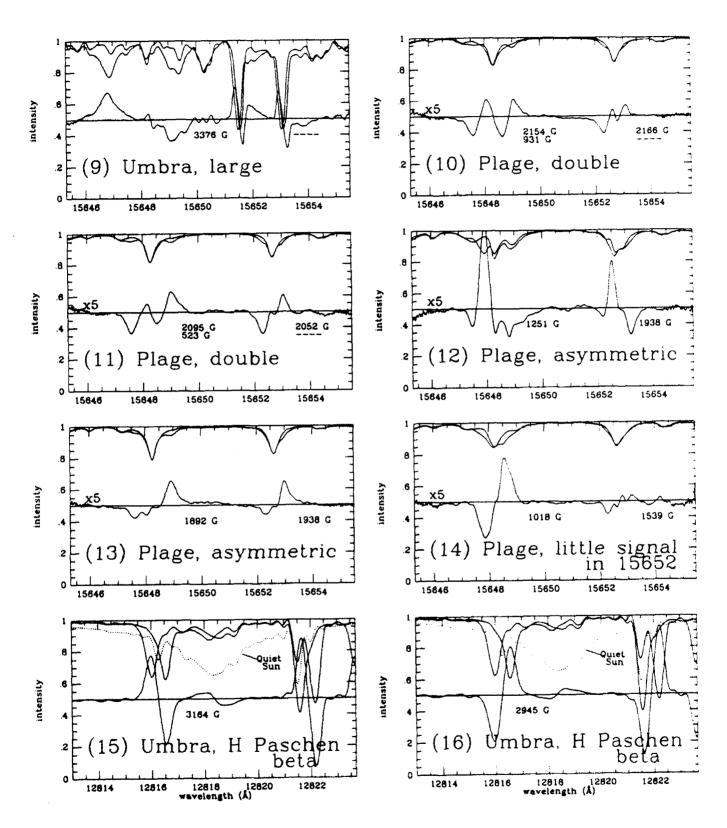


Fig. 2 More Samples of I and V Stokes profiles.

#### References

Deming, D.: 1990, Polarimetry in the IR, Solar Polarimetry.

Hall, D.N.B.: 1974, An Atlas of Infrared Spectra of the Solar Photosphere and of Sunspot Umbrae, Kitt Peak National Observatory.

Harvey, J., Hall, D.: 1975, Magnetic field observations with Fe I λ15648Å, Bull. Amer. Astron. Soc. 7, 459. Hewagama, T.: 1990, Polarimetry of the 12 Micron Lines, Solar Polarimetry.

Pierce, A.K.: The McMath Solar Telescope of the Kitt Peak National Observatory, Applied Optics, 3, 1337.

Rabin, D., Jaksha, D., Wagner, J. Iwata, K.: 1990, A Near Infrared Magnetograph, Solar Polarimetry.

Severny, A.B., Bumba, V.: 1960, On the penetration of solar magnetic fields into the chromosphere, Observatory, 78, 33.

Solanki, S.K.: 1990 Diagnostics of Flux Tubes from Infrared H-Band Lines, Solar Polarimetry.

Solanki, S.K., Biémont, E., Mürset, U.: 1990, Interesting lines in the infrared solar spectrum between λ 1.49 and λ 1.8 μm, Astron. and Astrophys. Suppl. Ser., 83, 307.

Skumanich, A.: 1990, Velocity Gradients Across a Flaring Neutral Line from Stokes II Measurements, Solar Polarimetry.

### Discussion

**Henoux:** What is the depth of formation of the two 1.5  $\mu$  lines you used?

Bruls: As far as 15648Å is concerned I find the  $r_{v_0} = 1$  point is located at heights varying from +20 km in the umbra to +110 km in the quiet sun model.

- B. Lites: Do you know if the actual Zeeman splitting pattern in the  $1.5\mu$  lines departs from that predicted by LS coupling?
- S. Solanki: For the g=3 line LS coupling ought to be a good approximation according to Litzen (1976). However, if memory serves me right, for the other line the Landé factor on one of the levels appears to differ significantly from the LS coupling value. Therefore, the Zeeman pattern may also differ.
- J. Staude: I have a comment concerning possible interpretations of the observed reversal of the V profiles near the line center: From line formation theory it is known that the effect occurs already in a homogeneous magnetic field with a sufficiently strong transverse component, if anomalous dispersion is correctly taken into account. The effect can be increased by various mechanisms: (1) the action of line scattering in the reemission instead of pure absorption only; (2) a gradient of the azimuth of the transverse field component along line-of-sight (if the sign is suitable, the Faraday rotation is increased, otherwise it is reduced); (3) the rather sophisticated model of unresolved small magnetic fields with opposite polarity.
- E. Landi: Could you give an estimate of the ratio between the occurrence of "funny" V profiles and the occurrence of "regular" V profiles in your data?

Livingston: Abnormal V profiles are relatively rare in the total data set. However, once a region is found containing one irregular profile, I have the impression that more will likely occur over that area.

- J. Stenflo: If one looks carefully at our FTS recording of the 1.6  $\mu$ m region with 5 arcsec spatial resolution and long time integration, we see a deformation or "notches" of the core parts of the Stokes V profiles of the g=3.0 line, for which you saw frequent cases of sign reversals around the line core. This was observed both at and off disk center. Such a deformed Stokes V profile might result from an average of individual profiles of your type. We (Zayer et al., Astron. Astrophys., 1989) have tentatively suggested that this effect is due to weak flux surrounding the strong kilogauss flux tubes.
- S. Koutchmy: This is just a tentative comment, but I think it is justified by the quality of your data and excitation they induce. It seems that your S/N ratio and speed of recording would permit you to build time series sufficient for looking at MHD waves propagating in the flux tube region, not only in Doppler mode, but especially in magnetic modes. It would be so nice to see magnetic waves or oscillations which are needed to heat the high photosphere and the low chromosphere above flux tube region.

# Plage Magnetic Field Strengths from Near-Infrared Spectra

Douglas Rabin, David Jaksha, Claude Plymate, Jeremy Wagner
National Solar Observatory
National Optical Astronomy Observatories
P. O. Box 26732, Tucson, AZ 85726, U.S.A.

Koji Iwata

Department of Physics, University of Arizona

Tucson, AZ 85721, U.S.A.

Summary. We have measured magnetic field strengths in a small sample of plages from Stokes V spectra of two Zeeman-sensitive iron lines near 6388 cm<sup>-1</sup> (1.565  $\mu$ m). The detected fields are strong ( $\sim 10^3$  gauss), but their strength varies significantly from feature to feature. The individual  $\sigma$ -components are broader than an average quiet-Sun line profile; if this broadening is primarily magnetic, there is typically about a 20% range in field strength within a 2-arcsecond resolution element. These observations represent the first stage of a project to build a near-infrared magnetograph that will produce two-dimensional maps of local magnetic field strength in the low photosphere.

#### 1 Introduction

Almost two decades ago, inconsistencies between the apparent field strengths indicated by different Zeeman-sensitive lines in the visible spectrum led to the hypothesis that the photospheric magnetic field outside of sunspots is characteristically concentrated into subarcsecond fluxtubes of strength  $B \equiv |\vec{B}| \gtrsim 10^3$  gauss (Howard and Stenflo 1972). Since that time, fluxtubes have come to occupy a central place in theoretical models of the magnetic solar atmosphere. Recent observations, particularly those employing a Fourier transform spectrometer, have led to detailed empirical models of single fluxtubes (Keller et al. 1990a) which complement theoretical models of increasing sophistication (Steiner and Pizzo 1989). However, some questions call out for two-dimensional maps to provide a large sample of fluxtubes the properties of which can be related to the larger magnetic and thermal environment. For example, what is the distribution of peak field strengths among fluxtubes? How different are the distributions in different environments, such as old network, enhanced network, or within active regions? Do the thermal properties of fluxtubes differ systematically between regions?

Conventional solar magnetographs employing a single spectral line cannot distinguish a 1000-gauss field occupying 10% of a spatial resolution element from a 100-gauss field with 100% filling factor: magnetographs usually measure magnetic flux rather than magnetic field strength. It

<sup>&</sup>lt;sup>1</sup>Operated by the Association of Universities for Research in Astronomy, Inc. (AURA) under cooperative agreement with the National Science Foundation

is easier to make direct measurements of field strength in the infrared because Zeeman spiring increases as  $\lambda^2$  while thermal broadening increases only as  $\lambda$ . Single-element infrared measurements by Harvey and Hall (1975) and by Stenflo, Solanki, and Harvey (1987) have verified that kilogauss fields are normal in active network elements. However, relating individual measurements to the large body of knowledge built on imaging observations requires, in practice, an instrument based on an array detector. The observations reported here were obtained with a breadboard version of such an instrument, a Near-Infrared Magnetograph (NIM). Although labelled a magnetograph for lack of a better term, its primary goal is to measure intrinsic field strength rather than magnetic flux.

# 2 Observations

The 0.8-m east auxiliary telescope of the NSO McMath Telescope was used in conjunction with the 13.7-m vertical spectrograph and the NOAO  $58 \times 62$  indium antimonide array camera (Fowler et al. 1985) to obtain circularly-polarized spectra of two Zeeman-sensitive iron lines near 1.565  $\mu$ m. The lines are Fe I 6388.64 cm<sup>-1</sup> ( $e^7D_1 - 3d^64s5p^7D_1^o$ , Landé  $g_{\rm eff} = 3.00$ ,  $\chi_e = 5.36$  eV) and Fe I 6386.85 cm<sup>-1</sup> ( $f^7D_5 - (9/2)[7/2]_4^o$ ,  $g_{\rm eff} = 1.53$ ,  $\chi_e = 6.25$  eV) (Solanki, Biémont, and Mürset 1990). Both lines are formed in the low photosphere (the adjacent continuum lies in the opacity minimum).

The angular and spectral scales were 0.58 arcsec pixel<sup>-1</sup> and 0.072 cm<sup>-1</sup> pixel<sup>-1</sup>. The angular resolution in the spectra was limited by seeing to about 2 arcsec. The width of the entrance slit (200  $\mu$ m) was matched to the pixel size in the spectral direction, yielding a spectral resolution (two pixels) of 0.14 cm<sup>-1</sup>.

Images were taken alternately in states of left and right circular polarization using a fixed  $\lambda/4$  plate followed by two ferroelectric liquid crystal (FLC) bistable retarders (Patel and Goodby 1987) and an infrared (HR-type) polaroid. The optical train in front of the slit is shown in Figure 1. In practice, another  $\lambda/4$  plate followed the analyzer to produce circularly polarized light; although not strictly necessary, this ensures that the throughput of the spectrograph (which is sensitive to the state of linear polarization) will be the same each time the instrument is used. The two states of each FLC have the same retardance ( $\lambda/4$ ), but the direction of the fast axis switches by 45°. Two units with matched orientation were used in series because we could not obtain a single unit with  $\lambda/2$  retardance.

The infrared imager controlled the overall synchronization by issuing a TTL-level signal which triggered the FLC voltage controller; the imager paused for 150  $\mu$ s following the TTL signal to allow the retarders to change state and stabilize, after which the detector integrated for 30 ms. The system acquired fifteen circular-polarization pairs per second. Forty pairs were stored in memory and then written to disk. The computer could not co-add pairs in real time fast enough to reduce seeing noise, so polarization pairs were averaged during data reduction.

On 27 January 1990 (1800-2000 UT), we observed active region NOAA 5900 near disk center. The slit was oriented east-west (terrestrial). The NIM is intended to acquire spectra covering two spatial dimensions by precisely scanning the solar image across the entrance slit of the spectrograph.

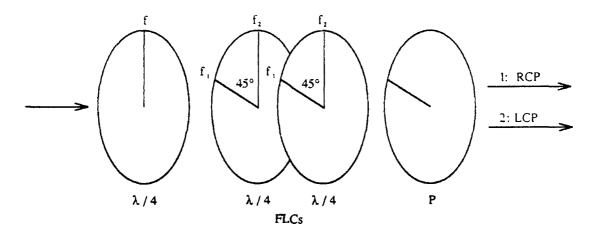


Figure 1: Polarizing optics in front of the spectrograph slit. FLC = ferroelectric liquid crystal, a two-state retarder in which the fast axis switches between the orientations indicated by  $f_1$  and  $f_2$ . P = polaroid analyzer.

In the breadform setup, however, the slit was positioned manually. Ten settings in the active region were made, beginning with a position in which the following spot appeared near one edge of the field. For each subsequent setting, the slit was displaced along its own 36-arcsec length by about 20 arcsec toward the leading complex, providing spatial overlap between successive fields. The trajectory of the slit was chosen to avoid any small spots and pores between the leader and follower. Either forty or eighty polarization pairs were taken at each setting.

# 3 Spectra

Figure 2 displays spectroscopic images from four consecutive slit settings that progressed across the polarity inversion line of the active region. Because the slit was moved manually, the spatial overlap of the spectra is not perfectly regular. The larger frequency splitting of the 6388.6 cm<sup>-1</sup> ( $g_{\text{eff}} = 3.0$ ) line is evident.

Three conclusions emerge from examination of the images. First, where the polarization signal is well above the noise, the corresponding magnetic field is strong,  $B \gtrsim 10^3$  gauss. Second, the field strength is not the same in all features: compare the features labelled B and C in Figure 2. Third, features with approximately the same field strength can have markedly different amplitudes: compare features A and B.

We illustrate these conclusions with one-dimensional spectra by integrating over the spatial extents of the labelled features (guided by the appearance of the feature and consistent with the estimated seeing). Figure 3 (left) compares two features with noticeably different field strengths,  $B \approx 1600$  gauss and  $B \approx 1100$  gauss (the next section discusses the measurement of field strength). Figure 3 (right) compares two features that have similar field strengths but V amplitudes that differ by more than a factor of two.

D. Rabin et al.

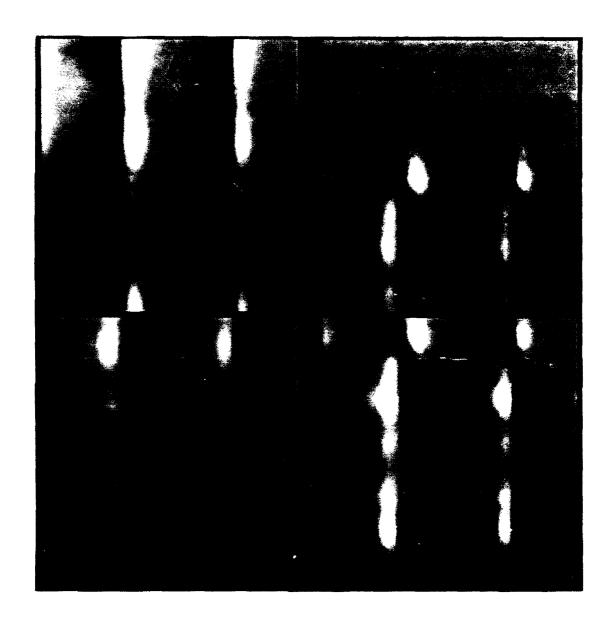


Figure 2: Spectroscopic images from four consecutive slit settings that progressed westward across the polarity inversion line of NOAA 5900 (clockwise from upper left). Wavenumber increases from right to left; east is toward the top.

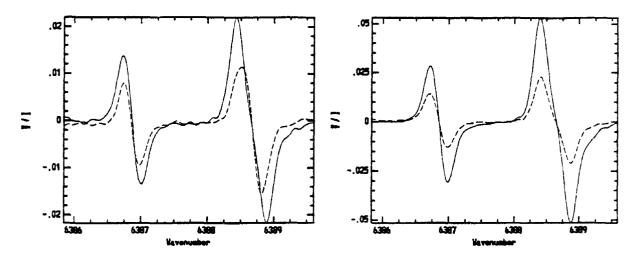


Figure 3: Left, features with different fields strengths (solid: feature B; dashed: feature C (with polarity reversed). Right, features with similar field strengths but different V amplitudes (solid: feature A; dashed: feature B.

To first approximation, the amplitude of the V profile,  $A_V = 0.5(V_{\rm max} - V_{\rm min})$ , is proportional to  $\mathcal{A} = \eta \alpha \cos \gamma$ , where  $\alpha$  is the area filling factor,  $\gamma$  is the inclination of the magnetic field to the line of sight, and  $\eta$  is the strength the absorption line would have in a feature of the same temperature and pressure but without a magnetic field (desaturation and other radiative transfer effects must also be considered in principle but are ignored here for simplicity and because the lines are relatively weak). The filling factor is perhaps the dominant influence on the V amplitude in a statistical sense because the present high-excitation lines are relatively insensitive to temperature (Muglach and Solanki 1991) and because buoyancy drives an isolated flux tube to a vertical orientation (Spruit 1981). However, within the small sample of features considered here, we cannot assess the relative importance of the several factors that affect the V amplitude.

# 4 Preliminary Analysis

Let  $\Delta\nu_V$  be half the frequency splitting between the two Stokes V "peaks" (positive and negative extrema),  $\Delta\nu_D$  the doppler width of Stokes I, and  $\Delta\nu_B$  the true frequency separation of each Zeeman component from the nominal line center.<sup>2</sup> When  $\Delta\nu_V \gtrsim 1.5 \Delta\nu_D$  — the strong splitting regime — then  $\Delta\nu_V \approx \Delta\nu_B$ , and, therefore,  $\Delta\nu_V$  directly measures B through the Zeeman relation  $\Delta\nu_B = 4.67 \times 10^{-5} g_{\rm eff} B$ ; the V amplitude is independent of B. When  $\Delta\nu_V \ll \Delta\nu_D$  — the weak splitting regime — then  $\Delta\nu_V \approx \Delta\nu_D$  independently of B; but the V amplitude decreases as B decreases.

A simple, empirical approach to extracting field strength B and amplitude factor A from Stokes V spectra is to calibrate the relationships between  $\Delta \nu_V$  and  $\Delta \nu_B$  and between  $\Delta \nu_V$  and  $A_V$  by numerically splitting an observed Stokes I profile. This technique is just the extension to full

<sup>&</sup>lt;sup>2</sup>Stokes I is normalized to unit continuum intensity, so V = V/I.

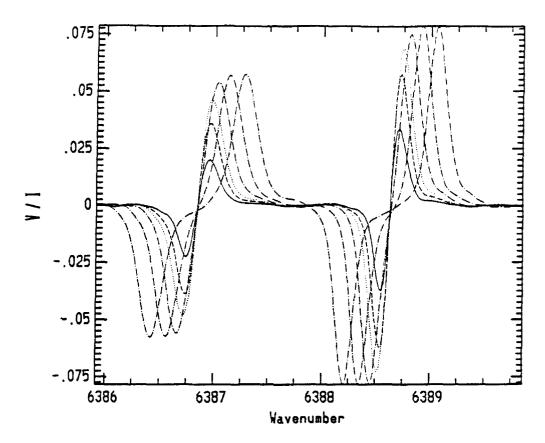


Figure 4: Synthetic V profiles used for calibration.

Seares profiles of the usual calibration method for magnetographs with discrete exit slits. Figure 4 shows synthetic V profiles derived in this way from a mean quiet-Sun I spectrum (weak lines that contaminate the two lines of interest were fitted and removed before splitting was introduced).<sup>3</sup> The advantage of this approach (besides simplicity) is that it avoids the use of theoretical line profiles, which may have the wrong shape and which must be adjusted for the optical transfer function of the spectrograph. The obvious disadvantage is that the empirical I profile, typically a mean profile from the quiet Sun, cannot account for changes in the strength or width of the line inside a magnetic feature. Ignoring possible changes in strength is justified in this preliminary analysis because the lines are insensitive to temperature and because the primary goal is to measure Zeeman splitting, which is insensitive to line strength in the strong-splitting regime. The widths of the individual V components are discussed below.

Figure 5 shows calibration curves derived from Figure 4. Plotting apparent field strength,  $B_{\rm app}=2.14\times 10^4\Delta\nu_V/g_{\rm eff}$ , in place of the raw frequency splitting  $\Delta\nu_V$ , we see that the transition between quasi-strong splitting (for which  $B_{\rm app}$  and  $B_{\rm true}$  differ by  $\lesssim 20\%$ ) and weak splitting takes place over a fairly narrow range in field strength (again about 20%). For the 6388.6 cm<sup>-1</sup> line, the calibration is usable down to  $B_{\rm true}\approx 650$  gauss. For fields strong enough to allow reliable determinations from both lines ( $B\gtrsim 1600$  gauss), comparison suggests an external uncertainty of

<sup>&</sup>lt;sup>3</sup>Figure 4 is not a synthetic V spectrum because the frequency splitting is the same for both lines, which have different Zeeman sensitivities; this is taken into account in the derived calibration curves.

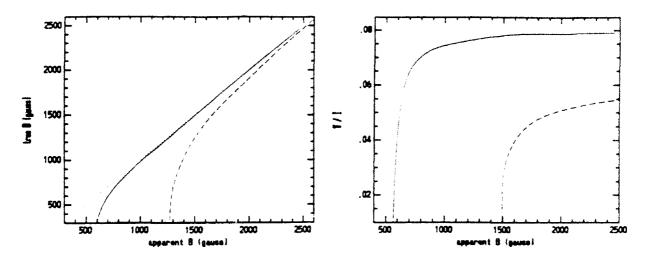


Figure 5: Calibration curves relating  $E_{\rm app}=2.14\times 10^4\Delta\nu_V/g_{\rm eff}$  to  $B_{\rm true}$  and  $A_V$ . Solid: Fe I 6388.6 cm<sup>-1</sup>. Dashed: Fe I 6386.9 cm<sup>-1</sup>. Dotted (left):  $B_{\rm eff}=B_{\rm true}$ .

about ±7%.

We are currently testing an elaboration of this measurement technique that retains its empirical character. Instead of measuring  $\Delta\nu_V$  and  $A_V$  and then entering calibration curves, we use nonlinear fitting to determine the splitting and amplitude of the Zeeman components. Each iteration generates a full V profile (by numerically splitting and renormalizing the I profile), which is then compared in a least-squares sense to the observed profile. In addition, a "three-point approximation" to line broadening is included by replacing the nominal I profile with three components of the same shape. The two outlying components are separated symmetrically from the central component by  $\Delta\nu_V$  to be determined in the fitting; the relative amplitude of the secondary components is fixed at a value 0.607 times the amplitude of the primary component (0.607 is the ordinate of a gaussian with unit amplitude at abscissae  $\pm 1\sigma$ ).

Figure 6 shows an example of the fitting. With no broadening added to the nominal I profile, the individual Zeeman components are clearly too narrow. In the fit with broadening, the secondary components are split from the primary component by the equivalent of  $\pm 330$  gauss, a  $\pm 21\%$  spread relative to the mean splitting (1540 gauss). Of course, this crude approximation makes no distinction between Zeeman and additional Doppler broadening. In principle, the different Zeeman sensitivites of the two lines allow magnetic and thermal broadening to be distinguished. In the present data, only the strongest measured fields can be tested. For this very small sample, Zeeman broadening alone produces better fits than Doppler broadening alone, consistent with the conclusion reached by Zayer, Solanki, and Stenflo (1988) in a detailed analysi. of FTS data.

<sup>\*</sup>beyond the turbulent broadening implicitly included in the reference I profile

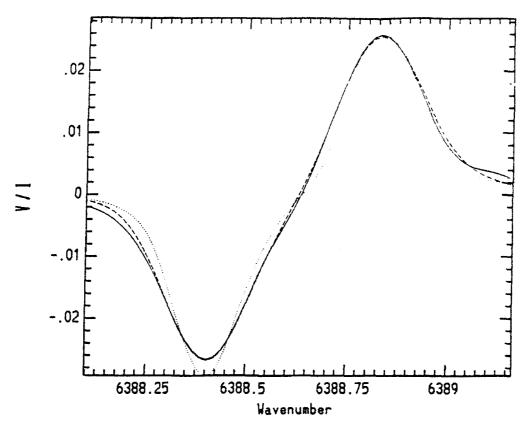


Figure 6: The results of nonlinear least-squares fitting, indicating the need to broaden the individual Zeeman components. Solid: observed profile. Dashed: fitted profile with Zeeman broadening. Dotted: fitted profile without Zeeman broadening.

# 5 Conclusion

The sample of features in Figure 2 is too small to reveal the joint distribution of points in the B-A plane. However, the spreads of B and A are separately significant. The measured field strengths span the range 800-1600 gauss. This is substantially larger than the range (<300 gauss) inferred by Stenflo and Harvey (1985), who applied the  $\lambda 5250.2/\lambda 5247.1$  line-ratio method to a sample of magnetic regions which spanned a factor of six in magnetic flux. Keller et al. (1990b) applied the same technique to narrowband filtergrams and concluded that their observations were compatible with a unique magnetic field strength in small-scale magnetic elements.

The present infrared observations are not compatible with the hypothesis of a unique mean field strength in plage fluxtubes.

One of the main goals of the NIM instrument, when it is fully operational in scanning mode, will be to relate the joint distribution of B and A to cospatial and cotemporal images, such as (conventional) magnetograms and chromospheric filtergrams.

Although the present data have lower spectral resolution than is desirable for analyzing thermal properties, the Zeeman components are nonetheless detectably broadened. In conjunction with other observations that place limits on the Doppler broadening in magnetic elements (Zayer, Solanki, and Stenflo 1988), it should therefore be possible to discover how much the magnetic field distribution within a fluxtube can vary from element to element.

We thank R. Probst, A. Fowler, K. Gillies, N. Buchholz and I. Gatley for accistance in connection with the infrared imager.

# REFERENCES

Fowler, A., Probst, R., Britt, J., Joyce, R., and Gillett, F. 1987, Opt. Eng., 26, 232.

Harvey, J., and Hall, D. 1975, Bull. Am. Astron. Soc., 7, 459.

Howard, R., and Stenflo, J. 1972, Solar Phys., 22, 402.

Keller, C., Solanki, S., Steiner, O., and Stenflo, J. 1990, Astron. Astrophys., 233, 583.

Keller, C., Solanki, S., Tarbell, T., Title, A., and Stenflo, J. 1990, Astron. Astrophys., 236, 250.

Muglach, K., and Solanki, S. 1991, in *Solar Polarimetry* (Proc. 11th Sacramento Peak Workshop), ed. L. November (NSO: Sunspot, NM).

Patel, J., and Goodby, J. 1987, Opt. Eng., 26, 373.

Solanki, S., Biémont, E., Mürset, U. 1990, Astron. Astrophys. Suppl., 83, 307.

Spruit, H. 1981, in The Sun as a Star (NASA SP-450), ed. S. Jordan (Washington: NASA), p. 385.

Steiner, O., and Pizzo, V. 1989, Astron. Astrophys., 211, 447.

Stenflo, J., and Harvey, J. 1985, Solar Phys., 95, 99.

Stenflo, J., Solanki, S., and Harvey, J. 1987, Astron. Astrophys., 173, 167.

Zayer, I., Solanki, S., and Stenflo, J. 1988, Astron. Astrophys., 211, 463.

Speaker: Rabin

#### Discussion

- S. Solanki: We have calculated the g=3 line in models with different temperatures and have found it to be relatively temperature insensitive. I can't say off-hand what its sensitivity actually is, but it is less than half as sensitive as FeI 5250.2Å.
- S. Koutchmy: On your last graphs you presented very nice measurements using the strong-field case (splitting). What about weaker fields? Why not use the same method (measure the amount of polarized light) as in the optical region (see the J. Jefferies contribution).
- D. Rabin: Techniques developed for weakly split lines in the visible can and should be applied to infrared lines, particularly if all the Stokes parameters are measured. This should allow weaker magnetic fields to be detected if they are present.
- D. Deming: Do you see any weaker fields, i.e. less than ~ 800 gauss?
- D. Rabin: Not in the small sample of data we have so far.
- J. Stenflo: The effect of Zeeman and Doppler broadening of the sigma components could be separated in the FTS data by comparing two FeI lines of different Zeeman sensitivities. The Zeeman broadening would be explained entirely in terms of the field strength variation along the line of sight, resulting from the divergence with height of the field in self consistent hydrostatic flux tube models.

# Section 4 Physical Interpretation chair: A. Skumanich

# DIRECT INFERENCE OF MAGNETIC FIELD VECTORS FROM STOKES PROFILES

John T. Jefferies
National Solar Observatory, NOAO \*
Tucson, Arizona 85726

Donald L. Mickey Institute for Astronomy University of Hawaii Honolulu, Hawaii 96822

In a publication by Jefferies, Lites, and Skumanich (1989) - here referenced JLS - it was shown that procedures could be developed which, in certain cases, would allow the inference of approximate values of the magnetic-field vector directly and simply from measured profiles of the Stokes parameters (I, Q, U, V) across a magnetically sensitive spectral line. The procedures were based on the so-called "weak-field" approximation (WFA) and were embodied in equations (55) and (56) of JLS which may be written:

$$|v_b|\cos\gamma = -V/\left(\frac{dl}{dv}\right) \tag{1a}$$

$$\left(\frac{v_b \sin \gamma}{2}\right)^2 = \frac{H'(a, v)}{H''(a, v)} \left(Q^2 + U^2\right)^{1/2} / \frac{dI}{dv}$$
 (1b)

$$\tan 2\chi = U/Q \tag{1c}$$

In these equations,  $\gamma$  and  $\chi$  are respectively the polar and azimuthal angles of the field vector in a reference frame where the vertical axis is along the line of sight and the axes in the x, y plane are arbitrarily established by the observer. The parameter v is the normalized line frequency  $(\Delta v/\Delta v_D)$  measured from the line center in units of the Doppler width  $\Delta v_D$ ; H', H" are the derivatives, with respect to v, of the Voigt function

H(a,v); a is the usual damping constant; and  $v_b$  is the line splitting in units of the Doppler width, i.e.,

$$v_b = \frac{eBg_L}{4\pi mc} \left( \frac{1}{\Delta v_D} \right) = \frac{eBg_L}{4\pi mc^2} \frac{\lambda^2}{\Delta \lambda_D}$$
 (2)

with B the field strength and gL the Lande factor for the spectral line.

The results (1) were derived on the assumption that  $v_b < 1$  (i.e., that the field B was "weak" in that sense) in which case the transfer equations for the Stokes parameters simplify greatly and require the conditions embodied in equations (1) for consistency. They also were based on the assumption that the parameters determining the Stokes vector do not change strongly with depth (except for the LTE source function  $B(\tau)$ , which may change arbitrarily with optical depth  $\tau$ ). To the extent that these approximations are valid, equations (1) apply at all frequencies across the line (and at all depths, too, although this is of less immediate interest). A considerable redundancy is potentially available, then, for determining the (assumed constant) value of the field vector from measurements of I, Q, U, V

Operated by the Association of Universities for Research in Astronomy, Inc. (AURA) under cooperative agreement with the National Science Foundation.

across a line. This redundancy may be used - as was done by Ronan, Mickey, and Orrall (1987) - to combat the inevitable noise in the often - weak polarization signals by using wavelength-integrated values of the Stokes parameters. In practice we can expect to find that inferences of the field vector made from data at different positions in the line do not always yield consistent results - and this will bring the assumption of depth-independence into question. Indeed the asymmetry in the Q, U, and V profiles, which is almost invariably seen in observational data, is a clear indicator that that assumption will normally be wrong. More positively, however, such variations may open a path for inferring the depth gradient in the field vector.

This study pursues the limits of applicability of the weak-field approximation. The more general methods involving non-linear least-squares fitting to special solutions of the Stokes transfer equations - see, e.g., Skumanich and Lites (1987), Keller et al (1990) and references cited therein - appear to give the best approach for inferring strong fields in the line core. They are, however, demanding computationally and impractical for on-line reduction. We might hope, then, that the WFA will turn out to be of sufficiently broad application to provide a "quick-look" assessment as data is being gathered, as well, perhaps, as giving a good starting value for more sophisticated approaches.

Our approach is consistent with that hope. We first show that the WFA can indeed be applied for very muci stronger fields than was previously believed the case, provided we work at wavelengths away from the immediat vicinity of the line core. For a broad range of circumstances which may be commonly encountered on the sun, then, simple algorithms can indeed be found for obtaining values of all three components of the vector field directly and simply from the Stokes parameters. The expressions we obtain are essentially equivalent to equations (1). For the line wings they take the explicit forms

$$B\cos\gamma = \frac{2.1 \times 10^{12}}{g_* \lambda^2} \left( V / \frac{dI}{d\lambda} \right) \qquad gauss, \qquad (3a)$$

$$B\sin\gamma = \frac{2.5 \times 10^{12}}{g_L \lambda^2} \left[ \frac{\Delta \lambda \left( Q^2 + U^2 \right)^{1/2}}{dI / d\lambda} \right]^{1/2} \qquad gauss \qquad (3b)$$

where wavelengths are measured in A. The azimuth angle  $\chi$  is again given by

$$tan 2\gamma = U/O (3c)$$

We should note, particularly, that application of these expressions requires no prior knowledge of the line strength, damping constant, doppler width, or depth dependence of the Planck function. The accuracy of these expressions decreases as the field strength increases, however they still remain valid at about the 80% level for fields as strong as 3500/gL gauss. Our theoretical discussion suggests that, by a simple calibration of these expressions, the systematic loss of accuracy with field strength can be corrected to yield a significant increase in the accuracy of estimating field strengths or, strictly speaking, of magnetic fluxes.

The theoretical results have been applied to determine the field vector, for a typical situation near a sunspot, using observations of the Stokes profiles of some Fe I lines (near 6300Å) obtained with the spectropolarimeter at the Mees Solar Observatory on Haleakala. The consistency found in the results of this application is reassuring and suggests that the approach may be broadly applicable both to high-resolution (spectrographic) polarimeters and to lower resolution imaging systems based, e.g., on monochromatic filters.

A full description of this work has been submitted for publication in The Astrophysical Journal.

# REFERENCES

Jefferies, J. T., Lites, B. W., and Skumanich, A. P., 1989, Ap. J., 343, 920. Keller, C. U., Solanki, S. K., Steiner, O., and Stenflo, J. O., 1990, Astr. Ap., 233, 583. Ronan, R., Mickey, D. L., and Orrall, F. Q., 1987, Solar Phys. 113, 353. Skumanich, A., and Lites, B. W., 1987, Ap. J., 322, 473.

#### Discussion

- J. Sterifio: It seems to me that the weak-field approximation has already been included and used in previous calibrations of vector magnetograph observations, going back to the work of Stepanov and Severny in 1962.  $dI/d\lambda$  was derived from artificial or known displacements of the line used in the magnetograph. For practical reasons this calibration could not be done for each single spatial point of observation, since Stokes profile measurements were not available, but the philosophy of the weak-field approximation was the underlying foundation of interpreting the observations.
- J. Jefferies: Perhaps I have misunderstood your question, but I can only say that I do not see how any calibration of the transverse field could possibly have been in 1962 since the relationship expressed in equation (1b), or (3b), was first published in 1989 in the paper by Jefferies, Lites, and Skumanich. Indeed the usual belief see e.g. your paper at the Huntsville conference ("Measurements of Solar Vector Magnetic Field", NASA SP 2374, 266) has been that the transverse field depended on the second derivative of the line intensity rather than the first derivative as our analysis has shown must be the case in the weak-field approximation. In these circumstances I cannot see how Stepanov and Severny could have had a basis for quantitative calibration.

The weak-field form of the longitudinal field has, of course, been known for a long time and has been used universally for calibration purposes. In fact the Landi's derived the expression in more generality well before our paper did but in much the same way – see their article in Solar Physics 31, 299.

- M. Semel: Magnetographs, in the past, used to be calibrated by a standard line profile (or its measured derivative at a particular wavelength). In the present proposal, one should use the actual derivative of the line profile measured at the observed solar point. The longitudinal component of the magnetic field is obtained independently of the field strength by the "center of gravity method", i.e., by measuring the first moment of V and dividing by the equivalent width of the line. The application of the integral method to the linear polarization depends only on the line broadening parameter. This last may be determined by using several lines of different factors.
- J. Jefferies: The basic expression (3a) can be integrated at once to give

$$B\cos\gamma = \frac{1.05 \cdot 10^{12}}{g_L \lambda^2} \frac{\int_{-\infty}^{+\infty} |V| d\lambda}{I_o - I_c}$$

which expresses the longitudinal field in terms of the ratio of the first moment of |V| and the depth of the line at its center. This form is exact in the weak-field limit and requires no knowledge of atomic or atmospheric parameters (other than the Landé factor) to apply.

Ronan, Mickey, and Orrall used a variant of this by replacing the line depth by the equivalent width, in the belief that this would reduce the error introduced by the noise in the data. Their expression is, however, no longer exact (in the weak-field limit) and the calibration constant will depend on such parameters as the line strength, damping constant, and Doppler width – as you say. Whether the attendant uncertainty thus introduced compensates for the potential error in estimating the central depth of the line I cannot say. This whole question is discussed in detail in the paper by Jefferies, Lites, and Skumanich.

- E. Landi: There is an important difference between the two formulae presented for the longitudinal and transverse component of the magnetic field. The first is more general, as it is valid also when velocity gradients are present and when there are variations with depth of the thermodynamical parameters (Doppler broadening, damping constant). On the contrary, the second formula is valid only for a static atmosphere with constant Doppler broadening and damping.
- J. Jefferies: I agree. You pointed this out some years ago (Solar Physics 31, 299, 1973). The expression is very robust indeed.

# The Derivation of Vector Magnetic Fields from Stokes Profiles: Derivative versus Least Squares Fitting Techniques

T. R. Metcalf, R. C. Canfield and D. L. Mickey Institute for Astronomy, University of Hawaii

B. W. Lites

High Altitude Observatory, National Center for Atmospheric Research

#### Abstract

We present a comparison of solar magnetic fields calculated using the weak field equations of Jefferies, Lites, and Skumanich and the least squares fitting method of Skumanich and Lites. The two calculations used Fe 1 6302 data from June, 1985, and are found to agree quite well up to at least 1200 G.

# I. Introduction

Recently, Jefferies, Lites, and Skumanich (1989, hereafter JLS) derived simple expressions for calculating the vector magnetic field from observations of the Stokes profiles in the weak field limit. Further study by Jefferies and Mickey (1990) demonstrated the practicality of this method for solar observations. In this work, we further test the method by comparing a large range of magnetic field strengths derived using both the JLS method and the least squares fitting method of Skumanich and Lites (1987, hereafter SL). For this purpose, we use data obtained in 1985 at the Mees Solar Observatory, Haleakala, Hawaii, which is the same dataset utilized by Ronan, Mickey and Orrall (1987, hereafter RMO) to compare the integral reduction method to the SL least squares fitting method.

The equations of JLS are straightforward to apply, with the only difficulties arising in the calculation of the derivative of the Stokes I profile and the line center wavelength position (particularly in dark sunspots). In §II we discuss the reduction method we have used, and in §III we demonstrate the method and compare the results to those obtained using the SL code.

# II. DATA REDUCTION

JLS give the following equations relating the magnetic field to the observed Stokes profiles:

$$B\cos\gamma = \frac{4\pi mc^2}{eg_L\lambda^2} \frac{V}{dI/d(\Delta\lambda)} \tag{1}$$

and

$$B\sin\gamma = \frac{8\pi mc^2}{eg_L\lambda^2} \left(\frac{H'}{vH''}\right)^{1/2} \left(\frac{(Q^2 + U^2)^{1/2}\Delta\lambda}{dI/d(\Delta\lambda)}\right)^{1/2}$$
(2)

$$\phi = \frac{1}{2} \tan^{-1} \left( \frac{U}{Q} \right) \tag{3}$$

Here, I, Q, U, and V are the Stokes profiles,  $dI/d(\Delta\lambda)$  is the derivative of the Stokes I profile with respect to the wavelength measured relative to line center, H' and H'' are the first and second derivatives of the Voigt profile with respect to v (the frequency measured relative to line center in units of the Doppler width), B is the total field strength, and  $\gamma$  is the polar angle and  $\phi$  the azimuthal angle of the field. To implement these equations, we need, in addition to the Stokes profiles, the derivative of the I profile, the wavelength position of line center, and the first and second derivatives of the Voigt function.

To calculate the derivative of the I profile in the presence of noise, we have followed the suggestions of Craig and Brown (1986) and have converted the calculation of the derivative to an integral equation which can, in turn, be converted to a smoothed matrix equation using the method of second order regularization. This makes the calculation of the derivative much less sensitive to the noise. With the derivative equation converted to the integral equation

$$\int_0^{\Delta \lambda} \left( \frac{dI}{dy} \right) dy = I(\Delta \lambda) - I(0),$$

the matrix equation for the derivative is

$$\mathbf{K}\left(\frac{d\vec{I}}{d(\Delta\lambda)}\right) = \vec{I} \quad \text{or} \quad \frac{d\vec{I}}{d(\Delta\lambda)} = \mathbf{K}^{-1}\vec{I}$$
,

and the smoothed matrix equation is

$$(\mathbf{K}^T \mathbf{K} + \alpha \mathbf{H}) \frac{d\vec{I}}{d(\Delta \lambda)} = \mathbf{K}^T \vec{I} . \tag{4}$$

Here, K is a lower triangular matrix which, when inverted and applied to a data vector. gives the first order finite differences, and  $K^T$  is the transpose of this matrix. H is a smoothing matrix which finds the most linear derivative consistent with the data,  $\alpha$  is a parameter which controls the amount of smoothing,  $\vec{I}$  is the Stokes intensity profile as a function of wavelength, and  $dI/d(\Delta\lambda)$  is the derivative we seek. Since the matrix on the left side of equation (4) does not depend on the data, it need be inverted only once, and the inverse applied to  $\mathbf{K}^T \vec{I}$  for each profile for which the derivative is calculated. Note that when  $\alpha$  is zero, the finite difference solution is regained and when  $\alpha$  is large, a linear derivative is obtained (i.e. the derivative of the best fit to a parabolic I profile). In practice,  $\alpha$  is computed by comparing the magnitude of the observational errors inherent in the data with the sum of the residual error incurred by introducing smoothing and the error due to the instability of the inversion, determined by the scatter present in the inversion of many random realizations of the Stokes I vector. This procedure avoids potential problems of oversmoothing in the solution (Metcalf et al, 1990). For the RMO dataset described below, the solution is very insensitive to the choice of  $\alpha$ ; we used a value of 10, but values of 1 and 100 were found to give almost identical solutions. The smoothing obtained by inverting equation (4) is quite helpful in reducing the noise in the derivative; however, we have found the RMO dataset to be good enough that magnetograms derived without smoothing are reasonably accurate.

378 T. R. Metcalf et al.

To find the position of the line center, we fit the minimum region of the I profile with a parabola. However, inside sunspots this method fails and we have taken line center as the wavelength intermediate between the peaks of the V profile.

Finally, Jefferies and Mickey have shown that the combination of the derivatives of the Voigt function in equation (2) is practically constant in the wings of the line regardless of the values of the Doppler width and Voigt parameter chosen. For generality, however, we have used the algorithm of Humlicek (1982) to compute this function exactly since it is computationally expedient.

# III. COMPARISON OF DATASETS

The RMO data used were obtained on June 8 and June 10, 1985, with the Haleakala Stokes Polarimeter (Mickey, 1985) and consist of the four Stokes parameters for the Fe1 6302.5 photospheric line rastered over a  $150'' \times 150''$  field of view. The point-wise observations have a 6'' instantaneous field of view with a 3.5 s integration time at each point. The red and blue sides of the line were averaged, and the derivative of the I profile was computed 110 mÅ from line center. Except in the sunspots, this point was far enough in the wings to allow the use of the weak field equations, yet still had sufficient polarization to give a good measurement of the field.

In Figures 1 through 4, the longitudinal and transverse fields and the polar and azimuthal angles derived using the JLS and the SL methods are compared, with the field from the SL method on the horizontal axis and the field from the JLS method on the vertical axis. The field parameters are consistent (±100 G) up to a field strength of at least 1200 G. In Figure 4, the 180 degree ambiguity in the azimuthal angle was accounted for by adding or subtracting multiples of 180 degrees from the value found with the JLS method until it was as close as possible to the value from the SL method. We have not used the scattered light correction in the SL analysis, since this correction is not included in the JLS method as formulated.

In Figures 1 and 2, the data points with longitudinal/transverse fields from the SL method falling between 1500 and 2000 G are within a sunspot where the line splitting was relatively large. At 110 mÅ, the weak field approximation is not valid for these field strengths, and the JLS method requires data further out into the line wings for a reliable calculation of the field strength. Unfortunately, a blend on the red side of the Fe i 6302 line interferes with the calculation and only the blue side can be used beyond 125 mÅ. Thus, it is not useful to look further into the wings of this line since the averaging of red and blue sides of the line cannot be accomplished, and line asymmetries conspire to make the field uncertain. Eliminating the fields derived from within the sunspots yields the comparison shown in Figures 6 and 7.

# IV. CONCLUSIONS

1. Fields derived with the JLS method compare very well with those derived with the SL method and require much less effort to obtain, suggesting that the JLS formulae will be very useful in analyzing Stokes profiles. The method may, in fact, be optimal for imaging type magnetographs which sample the full Stokes spectrum only sparsely.

2. Within sunspots or other strong field regions, the derivative of I must be calculated further from line center than in the weaker field regions. Due to the blend, this is not possible with the Fe i 6302 line and hence this line is not ideal for use with the JLS method.

# Acknowledgments

This work was supported by NASA grant NAGW-1542 and Lockheed Solar-A contract SE80D7850R.

# References

Craig, I. J. D. and Brown, J. C. 1986, Inverse Problems in Astronomy, Adam Hilger Ltd., Bristol.

Humlicek, J. 1982, J. Quant. Spect. Rad. Trans., 27, 437.

Jefferies, J. T., Lites, B. W. and Skumanich, A. 1989, Ap. J., 343, 920

Jefferies, J. T. and Mickey, D. L. 1990, Ap. J., submitted.

Metcalf, T. R., Canfield, R. C., Avrett, E. H., and Metcalf, F. T. 1990, Ap. J., 350, 463.

Mickey, D. L. 1985, Solar Phys., 97, 223.

Ronan, R. S., Mickey, D. L. and Orrall, F. Q. 1987, Solar Phys., 113, 353.

Skumanich, A. and Lites, B. W. 1987, Ap. J., 322, 473.

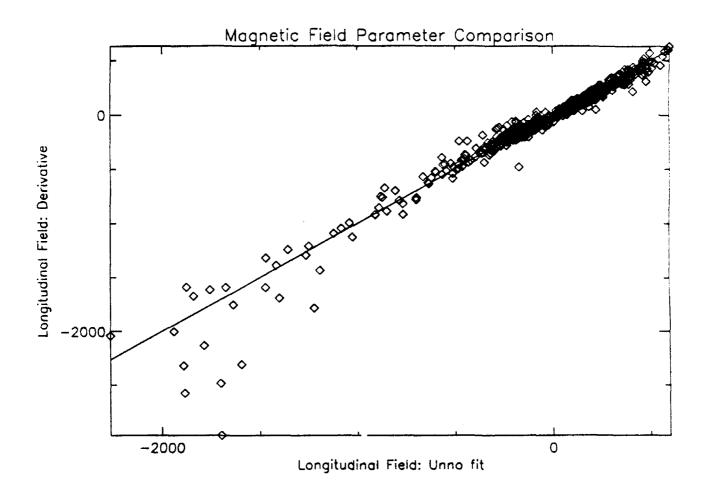


Fig. 1 A comparison of the longitudinal magnetic field strengths derived from the SL least squares method (horizontal axis) and the JLS derivative method (vertical axis). The large scatter at high field strengths is due to the difficulty of determining the derivative of I in sunspots when using the Fe I 6302 line.

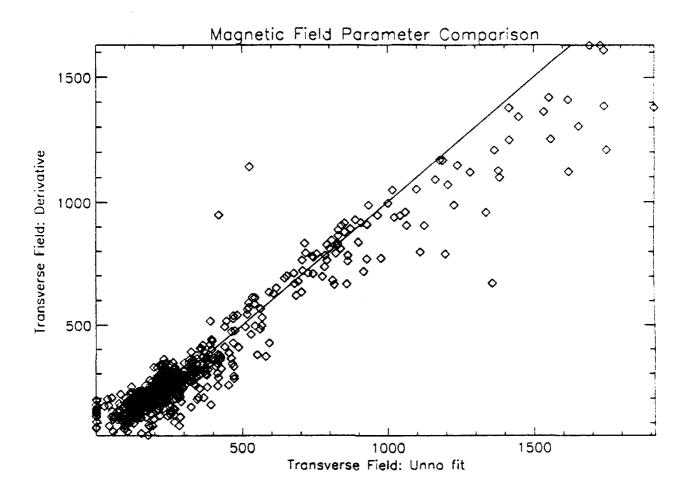


Fig. 2 A comparison of the transverse magnetic field strengths derived from the SL least squares method (horizontal axis) and the JLS derivative method (vertical axis). The large scatter at high field strengths is due to the difficulty of determining the derivative of I in sunspots when using the Fei 6302 line.

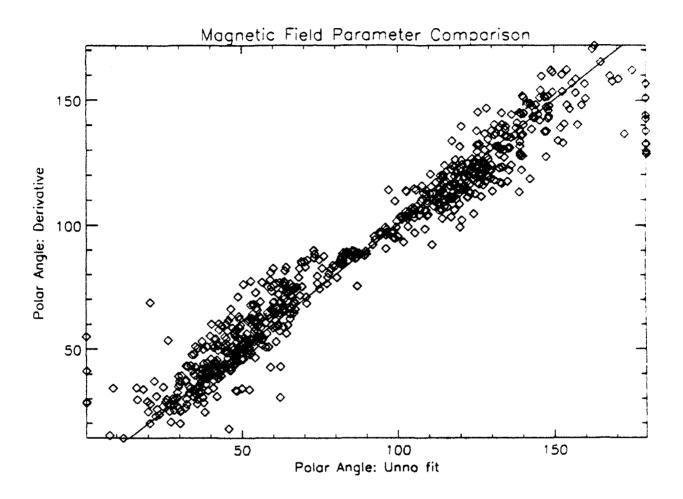


Fig. 3 A comparison of the polar angle (angle from line-of-sight) derived from the SL least squares method (horizontal axis) and the JLS derivative method (vertical axis).

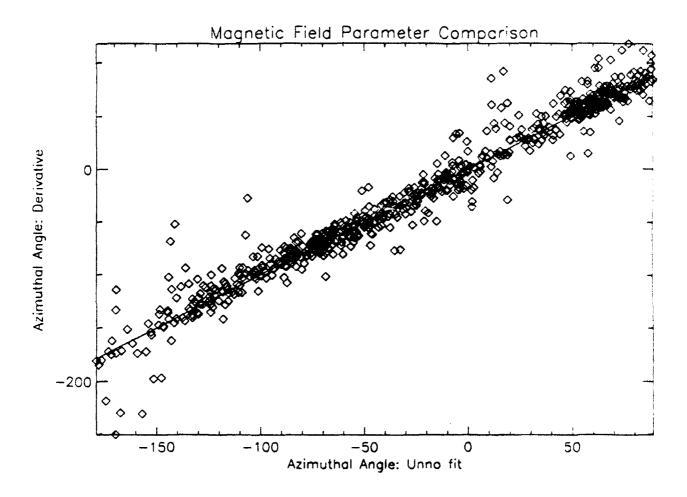


Fig. 4 A comparison of the azimuthal angle derived from the SL least squares method (horizontal axis) and the JLS derivative method (vertical axis).

T. R. Metcalf et al.

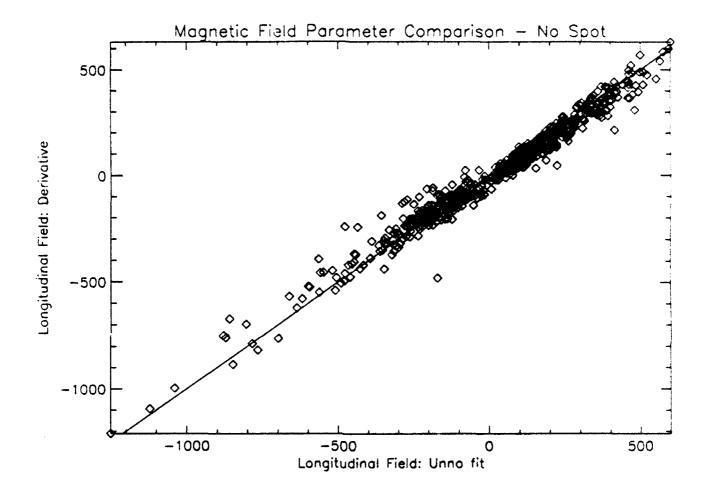


Fig. 5 A comparison of the longitudinal magnetic field strengths derived from the SL least squares method (horizontal axis) and the JLS derivative method (vertical axis) after excluding the data from the sunspot. The agreement between the two methods is good up to at least 1200 G.

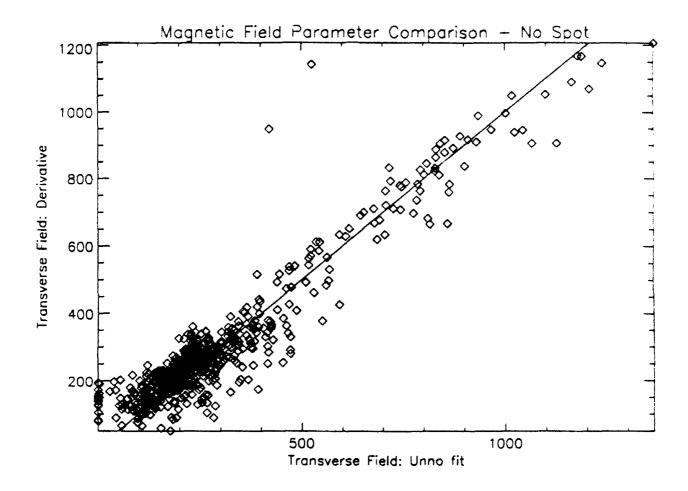


Fig. 6 A comparison of the transverse magnetic field strengths derived from the SL least squares method (horizontal axis) and the JLS derivative method (vertical axis) after excluding the data from the sunspot. The agreement between the two methods is good up to at least 1200 G.

# Discussion

- J.C. del Toro Iniesta: Have you tried to use the Fourier technique to derive the I derivatives? Any smoothing procedure implies some losses in high frequencies (not only noise).
- T. Metcalf: No. There are many techniques for smoothing the inversion problem; Fourier techniques should work as well.
- B. Lites: What might you expect to be the effect of degraded spectral resolution on the results of this method?
- T. Metcalf: We have not yet investigated this question, but it is clearly an important consideration and we will be looking into it.
- S. Keil: Do you have some good unblended candidate lines in mind for applying this technique?
- T. Metcalf: 6302.5Å.

# Inversion of Stokes V Profiles:

The structure of solar magnetic fluxtubes and its dependence on the filling factor

C.U. KELLER, S.K. SOLANKI, J.O. STENFLO, I. ZAYER

Institute of Astronomy
ETH-Zentrum, CH-8092 Zürich, Switzerland

Summary: We present results from an inversion procedure that derives the temperature stratification, the turbulent velocity, and the magnetic field strength of the photospheric layers of magnetic fluxtubes from observed Stokes V spectra near disk center. In a first step the inversion has been applied to 10 Fe I and Fe II Stokes V profiles of a plage and a network region to obtain reliable models of the fluxtubes. In a second step the dependence of the fluxtube structure on the filling factor has been studied with spectra of 3 Fe I lines from 23 different regions based on the models derived in the first step. We find a temperature excess at equal geometrical height in the upper photosphere with respect to the quiet photosphere and a deficit at the level of continuum formation. There the magnetic field strength is on the order of 2000-3000 G and turbulent velocities are considerably larger in the fluxtubes than in the quiet photosphere. Fluxtubes are found to become cooler and their field strengths, at a given optical depth, to become larger as the filling factor increases. The field strength stratification along the geometrical height axis, on the other hand, is very similar for all the investigated regions. Some evidence is also found for a slight decrease of the non-stationary velocity amplitude with increasing filling factor.

#### 1. Introduction

Most empirical fluxtube structures have been obtained by fitting synthetic Stokes I spectra from simple fluxtube models to observed facular spectra or by fitting the observed center-to-limb variations (CLV) of the continuum contrast of faculae (see the review by Solanki, 1990). However, these attempts have failed in finding a unique model that explains the observations and that is not heavily influenced by assumptions regarding the structure of the non-magnetic atmosphere between the fluxtubes (e.g. Walton, 1987). The few models derived from Stokes V profiles (Stenflo, 1975; Solanki, 1984, 1986) have the substantial advantage that the analysis can be performed independently of the spatial resolution. However, these efforts have been limited to just a few solar regions due to their reliance in the 1980s on FTS observations of a suitably large sample of carefully selected spectral lines. Therefore, comparatively little is known about the dependence of fluxtube structures on the filling factor  $\alpha$ , which is defined as the fraction of the observed solar surface covered by strong magnetic fields. For practical reasons this type of investigation is best carried out with a small number of spectral lines. The dependence of some fluxtube properties on  $\alpha$  has previously been studied by Stenflo and Harvey (1985). In Sect. 2 we present the inversion procedure, which is then applied to 10 lines of a plage and a network region near disk center (Sect. 3, see Keller et al., 1990, for more details) and in Sect. 4 to 23 spectra of different solar regions near disk center using only 3 lines (see Zayer et al., 1990, for more details).

# 2. Inversion procedure

The inversion of Stokes V profiles is based on the determination of a few model fluxtube parameters by a least-squares fitting algorithm. The fluxtube model used is the thin tube approximation (e.g. Roberts and Webb, 1978). The use of more elaborate models does not introduce any qualitative difference in the resulting fluxtube structures when using spectra from disk center (Keller et al., 1990). The free parameters of the models are the magnetic field strength at optical depth unity inside the fluxtube  $B(\tau_i)$  (subscript i denotes the atmosphere within the fluxtubes),

388 C. U. Keller et al.

the temperature as a function of the geometrical height, and the macroturbulent velocity as a function of the line strength and the excitation potential. The microturbulent velocity is kept at a height independent value of 0 6 km s<sup>-1</sup>. The inversion is started with prescribed initial values for the model parameters from which the corresponding fluxtube model is calculated. Then the synthetic Stokes V profiles resulting from the fluxtube model are compared with the observations. Based on this comparison improved model parameters are derived. We have tested the uniqueness of the derived fluxtube structures by starting the inversion with widely different initial values for the free model parameters. We always obtained the same final fluxtube structures within the accuracy of the program, which strongly supports the uniqueness of our solutions. Our experience with codes of different levels of sophistication lead to a rough estimate of the errors of the final code. They result in an uncertainty of 100 G in the magnetic field strength, of 200 K in the temperature stratification, and of 0.3 km s<sup>-1</sup> in the macroturbulent velocity.

#### 3. Fluxtube structure

We have applied the inversion procedure to the Fourier Transform Spectrometer observations of Stenflo et al. (1984). The selected data consist of the Stokes V profiles of 8 Fe t and 2 Fe ti lines in the range from 5000 to 5500 A observed in a plage and a network region near disk center. The true continuum contrast on the axis of fluxtubes is not well determined by observations, but has been chosen to be 1.3 for the plage and 1.4 for the network region. The temperature stratification is parameterized at five grid points along the geometrical height scale.

The speed of convergence and the uniqueness of the solution of the iterative fit algorithm are determined by the way in which the comparison between observed and synthetic Stokes V profiles is performed. In the ideal case a set of 'orthogonal' observables is extracted from the observed profiles such that each of the corresponding synthetic observables depends on only one fluxtube model parameter. By orthogonal Stokes V parameters we mean that no two Stokes V parameters depend on one and the same fluxtube model parameter. Due to the extremely non-linear response of spectral line profiles to changes in the model parameters, it is not possible to find an ideal set of observables. However, it is possible to find certain observables that are much closer to being 'orthogonal' to each other than just the Stokes V profile values at various wavelengths. We anti-symmetrize all observed Stokes V asymmetry (Solanki, 1989).

The first observables that have been selected are the logarithmic ratios of the areas of the Stokes V wings of the Fe I lines to the Stokes V wing areas of the Fe II 5197.6 Å line. Since strong Fe I lines are formed higher in the photosphere than weak Fe I lines, the temperature structure can be determined over different height ranges, by using Fe I to Fe II ratios with Fe I lines of different strength. In the present work we form the ratios of the Stokes V areas of Fet 5048.4 Å, Fet 5083.3 Å, Fet 5127.7 Å, Fet 5247.1 Å, Fet 5250.6 Å, Fet 5294.0 Å, Fet 5383.4 Å, and Fett 5414 1 Å, to that of Fe II 5197.6 Å. Another observable is the well-known magnetic line ratio, i.e. the ratio of the Fe I 5247.1 Å to the Fe  $_1$  5250.2 Å Stokes V amplitudes divided by the ratio of the corresponding Landé factors (Stenflo, 1973). Because these two lines have nearly the same atomic parameters except for the Landé factor, their ratio is insensitive to all model fluxtube parameters except for the magnetic field strength at their height of formation, the macroturbulent velocity, and the angle of inclination. Stenflo et al. (1987) used the Fe 1 5247.1 Å and Fe 1 5250.6 Å lines to form a thermal line ratio. These two lines have similar and not too large Landé factors (2.0 and 1.5, respectively) and similar line strengths in the quiet sun, so that they are affected by the magnetic field in much the same way. The difference in the excitation potential of their lower levels (0.09 eV as compared with 2.20 eV) gives rise to the substantial dependence of this line ratio on the thermodynamic properties of magnetic elements. To determine the macroturbulent velocity in fluxtubes we use the full width at half maximum (FWHM) of the Stokes V wings. The temperature in the higher photospheric layers of fluxtubes cannot be deduced from Fe 1 to Fe 11 ratios, because these observables are insensitive to temperature for strong Fe1 lines formed in those higher layers. Since Stokes I line widths of strong lines are sensitive to the temperature we expect the wavelength separation of the Stokes V extrema of strong lines to depend on the temperature as well (recall that  $V \sim \partial I/\partial \lambda$ ).

In Fig. 1 the temperature (left panel) and magnetic field stratifications (right panel) of the plage (short dashes)



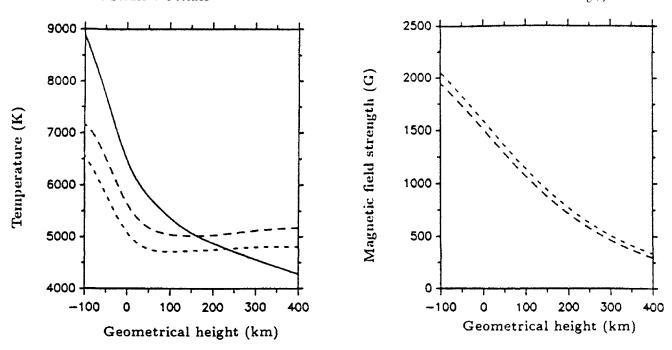


Fig. 1 Fluxtube models for the plage (short dashes) and the network region (long dashes) compared with the quiet photosphere (solid line) at equal geometrical heigh. The left panel shows the temperature, the right panel the magnetic field strength.

and the network (long dashes) regions versus the geometrical height are compared with the quiet photosphere (soli' line). The behavior of T(z) or  $T(\tau_i)$  near  $\tau_i = 1$  ( $z = -165 \,\mathrm{km}$ ) within the fluxtube should not be taken too literally, since there is only a single observational data point below  $\log \tau_i = -1$  ( $z = -65 \,\mathrm{km}$ ) to constrain the temperature stratification, namely the continuum contrast. Bearing this and other constraints in mind, we feel that the present fluxtube models are reliable only within the range  $-3 \leq \log \tau_i \leq -1$  ( $-65 \,\mathrm{km} \leq z \leq 200 \,\mathrm{km}$ ). The macroturbulent velocities of weak lines are comparable with the values measured from Stokes I profiles in the quiet photosphere whereas for strong lines the velocities exceed the values found in the quiet photosphere by roughly  $2 \,\mathrm{km} \,\mathrm{s}^{-1}$ . It is rather difficult to estimate the influence of possible errors and idealizations on the derived fluxtube structures. The small set of grid points and lines, the assumption of horizontally homogenous temperature structures, LTE, and the continuum contrast values are probably the most severe limitations. We feel that the combined microturbulence and macroturbulence approach, the neglect of the angle between the magnetic field and the vertical, and the antisymmetrization of the Stokes V profiles play only a minor role.

# 4. Dependence on the filling factor

To investigate the dependence of the fluxtube structures on the filling factor we use data from three different sources, namely the two FTS spectra used in Sect. 3, which contain the three chosen Fe I lines at 5247.1 Å, 5250.2 Å, and 5250.6 Å, the data obtained by Stenflo and Harvey (1985) with the vertical grating spectrometer of the McMath telescope, and data obtained with the Horizontal Telescope of the Arosa Astrophysical Observatory (HAT). The latter consist of simultaneous recordings of the Stokes I and V profiles of the three selected lines. In total 23 spectra obtained from regions of varying filling factors at  $\mu \ge 0.9$  are analysed in detail.

We assume a geometrical height independent temperature difference,  $\Delta T$ , with respect to the plage model from Sect. 3, which is used as a reference. Note that by choosing an appropriate  $\Delta T$  we can approximately reproduce the network model from Sect. 3. Therefore the simple temperature parameterization introduced above can be regarded as a rough interpolation between the temperature structures of magnetic elements in regions of quite different filling

390 C. U. Keller et al.

factors. Since Fe i 5247.1 Å and Fe i 5250.2 Å are sufficiently similar only two free parameters for the macroturbulent velocity are required,  $\xi_{\text{mac}1}$  for Fe i 5247.1 Å and Fe i 5250.2 Å, and  $\xi_{\text{mac}2}$  for Fe i 5250.6 Å. The observables extracted from the three lines are the magnetic and the thermal line ratio as well as the FWHM of the Stokes V wings of the three lines. Note that the use of only one line ratio as a proper temperature diagnostic does not allow whatle information on further temperature parameters (e.g. gradients) to be obtained in a straightforward manner.

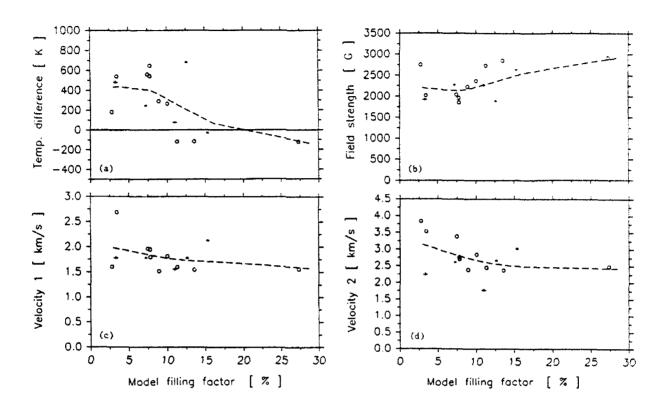


Fig. 2 Results of the Stokes V inversion using three lines only. (a) Temperature difference with respect to the plage model of Sect. 3, (b) field strength at continuum optical depth unity, (c) macroturbulence velocity of Fe I 52547.1 Å and Fe I 5250.2 Å, (d) macroturbulence velocity of Fe I 5250.6 Å. All quantities are plotted as a function of the filling factor as determined from the comparison of the observed and the synthetic spectra (stars: HAT; circles: McMath vertical grating spectrograph; crosses: FTS). The dashed curves are smoothed spline fits to the data.

The resulting values of the four free model parameters are shown in Fig. 2 as functions of the filling factor, which has been obtained from the ratio between the synthetic and the observed Stokes V amplitudes. Only those regions are represented which yield sufficiently good fits. For the other spectra (generally with high noise levels) we do not consider the derived atmospheric parameters to be reliable. Note the substantial decrease in temperature and the simultaneous increase in the magnetic field strength with increasing filling factor. The small  $\Delta T$  of the FTS plage data suggests that the present inversion procedure gives results consistent with those of the more elaborate one of Sect. 3 and increases our confidence in the simpler version of the inversion used here. The deduced macroturbulence velocities decrease slightly with increasing filling factor, although a constant  $\xi_{\text{mac}2}$  cannot be completely ruled out.

It is instructive to consider the behaviour of the temperature and the magnetic field of the best fit models along the continuum optical depth axis,  $\tau_{5000}$ , and also along the geometrical height axis. The temperature  $T(\tau_i)$  and the field strength  $B(\tau_i)$  are plotted in Fig. 3a and b, respectively, while T(z) and B(z) are plotted in Fig. 3c and d, respectively. The T(z) curves simply reflect the temperature parameterization. The difference between the T(z) and the  $T(\tau_i)$  curves is a measure of how strongly the continuum opacity is affected by temperature. The curves of the magnetic field strength B(z) all lie very close together. The relatively small scatter of the B(z) curves derived for the various regions is of the order of magnitude expected from the noise in the data and uncertainties in the inversion

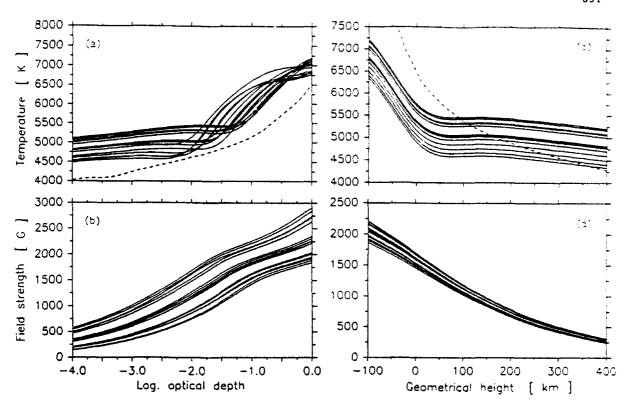


Fig. 3 Temperature (a) and field strength (b) as functions of  $\log(\tau_{5000})$ , and temperature (c) and field strength (d) as functions of geometrical height, z, resulting from the inversion of Stokes V data (solid curves). The dashed curves in a and c represent the temperature stratification of the quiet sun.

procedure. It therefore appears that magnetic elements have a unique or an almost unique field strength at a given height in the atmosphere. This is due to the strong evacuation of the fluxtubes in all the observed regions, so that the derived B(z) curves all resemble the asymptotic case of a completely evacuated fluxtube for which B(z) is exclusively determined by the pressure stratification of the surrounding non-magnetic atmosphere. The similarity between the various B(z) curves is in striking contrast to the large variation of  $B(\tau_i)$  in Fig. 3b. The latter is thus clearly induced by changes of the optical depth scale and the heights of formation of the spectral lines due to temperature variations alone.

Theoretical model calculations by Knölker and Schüssler (1988) suggest that there are two possible explanations for the dependence of the temperature within fluxtubes on the amount of magnetic flux. Their models show that fluxtubes grow cooler with increasing size. A decrease in temperature with  $\alpha$  may, therefore, be due to a greater average size of fluxtubes in regions with more magnetic flux. They also argue that fluxtubes could be cooler in regions of larger magnetic flux due to the denser packing, even if their size remains unaltered. Unfortunately, the present data cannot easily distinguish between the two proposed mechanisms.  $B(\tau_i = 1)$  varies approximately from 2000 to 3000 G as the filling factor increases from 3% to 30%. However the field strength as a function of geometrical height hardly varies at all with  $\alpha$ . Since the temperature stratification changes with the filling factor, the variation of  $B(\tau_i)$  with  $\alpha$  is a simple consequence of the  $\alpha$  independent B(z) structure and the varying temperature stratification.

The amplitude of the non-stationary velocity within magnetic elements (simulated by macroturbulence) is found to decrease somewhat with increasing filling factor. Thus it seems that the excitation mechanism for disturbances is reduced in regions with larger  $\alpha$ . One of the main proposed mechanisms for the generation of longitudinal waves is the compression of fluxtubes by granules (Musielak et al., 1989). Observations indeed suggest that granular velocities are reduced in active regions (Title et al., 1989), so that the efficiency of this mechanism is reduced as  $\alpha$  increases.

# Acknowledgements

The work of CUK and IZ was supported by grants No. 2.666-0.85, 2.417-0.87, and 2000-5.229 from the Swiss National Science Foundation. CUK and SKS received a travel grant from the Swiss Society for Astrophysics and Astronomy which is also gratefully acknowledged.

#### References

Keller, C.U., Solanki, S.K., Steiner, O., Stenflo, J.O.: 1990. Astron. Astrophys. 233, 583

Knölker, M., Schüssler, M.: 1988, Astron. Astrophys. 202, 275

Musielak, Z.E., Rosner, R., Ulmschneider, P.: 1989, Astrophys. J. 337, 470

Roberts, B., Webb, A.R.: 1978, Solar Phys. 56, 5

Solanki, S.K.: 1984, in The Hydromagnetics of the Sun, T.D. Guyenne, J.J. Hunt (Eds.). Proc. Fourth European Meeting on Solar Physics, ESA SP-220, p. 63

Solanki, S.K.: 1986, Astron. Astrophys. 168, 311

Solanki, S.K.: 1989, Astron. Astrophys. 224, 225

Solanki, S.K.: 1990, in Solar Photosphere: Structure, Convection, Magnetic Fields, J.O Stenflo (Ed.). IAU Symp. 138.

103

Stenflo, J.O.: 1973, Solar Phys. 32, 41

Stenflo, J.O.: 1975, Solar Phys. 42, 79

Stenflo, J.O., Harvey, J.W.: 1985, Solar Phys. 95, 99

Stenflo, J.O., Harvey, J.W., Brault, J.W., Solanki, S.K.: 1984, Astron. Astrophys. 131, 33

Stenflo, J.O., Solanki, S.K., Harvey, J.W.: 1987, Astron. Astrophys. 173, 167

Title, A.M., Tarbell, T.D., Topka, K.P, Ferguson, S.H., Shine, R.A., and the SOUP Team: 1989, Astrophys. J. 336, 475

Walton, S.R.: 1987, Astrophys. J. 312, 909

Zayer, I., Solanki, S.K., Stenflo, J.O., Keller, C.U.: 1990, Astron. Astrophys. 239, 356

# Measurement of Polarization-Dependent Stark Broadening as a Diagnostic of Electric Fields in the Solar Atmosphere

T. Moran and P. Foukal

Cambridge Research and Instrumentation Cambridge, MA, USA

#### Abstract

Electric fields play a key role in models of energy dissipation and charged particle acceleration in flares, as well as other dynamic solar phenomena. An instrument designed to observe the transverse (to the line of sight) component of such electric fields has been constructed and installed at the 40 cm coronagraph at Sacramento Peak. This "electrograph" measures the halfwidth of Stark-broadened hydrogen emission lines as a function of polarization in the sky plane. Thus, the instrument resembles a transverse magnetograph except that it operates on Stark-broadened hydrogen emission lines in coronal structures rather than on Zeeman-broadened absorption lines on the disk. We describe the principles behind the instrument, its design, and some first data.

#### 1. Introduction

While the study of magnetic fields in the solar atmosphere is a well established field, electric fields on the sun have received scant attention. This is explained partly by the belief that electric fields are weak on the sun, due to the high conductivity of solar plasmas, which tend to neutralize electric potential differences over short time scales. However, models of charged particle acceleration and magnetic energy dissipation in flares and other dynamic solar phenomena indicate that substantial E-fields must be present, although their intensity, time scales and associated plasma emission measures need to be measured (see review by Foukal and Hinata, 1991).

The possibility of measuring electric fields in solar plasmas was first pointed out by Wien (1916), in connection with motional electric fields associated with the strong magnetic fields in sunspots. More recently, researchers have attempted to measure electric fields through helium and silicon line spectra. Quadratic Stark shifts in neutral helium lines in flare emission suggest fields of 700 volt/cm (Davis,1977). Quadratic Stark shifts in neutral silicon absorption lines in sunspot spectra indicate fields of 300 volts/cm (Jordan er al.,1980).

The linear Stark effect in the high-n hydrogen Balmer and Paschen lines has seen used to search for fields in post-flare loops and eruptive prominences. Foulah Miller and Gilliam, 1983, Foukal, Hoyt and Gilliam, 1986, Foukal, Little and Gilliam, 1988). The data used in the hydrogen-line studies were photographic spectra obtained at the Evans Facility, National Solar Observatory, Sacraments Peak. We describe here an "electrograph", based on this technique, and optimized to improve the sensitivity and accuracy of electric field vector measurements

# 2. Theory

Shifts in the sublevels of the hydrogen atom in an electric field are computed by solving the perturbed hydrogen atom Schrodinger equation (Bethe and Salpeter, 1957)

$$(H_0 + \underline{P} \cdot \underline{F} + \underline{k} \, \underline{L} \cdot \underline{S}) \Psi = \underline{F} \, \Psi, \tag{1}$$

where  $H_o$  is the unperturbed hydrogen atom hamiltonian,  $\underline{P} = e\underline{R}$  is the dipole moment,  $\underline{F}$  is the electric field vector, k  $\underline{L} \cdot \underline{S}$  is the spin orbit interaction energy,  $\underline{E}$  is the total energy and  $\Psi$  is the atomic wavefunction. The total energy  $\underline{E}$  is the sum of the unperturbed atomic energy  $\underline{E}_o$  and the perturbation  $\Delta \underline{E}$  due to the electric field and the spin-orbit interaction

$$E = E_0 + \Delta^{r}$$

To obtain the first order perturbation due to the electric field, the unperturbed Schrödinger equation

$$H_{\mathbf{0}}\Psi - E_{\mathbf{0}}\Psi, \tag{3}$$

is first solved in a parabolic coordinate system. The resulting parabolic states are characterized by the quantum numbers  $n_1$ ,  $n_2$ , m and n. Here, n is the principal quantum number and is equivalent to the principal quantum number characterizing the spherical hydrogen atom states, and m is the orbital magnetic quantum number. The parabolic quantum numbers,  $n_1$  and  $n_2$ , have integer values ranging from 0 to n - 1. The difference,  $n_1$  -  $n_2$ , is an indicator of the asymmetry, or charge separation of the state. The four quantum numbers are not independent, since

$$n_1 + n_2 + m + 1 - n. (4)$$

The first order energy shift  $\Delta E$  of a state  $\Psi$  in an electric field of strength F is given by

$$\Delta E = < \Psi_{n_1, n_2, n} \mid \underline{P} \cdot \underline{F} + k \mid \underline{L} \cdot \underline{S} \mid \Psi_{n_1, n_2, n}>.$$

In computing the energy shift due to the electric field, the spin-orbit interaction term (fine structure) is initially ignored, and later included as a correction the shift arising from the fine structure varies as  $n^{-3}$ , so it is only considered in the splitting of the lower level in the transition. This term is almost always small compared to the electric field induced energy shift for relevant field strengths. The energy shift of level  $n,n_1,n_2$  is given in atomic units by

$$\Delta E = 3/2 \ n(n_1 - n_2)F$$
 (6)

There are 2n-1 sublevels. The mean value of  $n_1-n_2$  is proportional to n, so the mean energy splitting is proportional to  $n^2$ . The wavelength shift of the line component for the transitions from the n,  $n_1$ ,  $n_2$  state to the n',  $n'_1$ ,  $n'_2$  state is given by

$$\Delta \lambda = C \lambda^2 (n(n_1 - n_2) - n'(n_1' - n_2')) F,$$
 (7)

where C is a constant. In the lines measured for this study, the value of the upper n is at least a factor of four greater than that of the lower n. The wavelength splitting is thus determined mostly by the upper level, and varies as

$$\Delta \lambda \propto \lambda^2 \, n^2 \, F. \tag{3}$$

Consequently, higher n transitions will have greater sensitivity to electric fields. Also, since the shift depends quadratically on the wavelength, we choose to study the Paschen series lines (radiative decay to n=3), which have wavelengths between 8200 Å and 19000 Å, rather than the Balmer series lines, which have wavelengths between 3645 Å and 6563 Å.

The polarization of a line component will depend on  $\Delta m$ , the change in magnetic quantum number, which is limited by selection rules to 0, or  $\pm$  1. Transitions with  $\Delta m = 0$ , ( $\pi$  components) will be polarized along the electric field, while transitions with  $\Delta m = \pm$  1, ( $\sigma$  components) will be polarized perpendicular to the field. The mean wavelength shift of the  $\pi$  components lies near the maximum wavelength shift, while the mean wavelength shift of the  $\sigma$  components will lie at approximately half the maximum shift. Figure 1 shows a plot of the oscillator strengths of the  $\pi$  and  $\sigma$  components of the Paschen 18 (P18) ( $n = 18 \rightarrow n = 3$ ) line

in the presence of a 10 volt/cm electric field (oscillator strengths and wavelength shifts taken from Underhill and Waddell, 1959). Fine structure splitting, which would introduce 0.03 Å shifts (on the average) is ignored for simplicity.

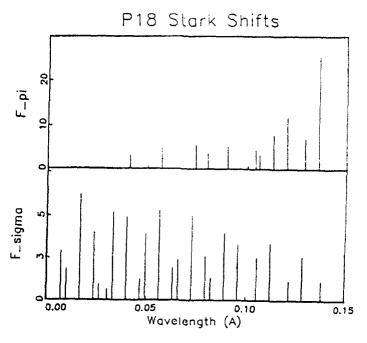


Fig 1 Paschen 18  $\pi$  and  $\sigma$  component oscillator strengths plotted against wavelength shift.

In solar plasmas thermal motion and other mechanisms broaden the lines, so individual Stark components would not be resolvable. Figure 2 shows the Pl8  $\pi$  and  $\sigma$  components separately convolved with a 0.5 Å gaussian, which is about the minimum thermal broadening observed for this line in coronal structure emissions. The calculated difference in half width between the two polarizations is 0.043 Å.

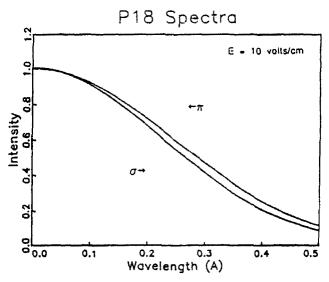


Fig 2 Paschen 18  $\pi$  and  $\sigma$  line shapes for 0.5 Å thermal broadening.

The typical width of the P18 line observed in solar prominences is 0.8 Å. Figure 3 shows a plot of the difference in half width (modulation) between the  $\pi$  and  $\sigma$  polarizations of the P18 line as a function of electric field strength for a width of 0.8 Å. The fine structure splitting is added to lower levels as a correction. The width modulation increases as the square of the electric field strength at low field strengths, since the various contributions to the broadening add quadratically. At higher fields the modulation is proportional to field strength.

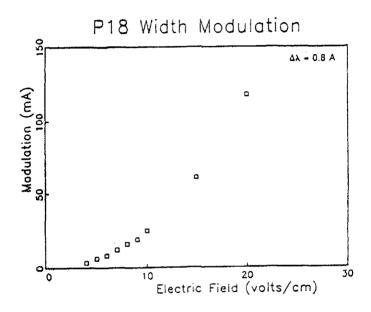


Fig 3 Paschen 18 half width modulation plotted against electric field strength.

#### 3. Instrumentation

The instrument (electrograph) which we have constructed is designed to record hydrogen Paschen line spectra emitted from coronal structures, as a function of linear polarization in the sky plane. The instrument consists of a near-infrared polarization analyzer and a PC-controlled Pulnix TM840N integrating GCD camera. The polarization analyzer is made up of an achromatic (for wavelengths between 8000 Å and 9000 Å) half-waveplate rotated by a PC-controlled stepping motor, and an infrared polarizer. The analyzer is located directly behind the occulting disk of the 40 cm coronagraph at the Evans Coronal Facility at Sacramento Peak. The CCD chip is positioned at the focal plane of the Evans Facility universal spectrograph (USG) and records Paschen line spectra in first order. A schematic diagram of the electrograph system mounted on the coronagraph and USG is shown in Figure 4. An enlarged view of the waveplate and polarizer assembly is shown in Figure 5.

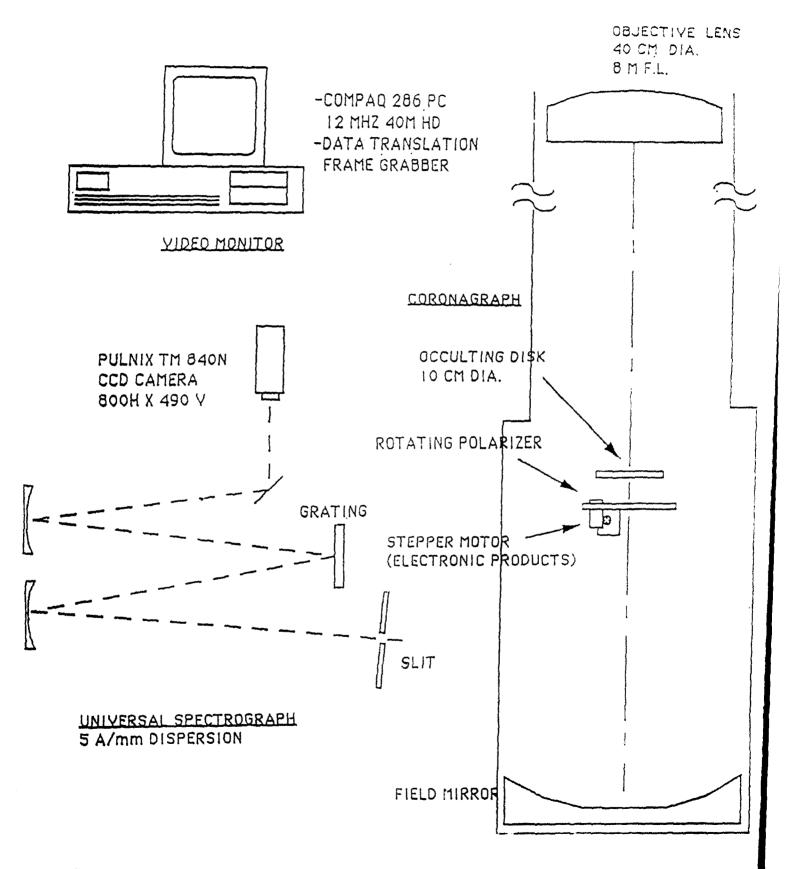


Fig 4 A shematic diagram of the CRI electrograph installed on the 40 cm coronagraph at the Evans Facility at Sacramento Peak.

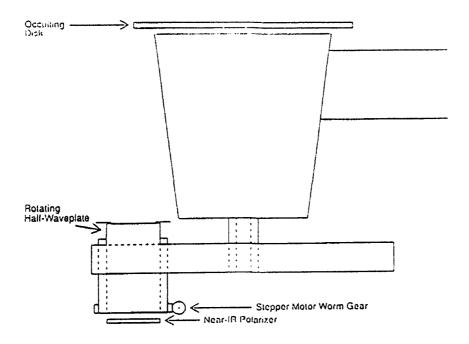


Fig 5 A schematic diagram of the electrograph polarization analyzer.

The CCD camera has a windowless Sanyo chip (800 h x 480 v) with high quantum efficiency (>30 %) at the Paschen line wavelengths of interest. The first order dispersion of the USG is 5 Å/mm and the CCD chip spans 32 Å. A 45  $\mu$ m slit yields a wavelength resolution of 0.25 Å and a projected slit width on the sun of 0.36 arcseconds. The chip is cooled by a Peltier cooler attached to the back of the chip. Dry ice is applied to the cooler's heat sink, bringing the chip temperature to - 30 C°. The resulting low dark count levels make 60 second exposures possible. Tests have shown that the CCD-based system is a factor of 20 more sensitive than IR-sensitive film at these wavelengths.

The camera is controlled through a Data Translation 2853 frame grabber board installed in a Compaq 286 PC (12 Mhz, 40 MB HD). Control software sets the camera exposure and averages a specified row section on the chip to obtain the spectrum. The stepper motor is controlled through a driver board installed in the Compaq. In data collection the waveplate is rotated in 30 degree steps and the CCD exposes a frame at each angular location. The spectra are stored on the PC's hard disk. A menu-driven program simultaneously controls the camera exposure, stepper motor, data collection and data storage.

#### 4. Observations and Discussion

The electrograph was used in an attempt to study hydrogen emissions from post-flare loops during five observing runs between May, 1989 and May, 1990. No post-flare loops occurred during these runs, but observations of several quiescent prominences were carried out.

The best data were recorded on April 21, 1990. Spectra from PlO and Pl8 were recorded in emission from a relatively bright quiescent prominence, using 10 and 40 second integration times at PlO and Pl8, respectively. The line widths at 180 degree separations were averaged since these waveplate orientations select identical polarizations. A plot of the Pl8 line width versus polarization orientation is shown in Figure 6.

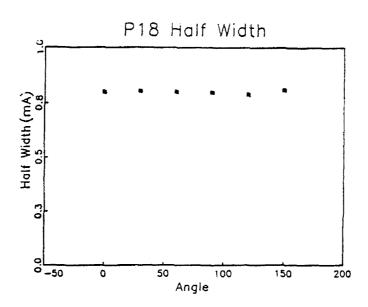


Fig 6 Paschen 18 line width plotted versus polarizer orientation measured in emission from a quiescent prominence.

The uncertainty in line width is determined by chip read-out electronics and digitization. Typical signal-to-noise ratios are 200-400 for sums of 2-3 spectra. This leads to uncertainties of 0.3-0.6 % in halfwidth for the P18 line, which correspond to electric field sensitivity of 5-8 volts/cm using the calibration described in section 2. Tests made using a slow-scanned CCD camera showed a factor of 10 increase in signal to noise, which corresponds to a factor of 3 gain in electric field sensitivity. We plan to use this camera in the electrograph in the future.

The prominence line widths measured on April 21, 1990 show no modulation of half width beyond noise limits. Thus, the measurements yield an upper limit for macroscopic electric field strength averaged over the slit area of 5 volts/cm in the Paschen-line emitting plasma. A more detailed interpretation of this result in terms of motional fields associated with the plasma thermal velocity, and with possible macroscopic motions will be presented in a later paper.

Our aim is to observe bright post-flare loops, which can be 10-100 times brighter in Paschen line emission than the prominences we have observed. These higher signal levels would make measurements of approximately 3 volt/cm accuracy possible, thus well within the 1-100 volt/cm range expected in reconnection models of flares.

We are also preparing for a NASA-sponsored expedition to the July 1991 eclipse in Baja, Mexico. We expect that around totality the absence of sky-scattered light in prominences may increase the accuracy of electric field measurements by a factor of three. A telescope and spectrometer are being assembled for the expedition.

#### Acknowledgements

We would like to thank Heinz Kochling and Ruel Little for assistance in the design and construction of the electrograph system. We are also grateful to Lou Gilliam, Brian Armstrong and Joe Elrod for observing assistance at the Evans Coronal Facility. This work at the Sacramento Peak Observatory has been supported under an Air Force SBIR contract #F19628-87-C-0110, and under NASA contract NASW 4538.

#### References

Bethe, H. and Salpeter E., 1957, "Quantum Mechanics of One- and Two-Electron Atoms," Springer Verlag, New York.

Davis, W., 1977, Solar Phys., 111, 1.

Foukal, P., Miller P., and Gilliam, L., 1983, Solar Phys., 83, 83.

Foukal, P., Hoyt C., and Gilliam, L., 1986, Astrophys. Journ., 303, 861.

Foukal, P. and Little, R., 1987, Solar Phys., 114, 65.

Foukal P. and Hinata, S., Solar Physics, 1991 in press.

Jordan, C., et al., 1980, Astrophys. Journ., 240, 702.

Underhill, A. and Waddell, A., 1959, "Stark Broadening Functions for the Hydrogen Lines," NBS CIRC. No. 604.

Wien, A., 1916, Ann. Physik, 49, 842.

#### Discussion

- J. Stenflo: Let me mention that the first attempt to measure linear polarization due to the Stark effect in electric fields produced by solar flares was done by Dravins back in 1970. He did it in  $H\alpha$  at the Big Bear Solar Observatory.
- T. Moran: We are aware of Dravins' attempt to measure polarization dependent effects on the  $H\alpha$  line shape from flare emission. The results were negative. That type of experiment could be tried again using CCD's.
- **D. Deming:** Have you considered using the hydrogen lines in the 10-12 micron region? They obviously have long wavelengths, but perhaps the n values are not large enough.
- T. Moran: In fact, we have considered those lines for electric field measurements in coronal structures, where some of them were observed. While the upper n-values are lower than the n values in the highest observable Paschen lines, the longer wavelengths of the IR lines more than compensate. Whether the signal to noise is high enough would have to be determined.
- W. Livingston: Is there no hope for electric field observations on the disk?
- T. Moran: We have investigated using Paschen lines in absorption emission in sunspots, but encountered problems with line blending. This requires more scrutiny. Other possibilities for observations on the disk are the Balmer lines in flare emission, the 12 micron lines in active region spectra, and the Brackett, Pfund and Humphreys-series hydrogen lines.
- R. Altrock: Why haven't any post-flare loops been obtained? We see CaXV emission on the limb frequently, and this emission is thought to be connected with post-flare loops. These observations could be used to trigger your observations.
- T. Moran: Unfortunately there have been very few loops on the limb during the past year, and none during our observing periods. We do monitor the daily CaXV limb emission for indications of activity on the limb during observing runs.

# Polarimetric Studies of Solar Magneto-Sensitive Spectral Lines

# YE SHI-HUI

Purple Mountain Observatory
Academia Sinica, Nanjing, 210008, China

Summary. This paper presents a comprehensive account of a series of researches on solar magneto—sensitive spectral lines made by the author and his coworkers. On the basis of numerical solutions of the equations of transfer of polarized radiation in magnetic fields, the following characteristics of solar magneto—sensitive lines have been studied: (1) profiles of Stokes parameters, (2)temperature sensitivity, (3)magnetic intensification, (4)depth of formation, (5)Zeeman components and Seares' formulae, (6)monochromatic images, (7)line asymmetry and gradient of sunspot magnetic fields, (8)relation with Alfven waves, (9)derivation of information of magnetic vector, (10)Faraday rotation and azimuth of the transverse magnetic field, (11)twist of magnetic lines of force in depth. In "Conclusion" we make some remarks about our own researches on magneto—sensitive spectral lines.

#### 1. Introduction

The importance of magnitic field observations to solar physics is well-known to everyone. In essence they are mainly the polarimetric measurements of the Zeeman components of magneto-sensitive spectral lines. Therefore, in order to get accurate information of the magnetic field, one has to make a deepgoing and detailed study of the properties of these lines. This may be considered to be one of the main contents of solar polarimetry. The theoretical foundation of this project was laid by Unno (1956). Since 1977 we have tried to improve his theory and apply it to attack a series of problems about solar magneto-sensitive lines. The results of our works are stated below.

# 2. Profiles of Stokes Parameters

A spectral line is defined to be magneto-sensitive if its Lande splitting factor is larger than certain value, say 1.5. In order to study its characteristics, one has to solve the following Unno's equations of transfer of its Stokes parameters:

$$\begin{cases} \cos\theta \frac{dI}{d\tau} = (1 + \eta_I)I + \eta_Q Q + \eta_V V - (1 + \eta_I)B, \\ \cos\theta \frac{dQ}{d\tau} = \eta_Q I + (1 + \eta_I)Q - \eta_Q B, \\ \cos\theta \frac{dV}{d\tau} = \eta_V I + (1 + \eta_V)V - \eta_V B. \end{cases}$$

$$(1)$$

Unno took U=0. This implies that the plane of polarization is fixed and the Faraday rotation cannot be taken into consideration. Besides, he adopted the following assumptions: (1) There exists the local thermodynamic equilibrium, so the source function is the Planckian function B. (2) B exhibits a linear distribution with depth. (3) The atmosphere can be fitted with Milne-Eddington's model, i.e.  $\eta$  does not depend on depth. (4) The magnitic field is homogeneous, i.e. its intensity does not vary with depth. Under these conditions which are evidently far from reality, Unno obtained an algebraic solution of Eq.(1). In our works we retained only the first assumption, abandoned all the others, and got numerical solutions of Eq.(1) and later of the more complete Unno-Beckers' equations. This allows us to calculate more accurate Stokes profiles.

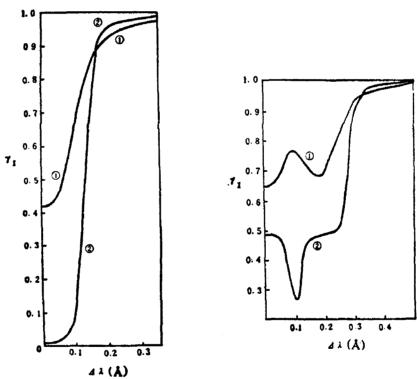


Fig.1. Comparison of our numerical solution ① with Unno's algebraic solution ②. On left side,  $\gamma = \pi/2$ , H = 1000G. On right side,  $\gamma = \pi/2$ , H = 4000G.

We (Ye Shi-hui et al., 1978a) used Stellmacher and Wiehr (1970) 's model of sunspot umbrae, adopted a series of values for the magnetic field intensity H and the angle formed by field line and line of sight  $\gamma$  and computed a lot of I, Q and V profiles for FeI $\lambda\lambda$ 6302.499, 6173. 341 and 5250.216. By comparison with the corresponding profiles given by Unno's algebraic solution, it can be said that our numerical solution is much better. This is shown by Figure 1. On the right side, in the case of pure transverse Zeeman effect, the I-profile of  $\lambda$ 6302 should have three com-

Polarimetric Studies 405

ponents. This agrees with the pattern of splitting given by our numercal soulation. However, Unno's algebraic solution gives rise to only two  $\sigma$  components. On the left side, our profile has a central residual intensity of 0.42, which is close to the observed value. The corresponding value given by Unno's solution is only 0.01. In practice, there is no any solar spectral line which is so deep at its center.

# 3. Temperature Sensitivity

The question of temperature sensitivity of magneto-sensitive lines was raised first of all for  $\lambda 5250$ . Due to its high magnetic sensitivity (g = 3), it was for many years used as the main working line in magnetic field measurements. However, in the late sixties it was discovered that this line is also very sensitive to temperature. So the results of magnetic field observations made with it may have large errors. Wittmann (1971) used  $W_u/W_{ph}$  to represent the degree of temperature sensitivity, where  $W_u$  and  $W_{ph}$  are the observed equivalent widths of one and the same line in a spot umbra and in the photosphere respectively. We think that this method is not quite reasonable, because the variatons of both magnetic field and temperature may affect the equivalent width. In order to lay special stress on temperature sensitivity, the influence of magnetic field should be put aside. So in calculating  $W_u$  we (Ye Shi-hui et al., 1978a) purposely took H to be equal to zero. In this way we have computed the degrees of temperature sensitivity of four magneto-sensitive lines (see Table 1). It can be readily seen that among them  $\lambda 5250$  indeed possesses the highest temperature sensitivity and  $\lambda 6302$  — the lowest one.

Line	$\mathbf{W}_{\mathbf{u}}(\mathbf{A})$	$W_{ph}(A)$	W <sub>u</sub> /W <sub>ph</sub>
Fe I \(\lambda 5324.191\)	0.718	0.364	1.97
λ6302.499	0.140	0.128	1.09
λ6173.341	0.0996	0.0576	1.72
λ5250.216	0.116	0.0480	2.42

Table 1. Temperature sensitivity of magneto-sensitive lines

#### 4. Magnetic Intensification

As first of all pointed out by Unno (1956), the presence of magnetic fields may not only cause deformation of the profiles but also increase of the equivalent widths of mangneto—sensitive lines. In order to make a complete study of this effect, we (Ye Shi—hui et al., 1978a) calculated the equivalent widths of  $\lambda 6302$  for five values of H (0, 1000, 2000, 3000, 4000G) and five values of  $\gamma$  (0, 30°, 45°, 60°, 90°). The results are shown in Figure 2 in which the magnetic intensification is represented by the quantity  $\Delta W_{\lambda} = W_{\lambda}(H) - W_{\lambda}(0)$ . From this Figure the following conclusions can be drawn: (1) The effect of magnetic intensification really exists. (2)  $W_{\lambda}$  depends on both H and  $\gamma$ . (3) When  $\gamma = 0$ ,  $\Delta W_{\lambda} = 0$ . This means that the pure longitudinal Zeeman effect does not cause magnetic intensification. (4) When  $\gamma \neq 0$ ,  $\Delta W_{\lambda} > 0$ . Moreover,  $\Delta W_{\lambda}$  increases with  $\gamma$ . (5) In the region of

 $\gamma > 60$ °,  $\Delta W_{\lambda}$  gradually becomes saturated. This does not agree with Unno's prediction that  $\Delta W_{\lambda}$  is maximum at  $\gamma = 55$ °. (6)The larger is H or  $\gamma$ , the more conspicuous is the effect of saturation.

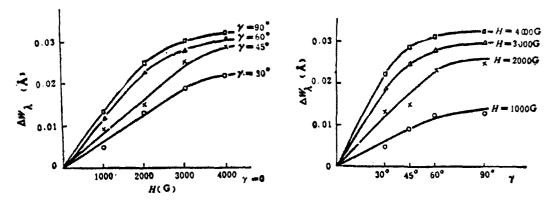


Fig.2. Magnetic intensification of  $\lambda 6302$ .

# 5. Depth of Formation

Jin Jie-hai (1980) defined the equivalent selective absorption coefficient  $k_l^*$  to be such that under its joint action with the continuous absorption coefficient  $k_c$  the change of I with h is the same as obtained by solving the equation of transfer in a magnetic field. Let  $d\tau = (k_l^* + k_c)\rho dh$ , then the equation of transfer can be reduced to be

$$\frac{d\tau}{d[lg\tau_c]} = \frac{\cos\theta \frac{dI}{d[lg\tau_c]}}{I - B}.$$
 (2)

Ye S.-H.

After getting  $\tau(lg\tau_c)$ , one may calculate the emergent intensity  $I(\tau=0)$ , the normalized contribution function  $F_I$ , and the depth of formation  $\overline{\tau}_I$  by solving the following three equations:

$$I(\tau=0) = \int_0^\infty \frac{S}{\cos\theta} e^{-\frac{\tau}{\cos\theta}} d\tau, \tag{3}$$

$$F_{I}(\tau) = \frac{\frac{S}{\cos \theta} e^{\frac{-\tau}{\cos \theta}}}{I(\tau = 0)} \tag{4}$$

$$\bar{\tau}_I = \int_0^\infty \tau F_I(\tau) d\tau. \tag{5}$$

The equivalent source functions  $S_0^*$ ,  $S_U^*$ , and  $S_V^*$  are defined to be

$$\begin{cases} S_{Q}^{*} = Q - \cos\theta \frac{dQ}{d\tau}, \\ S_{U}^{*} = U - \cos\theta \frac{dU}{d\tau}, \\ S_{V}^{*} = V - \cos\theta \frac{dV}{d\tau}. \end{cases}$$
 (6)

Then the normalized contribution functions of Q, U, and V have expressions similar to (4) and (5). Actual calculations for  $\lambda 6302$  show that the depths of formation of four Stokes parameters may be quite different.

# 6. Zeeman Components and Seares' Formulae

For a long time Hale and Nicholson (1938) applied the following Seares' formulae to calculate the angle  $\gamma$  with the relative intensities of Zeeman components.

$$\begin{cases} I_{\sigma_{1}} = \frac{1}{4} (1 \mp \cos \gamma)^{2}, \\ I_{\pi} = \frac{1}{2} \sin^{2} \gamma, \\ I_{\sigma_{2}} = \frac{1}{4} (1 \pm \cos \gamma)^{2}. \end{cases}$$
 (7)

Strictly speaking, these expressions were established for the direct Zeeman effect of emission lines and so in principle cannot be used for the inverse effect exhibited by absorption lines. However, for some time it was believed that Seares' formulae could still be applied to absorption lines. The first reason is that it is possible to derive these formulae from the algebraic solution of Unno's equations for very weak lines with  $\eta \ll 1$ . Secondly, according to the calculations of Stepanov (1958) for  $\lambda 6173$  and H=2500G the error of  $\gamma$  given by Seares' formulae does not exceed 4°. Nevertheless, we (Ye Shi-hui et al., 1978b) pointed out that both these arguments are questionable. Firstly, Unno's algebraic solution is rather crude and, moreover, spectral lines with  $\eta \ll 1$  practically do not exist. Secondly, Stepanov's computations were made only for one line and one value of H, so his conclusion may be incorrect in the general case. We derived the expressions of residual intensities of ordinary (o) and extraordinary (e) light to be

$$\begin{cases}
r_o = r_I + r_V, \\
r_e = r_I - r_V.
\end{cases}$$
(8)

They enabled us to compute the ratios of central depths of Zeeman components as functions of  $\gamma$ . Our results of calculations are represented by the solid lines in Figure 3. The broken lines are given by Seares' formulae and the dotted lines —Stepanov's calculations. Then the following conclusions can be drawn from this Figure: (1) The results of our computations differ much from those given by Seares' formulae. (2) According to our calculations the ratios of relative intensities of Zeeman components should depend on H, but Seares' formulae have no any relation with this quantity. (3) Stepanov's calculations lead to a relation of  $\lg(d\sigma_1/d\sigma_2)$  close to that given by Seares' formulae, but the case for  $\lg(d\sigma/d\pi) \sim \gamma$  is quite different. This implies that the former is possibly an accidental coincidence.

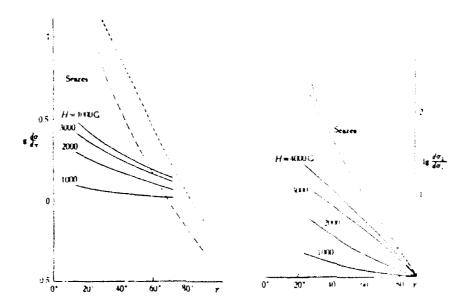


Fig.3. Relations between intensities of Zeeman components and y

In conclusion we may say that it is not a good method to measure the direction of sunspot magnetic fields with Seares' formulae.

# 7. Monochromatic Images

As we (Ye Shi-hui et al., 1978b) have shown, the "o" and "e" profiles of a magneto-senstive line depend on both H and y. Then the same can be said for the equivalent width and intensity of monochromatic images. Therefore, it is possible to derive H and y with the monochromatic images of a magneto-sensitive line.

In scanning a monochromatic image both the width  $(\triangle \lambda)$  and position (denoted by the distances of pass—band edges from line center a and b in Figure 4) of the exit slit can be chosen arbitrarily. Let the intensity of a certain point on the monochromatic image of a magneto—sensitive line be  $I(\triangle \lambda) = \int_a^b i_{\lambda} d\lambda$ , and that on the neighboring continuum be  $I_c(\triangle \lambda) = i_c\triangle \lambda$ , then it is easy to get the following relation:

$$\frac{I(\Delta\lambda)}{I_c(\Delta\lambda)} = 1 - \frac{W_{\lambda}(\Delta\lambda)}{\Delta\lambda},\tag{9}$$

where  $W_{\lambda}(\Delta \lambda) = \int_{a}^{b} \frac{i_{c} - i_{\lambda}}{i_{c}} d\lambda$  is the equivalent width of magneto-sensitive line in "o" or "e"

light. This quantity can be calculated with theoretical line profiles.  $I(\triangle \lambda) / I_c(\triangle \lambda)$  may be determined with observational data.

Polarimetric Studies 409

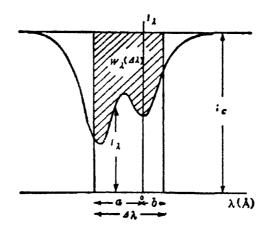


Fig.4. Relation between monochromatic intensity and equivalent width.

For expression of the relation of  $W_{\lambda}$  with H and  $\gamma$ , we (Ye Shi-hui et al., 1985) designed three methods. For two slit states this relation can be written as follows:

$$\begin{cases}
W_{\lambda}(\Delta\lambda_{1}) = f_{1}(H,\gamma), \\
W_{\lambda}(\Delta\lambda_{2}) = f_{2}(H,\gamma).
\end{cases}$$
(10)

Substituting these expressions into Eq.(9), we have

$$\begin{cases}
\frac{I(\Delta\lambda_1)}{I_c(\Delta\lambda_1)} = 1 - \frac{f_1(H,\gamma)}{\Delta\lambda_1}, \\
\frac{I(\Delta\lambda_2)}{I_c(\Delta\lambda_2)} = 1 - \frac{f_2(H,\gamma)}{\Delta\lambda_2}.
\end{cases} (11)$$

After measuring the intensities of one and the same point on two monochromatic images corresponding to the two slit states and with known functions  $f_1$  and  $f_2$ , one may calculate the values of H and  $\dot{\gamma}$  for the given point. By repeating this procedure for many points one can trace a 2D magnetic map. We used the monochromator attached to the solar spectrograph of Purple Mountain Observatory, applied this method to observation of the magnetic field of a sunspot group and got some reasonable results.

#### 8. Line Asymmetry and Gradient of Sunspot Magntic Fields

The method of determination of the gradient of spot magnetic fields with the asymmetry of  $\sigma$  components of a Zeeman triplet was proposed by Hubenet (1954) before the advent of Unno's theory. We (Ye Shi—hui et al., 1979) studied this method anew with the theory of inverse Zeeman effect.

As the first approximation, we supposed that magnetic field intensity exhibits a linear distribution with depth, i.e.

$$H = H_0(1 + alg\tau), \tag{12}$$

where a is the coefficient of gradient and Ho— magnetic field intensity on surface. We took for

410 Ye S.-H.

the optical depth gradient  $dH/dg\tau = H_o \alpha$  a series of values 100, 200, ...1000 which approximately correspond to the geometrical gradient dH/dz = 1,2,...10G/km. Then we computed the theoretical profiles of the  $\sigma$  components of  $\lambda 6302$ . It was found that in the case of zero gradient the  $\sigma$  components are symmetric and that with increase of the gradient the asymmetry becomes more and more pronounced. In order to find a quantity to represent line asymmetry, we may take two points on the profile with a depth equal to half of the depth at line center, find their middle point and define its distance  $\delta$  from line center with zero gradient to be a measure of asymmetry. Besides, for the point on a wing also with a depth equal to the half of the central value, we defined the displacement relative to the corresponding point in the case of absence of gradient to be the measure of rotation  $\varepsilon$  of a line wing. With the results of theoretical calculations, we constructed Figure 5 which shows the changes of  $\delta$  and  $\varepsilon$  with the magnetic field gradient. Thus, if one of the quantities  $\delta$  and  $\varepsilon$  can be measured by observations, the value of gradient may be determined. We applied this method to actual observations and found that the geometrical gradient of spot magnetic fields is about 1G/km.

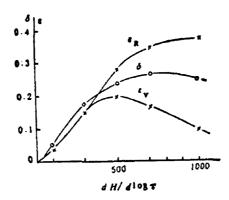


Fig.5. Line asymmetry and magnetic field gradient.

In passing it is worthwhile to point out that the rotation of line wings caused by magnitic field gradient might give rise to large errors in magnetographic observations.

#### 9. Relation with Alfven Waves

Waves propagating in a plasma may cause deformation of the spectral lines emitted by it. We studied the influence of Alfven waves on magneto-sensitive lines (Ye Shi-hui et al., 1981) and also the possible effect of Alfven waves in the cooling of sunspots (Ye Shi-hui et al., 1983a).

On the basis of Maltby (1968)'s work we took the relation between the flux of energy transported by Alfven waves  $(F_A)$  and the velocity of horizontal oscillations  $(\sigma_{hor})$  to be

$$F_{A} = \rho v_{A} \sigma_{hor}^{2}, \tag{13}$$

where  $v_A$  is the velocity of Alfven waves given by

$$v_A = \frac{H_0}{\sqrt{4\pi\rho}}. (14)$$

We supposed that the sunspot is circular with radius b and its magnetic field can be fitted with the

Polarimetric Studies 411

fan-shaped model. Then for a point in the spot and at distance r from center the Doppler half width of the magneto-sensitive line is

$$\Delta \lambda_D = \frac{\lambda}{c} \sqrt{\frac{2RT}{\mu} + v_i^2 + \sigma_{hor}^2 sin^2 (67.5 \circ \frac{r}{b} \pm \theta)}. \tag{15}$$

Besides, its Zeeman splitting becomes

$$\Delta \lambda_{H} = 4.67 \times 10^{-5} g \lambda^{2} H_{0} \sqrt{1 + \left(\frac{b_{y}}{B_{0}}\right)^{2}}, \qquad (16)$$

where by is the amount of disturbance of magnetic field intensity caused by Alfven waves. Substituting these expressions into Unno's equations, we computed the I, Q, and V profiles of the magneto—sensitive line under the action of Alfven waves. It is interesting to note that all these profiles should incessantly undergo violent oscillations. Figure 6 presents such an example. We proposed some methods to verify this phenomenon.

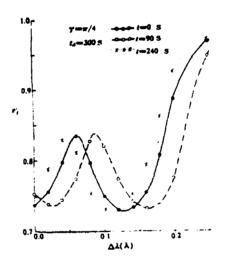


Fig.6. Changes of I-profile of  $\lambda 6302$  in a period of Alfven wave motions.

Moreover, Alfven waves can also exert a significant influence on magneto—insensitive lines and this may be used to verify Parker (1974) 's theory of cooling of sunspots. Beckers (1976) carried out such a justification. However, he took the value of gfA(A is the abundance of the chemical element to which the considered spectral line belongs) as an indefinite quantity and chose for it such a value that the observed line profile might be fitted by the theoretical one. This seems to be not quite reasonable. We calculated the accurate profiles of FeI $\lambda\lambda$ 5691.505 and 5434.534 and they satisfactorily agree with the observed ones. It is more important to say that with increase of  $F_A$  from 0 to  $10^{10}$  and  $10^{11}$  ergs/cm<sup>2</sup>—sec the degree of agreement becomes better and better. This might be a preliminary justification of the Alfven wave cooling of sunspots.

# 10. Derivation of Information of Magnetic Vector

Under the action of the magneto-optical effect the plane of polarization may rotate and so the aziumth cannot be taken to be always equal to zero. This requires us to abandon Unno's assumption of U = 0 and solve Unno-Beckers' equations of transfer of four Stokes parameters, i.e.

$$\begin{cases} \cos\theta \frac{dI}{d\tau} = (1 + \eta_I)(I - B) + \eta_Q Q + \eta_U U + \eta_V V, \\ \cos\theta \frac{dQ}{d\tau} = \eta_Q (I - B) + (1 + \eta_I)Q + \rho_R U + \rho_W \sin2\chi V, \\ \cos\theta \frac{dU}{d\tau} = \eta_U (I - B) - \rho_R Q + (1 + \eta_I)U - \rho_W \cos2\chi V, \\ \cos\theta \frac{dV}{d\tau} = \eta_V (I - B) - \rho_W \sin2\chi Q + \rho_W \cos2\chi U + (1 + \eta_I)V. \end{cases}$$

$$(17)$$

Beckers (1969) considered the magneto-optical effect to be equivalent to the joint action of a retarder of circular polarization and another of linear polarization. In the above equations they are represented by the coefficients:

$$\begin{cases} \rho_{R} = \frac{\eta_{0}}{H(0,a)} \cos\gamma [F(v-v_{H},a) - F(v+v_{H},a)], \\ \rho_{W} = \frac{\eta_{0}}{H(0,a)} \frac{\sin^{2}\gamma}{2} [F(v-v_{H},a) + F(v+v_{H},a) - 2F(v,a)], \end{cases}$$
(18)

where

$$F(v,a) = \frac{1}{2\pi} \int_{-\infty}^{\infty} \frac{v}{u^2 + a^2} e^{-(u-s)^2} du.$$
 (19)

There were some inexactitudes in Beckers' original equations and we made the necessary corrections. We (Ye Shi-hui et al., 1983b) performed numerical solutions of Unno-Beckers' equations and designed a method to derive the three characteristic quantities H,  $\gamma$  and  $\chi$  with observed Stokes profiles. It consists of the following three steps: (1) to get H from the wavelength difference of the highest point of V-profile and line center, (2) with known H to obtain  $\gamma$  from the maximum of V, (3) with both H and  $\gamma$  known to determine the azimuth of transverse field  $\chi$  with the value of Q at line center.

We applied this method to the Stokes profiles of two large sunspots observed at the Okayama Astrophysical Observatory and obtained values of H,  $\gamma$  and  $\chi$  for many points in each spot. It is intersting to note that our results differ much from those of Kawakami who treated just the same observational material. For instance, our values of H are about twice larger than his. Judging with results of direct Zeeman splitting observations, we can say that our values are nearer to reality than his.

#### 11. Faraday Rotation and Azimuth of the Transverse Magnetic Fields

After much controversy the existence of Faraday rotation in sunspots has been convincingly

Polarimetric Studies 413

demonstrated by Makita (1986) with observational data of Okayama. So the azimuth of plane of polarization  $\varphi[=\frac{1}{2}\tan^{-1}(\frac{U}{O})]$  given by direct measurements may deviate significantly from that of transverse magnetic field  $\chi$ . We (Ye Shi-hui et al.,1987) have shown that the influence of Faraday rotation is largest if measurements are made with radiation from line center. This is represented by the point A in Figure 7. The coordinates of this point are the Q and U parameters of the very center of  $\lambda$ 5250. Before starting to solve Unno-Beckers' equations we took  $\chi$  to be 10 °. But the angle  $\angle AOQ = 167^{\circ}$ , so at line center  $\varphi = 83.5^{\circ}$ . This means that direct measurements made at line center may give rise to an azimuth of plane of polarization which is far larger than that of transverse magnetic field. If the spectral region of observation is shifted step by step from line center to a wing, the observed values of Q and U yield points B, C, etc. The values of  $\varphi$  given by them become smaller and smaller. When measurements are made in a far wing, the soild line connecting points A,B, C, ... gradually approaches an asymptote OL. [See Figure 7 in which the dotted line is the curve predicted by Makita (1986)]. It is interesting to note that  $\angle LOQ = 20^{\circ}$ , i.e. the value of 2x. This tells us that the Faraday rotation exerts practically no influence on far wings. However, their reaction to magnetic fields is quite weak, so we still have to carry out magnetic measurements in the region of line core. In order to eliminate the influence of the Faraday rotation, we have designed a method to derive  $\chi$  from the directly measured  $\varphi$ . It can be used in practical observations.

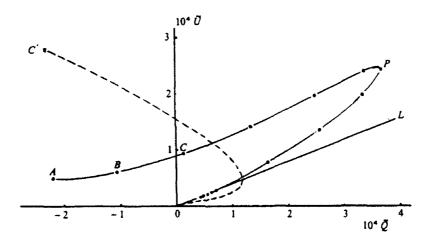


Fig.7. Change of  $\varphi$  from lines center to wing.

#### 12. Twist of Magnetic Lines of Force in Depth

In order to study the 3D structure of sunspot magnetic fields, it is necessary to determine whether the lines of force are twisted, i.e., if the angle  $\chi$  changes with depth. For this purpose we (Ye Shi—hui et al., 1990) proposed the following method. At a fixed point in a spot and in a certain wavelength interval of a magneto—sensitive line, one may measure Q and U and then calculate  $\varphi$ . If the spectral region of observation is moved successively from line center to a wing, one may draw the azimuth diagram with Q and U as coordinates. According to our theoretical calculations, if magnetic lines of force are sufficiently strongly twisted, the curve on this diagram

contains loop structures (see Figure 8). If the twist is rather weak, the curve is approximately semicircular. From the direction the curve winds (clockwise or counterclockwise) one may infer whether the magnetic field is twisting in one direction or in the opposite. In the case of no twist at all, the curve is comparatively simple and similar to a parabola.

When the sensitivity of observational facilities is high enough, our diagnostic method can also be applied to regions of weak magnetic fields outside sunspots.

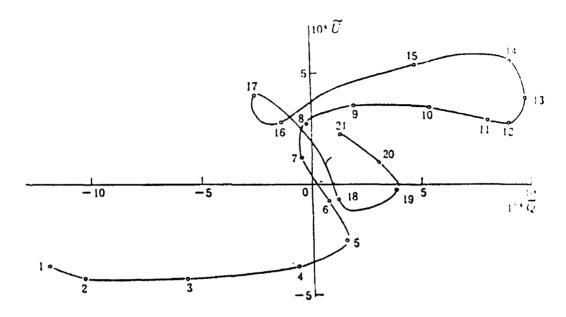


Fig.8. An azimuth diagram.

#### 13. Conclusion

In the above sections we have birefly reviewed the results of our studies of solar magneto-sensitive lines. Our work is rather comprehensive and systematic and we have made a series of improvements on predecessors' works. Concretely speaking, on the theoretical side, we abandoned some of Unno's unreasonable assumptions, for Unno's equations got numerical solutions which are much better than his algebraic solution, pointed out the inadequacy of applying Seares' formulae to the determination of direction of sunspot magnetic fields, corrected some inexactitudes in Beckers' equations of transfer of Stokes parameters, discovered that the depths of formation of various Stokes parameters may be quite different, investigated the oscillations of Stokes profiles caused by Alfven waves, preliminarily justified Parker's theory of sunspot cooling by Alfven waves, and studied the influence of magneto-optical effects, especially the Faraday rotation, on magneto-optical lines. On the practical side, we established a method of derivation of information of vector magnetic fields with Stokes profiles, improved the method of determination of gradient of magnetic fields with the asymmetry of Zeeman components, investigated the temperature sensitivity and magnetic intensification of magneto-sensitive lines, and designed a diagnostic method for probing the possible twist of magnetic lines of force. All these may be of some interest and use for the observations of solar magnetic fields.

Polarimetric Studies 415

However, our work is still far from being complete. First, we retain Unno's assumption of local thermodynamic equilibrium. Second, our research is restricted in the realm of Zeeman triplets. Besides, the fine structure of solar magnetic fields and the effects of MHD dynamical processes other than the Alfven waves have not been taken into consideration. Therefore, our polarimetric studies of solar magneto—sensitive spectral lines have to be further carried on.

#### References

Beckers, J.M.:1976, Astrophys.J., 203. 739.

Beckers, J.M.: 1969, Solar Phys., 9, 372.

Hale, G.E. and Nicholson S.B.: 1938, Magnetic Observations of Sunspots (1917-1924), Carnegie Institution.

Hubenet, H: 1954, Z.f.Ap., 34, 110.

Jin Jie-hai: 1980, Acra Astronomica Sinica, 21, 32.

Makita, M.: 1986, Solar Phys., 103, 1.

Maltby, P.: 1968, Solar Phys.,5, 3.

Parker, E.N.: 1974, Solar Phys., 36, 249.

Stellmacher, G. and Wiehr, E.: 1970, Astron. Astrophys., 7, 432.

Stepanov, V.E.: 1958, Izv. Krym. Astrofiz. Obs., 19, 20.

Unno, W.: 1956, Publ. Astron. Soc. Japan, 8, 108.

Wittamnn, A.: 1971, Solar Phys., 20, 78.

Ye Shi-hui and Jin Jie-hai: 1981, Acta Astronomica Sinica, 22, 265. = 1982, Chinese Astron. Astrophys., 6, 13.

Ye Shi-hui and Jin Jie-hai: 1983a, Acta Astrophysica Sinica, 3, 276. = 1984, Chinese Astron. Astrophys., 8, 21.

Ye Shi-hui and Jin Jie-hai: 1983b, Acta Astronomica Sinica, 24, 119. = 1983, Chinese Astron. Astrophys., 7, 255.

Ye Shi-hui and Jin Jie-hai: 1987, Solar Phys., 112, 305.

Ye Shi-hui and Jin Jie-hai: 1990, Solar Phys.,in press.

Ye Shi-hui, Jin Jie-hai and Jiang Min-han: 1985, in Measurements of Solar Vector Magnetic Fields, ed. M.J. Hagyard, 368.

Ye Shi-hui, Wang Zhen-yi and Jin Jie-hai: 1978a, Acta Astronomica Sinica, 19, 152. = 1979, Chinese Astron., 3, 258.

Ye Shi-hui, Wang Zhen-yi and Jin Jie-hai: 1978b, Studia Astronomica Sinica, No.2, 70. = 1979, Chinese Astron., 3, 394.

Ye Shi-hui, Wang Zhen-yi and Jin Jie-hai: 1979, Acta Astronomica Sinica, 20, 275. = 1980, Chinese Astron., 4, 273.

#### Acknowledgement

This work was supported by the National Natural Science Foundation of China under grant No. 9187006-01.

# Unified classical theory of line formation in a magnetic field

J.O. Stenflo

Institute of Astronomy, ETH-Zentrum, CH-8092 Zurich

Summary. A unified theory of line formation in a magnetic field is developed from first principles within a classical framework. Starting from Maxwell's equations for the electromagnetic field in vacuum and the Hamiltonian for an electron in a central potential, the theory of radiative transfer in a magnetic field is developed, including magnetooptical effects, scattering, coherence effects (the Hanle effect), and partial redistribution.

#### 1. Introduction

The theory of line formation in a magnetic field has been developed over the past decades in bits and pieces. Different authors have been using different formalisms and theoretical frameworks, and have generally addressed only certain aspects of the theory. Therefore a unified theory developed from first principles is needed.

The LTE theory was first formulated by Unno (1956) in a phenomenological way, and was independently developed by Stepanov (1958a), who made a more stringent classical derivation that implicitly also included the magnetooptical effects. Rachkovsky (1962a, b) extended Stepanov's approach and explicitly treated the magnetooptical effects. Jefferies et al. (1989) have made a new classical derivation of the same LTE theory. Their approach is similar to that of Stepanov and Rachkovsky. A quantum-mechanical derivation of the LTE equations was first obtained by Landi Degl'Innocenti and Landi Degl'Innocenti (1972).

Incoherent scattering in a magnetic field was first introduced by Stepanov (1958b) and Rachkovsky (1963). Later it became part of a more complete non-LTE theory of polarized radiative transfer, developed by Domke and Staude (1973), Dolginov and Pavlov (1973), Šidlichovský (1974), and House and Steinitz (1975). Non-LTE transfer with scattering of polarized radiation in multi-dimensional media was first treated by Stenholm and Stenflo (1978).

The quantum theory of coherent scattering (Hanle effect) was developed in various forms by House (1970a. b, 1971), Lamb and ter Haar (1971), Omont et al. (1973), and Bommier and Sahal-Bréchot et al. (1978). It was built into a non-LTE radiative-transfer theory for the weak-field case by Stenflo (1978).

The first unified derivation of the transfer equation from first principles, including both the Zeeman and Hanle effects, was done by Landi Degl'Innocenti (1983) within the framework of quantum electrodynamics (QED). The formalism has been further developed by Landi Degl'Innocenti et al. (1990) for practical applications. An independent QED derivation from first principles, but without coherence effects, has also been provided by Mathys (1983).

Although the QED framework is the physically most general one, it is difficult via the often cumbersome formalism to obtain a good intuitive understanding of the physics involved, beyond the application of the formalism as a "mathematical cookbook" for computations. To aid the physical insight I have therefore in the present paper developed a unified radiative transfer theory of the Zeeman and Hanle effects from first principles within a classical framework. The following sections outline (in abbreviated form, due to space limitations) the derivation of the theory. The lengthy considerations of partial redistribution in a magnetic field of arbitrary strength have been omitted in the present highly condensed presentation of the theory.

#### 2. Maxwell's equations

The standard set of equations for the electromagnetic field can be written

$$\nabla \cdot \mathbf{D} = \rho_{c},$$

$$\nabla \cdot \mathbf{B} = 0,$$

$$\nabla \times \mathbf{E} = -\frac{\partial \mathbf{B}}{\partial t},$$

$$\nabla \times \mathbf{H} = \mathbf{j} + \frac{\partial \mathbf{D}}{\partial t}.$$
(1)

In addition we need two equations relating D and B to E and H. We will only make use of the equations valid for vacuum, i.e.

$$\begin{aligned} \mathbf{D} &= \epsilon_0 \mathbf{E} \,, \\ \mathbf{B} &= \mu_0 \mathbf{H} \,. \end{aligned} \tag{2}$$

Often in electromagnetic theory the macroscopic effects of a medium are described by introducing a dielectric constant  $\epsilon$  and a magnetic permeability  $\mu$ . Such concepts however represent a phenomenological element of the theory, hides the underlying physics, and have led to physically inconsistent treatments in the past. We will therefore entirely refrain from introducing any  $\epsilon$  or  $\mu$  at all, to allow us to work from a rigorous version of Maxwell's theory. All the effects of matter will exclusively enter via the charge density  $\rho_{\epsilon}$  and the current density j.

#### 3. The electromagnetic wave equation

For the treatment of radiation problems it is convenient to reformulate Maxwell's equations in terms of a vector potential  $\boldsymbol{A}$  and a scalar potential  $\boldsymbol{\Phi}$ , defined by

$$\mathbf{B} = \nabla \times \mathbf{A}, 
\mathbf{E} = -\nabla \mathbf{\Phi} - \frac{\partial \mathbf{A}}{\partial t}. \tag{3}$$

These definitions assure that B is divergence free, and that E satisfies Faraday's law.

For radiation problems the natural gauge to choose is the so-called Coulomb or radiation gauge defined by

$$\nabla \cdot \mathbf{A} = 0. \tag{4}$$

If we introduce plane waves

$$\mathbf{A}(t,\mathbf{r}) = \mathbf{A}_0(\omega) e^{-i\omega t + i\mathbf{k}\cdot\mathbf{r}}, \qquad (5)$$

the gauge condition implies

$$\mathbf{k} \cdot \mathbf{A} = 0, \tag{6}$$

i.e., the waves must be transverse.

The scalar potential  $\Phi$  then decouples from the wave propagation problem, and the electromagnetic waves become described by the single equation

$$\nabla^2 \mathbf{A} - \frac{1}{c^2} \frac{\partial^2 \mathbf{A}}{\partial t^2} = -\mu_0 \mathbf{j}_t. \tag{7}$$

Only the transverse component of j (marked by index t), i.e., the component of the current density that is perpendicular to the propagation direction given by the wave vector k, can serve as a source for the waves.

#### 4. Dipole moment and the refractive index

Plane wave solutions of the type (5) to the wave equation (7) imply

$$\left(-k^2 + \frac{\omega^2}{c^2}\right) \mathbf{A}_0 e^{-i\omega t + i\mathbf{k} \cdot \mathbf{r}} = -\mu_0 \mathbf{j}_t. \tag{8}$$

If the currents j are carried by moving electrons, each electron i contributes to the current density by the amount

$$\mathbf{j}_i = -e\dot{\mathbf{r}}_i \,. \tag{9}$$

If we denote the electric dipole moment per unit volume by d, its time derivative is

$$\dot{d} = -\sum_{i} e \dot{r}_{i} \,, \tag{10}$$

i.e., it equals the total current density j.

Let us now define a refractive index n as embodying the dispersion relation between the wave number k and angular frequency  $\omega$  through

$$k \equiv n\omega/c \,. \tag{11}$$

Then we obtain from Eqs. (8), (9), and (10)

$$\dot{d}_t = \frac{\omega^2}{\mu_0 c^2} (n^2 - 1) A_0 e^{-i\omega t + ik \cdot r} , \qquad (12)$$

where index t denotes the transverse component. This constitutes a relation between the wave amplitude  $A_0$  and the amplitude of the electric dipole moment per volume element of the medium, expressed in terms of the complex refractive index n.

#### 4.1. Remarks on previous uses of a dielectric constant $\epsilon$

In previous approaches (Stepanov, 1958a; Jefferies et al., 1989)  $\epsilon$  (which is expressed in units of its vacuum value) has been calculated from the polarizability of the medium and identified as representing  $n^2$ . This however leads to inconsistencies, as will be explained below.

If we have a homogeneous medium with  $\epsilon \neq 1$  (but with  $\mu = 1$  for simplicity), then the wave equation (7) is the same except that  $1/c^2$  is replaced by  $\epsilon/c^2$ . Now we have two choices to account for the effect of the medium: Through the dielectric constant  $\epsilon$  or through the current density j. Let us first try to do it through  $\epsilon$  alone.

If we insert the plane-wave solutions (5) and denote the real and imaginary parts of the wave number vector k by  $k_R$  and  $k_I$ , respectively, it is readily shown that

$$\mathbf{k}_R \cdot \mathbf{k}_I = 0. \tag{13}$$

This means that absorption in the direction of propagation (along  $k_R$ ) is not possible, i.e., plane waves of the type

$$e^{-k_I x} \cos(\omega t - k_R x)$$

cannot be solutions to the homogeneous wave equation. These are however precisely the type of solutions that are needed to represent absorbing properties of the medium!

Thus we need an inhomogeneous term on the right hand side of the wave equation, and this is provided by the current density. However, if we let the influence of matter enter via the current density j, we cannot also let it enter via  $\epsilon$  by identifying  $\epsilon$  with  $n^2$ . Inserting our plane wave solution Eq. (5) in the wave equation, the left hand side becomes

$$(-k^2+\frac{\omega^2\epsilon}{c^2})\,A\,.$$

If we now insert both the definition (11) that  $k \equiv n\omega/c$  and make the identification  $\epsilon = n^2$ , the above expression vanishes, implying that the current density also has to vanish.

Thus, for the problem of absorption and refraction of radiation, the use of a dielectric constant to represent the effects of the medium leads to inconsistencies and therefore has to be abandoned. Furthermore there is no need for it, since the matter effects are fully taken care of by the current density term.

#### 5. Dipole radiation

The solution of the wave equation (7) for the vector potential A is

$$\mathbf{A}(\mathbf{r},t) = \frac{\mu_0}{4\pi} \int \frac{\mathbf{j}_t(\mathbf{r}',t')}{|\mathbf{r}-\mathbf{r}'|} \, \mathrm{d}V'$$
 (14)

(Biot-Savart's law), if we only consider the contribution to A from currents j within a localized region.

$$t' = t - |\mathbf{r} - \mathbf{r}'|/v \tag{15}$$

is the retarded time, where  $v = \omega/k$  is the speed of light in the medium.

The currents that are the sources of the vector potential A are due to oscillating electric dipoles. The oscillating part of the electric dipole moment d per unit volume (which is the only part of d that is of relevance for the radiation problem) can according to Eq. (12) be written

$$d_t(\mathbf{r}',t') = d_{0t}(\mathbf{r}') e^{-i\omega t'}. \tag{16}$$

Then follows from Eq. (9) and (10) that

$$j_t(\mathbf{r}',t') = -i\omega \mathbf{d}_{0t}(\mathbf{r}') e^{-i\omega t'}. \tag{17}$$

As

$$e^{-i\omega t'} = e^{-i\omega t}e^{ik|\mathbf{r} - \mathbf{r}'|}, \tag{18}$$

$$\mathbf{A}(\mathbf{r},t) = -\frac{i\mu_0\omega}{4\pi} e^{-i\omega t} \int \frac{\mathbf{d}_{0t}(\mathbf{r}') e^{ik|\mathbf{r}-\mathbf{r}'|}}{|\mathbf{r}-\mathbf{r}'|} dV'.$$
 (19)

We consider the "wave zone"  $(r \gg r')$ , where the waves become aymptotically plane, and use the "dipole approximation", implying that the dimension of the dipoles (the size of the atoms) is small in comparison with the wavelength of the radiation, i.e.,

$$e^{ik\mathbf{r}'\,\mathbf{e}_r} \approx 1$$
. (20)

If we let the vector potential A represent the wave-zone field due to dipoles within a region of unit volume, then the approximations we have introduced allow us to rewrite Eq. (19) in the form

$$A(\mathbf{r},t) = -\frac{i\mu_0\omega}{4\pi} \frac{e^{-i\omega t + ikr}}{r} d_{0t}. \tag{21}$$

The component  $E_{\alpha}$  of the electric field E that is parallel to some direction  $e_{\alpha}$  (which has to lie in a plane perpendicular to the propagation direction given by  $e_r$ ) then becomes

$$E_{\alpha} = \frac{\mu_0 \omega^2}{4\pi} \frac{e^{-i\omega t + ikr}}{r} d_0 \cdot e_{\alpha}. \tag{22}$$

This is a key expression for describing the polarization of the scattered radiation and the Hanle effect, as will be seen later.

# 6. Classical description of the electromagnetic interaction of an electron in a central potential

For a conservative system, the Hamiltonian for an electron in an electromagnetic field is

$$H = \frac{1}{2m}(p + eA)^2 + V(r), \qquad (23)$$

where the canonical momentum is

$$p = mv - eA, (24)$$

and we let V represent a Coulomb central potential that has its source in an atomic nucleus of charge +Ze:

$$V(r) = -\frac{Z e^2}{4\pi\varepsilon_0 r} \,. \tag{25}$$

The vector potential A contains both the external magnetic field and the external radiation field

The equation of motion for the electron is obtained from one of the Hamiltonian equations (here expressed in vector notation):

$$\dot{\mathbf{p}} = -\nabla H \,. \tag{26}$$

As the back-reaction force  $m\gamma v$  due to the radiative losses of the accelerated electron is about  $10^7$  times smaller than the  $\nabla V$  term (since at optical frequencies  $\gamma \approx 10^8$  and  $\omega_0 \approx 10^{15} \text{ s}^{-1}$ ), it may be added to the momentum equation as a small perturbation. The complete equation for the classical oscillator derived from Eq. (26) and adding the radiative back-reaction term then becomes

$$\ddot{\boldsymbol{x}} + \frac{e}{m}(\dot{\boldsymbol{x}} \times \boldsymbol{B}) + \gamma \dot{\boldsymbol{x}} + \omega_0^2 \boldsymbol{x} = -\frac{e}{m} \boldsymbol{E}, \qquad (27)$$

where the driving term from the external electromagnetic field has been placed on the right-hand side. This is the equation that we need to solve to obtain the dipole moment of the medium, which then allows us to find the refractive index from Eq. (12).

#### 7. Spherical vectors and the decoupling of the component equations

The complex spherical unit vectors  $e_q$ ,  $q = 0, \pm 1$ , can be defined in terms of the Cartesian linear unit vectors  $e_x$ .  $e_y$ , and  $e_z$  as

$$e_0 = e_z,$$

$$e_{\pm} = \mp (e_x \pm i e_y) / \sqrt{2},$$
(28)

where we have used the more compact notation  $e_{\pm}$  instead of  $e_{\pm1}$  .

Similarly, the relations between the vector components are defined to be

$$E_0 = E_z,$$

$$E_{\pm} = \mp (E_x \pm iE_y)/\sqrt{2}.$$
(29)

Then

$$E = \sum_{q} E_{q}^{*} e_{q} = \sum_{q} E_{q} e_{q}^{*} = \sum_{q} (-1)^{q} E_{q} e_{-q}.$$
 (30)

A scalar product becomes

$$\mathbf{a} \cdot \mathbf{b} = \sum_{q} a_{q} b_{q}^{*} = \sum_{q} (-1)^{q} a_{q} b_{-q} . \tag{31}$$

The fundamental role of the spherical vectors is seen if we choose a coordinate system such that the z axis is along the direction of the magnetic field  $\boldsymbol{B}$ , and express the momentum equation (27) in terms of the spherical vector components. The troublesome  $\boldsymbol{v} \times \boldsymbol{B}$  term then becomes

$$\boldsymbol{v} \times \boldsymbol{B} = -iB \sum_{q} q v_{q} \boldsymbol{e}_{q}^{*} \,. \tag{32}$$

where B = |B|.

Eq. (32) shows that the different components of v and B are no longer coupled to each other, in contrast to the Cartesian case. This means that the momentum vector equation (27) can be expressed as three independent, scalar equations,

$$C_q x_q = -\frac{e}{m} E_q \,, \quad q = 0, \pm 1,$$
 (33)

where the operator  $C_q$  is

$$C_q = \frac{\mathrm{d}^2}{\mathrm{d}t^2} - \left(qi\frac{eB}{m} - \gamma\right)\frac{\mathrm{d}}{\mathrm{d}t} + \omega_0^2 \,. \tag{34}$$

These three equations describe three independent, damped harmonic oscillators, which have different oscillation frequencies because of the q-dependent term in Eq. (34).

As the phases of the driving electric field components  $E_q$  are the same (see next section), there will be phase relations between the three oscillators, and it is these phase relations that are the reason for the polarization of the scattered radiation. The evolution of the phase relations depends both on the frequency differences (i.e., on B) and on the damping (lifetime of the excited state). The polarization effects arising from this fascinating interplay are collectively called the Hanle effect.

#### 8. Oscillatory solutions

We use our previous plane-wave expression

$$\mathbf{A} = \mathbf{A_0} \, e^{-i\omega t + i\mathbf{k} \cdot \mathbf{r}} \tag{5}$$

and search for oscillatory solutions of the form

$$x_q = x_{0q} e^{-i\omega t} \,. {35}$$

This gives us the solution

$$x_{0q} = \frac{-ie\omega A_{0q} e^{ik \cdot r}/m}{\omega_c - \omega^2 - 2q\omega_L \omega - i\gamma\omega},$$
(36)

where we have introduced the Larmor frequency

$$\omega_L = \frac{\epsilon}{2m} B \,. \tag{37}$$

#### 9. Solutions in terms of a complex refractive index

As

$$\dot{x}_0 = -i\omega x_{00} e^{-i\omega t} \tag{38}$$

and

$$\dot{d}_{a} = -eN\dot{x}_{a} \,, \tag{39}$$

where N is the number density of oscillators, Eq. (36) gives us

$$\dot{d}_{q} = \frac{N e^{2} \omega^{2} A_{0q} e^{-i\omega t + ik \cdot r} / m}{\omega_{0}^{2} - \omega^{2} - 2q\omega_{L}\omega - i\gamma\omega}.$$
(40)

This can be compared with our previous expression (12) in terms of a refractive index. If we by  $n_q$  denote the refractive index induced by the vector component q of the vibrations, (12) can be written

$$\dot{d}_q = \frac{\omega^2}{\mu_0 c^2} (n_q^2 - 1) A_{0q} e^{-i\omega t + i\mathbf{k} \cdot \mathbf{r}}$$
(41)

Identification of Eqs. (40) and (41) gives the refractive index:

$$n_q^2 - 1 = \frac{N\mu_0 c^2 e^2/m}{\omega_0^2 - \omega^2 - 2q\omega_L \omega - i\gamma\omega}.$$
 (42)

As  $|n_q - 1| \ll 1$  and  $|\omega_0 - \omega| \ll \omega_0$ , Eq. (42) can be simplified to

$$n_q - 1 \approx \frac{\mu_0 c^2 e^2 N}{4m\omega_0} \frac{1}{\omega_0 - \omega - g\omega_T - i\gamma/2}$$
 (43)

or

$$n_q - 1 \approx \frac{\mu_0 c^2 e^2 N}{4m\omega_0} \frac{\omega_0 - \omega - q\omega_L + i\gamma/2}{(\omega_0 - \omega - q\omega_L)^2 + (\gamma/2)^2}$$
 (44)

Let us now introduce dimensionless units by dividing all frequencies by a frequency width  $\Delta\omega_D$ , which we will later choose to be the Doppler width. If we further introduce the notation

$$v_d = (\omega_0 - \omega - q\omega_L)/\Delta\omega_D \tag{45}$$

and

$$a = \gamma/(2\Delta\omega_D), \tag{46}$$

the refractive index may be expressed as

$$n_q = 1 + \frac{k_N}{\pi} \frac{v_q + ia}{v_q^2 + a^2}, \tag{47}$$

where

$$k_N = \frac{\mu_0 c^2 e^2 N}{4m\omega_0 \Delta \omega_D}. (48)$$

#### 10. Absorption and dispersion of the electromagnetic wave

Let us now consider an electromagnetic wave propagating in a given direction s. The spherical vector components of the electric field are then represented by

$$E_q \propto e^{-i\omega t + in_q \omega s/c} \,. \tag{49}$$

The interactions with the medium of the three  $E_q$  vector components are mutually independent.

From Eq. (49) follows that the differential change in  $E_q$  caused by the medium is given by the scalar equation

 $\frac{\mathrm{d}E_q}{\mathrm{d}s} = in_q \frac{\omega}{c} E_q \,. \tag{50}$ 

which describes the absorption and dispersion effects in a magnetic field. This simple equation, together with the expression for  $n_q$ , e.g. as given by (47), contains all the physics needed to derive the transfer equation for polarized radiation (except for the scattering processes, which however can be dealt with in a similar manner).

As soon as another polarization basis is used instead of the spherical vectors. Eq. (50) no longer remains scalar, but has to involve matrix multiplication.

We may expand E in a linear polarization basis:

$$\boldsymbol{E} = \sum_{\alpha=1}^{2} E_{\alpha} \boldsymbol{e}_{\alpha} \,. \tag{51}$$

The linear unit vectors can on the other hand be expanded in complex spherical unit vectors eq.

$$\boldsymbol{e}_{\alpha} = \sum_{q} \varepsilon_{q}^{\alpha} \boldsymbol{e}_{q}^{*} = \sum_{q} \varepsilon_{q}^{\alpha*} \boldsymbol{e}_{q} , \qquad (52)$$

where  $\varepsilon_q^{\alpha}$  are the spherical vector components of the linear unit vector  $e_{\alpha}$ .

With these definitions we can derive

$$E_{\alpha} = \sum_{q} \varepsilon_{q}^{\alpha *} E_{q} \,, \tag{53}$$

and

$$E_q = \sum_{\alpha} \varepsilon_q^{\alpha} E_{\alpha} \,. \tag{54}$$

This can be used to obtain

$$\frac{\mathrm{d}}{\mathrm{d}s} \begin{pmatrix} E_1 \\ E_2 \end{pmatrix} = i \frac{\omega}{c} \begin{pmatrix} C_{11} & C_{12} \\ C_{21} & C_{22} \end{pmatrix} \begin{pmatrix} E_1 \\ E_2 \end{pmatrix} , \tag{55}$$

where

$$C_{\alpha\alpha'} = \sum_{q} n_{q} \varepsilon_{q}^{\alpha*} \varepsilon_{q}^{\alpha'} \,. \tag{56}$$

The physics is here cleanly separated in the different factors: While  $\varepsilon_q^{\alpha \epsilon} \varepsilon_q^{\alpha'}$  contains all the information on the geometry but nothing on absorption and dispersion, the opposite is the case for  $n_q$ .

#### 11. Evaluation of the spherical vector components

Let us now choose a linear polarization basis  $e_1$  and  $e_2$ , such that the projection  $B_{\pm}$  of the magnetic field vector makes an angle  $\chi$  (in the counter-clockwise direction) with  $e_1$  (which lies in the meridional plane with  $e_2$  perpendicular to it),  $\chi = \pi/2$  with  $e_2$ . Then simple trigonometry gives

$$\varepsilon_0^1 = \sin \gamma \cos \chi .$$

$$\varepsilon_0^2 = \sin \gamma \sin \chi .$$

$$\varepsilon_{\pm}^1 = \pm (\cos \gamma \cos \chi \mp i \sin \chi) / \sqrt{2} .$$

$$\varepsilon_{\pm}^2 = \pm (\cos \gamma \sin \chi \pm i \cos \chi) / \sqrt{2} .$$
(57)

For the special case that  $\chi = 0$  this system reduces to

$$\varepsilon_0^1 = \sin \gamma .$$

$$\varepsilon_0^2 = 0 ,$$

$$\varepsilon_{\pm}^1 = \pm \cos \gamma / \sqrt{2} ,$$

$$\varepsilon_{\pm}^2 = i / \sqrt{2} .$$
(58)

#### 12. Expansion of the absorption-dispersion matrix in terms of the Pauli matrices

It is convenient to introduce the following notation:

$$n_{\Delta} \equiv \frac{1}{2} \left( n_0 - \frac{n_- + n_+}{2} \right) ,$$

$$n^0 \equiv n_I \equiv n_{\Delta} \sin^2 \gamma + \frac{1}{2} (n_- + n_+) ,$$

$$n^1 \equiv n_Q \equiv n_{\Delta} \sin^2 \gamma \cos 2\chi ,$$

$$n^2 \equiv n_U \equiv n_{\Delta} \sin^2 \gamma \sin 2\chi ,$$

$$n^3 \equiv n_V \equiv \frac{1}{2} (n_- - n_+) \cos \gamma .$$
(59)

The absorption-dispersion matrix can then be written as

$$C = \begin{pmatrix} n_I + n_Q & n_U - in_V \\ n_U + in_V & n_I - n_Q \end{pmatrix} . \tag{60}$$

It is useful to expand C in the orthogonal basis of the Pauli spin matrices, which are given by

$$\sigma_0 = \begin{pmatrix} 1 & 0 \\ 0 & 1 \end{pmatrix}, \qquad \sigma_1 = \begin{pmatrix} 1 & 0 \\ 0 & -1 \end{pmatrix},$$

$$\sigma_2 = \begin{pmatrix} 0 & 1 \\ 1 & 0 \end{pmatrix}, \qquad \sigma_3 = \begin{pmatrix} 0 & -i \\ i & 0 \end{pmatrix}.$$
(61)

This gives

$$C = n_1 \sigma_0 + n_Q \sigma_1 + n_U \sigma_2 + n_V \sigma_3, \qquad (62)$$

or, using the alternative notation of Eq. (59),

$$C = \sum_{k=0}^{3} n^k \sigma_k \,. \tag{63}$$

Let us here recall that the imaginary part of C represents the absorption effects, the real part the anomalous dispersion (refraction) effects.

#### 13. Jones vector, density matrix, and Stokes vector

The Jones vector J is simply defined as

$$\boldsymbol{J} = \begin{pmatrix} E_1 \\ E_2 \end{pmatrix} . \tag{64}$$

The interaction with a medium can be described by a matrix w operating on J:

$$\mathbf{J}' = \mathbf{w}\mathbf{J}. \tag{65}$$

The  $2 \times 2$  density matrix  $\rho_R$  of the radiation field is obtained directly from the Jones vector by

$$\boldsymbol{\rho_R} = \boldsymbol{J} \boldsymbol{J}^{\dagger} \,. \tag{66}$$

where  $J^{\dagger}$  denotes the adjoint of J (transposition and complex conjugation of J).

The Stokes vector may be written as

$$\mathbf{S} = \begin{pmatrix} S_0 \\ S_1 \\ S_2 \\ S_3 \end{pmatrix} \equiv \begin{pmatrix} I \\ Q \\ U \\ V \end{pmatrix} , \tag{67}$$

which in a medium transforms according to

$$S' = MS. \tag{68}$$

M is the  $4 \times 4$  Mueller matrix. The formalism of calculating the effect of a medium or of an optical train on the Stokes vector is called Mueller calculus.

S can be obtained from the density matrix via

$$S_{k} = \operatorname{trace}(\sigma_{k} \rho_{R}). \tag{69}$$

This relation provides a direct link with quantum mechanics, due to the following. If the state of a statistical system is described by the quantum-mechanical density matrix  $\rho$ , then the expectation value of an observable represented by the operator X is given by trace( $\rho X$ ). If we now choose the measuring devices such that they are represented by the operators  $\sigma_k$  (corresponding in the classical case to the Jones matrices of the measuring systems), then the expectation values of these operators are given by Eq. (69). Thus when the Pauli spin matrices are chosen as the observables of the system, the Stokes parameters are their expectation values.

The inverse relation is

$$\rho_R = \frac{1}{2} \sum_k S_k \sigma_k \,, \tag{70}$$

i.e., the density matrix can be expanded in terms of the basis matrices  $\sigma_k$ , with the Stokes parameters divided by two as the expansion coefficients. Explicitly, in terms of a single matrix, Eq. (70) becomes

$$\rho_R = \frac{1}{2} \begin{pmatrix} I + Q & U - iV \\ U + iV & I - Q \end{pmatrix} . \tag{71}$$

J. O. Stenflo

# 14. Jones matrix for radiative scattering in a magnetic field

The scattering process consists of two physical components: (1) Excitation of a dipole moment d in the medium by the incident radiation. (2) Radiation from the dipoles.

For harmonically oscillating dipoles as described by Eqs. (16) or (35), we have

$$\dot{\mathbf{d}} = -i\omega \mathbf{d}_0 \, e^{-i\omega t} \,, \tag{72}$$

where  $d_0$  is the oscillation amplitude of the dipole moment per unit volume. The electric field of the scattered radiation has been given earlier in Eq. (22). If we make use of Eq. (72) and choose index 3 for the scattered linear vector components, Eq. (22) becomes

$$E_{\beta} = \frac{i\mu_0\omega}{4\pi} \frac{e^{ikr}}{r} \dot{\mathbf{d}} \cdot \mathbf{e}_{\beta} \,. \tag{73}$$

To calculate the  $E_{\beta}$  of the scattered radiation we need the expression for d, which is determined by the exciting, incident radiation. If we mark all incident radiation components by a prime, the spherical vector component of the *incident* electric field is

$$E_q' = i\omega A_{0q}' e^{-i\omega t + i\mathbf{k} \cdot \mathbf{r}} \,. \tag{74}$$

This allows us to write Eq. (41) as

$$\dot{d}_{q} = -\frac{2i\omega}{\mu_{0}c^{2}}E'_{q}(n_{q}-1). \tag{75}$$

As the expansion of d in terms of the spherical vectors is

$$\dot{\mathbf{d}} = \sum_{q} \dot{d}_{q} \mathbf{e}_{q}^{*} \,. \tag{76}$$

we obtain by inserting Eqs. (75) and (76) in Eq. (73)

$$E_{\beta} = \frac{\omega^2}{2\pi c^2} \frac{e^{ikr}}{r} \sum_{q} (n_q - 1) \, \varepsilon_q^{\beta^*} \, E_q' \,. \tag{77}$$

If we further use our previous expansion (54) of a spherical vector component in terms of linear vector components, and apply this for  $E'_q$  in Eq. (77), we obtain

$$E_{\beta} = \frac{\omega^2}{2\pi c^2} \frac{e^{ikr}}{r} \sum_{\alpha'} w_{\beta\alpha'} E'_{\alpha'}, \qquad (78)$$

where

$$w_{\beta\alpha'} = \sum_{q} (n_q - 1) \, \varepsilon_q^{\beta *} \varepsilon_q^{\alpha'} \tag{79}$$

are the components of the Jones scattering matrix w. This matrix determines the relation between the incident and scattered electrical vectors, both of which are given in terms of a real, linear polarization basis.

To derive explicit expressions for the components of w in their simplest form, we choose a special coordinate system with the polar axis along the direction of the magnetic field vector B, and the directions of the incident and scattered rays given by their colatitudes  $\theta'$  and  $\theta$ , and their azimuths  $\varphi'$  and  $\varphi$ .

With these definitions, and using the notation  $\mu = \cos \theta$ ,  $\mu' = \cos \theta'$ , we obtain from Eq. (57)

$$\varepsilon_0^1 = \sin \theta .$$

$$\varepsilon_0^2 = 0 .$$

$$\varepsilon_{\pm}^1 = \pm \mu e^{\pm i\varphi} / \sqrt{2} .$$

$$\varepsilon_{\pm}^2 = i e^{\pm i\varphi} / \sqrt{2} .$$
(80)

with the same expressions for the four  $\varepsilon_q^{\alpha'}$ , if all the angular quantities in Eq. (80) are replaced by the corresponding primed quantities.

Let us further define

$$b_q \equiv (n_q - 1) e^{iq (\varphi - \varphi')}, \qquad (51)$$

which makes the explicit expressions for the four components (79) of the Jones scattering matrix particularly simple:

$$w_{11'} = b_0 \sin \theta \sin \theta' + \frac{1}{2} \mu \mu' (b_- + b_+),$$

$$w_{22'} = \frac{1}{2} (b_- + b_+),$$

$$w_{12'} = \frac{i\mu}{2} (b_- - b_+),$$

$$w_{21'} = -\frac{i\mu'}{2} (b_- - b_+).$$
(82)

For the special case that  $\theta = \theta' = \gamma$  and  $\varphi = \varphi'$  (forward scattering), we get  $w = C - \sigma_0$ , as expected (C is the Jones matrix (56) for differential absorption-dispersion).

The above expressions (82) for the matrix components give a complete account of the polarization effects for a *single* scattering process. They contain all the information (for dipole scattering transitions) about the *Hanle effect*, with non-magnetic scattering polarization as a special case (when B = 0).

# 15. Stokes formulation of the transfer equation

The relation between the Stokes parameters  $S_k$  and the density matrix was given by Eq. (69). Since the derivative of this expression commutes with the trace operation, we obtain

$$\frac{\mathrm{d}S_k}{\mathrm{d}s} = \operatorname{trace}\left(\sigma_k \frac{\mathrm{d}\rho_R}{\mathrm{d}s}\right). \tag{83}$$

According to Eq. (66),

$$\frac{\mathrm{d}\boldsymbol{\rho_R}}{\mathrm{d}s} = \frac{\mathrm{d}\boldsymbol{J}}{\mathrm{d}s}\boldsymbol{J}^{\dagger} + \boldsymbol{J}\frac{\mathrm{d}\boldsymbol{J}^{\dagger}}{\mathrm{d}s}.$$
 (84)

The derivative of the Jones vector was obtained in our previous Eq. (55), which with the defining Eq. (64) may be written as

$$\frac{\mathrm{d}\boldsymbol{J}}{\mathrm{d}\boldsymbol{s}} = i\frac{\omega}{c}\boldsymbol{C}\boldsymbol{J}.\tag{85}$$

We then obtain, after some algebraic manipulations, after application of Doppler and collisional line broadening, and after adding an emission term,

$$\frac{\mathrm{d}S_k}{\mathrm{d}s} = -\frac{1}{4}\kappa_0 \sum_{i,j} [\mathcal{H}^i \operatorname{trace}(\sigma_k \sigma_i \sigma_j) + \mathcal{H}^{i*} \operatorname{trace}(\sigma_k \sigma_j \sigma_i)] S_j 
+ \frac{1}{2}\kappa_0 S \sum_i H^i \operatorname{trace}(\sigma_k \sigma_i).$$
(86)

S is an unpolarized line source function, which in the case of LTE equals the Planck function  $B_{\varepsilon}(T)$ . The form of the emission term follows from the requirement that detailed balance between emission and absorption (implying vanishing spatial gradients) should be achieved for an unpolarized radiation field of intensity S (which may in general differ from the Planck function).

The transfer equation (86) may be recast in the form

$$\frac{\mathrm{d}S_k}{\mathrm{d}s} = -\sum_j M_{kj}S_j + j_k \,, \tag{87}$$

or in matrix notation as

$$\frac{\mathrm{d}\mathbf{S}}{\mathrm{d}s} = -\mathbf{M}\mathbf{S} + \mathbf{j} \,. \tag{88}$$

where M is the Mueller absorption matrix, and j is the emission vector.

$$\mathcal{H}(a,v) = H(a,v) - 2iF(a,v). \tag{89}$$

H(a, v) is the Voigt function, F(a, v) the line dispersion function.

After some further algebra we obtain

$$\mathbf{M} = \kappa_0 \begin{pmatrix} H_I & H_Q & H_U & H_V \\ H_Q & H_I & 0 & 0 \\ H_U & 0 & H_I & 0 \\ H_V & 0 & 0 & H_I \end{pmatrix} + 2\kappa_0 \begin{pmatrix} 0 & 0 & 0 & 0 \\ 0 & 0 & F_V & -F_U \\ 0 & -F_V & 0 & F_Q \\ 0 & F_U & -F_Q & 0 \end{pmatrix}.$$
(90)

$$j = \kappa_0 S \begin{pmatrix} H_I \\ H_Q \\ H_U \\ H_V \end{pmatrix} . \tag{91}$$

This relation is valid quite generally for non-LTE problems without coherent scattering. The non-LTE physics enters in the calculation of the value of the scalar source function S.

$$H_{I} = H_{\Delta} \sin^{2} \gamma + \frac{1}{2} (H_{-} + H_{+}),$$

$$H_{Q} = H_{\Delta} \sin^{2} \gamma \cos 2\chi,$$

$$H_{U} = H_{\Delta} \sin^{2} \gamma \sin 2\chi,$$

$$H_{V} = \frac{1}{2} (H_{-} - H_{+}) \cos \gamma.$$
(92)

with

$$H_q = H(a, v - qv_H), \quad q = 0, \pm 1,$$
  
 $H_\Delta = \frac{1}{2}[H_0 - \frac{1}{2}(H_- + H_+)].$  (93)

The corresponding expressions for  $F_{I,Q,U,V}$  are obtained if we simply replace H in Eqs. (92) and (93) by F.

Finally, if we add a continuum and an optical depth scale, and denote the Stokes vector by  $I_{\nu}$  instead of S, the Stokes transfer equation (88) may be written

$$\frac{\mathrm{d}I_{\nu}}{\mathrm{d}\tau_{\nu}} = (\eta + E)I_{\nu} - (S_L \eta \mathbf{1} + B_{\nu} \mathbf{1}), \qquad (94)$$

where  $S_L$  is a scalar line source function, which may quite generally be determined by non-LTE processes, excluding coherent scattering (Hanle effect). Thus while the continuum is here assumed to be formed in LTE, the line radiation can be treated in general non-LTE.

$$\eta/\eta_0 = \begin{pmatrix} H_I & H_Q & H_U & H_V \\ H_Q & H_I & 2F_V & -2F_U \\ H_U & -2F_V & H_I & 2F_Q \\ H_V & 2F_U & -2F_Q & H_I \end{pmatrix} .$$
(95)

$$\eta_0 = \kappa_0 / \kappa_c \,. \tag{96}$$

 $\kappa_0 H(a,0)$  is the line center opacity,  $\kappa_c$  the continuum opacity.

E is the identity matrix with the diagonal elements equal to unity while the off-diagonal elements are zero. 1 is a four-vector representing unpolarized light with an intensity of unity, i.e., the first position is unity while the remaining three are zero.

#### 16. Coherent scattering in the rest frame

The  $2 \times 2$  density matrix can also be represented in the form of a 4-dimensional vector D, defined as

$$\mathbf{D} = \begin{pmatrix} \rho_{11} \\ \rho_{12} \\ \rho_{21} \\ \rho_{22} \end{pmatrix}, \tag{97}$$

where  $\rho_{ij}$  are the components of  $\rho_R$ . This vector is transformed by a medium according to

$$\mathbf{D}' = \mathbf{W}\mathbf{D},\tag{98}$$

where

$$\boldsymbol{W} = \boldsymbol{w} \otimes \boldsymbol{w}^* \,. \tag{99}$$

The symbols 3 and \* denote tensor product and complex conjugation, respectively.

The transformation matrix W for the vector version D of the density matrix, as defined in Eqs. (98) and (99), can be transformed into a Mueller matrix through

$$\mathbf{M} = \mathbf{T}\mathbf{W}\mathbf{T}^{-1},\tag{100}$$

where

$$T = \begin{pmatrix} 1 & 0 & 0 & 1 \\ 1 & 0 & 0 & -1 \\ 0 & 1 & 1 & 0 \\ 0 & i & -i & 0 \end{pmatrix}$$

$$T^{-1} = \frac{1}{2} \begin{pmatrix} 1 & 1 & 0 & 0 \\ 0 & 0 & 1 & -i \\ 0 & 0 & 1 & i \\ 1 & -1 & 0 & 0 \end{pmatrix}$$

$$(101)$$

The incoherent superposition of many scattering events cannot be done within the Jones formalism, but requires the density matrix or the Stokes formalisms. The Mueller matrix  $M_{sc}$  for a single scattering process can be directly derived from the corresponding Jones matrix, which according to Eq. (78) is

$$\frac{\omega^2}{2\pi c^2} \frac{e^{ikr}}{r} \boldsymbol{w} \,. \tag{102}$$

Using Eqs. (99) and (100) we then obtain

$$M_{sc} = \frac{\omega^{4}}{4\pi^{2}c^{4}} \frac{1}{r^{2}} T(\mathbf{w} \odot \mathbf{w}^{*}) T^{-1}. \tag{103}$$

where the transformation matrices T and  $T^{-1}$  are given by (101).

If the incident Stokes vector (per unit solid angle) is I', propagating in a direction characterized by colatitude  $\theta'$  and azimuth  $\varphi'$ , then the Stokes vector per unit solid angle, scattered in the direction given by  $\theta$  and  $\varphi$  and denoted by the vector  $j_{sc}$ , is obtained by integrating over all the incident directions (differential solid angles  $d\omega'$ ), thus adding up the stochastically independent contributions from all the incident solid angles:

$$j_{sc} = \int r^2 M_{sc} I' \, \mathrm{d}\omega'. \tag{104}$$

The  $r^2$  factor compensates for the  $1/r^2$  factor in  $M_{sc}$ , such that  $r^2M_{sc}$  represents scattering from one unit solid angle into another unit solid angle.

Inserting Eq. (103) into (104), we thus obtain

$$j_{sc} = \frac{\omega^4}{\pi c^4} \int T(\boldsymbol{w} \otimes \boldsymbol{w}^*) T^{-1} I' \frac{\mathrm{d}\omega'}{4\pi}. \tag{105}$$

The tensor product  $\mathbf{w} \otimes \mathbf{w}^*$  in Eq. (105) contains not only the squared terms, but also the cross products connecting different q values with each other. It is these terms that represent the interference or coherence effects, and these interference effects depend on the strength and direction of the magnetic field. The magnetic-field dependent polarization phenomena resulting from this interference are commonly denoted by the term Hanle effect.

## 17. Frequency averaging of the scattering matrix

Physically the frequency averaging is done by the Doppler broadening within the overall process of frequency and angular redistribution of the scattered radiation. The frequency-dependent terms to be averaged in the tensor product  $w \otimes w^*$  are of the type  $(n_q - 1)(n_{q'}^* - 1)$ . It may be shown that

$$\int_{-\infty}^{+\infty} (n_q - 1)(n_{q'}^* - 1) \, \mathrm{d}y \propto \cos \alpha_{q-q'} \, e^{i \, \alpha_{q-q'}} \,. \tag{106}$$

We have here defined an angle  $\alpha_{q-q'}$  by

$$\tan \alpha_{q-q'} = \frac{(q-q')v_H}{2a} = \frac{(q-q')g_b\omega_L}{\gamma} \,, \tag{107}$$

where the Landé factor  $g_b$  of the excited level appears in a quantum-mechanical treatment (in the classical framework  $g_b = 1$ ).

#### 18. Origin and nature of the Hanle effect

The essence of the Hanle effect is contained in the angle  $\alpha_{q-q'}$ . Only when interference effects are present, i.e., when  $q-q'\neq 0$ , does this angle differ from zero, provided that the field strength, which enters via  $v_H$  or  $\omega_L$ , is also non-zero. q-q' may assume the values  $\pm 2$ ,  $\pm 1$ , or 0.

The Hanle effect (magnetic-field dependence of the interference terms) manifests itself via the two factors  $\cos \alpha$  and  $e^{i\alpha}$ . The  $\cos \alpha$  factor is a scaling factor that decreases from unity towards smaller values when the field strength increases from zero to larger values. This factor corresponds to depolarization caused by the magnetic field. The phase factor  $e^{i\alpha}$  on the other hand gives rise to a rotation of the plane of linear polarization. The rotation angle increases with the strength of the magnetic field.

To see how these effects explicitly appear in the scattering matrix, let us calculate the component  $W_{44}$  of the matrix  $W = w \otimes w^*$ .

$$W_{44} = w_{22'} w_{22'}^* = \frac{1}{4} (|b_-|^2 + |b_+|^2 + b_- b_+^* + b_-^* b_+). \tag{108}$$

where  $b_q$  is given by Eq. (81).

In the case of the non-interference terms  $|b_{\pm}|^2$ , not only the angle  $\alpha_{q-q'}$ , but also the phase term in  $b_q$  involving the azimuth angles, vanishes. The frequency averaged value of  $W_{44}$  is obtained by inserting the result (106) for the different terms in Eq. (108), giving

$$W_{44} \propto 1 + \cos \alpha_2 \cos[2(\phi - \phi') - \alpha_2]. \tag{109}$$

The first, constant term on the right-hand side of Eq. (109) represents the incoherent contribution from the squared terms, while the second term represents the coherent contribution from the interference terms.

## 19. The Hanle effect phase matrix

For the special coordinate system where the polar axis is along the magnetic field vector the Hanle effect phase matrix (normalized Mueller scattering matrix) in the weak-field limit  $(\Delta \nu_H \ll \Delta \nu_D)$  can be written as

$$\mathbf{P}(\theta', \phi'; \theta, \phi) = \mathbf{E}_{11} + \frac{3}{4} (W_1 \mathbf{P}^1 + W_2 \mathbf{P}^2). \tag{110}$$

 $E_{ij}$  denotes a matrix that has element  $E_{ij} = 1$ , while all the remaining elements are zero.

$$P^{1} = [\mu \mu' + 2\cos \alpha_{1} \sin \theta \sin \theta' \cos(\phi - \phi' - \alpha_{1})] E_{44}, \qquad (111)$$

$$P^{2} = P_{0}^{2} + 2\cos\alpha_{1}\sin\theta\sin\theta' \left[P_{1}^{2}\cos(\phi - \phi' - \alpha_{1}) + P_{-1}^{2}\sin(\phi - \phi' - \alpha_{1})\right] + \cos\alpha_{2}\left\{P_{2}^{2}\cos[2(\phi - \phi') - \alpha_{2}] + P_{-2}^{2}\sin[(\phi - \phi') - \alpha_{2}]\right\}.$$
(112)

where

$$\boldsymbol{P}_{0}^{2} = \frac{1}{2} \begin{pmatrix} \frac{1}{3} (1 - 3\mu^{2})(1 - 3\mu'^{2}) & (1 - 3\mu^{2})(1 - \mu'^{2}) & 0 & 0\\ (1 - \mu^{2})(1 - 3\mu'^{2}) & (1 - 3\mu^{2})(1 - \mu'^{2}) & 0 & 0\\ 0 & 0 & 0 & 0\\ 0 & 0 & 0 & 0 \end{pmatrix}.$$
(113)

$$\mathbf{P}_{-1}^{2} = \begin{pmatrix} 0 & 0 & \mu & 0 \\ 0 & 0 & \mu & 0 \\ -\mu' & -\mu' & 0 & 0 \\ 0 & 0 & 0 & 0 \end{pmatrix}, \tag{115}$$

$$\boldsymbol{P}_{2}^{2} = \frac{1}{2} \begin{pmatrix} (1-\mu^{2})(1-\mu'^{2}) & -(1-\mu^{2})(1+\mu'^{2}) & 0 & 0\\ -(1+\mu^{2})(1-\mu'^{2}) & (1+\mu^{2})(1+\mu'^{2}) & 0 & 0\\ 0 & 0 & 4\mu\mu' & 0\\ 0 & 0 & 0 & 0 \end{pmatrix},$$
(116)

$$\boldsymbol{P}_{-2}^2 = \begin{pmatrix} 0 & 0 & -(1-\mu^2)\mu' & 0\\ 0 & 0 & (1+\mu^2)\mu' & 0\\ \mu(1-\mu'^2) & -\mu(1+\mu'^2) & 0 & 0\\ 0 & 0 & 0 & 0 \end{pmatrix}. \tag{117}$$

432 J. O. Stenflo

The factors  $W_1$  and  $W_2$  depend on the J (total angular momentum) quantum numbers of the upper and lower levels of the transition. For the purely classical case they are both equal to unity.

#### 20. Stokes transfer equation, including the Zeeman and Hanle effects

We can now summarize our results by incorporating them into a final radiative transfer equation, obtained by replacing the emission vector  $S_L \eta \mathbf{1}$  in Eq. (94) by  $j/\kappa_c$ . The line emission vector can be described as the sum of three contributions:

$$\mathbf{j} = \mathbf{j}_{coh} + \mathbf{j}_{ic} + \mathbf{j}_{th} \,. \tag{118}$$

 $j_{coh}$  represents coherent scattering (undisturbed by collisions),  $j_{ic}$  incoherent (collisionally disturbed) scattering, and  $j_{th}$  "thermal" emission, i.e., emission that does not represent a scattering process.

The transfer equation then becomes

$$\frac{\mathrm{d}\boldsymbol{I}_{\nu}}{\mathrm{d}\tau_{\nu}} = (\boldsymbol{\eta} + \boldsymbol{E})\boldsymbol{I}_{\nu} - B_{\nu}\boldsymbol{1} - S_{L}[\alpha_{ic}(1 - k_{c})\boldsymbol{e} + \alpha_{th}]\boldsymbol{\eta}\boldsymbol{1} - \boldsymbol{j}_{coh}/\kappa_{c}. \tag{119}$$

Here  $\alpha_{ic}$  and  $\alpha_{th}$  are coefficients indicating the relative weights of incoherent and thermal emission. respectively. They depend on the atomic level populations and transition probabilities.  $k_c$  denotes the fraction of all the scattering processes that occur as coherent scattering, which means that the fraction  $1 - k_c$  occurs as incoherent scattering.

$$k_c = \frac{\gamma_N}{\gamma_N + \gamma_c},\tag{120}$$

where  $\gamma_N$  and  $\gamma_c$  are the radiative and collisional rates, respectively.

$$e = \int \frac{d\omega'}{4\pi} \int d\nu' \left( K_I' I_{\nu'} + K_Q' Q_{\nu'} + K_U' U_{\nu'} + K_V' V_{\nu'} \right). \tag{121}$$

 $K_{I,Q,U,V} = H_{I,Q,U,V}/\sqrt{\pi}$ , where  $H_{I,Q,U,V}$  have been given by (92). The coherent scattering vector  $j_{coh}$ , which generally has a very complicated dependence on the scattering geometry, the magnetic field vector, and the partial redistribution processes, can in the weak-field limit be approximated by

$$j_{coh} \approx k_c \sigma \varphi_{\nu} \left[ a_{\nu} \int \varphi_{\nu'} J_{\nu'} d\nu' + (1 - a_{\nu}) J_{\nu}^{0} \right], \tag{122}$$

where  $\sigma$  is the scattering cross section,  $a_{\nu} \approx 1$  in the line core  $(|\Delta \nu| \lesssim 3\Delta \nu_D)$ , and  $a_{\nu} \approx 0$  in the wings. The vector  $J_{\nu}$  is defined by

$$J_{\nu} = \int P I'_{\nu'} \frac{\mathrm{d}\omega'}{4\pi} \,. \tag{123}$$

 $J_{\nu}^{0}$  is the non-magnetic counterpart of  $J_{\nu}$ . While the core expression (the first term) is only valid in the weak-field regime ( $\Delta\nu_{H}\ll\Delta\nu_{D}$ ), the wing expression (the second term) is valid independent of the field strength, as long as frequencies with  $|\Delta\nu|\gg\Delta\nu_{H}$  are considered. At intermediate frequencies, or for arbitrary field strengths, a more complete partial redistribution treatment is needed, the results of which would appear too messy if expressed in analytical form, so this is a problem for numerical computation.

Due to space limitations we have not here exposed the rather lengthy treatment of partial redistribution of polarized radiation, which as a special case contains the complete derivation of Eqs. (119)-(122), including explicit expressions for the parameters in these equations. Some heuristic arguments for writing Eqs. (119)-(122) in the present form can be found in Stenflo (1978) and Stenholm and Stenflo (1978).

#### References

```
Bommier, V., Sahal-Bréchot, S.: 1978, Astron. Astrophys. 69, 57.
Dolginov. A.Z., Pavlov. G.G.: 1973, Astron. Zhurnal 50, 762.
Domke, H., Staude, J.: 1973, Solar Phys. 31, 279.
House, L.L.: 1970a, J. Quant. Spectrosc. Radiat. Transfer 10, 909.
House, L.L.: 1970b, J. Quant. Spectrosc. Radiat. Transfer 10, 1171.
House, L.L.: 1971. J. Quant. Spectrosc. Radiat. Transfer 11, 367.
House, L.L., Steinitz, R.: 1975, Astrophys. J. 195, 235.
Jefferies, J.T., Lites, B.W., Skumanich, A.: 1989, Astrophys. J. 343, 920.
Lamb, F., ter Haar, D.: 1971, Phys. Rep. 2C, 253.
Landi Degl'Innocenti, E.: 1983, Solar Phys. 85, 3.
Landi Degl'Innocenti, E., Bommier, V., Sahal-Bréchot, S.: 1990, Astron. Astrophys. 235, 459.
Landi Degl'Innocenti, E., Landi Degl'Innocenti, M.: 1972, Solar Phys. 27, 319.
Mathys. G.: 1983, Ph.D. Thesis. Univ. Liège, Belgium.
Omont. A., Smith, E.W., Cooper, J.: 1973, Astrophys. J. 182, 283.
Rachkovsky, D.N.: 1962a. Izv. Krymsk. Astrofiz. Obs. 27, 148.
Rachkovsky, D.N.: 1962b. Izv. Krymsk. Astrofiz. Obs. 28, 259.
Rachkovsky, D.N.: 1963, Izv. Krymsk. Astrofiz. Obs. 29, 97.
Sidlichovský, M.: 1974, Bull. Astron. Inst. Czech. 25, 198.
Stenflo, J.O.: 1978, Astron. Astrophys. 66, 241.
Stenholm, L.G., Stenflo, J.O.: 1978, Astron. Astrophys. 67, 33.
Stepanov. V.E.: 1958a, Izv. Krymsk. Astrofiz. Obs. 18, 136.
Stepanov, V.E.: 1958b, Izv. Krymsk. Astrofiz. Obs. 19, 20.
Unno, W.: 1956, Publ. Astron. Soc. Japan 8, 108.
```

#### Discussion

E. Landi Although the results obtained by the classical theory are known for a long time, and are just a particular case of the more general ones deduced through the quantum theory, a classical derivation of the transfer equation for polarized radiation from first principles is however useful to have an intuitive grasp of the physical phenomena involved.

# DIAGNOSTIC OF THE MAGNETIC FIELD VECTOR USING THE ATOMIC DENSITY MATRIX FORMALISM

Véronique BOMMIER<sup>(1)</sup>
Egidio LANDI DEGL'INNOCENTI<sup>(1,2)</sup>
Sylvie SAHAL-BRÉCHOT<sup>(1)</sup>

(1) Laboratoire Astrophysique, Atomes et Molécules, URA 0812 du C.N.R.S. Département Atomes et Molécules en Astrophysique
Observatoire de Paris, Section de Meudon
F-92195 MEUDON Cedex, France

Dipartimento di Astronomia e Scienza dello Spazio Università di Firenze Largo E. Fermi, 5 I-50125 FIRENZE, Italia

#### **Abstract**

We present in the following the work which has been done and which is being done using the atomic density matrix formalism, for the interpretation of linear polarization measurements, leading to the magnetic field diagnostic in astrophysical media. This formalism has been used for interpreting polarization data from solar prominences, leading to original results on the prominence magnetic field obtained through the Hanle effect. An attempt is made to solve the coupled problem of polarized radiative transfer and statistical equilibrium in the case of weak, intermediate and strong magnetic fields, using a method of the *integral method* type; the advantages of this method, with respect to other methods, of the differential method type, are briefly discussed.

## I-INTRODUCTION

The density matrix formalism is born in the sixties (Fano, 1957), in order to have a quantum formalism able to describe the interaction between a "small" system (an ensemble of atoms) and a "large reservoir" (a bath of photons and/or perturbers). The main advantage of the density matrix formalism, with respect to the wave function formalism, is its ability of treating in an average manner an ensemble of identical physical systems, without mutual interaction, whereas the wave function formalism is adapted to the description of one individual system. The first attempt was made by Cohen-Tannoudji (1962) (see also Happer, 1972), in view of developing a quantum theory of optical pumping (atom-photon interaction); the development of the density matrix on the basis of irreducible tensors, well adapted for taking into account the symmetries of the problem, was furtherly introduced in the formalism by Omont (1965, 1977), together with the atom-perturber interaction.

Another advantage of the density matrix formalism is its ability of evaluating the atomic Zeeman coherences, or wave function interference effects between different Zeeman sublevels. The atomic coherences are given by the non-diagonal elements of the atomic density matrix, whereas the diagonal elements give the sublevels populations. The atomic Zeeman coherences play an important role in the Hanle effect; more precisely, they are created by the

anisotropy of the incident radiation, and partially destroyed by the magnetic field, this effect being the Hanle effect itself, leading to a partial depolarization or increasing in polarization (in some particular scattering geometries) and rotation of the linear polarization direction. Therefore, the density matrix formalism is the most adapted formalism to be used for the interpretation of Hanle effect measurements in Astrophysics.

In the following, we present the work which has been done and which is being done using the atomic density matrix formalism, for the diagnostic of magnetic fields in astrophysical media. We present as an introductoring step a classification of the different magnetic field regimes which can be found, namely the weak, intermediate and strong field regimes (section  $\Pi$ ), and we discuss for each regime the sensitivity to the Hanle and Zeeman effects.

In a first step, the case of weak magnetic fields (Hanle effect) has been tackled, for interpreting polarization data from solar prominences, in optically thin (HeI  $D_3$ , H $\beta$ ) and optically thick (H $\alpha$ ) lines; the interpretation of measurements in lines of different optical thickness is a method capable of solving the fundamental ambiguity which remains in any polarimetric measurement of the magnetic field. Firstly, we have used the density matrix formalism, by taking into account the non-vanishing Zeeman coherences, for computing the magnetic field effect on an optically thin line. These computations have led to the interpretation of measurements in terms of magnetic field diagnostic and original results have been obtained for solar prominences (section III).

We have then tackled the coupled problem of polarized radiative transfer and statistical equilibrium of the atomic density matrix, for computing the emergent polarization of an optically thick line in the weak field regime (section IV.1). Two methods have been developed in this aim: firstly, an iterative method, which is capable of treating the case of a multi-level atom; secondly, a "global" (non-iterative) method, for a two-level atom, which has been used to validate the results of the iterative method, which has been restricted to the first iteration. The advantages of our method, which is of the integral method type, with respect to other methods, of the differential method type, are briefly discussed in this section.

In a second step, we have tackled the computation of the emergent polarization of an optically thick line in stronger fields, when the Zeeman shift of the components can no more be neglected (section IV.2). We present a theoretical approach of the coupled problem of polarized radiative transfer and statistical equilibrium, using the atomic density formalism, in the case of a two-level atom.

#### II-CLASSIFICATION OF THE MAGNETIC FIELD REGIMES

Three magnetic field regimes can be distinguished, if one compares the Zeeman splitting to the natural width and to the Doppler width of the line. In the weak field regime, the Zeeman splitting is of the order of magnitude of the natural width; in the intermediate field regime, the Zeeman splitting is much larger than the natural width, but much smaller than the Doppler width; in the strong field regime, the Zeeman splitting is of the order of magnitude of the Doppler width.

For a more quantitative description of these regimes, one can introduce the two parameters  $\Gamma$  and  $\gamma$ , giving the ratio between the Zeeman splitting and the natural width on the one hand, and between the Zeeman splitting and the Doppler width on the other hand, and which are defined by:

$$\Gamma = g_{J'} \frac{2\pi v_L}{A} \qquad , \tag{1}$$

$$\gamma = g_F \frac{v_L}{\Delta v_D} \qquad , \tag{2}$$

where  $g_{j'}$  is the Landé factor for the upper level,  $y_{j'}$  is the Larmor frequency given by:

$$v_L = \frac{eB}{4\pi m_e c} \qquad , \tag{3}$$

where B is the magnetic field strength, A the Einstein coefficient for spontaneous emission, and  $\Delta v_D$  the Doppler broadening of the line, given by:

$$\Delta v_D = \frac{v_T}{\lambda_0} = \frac{1}{\lambda_0} \sqrt{\frac{2kT}{m}} \qquad , \tag{4}$$

where  $u_T$  is the thermal velocity,  $\lambda_0$  the wavelength of the line, k the Boltzmann constant, T the temperature, m the mass of the atom.

For a typical visible line, one has:  $A = 10^8 \,\mathrm{s}^{-1}$ 

$$A = 10^8 \, \mathrm{s}^{-1}$$

$$\lambda_0 = 5000 \text{ Å} \qquad ,$$

$$g_{J'} = 1$$
 ,  $v_T = 2 \text{ km s}^{-1}$  , (5)

which corresponds to a temperature of 5800 °K for an atom with m = 12 u.m.a.. Taking into account these typical values, and the fact that:

$$\frac{v_L}{R} = 1.4 \text{ MHz/Gauss} , \qquad (6)$$

one obtains that  $\Gamma = 1$  for a magnetic field B = 11 Gauss, which means that, for this magnetic field strength, the Zeeman splitting is equal to the natural width, and  $\gamma = 1$  for a magnetic field B = 2850 Gauss, which means that for this magnetic field strength, the Zeeman splitting is equal to the Doppler width of the line. As for the ratio  $\Gamma/\gamma$ , which is the ratio between the Doppler and the natural width:

$$\frac{\Gamma}{\gamma} = \frac{2\pi\Delta v_D}{A} = \frac{2\pi v_T}{\lambda_0 A} \quad , \tag{7}$$

one has for these typical values:

$$\frac{\Gamma}{\gamma} = 2.5 \times 10^2 \qquad . \tag{8}$$

## One can then define the 3 magnetic field regimes:

- i) the weak field regime, defined by  $\Gamma = 1$  and  $\gamma \ll 1$ , which leads to a magnetic field strength B = 11 Gauss for the typical values; in this field regime, the Zeeman splitting is of the order of magnitude of the natural width, and interferences can be found between the Zeeman sublevels, which are destroyed only partially by the magnetic field; this leads to non-vanishing non-diagonal elements of the density matrix, which are called "Zeeman coherences"; these coherences are modified by the magnetic field, leading to the Hanle effect, and this field regime is the Hanle effect regime. In this regime, the Zeeman shifts of the line components are very small with respect to the line width, and can be neglected for computing the line polarization.
- ii) the intermediate field regime, defined by  $\Gamma \gg 1$  and  $\gamma \ll 1$ , which leads to a magnetic field strength  $B \approx 250$  Gauss for the typical values; in this field regime, the Zeeman splitting is much larger than the natural width, but much smaller than the Doppler width; owing to the first inequality, the Zeeman coherences are completely destroyed by the magnetic field (in the reference frame where the magnetic field direction is the quantization axis) and no Hanle effect can be found; owing to the second inequality, the Zeeman components of the line are not separated, and some approximations (based on the fact that the Zeeman shift is small an empared to the line width) can be introduced in the radiative transfer theory, in which this regime is called weak field regime, which must not be confused with the Hanle effect regime described above.
- iii) the strong field regime, defined by  $\Gamma \gg 1$  and  $\gamma \approx 1$ , which leads to a magnetic field strength  $B \approx 2850$  Gauss for the typical values; in this field regime, the Zeeman splitting is of the order of magnitude of the Doppler broadening of the line, and the approximations introduced in the weak field hypothesis in the radiative transfer theory can no more be used. One has to take into account in a non-approximated manner the Zeeman shift of the components of the line.

## III-OPTICALLY THIN LINES AND THE HANLE EFFECT

The first problem which has been tackled using the density-matrix formalism is the statistical equilibrium of an atom, submitted to an anisotropic incident radiation field and to a weak magnetic field, in the Hanle effect regime. Namely, the HeI  $D_i$  and  $H\beta$  lines of solar prominences, which are optically thin, have been studied; as a first step, the theory of the statistical equilibrium for the atomic density-matrix has been established; in a second step, computations of the magnetic field effect have been achieved and the method of diagnostic of the magnetic field vector using the linear polarization data has been derived, leading to some results in a final step.

## III.1 - Theory and computation of diagrams

The theory of the statistical equilibrium of the density-matrix has been firstly established, for an atom submitted to an anisotropical incident radiation field and to a weak magnetic field, by completing for the case of a multi-level atom the formalism which had been previously established for laboratory purposes (Cohen-Tannoudji, 1975), in which one considers a two-level atom submitted to a totally directive incident radiation field. Such a theory can be found in Bommier (1977), Bommier and Sahal-Bréchot (1978), and Landi Degl'Innocenti (1982).

The magnetic field effect (Hanle effect) on the line polarization has been computed, and the results are generally given in diagrams, giving the line linear polarization as a function of the magnetic field strength and direction. The diagrams for the HeI D, line, unresolved in its two main components, can be found in Bommier (1977) and Sahal-Bréchot, Bommier and

Leroy (1977); the HeI D<sub>3</sub> line was unresolved in this work, devoted to the interpretation of data from Pic-du-Midi, obtained by J.L. Leroy, who used a polarimeter with a Lyot filter. The diagrams for the two main components of the HeI D<sub>3</sub> line can be found in Landi Degl'Innocenti (1982), whose work was devoted to the interpretation of data obtained by R.N. Smartt at Sacramento Peak, using the Stokes II spectro-polarimeter.

Furtherly, the diagrams have been completed for stronger fields by Bommier (1980), who has introduced the coherences corresponding to level-crossings in non-zero magnetic field, which occur for the HeI D line in the Hanle effect regime owing to the small fine structure splitting between the HeI D and D levels; these level-crossings have a polarizing effect, which leads to "loops" in the diagrams, which can be found in Bommier (1980) and Landi Degl'Innocenti (1982) for the HeI D line unresolved and resolved in its two main components respectively.

## III.2 - "Inversion" of diagrams and multi-line diagnostic

The next step is to "invert" the diagrams, in order to obtain the magnetic field as a function of the line polarization, in order to achieve the magnetic field diagnostic. The polarization data can then be interpreted in terms of magnetic field vector solutions. In the case of a one-line diagnostic, the number of magnetic field solutions is infinite, because one has to determine the 3 coordinates of the magnetic field vector, and one observes 2 parameters only, the linear polarization parameters of the line. In the case of one-line observations, as in the Pic-du-Midi data where the HeI D<sub>3</sub> line is not resolved, one hypothesis on the field direction has to be added in order to determine completely the field vector; in the prominences case, this hypothesis was the horizontality of the field line. The complete determination of the field vector requires in fact a multi-line diagnostic. Bommier, Leroy and Sahal-Bréchot (1981), have shown that 2 lines with different sensitivity to the magnetic field strength (different values of the  $\Gamma$  parameter) are sufficient to determine completely the field vector. This is the case of the Sacramento Peak data, where the HeI D<sub>4</sub> line is resolved in its two main components.

However, an ambiguity remains, which gives as undistinguishable solutions two field vectors symmetrical with respect to the line-of-sight. This ambiguity, which is called the fundamental ambiguity because of its fundamental origin, is due to the fact that the atom is insensitive to the propagation sense of the incident radiation, because the atomic size is very small with respect to the wavelength of the radiation. Such an ambiguity is found in any polarimetric diagnostic of the magnetic field. Bommier, Leroy and Sahal-Bréchot (1981) have shown that a possible method to solve this ambiguity in the case of prominences observations is to compare the two solutions obtained during several following days, when the scattering geometry is modified from day to day. However, the number of such observations remains too small to lead to significant results, but a trend can be observed: within the 9 cases observed, the magnetic field line lies along the prominence long axis is 2 cases, an angle of 15° between the filed line and the prominence long axis is found in 4 cases, and an angle of 20° is found in 3 cases.

## III.3 - Results of prominences magnetic field diagnostic

The interpretation of linear polarization data from prominences has led to the results which are summarized hereafter.

Using the Pic-du-Midi coronagraph, the polarization of the HeI D<sub>3</sub> line, unresolved in its two main components, has been firstly measured. As mentioned above, the interpretation of data requires a supplementary hypothesis on the field direction, which has been the horizontality of the field lines. Taking into account this hypothesis, the data have been

interpreted in terms of magnetic field diagnostic in 120 prominences of the Polar Crown (Leroy, Bommier and Sahal-Bréchot, 1983), and in 256 prominences of medium and low latitude (Leroy, Bommier and Sahal-Bréchot, 1984), observed during the ascending phase of Cycle XXI. For each object, two solutions symmetrical with respect to the line-of-sight are found, owing to the fundamental ambiguity. As a consequence, the field intensity is determined without ambiguity, and is found to be in average 6 Gauss at the beginning of the cycle, and 12 Gauss just before the maximum, in the Polar Crown prominences sample. In these prominences, which are most often seen edge-on, the field component along the prominence long axis is determined without ambiguity also, and its direction seems to depend closely on the polarities of the high latitude photospheric field (see Fig. 5 of Leroy et al., 1983). In the medium and low latitude sample, the fundamental ambiguity has been solved through a statistical analysis of the directions of the two solutions; the statistical result is the following: on the one hand, the prominences of total height lower than 30,000 km are found to have the normal polarity with respect to the photospheric field; the average angle between the field and the prominence long axis is 20° and the average field strength is 20 Gauss; on the other hand, the prominences of total height higher than 30,000 km are found to have the inverse polarity with respect to the photospheric field; the average angle between the field and the prominence long axis is 25° and the average field strength is 5-10 Gauss.

With the Stokes II polarimeter operating at Sacramento Peak, the two main components of the HeI D, line were resolved, which has given the possibility of a multi-line diagnostic, leading to the complete determination of the field vector. 2 prominences (Quefeld, Smartt, Bommier, Landi Degl'Innocenti and House, 1985) and 14 prominences (Athay, Querfeld, Smartt, Landi Degl'Innocenti, Bommier, 1983) have been analyzed; for each observed point, two solutions symmetrical with repect to the line-of-sight are obtained, owing to the fundamental ambiguity. The two solutions are always found to lie near the horizontal plane, and the horizontality of the field is therefore established. The same statistical analysis of the field direction as the one performed on the Pic-du-Midi data has been performed, and has led to the same results (Bommier, Leroy and Sahal-Bréchot, 1985).

The Pic-du-Midi coronagraph polarimeter has then been adapted to observe simultaneously the HeI D<sub>3</sub> line and one Hydrogen line, H $\alpha$  or H $\beta$ . The interpretation of the H $\alpha$  data requires to take into account the radiative transfer, which has been the aim of a further work; the interpretation of the data in HeI D<sub>3</sub> and H $\beta$  has provided another multi-line diagnostic, which has been performed on 14 prominences; as a result, the horizontality of the field line is confirmed; in this case, in addition of the 3 coordinates of the magnetic field, another parameter, namely the electron density, is derived through the analysis of the 4 observed linear polarization parameters. The electron density is determined through the depolarizing effect of collisions of electrons and protons with the hydrogen atom, and is found to be in average  $10^{10}$  cm<sup>-3</sup> (Bommier, Leroy and Sahal-Bréchot, 1986). It must be emphasized that, at these electron densities, the Stark effect is too small to be measurable and can therefore not be used for the electron density diagnostic.

## IV-OPTICALLY THICK LINES

The computation of the linear polarization emitted in optically thick lines has been tackled, in order to interpret the data obtained at the Pic-du-Midi in the Hydrogen Ha line of solar prominences (Leroy, 1981), and in order to interpret data obtained on the disk, where optically thick lines are formed, by the future polarization-free telescopes. This requires to solve the coupled problem of statistical equilibrium equations for the atomic density-matrix, and of the radiative transfer equations for polarized radiation, which have been derived in the density-matrix formalism from the basic equations of Quantum Mechanics by Landi Degl'Innocenti (1983a, 1984). This is a coupled problem, the polarized radiation entering the statistical equilibrium equations for the atomic density-matrix, and the density-matrix elements

V. Bommier et al.

entering the radiative transfer equations for polarized radiation, as described by Landi Degl'Innocenti (1983b). The solution of this coupled problem can be obtained, either by an iterative method, the statistical equilibrium equations for the atomic-density matrix being solved at step N taking into account the intensity and anisotropy of radiation in each point of the medium obtained by integrating the radiative transfer equations from the solution at step N-1, or by a "global" method, which is of the *integral method* type.

## IV.1 - Case of the weak field regime and the Hanle effect

IV.1.1 - Iterative method for computing the emergent polarization of the  $H\alpha$  line of prominences

The interpretation of simultaneous measurements in one optically thin line (HeI  $D_3$ ) and one optically thick line (H $\alpha$ ) is actually the only method able to solve the fundamental ambiguity on individual cases: in fact, the anisotropy of the incident radiation, and then the scattering geometry, is not the same in the optically thin case and in the optically thick case. Therefore, the two solutions obtained with the optically thin line are symmetrical with respect to the line-of-sight, whereas the two solutions obtained with the optically thick line are not; the parasitic solution can then be eliminated by comparing the two two-fold solutions.

The polarization of the H $\alpha$  line of solar prominences has been computed using the iterative method, for prominences seen at the limb (Landi Degl'Innocenti, Bommier and Sahal-Bréchot, 1987) and for prominences seen on the disk (Bommier, Landi Degl'Innocenti and Sahal-Bréchot, 1989). One starts from a solution of the coupled problem without polarization (Heasley and Milkey, 1978), which provides the source function for intensity in each point of a grid of points; the radiative transfer equations are then integrated, in order to provide the intensity and anisotropy of the incident radiation in each grid-point; the statistical equilibrium equations for the atomic-density matrix are then solved in each grid point, taking into account the magnetic field and depolarizing collisions effects; at a final step, the radiative transfer equations for polarized radiation are integrated along the line-of-sight, in order to provide the emergent polarization. This is the first iteration of the iterative method, which has been applied to the multi-level case of the Hydrogen atom (H $\alpha$  line) in a 2-dimensional medium (solar prominences); the validity of the restriction to one iteration has been tested later, by comparison with results given by the "global" method (see next sub-section).

In the case of prominences seen at the limb, a preliminary interpretation of data for 2 prominences can be found in Bommier, Landi Degl'Innocenti and Sahal-Bréchot (1990), which shows that the ambiguity is solved in the two objects, which are both found to be of the inverse polarity. As for prominences seen on the disk, the Hanle effect is found to be a polarizing effect in this scattering geometry, instead of the depolarizing one observed for right-angle scattering (see Fig. 8, 9 and 10 of Bommier, Landi Degl'Innocenti and Sahal-Bréchot, 1989); this leads to an observable linear polarization, of the order of 1-2%, which could be observed by future polarization-free telescopes; the fundamental ambiguity could be solved either by comparing several points observed perpendicularly to the filament axis, or by observing the same filaments at different positions on the disk, and by comparing the obtained solutions.

## IV.1.2 - "Global" method for a two-level atom

The global method has been developed, in order to study the validity of the results obtained with the iterative method restricted to one iteration, used for computing the polarization of the H $\alpha$  line of solar prominences. The global method has been developed for a two-level atom, without polarization in the lower state; in this case, the statistical equilibrium equations

for the atomic density matrix can be analytically solved, in terms of the intensity, anisoptropy and polarization of the incident radiation; the radiative transfer equations for polarized radiation is considerably simplified because the absorption matrix is diagonal, and the solution of the radiative transfer equations in terms of source functions involving the density-matrix elements can be reported into the statistical equilibrium equations for the atomic-density matrix, leading to a system of integral equations coupling the density-matrix elements in all points of the medium, which has to be numerically solved. This method is of the integral method type. The general equations, which do not take into account the Zeeman shift of the components in the profiles computations and are then valid in the weak field regime only, have been developed by Landi Degl'Innocenti, Bommier and Sahal-Bréchot (1990) for a two-level atom imbedded in a 3-dimensional medium; the particular cases on 1-dimensional and 2-dimensional media are treated.

This method, together with the iterative method, has been applied to the computation of the polarization emitted by a two-level atom imbedded in a plane-parallel atmosphere, in the presence of a weak magnetic field. The convergence of the iterative method has been studied; it has been found that, in the case of a normal Zeeman triplet line  $(J=0 \rightarrow J'=1)$ , the result of the iterative method restricted to one iteration is half of the converged or global result; in this case, the iterative method restricted to 1 iteration is then not valid; on the contrary, in the case of a line simulating very roughly the Hydrogen  $H\alpha$  line, namely the  $J=3/2 \rightarrow J'=5/2$  line, the result of the iterative method restricted to the first iteration agrees with the converged or global result, if one considers the measurements uncertainties, which validates the results previously obtained for the  $H\alpha$  line using the iterative method restricted to one iteration (Bommier, Landi Degl'Innocenti and Sahal-Bréchot, 1991, see Fig. 7 and 8). The difference in the results obtained for these two lines is due to the fact that the coupling between the density-matrix elements of different grid-points is the strongest in the case of the normal Zeeman triplet, and weaker for any other line.

Other methods could be employed to solve the transfer equations for polarized radiation, in particular the methods of the differential method type. In this type of methods, the unknowns to be computed are the Stokes parameters I, Q, U, V at each depth  $\tau$ , at each frequency v, and in each direction  $\Omega$ , which requires 3 discretizations in the computation. In our method, where we use the atomic density-matrix formalism, the unknowns to be computed are the 6 elements of the density-matrix  $\rho_0$  at each optical depth  $\tau$ . The frequency integration is contained in the computation of the kernels coupling the density-matrix elements at different depths. Then, 1 discretization only  $(on\tau)$  is required in the computation. The discretization on v is achieved in the kernels computation. The discretization on v is completely avoided, all the information on the anisotropy of the radiation being contained in the density-matrix elements. Therefore, the needed computer power is reduced, for our method, with respect to differential methods, to reach the same precision of the results.

## IV.2 - Case of intermediate and strong fields

Recently, the global method employed in the case of weak magnetic fields for computing the emergent polarization of an optically thick line emitted by a two-level atom, has been generalized to the case of intermediate and strong fields. This has been done by taking into account the Zeeman shift of the line components in the line profile computation. The general formalism, in which a generalized profile in the irreducible tensorial basis has been introduced in this aim, has been developed for a two-level atom without polarization in the lower state, imbedded in a 3-dimensional medium and in an arbitrary magnetic field (Landi Degl'Innocenti, Bommier and Sahal-Bréchot, 1991a). The atomic coherences, responsible of the Hanle effect, are taken into account. This formalism has been then particularized to the case of a plane-parallel atmosphere, and intermediate and strong fields, by neglecting the atomic coherences, which are non-vanishing in the weak field regime only, in the reference frame

V. Bommier et al.

where the quantization axis is the magnetic field direction (Landi Degl'Innocenti, Bommier and Sahal-Bréchot, 1991b). This formalism can be applied to numerical computations, which will show if the anisotropy effects, which are fully taken into account in the density-matrix elements, are of some importance on the emitted Stokes profiles in the intermediate and strong field regimes.

## **V-CONCLUSION**

The density-matrix formalism is well-adapted to take into account the anisotropy effects, which can appear in the upper layers of solar or stellar atmospheres, or in anisotropical scattering in objects located above the atmosphere, like solar prominences. These anisotropy effects are fully contained in the density-matrix elements. This formalism is well-adapted also to take into account the magnetic field effects, namely the Hanle effect, which acts on the non-diagonal elements of the density-matrix, the so-called "Zeeman coherences", and the Zeeman effect, which plays a role in the profile computation through the Zeeman shift of the line components.

The use of the density-matrix formalism for linear polarization computation in prominences has led to original results on the magnetic field vector diagnostic through the Hanle effect, and to an electron density diagnostic in a domain where the Stark broadening is too small to be measurable, in the case of optically thin lines. In the case of optically thick lines, the use of the density-matrix formalism reduces the number of unknowns to be computed for solving the transfer equations for polarized radiation in the presence of a magnetic field. Therefore, computations of the emergent polarization emitted by a two-level atom in a plane-parallel atmosphere imbedded in a weak magnetic field (Hanle effect), as well as that emitted in H\alpha in solar prominences, have been achieved. Recent advances in the formalism for computing the emergent polarization emitted by a two-level atom in a plane-parallel atmosphere imbedded in an intermediate or strong magnetic field (where the Zeeman shift can no more be neglected) will lead to computations, which will show if the anisotropy effects, which are fully taken into account in the density-matrix elements, are of some importance on the emitted Stokes profiles.

Such a formalism is a powerful tool for the interpretation of polarization data, like those which will be obtained by the future polarizatrion-free telescopes, from the upper layers of the solar atmosphere, in which the anisotropy and magnetic field effects play an important role.

#### References

Athay, R.G., Querfeld, C.W., Smartt, R.N., Landi Degl'Innocenti, E., Bommier, V.: 1983, Solar Phys. 89, 3

Bommier, V.: 1977, Thèse de 3ème cycle, Paris VI University

Bommier, V., Sahal-Bréchot, S.: 1978, Astron. Astrophys. 69, 57

Bommier, V.: 1980, Astron. Astrophys. 87, 109

Bommier, V., Leroy, J.L., Sahal-Bréchot, S.: 1981, Astron. Astrophys. 100, 231

Bommier, V., Leroy, J.L., Sahal-Bréchot, S.: 1985, Proceedings of the MSFC Workshop "Measurements of Solar Vector Magnetic Fields", Huntsville (Alabama), May 15-18 1984, NASA Conference Publication 2374.

Bommier, V., Leory, J.L., Sahal-Bréchot, S.: 1986, Astron. Astrophys. 156, 79 and 90

Bommier, V., Landi Degl'Innocenti, E., Sahal-Bréchot, S.: 1989, Astron. Astrophys. 211, 230

Bommier, V., Landi Degl'Innocenti, E., Sahal-Bréchot, S.: 1990, Proceedings of the IAU Colloquium n°117 "Dynamics of Quiescent Prominences", Hvar (Yugoslavia), September 25-29 1989, V. Ruzdjak and E. Tandberg-Hanssen eds., Lecture Notes in Physics 363, Springer-Verlag

Bommier, V., Landi Degl'Innocenti, E., Sahal-Bréchot, S.: 1991, Astron. Astrophys., in press

Cohen-Tannoudji, C.: 1962, Ann. Phys. 7, 423

Cohen-Tannoudji, C.: 1975, in Frontiers in Laser Spectrospeopy, École d'été des Houches, Session XXVII, R. Balian, S. Haroche and S. Liberman ed., North-Holland Publ.

Fano, U.: 1957, Rev. Mod. Phys. 29, 74

Happer, W.: 1972, Rev. of Modern Physics 44, n°2, 169
Heasley IN Milley P.W.: 1978, Astrophys. J. 221, 67

Heasley, J.N., Milkey, R.W.: 1978, Astrophys. J. 221, 677 Landi Degl'Innocenti, E.: 1982, Solar Phys. 79, 291

Landi Degl'Innocenti, E.: 1983a, Solar Phys. 85, 3 Landi Degl'Innocenti, E.: 1983b, Solar Phys. 85, 33

Landi Degl'Innocenti, E.: 1984, Solar Phys. 93, 3 Landi Degl'Innocenti, E.: 1984, Solar Phys. 91, 1

Landi Degl'Innocenti, E., Bommier, V., Sahal-Bréchot, S.: 1987, Astron. Astrophys. 186, 335 Landi Degl'Innocenti, E., Bommier, V., Sahal-Bréchot, S.: 1990, Astron. Astrophys. 235, 459 Landi Degl'Innocenti, E., Bommier, V., Sahal-Bréchot, S.: 1991a Astron. Astrophys., in press

Landi Degl'Innocenti, E., Bommier, V., Sahal-Bréchot, S.: 1991b Astron. Astrophys., in press

Leroy, J.L.: 1981, Solar Phys. 71, 285

Leroy, J.L., Bommier, V., Sahal-Bréchot, S.: 1983, Solar Phys. 83, 135

Leroy, J.L., Bommier, V., Sahal-Bréchot, S.: 1984, Astron. Astrophys. 131, 33

Omont, A.: 1965, Journal de Physique 26, 26

Omont, A.: 1977, Prog. Quantum Electronics 5, 69

Querfeld, C.W., Smartt, R.N., Bommier, V., Landi Degl'Innocenti, E., House, L.L.: 1985, Solar Phys. 96, 277

Sahal-Bréchot, S., Bommier, V., Leroy, J.L.: 1977, Astron. Astrophys. 59, 223

#### Discussion

- J. Staude: Do you expect a decrease in the non-isotropy of the population of Zeeman sublevels, if more than 2 levels are considered in the model atom?
- V. Bommier: The non-isotropy of the populations of Zeeman sublevels is transmitted from one level to a lower one through the spontaneous emission process; by this process, it is not destroyed at all. Such an effect (non-isotropy of several levels) can be observed on the diagrams giving the Hanlé effect for the  $HeID_3$  line of prominences, where the alignment of the lower levels lead to shoulders which can be seen on the diagrams (Sahal-Brichot, Bommier, Leroy, 1977, Astron. Astrophys. 59, 223; Bommier, 1980, Astron. Astrophys. 87, 109); however, our theory developed for optically thick lines is not able, at the present time, to consider more than 2 levels and alignment on the lower level.
- J. Stenfio: About 10 years ago we produced an atlas of linear polarization 10 second of arc inside the solar limb, using the FTS and the grating spectrometer of the McMath telescope. It revealed a large number of lines (some hundred) showing coherent scattering polarization, i.e. atomic transitions with significant atomic polarization of the excited state.

## Non-LTE formation heights of Stokes profiles of Fe I lines

J.H.M.J. Bruls

Sterrekundig Instituut Utrecht
P.O. Box 80 000, NL-3508 TA Utrecht, The Netherlands

B.W. Lites, G.A. Murphy

High Altitude Observatory

National Center for Atmospheric Research<sup>1</sup>

P.O. Box 3000, Boulder, CO 80307, U.S.A.

Summary. We study the formation properties of the diagnostically important FeI lines at 6302.5 Å and 5250.2 Å in four different model atmospheres, ranging from cool umbra to hot network. Its weak temperature sensitivity makes FeI 6302.49 Å a very suitable diagnostic, whereas the formation of FeI 5250.2 Å is more problematic. Its formation is shifted upward considerably in the cooler models, so that its source function senses the chromospheric temperature rise; magneto-optical effects dominate its linear polarization.

## 1 Introduction

In work in progress we are studying the formation of a number of diagnostically important Fe I lines with the goal to check and interpret results from the Lites-Skumanich inversion procedure for Stokes profile observations (Skumanich and Lites, 1987). Here we report preliminary results concerning Fe I 6302.5 Å and Fe I 5250.2 Å. These lines are representative of two major classes of iron lines:  $\lambda 6302.5$  Å represents lines with excitation energy above about 3 eV,  $\lambda 5250.2$  Å lines below 3 eV excitation. More detailed results, including other lines (Fe I 6301.5, 5247.05, 5434.5, 8688.6, 6173.3, 5576.1, 15648.5 and 15822.8 Å) will be published elsewhere. We compare results for four different atmospheric structures: quiet Sun, bright network, penumbra, and umbra.

We employ the Carlsson-Scharmer operator-perturbation code (Scharmer and Carlsson, 1985; Carlsson, 1986) to compute field-free radiative transfer and statistical equilibrium, and the Rees-Murphy DELO code (Rees et al., 1989) to evaluate Stokes profiles from the opacities and source functions from the field-free computation. The latter code generates Stokes profiles from the CRD line source function, including magneto-optical effects and assuming L-S coupling. We also use this code to compute line depression contribution functions as an indicator for the formation depth, in the magnetic as well as the non-magnetic cases (Murphy, 1990; see also Grossmann-Doerth et al. 1988).

# 2 Field-free radiative transfer and statistical equilibrium

## 2.1 Input parameters and model atom

Our sample of lines includes low and medium excitation lines in the visible and high excitation lines in the infrared; it requires a model atom with only quintet and septet terms. We use a partial and modified version of the Fe I model atom of Steenbock (1985) and Gigas (1986).

The collision cross sections were all set to  $\pi a_0^2$ , rather than using values that result from fitting line profiles, e.g. Steenbock (1985). The photoionization cross sections were also revised. For the lower levels we use the values adopted by Lites (1972) with hydrogenic wavelength dependence; the other cross sections are assumed to be fully hydrogenic. The ionization is dominated by photoionization out of levels at intermediate (3-4 eV) excitation energy, using near-ultraviolet radiation, and is balanced by radiative recombination to the lower levels. The ionization equilibrium is mainly sensitive to the overall ratio of the bound-free

<sup>&</sup>lt;sup>1</sup>The National Center for Atmospheric Research is sponsored by the National Science Foundation.

cross sections of the intermediate levels to the cross sections of the lower levels. For example, adopting hydrogenic cross sections for all levels produces 30 to 40% less neutral iron in the line formation region. The sensitivity to the absolute scaling of the cross sections is of secondary importance.

In order to obtain computed quiet Sun profiles that resemble the observed ones we multiply the standard Van der Waals broadening width, computed following Unsöld (1955) from the  $\overline{r^2}$  values of Hofsäss (1975), by 2.8 in the case of  $\lambda 5250.2$  Å and increase the gf value of  $\lambda 6302.5$  Å by a factor of 1.8. We do not explicitly introduce macroturbulent broadening.

## 2.2 Model atmospheres

We select the four semi-empirical model atmospheres shown in Fig. 1 and combine these with the depth-independent magnetic fields of various strengths and inclinations specified in Table 1. This selection is representative of many solar surface features.

Table 1: Magnetic field configurations. The quiet Sun model is without magnetic field. For all configurations the azimuth angle  $\chi$  is zero.

Model and reference	Field strength (Gauss)	Inclination angle $\gamma$
Quiet Sun, VAL-C, Avrett (1990)	0	0°
Bright network, VAL-F, Avrett (1990)	1600	0°
Penumbra, Ding and Fang (1989)	1200	75°
Umbra model M, Maltby et al. (1986)	2500	10°

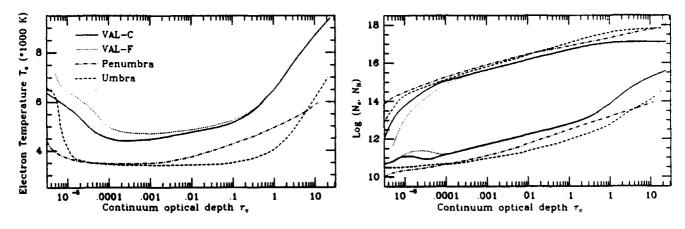


Figure 1: Atmospheric parameters for all four models: VAL-C (solid), VAL-F (dotted), penumbra (dot-dashed) and umbra (dashed). Left: electron temperature. Right: electron density (lower curves) and total hydrogen density. The electron density of the published umbra model contains peaks for  $\tau_c < 10^{-5}$  which were removed because they caused convergence problems.

## 2.3 Background opacities

The opacity package of the Carlsson-Scharmer code was adopted from LINEAR (Auer et al., 1972), and has insufficient opacity in the ultraviolet because the influence of the 'line haze' is neglected. We therefore multiplied the computed hydrogen opacities with suitable wavelength-dependent fudge factors, fitting computed emergent continua for VAL-C to the observed values from the quiet Sun. The same factors were then also applied to the opacities in the other three models. Results are shown in Fig. 2.

For the umbra and penumbra this procedure is questionable due to the significant contributions by molecules in the cooler layers. However, curves d-f in Fig. 2 show that the emergent umbral intensities are only moderately sensitive to these opacity fudge factors. The overall ionization equilibrium (inset of Fig. 3) is even less sensitive: the total neutral iron number densities change by less than 2% for factor 2 changes in opacity. The same holds for the populations of single levels because the excitation equilibrium is determined mainly by the stronger lines, which are insensitive to changes in the continuum opacity. Other experiments show that the spectral region shortward of the AlI edge at 2076 Å is less important because of its steep intensity decrease towards shorter wavelengths.

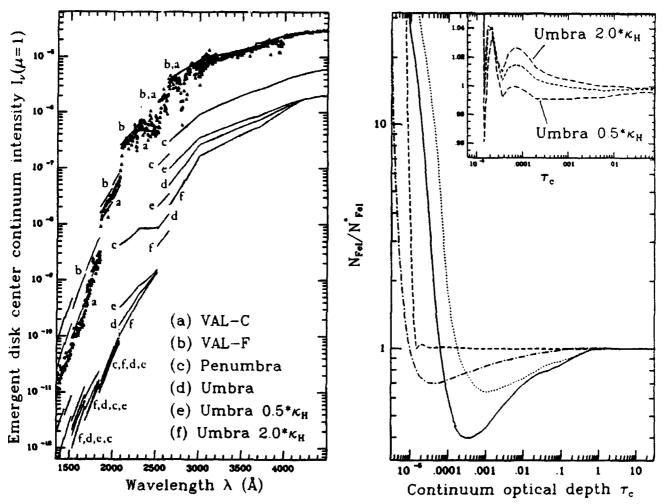


Figure 2: Emergent continuum intensities. The computed intensities are compared to observed quiet Sun values (triangles) from Vernazza et al. (1976). The three curves labeled 'umbra' are for different opacity fudge factors, respectively standard added opacity (d), half the standard added opacity (e), and double the added opacity (f).

Figure 3: Ionization equilibrium: neutral iron populations  $N_{\rm Fe~I}$  relative to LTE values  $N_{\rm Fe~I}^*$ . The dash patterns represent the same models as in Fig. 1. The inset shows the small differences in the neutral iron populations for the continuum opacity experiments in the umbra. The middle curve is for standard added opacity.

## 3 Results

## 3.1 Ionization and excitation equilibrium

The ionization equilibrium (Fig. 3) behaves as one may expect from the temperature stratifications in Fig. 1. Model VAL-C produces the largest overionization because its Planck function is very steep at

the  $\tau \approx 1$  point where the UV continuum becomes optically thin, reaching a minimum that is much lower than the local UV radiation temperature. VAL-F is equally steep in the photosphere but it has a higher minimum temperature and produces appreciably less overionization. The penumbra model has a less steep temperature gradient which extends to large height. It produces a similar overionization pattern to that of VAL-F, but it is shifted outward. Below the sharp chromospheric temperature rise the umbral model has an LTE neutral iron population because the neutral stage is the dominant one at the low umbral temperatures.

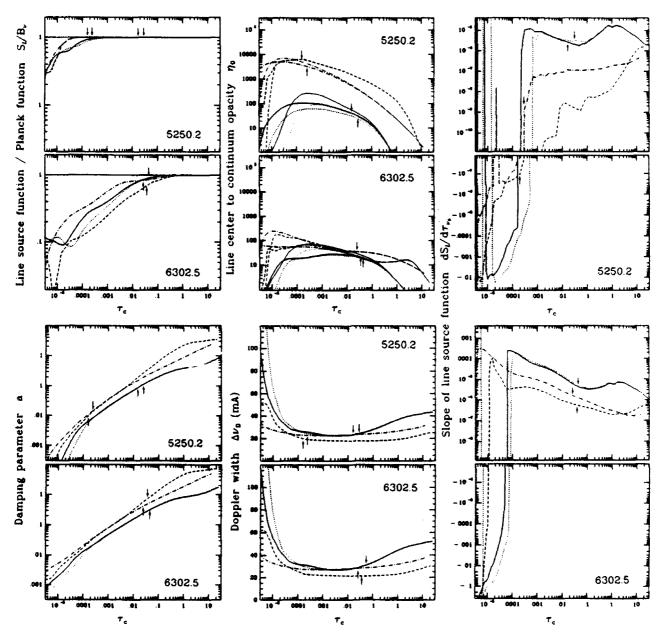


Figure 4: Thermodynamic parameters of two representative lines,  $\lambda 5250.21$  Å and  $\lambda 6302.49$  Å. For each line we plot the ratio of the line source function to the Planck function (top left), the line to continuum opacity ratio  $\eta_0$  (top middle; thick lines indicate the NLTE values, thin lines the LTE values), the damping parameter a (bottom left), the Doppler width  $\Delta \nu_D$  in mÅ (bottom middle), and the slope of the line source function  $dS_l/d\tau_{\nu_0}$  (righthand column). The dash patterns represent the same models as in Fig. 1. Arrows indicate the location of line center optical depth unity.

J. H. M. J. Bruls et al.

Fig. 4 displays departures from LTE in the line source functions and line opacities, and other line formation parameters. For all models the line source functions (upper left panel) are near LTE throughout the photosphere and temperature minimum region, because all neutral iron levels share the ionization departures equally due to strong radiative and collisional coupling; the source functions only drop below the Planck function due to photon losses where the strongest lines out of each upper level become optically thin, at a height slightly below their line center optical depth unity. For example the line source function of  $\lambda 6302.5$  Å is determined by stronger lines such as Fe i 5576.1 Å from the same upper level. The  $\lambda 5250.2$  Å line is much more opaque than  $\lambda 6302.5$  Å; in the umbra its source function drops below the Planck function only just above the temperature minimum, causing a tiny emission core in its field-free line profile.

On the basis of the line-to-continuum opacity ratios  $\eta_0$  (Fig. 4, top middle panel) the lines can be divided into two groups, represented here by the  $\lambda 5250.2$  Å and  $\lambda 6302.5$  Å lines. The  $\lambda 5250.2$  Å line shows a distinct separation between the hot and cool models, combined with strong depth-dependence of  $\eta_0$ . The  $\lambda 6302.5$  Å line displays smaller differences between the hot and cool atmospheres, and the curves are virtually flat throughout the line formation region. This different behaviour results from the temperature-dependence of the ionization and excitation equilibria. Lines with excitation energy below about 3 eV are of the first type; they are temperature sensitive and are formed considerably higher in the cooler models than in the hotter ones. The second group consists of higher excitation lines that are temperature insensitive and have line center optical depth unity at approximately the same continuum optical depth for all four models.

The damping parameter a (Fig. 4, lower left panel) varies rapidly with depth due to the strong dependence of the Van der Waals broadening on the hydrogen density. The Doppler width (lower middle panel) has only mild temperature dependence and is nearly constant over the line formation region, except for the strongest lines that feel part of the chromospheric rise in temperature and microturbulent velocity. The rightmost column displays the slope of the line source function  $dS_l/d\tau_{\nu n}$ . For a purely photospheric line like  $\lambda 6302.5$  Å this parameter is fairly constant throughout the line formation region; it changes sign due to the chromospheric temperature rise at a height where the line has already become optically thin. However, the  $\lambda 5250.2$  Å line does sense this change of sign in the cooler models because it becomes optically thin much higher than in the VAL models and its source function follows the Planck function more closely than for the  $\lambda 6302.5$  Å line, giving rise to a deeper location of the point where the sign change occurs.

## 3.2 Contribution functions: depth of formation

Figures 5 through 8 show line depression contribution functions (CF). In general these consist of four panels per line, one CF for each of the Stokes parameters I, Q, U, and V. We will refer to these curves as  $C_{R,I}, C_{R,Q}, C_{R,U}$ , and  $C_{R,V}$ , although what is plotted is actually  $\tau_c I_c C_{R,X}(\Delta \lambda, \tau_c)$  as defined by Murphy (1990), where X stands for each of the Stokes parameters. The reason for plotting this quantity is that it is better normalized: its depth integral can be directly compared to the matching Stokes parameter. We only show CF's for the shorter wavelength side of the line profile because the absense of macroscopic velocities implies that the Stokes parameters and CF's are either symmetrical or anti-symmetrical functions of  $\Delta \lambda$ .

For the field-free case only Stokes I is non-zero, requiring only one CF per line. For  $\lambda 6302.5$  Å the field-free CF's (top 4 panels of Fig. 5) are similar for all four models, except that an increase in line strength for the cooler models manifests itself as a slower inward decrease of the maxima towards the line wings. The umbral  $C_{R,I}$  shows the onset of the separation between the formation regions of the line core and the wings. For  $\lambda 5250.2$  Å the CF's show a striking difference between the hot and the cool models. In the cool models the inner line core is formed much higher than the rest of the line; in fact the Doppler core formation region is nearly completely separated from the wing formation region. The locations at which  $\tau = 1$  are indicated by tickmarks for a few  $\Delta \lambda$ 's and coincide with the CF maxima.

The magnetic cases are shown in Figs. 6-8. The CF's  $C_{R,I}$ ,  $C_{R,Q}$ ,  $C_{R,U}$ , and  $C_{R,V}$  show that radiation at the wavelengths of the separate Zeeman components originates generally deeper than the line center radiation of the unsplit line, because the opacity per component is lower than for the unsplit line. Often it

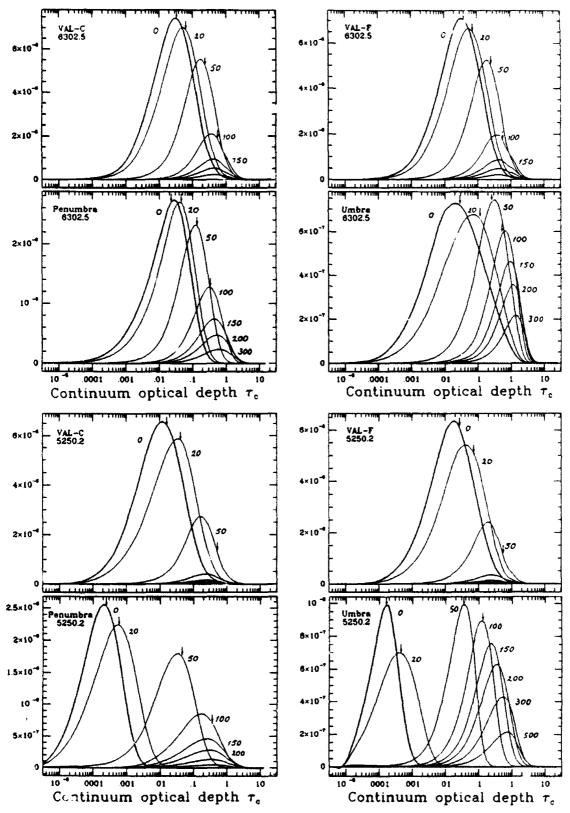


Figure 5: Field-free line depression contribution functions  $C_{R,I}$  for  $\lambda 6302.5$  Å (top half of figure) and  $\lambda 5250.2$  Å (bottom half) for all four models: VAL-C (upper left), VAL-F (upper right), penumbra (lower left) and umbra (lower right). The quantity actually plotted is not  $C_{R,I}$  but  $\tau_c I_c C_{R,I}(\Delta \lambda, \tau_c)$ . The labels for each curve specify the distance from line center in mÅ. All CF's are drawn on the optical depth scale of the adjacent continuum. Arrows indicate the corresponding  $\tau_{\nu}=1$  heights.

450 J. H. M. J. Bruls et al.

Table 2: Formation depths in terms of physical height h (in km) and continuum optical depth  $\tau_{in}$  at line center optical depth  $\tau_{in} = 1$ , and line to continuum opacity ratio  $\eta_0$  at continuum optical depth unity, all for the field-free case.

<u> </u>		VAL-C		<del></del> .	VAL-F	<del></del>	]	Penumb	ra		Umbra	
$\lambda$ (Å)	h	$\log  au_c$	$\eta_0$	h	$\log  au_c$	$oldsymbol{\eta}_{\mathrm{O}}$	h	$\log  au_c$	$\eta_0$	h	$\log  au_c$	$\eta_0$
LTE												
6302.494	249	-1.60	2.71	232	-1.50	2.64	194	-1.62	18.2	190	-1.50	13.9
6301.497	337	-2.21	8.04	314	-2.07	7.84	253	-2.19	54.9	321	-2.22	42.7
6173.338	276	-1.80	1.45	247	-1.61	1.40	276	-2.41	21.8	385	-2.55	37.8
5576.090	310	-2.06	4.93	288	-1.92	4.84	243	-2.13	39.9	302	-2.17	36.8
5434.521	556	-3.88	64.7	523	-3.54	63.0	596	-4.99	2006	752	-4.77	6943
5250.210	312	-2.10	0.47	259	-1.74	0.46	425	-3.74	24.1	590	-3.74	135
5247.059	319	-2.15	0.49	265	-1.78	0.48	431	-3.79	25.6	597	-3.78	147
8688.615	475	-3.21	22.9	437	-2.91	21.9	475	-4.09	333.	638	-3.97	575
15648.54	135	-1.40	1.81	126	-1.34	1.78	95	-1.42	13.2	19	-0.94	16.8
15822.81	188	-1.80	3.94	181	-1.74	3.88	117	-1.69	26.7	33	-1.17	33.7
NLTE												
6302.494	218	-1.39	2.70	209	-1.35	2.63	190	-1.58	18.3	183	-1.46	13.9
6301.497	294	-1.92	8.00	287	-1.87	7.81	245	-2.11	55.2	303	-2.13	42.7
6173.338	238	-1.54	1.44	223	-1.44	1.40	266	-2.31	21.9	386	-2.55	37.8
5576.090	272	-1.80	4.92	263	-1.74	4.82	238	-2.08	40.1	294	-2.13	36.8
5434.521	543	-3.80	64.4	532	-3.60	62.7	618	-5.11	2017	766	-4.85	6926
5250.210	260	-1.74	0.47	230	-1.54	0.45	406	-3.59	24.2	592	-3.75	134
5247.059	266	-1.78	0.49	236	-1.58	0.47	412	-3.64	25.8	598	-3.79	146
8688.615	432	-2.88	22.8	421	-2.79	21.8	461	-3.97	335	644	-4.01	573
15648.54	112	-1.25	1.81	107	-1.21	1.78	92	-1.39	13.2	18	-0.93	16.8
15822.81	156	-1.58	3.94	152	-1.54	3.88	111	-1.64	26.7	29	-1.13	33.7

also originates less deep than the line center radiation of the split line, but that depends sensitively upon the splitting pattern.

Fig. 6 shows  $C_{R,I}$  and  $C_{R,V}$  for the VAL-F model with  $B=1600\,G$  and  $\gamma=0^\circ$ . The longitudinal field suppresses the central  $\pi$ -component and creates a simple doublet profile for both  $\lambda6302.5$  Å and  $\lambda5250.2$  Å, with only left and right circularly polarized  $\sigma$ -components. The opacity difference between line center and the  $\sigma$ -components clearly shows up in both  $C_{R,I}$  and  $C_{R,V}$ : the radiation at wavelengths close to the centers of the  $\sigma$ -components ( $\Delta\lambda\approx75$  mÅ for  $\lambda6302.5$  Å,  $\Delta\lambda\approx50$  mÅ for  $\lambda5250.2$  Å) originates higher in the atmosphere than the line center radiation. The depth integral of  $C_{R,I}$  at line center is considerably smaller than at 50 or 100 mÅ from line center, so that the resulting Stokes I profiles (not shown) are clearly split. The field strength is such that the Zeeman splitting is about twice as large as the Doppler width. This is sufficient to get a clear (though incomplete) split in Stokes I, but insufficient to measure B directly from Stokes V splitting: the location of the Stokes V peaks is still nearly insensitive to the field strength (cf. Murphy 1990, p. 72).

Fig. 7 displays penumbral CF's. For  $\lambda 6302.5$  Å the  $C_{R,I}$  curves within 50 mÅ from line center show only small variation in depth of formation or depth integral (= total line depression). Since the Zeeman splitting for this line is 46.4 mÅ/kG and the inclination of the field is 75°, the magnetic field gives rise to a strong central  $\pi$ -component so that the Stokes I profile is not split; the magnetic field broadens the line and makes the core shallower. Towards the wings the CF's display non-magnetic behaviour, with a small shift deeper into the atmosphere which results from decreased line opacity. The  $\lambda 5250.2$  Å  $C_{R,I}$  curves are

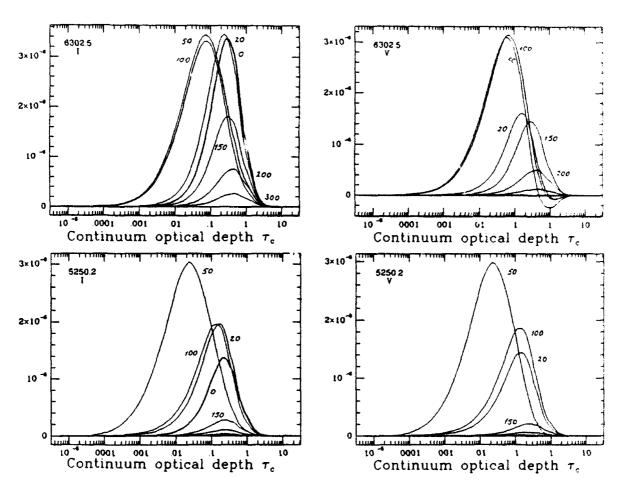


Figure 6: Line depression contribution functions  $C_{R,I}$  and  $C_{R,I'}$  for the VAL-F model for  $\lambda 6302.5$  Å (top panels) and  $\lambda 5250.2$  Å (bottom panels).  $C_{R,Q}$  and  $C_{R,U}$  are omitted because Stokes Q and U and the corresponding CF's are zero due to the longitudinal field. The labels for each curve indicate the distance from line center in mÅ measured towards the shorter wavelength side.

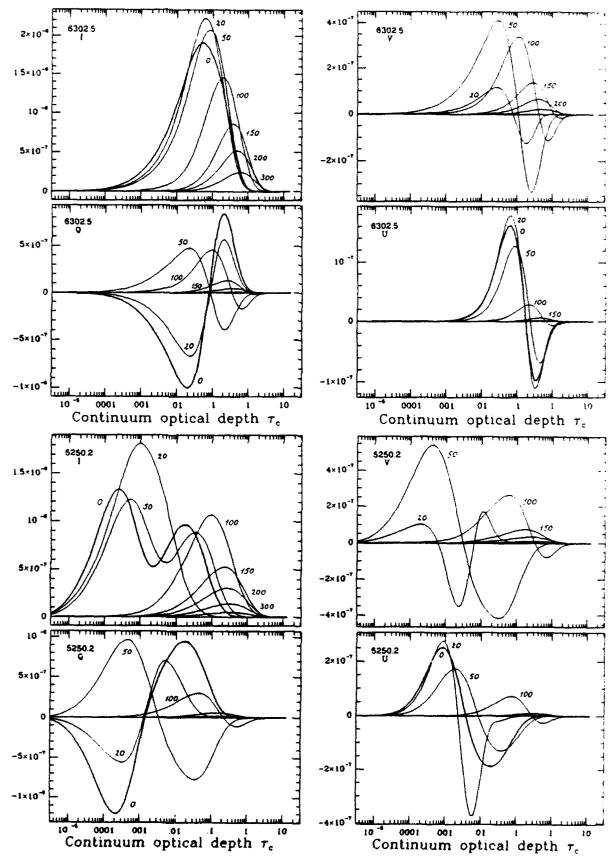


Figure 7: Line depression contribution functions  $C_{R,I}$ ,  $C_{R,Q}$ ,  $C_{R,U}$ , and  $C_{R,V}$  for  $\lambda 6302.5$  Å (top half of figure) and  $\lambda 5250.2$  Å ("ottom half) for the penumbra model. Labels as in Fig. 6.

doubly peaked near line center, except for the  $\Delta\lambda=20$  mÅ curve. This pattern results from the difference in formation heights for the two linear directions of polarization, which are prominently present due to the large field inclination. The presence of non-zero  $C_{R,C}$  values indicates that some Faraday rotation occurs for both lines.

In the umbral CF's for  $\lambda 6302.5$  Å (Fig. 8) the  $C_{R,I}$  curve at  $\Delta \lambda = 100$  mÅ is close to the center of a  $\sigma$ -peak and has a bump just below its maximum. That indicates that the formation heights of the two circularly polarized components are starting to separate. The linearly polarized components, which cause a similar but incomplete separation in the penumbra, are negligible due to the almost longitudinal field. This separation is better seen for  $\lambda 5250.2$  Å because the  $C_{R,I}$  curve for  $\Delta \lambda = 100$  mÅ has two completely separated peaks. The oscillatory character of the  $\lambda 5250.2$  Å  $C_{R,Q}$  and  $C_{R,U}$  curves is a strong indication that Stokes Q and U are dominated by magneto-optical effects. There is a tight relation between  $C_{R,Q}$  and  $C_{R,U}$  close to the line core, which is the part of the line that is most sensitive to magneto-optical effects, in the sense that  $C_{R,Q}$  has a maximum where  $C_{R,U}$  crosses zero and the other way around.  $C_{R,U}$ , especially for  $\Delta \lambda = 10$  mÅ (not shown), displays oscillatory irregularities with considerably smaller amplitude, pointing to interactions between circular and linear polarization. Although the oscillations are of numerical origin (Murphy, 1990) these relations suggest that multi-cycle Faraday-rotation is the most likely explanation of the oscillatory behaviour.

The good correspondence in Fig. 5 between the locations of the maxima of  $C_{R,l}$  and the  $\tau_{\nu}=1$  levels shows that both criteria give approximately the same 'depth of formation'. We therefore add the depth of formation for the other 8 lines in our study in Table 2, listing the location of line center optical depth unity in the field-free case. We caution the reader that this is not a very good representation of the depth of formation of lines that have a strongly developed Doppler core, formed much higher in the atmosphere than the line wings. Most of our lines indeed have such Doppler cores, especially for the cooler models. However, the  $\tau_{\nu_0}=1$  heights do indicate depths of formation of the centers of the strongest components of a magnetically split line; corrections for the smaller opacity per component can be applied straightforwardly by evaluating the fraction of the total opacity present in a particular component from the splitting pattern.

## 4 Conclusions

Medium excitation Fe I lines such as  $\lambda 6302.5$  Å represent better diagnostics than lines with low excitation energy such as  $\lambda 5250.2$  Å because they are less temperature sensitive: their line-to-continuum opacity ratio  $\eta_0$  is rather depth-independent within one model atmosphere, and it shows smaller variations from one model to another. For photospheric lines the assumption of an LTE source function is justified, but the line opacity depends on the overall ionization equilibrium which is model dependent.

The  $\lambda 6302.5$  Å line is formed at approximately the same geometrical height in all four models, which makes it an excellent choice for magnetic field measurements in the middle photosphere. The splitting of Stokes V is a direct measure of the field strengths only for field strengths at or above umbral values (cf. Lites and Scharmer 1989). At lower field strengths one has to use more indirect techniques, such as line ratios or profile fitting. The  $\lambda 5250.2$  Å line is a less suitable diagnostic because its formation height is very model dependent. Field strengths determined from  $\lambda 5250.2$  Å will not necessarily apply to the same physical height in different atmospheres.

Future work will focus on inversion of the line profiles that result from this analysis. The Lites-Skumanich inversion procedure derives a Milne-Eddington type atmosphere that reproduces observed Stokes profiles. Our goal is to establish the sensitivity of the derived atmospheric parameters, which are all depth-independent, to the depth-dependence of the actual parameters. It seems advantageous to invert lines that have little depth and model dependence. The  $\lambda 6302.5$  Å line satisfies this criterion better than  $\lambda 5250.2$  Å does.

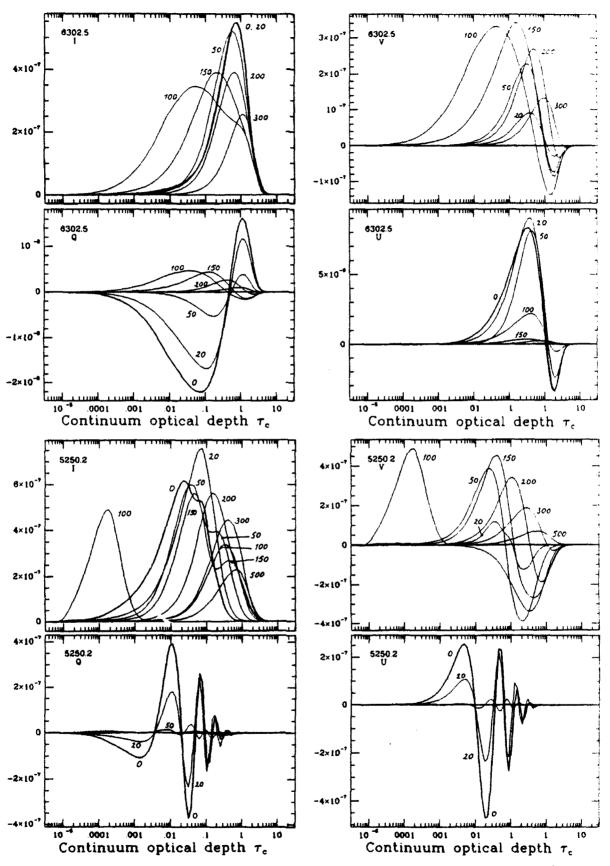


Figure 8: Line depression contribution functions  $C_{R,I}$ ,  $C_{R,Q}$ ,  $C_{R,U}$ , and  $C_{R,V}$  for  $\lambda 6302.5$  Å (top half of figure) and  $\lambda 5250.2$  Å (bottom half) for the umbra model. Labels as in Fig. 6.

## 5 References

Auer, L.H., Heasley, J.N., Milkey, R.W. 1972, Kitt Peak National Observatory Contr., 555

Avrett, E.H. 1990, in Heidelberg Conference on Mechanisms of Chromospheric and Coronal Heating, P. Ulmschneider (ed.), Springer, Berlin

Carlsson, M. 1986, Thesis. Uppsala Astronomical Observatory, Report, 33

Ding, M.D., Fang, C. 1989, Astron. Astrophys., 225, 204

Gigas, D. 1986, Astron. Astrophys., 165, 170

Grossmann-Doerth, U., Larsson, B., Solanki, S.K. 1988, Astron. Astrophys., 204, 266

Hofsäss D. 1975, J. Quant. Spectrosc. Radiat. Transfer, 15, 901

Lites, B.W. 1972, NCAR Cooperative thesis No. 28, Boulder

Lites, B.W., Scharmer, G.B. 1989, in High Spatial Resolution Solar Observations, O. von der Lühe (ed.), National Solar Observatory, Sunspot, N.M., p.286

Maltby, P., Avrett, E.H., Carlsson, M., Kjeldseth-Moe, O., Kurucz, R.L., Loeser, R. 1986, Ap. J., 306, 284

Murphy, G.A. 1990, NCAR Cooperative thesis No. 124, Boulder

Rees, D.E., Murphy, G.A., Durrant, C.J. 1989, Ap. J., 339, 1093

Scharmer, G.B., Carlsson, M. 1985, J. Comp. Phys., 59, 56

Skumanich, A., Lites, B.W. 1987, Ap. J., 322, 473

Steenbock, W. 1985, in Strassbourg Colloquium on Cool Stars with Excesses of Heavy Elements, M. Jaschek and P.C. Keenan (eds.), Reidel, Dordrecht

Unsöld, A. 1955, Physik der Sternatmosphären, Springer, Berlin

Vernazza, J.E., Avrett, E.H., Loeser, R. 1976, Ap. J. Suppl. Ser., 30, 1

#### Discussion

- **J. Staude**: Did you try calculations for simpler atomic models, such as those of Bruce Lites ( $\sim 1972$ )? Are there strong differences to the results from the more complex model?
- J. Bruls: Yes I did, though with slightly different model atom than I use here, and the differences are small. I believe it is mainly the ionization balance that can shift because of the added higher levels.
- J. Staude: What is the meaning of a negative contribution function?
- **J. Bruls**: Since Q, U, and V are differences of two orthogonal polarization states, we may expect their contribution functions to be bipolar as well.
- **K.S. Balasubramaniam**: How would you reconcile the factor of 2 difference in  $g_f$  for the FeI 6301.5Å and 6302.5Å lines?
- J. Bruls: I don't know; it may be that inhomogeneities make the adjustment unnecessary, but experiments I plan to do in the near future will have to tell.
- J. Stenflo: You say that a future aim is to improve the thermodynamic diagnostic instrumentation in the Lites-Skumanich inversion code. What type of improvement do you have in mind? The mentioned inversion code is based on a Milne-Eddington atmosphere with the parameter  $\eta_0$  depending on the thermodynamics. Do you plan to calibrate  $\eta_0$  in terms of the real physical parameters, e.g. the temperature at the height of line formation?
- A. Skumanich: Parameters in the Milne-Eddington representation yield average values. The heights to which these refer in the atmosphere needs to be calibrated. In addition the various other approximations. e.g. constant Doppler width, can be corrected for. Such a study has been done by Lites et al. for the strong Mgb line, and I refer you to that study.
- B. Lites: Besides quantifying the restrictions of the Milne-Eddington approximation when the inversion is presented with profiles from fully variable atmospheres, these simulations may be used to test revised versions of the inversion code which allow, for example, for variable line/continuum opacity ratios.

Canfield: How does one calculate a mean height of formation for Q, U, or V, which have contribution functions that are both positive and negative?

- J. Bruls: One should probably not speak about mean formation heights of Stokes Q, U or V because these are differences of orthogonal polarization states. One should look at one single state, by comparing also to the contribution function for Stokes I. In that case the sign changes in e.g.  $C_{R,V}$  disappear and we can speak of mean formation heights of left polarized light or right polarized light. Same for Q and U.
- S. Koutchmy: Is it correct to say that your results will not change in case we consider different kinds of stratification like in the case of 2 magnetic regions with a sub-hydrostatic vertical gradient of pressure?
- A. Skumanich: If the shape of the source function in optical depth is affected as well as the mean Doppler width, the results will change if not then not.

# Multiple Line Stokes Profile Inversion

Graham A. Murphy

High Altitude Observatory

National Center for Atmospheric Research

P.O. Box 3000

Boulder, Colorado, U.S.A.

Summary. Stokes vector observations of multiple spectral lines have generally concentrated upon multiplets. With the use of suitable multiplets, an inversion procedure's sensitivity to the magnetic field vector can be significantly increased. This paper presents the results of an analysis of three lines that share no special properties. The primary aim was to assess the self-consistency of the High Altitude Observatory's Stokes profile inversion technique. While self-consistency was confirmed, the results also suggest the feasibility of using a multiple line approach to study depth-dependence of magnetic fields on the Sun.

## I. Introduction

A number of authors have studied least-squares inversion of Stokes vector profiles to determine the magnetic field and thermodynamic parameters in the line formation region. Auer et al. (1977) fitted observed Stokes vector profiles with the analytic solution derived by Unno (1956). Their approach was limited to the field strength,  $|\mathbf{B}|$ , the field inclination,  $\gamma$ , the line center to continuum absorption coefficient (zero damping),  $\eta_0$ , and the Doppler width,  $\Delta\lambda_D$ , and neglected damping and magneto-optics. The importance of these latter effects was demonstrated by Skumanich and Lites (1985), who also included the field's azimuth,  $\chi$ , and the source function in the procedure. Both approaches entailed fitting the Stokes vector profile of a single line.

An important advance was made by the simultaneous inversion of multiplets, as described in Lites et al. (1988). This made it feasible to include an exponential term in the source function and correct for the effect of scattered light, as well as significantly increase the accuracy of the inversion generally. Such improvements are only possible when special relationships exist between the multiplets. These relationships allow essentially twice as much information to be processed at the cost of only one extra inversion parameter: the overall result being potentially a more stable and accurate inversion scheme.

Given a more general set of magnetically-sensitive spectral lines, the number of inversion parameters must be expanded in direct proportion to the additional information. There is thus generally no advantage in terms of stability. However, it is then possible to study depth-dependent behaviour if the physical trends are large enough to be distinguished from errors.

Alternately, a multiple line inversion can be applied to a more immediate problem: to test the self-consistency of the inversion procedure itself. The magnetic field vectors deduced from a pair of independent spectral lines should maintain a consistent relationship over a wide range of solar conditions: assuming that the lines do not interchange their relative levels of formation and that

<sup>&</sup>lt;sup>1</sup>The National Center for Atmospheric Research is sponsored by the National Science Foundation.

Table 1: Conditions for the Three Sets of Observations of McMath Region 15697.

G. A. Murphy

Data Set	04	07	15
Date	1978 Dec 09	1978 Dec 11	1978 Dec 14
Start (UT)	1713	1737	2101
Finish (UT)	1924	1900	2304
Latitude <sup>1</sup>	15.2° S	16.6° S	14.9° S
Carrington Longitude <sup>1</sup>	332.4°	332.5°	333.9°
$\mu^1$	0.70	0.92	0.88
Line of sight inclination1	46°	23°	28°
Dispersion (pm/pixel)	2.74	1.24	2.74
Pixels included	128	256	128
Minutes/spatial point	4.5	3.0	4.5

<sup>&</sup>lt;sup>1</sup>First raster point.

the magnetic field strength varies monotonically with height. (Both assumptions are likely to be valid under the conditions being studied.) A poor inversion scheme might then be indicated by either an absence of a relationship between a pair of lines or an erratic one. Since such a test can be conducted with observations, it complements single line analyses based upon synthesized data. While the latter can assess absolute accuracy, they depend upon modelling at some level and so might exclude significant effects.

The primary aim of this work was to confirm the self-consistency of the inversion scheme developed by Lites and Skumanich (1985a). This scheme has been extensively tested using synthesized and observed data. However, by comparing the magnetic field vectors deduced from three independent spectral lines, it was hoped to establish error levels in real conditions and discern whether problems existed in overall physical plausibility.

In the following section, aspects of the data used in this analysis are examined, including the data's source and limitations as well as difficulties introduced by the collecting instrument. To obtain Stokes profile data for three spectral lines, it was necessary to include two blended lines. The Stokes vector profiles of both blends were distorted by the presence of the strong central line. In §III the special methods developed to deal with the blending problem are discussed. In §IV the results of the inversion analysis are presented. Because of behaviour intrinsic to the formation of polarized radiation, the inversion parameters,  $|\mathbf{B}|$  and  $\gamma$ , are not displayed. Instead the longitudinal and transverse components of the magnetic field vector are presented, allowing trends to be more readily evaluated for weak Zeeman splitting. Finally in §V, the potential of a multiple line inversion to evaluate depth-dependence in the magnetic field vector is examined.

## II. Data

An obvious necessary condition to achieve a meaningful multiple line inversion is that the spectral lines should be formed co-spatially and be measured simultaneously. Any severe departures from this could result in an invalid interpretation of the results.

Observations of a sunspot suitable for analysis were made on three separate days by the High Altitude Observatory (HAO) Stokes I Stokes polarimeter. Each observation set involved a

Element	Fei	MgI	Tit
Wavelength (nm)	517.1610	517.2698	517.3749
Transition	$^3F_4 \rightarrow ^3F_4$	$^3P_1 \rightarrow ^3S_1$	$^3F_2 \rightarrow ^3F_2$
Landé $g_{\it eff}$	1.25	1.75	0.667
Atomic Weight	55.847	24.305	47.90
$12 + \log_{10}(\text{Rel. Abundance})$	7.57	7.42	5.13
gf	0.0525	1.41	0.0813
Excitation (eV)	1.48	2.71	0.00
Ionization (eV)	7.897	7.646	6.82

Table 2: ATOMIC DATA FOR THE THREE ABSORPTION LINES BEING STUDIED.

boustrophedonic scan of three lines, with nine measurements along each line, covering a total area approximately 40" by 10". Limitations of the instrument and the seeing restricted the spatial resolution to the order of 6". Because of the coarse spatial sampling and resolution, an accurate registration between the three days' observations was impossible, preventing any study of sunspot evolution. Accordingly, the three sets have been treated as being independent. The complete details of the circumstances of the observations are given in Table 1.

The original goal of the observations was to obtain the Stokes vector profiles of the MgIb line at 517.27 nm and of the associated multiplet at 518.3 nm. The formation of these strong chromospheric lines has been discussed at length in Lites et al. (1988). The importance of the 517.27 nm line for this work is that lines due to FeI and TiI occur in its blue and red wings, respectively. As MgIb and both blends exhibit the Zeeman effect strongly, these lines can meet the desired criteria for being co-spatial and were nearly simultaneously measured. Table 2 summarizes the atomic data for the three lines.

A number of problems were encountered with these data sets. One resulted from using blends rather than distinct lines: the MgIb line influences the Stokes profiles of the FeI and TiI lines. This is seen in Figure 1: the blends' peaks in Q, U, and V closer to the core of MgIb are generally lower in magnitude; the V signals are also displaced vertically. The task of correcting for these effects is discussed in the next section.

Further problems resulted from the limitations of the instrument used to obtain the data. The Stokes I polarimeter operated with a single detector so a complete scan in wavelength was required at each position. As noted in Table 1, the wavelength scan required at least three minutes, with the full data set taking about two hours. This led to large variations in seeing-induced noise not only between spatial points (as one might expect) but even between the three spectral lines. This also resulted in the three lines not being measured with the degree of simultaneity desired. However, any effects from this are likely to be dominated by the seeing-induced noise.

The instrument also had lower spatial resolution than desired for a study of this kind. By sampling a large area, a wide range of magnetic field strengths might be observed, making it difficult to discern real physical properties.

Finally, the spectral resolution available in two of the data sets was poor. Data sets 04 and 15 were both sampled at 2.74 pm: of the same order as the Doppler widths of the blends. This situation severely restricts the information available for fitting.

G. A. Murphy

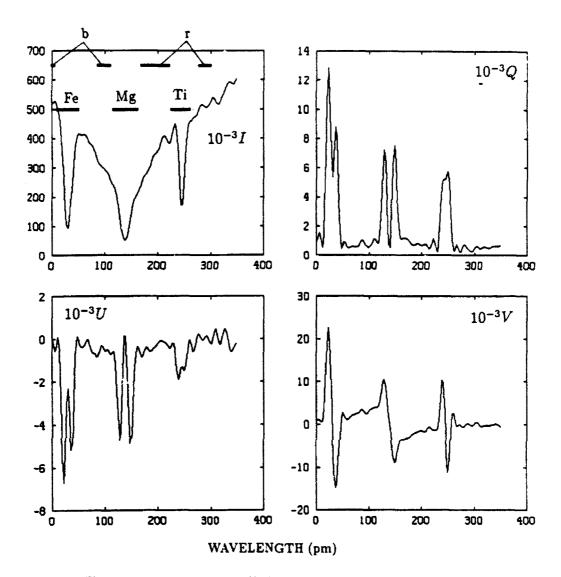


Figure 1: Stokes spectral profile for raster point 1 of the 15 data set. The bandpasses are indicated on the I profile: Fe, Mg, and Ti mark the bandpasses for the three lines; b and r mark the two parts of the blue and red Mg wing bandpasses, respectively. The MgI line induces in FeI and TiI offsets in the V profiles and asymmetry in the Q and U.

## III. Extension to the Profile Inversion Method

The details of least-squares inversion of Stokes vector profiles have been described at length in Lites and Skumanich (1985a, b). Only those aspects relevant to this problem will be discussed here.

The unusual features in the Stokes vector profiles of Fe I and Ti I lines shown in Figure 1 could lead to systematic errors if not corrected. When studying intensity profiles a technique commonly applied to compensate for blending involves fitting the continuum across the blend and rescaling to give an effectively flat continuum. Unfortunately, the interaction of polarized radiation does not permit such an approach. This is particularly apparent in V. Clearly for Stokes vector profiles, a

more sophisticated approach is necessary.

The most obvious solution would be to apply the least-squares inversion to all three lines simultaneously. While this would be the most satisfying, it would be complex and difficult to implement. The HAO inversion scheme employs a basic set of nine parameters for a spectral line so three lines would require about 27 parameters. However, it has been shown in Lites et al. (1988) that it is not possible to successfully fit both the core and the wings of a strong line such as MgIb because the wide physical range of thermodynamics cannot be adequately represented by an Unno-Rachkovsky model. Therefore a further nine parameters would be required to account for the MgIb wings, likely making the fitting process unmanageable. Moreover, a substantial rewriting of the inversion code would be required to handle this expanded problem.

A compromise was developed between the complexity of this latter technique and the need to represent the polarization's interaction.

A two-stage scheme was adopted. In the first stage, the MgI b line was fitted in three sections: the line core and the blue and red wings. The wings, excluding the blended region, were fitted individually to prevent introducing errors due to line asymmetries. The three separate fits to the core and wings of the Magnesium line were made with the usual Unno-Rachkovsky solution:

$$\mathbf{I} = B_0 \mathbf{I_0} + \mu B_1 \left[ \mathbf{1} + \eta_0 \mathbf{\Phi} \right]^{-1} \mathbf{I_0}. \tag{1}$$

There was no attempt to correct for scattered light or to include an exponential line source function: tests indicated that these provided no significant benefit for the single line profile inversions studied out here.

The MgIb core fit was used in the subsequent multiple line analysis. However, the fits to the wings were used only to correct the blends—the estimates of the magnetic field vectors were not extracted for further use. The Stokes vector radiative transfer equation for a spectral region that includes a blend can be written:

$$\mu \frac{d\mathbf{I}}{d\tau_c} = -\left(\mathbf{1} + \eta_0^{\text{MgW}} \mathbf{\Phi}^{\text{MgW}} + \eta_0^{\text{b}} \mathbf{\Phi}^{\text{b}}\right) \mathbf{I} + S_c \mathbf{I}_0 + S_l^{\text{MgW}} \eta_0^{\text{MgW}} \mathbf{\Phi}^{\text{MgW}} \mathbf{I}_0 + S_l^{\text{b}} \eta_0^{\text{b}} \mathbf{\Phi}^{\text{b}} \mathbf{I}_0,$$
(2)

where I is the Stokes vector at depth  $\tau_c$ ,  $S_l$  is the line source function,  $S_c$  is the continuum source function,  $\Phi$  is the absorption matrix, and  $I_0 = (1,0,0,0)^{\mathsf{T}}$ . (See Rees *et al.* 1989 for a more complete description of the terms.) The superscripts  $^{\mathsf{MgW}}$  and  $^{\mathsf{b}}$  denote terms associated with the wings of MgI or the blend, respectively. Note that the interaction between Iron and Titanium is taken to be negligible. By assuming that  $(\eta_0^{\mathsf{MgW}}\Phi^{\mathsf{MgW}} + \eta_0^{\mathsf{b}}\Phi^{\mathsf{b}})$  was constant with depth and that the source function terms could be represented as a linear function of  $\tau_c$ , the emergent Stokes vector could be written:

$$\mathbf{I} = B_0 \mathbf{I}_0 + \mu B_1 \left[ \mathbf{1} + \eta_0^{MgW} \mathbf{\Phi}^{MgW} + \eta_0^b \mathbf{\Phi}^b \right]^{-1} \mathbf{I}_0.$$
 (3)

In the second stage of the inversion process, the two blends were fitted separately using Equation (3), with the term,  $\eta_0^{MgW} \Phi^{MgW}$ , calculated directly from the respective wing fit rather than being inversion parameters. By virtue of the robustness of the routine, it was not necessary to adjust the derivatives of I for this change.

The procedure was found to work well. However, because of uncertainty in the determination of the thermodynamic parameters inherent in an Unno-Rachkovsky least-squares inversion, the blend correction was not as complete as desired. This led to errors that are discussed later.

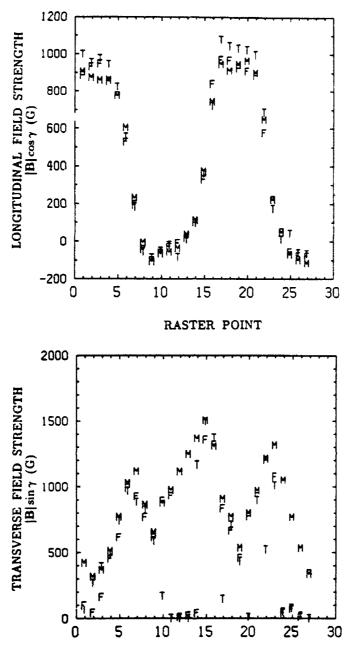


Figure 2: The longitudinal and transverse field strengths obtained from  $|\mathbf{B}|$  and  $\gamma$  for Fe1, Mg1, and Ti1 for the  $\theta i$  data set at each raster point. F - Fe1; M - Mg1; T - Ti1.

# IV. Results

The HAO inversion code includes the magnetic field strength and inclination in its parameter set so the initial examination of the results was done using these variables. Agreement between the three lines was generally good. However, at a number of points,  $|\mathbf{B}|$  for the blends was  $\approx 0\,\mathrm{G}$ , compared to  $\approx 1\,\mathrm{kG}$  from Magnesium, with corresponding discrepancies in the inclinations and azimuths.

The appearance of such differences suggested a fault in the inversion rather than some physical

interpretation. Three possible causes were investigated: (a) the inversion routine failing; (b) the blending-correction algorithm being inadequate; or (c) the high noise level of the data preventing good profile fitting.

Based upon a detailed examination of the fits, it was concluded that the last suggestion was the most likely. As the Magnesium line is much wider and stronger than either of the blends, its Stokes vector signal is less affected by noise. This generally resulted in good fits to this line even when the blends were poorly fitted. This difference was particularly apparent in linear polarization in which the peaks tend to be narrower and the signal much weaker than either the I or V Stokes parameters.

In the so called weak field case, the Zeeman splitting of a line is small compared to its Doppler broadening. In this regime, two approximations can generally be made: that  $V \propto |\mathbf{B}| \cos \gamma$  and that  $Q \propto |\mathbf{B}|^2 \sin^2 \gamma$  given  $\chi = 0$  (Stenflo 1985; Jefferies *et al.* 1989). These relations provide one link between the longitudinal component of the magnetic field,  $|\mathbf{B}| \cos \gamma$ , and the circular polarization, and another link between the transverse component,  $|\mathbf{B}| \sin \gamma$ , and the linear polarization. Since all the spectral lines in these data were weakly split, this suggests that errors in a particular polarization should appear predominantly in the associated magnetic field component.

Figure 2 confirms this prediction: the deduced fields are presented in terms of their longitudinal and transverse components. The longitudinal fields deduced from the three lines show excellent agreement at all field strengths. The transverse fields display the signature of the problem in fitting linear polarization discussed above: Iron or Titanium field strengths less than 200 G in contrast to much higher values from Magnesium. Points with these characteristics were discarded in the subsequent analyses as they were principally a product of the data sets' noise levels rather than features of the inversion.

It should be noted that Figure 2 demonstrates that in the weak-field regime  $|\mathbf{B}|\cos\gamma$  and  $|\mathbf{B}|\sin\gamma$  were the canonical variables to the inversion rather than  $|\mathbf{B}|$  and  $\gamma$ , even though the latter pair were actually used.

Additional insight may be gained from scatter plots comparing the three lines using all the data sets. In Figure 3, the longitudinal and transverse components from Fe I and Mg I b are compared. The longitudinal fields have a strong correlation at all field strengths, while the transverse fields display very good correlation but with more noise: this is to be expected given the greater noise sensitivity of the linear polarization previously discussed. Note that points where the blend fits failed appear near the horizontal axis (and should be ignored). The comparison of Ti I and Mg I b presented in Figure 4 is similar, though with still higher noise levels in the transverse component.

The HAO Inversion routine has proven to have a high level of self-consistency, as defined by the degree of correlation between the three lines being good in all but pathological cases. The relatively poor quality of the data makes it difficult to assess the true precision of the routine, though it would appear to be better than  $\pm 200\,\mathrm{G}$  in  $|\mathbf{B}|\cos\gamma$  and  $\pm 300\,\mathrm{G}$  in  $|\mathbf{B}|\sin\gamma$ . Overall from these results, the support is strong that Unno-Rachkovsky least-squares fitting of Stokes vector profiles can provide an effective means to estimate sunspot magnetic fields when Zeeman splitting is weak.

# V. Depth-dependence

It was noted in the introduction that multiple line Stokes vector profile inversion can be applied to the study of the depth-dependence of a sunspot's magnetic field. While the data studied did

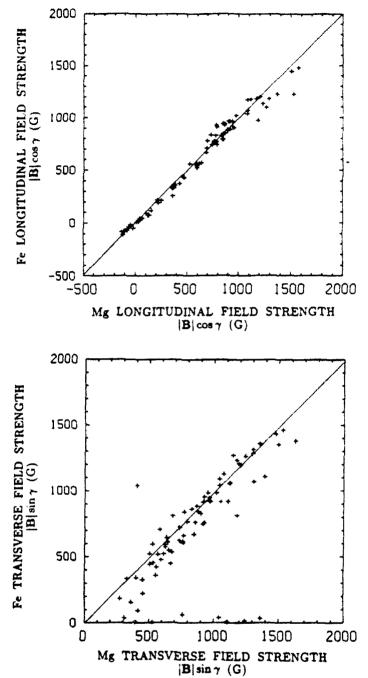


Figure 3: Comparison of the longitudinal and transverse field strengths between Fe 1 and Mg 1 for all data sets. Unit diagonals are shown.

not allow this to be done directly, statistical assessments can be used to gather the overall trends presented in Figures 3 and 4. The relationships are generally close to the unit diagonals indicated on the graphs both for Fe I to Mg I b, and also Ti I to Mg I b. Table 3 gives the best fits to the data using a linear relationship with zero intercept. All data with values less than 200 G have been excluded.

While the table suggests that there are differences in the magnetic field strengths deduced from the three lines, the physical interpretation is not straightforward. If the magnetic field strength

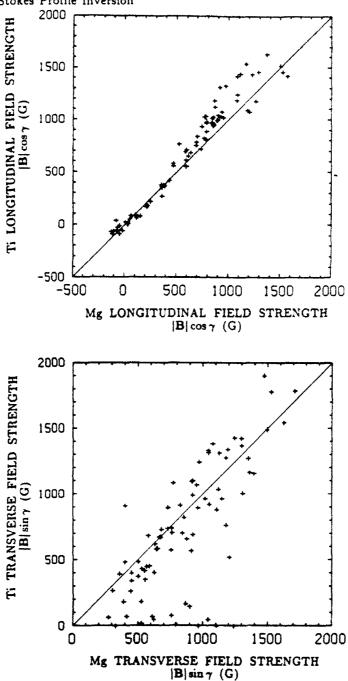


Figure 4: Comparison of the longitudinal and transverse field strengths between Ti I and Mg I for all data sets. Unit diagonals are shown.

increased with depth, the longitudinal components would imply that the FeI line is formed above MgIb and TiI below. However, this does not concur with the ratios for the transverse components.

Sunspot geometry might account for such a discrepancy. Therefore, simulations were conducted with a self-similar sunspot model (Murphy 1990) to provide a physically plausible magnetic field structure. In all the simulations, it was found that the increase in the field strength with depth was much greater than the change in field inclination. Accordingly, the ratios of longitudinal and transverse field strengths from any pair of lines should be equal to within a few percent—in

466 G. A. Murphy

Table 3: Ratios of the Longitudinal and Transverse Field Strengths. (Standard errors are shown.)

Field	Ratio	All data sets
	Fe/Mg	0.96 ±0.01
$ \mathbf{B} \cos\gamma$	Ti/Mg	1.11 ±0.02
	Fe/Mg	0.93 ±0.02
B sin $\gamma$	Ti/Mg	$0.98 \pm 0.03$

contradiction to the values presented in Table 3.

Such modelling cannot provide a definitive answer. However, detailed examination of the profile fits suggested that blending was only partially compensated in Q and U. This was apparently due to errors in the estimates of  $\eta_0^{\text{MgW}}$ —thermodynamic parameters are generally poorly determined with Unno-Rachkovsky based inversions. Using Stokes vector profiles synthesized from a solar atmosphere model, the partial compensation of the linear polarization was found to result in the transverse fields from the blends being under-estimated. This would result in the ratios for the transverse component being systematically lower than for the longitudinal field.

Assuming this occurred then the total magnetic field strength deduced from the TiI line was probably  $\approx 10\%$  greater than from MgIb, while FeI and MgIb were approximately the same. This could then be interpreted as implying that TiI was formed below MgIb, which is reasonable given that the TiI is likely to be a photospheric line. However, the FeI line was also expected to be formed in the photosphere (Lites et al. 1988) but the results do not agree with that proposition. Detailed non-LTE modelling of this particular line (for example, Bruls et al. 1990 in these proceedings) would be required to adequately answer this question.

Alternative explanations for the differences in the fields from the lines do exist. In particular, variations in the Landé g-factors from those predicted by Russell-Saunders coupling, or inequalities in the fill-factors for the three lines. However, there is no reason to suspect that LS coupling has failed for any of these lines, and evaluation of the relative intensities of the lines from the data indicate no systematic variations that would result in the observed behaviour.

#### VI. Conclusion

The self-consistency of HAO's least-squares Stokes profile fitting procedure has been demonstrated with a high level of confidence. Moreover, multiplet fitting should give more accurate results than the single line method applied here (Lites et al. 1988).

It has also been shown that it is feasible to fit more than one independent spectral line simultaneously, offering the potential for studying depth-dependence in detail. However, there is also a clear requirement that care be taken to avoid problems that could introduce systematic errors. In addition, questions that limit accuracy, such as variations in scattered light, need to be closely examined.

I thank Bruce Lites for his help in the preparation of this manuscript, and the High Altitude Observatory for its financial support through a Newkirk Graduate Research Assistantship during the period this research was conducted.

#### References

- Auer, L.H., Heasley, J.N., and House, L.L. 1977, Solar Phys., 55, 47.
- Bruls, J.H.M.J., Lites, B.W., and Murphy, G.A. 1990, in *Solar Polarimetry*, ed. L.J. November. (Sunspot, NM:National Solar Observatory), forthcoming.
- Jefferies, J.T., Lites, B.W., and Skumanich, A. 1989, Ap. J., 343, 920.
- Lites, B.W., and Skumanich, A. 1985a, in Measurements of Solar Vector Magnetic Fields, ed. M.J. Hagyard, NASA Conf. Publ. 2374 (Washington, DC:US GPO), p. 342.
- . 1985b, NCAR Technical Note, NCAR/TN-248+1A (Boulder, Co:National Center for Atmospheric Research).
- Lites, B.W., Skumanich, A., Rees, D.E., and Murphy, G.A. 1988, Ap. J., 330, 493.
- Murphy, G.A. 1990, NCAR Cooperative Thesis No. 124 (Boulder, Co:National Center for Atmospheric Research).
- Rees, D.E., Murphy, G.A., and Durrant, C.J. 1989, Ap. J., 339, 1093.
- Skumanich, A., and Lites, B.W. 1985, in Measurements of Solar Vector Magnetic Fields, ed. M.J. Hagyard, NASA Conf. Publ. 2374 (Washington, DC:US GPO), p. 341.
- Stenflo, J.O. 1985, in Measurements of Solar Vector Magnetic Fields, ed. M.J. Hagyard, NASA Conf. Publ. 2374 (Washington, DC:US GPO), p. 263.
- Unno, W. 1956, Publ. Astron. Soc. Jap., 8, 108.

#### Discussion

- R. Altrock: Is this technique insensitive to the strongly-inclined "continuum" level (wing of the Mg line) in the Fe and Ti lines? This will produce an asymmetric profile, even in the vicinity of the core.
- G. Murphy: Unfortunately, not as insensitive as I had wanted, as the wing fits did not accurately represent the Magnesium behavior. The asymmetric profiles in Q and U were not completely corrected for leading to an under-estimate of the transverse fields.
- J. Staude: Did you take into account the blending of all 3 lines in the synthesis of Stokes profiles which you calculated for comparison?
- G. Murphy: Yes, all three lines were included though I only had a detailed non-LTE model for Magnesium. An extended version of the DELO code (Rees et al. 1989) was developed to handle this synthesis problem.

#### CENTER-TO-LIMB VARIATION OF THE STOKES V ASYMMETRY IN SOLAR MAGNETIC FLUX TUBES

M. Bünte, O. Steiner, and S.K. Solanki

Institute of Astronomy, ETH Zentrum, CH-8092 Zürich, Switzerland

Summary. The center-to-limb-variation (CLV) of synthetic Stokes V line profiles of the spectral line Fe I 5250.22 A is presented and compared with observations. These synthetic profiles are calculated using models that contain the main features of the current basic picture of small scale magnetic fields on the sun. This basic picture consists of a flux tube in magnetohydrostatic equilibrium, which is separated from the surrounding non-magnetic atmosphere by a thin current sheet. Whereas the magnetic plasma is considered to be at rest the non-magnetic plasma is in convective motion which results in cool downflows along the flux tube boundary and warm upflows further away from it. The area asymmetry of Stokes V profiles observed at disk center can be explained by the presence of such non-magnetic downflows close to the boundary of the expanding flux tube. This mechanism also accounts for the unshifted zero-crossing wavelength of the Stokes V profiles. It is shown that the basic picture outlined above also reproduces the peculiar center-to-limb variation of the Stokes I asymmetry, in particular the sign reversal of the asymmetry near the limb (at  $\mu \simeq 0.4$  for Fe I 5250.22 A). The ingredients of the model mainly responsible for the sign reversal are identified. The fact that the agreement between theoretical and observational Stokes V profiles improves as more realistic features (like the temperature-velocity correlation of the granulation) are added to the model, leads us to conclude that the basic picture is correct and that the Stokes V parameter for small values of  $\mu$ . i.e. near the limb, has the potential to serve as a sensitive diagnostic of convection in active regions

#### 1. Introduction

Although most of the photospheric magnetic fine structure can still not be spatially resolved by observations, it can be studied indirectly through the spectro-polarimetric signature of the Zeemann effect on atomic lines formed in photospheric magnetic fields. In this context the directly observable Stokes parameters I, Q, U, and V of a spectral line have proven to be a powerful tool in deriving semi-empirical models of photospheric magnetic elements in plages and the network (see reviews by Solanki, 1987b; Stenflo, 1989). Such investigations have led to the following basic picture of the photospheric magnetic field. It is thought to be concentrated into kilo Gauss flux tubes that are situated in the dark and downflowing intergranular spaces as a consequence of flux expulsion (see e.g. Schüssler, 1990). Although the individual flux tubes are surrounded by downflowing gas, there is no sizeable downflow within them. In the photospheric layers flux tubes spread rapidly with increasing height due to the exponentially decreasing gas pressure until they merge and fill almost the entire atmosphere above the merging height.

One remarkable feature of Stokes V profiles observed in active region plages and the quiet solar network is their pronounced asymmetry (Stenflo et al., 1984; Wiehr, 1985). Near disk center the area and amplitude of the blue wing exceed those of the red wing by several percent (Solanki and Stenflo. 1984), i.e.  $\delta A = (A_b - A_r)/(A_b + A_r) > 0$  and  $\delta a = (a_b - a_r)/(a_b + a_r) > 0$ , where  $A_b$ ,  $A_r$  denote the areas.

 $a_b$ ,  $a_r$  the amplitudes of the blue and red wing, respectively. For LTE. Auer and Heasley (1978) have shown that the area asymmetry can only be explained in terms of velocity gradients. The first mechanism based on velocity gradients was proposed by Illing et al. (1975) and relied on the overlap of gradients in magnetic field strength and velocity. However, if we accept the current basic picture outlined above, in particular that the field strength decreases with height, then, as shown by Solanki and Pahlke (1988), a stationary flow within the magnetic flux tube implies a shift of the zero-crossing wavelength of the Stokes V profile larger than the observed upper limit of  $\pm 250 \text{ ms}^{-1}$  (Stenflo and Harvey, 1985; Solanki, 1986; Stenflo et al., 1987; Wiehr, 1987; Solanki and Pahlke, 1988). Other combinations of overlapping magnetic and velocity gradients have been proposed which can also produce asymmetric Stokes V profiles with only small zero-crossing shifts (Sánchez Almeida et al., 1988, 1989). However, such combinations invariably contradict the basic picture outlined above, since they require the field strength to increase with height. Van Ballegooijen (1985) pointed out that plasma flows in the non-magnetic surroundings of the flux tubes may also produce asymmetric Stokes V profiles. Grossmann-Doerth et al. (1988–1989) then showed that if the velocity and the magnetic field are spatially separated, as proposed by Van Ballegooijen (1985), asymmetric, but unshifted, Stokes V profiles are produced.

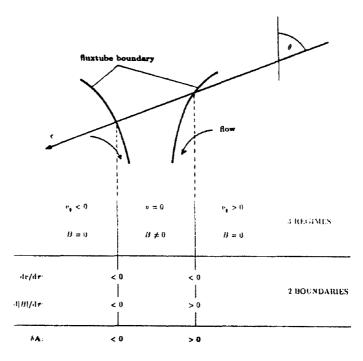


Fig. 1. Schematic illustration of the line of sight gradients of the magnetic and velocity fields for a highly inclined ray passing through a flux tube. According to Eq. (1) the contributions to the Stokes V asymmetry from the two intersections of the ray with the flux tube boundary counteract.

Solanki and Pahlke (1988) pointed out that the sign of the Stokes V area asymmetry depends on the signs of the line of sight gradients of the magnetic and the velocity fields alone:

$$\frac{d|\mathbf{B}|}{d\tau} \frac{dv(\tau)}{d\tau} \begin{cases} < 0, \implies \delta A > 0, \\ > 0, \implies \delta A < 0. \end{cases}$$
(1)

Note that only the absolute value of the magnetic field is of importance, not its polarity, whereas the sign of the velocity plays a vital role. At solar disk center in the standard picture the observer's line of sights only pass from the magnetic into the non-magnetic atmosphere, but not the other way around.

Closer to the limb, however, a particular ray may cross the border between magnetic and non-magnetic regimes in both directions. Such a case is schematically illustrated in Fig. 1. If we assume the same velocity fields on both sides of the flux tube profile then the Stokes V asymmetries produced at the two interfaces will, in general<sup>1</sup>, be of opposite sign. It is therefore not obvious whether the basic picture can account for the change in sign of the area asymmetry near the limb observed for Fe I 5250.22 Å by Stenflo et al. (1987) and for a larger sample of spectral lines by Pantellini et al. (1988). The aim of the present study is to find out under what conditions the area asymmetry changes sign near the limb. We also aim to obtain an idea of the diagnostic potential of the center-to-limb variation (CLV) of  $\delta A$ . In the present investigation we restrict our attention to the area asymmetry  $\delta A$  since the mechanism for its production at disk center is well understood. The amplitude asymmetry  $\delta A$  in contrast, may be produced or changed by a much larger variety of causes (e.g. velocity changes along the line of sight, perpendicular to it, or in time, macroturbulence, etc.), so that its production, even at disk center, is still partially unclear.

#### 2. The model

The basic structure of our model is shown in Fig. 2. A rotationally symmetric flux tube in magneto-hydrostatic equilibrium is surrounded by non-magnetic plasma in stationary motion. The magnetic field is calculated by numerically solving the force balance equation including all tension forces. For further details regarding various aspects of the magnetohydrostatic solutions we refer to Steiner et al. (1986). We prescribe the gas temperature, pressure and density in the interior of the flux tube according to the plage model of Solanki (1986).

In the photosphere the magnetic pressure and the gas pressure are comparable in magnitude, i.e.

$$\frac{B^2}{8\pi} \simeq p_{\text{gas}}.\tag{2}$$

For subsonic motions of a plasma with  $v^2/C_s^2 = 2p_{\rm dyn}/(\gamma p_{\rm gas}) \ll 1$ , the dynamic pressure is small compared to the gas pressure, so that by virtue of Eq. (2) the contribution of the former to the total pressure outside the flux tube can be neglected without changing the magnetic field structure noticeably. In the photosphere where typical maximal flow speeds are of the order of  $10^5$  cm/s this approximation seems to be justified which simplifies the numerical procedure considerably.

In the non-magnetic surroundings of the flux tube we initially prescribe an atmosphere similar to the quiet sun model, the HSRA (Gingerich et al., 1971), but systematically cooler by 300 K. Such an atmosphere provided the best fit to the observed  $\delta A$  values of four spectral lines at disk center (Solanki. 1989).

In addition various velocity fields are constructed which mimic some features of typical granular flow fields at various levels of sophistication. For example, we consider a pure downflow, following investigations of  $\delta A$  at disk center (Grossmann-Doerth et al., 1988, 1989 Solanki, 1989), or a purely horizontal inflow, i.e. a flow towards the flux tube axis. Of course, these velocity fields are unphysical, but help to identify some basic effects.

For a more physical representation, in a next step we calculate an irrotational downflow in the closer environment of the flux tube boundary (i.e. in a region  $R(z) \le r \le [W+R(0)]/2$ , where R(z) is the flux tube radius at height z, 2W the distance between two neighbouring flux tubes, and R(0) the radius at height z = 0, i.e.  $r_{5000} = 1$  in the non-magnetic atmosphere at disk center). The flow pattern is determined by the equation of continuity which poses a nonseparable elliptic boundary value problem for the velocity potential (Bünte, 1989). For an adequate choice of the boundary conditions the resulting velocity field can serve as an approximation to the intergranular downflow resulting from convection models, such as those of Steffen et al. (1989), but at much lower computational costs.

<sup>&</sup>lt;sup>1</sup> The velocity field must have sufficiently strong horizontal components for this to be valid.

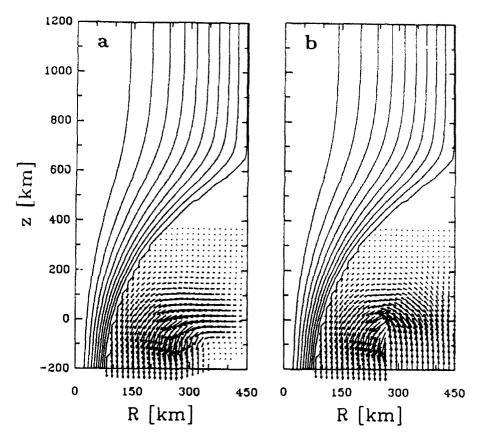


Fig. 2. Rotationally symmetric magnetic flux tubes in magnetohydrostatic equilibrium surrounded by non-magnetic plasma with two different stationary velocity fields. In Fig. 2a the flow is purely horizontal further away from the tube wall, whereas in Fig. 2b an upflow motion in that region prevails. Both flux tubes have a magnetic field strength of 1600 G, a radius of 100 km and a filling factor of 5 %. All these values refer to z = 0 ( $r_{0000} = 1$  in the quiet sun at disk center). Maximum flow velocities are  $\approx 4 \text{ km/s}$ .

In the outer part of the non-magnetic region (i.e. for  $[W+R(0)]/2 \le r \le W$ ) we either prescribe purely horizontal velocities which drop to zero at r=W (the radial scale of our model), as shown in Fig. 2a, or an upflowing velocity field, which is simply the mirror-image of the downflow but with a reversed z-component (see Fig. 2b). The latter case very roughly resembles a granular flow pattern (Steffen et al., 1989) or the baroclynic convection cell bordering the flux tube model of Deinzer et al. (1984). As a final step in the direction of realism we have introduced a correlation between velocity and temperature. This correlation consists of a velocity dependent temperature rise in upflow regions, e.g. in the following way:

$$T(z) = \begin{cases} T_{\text{HSRA}}^*(z), & \text{in downflow regions,} \\ T_{\text{HSRA}}^*(z) + \frac{v_z}{v_{z \text{ max}}} \Delta T, & \text{in upflow regions,} \end{cases}$$
(3)

where  $v_{z \text{ max}}$  is the maximum upflow velocity (typically  $\approx 3.8 \text{ km/s}$ ) and  $T_{\text{HSRA}}^*(z) = T_{\text{HSRA}} - 300 \text{ K}$ . For  $\Delta T$  we have chosen values of typically 500 - 1000 K for consistency with the 3-D model calculations of Nordlund (1985, Fig. 4b) and the most recent 2-D results of Steffen (1990).

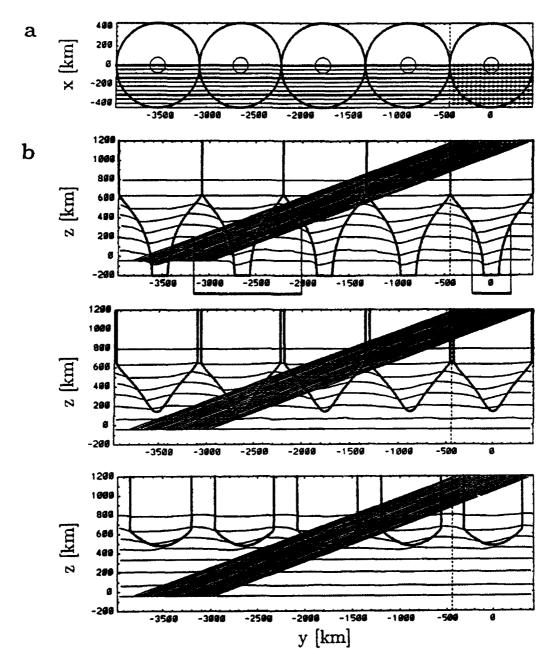


Fig. 3. Illustration of the model geometry for Stokes V calculations near the limb. a An array of merged flux tubes as seen from above (thick circles). Each horizontal line is the projection of a vertical plane cutting the model (the thick lines represent the planes shown in Fig. 3b). Each point to the right of the dashed line is the entry point into the top of the model of a ray lying in one of the vertical planes. b Illustration of the three vertical cuts that were indicated in Fig. 3a. The first frame represents the plane of symmetry (upper thick line in Fig. 3a), the middle and bottom frames correspond to the lower two heavy lines in Fig. 3a. The rays entering the model to the right of the dashed line for an "observation" close to the limb ( $\theta = 70^{\circ}$ , i.e.  $\mu = 0.34$ ) are visible as the group of stanted parallel lines. The thick lines are the contours where the flux tubes intersect with the vertical planes. The thin horizontal lines represent surfaces of equal optical depth  $\tau$ , in steps of  $\Delta \log \tau = 1$  from  $\log \tau = -6.0$  to +1.0. For a spectral line which is formed in the layer  $-3 \lesssim \log \tau \lesssim -1$  the horizontal range affecting Stokes V on both sides of a given flux tube is indicated below the first frame, for observations near the limb (left) and at disk center (right).

#### 3. Calculation of the Stokes parameters at different disk positions

The computation of the hydromagnetic parameters (cf. Sect. 2) is followed by a diagnostic procedure which serves to determine the spectral signature of the model, i.e. the values of the emergent Stokes parameters. In the present contribution we are only interested in Stokes V.

The diagnostics involve two steps: (1) First the atmospheric quantities must be determined along a number of parallel rays (line of sight) passing at an angle  $\theta$  (to the vertical) through the model. Only the line profiles averaged over all rays are finally compared with the spatially unresolved observations (1.5-D radiative transfer). Since flux tubes often come in groups we have assumed a periodic arrangement with a fixed filling factor at z=0. This is an important aspect, since close to the limb a ray may pass through more 'han one single flux tube (see below). Fig. 3a shows the "merged" magnetic flux tubes from above. In reality, of course, flux tubes lose their identity as they merge, in particular the rotational symmetry breaks down and the field should also fill the gaps between the circles in Fig. 3a. However, the spectral line under consideration (Fe I 5250.22 Å) is formed in layers well below the height where merging occurs, so that the topological details of merging fields do not have to be taken into account.

A set of parallel planes, one of which contains the symmetry axes of the tubes, are chosen (indicated by the horizontal parallel lines). Each of the dots on these lines is the beginning of one particular ray which lies in the corresponding plane and forms an angle  $\theta$  with the vertical of the atmosphere. Along each ray a set of points is chosen on the basis of an adaptive step size procedure with respect to the logarithm of the optical depth  $\tau$ .

Fig. 3b shows sets of rays through three different planes of the model. The code used to place the rays and evaluate the atmospheric data along them is a greatly modified and extended version of the one described by Ringenbach (1987) and De Martino (1986). For the current work typically  $10 \times 19$  rays are laid through the model (cf. Fig. 3a). In the following we consider a cluster of magnetic flux tubes with a field strength of 1600 G, a diameter of 200 km, and a filling-factor of 5%, all values given at z=0. The fields merge at a height of approximately 650 km. The non-magnetic plasma in between the flux tubes is in stationary motion (with maximum velocities of  $\approx 4$  km/s).

(2) The Stokes parameters for a particular spectral line are calculated numerically in LTE along each ray using a code based on the one described by Beckers (1969 a,b). For more details, see Solanki (1987a). Finally, all the calculated profiles are added together. The resulting Stokes V profiles can be directly compared with observations.

#### 4. Results

In the following we briefly describe the steps we have taken to test various mechanisms which may be responsible for the center-to-limb variation of  $\delta A$ .

- (1) As  $\theta$  is changed, so is the angle between the line of sight and the magnetic field, so that the  $\pi$ -component of the line becomes more prominent near the limb. It is this effect which is mainly responsible for the CLV of  $\delta A$  found by Auer and Heasley (1978). To test the importance of this effect we first calculated the CLV using the model described in Sect. 2, but with only pure downflows in the surroundings of the flux tubes, so that the observed  $\delta A$  at disk center is reproduced. This model completely fails to reproduce the observed CLV of  $\delta A$ . The calculated  $\delta A$  remains strictly positive and actually increases towards the limb.
- (2) While observations at disk center are only sensitive to the vertical component of the velocity field its horizontal component becomes relevant for observations closer to the limb. Schüssler (1990) proposed that this is the main mechanism giving rise to the change in sign of  $\delta A$ . However, this is not a priori clear, since Fig. 1 illustrates that as one follows a typical line of sight the areas around the two points where it enters and leaves a flux tube give opposite contributions to  $\delta A$ . In this step we therefore considered a purely horizontal inflow in the non-magnetic surroundings of the tubes. Of course  $\delta A = 0$  at  $\mu = 1$ . At the limb  $\delta A$  is small but positive in our calculations. We therefore conclude that

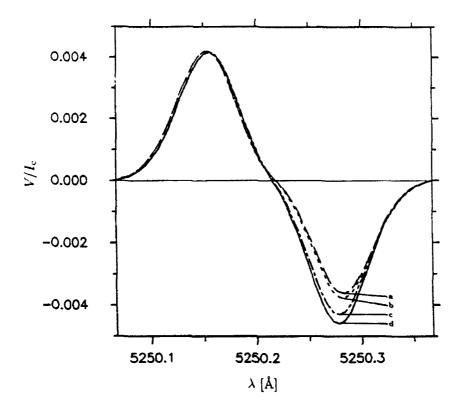


Fig. 4. Stokes V profiles of Fe I 5250.22 Å at  $\theta = 70^{\circ}$  ( $\mu = 0.34$ ) arising from an array of flux tubes (see Figs. 2 and 3). Different profiles correspond to different velocity fields that were used in steps 1-6 (Sect. 4). Curve a: inflow and downflow without any upflow (step 3); curve b: upflow instead of inflow in the outer parts of the model (step 4), curve c: like curve b, but including a temperature-velocity-correlation (step 5), curve d: like curve c, but with enhanced horizontal velocity components (step 6).

the presence of a horizontal inflow by itself is not sufficient to produce the observed sign reversal. although it turns out to be a necessary ingredient (within the confines of the basic picture).

- (3) In a third step we have combined an inflow with a downflow, as illustrated in Fig. 2a. Again, although the observations at disk center may be reproduced, the asymmetry does not change sign near the limb.
- (4) Next an upflow has been introduced, leading to a model of type shown in Fig. 2b. This model, finally, reproduces the observed (positive)  $\delta A$  at disk center, and, at the same time, yields a negative  $\delta A$  near the limb. However,  $\delta A$  changes sign only very close to the limb ( $\mu \approx 0.2$ ) for Fe I 5250.22 Å and does not drop below -1% to -2% for  $\mu \gtrsim 0.1$ , whereas observations show the sign reversal at  $\mu \approx 0.4$  and values of -5% to -10% for  $0.1 \le \mu \le 0.3$ . Apparently some important ingredient is still missing in the models.
- (5) In a next step a temperature-velocity-correlation of the type described in Sect. 2, Eq. (3) has been added, i.e. a warm upflow and a cool downflow. This model is able to produce both a large positive  $\delta A$  at  $\mu = 1$  and a large negative  $\delta A$  for small values of  $\mu$ .
- (6) Finally, the behaviour of the asymmetry can be considerably influenced by changing the ratio of the maximum horizontal flow velocity to the maximum up—, respectively, downflow component. Enhanced horizontal velocities result in more pronounced negative values of  $\delta A$  near the limb if the temperature and the velocity are correlated as in step 5.

The effect on the line profile of some of the steps described above are illustrated in Fig. 4 which shows calculated Stokes V profiles of the line Fe I 5250.22 Å at  $\mu = 0.34$ , i.e. at an angle  $\theta = 70^{\circ}$ . At this

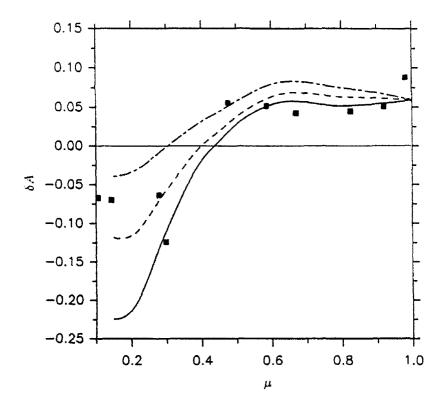


Fig. 5. Observed (squares) and calculated (curves) center-to-limb variation of the relative area asymmetry of Stokes V profiles of Fe I 5250.22 Å. The velocity fields used consist of a cool downflow near the flux tube boundary and a warm upflow further away from it (dashed curve, step 5). The dot-dashed curve results for suppressed, the solid curve for enhanced horizontal velocities (step 6).

position on the solar disk (close to the limb) the area asymmetry of the observed Stokes V profile has already changed sign, i.e. the red wing dominates the blue. The synthetic profiles in Fig. 4 all result from the same magnetic field configuration but from different velocity fields in the non-magnetic atmosphere between the flux tubes. Curve a represents the results from step 3, curve b corresponds to step 4, curve c to step 5 (where in comparison to step 4 a temperature-velocity-correlation has been introduced), and curve d shows the effect of enhancing the horizontal velocities by a factor of two while leaving the vertical components and the associated temperature structures unchanged (step 6).

Having identified some of the main parameters controlling the CLV and the sign reversal of  $\delta A$ , we have compared the synthetic profiles with the observations. Only the results of steps 5 and 6 are discussed further. Fig. 5 shows the observed (squares, data taken from Stenflo et al., 1987) and calculated relative area asymmetry of the Stokes V profiles of the line Fe I 5250.22 Å as a function of  $\mu = \cos \theta$ . The dashed curve corresponds to the  $\delta A(\mu)$  produced with the model of step 5. The maximum horizontal inflow is 2.9 km/s, the maximum vertical velocity components are 3.8 km/s. The  $\Delta T$  parameter of Eq. (3) is chosen to be 1000 K. The solid curve results when the horizontal velocity component is enhanced by a factor of 2, while the dot-dashed curve is obtained if the horizontal velocity is reduced by the same factor. The correspondence of these models to the observations is gratifying.

#### 5. Conclusions

The center-to-limb variation of synthetic Stokes V line profiles of the spectral line Fe I 5250.22 A has been investigated. The underlying hydromagnetic model consists of a cluster of rotationally symmetric magnetic flux tubes surrounded by granular non-magnetic plasma in stationary motion. From the variation of the velocity fields we come to the following conclusions:

- 1. Velocity fields in the non-magnetic environment are able to quantitatively reproduce not only the observed Stokes V area asymmetry ( $\delta A$ ) of Fe I 5250.22 Å at disk center, but also its center-to-limb variation including the sign reversal of the asymmetry around  $\mu = 0.4$  ( $\theta \simeq 60^{\circ}$ ).
- 2. The closer the assumed non-magnetic atmospheric dynamics (in the environment of the flux tubes) correspond to the solar granulation (i.e. warm central upflows, strong horizontal velocities, and cool downflows), the better the observed center-to-limb behaviour of the Stokes V asymmetry &A is reproduced. This is a sign that the basic picture of magnetic flux tubes and of their relations to the surroundings outlined in Sect. 1 is correct.
- 3. The center-to-limb variation of the area asymmetry of Stokes V profiles can be used as a sensitive tool for investigating the velocity and temperature structure of the granulation in solar active regions.
- 4. The temperature-velocity-correlation of granular convective motions is an essential ingredient for reproducing the observed  $\delta A$  away from disk center.
- 5. The calculated line profiles do not show any shift of the zero-crossing wavelength at any position on the disk, in agreement with the observations of Stenflo et al. (1987), Pantellini et al. (1988), and Wiehr (private communication). This is a direct result of the fact that the present models do not include any velocity within the magnetic features. As proved by Grossmann-Doerth et al. (1988, 1989) such a segregation of velocity and magnetic fields always leaves the V profiles unshifted, irrespective of the geometrical details. However, we do foresee possible problems for mechanisms which make use of velocities within the flux tubes to produce a non-zero δA and rely on special geometries to keep the zero-crossing shift small, since the geometry of the field and of the velocity along the line of sight is strongly dependent on θ. For example, near disk center the main contribution to the Stokes V signal comes from rays which remain completely within the magnetic features, Solanki, 1989), whereas near the limb every ray passes at least partially through the non-magnetic atmosphere.

Acknowledgements. We thank J.O. Stenflo for helpful discussions and careful reading of the manuscript. The work of two of us (M.B. and O.S.) has been supported by grant No. 20-26'436.89 of the Swiss National Science Foundation.

#### References

Auer, L.H., Heasley, J.N.: 1978, Astron. Astrophys. 64, 67.

Beckers, J.M.: 1969a, Solar Phys. 9, 372.

Beckers, J.M.: 1969b, Solar Phys. 10, 262.

Bünte, M.: 1989, Diplomarbeit, ETH Zürich.

Deinzer, W., Hensler, G., Schüssler, M., Weisshaar, E.: 1984, Astron. Astrophys. 139, 435.

De Martino, S.: 1986, Diplomarbeit, ETH Zürich.

Gingerich, O., Noyes, R.W., Kalkofen, W., Cuny, Y.: 1971, Solar Phys. 18, 347.

Grossmann-Doerth, U., Schüssler, M., Solanki, S.K.: 1988, Astron. Astrophys. 206, L37.

Grossmann-Doerth, U., Schüssler, M., Solanki, S.K.: 1989, Astron. Astrophys. 221, 338.

Illing, R.M.E., Landman, D.A., Mickey, D.L.: 1975, Astron. Astrophys. 41, 183.

Nordlund, A.: 1985, in H.U. Schmidt (Ed.), Theoretical Problems in High Resolution Solar Physics, Max. Planck Inst. f. Astrophys., München, p.1.

Pantellini, F.G.E., Solanki, S.K., Stenflo, J.O.: 1988, Astron. Astrophys. 189, 263.

Ringenbach, A.: 1987, Diplomarbeit, ETH Zürich.

Sánchez Almeida, J., Collados, M., Del Toro Iniesta, J.C.: 1988, Astron. Astrophys. 201, L37

Sánchez Almeida, J., Collados, M., Del Toro Iniesta, J.C.: 1989, Astron. Astrophys 222, 311.

Schüssler, M.: 1990, in J.O. Stenflo (Ed.), Solar Photosphere: Structure, Convection, and Magnetic Fields, IAU Symp. 138, 161.

Solanki, S.K.: 1986, Astron. Astrophys. 168, 311.

Solanki, S.K.: 1987a, Ph.D. Thesis, ETH Zürich.

Solanki, S.K.: 1987b, in E.-H. Schröter, M. Vázquez, A.A. Wyller (Eds.), The Role of Fine-Scale Magnetic Fields on the Structure of the Solar Atmosphere, Cambridge University Press, p.67.

Solanki. S.K.: 1989, Astron. Astrophys. 224, 225.

Solanki, S.K., Pahlke, K.D.: 1988, Astron. A. 'cophys. 201, 143.

Solanki, S.K., Stenflo, J.O.: 1984, Astron. Assorblys. 140, 185.

Steffen, M.: 1990, in L. Crivellari, I. Hubeny (Eds.), Stellar Atmospheres: Beyond Classical Models. Kluwer, Dordrecht, (in press).

Steffen, M., Ludwig, H.-G., Krüß, A.: 1989, Astron. Astrophys. 213, 371.

Steiner, O., Pneuman, G.W., Stenflo, J.O.: 1986, Astron. Astrophys. 170, 126.

Stenflo, J.O. 1989, Astron. Astrophys. Rev. 1, 3.

Stenflo, J.O., Harvey, J.W.: 1985, Solar Phys. 95, 99.

Stenflo. J.O., Harvey, J.W., Brault, J.W., Solanki, S.K.: 1984, Astron. Astrophys. 131, 33.

Stenflo, J.O., Solanki, S.K., Harvey, J.W.: 1987, Astron. Astrophys. 171, 305.

Van Ballegooijen, A.A.: 1985, in H.U. Schmidt (Ed.), Theoretical Problems in High Resolution Solar Physics, Max Planck Inst. f. Astrophys., München, p.177.

Wiehr. 21: 1985, Astron. Astrophys. 149, 217.

Wiehr, E.: 1987, in J.L. Linsky, R.E. Stencel (Eds.) Cool Stars, Stellar Systems, and the Sun. V. Lecture Notes in Physics Vol. 291, Springer Verlag, Berlin, p.54.

#### Discussion

- J.C. Henoux: What temperature difference did you assume?
- S. Solanki: We assumed a maximum temperature difference of 1000° K between the up- and the down-flowing part of the non-magnetic atmosphere at equal geometrical height. The difference at equal optical depth is smaller. This temperature difference lies well within the maxima and minima of temperatures plotted by Nordlund (1986, Sac Peak Conference) from a scan through his models.
- B. Lites: Are size scales for the "upflow/downflow" regions surrounding the flux tube and their signature in white light consistent with the flux tube residing in an intergranular lane?
- S. Solanki: Yes. For the model I have shown the horizontal size of the full "granule" is approximately 700-800 km, which corresponds to about the size of a small or abnormal granule, as observed in active regions. However, we do intend to look at models with other flux tube diameters and other sizes of "granular" cells.
- **D. Deming:** The 5-minute oscillation is prominent in field-free regions, and is known to produce "velocity/intensity" correlations in spectral lines. Can it play a role in Stokes V asymmetries?
- S. Solanki: In active regions the 5-minute oscillations have an amplitude of approximately 250 m/s, while we require velocities of approximately 1 km/s to reproduce the asymmetry. I therefore feel that the 5 minute oscillations do not have a significant effect on the asymmetry, although they probably do affect the details.
- S. Koutchmy: The lifetime of a magnetic flux tube region is large compared to the lifetime of a bright granule which would show the velocity pattern you need in your model. Additionally, y ur model is magnetostatic and moreover stationary; accordingly for self-consistency the flux tube should be stable or

- at least should not rise quickly due to instability. Obviously, this cannot be the case when large velocity gradients are present near the tube, especially for velocities directed perpendicular to the magnetic field lines!
- A. Skumanich: Does your model predict a bright ring around the flux tube region at the center of the disc?
- S. Solanki: First to answer your question: No, our model does not predict a bright ring around the flux tube. Rather, it predicts that the bright flux tubes are embedded in cool, i.e. dark, intergranular lanes. To your comment, Serge: Our calculations are a simple approach to try to reproduce a substantial body of data, i.e. FTS Stokes V spectrum of active regions (note, that the small models simultaneously also reproduce many other spectral diagnostics). These observations are spatially and temporally averaged, so that the models also represent an "average" magnetic element. As for as the stability of flux tubes is concerned, the question is not completely resolved. However, calculations including velocities in the surroundings of magnetic elements do suggest that they can be stabilized by external flows. I suggest that you read the paper by Schusler (Astron. Astrophys., 1984).
- R. Canfield: What are the free parameters of your models?
- S. Solanki: The magnetic free parameters are the field strength and horizontal profile at one height. They have been chosen to correspond to observations. The temperature specifications have whenever possible been taken from empirical models. The velocity profile is prescribed at the boundary. We have used a couple of different profiles, but found no great difference in the profiles. I feel this is due to the fact that close to the limb the Stokes V profile "feels" a large horizontal region around the magnetic features.
- L. November: Koutchmy observes fine-structure unresolved in the vicinity of flux tubes. Your model is not unique. Is it possible that spatially unresolved elements could also produce the observed V asymmetry and sign reversal near the limb?
- S. Solanki: One of the things we have learned from this investigation is that the change in sign of the area asymmetry near the limb is a subtle effect due to the balancing of the asymmetry produced at two different boundaries between the magnetic and the non-magnetic atmosphere. It is therefore very difficult, if not impossible, to tell how the asymmetry will behave in a qualitatively different model, without a complete numerical calculation.
- S. Koutchmy: I am referring to the Larry November question which is addressing the problem of including the red-shifted mixed polarity of the weak field "contained" in the region of the flux tubes of dominant polarity. Either this spatial mixing effect or the fast decrease of the mixed polarity with height will show a reversing of the sign of the blue-red asymmetry when you go to the limb or when magnetograms made in a photospheric line are compared to magnetograms taken just above in the low chromosphere ( $B_2$  line of MgI). At the photospheric level the area asymmetry is obviously a result of the very complicated pattern we have among the flux tubes region: a strong unshifted field and red-shifted weak field of the mixed polarity, and a variation with heights. Accordingly, the "blue/red" asymmetry of Stokes parameters is a good diagnostic also for high spatial resolution observations.
- S. Solanki: I'm afraid I do not understand the mechanism you propose to produce a sign reversal of the area asymmetry. As I already pointed out to Larry November, it is not currently possible to say without a proper calculation whether a particular model (including yours) will produce a sign reversal. I personally believe in Ockham's razor, i.e. we keep a model as simple as possible as long as there is no very compelling reason to make it more complex. I feel that the reality of small scale mixed polarities can only be firmly established by IR observations.
- J.C. Henoux: Is the 1000° K temperature difference you used in agreement with other observations?
- S. Solanki: I don't know, but it is probably quite difficult to determine the true velocity in granules from observations. We have also calculated a model with a difference of 500° K and have also obtained the sign reversal, although we did not reproduce the data as well. But we need to do more calculations.

## STOKES PROFILE FORMATION HEIGHTS IN SOLAR MAGNETIC FLUX TUBES

Birgitta Larsson<sup>1</sup>, Sami K. Solanki<sup>2</sup> and Ulrich Grossmann-Doerth<sup>3</sup>

IMR, University of Tromsø, Box 953, N-9001 Tromsø, Norway
 Institut für Astronomie, ETH-Zentrum, CH-8092 Zürich, Switzerland
 Kiepenheuer Institut für Sonnenphysik, Schöneckstrasse 6,
 D-7800 Freiburg/Br, Federal Republic of Germany

Abstract: The formation heights of magnetically split lines in small solar magnetic flux tubes are investigated. In particular, we are interested in how the heights of formation depend on different flux tube parameters, like magnetic field strength, temperature and temperature gradient, as well as on line parameters, such as line strength, excitation potential and ionisation stage. The results should help to improve the construction of empirical models of magnetic features and improve our understanding of the spectral diagnostics used in the study of the solar magnetic field.

#### 1. Introduction

Depth-dependent parameters of the solar photosphere, such as temperature, magnetic field and velocity are generally studied by observing spectral lines. For the interpretation of observational data it is importent to know at which height a given wavelength in a spectral line is formed. Heights of formation (HOFs) of lines in the non-magnetic atmosphere have been relatively well studied, through both their contribution and their response functions. The situation for magnetically split lines is much less satisfactory. Although the problem has been addressed by a number of investigations (e.g. Wittman 1973, 1974, Landi Degl'Innocenti and Landi Degl'Innocenti 1977, Van Ballegooijen 1985, Grossmann-Doerth et al. 1988a, Rees et al. 1989, Murphy 1990) there does not, to our knowledge, exist any systematic study of how the heights of formation of magnetically split lines depend on different atmospheric and atomic parameters. In this paper we present such a study. In a sense the present investigation is complementary to that of Bruls et al. (1990). Their calculations are in NLTE and cover 4 models ranging from a sunspot umbra to an average 1-component network model. We restrict ourselves to LTE and small-scale magnetic structures, but consider in detail the effects of varying atmospheric and atomic parameters, besides listing the heights of formation of a number of lines in empirical flux tube models of magnetic elements. Since small-scale magnetic features may cover a wide range of properties (e.g. in temperature, cf. Solanki and Stenfio 1984, Zayer et al. 1990), it is not sufficient, although useful, to simply list the HOFs in one or two models of magnetic elements. A systematic study of the type reported on here is necessary to obtain an idea of the range of variation of the formation heights for different possible models and lines and thus to help improve diagnostics of the internal structure of magnetic features.

Grossmann-Doerth et al. (1988a, hereafter refered to as paper I) discussed the general problem of determining the heights of formation of magnetically split lines. Combining the approaches of Van Ballegooijen (1985a) and of Magain (1986) they derived the contribution function of the relative "line depression" Stokes vector,  $R^{\dagger} = (1 - I/I_c, -Q/I_c, -U/I_c, -V/I_c)$ , for magnetically split lines. They also demonstrated that this is a more useful diagnostic tool than the contribution function to the intensity. For example, the line depression contribution function is much more sensitive to changes in the magnetic field and its dependence on B can be interpreted in a straight forward manner. Therefore, in the present paper we exclusively discuss the line depression contribution functions calculated using the FORTRAN code presented in paper I for the numerical solution of the Unno-Rachkovsky equations based on Jones calculus, as proposed by Van Ballegooijen (1985a). The CFs are expressed per unit length and represented in a normalised form (i.e. divided by their peak value).

#### 2. Spectral Lines and Flux Tube Models

480

In the present study of the heights of formation (HOF) of magnetically split lines we have calculated contribution functions (CFs) of a set of 20 Fe I and Fe II lines in 11 different flux tube models each. With few exceptions all the calculations presented here have been made assuming LTE, plane parallel atmospheres and vertical incidence. Except for some illustrative examples we only consider the central ray corresponding to the axis of symmetry of a cylindrically symmetric flux tube, since for vertical incidence the largest fraction of the Stokes V signal arises from the central part of the flux tube. The lines have been chosen to form a representative sample of the Fe I and Fe II lines in the visible solar spectrum. Fe I and Fe II lines lie at the heart of most empirical models and of most diagnostic techniques of small-scale magnetic features (e.g. Harvey and Livingston 1969, Stenfio 1973, Chapman 1977, Stellmacher and Wiehr 1979, Solanki and Stenfio 1984, 1985, Solanki 1986, Keller et al. 1990a, Zayer et al. 1989). The chosen lines are listed in Table 1. They can be divided into two groups, one consisting of 9 hypothetical lines, the other of 11 real lines. Among the hypothetical lines there are 3 Fe I lines with low excitation potential, 3 with high excitation potential and 3 Fe II lines. Each of these subgroups is composed of a weak, a medium strong and a relatively strong line. The group of real lines also consists of Fe I and Fe II lines with different line strength, excitation potentials and Landé factors. Most of the real lines correspond to the ones chosen by Solanki (1986) and Keller et al. (1990a) to construct empirical models of the atmosphere in magnetic elements.

The flux tube models used here have been chosen to test the dependence of the HOF on magnetic field strength, temperature and temperature gradient. In addition, we have used two empirical flux tube models, one for network and one for plage regions (Solanki 1986). From these we hope to obtain an idea of the typical formation heights of the chosen lines in small scale solar magnetic features. Finally, as a reference, CFs have also been calculated for the quiet sun model, the HSRA (Gingerich et al. 1971).

In addition to the CFs we have calculated an average HOF at each wavelength of interest of each line in the different models. It is not obvious how to define such an average, in particular for the CFs of Stokes Q, U and

Table 1: List of Fe lines

Ion	$\lambda( ilde{\mathbf{A}})$	$\chi_e(eV)$	geffla	g <sub>eff</sub> emp	log <i>gf</i>
Fe I	5048.44	3.96	1.500	1.431	-1.02
Fe I	50 <b>83.34</b>	0.96	1.250	1.250	-3.10
Fe I	5127.68	0.91	1.500	1.497	-3.03
Fe II	5197.57	3.23	0.700	0.671	-2.31
Fe I	5247.06	0.09	2.000	1.992	-4.95
Fe I	5250.22	0.12	3.000	2.999	-4.94
Fe I	5250.65	2.20	1.500	1.502	-2.12
Fe I	5293.96	4.14	1.000	0.976	-1.63
Fe I	5383.38	4.31	1.083	1.123	0.32
Fe II	5414.07	3.22	1.206	1.190	-3.23
Fe I	5445.05	4.39	1.200	1.248	-0.06
Fe I	5000.00	0.0	0.500		-6.50
Fe I	5000.00	0.0	0.500		-4.93
Fe I	5000.00	0.0	0.500		-3.07
Fe I	5000.00	4.0	0.500		-3.01
Fe I	5000.00	4.0	0.500		-1.20
Fe I	5000.00	4.0	0.500		
Fe II	5000.00	3.0	0.500		-0.10
Fe II	5000.00	3.0 3.0	0.500		-4.65
Fe II	5000.00	3.0 3.0			-3.30
LeTT	3000.00	J.U	0.500		-2.00

The abundance used is 7.56 relative to log(A(H))=12

V, which can and generally do have different signs at different heights due to the fact that these Stokes parameters measure intensity differences between two orthogonal modes of polarisation. Since, at a given wavelength, the opacity for the two modes is in general different they will be formed at different heights in the atmosphere. We have taken the centre-of-gravity of the contribution function to represent the average height at which the line is formed, although we also tabulate the centre-of-gravity of the absolute value of the contribution function. In the following the expressions 'height of formation' and HOF refer to the centre-of-gravity of the CF. However, we wish to stress that each line, and even each individual wavelength of a line, is formed over a rather extended region in the atmosphere and such average HOF values determined here only give a very rough indication of the layers over which the lines are formed.

#### 3. General Properties of the Contribution Function

Magnetooptical effects influence the shapes of the CFs of Stokes Q and U, which may exhibit strong oscillations as a function of optical depth  $\tau$  in the flanks of sufficiently strong lines, where the imaginary part of the eigenvalue of the absorption matrix becomes larger than its real part. For more details we refer to Rees et al. (1989), who discovered and first explained this phenomenon. Our calculations confirm the presence of these oscillations for our stronger lines. Although the shapes of the CFs gets more complicated due to the oscillations, we find that the average height of formation is, at the most, only slightly shifted.

In the following we concentrate on Stokes I and V, since most Stokes diagnostics so far applied to small-scale magnetic features depend on only these two Stokes parameters. We are more interested in basic effects than in the detailed CFs at many wavelengths of each individual line. For this reason and in order to maintain clarity we have decided to present and discuss the CFs only at line centre of Stokes I and at the wavelength of the Stokes V wing maximum,  $\lambda(V_{\max})$ . Since often the CF(I) at  $\lambda(V_{\max})$ , as well as CF(Q) and CF(U) at the wavelength of  $Q_{\max}$  and  $U_{\max}$  are rather similar to CF(V), it may in many cases be taken as an approximation for the other CFs in the line flanks. Of course, there are situations when this approximation does not hold. For example CF(I) differs considerably from the rest if only a part of the atmosphere along the line of sight is magnetic.

The HOF can depend considerably on the model atmosphere and the line parameters. At disk centre we find for the Stokes I core average heights of formation in the range  $-4.4 \le \log \tau \le -0.6$ . For the Stokes V peaks the corresponding values are -3.0 and -0.6. The somewhat lower Stokes V HOFs basically reflect the fact that the Stokes V CF refers to the line flank. Some of the factors determining the HOFs are discussed in the following sections.

One of the questions we have addressed is what does the CF look like when the magnetic field fills only a part of the atmosphere and a particular ray passes through both the magnetic and the non-magnetic parts. This situation is pertinent to small-scale solar magnetic features (e.g., Rees and Semel 1980, Van Ballegooijen 1985a,b) and has important consequences for observed Stokes profiles, e.g. the Stokes V asymmetry (Grossmann-Doerth et al. 1988b, 1989, Solanki 1989). To address this question we have considered two simple cases. In the first case the atmosphere is field free above  $\log \tau = -1.5$ . At this height there is a sharp transition to a field of 1000G that stays constant to the bottom of the tabulated atmosphere. In the second case the field is 1000G above  $\log \tau = -1.5$ , and 0 below that level. Fig. 1 illustrates the contribution functions resulting from the two cases. Interestingly, in the first case the CFs of Q, U and V disappear whenever B=0, but in the second case they can be non-sero in the non-magnetic part of the atmosphere. Therefore, under certain circumstances, Stokes V, Q and U can obtain a contribution from the non-magnetic part of the atmosphere.

The apparent inconsistency between the two cases can be explained by considering the way in which the CF is calculated. We briefly illustrate this for the density matrix notation of the transfer equation (Van Ballegooijen 1985a). For the Müller matrix formalism the arguments are analogous to those outlined here. They are also independent of the numerical method of solution of the equation and in particular are also valid for the Feautrier and DELO techniques (Rees et al. 1989). If C is the 2 × 2 complex contribution matrix (cf. Van Ballegooijen 1985a or Paper I) then

$$C = (T)^{-1}F(T^*)^{-1},$$

where F is the Source function matrix and T is the density matrix analogue to the matrix attenuation operator

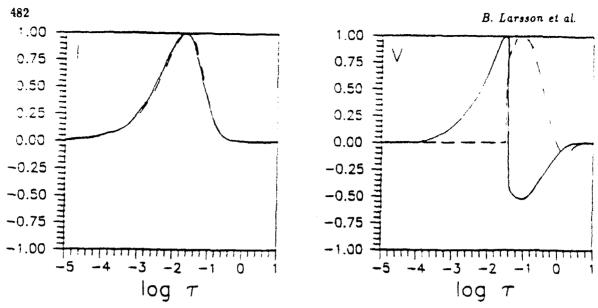


Fig. 1 The Stokes I contribution function (CF) at line center and the Stokes V CF at the wavelength of the V peaks of a high excitation Fe I line plotted vs. the continuum optical depth  $\log \tau$  for two test atmospheres. Case 1 (dashed curve): The upper part of the atmosphere, above  $\log \tau_{\rm crit} = -1.5$ , is field free, while below this height a constant vertical field of strength 1000G is present. Note, that the CF is zero wherever there is no field. Case 2 (solid curve): A constant field of 1000G is now present above  $\log \tau_{\rm crit} = -1.5$ , while the atmosphere below that height is field free. The CF of Stokes V is now non-zero also in the field free part of the atmosphere.

(e.g. Landi Degl'Innocenti and Landi Degl'Innocenti 1985). T is found by integrating a set of 4 complex ordinary differential equations,

$$d\mathbf{T}/d\tau = \mathbf{AT}$$
, with  $\mathbf{T}(\tau = 0) = 1$ ,

downwards from  $\tau=0$ . This implies that in the first case (i.e. B=0 for  $\tau \leq \tau_{\rm crit}$ ) in the field free part of the atmosphere  $\mathbf{T}(\tau \leq \tau_{\rm crit})$  is diagonal since  $\mathbf{A}(\tau \leq \tau_{\rm crit})$  is diagonal (both  $\mathbf{T}$  and  $\mathbf{A}$  are proportional to the unity matrix there).  $\mathbf{F}(\tau \leq \tau_{\rm crit})$  is also proportional to the unity matrix, so that  $C_Q=C_U=C_V=0$  for  $\tau < \tau_{\rm crit}$  in this case. For the second case (i.e. B=0 for  $\tau > \tau_{\rm crit}$ )  $\mathbf{T}(\tau > \tau_{\rm crit})$  is not diagonal, although  $\mathbf{A}(\tau > \tau_{\rm crit})$  and  $\mathbf{F}(\tau > \tau_{\rm crit})$  are, since  $\mathbf{A}(\tau < \tau_{\rm crit})$  also influences  $\mathbf{T}(\tau > \tau_{\rm crit})$ . Therefore,  $C_Q$ ,  $C_U$  and  $C_V$  do not necessarily disappear in the part of the atmosphere where there is no field.

This behaviour warns us to bear the exact meaning of contribution functions in mind whenever discussing them or formation heights derived from them: The intensity CF tells us how much light of a given frequency is emitted at a given depth  $\tau$  and escapes at the upper boundary of the atmosphere. This definition of the CF shows that the CF depends only on the properties of the atmosphere above the depth in question. Similarly, the line depression CF tells us how strongly the light intensity at a given wavelength is suppressed at a given depth and is not reemitted at that wavelength until the upper boundary of the atmosphere is reached. Basically, the current tests imply that the CF is sensitive to the atmosphere above the height of interest, but not below it.

#### 4. Temperature Dependence

Like the Stokes profiles themselves their heights of formation depend in a complex manner on the temperature stratification. This dependence is itself a function of ionisation stage and excitation potential. In order to examine the dependence on the absolute value of temperature we have used four models (HSRA, TEMP1, TEMP2 and TEMP3). Each of the latter 3 models is about 400K hotter than the preceding one. Our computational results may be summarised as follows: A low excitation Fe I line is greatly weakened when the temperature is increased, and hence its HOF is shifted downwards. The shift is much larger for the line core than for the flanks. For a temperature increase of 1200K the decrease in its HOF is approximately 1.6 in units of log  $\tau$  for the line centre and 0.5 for the

flanks. For the high excitation Fe I line both the line weakening and the shift of the HOF due to the temperature increase are much smaller. The HOF of the line core is shifted downwards by 0.8 in  $\log \tau$ , while the HOF of the flanks is almost unaffected. The Fe II line shows a completely different behaviour. The temperature hardly affects the line strength at all and the HOF actually increases with temperature instead of decreasing. The amount of increase is similar for both the line flank and core,  $\delta \log \tau = 0.5$  for a temperature difference of 1200K.

To reliably determine the temperature in unresolved magnetic features we have to use Stokes V, Q, or U profiles, since Stokes I is in general contaminated by light from the non-magnetic atmosphere. Due to the rough proportionality of Stokes V, Q, and U to the magnetic flux, ratios between the V, Q, or U profiles of two or more lines that differ strongly in their temperature sensitivities must be considered (e.g. Stenflo 1975, Landi Degl'Innocenti and Landolfi 1982), although diagnostics of the temperature that rely on the line profile shape do exist (e.g. Solanki et al. 1987, Lites et al. 1987). If the HOFs of the two lines have different temperature dependences, their relative heights of origin in the atmosphere will change with temperature, complicating the interpretation of such line ratios. As can be seen from the last paragraph, this is generally the case if the ratio is formed between two lines with strongly different excitation potentials or belonging to different ions. Exactly such line ratios (often termed "thermal line ratios") have been proposed and used to construct empirical models of magnetic elements (Landi Degl'Innocenti and Landolfi 1982, Zayer et al. 1990). Note, that for weak Zeeman splitting the situation is worse at line centre than in the flanks. Therefore, Stokes V line ratios and ratios involving only Q and U  $\sigma$  components should be less affected. Unfortunately, the line-centre line ratios (between the  $\pi$ -components of Stokes Q and or U profiles) show the best promise of providing diagnostics of the temperature in the higher layers of flux tubes.

Note that the  $\sigma$ -components are simpler to interpret only if the Zeeman splitting is small compared to the Doppler width, since otherwise the peaks of the  $\sigma$ -components also correspond to the line core and are affected in a similar manner as the core of the  $\pi$  component. However, this should not be a major problem for lines in the visible. The most strongly split lines in the near infrared are all high excitation Fe I lines (5eV  $\lesssim \chi_e \lesssim 6.5$ eV), which are of only limited use for the determination of the temperature in small magnetic features (Muglach and Solanki 1990).

The parameter which influences the HOFs the most is the temperature gradient. Not only does the average HOF change dramatically between models with different temperature gradients, but so does the width of the contribution functions. The  $T(\tau)$  structure of the three models used to test the dependence on temperature gradient is shown in Fig. 2. The models have been chosen such that the lines formed in all three of them have roughly similar equivalent widths, although certain differences in equivalent width and profile shape are unavoidable. In particular, the equivalent widths of the Fe I lines for the three models are considerably closer together than for the TEMP1.2 and 3 models. In this manner we ensure that differences between the HOFs resulting from different models are not mainly due to changes in the equivalent widths of the lines. As pointed out earlier TEMP1 has a gradient much like that of the HSRA. TEMP4 has a very flat temperature profile above  $\log \tau \approx -1$ , with the temperature actually increasing again outwards above  $\log \tau \approx -2.5$ . This model is roughly similar to the empirical flux tube models of Stenfio (1975) and Chapman (1977, 1979). TEMP5 is in many ways the opposite to TEMP4, since it has an almost constant gradient throughout the photosphere, whereas  $dT/d\tau$  of TEMP4 changes dramatically around  $\log \tau = 1$ .

Examples of profiles and their line core CFs resulting from these 3 models are shown in Fig. 3. The CFs of the low excitation Fe I line are again more sensitive to changes in the temperature structure than the CFs of the high excitation Fe I and the Fe II line. In a model like TEMP5, with a steeper temperature gradient in the line forming layers than both the HSRA, the low excitation Fe I line are formed much higher in the atmosphere than the high excitation Fe I line and the Fe II line, while in a model with a temperature minimum deep in the photosphere (TEMP4) all the lines are formed at almost the same height. The temperature gradient does not change the difference in HOF between the line flank and the core. This implies that the large variations of the line core CFs seen in Fig. 3 are mirrored by the CFs at, say, the Stokes V peaks or the Q or U  $\sigma$ -component peaks. The strong influence of the temperature gradient on the HOFs again has serious consequences for the interpretation of thermal line ratios. Now, since the Stokes V peak CFs are affected in a similar manner as the line core CFs the Stokes V line ratios become as complex to interpret as those of the Stokes Q and U  $\pi$ -components.

As a concrete example we have considered the often used Stokes V line ratio between Fe I 5247.1Å and 5250.6Å (Stenflo et al. 1987, Keller et al. 1990a, Zayer et al. 1990). According to our calculations it should be easily

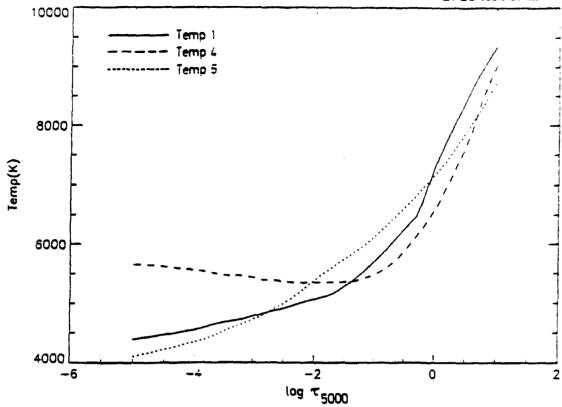


Fig. 2 Temperature as a function of  $\log \tau$  for three flux tube models. The solid curve represents TEMP1, which has a temperature gradient very similar to the quiet sun HSRA model. The dashed curve represents the TEMP4 model and the dotted curve the TEMP5 model.

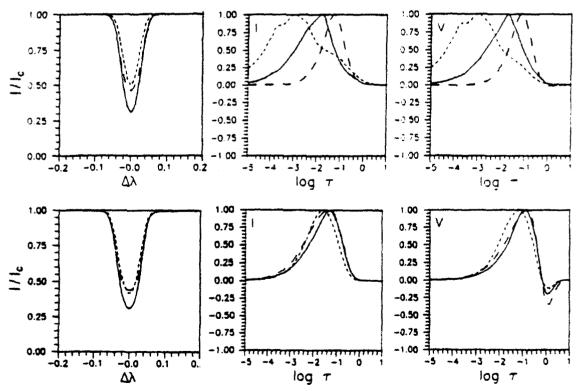


Fig. 3 Stokes I line profiles (left panels) and Stokes I (middle panels) and Stokes V (right panels) contribution functions of a low excitation Fe I line (upper three panels), and an Fe II line (lower three panels) showing the dependence on temperature gradient. The symbols refer to the same asmospheres as in Fig. 2. The CF to Stokes I is for the line centre, while the CF to Stokes V is for the wavelength at which Stokes V has its maximum.

interpretable, since the V maxima of these lines are formed at almost the same heights in all models. (However, the cores of these two lines are often formed at rather different heights.)

#### 5. Dependence on Magnetic Field Strength

In general for Zeeman splittings larger than the line width the HOFs depend strongly on field strenght. Starting from an unsplit line, an increase in the splitting due to a longitudinal field causes the line centre to be formed deeper and deeper in the atmosphere and the HOF of the line flanks, particularly at the wavelength where Stokes V has its maximum, to increase. This increase continues until the line is fully split. Let us now consider the specific case of the two Fe I lines 5250.2Å ( $g_{\rm eff}=3$ ) and 5247.1Å ( $g_{\rm eff}=2$ ). We have calculated the HOFs of these two lines in a standard atmosphere, the HSRA, assuming constant magnetic fields of different strengths. The CFs for 3 cases 100G, 1000G and 3000G are illustrated in Fig. 4. As tan be seen from the figure the lines are formed at the same

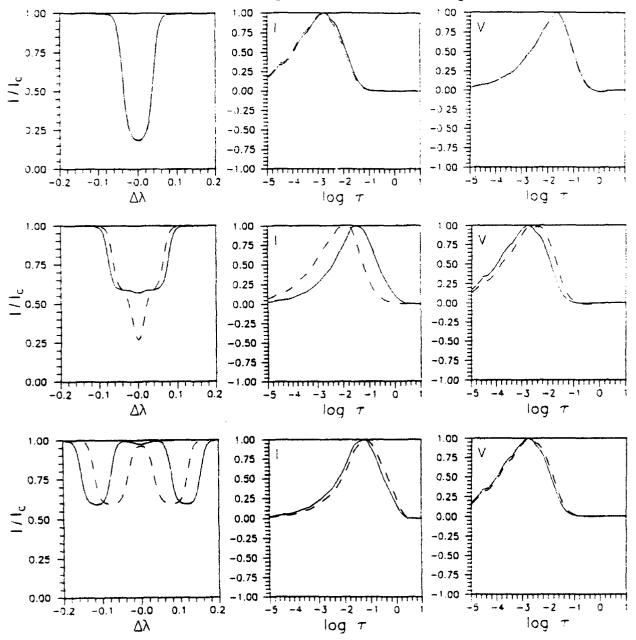


Fig. 4 Stokes I profiles of Fe I 5250.2Å and 5247.1Å (left) and their Stokes I (center) and Stokes V (right) contribution function for 100G (upper three panels), 1000G (middle panels) and 3000G (lower panel). The solid curve is for 5250.2 Å and the dashed curve for 5247.1 Å.

486 B. Larsson et al.

height for both weak and strong fields, when either both lines show no effect on their line profile shapes due to the magnetic field, or both are completely split. However, there is an intermediate field strength range for which the cores of the 2 lines are not formed at the same height. Fortunately, the difference in HOF is relatively small at  $\lambda(V_{\rm max})$ , so that that the ratio between the  $V_{\rm max}$  of these two lines is always sensitive to the field strength at a given height and the field strength gradient does not directly affect the line ratio. However, the gradient can have a substantial indirect effect on the line ratio, via the temperature. Recall that both lines have low excitation potentials and are thus extremely temperature sensitive. Fig. 3 shows the spread of the CFs of similar lines, due to variations of the temperature stratification of the magnetic features. Thus, due to its strong dependence on height, the magnetic field strength at the HOF can be quite different from model to model, although as a function of geometrical height it may be relatively unaffected by the temperature (cf. Zayer et al. 1990, Grossmann-Doerth and Solanki 1990).

Note, that it is better to use the  $V_{\rm max}$  values, instead of the ratio between the V profiles at some fixed wavelength (as is the case for magnetograms, Stenflo 1973, Frasier and Stenflo, Wiehr 1978, and filtergrams, Keller et al. 1990b), since the differences in HOF between the two lines can be considerably larger at a fixed wavelength than if the HOFs at the two  $\lambda(V_{\rm max})$  are compared.

The behaviour described here is only true as long as B is almost parallel to the LOS. When observing the field at an angle at which the  $\pi$ -component is equally strong as the  $\sigma$ -components the decrease of the HOF at line centre with increasing B is negligible. This is encouraging for the line ratio between the  $\pi$ -components of 5250.2Å and 5247.1Å (in particular of their Q and U profiles), which could provide a diagnostic of the magnetic field strength in higher layers of the atmosphere.

#### 6. Estimated Formation Heights in Solar Magnetic Elements

In Table 2 we present average values of HOFs of Stokes I and V for the 11 selected lines actually present in the solar spectrum, calculated in the empirical network flux tube model of Solanki (1986). The corresponding model of Keller et al. (1990) give relatively similar results. Therefore we consider the values listed in Table 2 to represent the current best estimate of the formation heights of these typical iron lines in small-scale magnetic features.

#### 7. Conclusions

We have calculated the Stokes contribution functions of a variety of magnetically split Fe I and II lines in a number of atmospheres. Thereby we have been able to obtain a better understanding of some of the diagnostics of the temperature and magnetic field within small-scale magnetic features. We find that among the atmospheric parameters the temperature gradient plays the dominant role in determining the heights of formation of temperature sensitive lines. The interpretation of many diagnostics cannot be assumed to be so straightforward as has been thought in the past. In particular, diagnostics based on multiple lines can become rather complex to interpret, since the differences between the heights of formation of the different lines changes with the assumed temperature structure. However, other diagnostics turn out to be relatively unaffected, a prime example being the magnetic line ratio between Fe I 5250.2Å and Fe I 5247.1Å of Stenflo (1973).

We have also presented estimates of the heights of formation in small-scale solar magnetic elements of 11 typical Fe I and II lines. One of the conclusions which can be drawn from this tabulation is that the Stokes V maxima of all these lines are formed at not too different heights. This implies that current Stokes V based empirical models of magnetic elements are only reliable over a rather limited range of the atmosphere (approximately  $-3 \leq \log \tau \leq -1$ ). To increase this height range upwards either the line profile shapes of Stokes V near the line cores will have to be employed, or the  $\pi$ -components of Stokes Q and U.

Table 2: Height of Formation of Fe lines in an empirical network fluxtube model

Ion	λ (Å)	HOF I (log $ au$ )	HOL V (log $\tau$ )	HOF V*
Fe I	5048.44	-1.7	-2.0	-1.9
Fe I	5083.34	-2.9	-2.9	-2.6
Fe I	5127.68	-3.0	-2.5	-2.4
<b>Fe II</b>	5197.57	-2.7	-2.0	-1.6
Fe I	5247.06	-2.0	-2.2	-2.2
Fe I	5250.22	-1.8	-2.2	-2.2
Fe I	5250.65	-2.5	-2.6	-2.4
Fe I	5293.96	-1.3	-1.3	-1.3
Fe I	5383.38	-2.9	-3.1	-2.0
Fe II	5414.07	-1.5	-1.6	-1.5
Fe I	5445.05	-2.4	-2.2	-1.8

HOF V is the center-of-gravity of the contribution function. HOF V\* is the center-of-gravity of the absolute value of the contribution function.

#### References

Bruls, J.H.M.J., Lites, B.W., Murphy, G.A., (1990), these proceedings

Chapman, G.A., (1977), Astrophys. J. Suppl. Ser. 33, 35

Chapman, G.A., (1979), Astrophys. J. 232, 923

Frazier, E.N., Stenflo, J.O., (1978), Astron. Astrophys. 70, 789

Gingerich, O., Noyes, R.W., Kalkofen, W., Cuny, Y., (1971), Solar Phys., 10, 220

Grossmann-Doerth, U., Larsson, B., Solanki, S.K., (1988a) Astron. Astrophys. 204, 266-274

Grossmann-Doerth, U., Schüssler, M., Solanki, S.K., (1988b), Astron. Astrophys. 206, L37

Grossmann-Doerth, U., Schüssler, M., Solanki, S.K., (1989), Astron. Astrophys. 221, 338

Grossmann-Doerth, U., Solanki, S.K., (1990), Astron. Astrophys. in press

Harvey, J.W., Livingston, W., (1969), Solar Phys. 10, 283

Keller, C.U., Solanki, S.K., Steiner, O., Stenflo, J.O., (1990a), Astron. Astrophys. 233, 583

Keller, C.U., Solanki, S.K., Tarbell, T.D., Title, A.M., Stenflo J.O., (1990a), Astron. Astrophys. 236, 250

Landi Degl'Innocenti, E., Landi Degl'Innocenti, M., (1977), Astron. Astrophys., 56, 111

Landi Degl'Innocenti, E., Landi Degl'Innocenti, M., (1985), Sciar Phys. 97, 239

Landi Degl'Innocenti, E., Landolfi, M., (1982), Solar Phys. 77, 13

Lites, B.W., Skumanich, A., Rees, D.A., Murphy, G.A., Carlsson, M., (1987),, Astrophys. J. 318, 930

Magain, P., (1986) Astron. Astrophys. 163, 135

Muglach, K., Solanki, S.K., (1990), these proceedings

Murphy, G.A., (1990), NCAR Cooperative Thesis No. 124

Rees, D.E., Murphy, G.A., Durrant, C.J., (1989), Astrophys. J. 339, 1093

Rees, D.E., Semel, M.D., (1979), Astron. Astrophys. 74, 1

Solanki, S.K., (1986) Astron. Astrophys. 168, 311

Solanki, S.K., (1989), Astron. Astrophys. 224, 225

Solanki, S.K., Keller, C., Stenflo, J.O., (1987), Astron. Astrophys. 188, 183

Solanki, S.K., Stenflo, J.O., (1984), Astron. Astrophys. 140, 185

Solanki, S.K., Stenflo, J.O., (1985), Astron. Astrophys. 148, 123

Stellmacher, G., Wiehr, E., (1970), Astron. Astrophys. 75, 263

Stenflo, J.O., (1973), Solar ".ys. 32, 41

Stenflo, J.O., (1975), Sciar Phys. 42, 79

Stenflo, J.O., Solanki, S.K., Harvey, J.W., (1980), Astron. Astrophys. 171, 105

Van Ballegooijen, A.A., (1985a), in Measurements of Solar Vector Magnetic Fields, ed. M.J. Hagyard, NASA Conf. F. i. 2374, p. 322

Van Ballegooijen, A.A., (1985b), in Theoretical Problems in High Resolution Solar Physics, H.U. Schmidt (Ed.), Max Planck Inst. f. Astrophys., Munich, p. 167

Wiehr, E., (1978), Astron. Astrophys. 69, 279

Wittmann, A., (1973), Solar Phys. 33, 107

Wittmann, A., (1974), Solar Phys. 35, 11

Zayer, I., Solanki, S.K., Stenflo, J.O., Keller, C.U., (1990), Astron. Astrophys. in press

#### FLUX TUBE DIAGNOSTICS BASED ON THE STOKES V PROFILES OF INFRARED H-BAND LINES

#### K. Muglach<sup>1</sup> and S. K. Solanki<sup>2</sup>

<sup>1</sup>Institut für Astronomie, Universität Graz, 8010 Graz, Austria <sup>1</sup>Institut für Astronomie, ETH-Zentrum, 8092 Zürich, Switzerland

Abstract: Stokes V profiles of the unblended Fe I lines in the wavelength range 1.5-1.8  $\mu$  (H-band) observed in the solar network are analysed. The data are consistent with an absence of stationary flows larger than 0.3 km s<sup>-1</sup>. The infrared Stokes V profiles are asymmetric in the same sense as lines in the visible, but tend to be of smaller magnitude, in particular the area asymmetry. The widths of the Stokes V profiles are consistent with kG field strengths. Finally, model calculations allow an upper limit of 2 to be set on the continuum intensity of small magnetic features relative to the quiet sun.

#### 1. Introduction

A large part of the magnetic field in the solar photosphere is concentrated into small-scale magnetic elements or flux tubes. Information on the deeper photospheric layers of such flux tubes is particularly important for the following reasons:

- 1. Waves and oscillations, which partially heat the chromosphere and possibly the corona, are excited in these layers and the radiation that heats the upper photosphere is channelled into the flux tubes at these depths.
- 2. The visible continuum intensity, formed in these layers, is important for the interpretation of observations. It influences measurements of the magnetic flux and also determines the ionization balance and thus the departures from LTE for many atomic species. In addition, it influences the variation of the global solar luminosity.

We present the results of an analysis of a spectrum each of Stokes I, V and Q covering the wavelength range between 1.5 and 1.8  $\mu$  (H-band) obtained simultaniously at solar disk centre ( $\mu = 0.99$ ) in a network region with a Fourier Transform Spectrometer (FTS). The analysis presented here concentrates on Stokes V, which originates only in the spatially unresolved magnetic elements.

Observing in the infrared H-band has two advantages: 1. Due to the continuum opacity minimum and the presence of very high excitation lines we see deeper layers of the photosphere than in the visible. 2. The Zeeman sensitivity is approximately three times larger at  $1.6 \mu$  than at  $0.5 \mu$ .

The analysis is carried out in two main steps. Some properties of the lower photospheric layers of the magnetic elements can be derived from a statistical multi-line analysis. To determine information on additional flux tube parameters numerical radiative transfer calculations are required. These are carried out for a sample of 16 lines.

#### 2. Line Parameters and Regression Analysis

In the first step various observed parameters of the Stokes V profiles of approximately 100 unblended Fe I lines are determined. The main results are illustrated in Figs. 1-3.

Fig. 1 shows the difference in km s<sup>-1</sup> between the zero-crossing wavelength of Stokes V,  $\lambda_V$ , and the wavelength of the Stokes I minimum,  $\lambda_I$ , as a function of Stokes I line strength,  $S_I$  (in Fraunhofer, F). Each symbol corresponds to a spectral line, a weighted linear regression is also plotted. The blueshift of Stokes I due to solar granulation has been compensated for according to the accurate empirical formula of Nadeau (1988). Since the average filling factor

of the observed region is relatively small (approximately 10 %) this correction formula, which is strictly valid only for the quiet sun, may also be used here.

In contrast to previously published infrared observations (e.g. Harvey, 1977; Stenflo et al. 1987), which show downflows of 0.5-2 km s<sup>-1</sup>, Fig. 1 suggests that the deeper layers of flux tubes are free from stationary flows larger than approximately 0.3 km s<sup>-1</sup>, in agreement with high spectral resolution results in the visible (Stenflo and Harvey 1985; Solanki, 1986). The previous IR measurements were restricted to the  $\lambda 1.5648\mu$  line, which shows a redshift in our data set as well, but is not typical for the other lines.

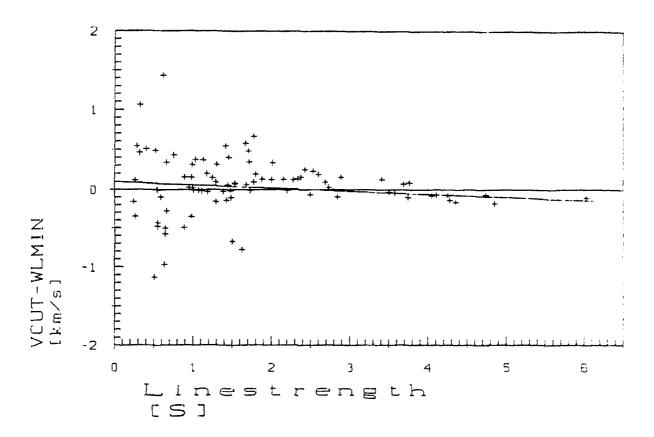


Fig. 1  $\lambda_V - \lambda_I$  vs.  $S_I$ . The solar granulation induced blueshift of Stokes I has been corrected according to the formula given by Nadeau.

The Stokes V relative amplitude asymmetry,  $\delta a = (a_b - a_r)/(a_b + a_r)$ , is plotted vs.  $S_I$  in Fig. 2a. Here  $a_b$  and  $a_r$  are the unsigned amplitudes of the blue and the red wings of the V profile, respectively. Fig. 2b shows the relative area asymmetry,  $\delta A = (A_b - A_r)/(A_b + A_r)$ , vs.  $S_I$ , where  $A_b$  and  $A_r$  are the unsigned areas of the blue and the red wings of the V profile, respectively. Lines with  $S_I < 0.5$ F have been omitted since they are strongly affected by noise.

As in the visible the Stokes V profiles are asymmetric with stronger blue than red wings, i.e.,  $\delta A$  and  $\delta a$  are positive (recall that the data were obtained near solar disk center). The V asymmetry of H-band lines appears to be is smaller than that of lines in the visible (Solanki and Stenflo, 1984), in particular  $\delta A$ , which is smaller by approximately a factor of two. Since  $\delta A$  is caused by downflows in the surroundings of flux tubes (Grossmann-Doerth et al., 1988), this may be caused by a decrease in the granular downflow velocity with depth in the photosphere. On the other hand, this effect may simply be due to the much larger Zeeman splitting of the infrared H-band lines, which should lead to a reduction of  $\delta A$  according to Grossmann-Doerth et al. (1989) and Sánchez Almeida et al. (1989). Model calculations are required to resolve this question.

To investigate the effect of the field strength on the Stokes V profiles we carry out multi-variate regressions of various line parameters. As an illustration we summarize the results of such an analysis for the difference of the

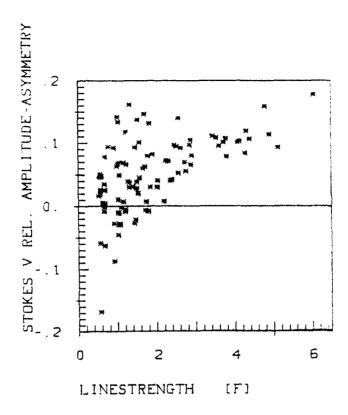


Fig. 2a The Stokes V relative amplitude asymmetry,  $\delta a = (a_b - a_r)/(a_b + a_r)$ , vs.  $S_I$ 

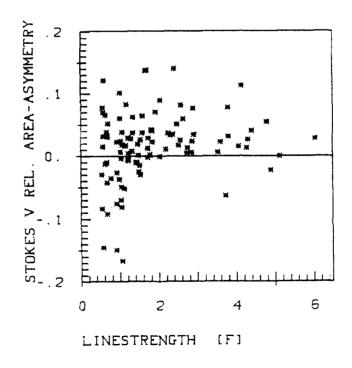


Fig. 2b The Stokes V relative area asymmetry,  $\delta A = (A_b - A_r)/(A_b + A_r)$ , vs.  $S_I$ 

centre-of-gravity wavelengths of the red and the blue Stokes V wings,  $\lambda_r - \lambda_b$ . The regression equation takes into account the influence of line strength, excitation potential, Zeeman splitting and wavelength on  $\lambda_r - \lambda_b$ . We find a better fit to the data if we assume the lines to be completely split [i.e.  $\lambda_r - \lambda_b \sim g_{\rm eff}\lambda^2$ ] than if we use the weak field approximation formula of Stenflo and Lindegren (1977) generally applied in the visible (i.e.  $\lambda_r - \lambda_b \sim g_{\rm eff}^2\lambda^2/(\lambda_r - \lambda_b)$ ). In Fig. 3  $\lambda_r - \lambda_b$ , with all regression terms except the one describing the Zeeman splitting subtracted from it. is plotted vs.  $g_{\rm eff}\lambda^2$ . The strong influence of the Zeeman splitting on the "width" (i.e.  $\lambda_r - \lambda_b$ ) of the Stokes V profiles is evident. Similar plots in the visible (Solanki and Stenflo, 1984) show a considerably less clear signature of the Zeeman splitting. The point in the upper right-hand corner is the magnetically very sensitive g=3 line at  $\lambda 1.5648\mu$ . The magnetic field strength determined from the regression coefficient of the Zeeman term lies around 1300 kG (if the most weakly split lines are neglected, since for them the approximation of complete splitting is not a good one), which compares well with the value of 1500 G obtained directly from the splitting of the 1.5648 $\mu$  line (Stenflo et al., 1987; Zayer et al., 1989).

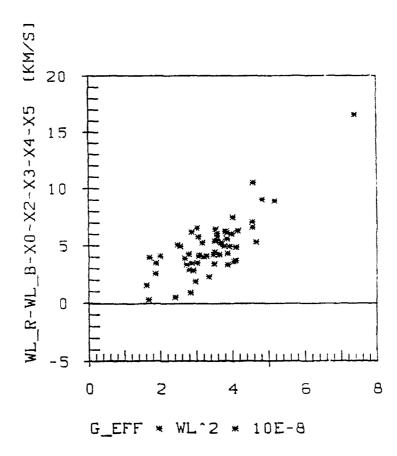


Fig. 3  $\lambda_r - \lambda_b - x_0 - x_2 - x_3 - x_4 - x_5$  vs. Zeeman splitting  $g_{\text{eff}}\lambda^2$ .  $\lambda_r - \lambda_b$  is the difference between the two Stokes V centre-of-gravity wavelengths.  $x_0, x_2, x_3, x_4$  and  $x_5$  represent the regression terms taking the influence of  $S_I$ ,  $\chi_c$  and  $\lambda$  on  $\lambda_r - \lambda_b$  into account. Note that the term describing the Zeeman splitting has not been subtracted from  $\lambda_r - \lambda_b$ .

#### 3. Modelling

To determine the temperature and the turbulence velocity in the lower layers of magnetic elements we calculate Stokes V profiles numerically in LTE along multiple vertical rays passing at various radii through flux tube models that are based on the thin tube approximation. The spatially averaged synthetic profiles are then compared with the observations. For the transfer calculations we have chosen 16 unblended Fe I lines. 14 of them, covering the

whole available line strength range, have small  $g_{\rm eff}$  values between 0.5 and 1.5 and are used to diagnose temperature. The remaining two have g=3 and  $g_{\rm eff}=2$ , respectively, and are used to determine the magnetic field strength. Simultaneous field strength diagnostics are required to derive the temperature properly. To determine the oscillator strengths of the 16 lines, synthetic Stokes I profiles are calculated using a model of quiet solar photosphere and they are fitted to the measured FTS profiles.

Fig. 4 shows temperature, T, vs. the logarithmic continuum optical depth at 1.6  $\mu$ ,  $\log \tau_{1.6}$ , of six model atmospheres used for Stokes profile calculations. The solid line represents the empirical Network flux tube model of Solanki (1986), NET. The other models are: double-dot-dashed curve: NETH1, long dashes: NETH2, dot-dashes: NETH3, short dashes: NETC1, dots: NETC2. All the employed models correspond to NET in their upper layers. Models with even lower temperatures have also been used, but are not shown since they were unable to reproduce the measured Stokes V profile shapes correctly (the synthetic profiles of some of the lines were too broad).

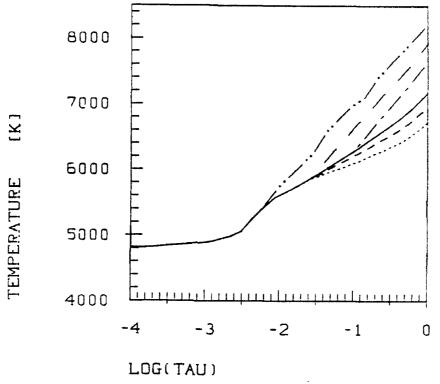


Fig. 4 Temperature T vs. continuum optical depth an  $1.6\,\mu$ ,  $\tau_{1.6}$ , of the models NETH1 ( - · · - ), NETH2 ( - · · · · ), NETC1 ( - · · · · ), NETC2 ( · · · · )

Since we have no a priori knowledge of the filling factor of the observed region, we calculate the profiles along rays out to a fixed radius in the 2-D flux tube model. This corresponds to calculating the line profiles for a fixed magnetic filling factor at a given level in the atmosphere. Therefore, the synthetic Stokes V profiles must still be multiplied by a fitting factor F to make them correspond in amplitude to the observed profiles. If the temperature stratification of the model used to calculate the profiles is correct, then the factor F is the same for all lines. For a too hot, or a too cold model F changes with line strength and excitation potential,  $\chi_e$ . Since the Fe I lines in the H-band all have very similar excitation potentials ( $5eV \leq \chi_e \leq 6eV$ ), a plot of F vs.  $S_I$  is a good diagnostic of the temperature, as extensive test calculations have shown.

In Fig. 5 the F values for each of the chosen lines and the 6 models of Fig. 4 are plotted against  $S_I$  (triangles: NETH1, crosses: NETH2, circles: NETH3, squares: NET, stars: NETC1, plusses: NETC2). Best fit straight lines are also plotted. Both the points and and the regression lines are shifted vertically for clarity (only the gradient of F vs.  $S_I$  contains diagnostic information on the temperature). Unfortunately, the H-band lines turn out to be rather insensitive to temperature in the range covered by the models NET and NETC2, so that it is not possible to accurately derive the temperature in the deeper layers of flux tubes.

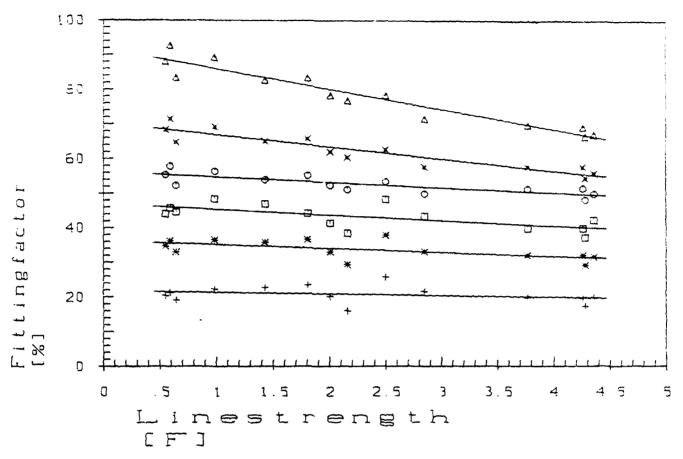


Fig. 5 F vs.  $S_I$  resulting from a fit of the synthetic profiles calculated using (from top to bottom) NETH1, 2, 3, NET, NETC1, 2 to the observed Stokes V profiles. F is the "fitting factor" (see text).

However, we can still set limits on the continuum contrast of the unresolved magnetic flux tubes at  $\lambda=0.5\,\mu$ :  $\delta_c=I_{c0.5}^{\rm fluxtube}/I_{c0.5}^{\rm quiet}$ . We find that  $\delta_c\leq 2$  at the  $2\sigma$  level and  $\delta_c\leq 1.75$  at the  $1.5\sigma$  level. A lower limit of  $\delta_c>0.8$  can be set by virtue of the bad fits to the observed line shapes produced by profiles from models cooler and darker than NETC2. Our upper limit suggests that the bright point observed by Koutchmy (1977) with  $\delta_c=2$  probably does not represent a typical fluxtube, although it may be a particularly bright one.

The macroturbulence broadening of the Stokes V profiles is found to be approximately  $2 \text{ km s}^{-1}$  and is therefore of the same order as in the visible (we assume a microturbulenz of  $1 \text{ km s}^{-1}$ ).

Fig. 6 gives 4 representative examples of the 16 selected lines showing the quality of the fit for the model NET which (besides reproducing observations in the visible) gives a slope of F vs.  $S_I$  which is zero within the error bars. The solid curves are observed and symmetrized Stokes V profiles, dashed ones are synthetic profiles. Note the good fit to the Stokes V profile of  $\lambda 1.5648 \text{\AA}$ , including its width and splitting. A field strength of 1500-1600 G at the  $\log \tau_{0.5} = 1$  level in the quiet sun is required to reproduce the profile shape of this and the other lines with  $g_{\text{eff}} \gtrsim 1$ . We confirm the field strength determined by Zayer et al. (1989) with a larger number of lines than used by those authors. The fact that the shapes and the amplitudes of the V profiles of both weakly and strongly Zeeman split lines can be reproduced simultaneously also suggests that for the observed region the amount of magnetic flux in weak field form is small ( $\lesssim 10 \%$ ).

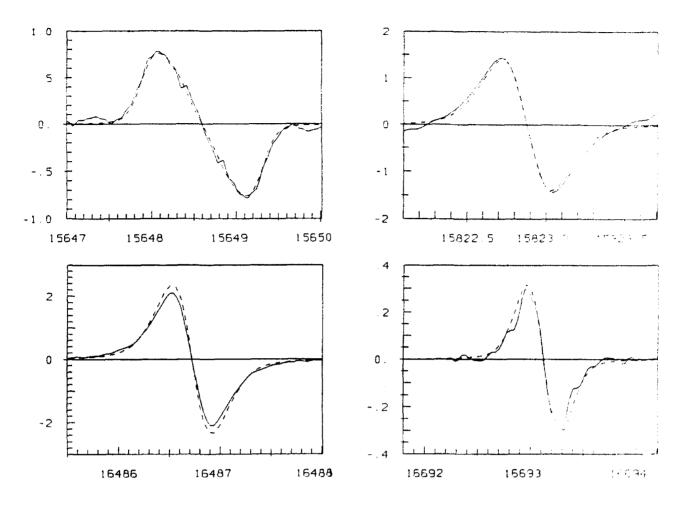


Fig. 6 Observed and symmetrized (solid) and synthetic (dashed) Stokes V profiles of four lines. The synthetic profiles have been calculated using the NET model.

#### References

Grossmann-Doerth, U., Schüssler, M., Solanki, S.K.: 1988, Astron. Astrophys. 206, L37

Grossmann-Doerth, U., Schüssler, M., Solanki, S.K.: 1989, Astron. Astrophys. 221, 338

Harvey, J.W: 1977, in Highlights of Astronomy, E.A. Müller (Ed.), Vol. 4, Part II, p. 223

Koutchmy, S.: 1977, Astron. Astrophys. 61, 397

Nadeau, D.: 1988, Astrophys. J. 325, 480

Sánchez Almeida, J., Collados, M., Del Toro Iniesta, J.C.: 1989, Astron. Astrophys. 222, 311

Solanki, S.K., Stenflo, J.O.: 1984, Astron. Astrophys. 140, 185

Solanki, S.K.: 1986, Astron. Astrophys. 168, 311

Stenflo, J.O., Harvey, J.W.: 1985, Solar Phys. 95, 99

Stenflo, J.O., Lindegren, L.: 1977, Astron. Astrophys. 59, 367

Stenflo, J.O., Solanki, S.K., Harvey, J.W.: 1987, Astron. Astrophys. 173, 167

Zayer, I., Solanki, S.K., Stenflo, J.O.: 1988, Astron. Astrophys. 211, 463

# THEMIS Un télescope pour comprendre le magnétisme solaire

Jean RAYROLE

Observatoire de Paris

L'Institut National des Sciences de l'Univers (CNRS-INSU) construit actuellement un télescope solaire d'un type tout à fait nouveau appelé "THEMIS" (Télescope Héliographique pour l'Étude du Magnétisme et des Instabilités de l'atmosphère Solaire).

Ce télescope sera prochainement installé aux îles Canaries à l'Observatoire du Teide, l'un des deux sites ouverts par l'Espagne aux investissements étrangers à la suite d'une campagne de recherche du meilleur site astronomique à proximité de l'Europe. Les deux sites des îles Canaries, l'Observatoire du Teide dans l'île de Tenerife et l'Observatoire du Roque de los Muchachos dans l'île de la Palma font partie de l'Institut d'Astrophysique des Canaries (IAC). Las îles Canaries ont été sélectionnées, parmi plus de 40 sites, grâce aux efforts conjoints de tous les pays européens au cours des années 1970.

#### **POURQUOI THEMIS?**

L'intérêt de la physique solaire réside dans le fait que notre étoile est assez proche pour qu'on puisse entreprendre toutes les études détaillées qu'on ne pourra faire sur aucune autre.

Le champ magnétique est le paramètre fondamental qui gouverne tous les phénomènes observés dans les atmosphères stellaires. On devine aisément qu'en présence d'un champ magnétique, les propriétés du gaz solaire, composé pour une large part de particules électrisées, peuvent être profondément modifiées par les phénomènes électromagnétiques. Le champ incurve les trajectoires des charges électriques, conduisant à des mouvements différents pour les ions et les électrons, c'est-à-dire à des courants électriques. Ceux-ci créent à leur tour un champ magnétique qui s'oppose au champ initial.

Les structures les plus connues observées dans l'atmosphère solaire sont les filaments (vus au bord sous la forme des protubérances) et les centres d'activités avec leurs taches et leurs facules. Les régions actives, associations de plusieurs centres actifs, sont des perturbations qui s'étendent à toutes les couches de l'atmosphère solaire, prolongeant leurs effets dans le milieu interplanétaire jusqu'à la Terre. Un centre actif prend naissance chaque fois qu'un tube de flux magnétique émerge à la surface du Soleil (photosphère). Une région active se forme par émergence successive de plusieurs tubes de flux et réorganisation des lignes de forces par interaction avec les mouvements de la matière. Au cours de sa vie, une région active est souvent le siège de phénomènes violents, les éruptions chromosphériques. Elles ont lieu en des points particuliers présentant toujours la même structure caractéristique du champ magnétique et des mouvements de la matière. L'observation des courants électriques sur les sites éruptifs est capitale pour comprendre le mécanisme du déclenchement des éruptions.

L'influence de l'activité solaire sur l'environnement terrestre est relativement bien connue, au moins par les effets perturbateurs des éruptions solaires sur le champ géomagnétique. La prévision des éruptions est donc importante pour les télécommunications et pour les activités spatiales, notamment lors des vols habités. Elle passe par l'observation des phénomènes précurseurs, en particulier les perturbations du champ magnétique dans les régions actives et des courants électriques associés qui annoncent la déstabilisation de la configuration magnétique. La mesure des courants électriques est très difficile et pratiquement impossible avec les télescopes actuellement en service (effets des polarisations instrumentales).

Une des découvertes les plus intéressantes des dix dernières années est la mise en évidence des concentrations du champ magnétique dans des structures de très petites dimensions (0.2 seconde d'arc soit 150 km). Ces structures apparaissent aussi bien dans les régions calmes (maille de la supergranulation) que dans les régions actives (facules). L'observation spectroscopique à très haute résolution spatiale (nécessitant des temps de pose supérieurs au temps caractéristique d'évolution des perturbations atmosphériques) est impossible avec des télescopes de conception classique, même s'ils sont placés dans le meilleur site possible. Beaucoup plus que de grossissement, c'est un problème de résolution, c'est-à-dire de séparation de points observables. Or, l'atmosphère terrestre, non seulement agit comme un filtre, mais encore brouille l'observation.

### LES LIMITATIONS INSTRUMENTALES ACTUELLES

La mesure du champ magnétique solaire se fait par l'analyse de la polarisation des raies spectrales par effet Zeeman. Seule la composante longitudinale du champ (projection du vecteur sur la ligne de visée) est mesurable facilement avec les instruments actuels.

La mesure de la composante transversale se heurte aux limites :

- de la résolution spatiale des observations spectroscopiques;
- de la polarisation instrumentale parasite introduite par les miroirs des instruments basés sur le concept classique des tours solaires;
- des incertitudes sur l'influence des conditions thermodynamiques locales dans le profil des raies observées.

Si la dimension des structures observées (fig. 1) est plus petite que la résolution des observations, la lumière reçue dans chaque élément résolu de l'image est un mélange de la lumière émise dans les régions magnétiques et non magnétiques. Chaque raie spectrale est le mélange des raies produites par l'atome considéré dans les régions magnétiques et non magnétiques. Le profil observé de la raie sera fonction de l'intensité et de la direction du champ magnétique dans les structures magnétiques, du nombre de ces structures dans l'élément résolu par l'observation, de la différence des températures et des vitesses radiales entre les régions magnétiques et non magnétiques.

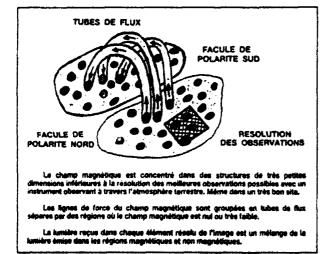


Fig. 1. - Structures fines du champ magnétique dans l'atmosphère du Sciati

Pour accéder à la mesure de vecteur champ magnétique (intensité et direction) à plusieurs niveaux dans l'atmosphère du Soleil, il est indispensable d'observer simultanément un grand nombre de raies se formant à des altitudes différentes et à chaque niveau pour séparer les effets du champ magnétique des variations locales des paramètres thermodynamiques.

#### LE CONCEPT DE THEMIS

THEMIS permettra de mesurer les trois composantes du champ magnétique ainsi que le champ de vitesses associé avec une excellente résolution spatiale en utilisant simultanément jusqu'à vingt raies spectrales choisies en fonction de leurs décompositions Zeeman et de leurs sensibilités aux variations des paramètres thermodynamiques.

Le concept de l'instrument est totalement original :

- Un télescope pointé directement sur le Soleil pour éviter les effets de la polarisation instrumentale provoquée par les miroirs du concept traditionnel coelostat/tour.
- Le vide dans le télescope pour éviter les turbulences internes.
- Le refroidissement des pièces optiques (lames de fermeture, miroir secondaire) pour supprimer les effets dus au chauffage par le faisceau lumineux.
- Un analyseur de la polarisation achromatique dans un large domaine spectral placé au foyer du télescope avant que la symétrie de révolution des faisceaux soit détruite.
- Une optique adaptative (miroir actif) pour corriger en temps réel les déplacements de l'image dus à l'agitation atmosphérique.
- Deux spectrographes en série (prédisperseur et échelle) pour pouvoir observer simultanément un grand nombre de raies avec une haute résolution spatiale et spectrale.
- Une conception architecturale du bâtiment très poussée pour limiter les perturbations thermiques et aérodynamiques de l'environnement immédiat du bâtiment.
- Des récepteurs modernes (caméras CCD) et une informatique très puissante pour maîtriser et traiter l'important débit de données nécessaires à une acquisition à cadence élevée.

#### LE SCHÉMA OPTIQUE

Le schéma optique se compose de trois parties principales (fig. 2) et de plusieurs instrumentations interchangeables en fonction du mode de fonctionnement choisi.

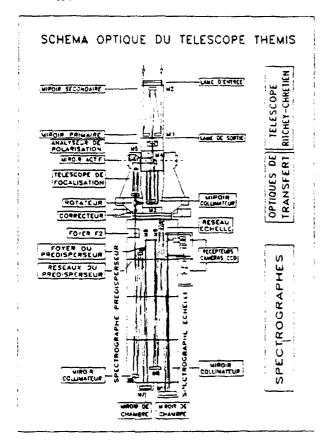


Fig. 2. - Schema optique et structure mécanique de THEMIS

#### 1) Le télescope Ritchey-Chrétien sous vide

Le miroir primaire M1 a un diamètre utile de 90 cm et une distance focale de 3145 mm (F/3.5). Le miroir secondaire M2 porte la distance focale équivalente de la combinaison à 15 mètres. L'ouverture F/17 des faisceaux a été choisie pour que l'analyse de la polarisation de la lumière puisse se faire correctement dans un champ de 4' de diamètre.

Comme le télescope est sous vide, le tube doit être fermé par deux lames de verre. Le bloc de verre (BK7 Schott) de la lame d'entrée a été sélectionné avec le plus grand soin. Les variations de l'indice de réfraction ne dépassent pas une unité de la sixième décimale. Cette lame a un diamètre de 1.10 mètre et une épaisseur de 65 mm. Pour éviter les images parasites et les franges d'interférence produites par les réflexions multiples sur les deux faces la lame est biconcave (distance focale de 5500 mm).

Le miroir secondaire reçoit une concentration importante du flux lumineux incident. En absence d'un système efficace de refroidissement, la température de ce miroir dépasserait la valeur critique de 150 degrés au delà de laquelle des réactions chimiques irréversibles se produiraient dans le bloc de verre (Zérodur de Schott).

Au foyer (F1) du télescope se trouve l'analyseur de polarisation. Comme pour le miroir secondaire, des précautions doivent être prises pour éviter l'échauffement des pièces optiques et du support mécanique. Un diaphragme refroidi limite le champ à la valeur utile de façon que le faisceau lumineux ne touche pas les barillets des lames cristallines qui elles-mêmes doivent être pré-chauffées avant introduction dans le faisceau.

#### 2) L'optique de transfert

L'optique de transfert sert à transporter le faisceau vers les spectrographes placés verticalement sous le télescope. Une amplification de 3 8 amène la distance focale équivalente à 57 mètres avec un rapport d'ouverture de F/63. En suivant le faisceau lumineux, nous avons :

- Un miroir collimateur M3 qui focalise une image de la pupille d'entrée sur le miroir actif M5.
- Un miroir plan troué M4, laissant passer le champ coude le faisceau le long de l'axe d'élévation de la monture azimutale.
- Le miroir actif M5 qui sert au balayage précis du champ et à la correction en temps réel de l'agitation atmosphérique.
- Une optique (Télescope Cassegrain M6, M7) pour refocaliser l'image sur la fente des spectrographes
- Un rotateur de champ pour compenser la rotation introduite par la monture azimutale et pour orienter le balayage du champ dans une direction quelconque par rapport à l'image.
- Un correcteur de champ pour compenser le chromatisme et l'aberration sphérique résiduelle de l'analyseur de pharisation.

Au foyer F2 (entrée des spectrographes) plusieurs intrumentations peuvent être mises en service simultanément :

- Un dispositif de visée de la fente permettant de connaître les structures observées avec les spectographes. Plusieurs combinaisons de filtres sont possibles pour sélectionner des images de la photosphère ou de la chromosphère (filtres de Lyot, interférentiels etc.).
- Des optiques correctrices du chromatisme transversal de l'analyseur de polarisation.
- Les capteurs du dispositif de mesure du déplacement de l'image (signaux pour le miroir actif).

#### 3) Les spectrographes

L'observation simultanée d'un grand nombre de raies choisies dans le plus grand domaine spectral possible impose deux spectrographes en série. Le premier, appelé spectrographe prédisperseur, permet de sélectionner plusieurs domaines au moyen de masques placés dans le plan de son spectre. La lumière qui passe dans chaque domaine ainsi sélectionné est envoyée sur le deuxième spectrographe échelle. Si les caractérisques des deux spectrographes sont correctement choisies, nous obtenons à la sortie autant de spectres qu'il y a de domaines sélectionnés et ces spectres sont séparés les uns des autres.

L'optique des spectrographes se compose de 4 parties :

- le spectrographe prédisperseur avec 3 réseaux interchangeables ;
- le spectrographe échelle ;
- les optiques de transfert entre les deux spectrographes;
- les séparateurs de faisceaux devant les caméras CCD.

Un tel dispositif donne une grande souplesse pour choisir la meilleure combinaison en fonction des raies sélectionnées pour l'observation. Les deux spectrographes peuvent être utilisés soit en mode additif (les dispersions s'ajoutent) soit en mode soustractif (les dispersions se retranchent).

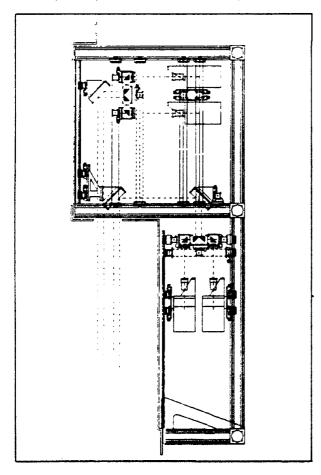


Fig. 3 - Implantation des caméras CCD

En mode additif classique, l'optique de transfert se compose de deux miroirs plans (M8, M9 fig. 2). Si l'on place dans le plan du spectre du prédisperseur des masques constitués de plusieurs fentes larges, isolant des bandes spectrales couvrant les différentes raies choisies, on obtiendra à la sortie du spectrographe échelle simultanément les profils de plusieurs raies pour tous les points de l'image sélectionnés par la fente d'entrée.

Un cas particulier du mode soustractif est celui connu sous le nom de DPSM (Double Passage Soustractif Multicanal). Le réseau du spectrographe prédisperseur est choisi de façon que les deux dispersions s'annulent complètement. Dans ce mode, la fente d'entrée est remplacée par une fenêtre laissant passer un champ bi-dimensionnel (au lieu d'une ligne). Si l'on place dans le spectre fourni par le prédisperseur, à l'emplacement d'une raie spectrale, une série de fentes fines équidistantes associées à une série de prismes à réflexion totale (pour ajuster l'écartement des faisceaux ainsi sélectionnés), on obtient à la sortie du spectrographe échelle autant d'images monochromatiques de la portion du Soleil observée (définie par la fenêtre d'entrée) qu'il y a de fentes sélectrices au niveau du spectre du prédisperseur. Si l'écartement entre les faisceaux est correctement ajusté, les différentes images sont séparées à la sortie et la longueur d'onde varie d'une image à l'autre en fonction de la dispersion du spectre (prédisperseur) et de la distance entre les fentes. La résolution spectrale de chaque image dépend de la largeur de chaque fente. Les deux spectrographes se comportent comme plusieurs filtres monochromatiques, à bande passante étroite, observant simultanément la même région sur le Soleil.

Suivant le mode de fonctionnement choisi, on peut, soit observer simultanément les profils d'un grand nombre de raies pour tous les points de l'image sélectionnés par la fente d'entrée (fine), soit observer les profils d'une raie (ou de 2 raies) simultanément pour tous les points de l'image sélectionnée par la fenêtre d'entrée.

THEMIS sera équipé de 20 caméras CCD (matrice Thomson de 288 × 384 éléments photosensibles) placées à la sortie du spectrographe échelle. Un ensemble de bancs d'optique (fig. 3) permet de répartir les caméras et leurs optiques associées, soit sur les différentes raies sélectionnées, soit sur les images monochromatiques fournies par le DPSM. La chaîne d'acquisition permet de traiter 2 millions d'octets par seconde, soit 8000 profils de raies toutes les 4 secondes.

#### CORRECTION DE LA TURBULENCE ATMOSPHÉRIQUE

L'échauffement du sol par le Soleil et le vent produisent autour d'un télescope un environnement turbulent caractérisé par des masses d'air à des températures différentes. Ces bulles d'air, plus ou moins chaudes ou froides, défilent constamment devant la ligne de visée du télescope. L'indice de réfraction de l'air étant fonction de la température, un rayon lumineux sera dévié à chaque transition entre des bulles d'air de température différente. Les bulles d'air, plus chaudes ou plus froides, jouent également le rôle de lentilles optiques convergentes ou divergentes, introduisant une défocalisation locale de l'image fournie par le télescope. Ces différentes perturbations ne sont pas cohérentes sur tout le champ et leurs effets dépendent de la fréquence. On peut définir la turbulence atmosphérique au moyen des trois paramètres suivants :

- Le paramètre de Fried "Ro". C'est le diamètre du télescope qui, dans le vide, donnerait la même résolution que l'atmosphère.
- Le domaine d'isoplanéité "i". C'est le champ angulaire pour lequel les perturbations sont cohérentes entre elles.
- Le temps caractéristique "t". C'est la durée moyenne d'évolution des perturbations en chaque point de l'image.

Pour un site de plaine, la valeur moyenne de Ro est de 5 cm, le domaine d'isoplanéité de 4 secondes d'arc et le temps caractéristique de 10 millisecondes. Le brouillage de l'image produit par cette atmosphère peut être comparé à celui de l'image de "Canal +" reçue sans décodeur. Les grandes lignes de l'image sont visibles mais il est impossible de voir tous les détails.

L'aspect de l'image fournie par un télescope dépend non seulement des paramètres atmosphériques (Ro,i,t) mais aussi du diamètre "D" du télescope. Bien que la résolution théorique d'un télescope augmente avec son diamètre, la résolution du couple atmosphère + télescope passe par un maximum pour D/Ro = 3 pour des poses longues par rapport à la valeur du temps caractéristique "t" d'évolution des perturbations.

**Pour D/Ro > 6** l'effet principal est dû aux variations de courbure de la surface d'onde. L'image sera floue et peu agitée.

**Pour D/Ro** < 6 l'effet principal est dû aux variations d'inclinaison de la surface d'onde L'image sera nette mais agitée.

Sur le site des îles Canaries, la valeur moyenne de Ro = 10 cm et 60 % du temps elle dépasse 15 cm avec un maximum de l'ordre de 45 cm 5 % du temps. Avec un télescope de 90 cm de diamètre (THEMIS) en corrigeant uniquement les effets du premier ordre (inclinaison de la surface d'onde) on obtiendra, dans le cas des observations spectroscopiques (pose longue), une résolution effective de 0"2 (60 % du temps) et un gain en résolution d'un facteur 3 pour les valeurs de D/Ro comprises entre 6 et 9.

Les déplacements de l'image dépendent de la fréquence. À 100 Hz il reste encore 1 % de l'amplitude des déplacements à basse fréquence (1 Hz) et environ 10 % à 12 Hz. Pour corriger une agitation de l'image de plus ou moins 1 seconde d'arc à 1 Hz et restituer une résolution effective de 0"16 (résolution théorique du télescope à 6000 Å) il faut agir sur l'orientation du miroir actif (2 axes) 800 fois par seconde, soit toutes les 1.25 milli-secondes.

Seuls les développements technologiques dans le domaine des matériaux composites (miroir léger très rigide) et dans celui de la micro-informatique (processeur très rapide) ont permis de résoudre ce problème très difficile.

L'orientation du miroir actif, supporté par une structure mécanique déformable (axe élastique). change 800 fois par seconde sous l'action de 2 quartz piézo-électriques agissant dans deux directions perpendiculaires. Les signaux envoyés aux deux quartz proviennent d'un calculateur très rapide qui analyse, également 800 fois par seconde, les variations de la position de l'image fournie par le télescope. Une caméra CCD enregistre en permanence une image de la granulation solaire obtenue en prélevant 10 % du flux sur le faisceau lumineux. Si, à un instant donné, on mémorise une image de cette granulation et que l'on compare les images suivantes à cette image mémorisée, on obtient les déplacements relatifs et l'on peut ramener toutes les images successives en coïncidence avec l'image mémorisée. On a ainsi stabilisé l'image sur la fente des spectrographes.

THEMIS 501

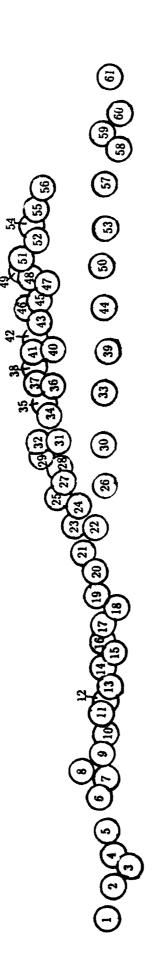
Note from the editor: The paper on the French project "Themis" by J. Rayrole, P. Mein, and M. Tournaire of Paris Observatory and of INSU-CNRS was presented by M. Semel. Unfortunately, we did not receive the manuscript in time so we asked the permission of Societe Astronomique de France to reprint a version of that paper published in French in L'Astronomie.

Speaker: Semel

#### Discussion

- **E. West:** I have a question on your polarimeter. You have a 2  $MgF_2$  and 2 KDPs. How are they aligned? Are the  $MgF_2$  plates one wave plate and the KDPs the second?
- M. Semel: The  $MgF_2$  plates are crossed and the 2 KDPs are aligned as well. The width of each plate is calculated to yield a super achromatic 1/4 wave plate when all the four plates are combined.
- **J.** Harvey: The immersion oil used to reduce surface reflections from the KDP and  $MgF_2$  plates will not match all the indices of refraction. Will the residual multiple reflections cause any difficulties?
- M. Semel: We expect very small effects.
- **J. Stenflo:** Do I understand it correctly that you do not measure all four Stokes parameters I, Q, U, and V simultaneously with THEMIS? If this is so,then variable seeing will seriously affect the construction of Stokes vectors. As the objective of using a "polarization-free" telescope is to obtain accurate Stokes vectors, how do you plan to deal with this fundamental problem?
- M. Semel: It is a misunderstanding. Themis may use any mode of Stokes polarimetry. However the best spatial resolution will be obtained in the two particular modes of observations I have mentioned.

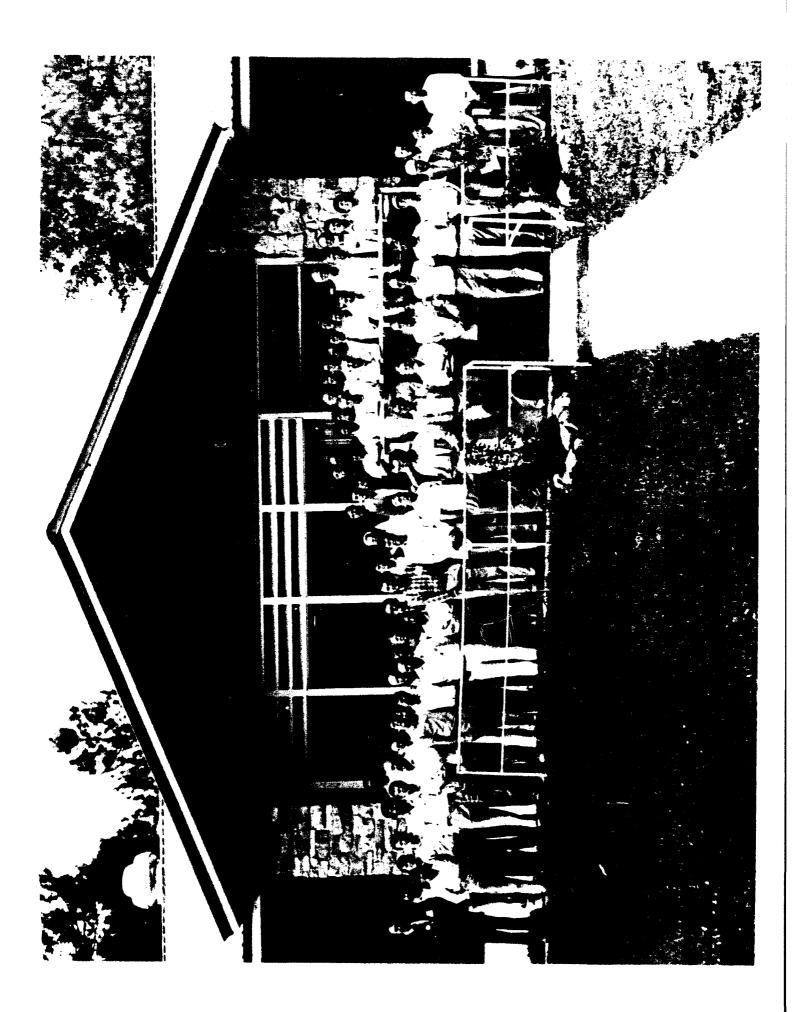
# NATIONAL SOLAR OBSERVATORY/SACRAMENTO PEAK ELEVENTH SUMMER WORKSHOP 27—31 AUGUST, 1990



							i
-	Larry November	17.	Steve Keil	35.	Egidio Landi	47.	George Simon
2	Brian Armstrong	œ.	Iraida Kim	33	Bill Livingston	<del>48</del> .	John Jefferies
eri	Tarla Leighton	19.	Julius Sykora	34.	Veronique Bommier	49.	Jose Carlos del Toro
i <del>- i</del>	Herve Auffret	20.	Jack Harvey	35.	Birgitta Larsson	20.	Jan Stenflo
\ci	Tom Moran	21.	Tom Metcalf	36.	Boris Ioshpa	51.	Dick Dunn
ó	K.S. Balasubramaniam	22.	William Henze Jr.	37.	Alessandro Cacciani	52.	Slava Zhurin
<i>.</i> :	Richard Canfield	23.	Jean-Louis Leroy	38	Tron Darvann	53.	Peter Povel
œ	Dick Altrock	24.	Tilak Hewagama	39.	Gary A. Chapman	54.	John Leibacher
o di	Serge Koutchmy	25.	Graham Murphy	40.	Andrew Skumanich	55.	Doug Rabin
10.	Juergen Staude	26.	Steven Tomcsyk	41.	Jo Bruls	56.	Haimin Wang
=======================================	G. Allen Gary	27.	Sergio Restaino	42.	Sami K. Solanki	57.	Jim Fowler
12,	Jean-Claude Henoux	28.	Kevin Reardon	43.	Drake Deming	58.	Jack Evans
13.	Kenneth P. Topka	29.	Jack Zirker	44	David Rust	59.	John O'Byrne
14.	Don Neidig	30.	Dirk Soltau	45.	Christoph Keller	.09	Ai Guoxiang
15.	Meir Semel	31.	Gianna Cauzzi	46.	Bruce Lites	61.	Ray Smartt

Ed West

16.



#### List of Participants

Ai Guoxiang
Beijing Astronomical Observatory
Beijing 100080, CHINA
telex=22940 BAOAS CN+

Richard Altrock
Solar Research Branch, AFGL
Sacramento Peak Observatory
Sunspot NM 88349,USA
tel=(505)434-7000
fax=(505)434-7029
telex=1561030 AURANSO UT
email=raltrock@solar

Herve Auffret
Observatoire de Pic-du-Midi
9 rue de Pont de la Moulette
F-65200 Bagneres-de-Bigorre
FRANCE
tel=62-95-19-69

K.S. Balasubramaniam
ES-52
NASA Marshall Space Flight Center
Huntsville, Al 35812, USA
tel=205-544-2280
email=balasub@solar

Veronique Bommier
DAMAP Observatoire de Meudon
92195 Meudon Principal Cedex
FRANCE
tel=(1)45077954
telex=201571
email=bommier@frmeu51,28726::
bommier,bommier%mesioa.dnet@solar

Jo Bruls
Sterrekundig Instituut
Postbus 80 000
3508 TA Utrecht, NETHERLANDS
Stel=(31)-30 535225
fax=(31) 30 531601
telex=40048 (fylut)
email=bruls%hutruu51.bitnet,
nbruls@ruunsa.fys.ruu.nl

Alessandro Cacciani
Physics Department
University "La Sapienza"
2 Aldo Moro
00185 Roma, ITALY
tel=(6)4991-4462
fax=39-6-4957697
email=acacciani@solar

Richard Canfield
Institute for Astronomy
University of Hawaii
Honolulu, HI 96822, USA
tel=(808)948-6898
email=canfield@mamane.ifa.
hawaii.edu

Gianna Cauzzi
National Solar Observatory
Sunspot NM 88349, USA
tel=(505)434-7000
fax=(505)434-7029
telex=1561030 AURANSO UT

Gary A. Chapman
San Fernando Observatory
14031 San Fernando Rd
Sylmar CA 91342, USA
email=gchapman@solar

Steven Colley
National Solar Observatory
Sunspot NM 88349, USA
tel=(505)434-7000
fax=(505)434-7029
telex=1561030 AURANSO UT

Jean-Marc Conan National Solar Observatory Sunspot NM 88349, USA tel=(505)434-7000 fax=(505)434-7029 telex=1561030 AURANSO UT

Roy Coulter
National Solar Observatory
Sunspot NM 88349, USA
tel=(505)434-7000
fax=(505)434-7029
telex=1561030 AURANSO UT

Tron A. Darvann
Inst. of Theoretical Astrophysics
University of Oslo
N0315 Oslo 3, NORWAY
tel=(505)434-7000

Jose Carlos del Toro Iniesta
Inst. de Astrofisica de Canarias
38200 La Laguna
Tenerife, Canary Islands, SPAIN
tel=9-22 26 3005
fax=9-22-263005
telex=92640 IACE
email=JDELTORO@SOLAR,
jti%iac.dnet@solar

Drake Deming
NASA/Goddard Space Flight Center
Code 693
Greenbelt, MD 20771, USA
tel=(301)286-6519
email=ddeming@solar

Richard B. Dunn
National Solar Observatory
Sunspot NM 88349, USA
tel=(505)434-7000
fax=(505)434-7029
telex=1561030 AURANSO UT

Jack W. Evans Jr. 1 Baya Rd, Eldorado Sante Fe NM 87505, USA tel=(505)983-5705

Jim Fowler
Apache Point Observatory
Sunspot NM 88349, USA
tel=(505)434-7000
fax=(505)434-7029
telex=1561030 AURANSO UT

G. Allen Gary
ES-52
Marshall Space Flight Center
Huntsville, AL 35812, USA
tel=205-544-7609
email=gagary@solar

Jack W. Harvey
National Solar Observatory, NOAO
950 Cherry, POB 26732
Tucson AZ 85726, USA

tel=(602)325-9337 email=jharvey@noao.edu

Steven Hegwer
National Solar Observatory
Sunspot NM 88349, USA
tel=(505)434-7000
fax=(505)434-7029
telex=1561030 AURANSO UT

Jean-Claude H'enoux
Observatoire de Meudon
DASOP 92195 Meudon Principal Cedex
FRANCE
tel=45077803
fax=45 07 7469
telex=201571
email=HENOUXOFRMEU51.BITNET

William Henze Jr.
MS 52, Teledyne Brown Engineering
Research Park
Huntsville AL 35807, USA
tel=(205)544-7616

Tilak Hewagama
NASA/Goddard Space Flight Center
Code 693
Greenbelt, MD 20771, USA
tel=(301)286-6517
email=ys2th@LEPVAX.SPAN

Boris Ioshpa
IZMIRAN, USSR Acad. of Sciences
142092 Troitsk
Moscow Region, USSR
telex=412623 SCSTD SU

John T. Jefferies
National Solar Observatory, NOAO
950 N. Cherry Ave
Tucson AZ 85786, USA
tel=(602)322-8501
email=jtj@noao.edu

Stephen L. Keil
Solar Research Branch, AFGL
Sacramento Peak Observatory
Sunspot NM 88349, USA
tel=(505)434-7000
fax=(505)434-7029
telex=1561030 AURANSO UT
email=skeil@solar

Christoph Keller
Institute of Astronomy
ETH-Zentrum
CH-8092 Zurich, SWITZERLAND
tel=41-1-2563815
fax=41-1-252-01-92
telex=817379ethgch
email=ckeller@solar

Iraida Kim
Sternberg State Astronomical Inst.
University of Moscow
Universitetskij Prosp 13
Moscow 119899, USSR
tel=939-23-82
fax=(7095)2302081
telex=411576 ASCON SU

Serge Koutchmy
Institute d'Astrophysique
98 Bis BD Arago
F-75014 Paris, FRANCE
tel=33-1-4320-1425
fax=40512100
telex=205671F
email=solaire@friap51.bitnet

Egidio Landi Degl'Innocenti Osservatorio Astrof. Di Arcetri Largo E. Fermi 5 I-50125 Firenze, ITALY email=28726::LANDIE

Birgitta Larsson
University of Tromso
P.O. Box 953N-9001 Tromso, NORWAY
tel=47-83-86060
fax=47-83-89852
telex=64124 AUROB.N
email=FYBLQES.UIT.UNINETT,
blarssonQsolar.

John Leibacher
National Solar Observatory, NOAO
950 Cherry,
POB 26732
Tucson AZ 85726-6732, USA
email=jleibacher@solar

Jean-Louis Leroy
Observatoires du Pic-du-Midi
et de Toulouse
14, Avenue Edouard-Belin
31400 Toulouse, FRANCE

tel=61 33 2929 fax=61 53 67 22 telex=530 776

Bruce W. Lites
High Altitude Observatory
NCAR POB 3000
Boulder CO 80307-0440, USA
tel=(303)497-1517
fax=303-497-1137
email=lites@hao.ucar.edu

William C. Livingston
National Solar Observatory, NOAO
950 Cherry,
POB 26732
Tucson AZ 85726,
USA
tel=(602)325-9374
email=wci@noao.edu

Richard Mann
National Solar Observatory
Sunspot NM 88349, USA
tel=(505)434-7000
fax=(505)434-7029
telex=1561030 AURANSO UT

Tom Metcalf
Institute for Astronomy
University of Hawaii
2680 Woodlawn Drive
Honolulu, HI 96822, USA
tel=808-948-8306
fax=808-988-2790
email=tmetcalf@solar

Thomas G. Moran
Cambridge Research and Instrumen.
21 Erie Street
Cambridge, MA 02139, USA
tel=617-491-2627
fax=617-864-3730

Graham Murphy
High Altitude Observatory
NCAR POB 3000
Boulder CO 80307-3000, USA
tel=(303)497-1565
fax=(303)497-1137
email=murphy@hao.UCAR.EDU,
GMurphy@SOLAR

Donald F. Neidig
Solar Research Branch, AFGL
Sacramento Peak Observatory
Sunspot NM 88349, USA
tel=(505)434-7019
fax=(505)434-7029
telex=1561030 AURANSO UT
email=dneidig@solar

Laurence J. November
National Solar Observatory
Sunspot NM 88349, USA
tel=(505)434-7000
fax=(505)434-7029
telex=1561030 AURANSO UT
email=lnovember@solar

John W. O'Byrne School of Physics Univ of Sydney N.S.W. 2006, AUSTRALIA

Marc Pic
National Solar Observatory
Sunspot NM 88349, USA
tel=(505)434-7000
fax=(505)434-7029
telex=1561030 AURANSO UT

Hans Peter Povel
Institut fur Astronomy
ETH-Zentrum
CH-8092 Zurich, SWITZERLAND
tel=01-256-4222
telex=81-73-79 ehhg ch
fax=01-251-2172

Douglas M. Rabin
National Solar Observatory, NOAO
950 Cherry, POB 26732
Tucson AZ 85726, USA
tel=(602)325-9331
fax=602-325-9278

Richard Radick
Solar Research Branch, AFGL
Sacramento Peak Observatory
Sunspot NM 88349, USA
tel=(505)434-7000
fax=(505)434-7029
telex=1561030 AURANSO UT
email=rradick@solar

Sergio Restaino
National Solar Observatory
Sunspot NM 88349, USA
tel=(505)434-7000
fax=(505)434-7029
telex=1561030 AURANSO UT
email=srestaino@solar

David M. Rust
Applied Physics Lab
Johns Hopkins University
Johns Hopkins Rd
Laurel MD 20723-6099, USA
tel=(301)953-5414
fax=(301)953-1093
telex=511303
email=drust@solar,drust@aplsp

Meir Semel
Observatoire de Meudon
5 Pl Janssen
F-92195 Meudon Principal Cedex
FRANCE
email=SEMEL%FRMEU51.BITNET

George W. Simon
Solar Research Branch
Air Force Geophysics Lab
Sacramento Peak Observatory
Sunspot NM 88349, USA
tel=(505)434-7000
fax=(505)434-7029
telex=1561030 AURANSO UT

Andrew P. Skumanich
High Altitude Observatory
NCAR POB 3000
Boulder CO 80307-0440, USA
tel=(303)497-1528
email=mesioa::heritichi sku@hao.
ucar.edu

Raymond Smartt
National Solar Observatory
Sunspot NM 88349, USA
tel=(505)434-7000
fax=(505)434-7029
telex=1561030 AURANSO UT
email=rsmartt@olar

Jesse B. Smith, Jr. ES-52, SSL/Solar Science Branch Marshall Space Flight Center Huntsville AL 35812, USA tel=205-544-7614, FTS 824-7614

Sami K. Solanki
Institute of Astronomy
ETH-Zentrum
8092 Zurich, SWITZERLAND
tel=+41/1/256 3810
fax=+41/1/251 2172
email=solanki@ifa.ethz.ch(.ean),
ssolanki@susolar(.bitnet)

Dirk Soltau
Kiepenheuer-Inst. fur Sonnenphysik
Schoeneckstr. GD-78 Freiburg
GERMANY
tel=761-382067
fax=764-32280
telex=772-1552 kis d
email=dirk.soltau%kis.
uni-freiburg.dbp.de@solar

Juergen Staude
Zentralinstitut fur Astrophysik
Sonnenobs Einsteinturm
Rosa-Luxemburg Strasse 17a
DDR-1591 Potsdam, GERMANY
telex=15305 VDEPDM

Frits Stauffer
National Solar Observatory
Sunspot NM 88349, USA
tel=(505)434-7000
fax=(505)434-7029
telex=1561030 AURANSO UT
email=fstauffer@solar

George Streander
National Solar Observatory
Sunspot NM 88349, USA
tel=(505)434-7000
fax=(505)434-7029
telex=1561030 AURANSO UT

Jan Stenflo
Institute of Astronomy, ETH-Zentrum
CH-8092 Zurich, SWITZERLAND
tel=+41-1-2563804
fax=+41-1-252 0192
telex=81-73-79 ehhg ch

email=jstenflo@solar, stenflo@ifa.ethz.ch

M.T. Sun
Cntr for Space Plasma
and Aeronomic Res
Dept of Mech Eng
University of Alabama
Huntsville AL 35899, USA
tel=(205)895-6413
fax=(205)895-6758

Július Sýkora
Astronomical Institute
059 60 Tatranska Lomnica
CZECHOSLAVAKIA
tel=(0969)967866
telex=78277

Steven Tomcsyk
High Altitude Observatory
NCAR POB 3000
Boulder CO 80307-0440, USA
tel=303-497-1579
email=tomcsyk@hao.ucar.edu

Kenneth P. Topka
Solar Physics, Dept 91-30, Bldg 256
Lockheed Palo Alto Res Lab
3251 Hanover St.
Palo Alto CA 94304, USA
tel=(415)424-4030 4027
fax=415-424-3994
email=ktopka@solar

Haimin Wang
Solar Astronomy
Caltech, 264-33
Pasadena CA 91125, USA
tel=(818)356-3858
email=haimin@sundog.caltech.edu

Ed West
ES52
NASA Marshall Space Flight Ctr
Huntsville AL 35812, USA
tel=205-544-7625
fax=205-544-5862
email=ewest@solar

S.T. Wu
Cntr for Space Plasma
and Aeronomic Res
Dept of Mech Eng
University of Alabama
Huntsville AL 35899, USA
tel=(205)895-6413
fax=(205)895-6758
email=wu@cspara.span

Slava Zhurin
Deputy Director, IZMIRAN
USSR Acad of Sciences
142092 Troitsk
Moscow Region, USSR
tel=3340929
telex=412623 SCSTP SU

Jack B. Zirker
National Solar Observatory
Sunspot NM 88349, USA
tel=(505)434-7000
fax=(505)434-7029
telex=1561030 AURANSO UT
email=jzirker@solar

#### **NSO/SP SUMMER WORKSHOP SERIES**

Large-Scale Motions of the Sun: Summer Workshop, Sunspot, N.M., 1-2 September, 1977. S.A. Musman, chairman. \*(NSO/SP Summer Workshop no. 1) 45 participants

Summary: This first (unpublished) meeting of the NSO/SP Summer Series focused on solar oscillations, both in theory and observation, and on the application of oscillation data to the determination of differential interior rotation. A proposed model of solar rotation was also presented. The application of solar p-modes as a tracer of large-scale horizontal motions was discussed, together with studies of the dynamics of gas and magnetic fields in the outer solar layers.

Small-Scale Magnetic Fields in the Solar Atmosphere: Summer Workshop, Sunspot, N.M., 16-20 July, 1979. L.E. Cram, chairman. \*(NSO/SP Summer Workshop no. 2) 50 participants

Summary: Observed properties and theoretical consequences of the structure and intensity of solar magnetic fields were major areas of focus. Observations show that almost all the solar magnetic flux is concentrated in 1-2 kG bundles which occupy only a small fraction of the observed area. Processes responsible for this concentration, as well as the implication to solar cycle dynamo theories, were examined. There was demonstrated a strong need to study in detail the physical processes occurring in single small flux tubes. Such studies require sensitive velocity and magnetic field measurements over relatively long periods, with excellent spatial resolution.

Solar Instrumentation: What's Next? Conference Proceedings, Sunspot, N.M., 14-17 October, 1980. R.B. Dunn, ed. 618 p. (NSO/SP Summer Workshop no. 3) 56 participants

Summary: This workshop, the first to be published in the NSO/SP Summer Series, explored the observational needs of solar and solar-stellar astronomers, and the required instrumentation to fulfill those needs. Sessions were dedicated to LEST, in its initial planning stages, and to image stabilization techniques. The use of interferometry for solar observations, as well as the importance of the solar-stellar connection to further the understanding of the Sun, were also discussed.

The Physics of Sunspots: Conference Proceedings, Sunspot, N.M., 14-17 July, 1981. L.E. Cram and J.H. Thomas, eds. 495 p. (NSO/SP Summer Workshop no. 4) 57 participants

Summary: The workshop began with the discussion of relevant observations on the birth, evolution and emergence of sunspots, as well as with the analysis of magnetic features and vector magnetic fields of active regions; and continued with empirical and theoretical models of sunspots. A study of starspots was presented, as were studies of solar dynamical phenomena, such as umbral flares, Evershed flow, oscillations, and the influence of sunspots on the output of solar radiation.

Small-Scale Dynamical Processes in Quiet Stellar Atmospheres: Conference Proceedings, Sunspot, N.M., 25-29 July, 1983. S.L. Keil, ed. 469 p. (NSO/SP Summer Workshop no. 5) 66 participants

Summary: The study of small-scale dynamical processes in the solar atmosphere was the major focus, including the implication of this work to the interpretation of unresolved observations of stellar atmospheres in general. Sessions were dedicated to high-resolution observations of small-scale solar phenomena, and their interpretation; to the modelling of small-scale processes, such as granulation; to the interaction of convection and magnetic fields; and to low-resolution observations, bearing on small-scale dynamical processes such as line asymmetries and wavelength shifts.

<sup>\*</sup> NSO/SP Summer Workshops nos. 1 and 2 are unpublished

Chromospheric Diagnostics and Modelling: Workshop Proceedings, Sunspot, N.M., 13-16 August, 1984. B.W. Lites, ed. 314 p. (NSO/SP Summer Workshop no. 6) 69 participants

Summary: The OSO-8 observations had revealed that chromospheres (and coronae) are the rule, rather than the exception, for most classes of stars. The aim of the meeting was to enhance the understanding of chromospheres. Sessions dedicated to the observations of chromospheric structures and magnetic fields were followed by talks on the calculation of chromospheric models and heating processes. Working groups were organized on Line Synthesis and Atmospheric Modelling; Magnetic Fields; Space and Ground-Based Collaborative Observations, and on Chromospheric Heating and Energy Balance.

The Lower Atmosphere of Solar Flares: Relationships Between Low Temperature Plasmas and High Energy Emissions. Proceedings of the National Solar Observatory/ Solar Maximum Mission Symposium, Sunspot, N.M., 20-24 August, 1985. Don Neidig, ed. 503 p. (NSO/SP Summer Workshop no. 7) 58 participants

Summary: The meeting analyzed flare phenomena in the chromosphere (impulsive phase, shocks and condensations, observations of flares in helium lines) and included white light flares, which had, until recently, been often considered a separate flare class. High energy emissions in solar, and stellar, flares were also reviewed. The meeting ended with sessions on the origin of flare energy, its transport, and on the evidence for and against electron beams as the agent generating hard X-ray bursts in Solar Flares.

The Internal Solar Angular Velocity: Theory, Observations and Relationship to Solar Magnetic Fields. Symposium Proceedings, Sunspot, N.M., 11-14 August, 1986. B.R. Durney and S. Sabatino, eds. 374 p. (NSO/SP Summer Workshop no. 8) 60 participants

Summary: The meeting aimed at the study of the internal solar angular velocity, both in the radiative zone (where the angular momentum loss due to the solar wind and magnetic fields must play an essential role) and in the convection zone, where the interaction of rotation with convection generates differential rotation—an essential link in the generation of solar magnetic fields. Sessions were also dedicated to observations, at the surface, as well as of normal modes of oscillations of the sun, which eventually will provide accurate information of the internal solar angular velocity.

Solar and Stellar Coronal Structure and Dynamics: a Festschrift in Honor of Dr. John W. Evans, Sunspot, N.M., 17-21 August, 1987. R.C. Altrock, ed.

577 p. (NSO/SP Summer Workshop no. 9) 60 participants

Summary: The festschrift was dedicated to honoring the leadership and accomplishments of John W. Evans, first director of Sacramento Peak Observatory. The primary focus was on physical processes that result in observable phenomena in coronae of the sun and stars. The meeting began with talks on stellar coronae, and continued with the solar corona, including processes such as coronal holes and loops, and theories concerning the mechanism for coronal heating. Sections were dedicated to the solar-cycle variations of the corona, to the observations of magnetic fields and their numerical modelling, and to solar mass ejections, transients and flares.

High Spatial Resolution Solar Observations: Proceedings of the Tenth Sacramento Peak Summer Workshop, Sunspot, New Mexico, 22-26 August, 1988. O. von der Lühe ed. 573 p. (NSO/SP Summer Workshop no. 10) 56 participants

Summary: This workshop studied a number of modern concepts to advance high angular resolution observation of the Sun. It was the intent of the workshop to bring together those who develop high resolution instrumentation with those who intend to use them in their experiments. The topics ranged from planned and newly commissioned solar telescopes, active and adaptive optics, interferometry, and data analysis methods, to observational results of spectroscopy with high spatial resolution, polarimetry, velocity field measurements, and coronal observations.